frontiers | Research Topics

Hydrothermal and submarine volcanic activity: impacts on ocean chemistry and plankton dynamics

Edited by
Sophie Bonnet, Ilana Berman-Frank, Douglas G. Capone, Jessica Nicole Fitzsimmons, Cecile Guieu and Joseph A. Resing

Published in
Frontiers in Marine Science
Frontiers in Microbiology

ISSN 1664-8714
ISBN 978-2-8325-7029-6
DOI 10.3389/978-2-8325-7029-6

Generative AI statement
Any alternative text (Alt text) provided alongside figures in the articles in this ebook has been generated by Frontiers with the support of artificial intelligence and reasonable efforts have been made to ensure accuracy, including review by the authors wherever possible. If you identify any issues, please contact us.

About Frontiers

Frontiers is more than just an open access publisher of scholarly articles: it is a pioneering approach to the world of academia, radically improving the way scholarly research is managed. The grand vision of Frontiers is a world where all people have an equal opportunity to seek, share and generate knowledge. Frontiers provides immediate and permanent online open access to all its publications, but this alone is not enough to realize our grand goals.

Frontiers journal series

The Frontiers journal series is a multi-tier and interdisciplinary set of open-access, online journals, promising a paradigm shift from the current review, selection and dissemination processes in academic publishing. All Frontiers journals are driven by researchers for researchers; therefore, they constitute a service to the scholarly community. At the same time, the *Frontiers journal series* operates on a revolutionary invention, the tiered publishing system, initially addressing specific communities of scholars, and gradually climbing up to broader public understanding, thus serving the interests of the lay society, too.

Dedication to quality

Each Frontiers article is a landmark of the highest quality, thanks to genuinely collaborative interactions between authors and review editors, who include some of the world's best academicians. Research must be certified by peers before entering a stream of knowledge that may eventually reach the public - and shape society; therefore, Frontiers only applies the most rigorous and unbiased reviews. Frontiers revolutionizes research publishing by freely delivering the most outstanding research, evaluated with no bias from both the academic and social point of view. By applying the most advanced information technologies, Frontiers is catapulting scholarly publishing into a new generation.

What are Frontiers Research Topics?

Frontiers Research Topics are very popular trademarks of the *Frontiers journals series*: they are collections of at least ten articles, all centered on a particular subject. With their unique mix of varied contributions from Original Research to Review Articles, Frontiers Research Topics unify the most influential researchers, the latest key findings and historical advances in a hot research area.

Find out more on how to host your own Frontiers Research Topic or contribute to one as an author by contacting the Frontiers editorial office: frontiersin.org/about/contact

Hydrothermal and submarine volcanic activity: impacts on ocean chemistry and plankton dynamics

Topic editors

Sophie Bonnet — Institut de Recherche Pour le Développement (IRD), France
Ilana Berman-Frank — University of Haifa, Israel
Douglas G. Capone — University of Southern California, United States
Jessica Nicole Fitzsimmons — Texas A and M University, United States
Cecile Guieu — UMR7093 Laboratoire d'océanographie de Villefranche (LOV), France
Joseph A. Resing — Cooperative Institute for Climate, Ocean and Ecosystem Studies University of Washington and NOAA Pacific Marine Environmental Laboratory, United States

Citation

Bonnet, S., Berman-Frank, I., Capone, D. G., Fitzsimmons, J. N., Guieu, C., Resing, J. A., eds. (2025). *Hydrothermal and submarine volcanic activity: impacts on ocean chemistry and plankton dynamics*. Lausanne: Frontiers Media SA.
doi: 10.3389/978-2-8325-7029-6

Table of contents

frontiers | Frontiers in Microbiology

TYPE Editorial
PUBLISHED 09 October 2025
DOI 10.3389/fmicb.2025.1703123

OPEN ACCESS

EDITED AND REVIEWED BY
Eva Sintes,
Spanish Institute of Oceanography (IEO), Spain

*CORRESPONDENCE
Sophie Bonnet
✉ sophie.bonnet@mio.osupytheas.fr
Cecile Guieu
✉ cecile.guieu@imev-mer.fr

RECEIVED 10 September 2025
ACCEPTED 22 September 2025
PUBLISHED 09 October 2025

CITATION
Bonnet S, Guieu C, Berman-Frank I, Capone DG, Fitzsimmons JN and Resing JA (2025) Editorial: Hydrothermal and submarine volcanic activity: impacts on ocean chemistry and plankton dynamics. *Front. Microbiol.* 16:1703123. doi: 10.3389/fmicb.2025.1703123

Editorial: Hydrothermal and submarine volcanic activity: impacts on ocean chemistry and plankton dynamics

Sophie Bonnet[1]*, Cecile Guieu[2]*, Ilana Berman-Frank[3], Douglas G. Capone[4], Jessica Nicole Fitzsimmons[5] and Joseph A. Resing[6,7]

[1]Aix Marseille University, Université de Toulon, CNRS, IRD, MIO, Marseille, France, [2]Sorbonne Université, Centre National de la Recherche Scientifique, Laboratoire d'Océanographie de Villefranche, LOV, Villefranche-sur-Mer, France, [3]Department of Marine Biology, Leon H. Charney School of Marine Sciences, University of Haifa, Haifa, Israel, [4]Department of Biological Sciences, University of Southern California, Los Angeles, CA, United States, [5]Texas A&M University, College Station, TX, United States, [6]Cooperative Institute for Climate, Ocean, and Ecosystem Studies, University of Washington, Seattle, WA, United States, [7]NOAA-Pacific Marine Environmental Laboratory, Seattle, WA, United States

KEYWORDS

hydrothermal activity, iron, plankton, trace metals, ocean

Editorial on the Research Topic
Hydrothermal and submarine volcanic activity: impacts on ocean chemistry and plankton dynamics

Iron (Fe) is a key limiting factor for primary productivity across vast regions of the global ocean (Tagliabue et al., 2017; Browning and Moore, 2023). Traditionally, atmospheric dust deposition and continental margin fluxes have been considered the dominant sources of Fe to surface waters (Moore et al., 2004). However, deep-sea hydrothermal systems also release substantial amounts of dissolved Fe (dFe) into the overlying water column via hydrothermal plumes. These plumes can be transported over long distances across ocean basins, thereby influencing large-scale ocean chemistry (Nishioka et al., 2013; Saito et al., 2013; Fitzsimmons et al., 2014; Resing et al., 2015). Furthermore, global biogeochemical models estimate that hydrothermal fluxes from mid-ocean ridges contribute nearly 23% of the dFe inventory in the oceanic water column (Tagliabue et al., 2017).

Unlike deep hydrothermal systems associated with mid-ocean ridges (>2,000 m), hydrothermal activity can also occur at much shallower depths, such as in proximity to island arcs and hotspot volcanoes, thereby delivering substantial fluxes of trace metals to the upper ocean waters (ca. 500–1,000 m; Massoth et al., 2007; Hawkes et al., 2014) and in some cases directly to the euphotic zone (0–150 m; Chemine et al., 1991; Resing et al., 2009; Santana-Casiano et al., 2016; Guieu et al., 2018; Tilliette et al., 2022). However, unlike deep hydrothermal plumes, dFe concentrations in these shallow environments decrease rapidly with distance from the source due to the much stronger water mass dynamics that prevail at shallow depths (Tilliette et al., 2022). In deep hydrothermal systems, particulate dFe losses are mitigated through stabilization with organic Fe-binding ligands (Bennett et al., 2008; Toner et al., 2009). In contrast, in shallow hydrothermal systems, both the concentration

and chemical nature of these ligands are poorly characterized, thereby constraining our ability to assess Fe stabilization, residence times, and bioavailability in these environments.

This Research Topic includes, among other contributions, several studies investigating the occurrence, composition, and functional role of ligands in stabilizing Fe near the shallow hydrothermal vents of the Tonga-Kermadec arc (Western subtropical South Pacific). Mahieu et al. identified elevated conditional concentrations of Fe-binding ligands peaking near hydrothermal sites, primarily composed of intermediate-strength L2 types. Despite this, their analysis revealed that ligand concentrations were largely in excess relative to DFe, suggesting limited effectiveness in stabilizing hydrothermal Fe inputs. Consistent with this finding, Portlock et al. reported unusually high concentrations of reduced sulfur substances (phytoplankton-derived biomolecules that associate with trace metals under elevated exposure levels), thereby mitigating toxicity. Complementing these studies, Dulaquais et al. investigated the contribution of soluble humic-like substances produced during phytoplankton degradation to Fe complexation at various sites impacted differently by hydrothermal fluids. The authors showed that the humic-ligands were unsaturated likely due to their inability to access colloidal DFe, Fe(II) and FeOx species. The humic ligands only complexed 1–5.5% of the total DFe pool close to the vent, thereby solubilizing only a small fraction of the hydrothermal Fe released. Beyond Fe, hydrothermal vents release a variety of trace elements and gases. Zhao et al. investigated the impact of hydrothermal activity on the barium cycle. They showed that Ba isotopes in vent waters and sediments are lighter than those in the water column, indicating the preferential removal of lighter isotopes during fluid–seawater mixing and highlighting their value as tracers of hydrothermal influence on sediments. In a shallow Southern Ocean bay, Belyaev et al. demonstrated how hydrothermal activity alters seawater biogeochemistry by linking vent inputs with elevated concentrations of vanadium, cobalt, nickel and Fe, along with methane and carbon dioxide. In addition to the continuous hydrothermal inputs, sporadic volcanic eruptions in many of these systems also deliver material and chemical elements. Chavagnac et al. showed that strontium (Sr) and lithium (Li) isotopic signatures can distinguish between volcanic and hydrothermal sources. Volcanic activity boosts the total Sr and Li through ash dissolution, while hydrothermal inputs drive concurrent increases of both elements in the water column.

These studies suggest that, although shallow hydrothermal systems provide substantial amounts of Fe and other trace elements, limited ligand stabilization may restrict their persistence in surface waters. This, in turn, raises important questions about the residence time, bioavailability, and ecological impact of hydrothermal Fe on plankton communities.

How do these shallow hydrothermal environments (<500 m deep) impact phytoplankton dynamics? The proximity of Fe release to the euphotic layer greatly increases the likelihood of a direct and immediate biological response. Evidence from the Tonga–Kermadec arc indicates that Fe-rich fluids entering surface waters can stimulate intense diazotrophic activity, thereby fueling enhanced net community production, N_2 fixation, and ultimately increased carbon export to the deep ocean (Bonnet et al., 2023). Strikingly, the carbon sequestration efficiency observed in these natural, shallow-vent systems is higher than that of artificial, mesoscale Fe-fertilization experiments, underscoring the ecological significance of shallow hydrothermal inputs as natural "fertilization hotspots" for surface ecosystems.

This Research Topic brings together several complementary studies that explore the complex biological responses elicited by the diverse suite of chemical elements supplied through hydrothermal inputs. Tilliette et al. demonstrated experimentally that increasing fluid inputs initially exerts toxic effects on planktonic communities, but subsequently stimulates net community production, N_2 fixation, and enhanced export relative to controls. Consistent with the findings of Portlock et al., this fertilization effect is likely sustained by planktonic detoxification via thiol-based ligands that bind toxic trace metals (e.g., Cu, Cd, and Hg). Mériguet et al. provided *in situ* evidence that these shallow hydrothermal inputs structure the entire ecosystem's trophic dynamics. Using imaging and acoustic approaches, the authors demonstrated that the elevated diazotrophic biomass stimulated by hydrothermal fluids propagates through meso- and macrozooplankton communities, which in turn may enhance organic matter export via the production of fast-sinking fecal pellets. Consistent with this, Ababou et al. showed that zooplankton-derived material (fecal aggregates, carcasses, and cylindrical fecal pellets) represents more than 90% of the carbon flux exported below the euphotic zone in the vicinity of hydrothermal vents. In parallel, nitrogen isotope budgets analyzed by Forrer et al. revealed that this export is predominantly fueled by diazotrophy, which requires high Fe availability.

Together, these findings indicate that, in this system, newly fixed nitrogen is efficiently transferred up to zooplankton and repackaged into dense fecal pellets. This highlights an overlooked but highly effective pathway by which diazotroph activity indirectly sustains particulate organic carbon export, strengthening the coupling between nitrogen fixation and the efficiency of the biological carbon pump in shallow hydrothermal regions. In the much deeper environments of the Arctic Ocean, Wegener et al. reported a clear biological response within hydrothermal plumes, characterized by elevated carbon fixation rates compared to surrounding waters, suggesting enhanced chemoautotrophy fueled by hydrogen and sulfide as energy sources.

Taken together, the studies reported in this Research Topic reveal that the fate of hydrothermal Fe in shallow systems is governed by a delicate balance between its limited chemical stabilization by organic ligands and rapid biological utilization in the euphotic zone. While the weak role of binding ligands may constrain the long-term persistence of hydrothermal Fe, its immediate availability fuels primary productivity, diazotroph activity and production, trophic transfer, and greater carbon export. This coupling of trace metal chemistry and biological responses underscores the role of shallow hydrothermal systems as natural laboratories where geochemical processes and ecosystem functioning are tightly interconnected, with potentially significant implications for the oceanic carbon and nitrogen cycles.

Author contributions

SB: Conceptualization, Data curation, Formal analysis, Funding acquisition, Investigation, Methodology, Project administration, Supervision, Validation, Writing – original draft, Writing – review & editing. CG: Conceptualization, Data curation, Formal analysis, Funding acquisition, Investigation, Methodology, Project administration, Supervision, Validation, Writing – review & editing. IB-F: Writing – review & editing. DC: Writing – review & editing. JF: Writing – review & editing. JR: Writing – review & editing.

Funding

The author(s) declare that financial support was received for the research and/or publication of this article. Several article of this Research Topic are a contribution of the TONGA project (Shallow hydroThermal sOurces of trace elemeNts: potential impacts on biological productivity and the bioloGicAl carbon pump; TONGA cruise doi: 10.17600/18000884) funded by the Agence Nationale de la Recherche (grant TONGA ANR-18- CE01-0016 0014), the LEFE-CyBER program (CNRS-INSU), the A-Midex foundation, the Institut de Recherche pour le Développement (IRD). Joseph Resing was funded by NOAA Ocean Exploration and the Pacific Marine Environmental Laboratory. This publication is CICOES # 2025-1484 and PMEL # 5819.

Conflict of interest

The authors declare that the research was conducted in the absence of any commercial or financial relationships that could be construed as a potential conflict of interest.

Generative AI statement

The author(s) declare that no Gen AI was used in the creation of this manuscript.

Any alternative text (alt text) provided alongside figures in this article has been generated by Frontiers with the support of artificial intelligence and reasonable efforts have been made to ensure accuracy, including review by the authors wherever possible. If you identify any issues, please contact us.

Publisher's note

References

Bennett, S. A., Achterberg, E. P., Connelly, D. P., Statham, P. J., Fones, G. R., and German, C. R. (2008). The distribution and stabilisation of dissolved Fe in deep-sea hydrothermal plumes. *Earth Planet. Sci. Lett.* 270, 157–167. doi: 10.1016/j.epsl.2008.01.048

Bonnet, S., Guieu, C., Taillandier, V., Boulart, C., Bouruet-Aubertot, P., Gazeau, F., et al. (2023). Natural iron fertilization by shallow hydrothermal sources fuels diazotroph blooms in the ocean. *Science* 380, 812–817. doi: 10.1126/science.abq4654

Browning, T. J., and Moore, C. M. (2023). Global analysis of ocean phytoplankton nutrient limitation reveals high prevalence of co-limitation. *Nat. Commun.* 14:5014. doi: 10.1038/s41467-023-40774-0

Chemine, J.-L., Stoffers, P., Mcmurtry, G., Richnow, H., Puteanus, D., and Sedwick, P. (1991). Gas-rich submarine exhalations during the 1989 eruption of Macdonald Seamount. *Earth Planet. Sci. Lett.* 107, 318–327. doi: 10.1016/0012-821X(91)90079-W

Fitzsimmons, J. N., Boyle, E. A., and Jenkins, W. J. (2014). Distal transport of dissolved hydrothermal iron in the deep South Pacific Ocean. *Proc. Nat. Acad. Sci. U. S. A.* 111, 16654–16661. doi: 10.1073/pnas.1418778111

Guieu, C., Bonnet, S., Petrenko, A., Menkes, C., Chavagnac, V., Desboeufs, K., et al. (2018). Iron from a submarine source impacts the productive layer of the Western Tropical South Pacific (WTSP). *Sci. Rep.* 8:9075. doi: 10.1038/s41598-018-27407-z

Hawkes, J. A., Connelly, D. P., Rijkenberg, M. J. A., and Achterberg, E. P. (2014). The importance of shallow hydrothermal island arc systems in ocean biogeochemistry. *J. Geophys. Res.* 41, 942–947. doi: 10.1002/2013GL058817

Massoth, G., Baker, E., Worthington, T., Lupton, J., De Ronde, C., Arculus, R., et al. (2007). Multiple hydrothermal sources along the south Tonga arc and Valu Fa Ridge. *Geochem. Geophys. Geosyst,* 8, 1–26. doi: 10.1029/2007GC001675

Moore, J. K., Doney, S. C., and Lindsay, K. (2004). Upper ocean ecosystem dynamics and iron cycling in a global three-dimensional model. *Glob. Biogeochem. Cycles* 18, 1–21. doi: 10.1029/2004GB002220

Nishioka, J., Obata, H., and Tsumune, D. (2013). Evidence of an extensive spread of hydrothermal dissolved iron in the Indian Ocean. *Earth Planet. Sci. Lett.* 361, 26–33. doi: 10.1016/j.epsl.2012.11.040

Resing, J. A., Baker, E. T., Lupton, J. E., Walker, S. L., Butterfield, D. A., Massoth, G. J., et al. (2009). Chemistry of hydrothermal plumes above submarine volcanoes of the Mariana Arc. *Geochem. Geophys. Geosyst.* 10, 1–23. doi: 10.1029/2008GC002141

Resing, J. A., Sedwick, P. N., German, C. R., Jenkins, W. J., Moffett, J. W., Sohst, B. M., et al. (2015). Basin-scale transport of hydrothermal dissolved metals across the South Pacific Ocean. *Nature* 523, 200–203. doi: 10.1038/nature 14577

Saito, M. A., Noble, A. E., Tagliabue, A., Goepfert, T. J., Lamborg, C. H., and Jenkins, W. J. (2013). Slow-spreading submarine ridges in the South Atlantic as a significant oceanic iron source. *Nat. Geosci.* 6, 775–779. doi: 10.1038/ ngeo1893

Santana-Casiano, J. M., Fraile-Nuez, E., González-Dávila, M., Baker, E., Resing, J., and Walker, S. (2016). Significant discharge of CO2 from hydrothermalism associated with the submarine volcano of El Hierro Island. *Sci. Rep.* 6:25686. doi: 10.1038/srep25686

Tagliabue, A., Bowie, A. R., Boyd, P. W., Buck, K. N., Johnson, K. S., and Saito, M. A. (2017). The integral role of iron in ocean biogeochemistry. *Nature* 543, 51–59. doi: 10.1038/nature21058

Tilliette, C., Taillandier, V., Bouruet-Aubertot, P., Grima, N., Maes, C., Montanes, M., et al. (2022). Dissolved iron patterns impacted by shallow hydrothermal sources along a transect through the Tonga-Kermadec Arc. *Glob. Biogeochem. Cycles* 36:e2022GB007363. doi: 10.1029/2022GB007363

Toner, B. M., Fakra, S. C., Manganini, S. J., Santelli, C. M., Marcus, M. A., Moffett, J. W., et al. (2009). Preservation of iron (II) by carbon-rich matrices in a hydrothermal plume. *Nat. Geosci.* 2, 197–201. doi: 10.1038/ngeo433

frontiers | Frontiers in Marine Science

TYPE Original Research
PUBLISHED 12 May 2023
DOI 10.3389/fmars.2023.1082077

OPEN ACCESS

EDITED BY
Ilana Berman-Frank,
University of Haifa, Israel

REVIEWED BY
Ruifeng Zhang,
Shanghai Jiao Tong University, China
Zhibing Jiang,
Ministry of Natural Resources, China

*CORRESPONDENCE
Chloé Tilliette
chloe.tilliette@imev-mer.fr
Frédéric Gazeau
frederic.gazeau@imev-mer.fr
Cécile Guieu
cecile.guieu@imev-mer.fr

RECEIVED 27 October 2022
ACCEPTED 22 March 2023
PUBLISHED 12 May 2023

CITATION
Tilliette C, Gazeau F, Portlock G, Benavides M, Bonnet S, Guigue C, Leblond N, Lory C, Marie D, Montanes M, Pulido-Villena E, Sarthou G, Tedetti M, Vorrath M-E, Whitby H and Guieu C (2023) Influence of shallow hydrothermal fluid release on the functioning of phytoplankton communities. *Front. Mar. Sci.* 10:1082077. doi: 10.3389/fmars.2023.1082077

Influence of shallow hydrothermal fluid release on the functioning of phytoplankton communities

Chloé Tilliette[1*], Frédéric Gazeau[1*], Gemma Portlock[2], Mar Benavides[3], Sophie Bonnet[3], Catherine Guigue[3], Nathalie Leblond[1], Caroline Lory[3], Dominique Marie[4], Maryline Montanes[1], Elvira Pulido-Villena[3], Géraldine Sarthou[5], Marc Tedetti[3], Maria-Elena Vorrath[6], Hannah Whitby[2] and Cécile Guieu[1*]

[1]Sorbonne Université, CNRS, Laboratoire d'Océanographie de Villefranche, LOV, Villefranche-sur-Mer, France, [2]Department of Earth, Ocean and Ecological Sciences, School of Environmental Sciences, University of Liverpool, Liverpool, United Kingdom, [3]Aix Marseille Univ., Université de Toulon, CNRS, IRD, MIO, Marseille, France, [4]CNRS, Sorbonne Université, UMR7144, Team ECOMAP, Station Biologique de Roscoff, Roscoff, France, [5]University of Brest, CNRS, IRD, Ifremer, LEMAR, Plouzané, France, [6]Intitut für Geologie, University Hamburg, Hamburg, Germany

In the Western Tropical South Pacific (WTSP) Ocean, a hotspot of dinitrogen fixation has been identified. The survival of diazotrophs depends, among others, on the availability of dissolved iron (DFe) largely originating, as recently revealed, from shallow hydrothermal sources located along the Tonga-Kermadec arc that fertilize the Lau Basin with this element. On the opposite, these fluids, released directly close to the photic layer, can introduce numerous trace metals at concentrations that can be toxic to surface communities. Here, we performed an innovative 9-day experiment in 300 L reactors onboard the TONGA expedition, to examine the effects of hydrothermal fluids on natural plankton communities in the WTSP Ocean. Different volumes of fluids were mixed with non-hydrothermally influenced surface waters (mixing ratio from 0 to 14.5%) and the response of the communities was studied by monitoring numerous stocks and fluxes (phytoplankton biomass, community composition, net community production, N_2 fixation, thiol production, organic carbon and metal concentrations in exported material). Despite an initial toxic effect of hydrothermal fluids on phytoplankton communities, these inputs led to higher net community production and N_2 fixation rates, as well as elevated export of organic matter relative to control. This fertilizing effect was achieved through detoxification of the environment, rich in potentially toxic elements (e.g., Cu, Cd, Hg), likely by resistant *Synechococcus* ecotypes able to produce strong binding ligands, especially thiols (thioacetamide-like and glutathione-like compounds). The striking increase of thiols quickly after fluid addition likely detoxified the environment, rendering it more favorable for phytoplankton growth. Indeed, phytoplankton groups stressed by the addition of fluids were then able to recover important growth rates, probably favored by the supply of numerous fertilizing trace metals (notably Fe) from hydrothermal fluids and new nitrogen provided by N_2 fixation. These experimental results are in good agreement with *in-situ*

observations, proving the causal link between the supply of hydrothermal fluids emitted at shallow depth into the surface layer and the intense biological productivity largely supported by diazotrophs in the WTSP Ocean. This study highlights the importance of considering shallow hydrothermal systems for a better understanding of the biological carbon pump.

KEYWORDS

hydrothermal fluids, phytoplankton communities, trace metal, fertilizing effect, toxic effect, Western Tropical South Pacific, community functioning, thiol compounds

1 Introduction

The Western Tropical South Pacific (WTSP) Ocean (18-22°S, 160°E-160°W) has recently been recognized as a hotspot of dinitrogen (N_2) fixation, harboring some of the highest rates reported to date in the global ocean (Bonnet et al., 2017). Diazotrophs (i.e., N_2-fixing organisms) have high cellular iron (Fe) quotas relative to other plankton functional groups, as Fe is an essential component of the nitrogenase enzyme catalyzing N_2 fixation (Rueter et al., 1992; Berman-Frank et al., 2001). Hence, their biogeographical distribution has been closely related to ambient Fe concentrations, especially in the subtropical Atlantic Ocean and the WTSP Ocean (Schlosser et al., 2014; Lory et al., 2022). In the WTSP Ocean, diazotroph blooms have also been attributed to elevated, non-limiting concentrations of Fe, along with optimal conditions of temperature and phosphorus availability (Moutin et al., 2005; Moutin et al., 2008). Prior to the OUTPACE (Moutin and Bonnet, 2015) and TONGA (Guieu and Bonnet, 2019) cruises performed in the WTSP Ocean, our knowledge of the origin and distribution of Fe in the region was poor, as the Pacific Ocean is severely undersampled, especially for trace metals (Schlitzer et al., 2018). Accurate quantification of dissolved Fe (DFe) distribution along a 6000-km transect during the TONGA cruise has demonstrated that shallow hydrothermal sources (200-300 m) located along the Tonga-Kermadec arc accounted for these elevated DFe concentrations measured in the Lau Basin and Melanesian waters (Tilliette et al., 2022) and trigger the high N_2 fixation rates measured in the region (Bonnet et al., in rev.).

The Tonga-Kermadec subduction zone belongs to the Pacific Ring of Fire hosting nearly three-quarters of the world's active volcanoes (Rinard Hinga, 2015). It is the most linear, convergent and seismically active of the Earth's subduction boundaries (Timm et al., 2013) and consequently carries intense volcanic and hydrothermal activities (2.6 active vents/100 km; Pelletier et al., 1998; Massoth et al., 2007). Submarine hydrothermal activity occurs when water percolates through the fractured oceanic crust. As it penetrates downward, the water is heated (> 400°C) and undergoes chemical changes by reacting with nearby rocks. At this temperature, the fluid becomes buoyant and rises rapidly in the water column (German et al., 2016). Numerous chemical species can be introduced into the water column by hydrothermal plumes at concentrations much higher than those usually found in the water column (Dick et al., 2013; Lilley et al., 2013; González-Vega et al., 2020). These include gases (e.g., carbon dioxide: CO_2, hydrogen sulfide: H_2S, dihydrogen: H_2, helium: He) and macronutrients (e.g., nitrate: NO_3^- , silicate: Si(OH)4, phosphate: PO_4^{3-}). They also contain dissolved and particulate trace metals, some being essential although toxic at high concentrations (e.g., copper: Cu, zinc: Zn) and others non-essential and even harmful (e.g., cadmium: Cd, mercury: Hg, lead: Pb) for many organisms including phytoplankton (Thomas et al., 1980; DalCorso, 2012; Mehana, 2014; Azeh Engwa et al., 2019). Contrary to mid-ocean ridges where hydrothermal vents are located deep (3000-4000 m), in some regions such as the WTSP or the Aegean Sea, hydrothermal vents can be shallow (< 300 m) and inject such elements directly into the surface layer (Massoth et al., 2007; Zhang et al., 2020). Thus, besides fertilization by trace metals such as Fe (Ardyna et al., 2019; Schine et al., 2021), toxic effects may also occur for plankton communities due to the proximity of the vent, where fluids can be highly concentrated in these elements (Lilley et al., 2013). In addition, plumes from shallow hydrothermal sources supply fresher and more labile material (Hawkes et al., 2014) compared to inputs reaching surface waters from deep systems (Tagliabue et al., 2010) and thus may be more bioavailable to surface phytoplankton. These fluids could therefore affect (positively or adversely) the functioning of the planktonic ecosystem and the biological carbon pump.

Numerous studies have reported on the effects of trace metal additions, alone or in combination, in mono-specific cultures or on natural phytoplankton assemblages. They all revealed that plankton communities release binding ligands into the environment to face metal stress (e.g., Lage et al., 1996; Leal et al., 1999; Morel and Price, 2003; Dupont and Ahner, 2005; Horvatić and Peršić, 2007; Hoffmann et al., 2012; Wu and Wang, 2012; Permana and Akbarsyah, 2021). In particular, thiols, which are low molecular weight peptides comprising a sulfhydryl group (–SH; Buckberry and Teesdale-Spittle, 1996; Morrison et al., 2010), are an important component of the ligand pool and have been shown to be responsible for the near-complete complexation of several trace metals in surface waters, rendering them non-bioavailable (Satoh et al., 1999; Tang et al., 2000; Dupont et al., 2006). Such compounds may have a key role in detoxifying an environment rich in harmful elements (Grill et al., 1989; Ahner and Morel, 1995; Zenk, 1996). Yet to date, no study has explored the effect of natural metal-rich

shallow hydrothermal inputs on plankton communities. In the present study, we conducted an innovative experiment to investigate the effects of hydrothermal fluids from shallow sources located along the Tonga-Kermadec arc on natural plankton communities of the WTSP Ocean. During the TONGA cruise, different volumes of hydrothermal fluids collected from an identified active vent along the Tonga arc were added to surface waters collected in a remote area unaffected by hydrothermal fluids. This nine-day experiment allowed for the examination of the community functioning as a whole and for the investigation of the effects of hydrothermal fluids on numerous biological and biogeochemical stocks and fluxes (e.g., biomass, community composition, thiols and fluorescent dissolved organic matter (FDOM) concentrations, biological productivity, N_2 fixation, export of material) in a system mimicking the natural physico-chemical conditions prevailing in the region.

2 Materials and methods

2.1 Hydrothermal fluid enrichment experiment

2.1.1 Experimental design

The experiment was conducted as part of the TONGA cruise (GEOTRACES GPpr14, November 2019, R/V *L'Atalante*; Guieu and Bonnet, 2019) in 300 L high-density polyethylene (HDPE) and trace metal free experimental tanks (referred hereafter as minicosms; Figure 1A). Each minicosm was equipped with a lid supporting six rows of LEDs (Alpheus©) composed of blue, green, cyan and white units mimicking the natural light spectrum. A 250 mL HDPE bottle was screwed onto a polyvinyl chloride valve that remained open throughout the experiment to collect exported material at the conical base of each minicosm. Photosynthetically active radiation (PAR; 400-700 nm) and temperature were continuously monitored in each minicosm using a QSL-2100 irradiance sensor (Biospherical Instruments Inc©) and a HOBO TidbiT® v2 temperature data logger (Onset), respectively.

The experimental system was composed of nine minicosms installed in a light-isolated, air-conditioned, clean-room container (99.9% filtration of particles larger than 0.2 µm by a high efficiency particulate air filter; Figure 1B). Prior to the experiment, minicosms were meticulously washed with a high-pressure cleaner (Kärcher®) and filled with a mixture of fresh water and surfactant (Decon™) for 24 h. They were then refilled with fresh water and acidified with hydrochloric acid (Suprapure HCl; Supelco®; final pH ~2). After 24 h, minicosms were emptied and rinsed with deionized water. The temperature of the container was adjusted 2°C below *in-situ* temperature level to facilitate maintaining temperature close to the targeted level (i.e., *in-situ* temperature) using a temperature-control system placed in each minicosm during the experiment (see thereafter).

The experimental protocol followed a gradient approach, with one control and seven minicosms enriched with increasing volumes of hydrothermal fluids: from 1.8 to 14.5% of the total volume added to surface waters (Table 1). These ratios were chosen based on previous DFe measurements during the OUTPACE cruise (Guieu et al., 2018), where DFe likely from hydrothermal origin reached concentrations up to 66 nM while in surface waters (< 100 m) impacted by these fluids, [DFe] reached 1-2 nM. Depending on their vertical and horizontal distance from the source, communities will be subjected to different fluid-water mixing. Closer to the source, communities will be subjected to higher enrichments (5-12 nM at 100-150 m during OUTPACE, corresponding to mixing rates of 8-18%) while those more distal from the source will be subjected to lower mixing, due to high fluid dilution, similar to those observed at the surface during OUTPACE (corresponding to mixing of 1.5-4.5%). The gradient chosen thus covers the different conditions to which communities may be subjected. The ninth minicosm, labeled M9, was used to sample both end-members (hydrothermal fluids and surface waters unaffected by hydrothermal fluids) for all parameters and processes considered prior to their mixing (see Section 2.1.2).

2.1.2 End-member sampling and mixing protocol

The nine minicosms were first filled with surface water sampled on November 10, 2019, at the western boundary of the South Pacific Gyre (21.69°S, 174.74°W), located outside the influence of volcanic activity and characterized by low chlorophyll concentrations (< 0.1 mg m^{-3}; Figure 1C). Seawater was pumped at 5 m at 10 p.m. (local time) using a high flow peristaltic pump (TecamySer®). A volume of 275 L was evenly and synchronously distributed in the nine minicosms using nine HDPE pipes. M9 was sampled the next day at 6 a.m. for the measurement of all stocks and fluxes, which are necessary to characterize the properties of the surface end-member shortly before mixing. M9 was then emptied and rinsed with deionized water.

Hydrothermal fluids were sampled upon arrival at the station, on November 11, 2019, at 9:30 a.m. (local time). Sampling was performed at 21.15°S, 174.75°W above an active shallow hydrothermal source (Figure 1C). Seawater was pumped at 200 m (i.e., the depth at which the strongest acoustic and chemical anomalies were measured; Tilliette et al., 2022) to fill the minicosm M9 using the same pumping device as for the surface end-member. After having collected the samples for the parameters and processes needed to characterize the fluid end-member, M9 was used for the mixing. In each of the eight minicosms, different volumes of surface seawater were removed and replaced by the same volumes of fluid end-member, following the gradient approach described in Table 1. The entire process (pumping and mixing of the two end-members) required 13 h. Concurrently, a CTD cast (conductivity, temperature and depth; SeaBird SBE 911 Plus rosette-mounted) was performed above the hydrothermal source to compare parameters measured in the minicosms to the *in-situ* data (see below).

2.1.3 Final adjustments and launch of the experiment

Immediately after mixing, 260 mg of ^{13}C-labeled sodium bicarbonate (^{13}C-$NaHCO_3$; Sigma-Aldrich®) was added to each minicosm to monitor the incorporation of dissolved inorganic

10.3389/fmars.2023.1082077

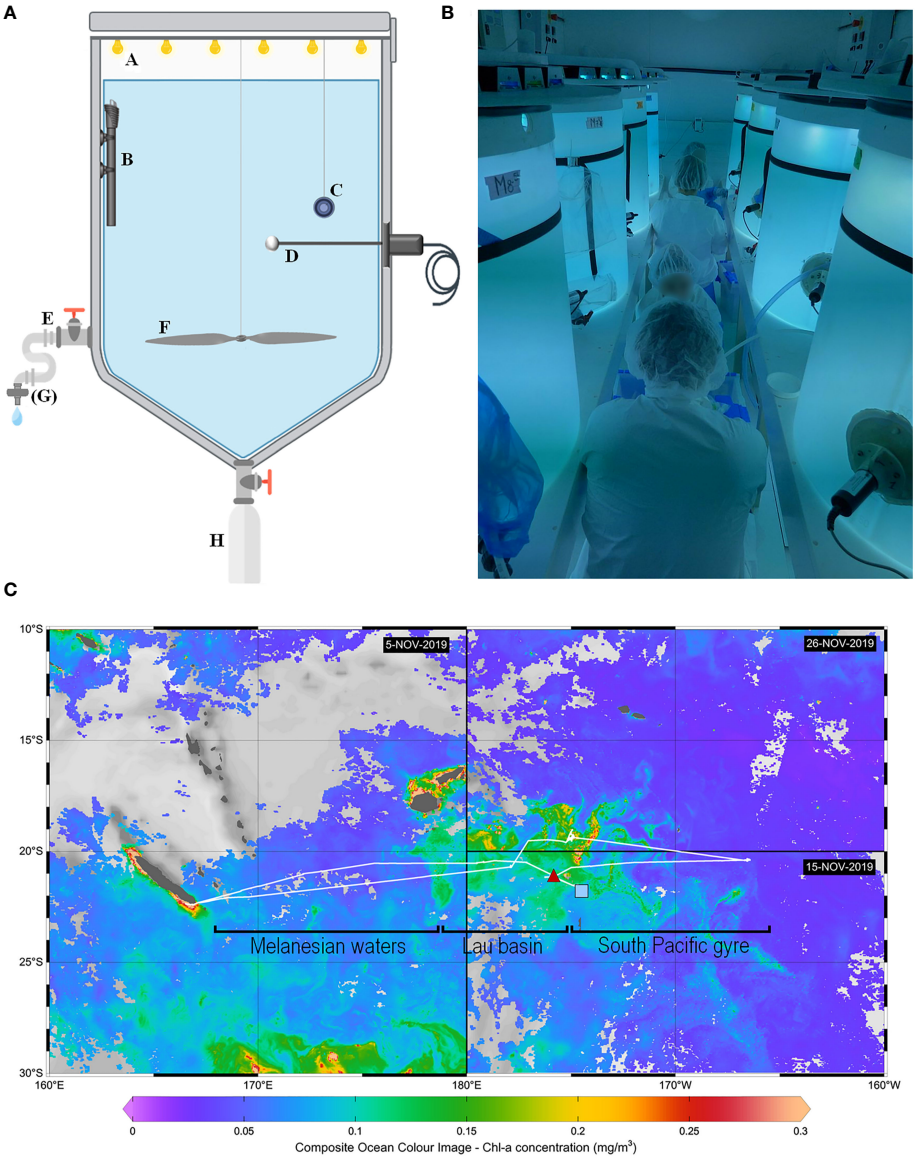

FIGURE 1
Methods used for the hydrothermal fluid enrichment experiment. **(A)** Scheme illustrating the different components of a minicosm with A LED cover, B heating resistor, C temperature data logger, D photosynthetically active radiation (PAR) sensor, E sampling tube, F motorized propeller, G filtration cartridge (used only for some parameters) and H particle trap. **(B)** Picture taken during sampling, showing eight of the nine minicosms used during the experiment and installed in the "clean-room" container. **(C)** Cruise transect superimposed on surface chlorophyll-*a* concentrations (mg m^{-3}). Chlorophyll-*a* concentrations were derived from satellite images acquired during the respective period of occupancy: 5 November 2019 for the western part of the transect, 15 November for the southeastern part, and 29 November for the northeastern part. The position of the end-members sampled for the minicosm experiment is represented by a red triangle for the fluid end-member and a blue square for the surface end-member. Note that an effort was made to sample waters relatively low in chlorophyll-*a* for the surface end-member (< 0.1 mg m^{-3}). The hooks under the transect represent the different subregions studied during the cruise: Melanesian waters and the Lau Basin at the west and the South Pacific Gyre at the east.

TABLE 1 Gradient approach considered for the mixing experiment between surface water and hydrothermal fluids.

Treatment	Control	1.8%	3.6%	5.5%	7.3%	9.1%	10.9%	14.5%
Volume of fluid (L)	0	5	10	15	20	25	30	40
Volume of surface water (L)	275	270	265	260	255	250	245	235

Treatment (in %) represents the proportion of hydrothermal fluid added to surface waters.

carbon (DIC) into particulate organic carbon (POC). An initial ^{13}C-DIC signature of ca. 500‰ was achieved. The rotating propellers fitted in each minicom (Figure 1A) were set at 9 rotations per minute, creating a slight turbulence allowing particles to remain in suspension. A 12:12 light cycle was simulated with a maximum irradiance of ~735 µmol photons m^{-2} s^{-1} reached between 9:30 a.m. and 5 p.m. (local time). The seawater temperature in each minicosm was regulated during the entire experiment to the surface *in-situ* value (25.7°C) using heating resistors (500 W; Aquamedic™) regulated by control units (Corema™).

2.1.4 Sampling

Sampling was performed on six occasions for most parameters during the nine-day experiment: 12 h (day 0.5), 24 h (day 1), 48 h (day 2), 96 h (day 4), 144 h (day 6) and 216 h (day 9) after mixing the two end-members. However, some parameters requiring low volume, such as for flow cytometry analyses, were sampled daily. The parameters studied included: photosynthetic pigment concentrations, phytoplankton abundances, net community production (NCP), N_2 fixation rates, DFe, thiols, FDOM and nutrients concentrations. All samples were collected from the sampling tube installed on each minicosm (Figure 1A) under the cleanest possible conditions by gravity and without filtration, except for thiol and macronutrient samples filtered on sterile Sartobran® 300 cartridges (0.45 µm pre-filtration and 0.2 µm final filtration) connected to the sampling tubes of each tank. Macro-nutrients were analyzed (see Text S1) and are described in detail in Bonnet et al. (in rev.). The sampling protocol is illustrated in Table S1. The duration of the experiment was imposed by the tight schedule of the cruise and the need to sample less than 50% of the initial volume by the end of the experiment to minimize the associated bias.

2.2 Analytical methods

2.2.1 Dissolved iron and particulate trace metals

DFe samples were collected in 60 mL LDPE bottles after filtration through sterile Sartobran® 300 cartridges (pre-filtration on 0.45 µm and final filtration on 0.2 µm). Right after collection, seawater samples were acidified to pH ~1.7 with 2‰ (v/v) hydrochloric acid (HCl, Ultrapure® Merck) under a class 100 laminar flow hood, double-bagged, and stored at ambient temperature in the dark before shore-based analysis. DFe concentrations were determined by flow injection and chemiluminescence detection as described in Tilliette et al. (2022).

Trace-metal clean rosette casts were conducted to sample dissolved and particulate trace metals above the hydrothermal source. DFe samples were analyzed as described above (see Tilliette et al. (2022) for further details). The protocol for other dissolved and particulate trace metal measurements is presented in Text S2.

2.2.2 Biological stocks

2.2.2.1 Photosynthetic pigments

Samples of 2.7 L were filtered within 2 h of collection through 25 mm glass fiber filters (GF/F; Whatman™; 0.7 µm). After filtration, filters were transferred to cryovials, flash-frozen in liquid nitrogen and stored at -80°C pending analysis. Nine months after collection, samples were processed by the SAPIGH analytical platform at the Institut de la Mer de Villefranche (IMEV, France). Filters were extracted at -20°C in 3 mL of methanol (100%) containing vitamin E acetate (Sigma-Aldrich®). They were crushed by sonication before being clarified one hour later by vacuum filtration. The extracts were analyzed within 24 h using a complete Agilent Technologies® 1200 series high-performance liquid chromatography (HPLC) system. The contribution of the identified pigments and their taxonomic significance were determined according to Uitz et al. (2006). The biomass of haptophyceae, diatoms and dinoflagellates was thus estimated from 19'-hexanoyloxyfucoxanthin, fucoxanthin and peridinin, respectively.

2.2.2.2 Abundance of Synechococcus and Prochlorococcus cells

Samples of 7 mL were fixed with a mixture of 0.25% glutaraldehyde and 0.01% Pluronic F-68, flash-frozen in liquid nitrogen and stored at -80°C pending analysis. Samples were analyzed at the Station Biologique de Roscoff as described in Marie et al. (1999). Briefly, 1 mL of thawed sample was transferred into a cryotube and analyzed using a BD FACSCanto™ II flow cytometer equipped with 488 and 633 nm lasers. Signal was triggered on red fluorescence and samples were run for 3 minutes with a flow rate around 100 µL min^{-1}. *Synechococcus* were discriminated from *Prochlorococcus* cells through the presence of the pigment phycoerythrin.

During the cruise, rosette casts were conducted to sample for photosynthetic pigments as well as *Prochlorococcus* and *Synechococcus* abundances above the hydrothermal source. The collected samples were analyzed as described above.

2.2.3 Biological fluxes

2.2.3.1 Net community production

Samples of 2.7 L were filtered through pre-combusted (450°C, 4 h) and pre-weighed GF/F filters. Filters were then stored in petri dishes and dried at 60°C for 24 h. Shortly before analysis, each sample was acidified by adding HCl (2 N) to remove the inorganic carbon fraction. POC concentrations and carbon isotopic signature were measured by an elemental analyzer coupled to an isotope ratio mass spectrometer (EA-IRMS; Vario Pyrocube-Isoprime 100, Elementar®). DIC concentrations were determined using the R package *seacarb* developed by Lavigne and Gattuso (2010) using the pre-requisite pH and total alkalinity data measured during the experiment (see Texts S3, S4). δ^{13}C-DIC concentrations were measured as described in Maugendre et al. (2017). NCP was finally calculated using all these parameters according to the method of de Kluijver et al. (2010).

2.2.3.2 N_2 fixation rates

Rates were measured using the $^{15}N_2$ bubble technique (Montoya et al., 1996), intentionally chosen to avoid any potential trace metal or dissolved organic matter contaminations (Klawonn et al., 2015), as both have been found to control N_2 fixation or *nifH* gene expression in

this region (Moisander et al., 2014; Benavides et al., 2017). Samples collected in 2.25 L acid-washed polycarbonate bottles were amended with 2 mL of 98.9% $^{15}N_2$ (Cambridge isotopes), incubated in on-deck incubators connected to surface circulating seawater and shaded at the specified irradiances using blue screening. Incubations were stopped by filtering the entire incubation bottle onto pre-combusted (450°C, 4 h) GF/F filters. Filters were subsequently dried at 60°C for 24 h before analysis of ^{15}N:^{14}N ratio and particulate N using an EA-IRMS (Integra 2, SerCon Ltd) as described in Bonnet et al. (2018). The^{15}N:^{14}N of the N_2 pool available for N_2 fixation (Montoya et al., 1996) was measured in all incubation bottles by membrane inlet mass spectrometry to ensure accurate rate calculations as fully described in Bonnet et al. (2018).

2.2.4 Dissolved organic compounds

2.2.4.1 Thiols

Thiol samples were collected in 125 mL trace metal-clean low-density polyethylene (LDPE) bottles (Nalgene®) after filtration through sterile Sartobran® 300 cartridges. Samples were then double-bagged and stored frozen at -20°C pending analysis. Samples were defrosted at room temperature in the dark, and thiol concentrations were measured electrochemically using a Metrohm μAutolab III. The working electrode was a hanging mercury drop electrode, the reference electrode was Ag/AgCl with a glass salt bridge filled with 3 M KCl, and the counter electrode a glassy carbon rod. The voltammetric method was taken from Pernet-Coudrier et al. (2013).

Briefly, a sample aliquot of 10 mL was transferred into an acid-cleaned voltammetric quartz cell under a laminar flow hood and acidified to pH 2 using trace-metal grade HCl. The solution was spiked with 30 μL of 10 ppm molybdenum(VI) and then purged with nitrogen (99.99%) for 5 minutes. A deposition potential of 0 V was applied for 150 s with stirring followed by a 5-s rest time. Using differential pulse mode, the potential scan ranged from 0 to -0.65 V. Compound concentrations were determined by standard addition of thioacetamide (TA, Fisher Scientific) and glutathione (GSH, reduced, Sigma-Aldrich) standards. Two additions were made for each sample, with four measurements per addition. The peak height was measured using ECDSOFT (Omanović and Branica, 1998).

2.2.4.2 Fluorescent dissolved organic matter

FDOM samples were collected in pre-calcined glass bottles and immediately filtered through pre-calcined GF/F filters using a low vacuum glass filtration system. The resulting filtrates were transferred to 100 mL pre-calcined amber glass bottles with Teflon®-lined caps. The ampoules were stored in the dark at -20°C until analysis.

Within three months of collection, FDOM measurements were performed with a F-7000 spectrofluorometer (Hitachi®). Excitation-emission matrices (EEMs) were conducted over the excitation (λ_{Ex}) and emission (λ_{Em}) wavelength ranges of 200-500 nm and 280-550 nm, respectively. EEMs were blank-corrected, Raman-normalized and converted into quinine sulfate unit (QSU). EEMs were treated with parallel factor analysis (PARAFAC) executed using the DOMFluortoolbox v1.6 (Stedmon and Bro, 2008) running under MATLAB® 7.10.0 (R2010a) for the identification of the main fluorophores according to Ferretto et al. (2017) and Tedetti et al. (2016); Tedetti et al. (2020).

2.2.5 Exported material

At the end of the experiment, particle traps were removed, closed and stored at 4°C in the dark in a 4% formaldehyde solution pending analysis. Samples were processed according to the standard protocol followed by the "Cellule Pièges" (INSU-CNRS). After removal of the swimmers (zooplankton), samples were rinsed three times in MilliQ water and lyophilized. The total amount of material collected was weighed to estimate the total exported flux. Three aliquots were then weighed to estimate total carbon, POC as well as particulate trace metals exported during the experiment: Fe and Cu.

Total carbon was measured with a CHN elemental analyzer (2400 Series II CHNS/O Elemental Analyzer, Perkin Elmer®) on weighted subsamples. POC was measured similarly, after removing inorganic carbon by acidification with 2 N HCl.

Particulate Fe and Cu concentrations were measured by ICP-OES (Inductively Coupled Plasma Optical Emission Spectrometry; Perkin-Elmer® Optima-8000) on acid-digested samples. Digestions were performed in Teflon® vials by adding Suprapur grade acids to weighed subsamples in two steps: (1) 1 mL of 65% nitric acid (HNO_3) followed by a mixture of (2) 500 μL of 65% HNO_3 and 500 μL of 40% hydrofluoric acid. After each step, samples were heated at 150°C for 5 h. Several aliquots of blanks and certified reference material (GBW, NRCC) were digested and analyzed under the same conditions. Blanks (reagent alone and reagent + blank filter) were below the detection limit (DL). The percentage recovery obtained with the certified reference material indicated accurate digestion and quantitative analysis for all elements (Fe: 94 ± 4%, Cu: 97 ± 3%).

2.2.6 Statistical analyses

To estimate whether the addition of different hydrothermal fluid volumes had an effect on the measured parameters as a function of time, multiple linear regressions with interaction were performed following James et al. (2013). These regressions were modeled to follow the formula $y = ax_1 + bx_2 + c$, with y, the parameter of interest; x_1, the mixing ratio (in %); x_2, the sampling time and c, the intercept. In order to compare the growth and decline phases of the control to the kinetics observed in the fluid-enriched treatments, regressions were performed independently at the start (12 h, 24 h, 48 h) and at the end (96 h, 144 h, 216 h) of the experiment *via* the *lm* function in R software. In case of significant interaction (*p-value (p)* < 0.05), a pairwise *post-hoc* comparison test was performed to determine the percentage(s) of enrichment having an effect on the considered parameter using the *emmeans* package (Lenth et al., 2019).

3 Results

Irradiance, temperature and pH on the total scale during the experiment are shown in Figure S1. Briefly, the different L:D cycles (Light : Dark) were stable for all minicosms. The targeted experimental temperature (25.7°C) was achieved in each minicosm, although a lower temperature (25.2°C) was recorded in

10.3389/fmars.2023.1082077

the +9.1% fluid treatment. However, this value was within the range of *in-situ* surface temperatures and likely did not significantly impact the results presented. Since the pH of the fluid end-member was very low (~6.5), decreases in pH proportional to the addition of fluid were observed. These pH values gradually returned to the values observed *in-situ* in surface waters, due to CO_2 outgassing during the experiment. Dilution curves performed on pH, nutrients and DFe data are shown in Figure S2 and attest the accuracy and quality of the mixing performed.

3.1 Dissolved iron

DFe concentration ([DFe]) in the fluid end-member was 15-fold higher than in the surface end-member. [DFe] followed quite similar dynamics in all fluid-enriched treatments (Figure 2). They increased until day 1, peaking at 3.2-19.5 nmol L^{-1}, before gradually decreasing until the end of the experiment.

In the following section, the results will be discussed according to two selected periods of the experiment: period 1 (P1) from the start of the experiment to day 2 and period 2 (P2) from day 2 to the end of the experiment.

3.2 Stocks and fluxes during the experiment

3.2.1 Biological stocks

3.2.1.1 Cyanobacteria

Prochlorococcus abundance increased in all minicosms during P1, independent of fluid treatment ($p > 0.05$; Figure S3A), although the maximum abundances reached were 1.1 to 2-fold higher in the fluid-enriched treatments relative to control (Table 2), except for the +3.6 and +10.9% fluid treatments. *Prochlorococcus* populations then gradually decreased until the end of P2, independently of the treatment ($p > 0.05$; Figure S3A). In contrast, *Synechococcus* populations showed significant differences between the fluid-enriched treatments and the control ($p < 0.05$; Figure S3B). Control populations increased until day 1 only, before decreasing. Population in the +7.3% fluid treatment followed the same kinetics as in the control, although the maximum abundance was two-fold higher (Table 2). Comparatively, *Synechococcus* grew in all other fluid-enriched treatments until day 2, reaching up to 8-fold higher maximum abundance as compared to the control. *Synechococcus* populations decreased in most minicosms during P2, even reaching a near-zero abundance in some treatments ($p > 0.05$; Figure S3B). Modest increases in abundance were observed for three of the seven fluid-enriched treatments between days 6 and 8. Only the +1.8% fluid treatment reached its maximum abundance in P2 (x3.7 relative to the control; Table 2).

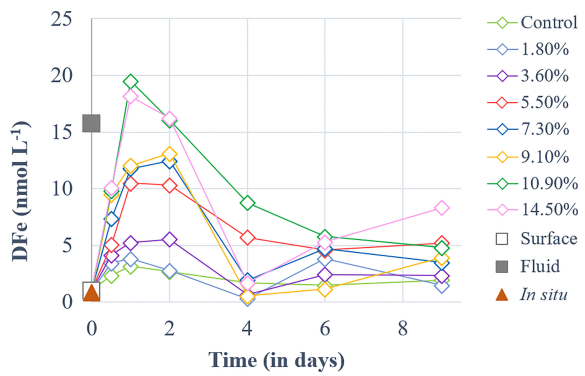

FIGURE 2
Temporal dynamics of dissolved iron (DFe) concentrations for a gradient of fluid addition (in % of total minicosm volume). DFe concentrations measured in the surface and fluid end-members are represented by an empty and a solid gray square, respectively. The red triangle represents the concentration measured *in-situ* above the sampled hydrothermal source at 5 m during the CTD casts of TONGA cruise.

3.2.1.2 Non-cyanobacterial phytoplankton

Haptophyceae biomass (B_{hapto}) in the control increased throughout P1 (Figure 3A) before decreasing during P2. In comparison ($p < 0.01$), no increase in biomass was observed in the fluid-enriched treatments during P1, as B_{hapto} decreased (reaching ~0.004 µg L^{-1}) relative to the initial biomass (0.01 µg L^{-1}). During P2, B_{hapto} continued to increase until day 4, peaking at 0.035 µg L^{-1}, before gradually decreasing (Figure 3A). Stagnant in P1, B_{hapto} in fluid-enriched treatments increased throughout P2, reaching values twice the one in the control (up to 0.1 µg L^{-1}, $p < 0.01$). Diatom biomass (B_{dia}) remained stable in the control (~0.0031 µg L^{-1}) within the first 24 h relative to the initial biomass (0.0025 µg L^{-1}). It then doubled at the end of P1 (Figure 3B) and remained stable throughout P2 (~0.0025 µg L^{-1}). B_{dia} in the fluid-enriched treatments remained stable during P1 at much lower values than those reached in the control ($p < 0.002$). It then increased from the start of P2 until day 6. B_{dia} then stabilized in most fluid-enriched treatments, except for the +5.5, +7.3 and +10.9% fluid treatments in which a significant increase was observed at the end of P2 (up to 0.043 µg L^{-1}; $p < 0.006$ relative to the control). Dinoflagellate biomass (B_{dino}) in the control increased throughout P1, peaking at 0.046 µg L^{-1} before decreasing until the end of P2 (Figure 3C). The opposite was observed in the fluid-enriched treatments, displaying a decreasing trend ($p < 0.001$) during P1 (~0.001 µg L^{-1}), which continued until day 4. It stabilized between 4 and 6 days before increasing significantly in the fluid-enriched minicosms until the end of P2 ($p < 0.05$ relative to control).

3.2.2 Biological fluxes

Cumulative NCP increased during P1 similarly in all treatments ($p > 0.08$, Figure 4A). At the start of P2, a slight shift occurred: while control NCP continued to increase, NCP in fluid-enriched treatments stabilized until day 6 (except for the +14.5% fluid treatment; Figure 4A). Control NCP stabilized after 4 days, peaking at 19.8 µmol C L^{-1}, before decreasing. In comparison, cumulative NCP in fluid-enriched treatments finally increased significantly at the end of P2, to higher levels than in the control (~30.6 µmol C L^{-1}, $p < 0.04$). A strong positive correlation was observed between the maximum cumulative NCP reached for each treatment and the percentage of fluid enrichment ($R^2 = 0.72$, $p < 0.05$; Figure 4B).

10.3389/fmars.2023.1082077

TABLE 2 Ratio of maximum relative changes in biomass of cyanobacteria populations in hydrothermal fluid-enriched treatments relative to the control.

Treatment	*Prochlorococcus*	*Synechococcus*
1.8%	1.1 (day 2)	3.7 (day 8)
3.6%	0.7 (day 2)	4.3 (day 2)
5.5%	1.4 (day 2)	4.6 (day 2)
7.3%	1.6 (day 2)	2.1 (day 1)
9.1%	1.5 (day 2)	7.5 (day 2)
10.9%	0.9 (day 2)	3.4 (day 2)
14.5%	2.0 (day 2)	4.3 (day 3)

The sampling time at which these maximum relative changes were observed is indicated in parentheses. The abundance of cyanobacteria (*Prochlorococcus* and *Synechococcus*) was measured by flow cytometry.

Cumulative N_2 fixation (Figure 4C) also increased in all minicosms during P1. It stabilized in the control at the end of P1 while it continued to increase, although less sharply, in the fluid-enriched treatments. Cumulative N_2 fixation in the control remained stable during P2, peaking at 15 nmol N L^{-1} (Figure 4C). In comparison, N_2 fixation continued to increase throughout P2 in the fluid-enriched treatments, reaching values 2.5-fold higher than the control. No significant correlation was found between the maximum cumulative N_2 fixation reached for each treatment and the percentage of fluid added (R^2 = 0.019, p = 0.96).

3.2.3 Dissolved organic compounds

3.2.3.1 Thiols

Two types of thiol compounds were identified during the experiment: TA and GSH compounds. TA concentrations ([TA]) remained stable in the control during both P1 and P2 (~92.8 nmol L^{-1}; Figure S4A). In contrast, [TA] increased at the start of P1 in all fluid-enriched treatments, reaching a maximum concentration 2.5- to 9.2-fold higher than in the control (p < 0.04; Table 3). However, no correlation between the percentage of fluid enrichment and [TA] increase was observed (R^2 = 0.41, p = 0.31). [TA] then decreased rapidly until the end of P2, reaching near-control levels. GSH concentrations ([GSH]) were null in all minicosms at the start of P1 (Figure S4B). They started to increase at P2, except for the +1.8% and the +9.1% fluid treatments, reaching concentrations 1.1 to 1.9-fold higher than in the control (Table 3).

3.2.3.2 Fluorescent dissolved organic matter

Three FDOM fluorophores were identified by the PARAFAC model: two protein-like fluorophores, i.e., tryptophan-like (TP; peaks T) and tyrosine-like (TY; peaks B), and one humic-like fluorophore (HS; peaks 1+C). These are the most prevalent FDOM fluorophores in the aquatic environment (Coble, 2007; Aiken, 2014). Below, fluorophore concentrations refer to their fluorescence intensities in QSU.

TP concentrations ([TP]) increased in all fluid-enriched treatments during P1 (Figure S5A), whereas [TP] remained stable in the control (p < 0.01). Only the +3.6% fluid treatment reached its maximum concentration during P1 which was lower than in the control (Table 3). [TP] slightly increased throughout P2 (Figure S5A), mainly in the fluid-enriched treatments, reaching maximum concentrations 1.3 to 3.3-fold higher than in the control (Table 3). A drastic increase of TY concentrations ([TY]) was observed in all minicosms during P1. Only [TY] in the control decreased after 24 h (Figure S5B). HS concentrations ([HS]) increased during the first 24 h in all minicosms before stabilizing until the end of P1 (Figure S5C, p > 0.05). [TY] and [HS] followed the same dynamics as [TP] during P2 (p < 0.03), reaching maximum concentrations 1.1 to 1.4 higher in the most enriched minicosms as compared to the control.

3.3 Trace metal and POC concentrations in exported material collected in particle traps throughout the experiment

The exported material from the control, +3.6% and +10.9% fluid treatments showed similar Fe concentrations ([Fe]; ~3.67 mg g^{-1}; Figure 5A). [Fe] from other fluid-enriched treatments doubled relative to the control. The highest [Fe] (x4 relative to the control)

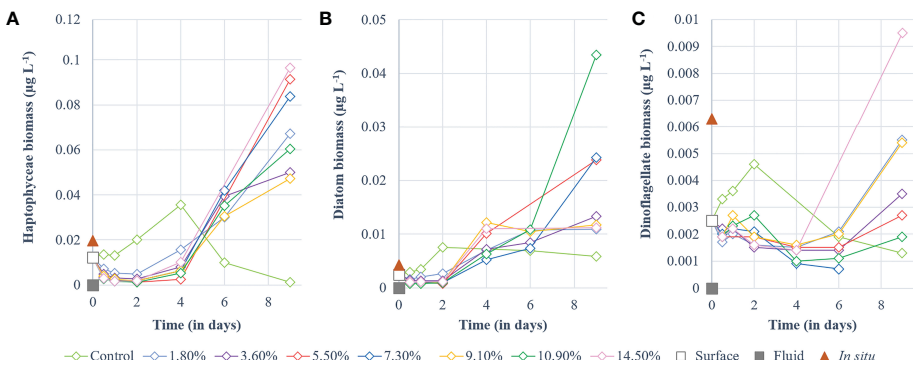

FIGURE 3
Temporal dynamics of non-cyanobacterial phytoplankton biomass (µg L^{-1}) for a gradient of fluid addition (in % of total minicosm volume). **(A)** haptophyceae (i.e., 19'-hexanoyloxyfucoxanthin), **(B)** diatoms (i.e., fucoxanthin) and **(C)** dinoflagellates (i.e., peridinin). Values measured for each pigment in the surface and fluid end-members are represented by an empty and a solid gray square, respectively. The red triangle represents the value measured *in-situ* above the sampled hydrothermal source at 5 m during the CTD casts of TONGA cruise.

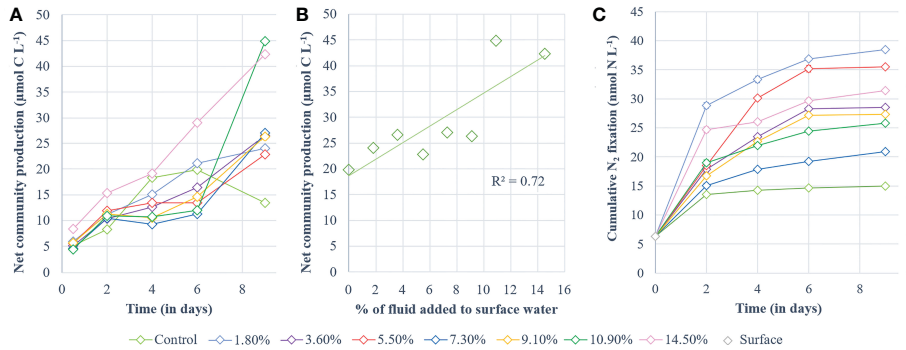

FIGURE 4
Processes studied during the experiment. **(A)** cumulative ^{13}C-net community production and **(B)** highest values of cumulative ^{13}C-net community production obtained for each minicosm (i.e., day 6 for the control and day 9 for the fluid-enriched treatments) correlated with the percentage of hydrothermal fluid added. Net community production is shown in µmol C L^{-1} and was determined according to the ^{13}C-labeling method described by de Kluijver et al. (2010). **(C)** Cumulative dinitrogen fixation (nmol N L^{-1}).

was observed in the most fluid-enriched treatment. Nevertheless, no significant correlation was found between the exported [Fe] and the percentage of fluid added (R^2 = 0.24, p = 0.57). High concentration of Cu ([Cu]) were exported in the most fluid-enriched treatments relative to the control (x2.4; Figure 5B). However, low [Cu] was exported in the +5.5% and +9.1% fluid treatments relative to the large volume of fluid added. Nevertheless, a positive relationship between the [Cu] exported and the percentage of fluid added was observed (R^2 = 0.6, p = 0.03). POC concentrations ([POC]) exported in the fluid-enriched treatments were higher than the control (x1.4), except for the +3.6% fluid treatment that exported lower [POC] (Figure 5C). The highest [POC] (x2 relative to the control) were exported in the least fluid-enriched treatment. No correlation between the [POC] and the percentage of fluid added was found (R^2 = 0.27, p = 0.52).

4 Discussion

Our primary concern was whether the dynamics observed for the major phytoplankton groups and thiols were a consequence of the biological response to the addition of hydrothermal fluids or a dilution effect following the mixing of the two end-members. Theoretical dilution lines were thus calculated for each treatment and compared to the measured values of the parameters at 12 h (Figure S6). For the cyanobacteria biomass, the measured values were always higher (~0.08 µg L^{-1}) compared to theoretical values (~0.05 µg L^{-1}), indicating that cyanobacteria developed rapidly after mixing. In comparison, measured values of B_{hapto} (~0.004 µg L^{-1}) and B_{diato} (~0.001 µg L^{-1}) were lower than theoretical values (~0.01 µg L^{-1} and ~0.003 µg L^{-1}, respectively) in the fluid-enriched treatments, showing a decline of both after mixing. The opposite was observed in the control (i.e., higher measured than theoretical values). Regarding thiols, while measured and theoretical [TA] of the control matched perfectly, [TA] measured in fluid-enriched treatments were up to 8 times higher than theoretical [TA]. This evidence shows that the dynamics observed during the first 12 h after mixing were rather a biological response to hydrothermal fluid enrichment than a simple dilution effect.

4.1 Primary effect of fluids

In the control minicosm, a small increase of biomass associated with picocyanobacteria, haptophyceae, diatoms and dinoflagellates was observed during P1. This increase lasted for only two days,

TABLE 3 Ratio of maximum relative changes in the concentrations of thiol compounds and fluorescent dissolved organic matter (FDOM) fluorophores in hydrothermal fluid-enriched treatments relative to control.

Treatment	Thiols		FDOM fluorophores		
	TA-like	GSH-like	Tryptophan-like	Tyrosine-like	Humic-like
1.8%	3.7 (day 0.5)	0.68 (day 9)	1.3 (day 9)	1.3 (day 9)	1.1 (day 9)
3.6%	3.8 (day 0.5)	1.7 (day 4)	0.8 (day 2)	1.2 (day 6)	1.2 (day 9)
5.5%	2.9 (day 0.5)	1.9 (day 4)	1.6 (day 9)	1 (day 6)	1.4 (day 9)
7.3%	2.5 (day 0.5)	1.2 (day 4)	2.3 (day 9)	1.2 (day 9)	1.4 (day 9)
9.1%	2.5 (day 0.5)	1 (day 9)	1.7 (day 9)	1.2 (day 4)	1 (day 9)
10.9%	2.6 (day 0.5)	1.3 (day 9)	3.3 (day 9)	1.2 (day 4)	1.2 (day 9)
14.5%	9.2 (day 0.5)	1.1 (day 9)	1.5 (day 6)	0.9 (day 9)	1.2 (day 9)

The sampling time at which these maximum relative changes were observed is indicated in parentheses. TA refers to thioacetamide-like thiol compounds while GSH refers to glutathione-like thiol compounds. FDOM is composed of two protein-like (tryptophan- and tyrosine-like) and one humic-like fluorophores. Concentrations of the three fluorophores refer to their fluorescence intensities in QSU.

10.3389/fmars.2023.1082077

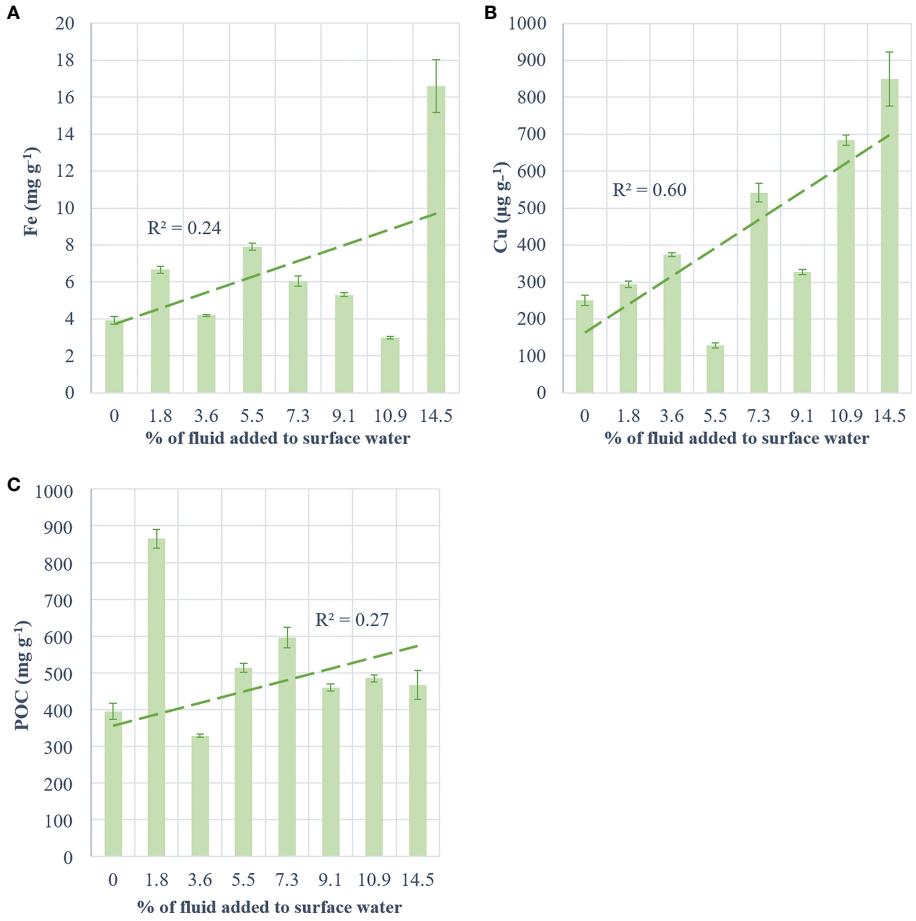

FIGURE 5
Concentration of metals and carbon per g of collected matter in traps at the end of the experiment for **(A)** iron (mg g^{-1}), **(B)** copper (µg g^{-1}) and **(C)** particulate organic carbon (mg g^{-1}) as a function of treatment (+0 to +14.5% hydrothermal fluid added). The green dotted line represents the regression line and its coefficient (R^2).

probably due to nutrient limitation, especially in nitrate (< 0.1 µmol L^{-1}, Figure S7; Bonnet et al., in rev.). The biomass associated with those groups then decreased rapidly until the end of the experiment. Nevertheless, this brief development at the start of the experiment resulted in fairly significant cumulative NCP and POC export into the traps. In contrast, N_2 fixation rates remained stable during this period in the control, and throughout the experiment.

Large differences were observed between the control and fluid-enriched treatments regarding community composition, plankton abundance and biological fluxes. Indeed, at the start of P1, only picocyanobacteria (mainly *Synechococcus)* developed after the mixing and at much higher abundances than in the control. Yet, the fluids provided a small amount of macronutrients that could have supported the growth of phytoplankton (+0.04-0.28 and +0.003-0.023 µmol L^{-1} of $NO_3^-$and PO_4^{3-} added by fluids, respectively, relative to the control; Bonnet et al., in rev.). Furthermore, active diazotrophs also likely provided new N sources to the system. Compared to the control, the large non-cyanobacterial species did not develop during P1 and dinoflagellate mortality (i.e., decreased abundance) was even observed. One possible hypothesis is that the observed patterns were the result of an initial toxicity of some elements supplied by the fluids. Such an effect would have decreased after 4 days of experiment, as species whose growth was stagnant finally started to grow. This implies that the studied waters had likely been detoxified, consistent with the dynamics of thiols at P1, as these compounds have been reported to selectively complex certain toxic trace metals (Grill et al., 1989; Ahner and Morel, 1995; Zenk, 1996). This mechanism will be explored in the following section.

4.2 Detoxification of the environment and candidate toxic elements

Environmental detoxification may occur through the excretion of metal-binding ligands by communities (e.g., Leal et al., 1999; Morel and Price, 2003; Dupont and Ahner, 2005; Hoffmann et al., 2012). Two types of organic ligands capable of detoxifying the environment were measured during the experiment: FDOM, protein- and humic-like fluorophores, and thiols, a pool of non-fluorescent matter (Chen et al., 2013). In this section, an in-depth exploration of thiol implication in environmental detoxification will be conducted. FDOM fluorophores will be discussed in accordance with their role as strong Cu ligands (Wong et al., 2019).

Thiol production by phytoplankton is triggered by the presence of various trace metals such as Cd, Cu, Hg, Pb and Zn (Grill et al., 1989; Ahner and Morel, 1995; Zenk, 1996). These metals, essential (Cu, Zn) or not (Cd, Hg, Pb), can cause numerous deleterious effects on communities at various concentrations (e.g., Sunda and Huntsman, 1998; Echeveste et al., 2012; Le Faucheur et al., 2014). During our experiment, communities immediately responded to fluid addition through striking thiol production (i.e., up to +823% [TA] relative to control produced during the 12 h after the mixing). Two types of thiol compounds were detected: TA and GSH. TA is actively exuded by phytoplankton (Leal et al., 1999) and precipitates trace metals, rendering them non-bioavailable to communities (Gharabaghi et al., 2012). GSH is the most common thiol ligand in surface waters (Le Gall and Van Den Berg, 1998; Leal et al., 1999; Tang et al., 2000) and is a precursor of phytochelatins (PC; Grill et al., 1989), a polypeptide that forms complexes with trace metals ultimately transported and degraded in the vacuole and/or chloroplasts (Cobbett, 2000; Worms et al., 2006). Thus, the decrease in [GSH] to near-zero levels reflects a high PC production (Romano et al., 2017). Previous studies reported that GSH levels in the presence of high metal concentrations could reach undetectable levels within a few hours (2-4 h; Scheller et al., 1987; Coppellotti, 1989; De Vos et al., 1992; Rijstenbil et al., 1994; Satoh et al., 1999), in agreement with the levels observed in minicosms 12 h after the mixing (< DL). After the probable environmental detoxification, [GSH] accumulated in minicosms. This result was expected as GSH also plays a homeostasis and environmental sensing role in phytoplankton (May et al., 1998; Noctor et al., 1998). Thus, these two thiol compounds had a key role in mitigating the deleterious effects of toxic trace metals added to the environment by fluids (Figure 6). The possible trace metals released by hydrothermal fluids will be explored in this section in accordance with their ability to trigger thiol production (i.e., Cd ≥ Cu > Pb > Hg; Grill et al., 1989; Ahner and Morel, 1995).

4.2.1 Cadmium

Cd has been reported as the most effective trigger of thiol production in most phytoplankton species (Ahner and Morel, 1995; Dupont and Ahner, 2005; Romano et al., 2017; Permana and Akbarsyah, 2021). Consistently, elevated concentrations of particulate Cd were measured in the fluid end-member relative to the surface end-member (x11.5; Table S2) suggesting that fluid addition supplied high Cd levels. This raises the possibility that Cd played a role in the preliminary toxicity induced by shallow hydrothermal fluid addition.

4.2.2 Copper

Cu has been reported to trigger significant phytoplankton production of thiols, both TA and GSH, their presence allowing for rapid and efficient detoxification of the environment (De Vos et al., 1992; Leal et al., 1999; Brown and Gordon, 2001; Dupont and Ahner, 2005). Although total dissolved Cu (DCu) concentrations were similar in fluid and surface end-members (~250 pmol L^{-1}), DCu toxicity depends solely on the concentration of the free Cu^{2+} form (not measured during TONGA), the only toxic form of DCu and also the most bioavailable (Brand et al., 1986; Ahner et al., 1994; Sunda, 1994; Ahner et al., 1998). Interestingly, shallow hydrothermal sources have been reported to release high concentrations of labile material, including Cu^{2+} (Valsami-Jones et al., 2005; Hawkes et al., 2014), suggesting that a significant portion of the DCu measured in the fluid end-member may be in the ionic form. Thus, the low concentration of DCu present in the fluid could still be extremely toxic to communities, as Cu^{2+} concentrations as low as 2.3 pmol L^{-1} have been reported to be toxic to some species (Leal et al., 1999; Mann et al., 2002). In contrast, an 82-fold enrichment of particulate Cu (pCu) in the fluid end-member relative to the surface end-member was measured (Table S2). A relationship between the percentage of fluid addition and the concentration of exported pCu (Figure 5) was also found. This pCu was probably a mixture between fluid-added hydrothermal particles and Cu-TA compounds (i.e., complexed thiols). However, based on pCu concentrations added by fluid and surface end-members (see Text S5 for further details), it can be stated that not all of the added pCu was recovered in the material exported in fluid-enriched treatments (~28-72% recovered depending on the fluid addition), in contrast to the control (101% pCu recovered). This could be explained by a possible redissolution of hydrothermal particles at the start of the experiment (favored by the low pH; Figure S1; Ain Zainuddin et al., 2019) or by the presence/formation of fine particles that may be slow to settle. This is likely as most hydrothermal particles have been reported to have a small diameter (< 2 µm; Walker and Baker, 1988) and Lou et al. (2020) demonstrated that particles smaller than 20 µm were

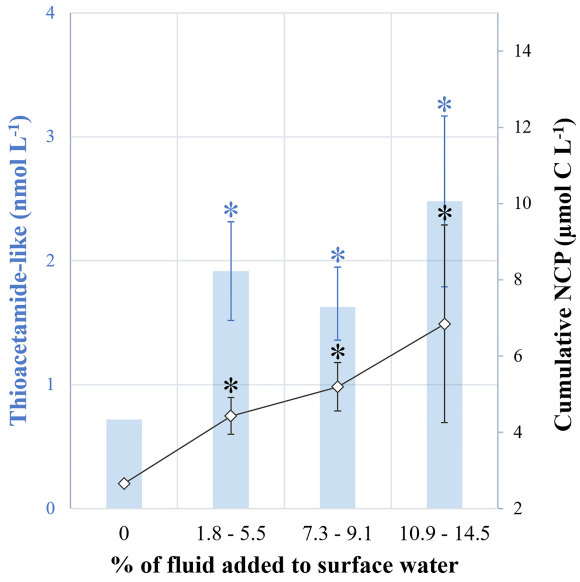

FIGURE 6
Summary diagram. (1) in blue, the ratio of thioacetamide-like compound concentrations measured 12 h after the mixing versus at the end of the experiment (D0.5:D9) and, (2) in black, the ratio of cumulative ^{13}C-net community production rates measured at the end versus at the start of experiment (D9:D0.5). Treatments were grouped: no addition (0, control), low (+1.8-5.5%), medium (+7.3-9.1%) and high (+10.9-14.5%) fluid addition. Asterisks represent the significance of each group relative to control (*unpaired Student test*, $p < 0.01$).

involved in the long-distance transport of the plume (and thus have a lower sedimentation rate). Furthermore, a high FDOM production was observed in the fluid-enriched treatments with significant increases in the concentrations of protein- and humic-like fluorophores during the experiment (Table 3). Besides thiols compounds, protein- and humic-like fluorophores have been clearly identified as organic ligands that present binding affinities with trace metals, particularly Cu^{2+} (Mounier et al., 2011; Chen et al., 2013). A recent study also showed a strong correlation between FDOM production, Cu^{2+} concentrations and L_1-class ligands in marine waters (Wong et al., 2019). All these observations suggest a release of protein-like FDOM by phytoplankton in response to Cu toxicity (Corbett, 2007; Wong et al., 2019). Thus, Cu may play an important role in the toxicity induced by fluid addition at the start of the experiment.

4.2.3 Lead

Pb is a known trigger for thiol production by phytoplankton, although less effective (Ahner and Morel, 1995). This element may have had a toxic effect on communities subjected to fluid enrichment at the start of the experiment, as particulate Pb was 91 times enriched in the fluid end-member relative to the surface end-member (Table S2).

4.2.4 Mercury

Hg has been reported as being one of the less effective triggers of thiol production by phytoplankton in response to toxic environments (Satoh et al., 2002; Wu and Wang, 2012). Despite such a fact, total Hg (THg) concentrations in the fluid end-member were 10 times higher than in the surface end-member (Table S2, Desgranges, pers. comm., 2022). THg was present primarily as elemental Hg (i.e., in gaseous form; Desgranges, pers. comm., 2022) that can (1) degas to the atmosphere and/or (2) be oxidized to Hg^{2+} reported to be extremely toxic to phytoplankton (Wu and Wang, 2011). Even if it is impossible to conclude which Hg form predominates in fluid-enriched treatments, high concentrations of Hg^{2+} could be toxic, or even lethal, to communities.

Other thiol-complexed trace metals, such as Zn or nickel, were not exported in significant amounts in traps relative to the control. It is therefore unlikely that these elements played a significant role in the biological dynamics observed during P1. Thus, the high production of thiols in response to the hydrothermal fluid addition is coherent and could be triggered by the presence of a cocktail of several toxic elements such as Cu, Hg, Pb and possibly Cd.

4.3 The most probable producers of thiol ligands

The question of which players produce thiols capable of detoxifying the environment is relevant. In the present experiment, picocyanobacteria could be the potential thiol producers (Moffett et al., 1990; Moffett and Brand, 1996; Croot et al., 2000). In fact, the first organisms to grow were picocyanobacteria such as *Synechococcus* and *Prochlorococcus* to a lesser extent, consistent with the striking increase of thiols that occurred 12 h after the mixing (Table 3). In line with these observations, *Prochlorococcus* has been reported to be more sensitive to trace metal addition than *Synechococcus* (Mann et al., 2002). However, *Synechococcus* has previously been reported as one of the most sensitive species to trace metal addition due to its large surface-to-volume ratio (Quigg et al., 2006). This was not observed in this experiment, as in several other studies, where *Synechococcus* was the most resistant species to trace metal addition while eukaryotic species were the most sensitive (Joux-Arab et al., 2000; Stauber and Davies, 2000; Le Jeune et al., 2006; Levy et al., 2007). Numerous studies have demonstrated the existence of *Synechococcus* ecotypes adapted to toxic trace metal concentrations, either genetically or physiologically (Huckle et al., 1993; Mann et al., 2002; Palenik et al., 2006; Stuart et al., 2009; Stuart et al., 2013). These ecotypes are primarily from environments where trace metal concentrations may be chronically high, such as coastal waters or near hydrothermal vents, and are adapted to a fast-changing environment (Mann et al., 2002; Stuart et al., 2009). They may also be related to their previous exposure to trace metals (Levy et al., 2007). Low abundance of cyanobacteria was measured in the fluid end-member (0.0035 $\mu g\ L^{-1}$). It is therefore possible that the thiol-producing *Synechococcus* adapted ecotypes found in fluid-enriched treatments originated from the environment near the shallow hydrothermal source and allowed for environmental detoxification. Molecular analyses would be necessary to confirm such a hypothesis. For all these reasons, it is very likely that *Synechococcus*, known to produce strong binding ligands, including thiols (Moffett et al., 1990; Moffett and Brand, 1996; Croot et al., 2000), was the major producer of these ligands that were needed to inhibit toxicity of ionic trace metal, allowing other species to grow. Moreover, Brand et al. (1986) demonstrated that *Synechococcus* growth rates subjected to high concentrations of Cu or Cd were inhibited in the absence of strong chelators.

Based on our experimental data, the largest non-cyanobacterial species (haptophyceae, diatoms and dinoflagellates) were probably not the major thiol producers, especially since eukaryotes have been reported to have more affinity for thiols-Cu complexes, in contrast to prokaryotes (Walsh et al., 2015) and to produce weaker ligands (Croot et al., 2000). Indeed, diatoms and haptophyceae only developed 2 and 4 days after the mixing, respectively, not coinciding with the thiol peaks measured 12 h after mixing. However, it is interesting to note that diatoms – known to be more tolerant to the addition of certain trace metals, such as Cu (Croot et al., 2000) – were the first to develop after environmental detoxification. Dinoflagellate mortality (i.e., decrease in biomass) was observed from the start of the experiment, rendering these species poor candidates for strong ligand production. This result is not surprising as dinoflagellates are known to be very sensitive to Cu, even at low concentrations, and to other trace metals (Anderson and Morel, 1978; Brand et al., 1986; Taylor, 1987; Lage et al., 2001). Encystment strategies have been developed by dinoflagellates to protect themselves from a harmful environment (Anderson and Morel, 1978; Pinto et al., 2003), allowing the persistence of plasma membrane and chlorophyll integrity (Lage et al., 2001). Recovery from trace metal exposure has been observed for numerous dinoflagellates species within 24 to 96 h after exposure (Lage et al., 1994; Okamoto et al., 1999). This excystation process may

explain the delayed growth of dinoflagellates (6 days after the mixing) relative to other species.

Abiotic factors such as pH and temperature and biotic factors such as uptake pathways and internal detoxification processes can influence trace metal tolerance. When mixing the two end-members, addition of one (or a cocktail of) trace metal(s) and H_2S-rich, low-pH and oxygen-poor fluid (Tilliette et al., 2022) temporarily altered the surface water chemistry and may have exacerbated the toxic effect of fluid addition. Nevertheless, due to the significant production of thiols by picocyanobacteria, especially by resistant *Synechococcus* ecotypes, potential toxic elements supplied by hydrothermal fluids have been modified into less harmful forms. This environmental detoxification allowed the larger species to grow and a late positive effect proportional to the fluid addition could be observed at the end of the experiment (see the following section).

4.4 Fertilizing effect of fluid addition and comparison with *in situ* data

As discussed above, the addition of hydrothermal fluids to surface waters first inhibited biological activity until the fluid chemistry was modified by the production of thiols making the mixed water less harmful or even fertilizing (Figure 6). Indeed, growth of non-cyanobacterial species was observed 4 days after the mixing, resulting in enhanced cumulative NCP rates (up to x3.3 relative to the control) at the end of the experiment. Moreover, an increasing fertilizing effect depending on the addition of hydrothermal fluid was observed, as the maximum cumulative NCP values were proportional to the percentage of fluid added (Figure 4B). This positive effect was also observed for N_2 fixation, which was up to 2.5-fold higher in fluid-enriched treatments relative to the control. Consequently, an increase of POC export was measured in the fluid-enriched treatments (x1.4 on average and up to x2.2 relative to the control). Such a positive effect on NCP and N_2 fixation is likely due to the introduction of high concentrations of fertilizing elements, such as Fe, along with rather low concentrations of macronutrients, so the system was likely still nitrate-limited. During the TONGA cruise (Guieu and Bonnet, 2019), the same stocks and fluxes studied in the minicosms were measured *in-situ* along a 6100-km transect through the Tonga volcanic arc. Cruise results show that N_2 fixation rates were the highest above hydrothermal sources and primarily supported by large (> 10 µm) species such as *Trichodesmium* (Bonnet et al., in rev.). In contrast, *in-situ* primary production was high a few kilometers from the source, but lower just above it (Bonnet, *unpublished*), likely reflecting the toxic effect of fluids evidenced during our experiment.

Fe is an essential element for phytoplankton growth and metabolism (Behrenfeld and Milligan, 2013). It is a known fertilizing element for all phytoplankton species, having a direct influence on photosynthesis (Sunda and Huntsman, 1995) and thus an important role in carbon export and sequestration in the ocean interior (Martin, 1990; Pollard et al., 2007). Fe is also often a limiting element for diazotrophs, as in addition to photosynthesis, the N_2 fixation process also requires high Fe amounts (Raven, 1988). During the experiment, hydrothermal fluids supplied high Fe concentrations, both in particulate and dissolved forms (Figure 4). Indeed, a 772- and 16-fold enrichment of particulate (Table S2) and dissolved Fe, respectively, could be observed in the fluid end-member relative to the surface end-member. These high DFe concentrations introduced by the fluid end-member ([DFe] = 15.8 nmol L^{-1}) were likely responsible for the high N_2 fixation and NCP rates measured in the fluid-enriched treatments. This was confirmed (see Text S6) by the higher Fe uptake rates of picocyanobacteria (mainly *Synechococcus* and bacteria), that consumed up to 16% of the total minicosm DFe stock over the course of the experiment, relative to non-cyanobacterial species, that consumed up to 8% of the total stock, in agreement with the uptake rates measured by Lory et al. (2022) during the TONGA cruise (~4-11 pmol Fe L^{-1} d^{-1}). Interestingly, consistent with these uptake rates, the DFe dynamics observed during the experiment were primarily driven by precipitation. This process can easily be explained by the presence of high H_2S concentrations in the fluid (Tilliette et al., 2022) and the gradual increase in pH, which was significantly decreased at the start of the experiment through the low pH fluid addition (pH of 6.5; Figure S1). Estimated precipitation rates in fluid-enriched treatments (66 ± 7%) were similar to those estimated *in-situ* above the shallow hydrothermal source (62-86%; Tilliette et al., 2022). As for Cu, only a small proportion of the particulate Fe was recovered in traps (< 10%), probably due to the small particle size that did not allow them to be exported.

The growth of the large non-cyanobacterial species occurred at days 2-4, when phosphate and nitrate concentrations were nearly depleted (Bonnet et al., in rev.; Figure S4). Nitrogen was made available to non-diazotrophic phytoplankton through N_2 fixation and the use of rather abundant DOP (~0.2 µmol L^{-1} after 4 days, *data not shown*) as an alternative P-source may have allowed their growth. Indeed, microbial utilization of DOP through alkaline phosphatase activity can be Fe-limited (Browning et al., 2017) and the alleviation of Fe stress leads to DOP loss (likely as a consequence of enhance uptake) under low phosphate availability at the global scale (Fernández-Juárez et al., 2019; Liang et al., 2022). Thus, the introduction of high concentrations of DFe by the fluid end-member mitigated the Fe limitation of surface end-member waters. This DFe fertilization by fluids is of great importance as diazotrophs can exploit these high concentrations to build biomass, as long as phosphate concentrations are sufficient or if these organisms also use DOP (Dyhrman et al., 2006; Dyhrman and Haley, 2006). The fluid addition also allowed an important enrichment in Al (x27.5 of particulate Al relative to control; Table S2). Interestingly, Al has been reported to promote Fe uptake (Shaked et al., 2005; Mujika et al., 2011; Ruipérez et al., 2012), DOP utilization and N_2 fixation (Liu et al., 2018) and may explain, in addition to DFe availability, the fertilizing effects observed on phytoplankton communities over half of the experiment. Subsequent nitrogen provision by these organisms in this N-poor environment likely allowed the development of larger non-diazotroph species (i.e., haptophyceae, diatoms and dinoflagellates), which in turn likely also explains the observed significant impact on primary production (Berthelot et al., 2016). Hydrothermal fluid-induced DFe fertilization, which resulted in higher primary production rates and POC export, indicated that such fertilization has a positive impact on the biological carbon pump, in line with *in-situ* results obtained during the TONGA cruise (Bonnet et al., in rev.). It should be noted that the experiment had to be stopped for logistic reasons, during the exponential phase of

10.3389/fmars.2023.1082077

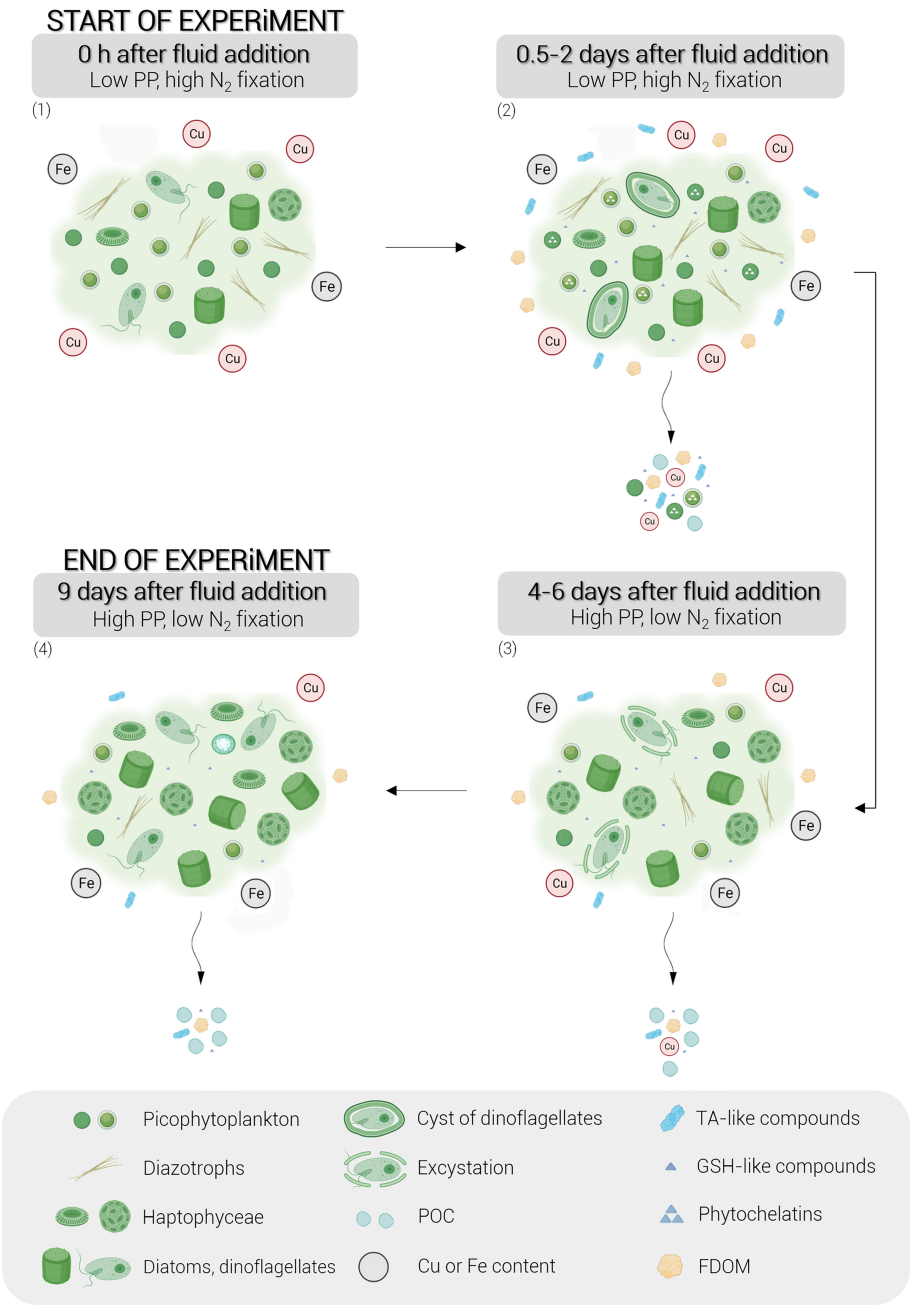

FIGURE 7
Conceptual diagram of the stepwise biological responses of natural phytoplankton communities to hydrothermal fluid addition during the nine-day experiment. Briefly, the following points can be observed: (1) the dominance of picocyanobacteria and diazotrophs at the start of the experiment due to the toxicity of the metals supplied by the hydrothermal fluid, (2) the production of organic ligands by *Synechococcus*, in particular thiols and FDOM, within 0.5 to 2 days after the fluid addition, (3) the development of eukaryotic phytoplankton following environmental detoxification, leading to high primary production and (4) the exponential growth of these eukaryotes until the end of the experiment. The schematic legend is represented in a grey frame. Cu, copper; Fe, iron; TA-like compounds, thioacetamide-like compounds; GSH-like compounds, glutathione-like compounds; FDOM, fluorescent dissolved organic matter; PP, primary production.

non-cyanobacterial species. Thus, POC export was likely supported by diazotrophs, as observed *in-situ* (Bonnet et al., 2023), and cyanobacteria, as larger non-diazotroph phytoplankton developed belatedly and were still in exponential phase when the experiment was stopped. This suggests that the effect of fluids on POC export was likely underestimated in our experiment due to the limited incubation time considered.

5 Conclusion

This nine-day experiment demonstrates that, although hydrothermal fluids triggered an initial toxic effect on phytoplankton communities, these hydrothermal inputs ultimately stimulated NCP, N_2 fixation and POC export, in line with *in-situ* observations. This fertilizing effect occurred notably through rapid detoxification of the

potentially toxic trace metal-rich environment (a cocktail of trace metals such as Cu, Cd, Hg and Pb) by *Synechococcus* ecotypes, which are capable of producing organic ligands, such as thiols (TA- and GSH-like compounds) and FDOM (protein-like fluorophores). These ligands have been reported to significantly reduce the bioavailability of harmful elements to the planktonic communities and have probably allowed the environment to become suitable for the development of more sensitive communities (i.e., eukaryotes). Thus, species stressed by high concentrations of trace metals (haptophyceae, diatoms and dinoflagellates) were able to increase their growth rates, which were further enhanced by the supply of essential and fertilizing elements, especially Fe, by hydrothermal fluids (Figure 7). The experimental results are consistent with the *in-situ* observations performed during the TONGA expedition in the region impacted by hydrothermal fluids. They confirm the causal link between the supply of hydrothermal fluids into the photic layer, the intense biological productivity and the high rates of diazotrophy. This study highlights the implication of shallow hydrothermal systems as a trigger for high biological productivity in oligotrophic ocean areas. Such sources may be widespread in the global ocean and may have a significant impact on the functioning and effectiveness of the biological carbon pump.

This study revealed some shortcomings that need to be addressed in future experiments. Additional analyses of trace metal ionic concentrations in fluids from hydrothermal sources of the Tonga-Kermadec arc would have helped confirm the level of toxicity of metals triggering the production of thiols. A precise measurement of the dynamics of ionic forms of trace metals and their ligands during the experiment could be of great interest to better understand environmental detoxification. It would also be possible to repeat this experiment but over a longer time period to accurately estimate the effect of fluids on material export. Molecular analyses could also validate the hypothesis of the presence of resistant thiol-producing ecotypes of *Synechococcus* in hydrothermal fluids.

Data availability statement

The datasets presented in this study can be found in online repositories. The names of the repository/repositories and accession number(s) can be found below: http://www.obs-vlfr.fr/proof/php/TONGA/tonga.php.

Author contributions

FG and CéG designed the research. CT, EP-V, FG and CéG carried out the 9-day experiment in minicosms. CT conditioned HPLC samples. DM performed flow cytometry analyses, SB, MB, and CL measured the N_2 fixation, CT analyzed the nitrate, NCP, A_T and DFe samples, NL and CT analyzed the exported material, GP analyzed the thiol compounds, CaG and MT analyzed FDOM, EP-V analyzed DOP, M-EV analyzed pTM and FG analyzed pH_T. CT analyzed the data with the help of CéG and FG. The original draft was written by CT, CéG, and FG. All authors contributed to the article and approved the submitted version.

Funding

This work was performed in the framework of the TONGA project (TONGA cruise GEOTRACES GPpr14, November 2019, https://doi.org/10.17600/18000884) managed by the LOV (CéG) and the MIO (SB). The project was funded by the TGIR Flotte Océanographique Française, the A-MIDeX of Aix-Marseille University, the LEFE-CYBER and GMMC program and the Agence Nationale de Recherche (ANR-18-CE01-0016). GP was supported by a Natural Environment Research Council Doctoral Training Scholarship (NE/L002469/1).

Acknowledgments

We warmly thank all the scientists, the captain and the crew of the R/V l'Atalante for their cooperative work at sea. We especially thank all the individuals involved in the minicosm experiment for their great contribution to its success. We thank Céline Dimier and the SAPIGH platform of the Institut de la Mer de Villefranche (IMEV) for performing the pigment analyzes. We thank Sandra Nunige for the nutrient analyses. We warmly thank Matthieu Bressac, Veronica Arnone and David González-Santana for collecting dissolved and particulate metal end-member samples during the cruise. We thank Hélène Planquette for the analysis of the particulate trace metal end-member samples and for her review of the manuscript.

Conflict of interest

The authors declare that the research was conducted in the absence of any commercial or financial relationships that could be construed as a potential conflict of interest.

The handling editor IB-F is currently organizing a Research Topic with the authors SB and CG.

Publisher's note

Supplementary material

The Supplementary Material for this article can be found online at: https://www.frontiersin.org/articles/10.3389/fmars.2023.1082077/full#supplementary-material

References

Ahner, B. A., Lee, J. G., Price, N. M., and Morel, F. M. M. (1998). Phytochelatin concentrations in the equatorial pacific. *Deep Sea Res. Part I: Oceanog. Res. Pap.* 45, 1779–1796. doi: 10.1016/S0967-0637(98)00043-0

Ahner, B. A., and Morel, F. M. M. (1995). Phytochelatin production in marine algae. 2. induction by various metals. *Limnol. Oceanogr.* 40, 658–665. doi: 10.4319/lo.1995.40.4.0658

Ahner, B. A., Price, N. M., and Morel, F. M. (1994). Phytochelatin production by marine phytoplankton at low free metal ion concentrations: laboratory studies and field data from Massachusetts bay. *Proc. Natl. Acad. Sci. U.S.A.* 91, 8433–8436. doi: 10.1073/pnas.91.18.8433

Aiken, G. R. (2014). "Fluorescence and dissolved organic matter: A chemist's perspective., in: Aquatic organic matter fluorescence,". Eds. P. G. Coble, J. Lead, A. Baker, D. M. Reynolds and R. G. M. Spencer (New York, NY, USA: Cambridge University Press), 35–74. doi: 10.1017/CBO9781139045452

Ain Zainuddin, N., Azwan Raja Mamat, T., Imam Maarof, H., Wahidah Puasa, S., and Rohana Mohd Yatim, S. (2019). Removal of nickel, zinc and copper from plating process industrial raw effluent *Via* hydroxide precipitation versus sulphide precipitation. *IOP Conf. Ser.: Mater. Sci. Eng.* 551, 12122. doi: 10.1088/1757-899X/551/1/012122

Anderson, D. M., and Morel, F. M. M. (1978). Copper sensitivity of gonyaulax tamarensis 1: Cooper sensitivity. *Limnol. Oceanogr.* 23, 283–295. doi: 10.4319/lo.1978.23.2.0283

Ardyna, M., Lacour, L., Sergi, S., d'Ovidio, F., Sallée, J.-B., Rembauville, M., et al. (2019). Hydrothermal vents trigger massive phytoplankton blooms in the southern ocean. *Nat. Commun* 10, 1–8. doi: 10.1038/s41467-019-09973-6

Azeh Engwa, G., Udoka Ferdinand, P., Nweke Nwalo, F., and N. Unachukwu, M. (2019). "Mechanism and health effects of heavy metal toxicity in humans," in *Poisoning in the modern world - new tricks for an old dog*. Eds. O. Karcioglu and B. Arslan (Kazimierz Dolny, Poland: IntechOpen). doi: 10.5772/intechopen.82511

Behrenfeld, M. J., and Milligan, A. J. (2013). Photophysiological expressions of iron stress in phytoplankton. *Annu. Rev. Mar. Sci.* 5, 217–246. doi: 10.1146/annurev-marine-121211-172356

Benavides, M., Berthelot, H., Duhamel, S., Raimbault, P., and Bonnet, S. (2017). Dissolved organic matter uptake by trichodesmium in the southwest pacific. *Sci. Rep.* 7, 41315. doi: 10.1038/srep41315

Berman-Frank, I., Cullen, J. T., Shaked, Y., Sherrell, R. M., and Falkowski, P. G. (2001). Iron availability, cellular iron quotas, and nitrogen fixation in *Trichodesmium*. limnol. *Oceanogr* 46, 1249–1260. doi: 10.4319/lo.2001.46.6.1249

Berthelot, H., Bonnet, S., Grosso, O., Cornet, V., and Barani, A. (2016). Transfer of diazotroph-derived nitrogen towards non-diazotrophicplanktonic communities: a comparative study between<i<Trichodesmium</i< <i<erythraeum</i<, <i<Crocosphaerawatsonii</i< and <i<Cyanothece</i< sp. *Biogeosciences* 13, 4005–4021. doi: 10.5194/bg-13-4005-2016

Bonnet, S., Benavides, M., Le Moigne, F. A. C., Camps, M., Torremocha, A., Grosso, O., et al. (2023). Diazotrophs are overlooked contributors to carbon and nitrogen export to the deep ocean. *ISME J.* 17, 47–58. doi: 10.1038/s41396-022-01319-3

Bonnet, S., Caffin, M., Berthelot, H., Grosso, O., Benavides, M., Helias-Nunige, S., et al. (2018). In-depth characterization of diazotroph activity across the western tropical south pacific hotspot of N<sub<2</sub< fixation (OUTPACE cruise). *Biogeosciences* 15, 4215–4232. doi: 10.5194/bg-15-4215-2018

Bonnet, S., Caffin, M., Berthelot, H., and Moutin, T. (2017). Hot spot of n $_2$ fixation in the western tropical south pacific pleads for a spatial decoupling between n $_2$ fixation and denitrification. *Proc. Natl. Acad. Sci. U.S.A.* 114, E2800–E2801. doi: 10.1073/pnas.1619514114

Bonnet, S., Guieu, C., Taillandier, V., Boulart, C., Bouruet-Aubertot, P. , Gazeau, F., et al. (in rev). Natural iron fertilization by shallow hydrothermal sources fuels diazotroph blooms in the ocean. *Science*.

Brand, L. E., Sunda, W. G., and Guillard, R. R. L. (1986). Reduction of marine phytoplankton reproduction rates by copper and cadmium. *J. Exp. Mar. Biol. Ecol.* 96, 225–250. doi: 10.1016/0022-0981(86)90205-4

Brown, A. C., and Gordon, A. S. (2001). Production of a novel copper-binding ligand by marine synechococcus (Cyanobacteria) in response to toxic concentrations of copper. *Virginia J. Sci.* 52. doi: 10.25778/3Z1J-A974

Browning, T. J., Achterberg, E. P., Yong, J. C., Rapp, I., Utermann, C., Engel, A., et al. (2017). Iron limitation of microbial phosphorus acquisition in the tropical north Atlantic. *Nat. Commun.* 8, 15465. doi: 10.1038/ncomms15465

Buckberry, L. D., and Teesdale-Spittle, P. H. (1996). *Sulfur–hydrogen compounds, in: Biological interactions of sulfur compounds* Vol. p (London, UK ; Bristol, PA, USA: Taylor & Francis), 32.

Chen, W. B., Smith, D. S., and Guéguen, C. (2013). Influence of water chemistry and dissolved organic matter (DOM) molecular size on copper and mercury binding determined by multiresponse fluorescence quenching. *Chemosphere* 92, 351–359. doi: 10.1016/j.chemosphere.2012.12.075

Cobbett, C. S. (2000). Phytochelatins and their roles in heavy metal detoxification. *Plant Physiol.* 123, 825–832. doi: 10.1104/pp.123.3.825

Coble, P. G. (2007). Marine optical biogeochemistry: The chemistry of ocean color. *Chem. Rev.* 107, 402–418. doi: 10.1021/cr050350+

Coppellotti, O. (1989). Glutathione, cysteine and acid-soluble thiol levels in euglena gracilis cells exposed to copper and cadmium. *Comp. Biochem. Physiol. Part C: Comp. Pharmacol.* 94, 35–40. doi: 10.1016/0742-8413(89)90140-0

Corbett, C. (2007). *Colored dissolved organic matter (CDOM) workshop summary report*.

Croot, P. L., Moffett, J. W., and Brand, L. E. (2000). Production of extracellular Cu complexing ligands by eucaryotic phytoplankton in response to Cu stress. *Limnol. Oceanogr.* 45, 619–627. doi: 10.4319/lo.2000.45.3.0619

DalCorso, G. (2012). "Heavy metal toxicity in plants," in *Plants and heavy metals, SpringerBriefs in molecular science*. Ed. A. Furini (Netherlands, Dordrecht: Springer), 1–25. doi: 10.1007/978-94-007-4441-7_1

de Kluijver, A., Soetaert, K., Schulz, K. G., Riebesell, U., Bellerby, R. G. J., and Middelburg, J. J. (2010). Phytoplankton-bacteria coupling under elevated CO_2 levels: a stable isotope labelling study. *Biogeosciences* 7, 3783–3797. doi: 10.5194/bg-7-3783-2010

De Vos, C. H. R., Vonk, M. J., Vooijs, R., and Schat, H. (1992). Glutathione depletion due to copper-induced phytochelatin synthesis causes oxidative stress in *Silene cucubalus*. *Plant Physiol.* 98, 853–858. doi: 10.1104/pp.98.3.853

Dick, G. J., Anantharaman, K., Baker, B. J., Li, M., Reed, D. C., and Sheik, C. S. (2013). The microbiology of deep-sea hydrothermal vent plumes: ecological and biogeographic linkages to seafloor and water column habitats. *Front. Microbiol.* 4. doi: 10.3389/fmicb.2013.00124

Dupont, C. L., and Ahner, B. A. (2005). Effects of copper, cadmium, and zinc on the production and exudation of thiols by *Emiliania huxleyi*. limnol. *Oceanogr* 50, 508–515. doi: 10.4319/lo.2005.50.2.0508

Dupont, C. L., Moffett, J., Bidigare, R. R., and Ahner, B. A. (2006). Distributions of dissolved and particulate biogenic thiols in the subartic pacific ocean. *Deep Sea Res. Part I: Oceanog. Res. Pap.* 53, 1961–1974. doi: 10.1016/j.dsr.2006.09.003

Dyhrman, S. T., Chappell, P. D., Haley, S. T., Moffett, J. W., Orchard, E. D., Waterbury, J. B., et al. (2006). Phosphonate utilization by the globally important marine diazotroph trichodesmium. *Nature* 439, 68–71. doi: 10.1038/nature04203

Dyhrman, S. T., and Haley, S. T. (2006). Phosphorus scavenging in the unicellular marine diazotroph *Crocosphaera watsonii*. *Appl. Environ. Microbiol.* 72, 1452–1458. doi: 10.1128/AEM.72.2.1452-1458.2006

Echeveste, P., Agustí, S., and Tovar-Sánchez, A. (2012). Toxic thresholds of cadmium and lead to oceanic phytoplankton: Cell size and ocean basin-dependent effects. *Environ. Toxicol. Chem.* 31, 1887–1894. doi: 10.1002/etc.1893

Fernández-Juárez, V., Bennasar-Figueras, A., Tovar-Sanchez, A., and Agawin, N. S. R. (2019). The role of iron in the p-acquisition mechanisms of the unicellular N2-fixing cyanobacteria halothece sp., found in association with the Mediterranean seagrass posidonia oceanica. *Front. Microbiol.* 10. doi: 10.3389/fmicb.2019.01903

Ferretto, N., Tedetti, M., Guigue, C., Mounier, S., Raimbault, P., and Goutx, M. (2017). Spatio-temporal variability of fluorescent dissolved organic matter in the rhône river delta and the fos-marseille marine area (NW Mediterranean Sea, France). *Environ. Sci. pollut. Res.* 24, 4973–4989. doi: 10.1007/s11356-016-8255-z

German, C. R., Casciotti, K. A., Dutay, J.-C., Heimbürger, L. E., Jenkins, W. J., Measures, C. I., et al. (2016). Hydrothermal impacts on trace element and isotope ocean biogeochemistry. *Philos. Trans. R. Soc. A: Math. Phys. Eng. Sci.* 374, 20160035. doi: 10.1098/rsta.2016.0035

Gharabaghi, M., Irannajad, M., and Azadmehr, A. R. (2012). Selective sulphide precipitation of heavy metals from acidic polymetallic aqueous solution by thioacetamide. *Ind. Eng. Chem. Res.* 51, 954–963. doi: 10.1021/ie201832x

González-Vega, A., Fraile-Nuez, E., Santana-Casiano, J. M., González-Dávila, M., Escánez-Pérez, J., Gómez-Ballesteros, M., et al. (2020). Significant release of dissolved inorganic nutrients from the shallow submarine volcano tagoro (Canary islands) based on seven-year monitoring. *Front. Mar. Sci.* 6. doi: 10.3389/fmars.2019.00829

Grill, E., Löffler, S., Winnacker, E.-L., and Zenk, M. H. (1989). Phytochelatins, the heavy-metal-binding peptides of plants, are synthesized from glutathione by a specific γ-glutamylcysteine dipeptidyl transpeptidase (phytochelatin synthase). *Proc. Natl. Acad. Sci. U.S.A.* 86, 6838–6842. doi: 10.1073/pnas.86.18.6838

Guieu, C., and Bonnet, S. (2019). *TONGA cruise 2019, L'Atalante R/V*. doi: 10.17600/18000884

Guieu, C., Bonnet, S., Petrenko, A., Menkes, C., Chavagnac, V., Desboeufs, K., et al. (2018). Iron from a submarine source impacts the productive layer of the Western tropical south pacific (WTSP). *Sci. Rep.* 8, 1–9. doi: 10.1038/s41598-018-27407-z

Hawkes, J. A., Connelly, D. P., Rijkenberg, M. J. A., and Achterberg, E. P. (2014). The importance of shallow hydrothermal island arc systems in ocean biogeochemistry. *Geophys. Res. Lett.* 41, 942–947. doi: 10.1002/2013GL058817

Hoffmann, L. J., Breitbarth, E., Ardelan, M. V., Duggen, S., Olgun, N., Hassellöv, M., et al. (2012). Influence of trace metal release from volcanic ash on growth of thalassiosira pseudonana and emiliania huxleyi. *Mar. Chem.* 132–133, 28–33. doi: 10.1016/j.marchem.2012.02.003

Horvatić, J., and Peršić, V. (2007). The effect of Ni2+, Co2+, Zn2+, Cd2+ and Hg2+ on the growth rate of marine diatom phaeodactylum tricornutum bohlin: Microplate growth inhibition test. *Bull. Environ. Contam Toxicol.* 79, 494–498. doi: 10.1007/s00128-007-9291-7

Huckle, J. W., Morby, A. P., Turner, J. S., and Robinson, N. J. (1993). Isolation of a prokaryotic metallothionein locus and analysis of transcriptional control by trace metal ions. *Mol. Microbiol.* 7, 177–187. doi: 10.1111/j.1365-2958.1993.tb01109.x

James, G., Witten, D., Hastie, T., and Tibshirani, R. (2013). *An introduction to statistical learning, springer texts in statistics* (New York, NY: Springer New York). doi: 10.1007/978-1-4614-7138-7

Joux-Arab, L., Berthet, B., and Robert, J.-M. (2000). Do toxicity and accumulation of copper change during size reduction in the marine pennate diatom haslea ostrearia? *Mar. Biol.* 136, 323–330. doi: 10.1007/s002270050690

Klawonn, I., Lavik, G., Böning, P., Marchant, H. K., Dekaezemacker, J., Mohr, W., et al. (2015). Simple approach for the preparation of 15–15N2-enriched water for nitrogen fixation assessments: evaluation, application and recommendations. *Front. Microbiol.* 6. doi: 10.3389/fmicb.2015.00769

Lage, O. M., Parente, A. M., Soares, H. M. V. M., Vasconcelos, M. T. S. D., and Salema, R. (1994). Some effects of copper on the dinoflagellates *Amphidinium carterae* and *Prorocentrum micans* in batch culture. *Eur. J. Phycol.* 29, 253–260. doi: 10.1080/09670269400650711

Lage, O. M., Sansonetty, F., O'Connor, J.-E., and Parente, A. M. (2001). Flow cytometric analysis of chronic and acute toxicity of copper(II) on the marine dinoflagellateAmphidinium carterae. *Cytometry* 44, 226–235. doi: 10.1002/1097-0320(20010701)44:3<226::AID-CYTO1115>3.0.CO;2-9

Lage, O. M., Soares, H. M. V. M., Vasconcelos, M. T. S. D., Parente, A. M., and Salema, R. (1996). Toxicity effects of copper (II) on the marine dinoflagellate *Amphidinium carterae* : Influence of metal speciation. *Eur. J. Phycol.* 31, 341–348. doi: 10.1080/09670269600651571

Lavigne, H., and Gattuso, J.-P. (2010). *Seacarb: seawater carbonate chemistry with r*.

Leal, M. F. C., Vasconcelos, M. T. S. D., and van den Berg, C. M. G. (1999). Copper-induced release of complexing ligands similar to thiols by emiliania huxleyi inseawater cultures. *Limnol. Oceanogr.* 44, 1750–1762. doi: 10.4319/lo.1999.44.7.1750

Le Faucheur, S., Campbell, P. G. C., Fortin, C., and Slaveykova, V. I. (2014). Interactions between mercury and phytoplankton: Speciation, bioavailability, and internal handling: Mercury-phytoplankton interactions. *Environ. Toxicol. Chem.* 33, 1211–1224. doi: 10.1002/etc.2424

Le Gall, C., and Van Den Berg, C. M. G. (1998). Folic acid and glutathione in the water column of the north East Atlantic. *Deep Sea Res. Part I: Oceanog. Res. Pap.* 45, 1903–1918. doi: 10.1016/S0967-0637(98)00042-9

Le Jeune, A.-H., Charpin, M., Deluchat, V., Briand, J.-F., Lenain, J.-F., Baudu, M., et al. (2006). Effect of copper sulphate treatment on natural phytoplanktonic communities. *Aquat. Toxicol* 80, 267–280. doi: 10.1016/j.aquatox.2006.09.004

Lenth, R., Singmann, H., Love, J., Buerkner, P., and Herve, M. (2019). *Package "emmeans"*.

Levy, J. L., Stauber, J. L., and Jolley, D. F. (2007). Sensitivity of marine microalgae to copper: The effect of biotic factors on copper adsorption and toxicity. *Sci. Total Environ.* 387, 141–154. doi: 10.1016/j.scitotenv.2007.07.016

Liang, Z., Letscher, R. T., and Knapp, A. N. (2022). Dissolved organic phosphorus concentrations in the surface ocean controlled by both phosphate and iron stress. *Nat. Geosci.* 15, 651–657. doi: 10.1038/s41561-022-00988-1

Lilley, M. D., Feely, R. A., and Trefry, J. H. (2013). Chemical and biochemical transformations in hydrothermal plumes, in: Seafloor hydrothermal systems: Physical, chemical, biological, and geological interactions. *Am. Geophys. Union (AGU)* pp, 369–391. doi: 10.1029/GM091p0369

Liu, J., Zhou, L., Ke, Z., Li, G., Shi, R., and Tan, Y. (2018). Beneficial effects of aluminum enrichment on nitrogen-fixing cyanobacteria in the south China Sea. *Mar. pollut. Bull.* 129, 142–150. doi: 10.1016/j.marpolbul.2018.02.011

Lory, C., Van Wambeke, F., Fourquez, M., Berman-Frank, I., Barani, A., Tilliette, C., et al. (2022). Assessing the contribution of diazotrophs to microbial fe uptake using a group specific approach in the Western tropical south pacific ocean. *ISME Commun.* doi: 10.1038/s43705-022-00122-7

Lou, Y., He, Z., and Han, X. (2020). Transport and deposition patterns of particles laden by rising submarine hydrothermal plumes. *Geophys. Res. Lett.* 47. doi: 10.1029/2020GL089935

Mann, E. L., Ahlgren, N., Moffett, J. W., and Chisholm, S. W. (2002). Copper toxicity and cyanobacteria ecology in the Sargasso Sea. *Limnol. Oceanogr.* 47, 976–988. doi: 10.4319/lo.2002.47.4.0976

Marie, D., Partensky, F., Vaulot, D., and Brussaard, C. (1999). Enumeration of phytoplankton, bacteria, and viruses in marine samples. *Curr. Protoc. Cytomet.* 10. doi: 10.1002/0471142956.cy1111s10

Martin, J. H. (1990). Glacial-interglacial CO $_2$ change: The iron hypothesis. *Paleoceanography* 5, 1–13. doi: 10.1029/PA005i001p00001

Massoth, G., Baker, E., Worthington, T., Lupton, J., de Ronde, C., Arculus, R., et al. (2007). Multiple hydrothermal sources along the south Tonga arc and valu fa ridge. *Geochem. Geophys. Geosyst* 8. doi: 10.1029/2007GC001675

Maugendre, L., Gattuso, J.-P., de Kluijver, A., Soetaert, K., van Oevelen, D., Middelburg, J. J., et al. (2017). Carbon-13 labelling shows no effect of ocean acidification on carbon transfer in Mediterranean plankton communities. *Estuar. Coast. Shelf Sci.* 186, 100–111. doi: 10.1016/j.ecss.2015.12.018

May, M. J., Vernoux, T., Leaver, C., Montagu, M. V., and Inze, D. (1998). Glutathione homeostasis in plants: implications for environmental sensing and plant development. *J. Exp. Bot.* 49, 649–667. doi: 10.1093/jxb/49.321.649

Mehana, E.-S. (2014). Impact of water pollution with heavy metals on fish health:Overview and updates. *Global Veterinaria* 12, 219–231. doi: 10.5829/idosi.gv.2014.12.02.82219

Moffett, J. W., and Brand, L. E. (1996). Production of strong, extracellular Cu chelators by marine cyanobacteria in response to Cu stress. *Limnol. Oceanogr.* 41, 388–395. doi: 10.4319/lo.1996.41.3.0388

Moffett, J. W., Zika, R. G., and Brand, L. E. (1990). Distribution and potential sources and sinks of copper chelators in the Sargasso Sea. *Deep Sea Res. Part A. Oceanog. Res. Pap.* 37, 27–36. doi: 10.1016/0198-0149(90)90027-S

Moisander, P. H., Serros, T., Paerl, R. W., Beinart, R. A., and Zehr, J. P. (2014). Gammaproteobacterial diazotrophs and nifH gene expression in surface waters of the south pacific ocean. *ISME J.* 8, 1962–1973. doi: 10.1038/ismej.2014.49

Montoya, J. P., Voss, M., Kahler, P., and Capone, D. G. (1996). A simple, high-precision, high-sensitivity tracer assay for N(inf2) fixation. *Appl. Environ. Microbiol.* 62, 986–993. doi: 10.1128/aem.62.3.986-993.1996

Morel, F. M. M., and Price, N. M. (2003). The biogeochemical cycles of trace metals in the oceans. *Science* 300, 944–947. doi: 10.1126/science.1083545

Morrison, R. T., Boyd, R. N., and Bhattacharjee, S. K. (2010). *Organic chemistry*.

Mounier, S., Zhao, H., Garnier, C., and Redon, R. (2011). Copper complexing properties of dissolved organic matter: PARAFAC treatment of fluorescence quenching. *Biogeochemistry* 106, 107–116. doi: 10.1007/s10533-010-9486-6

Moutin, T., and Bonnet, S. (2015). *OUTPACE cruise,L'Atalante R/V*. doi: 10.17600/15000900

Moutin, T., Karl, D. M., Duhamel, S., Rimmelin, P., Raimbault, P., Van Mooy, B. A. S., et al. (2008). Phosphate availability and the ultimate control of new nitrogen input by nitrogen fixation in the tropical pacific ocean. *Biogeosciences* 5, 95–109. doi: 10.5194/bg-5-95-2008

Moutin, T., Van Den B, B., Beker, B., Dupouy, C., Rimmelin, P., and Le Bouteiller, A. (2005). Phosphate availability controls trichodesmium spp. *Biomass SW Pacific Ocean. Mar. Ecol. Prog. Ser.* 297, 15–21. doi: 10.3354/meps297015

Mujika, J. I., Ruipérez, F., Infante, I., Ugalde, J. M., Exley, C., and Lopez, X. (2011). Pro-oxidant activity of aluminum: Stabilization of the aluminum superoxide radical ion. *J. Phys. Chem. A* 115, 6717–6723. doi: 10.1021/jp203290b

Noctor, G., Arisi, A.-C. M., Jouanin, L., Kunert, K. J., Rennenberg, H., and Foyer, C. H. (1998). Glutathione: biosynthesis, metabolism and relationship to stress tolerance explored in transformed plants. *J. Exp. Bot.* 49, 623–647. doi: 10.1093/jxb/49.321.623

Okamoto, O. K., Shao, L., Woodland Hastings, J., and Colepicolo, P. (1999). Acute and chronic effects of toxic metals on viability, encystment and bioluminescence in the dinoflagellate gonyaulax polyedra. *Comp. Biochem. Physiol. Part C: Pharmacol. Toxicol. Endocrinol.* 123, 75–83. doi: 10.1016/S0742-8413(99)00013-4

Omanović, D., and Branica, M. (1998). Automation of voltammetric measurements by polarographic analyser PAR 384B. *Croatica Chemica Acta* 71, 421–433.

Palenik, B., Ren, Q., Dupont, C. L., Myers, G. S., Heidelberg, J. F., Badger, J. H., et al. (2006). Genome sequence of *Synechococcus* CC9311: Insights into adaptation to a coastal environment. *Proc. Natl. Acad. Sci. U.S.A.* 103, 13555–13559. doi: 10.1073/pnas.0602963103

Pelletier, B., Calmant, S., and Pillet, R. (1998). Current tectonics of the Tonga–new Hebrides region. *Earth Planet. Sci. Lett.* 164, 263–276. doi: 10.1016/S0012-821X(98)00212-X

Permana, R., and Akbarsyah, N. (2021). Phytoplankton susceptibility towards toxic heavy metal cadmium: Mechanism and its recent updates. *World News Natural Sci.* 38, 83–97.

Pernet-Coudrier, B., Waeles, M., Filella, M., Quentel, F., and Riso, R. D. (2013). Simple and simultaneous determination of glutathione, thioacetamide and refractory organic matter in natural waters by DP-CSV. *Sci. Total Environ.* 463–464, 997–1005. doi: 10.1016/j.scitotenv.2013.06.053

Pinto, E., Sigaud-kutner, T. C. S., Leitao, M. A. S., Okamoto, O. K., Morse, D., and Colepicolo, P. (2003). Heavy metal-induced oxidative stress in algae. *J. Phycol* 39, 1008–1018. doi: 10.1111/j.0022-3646.2003.02-193.x

Pollard, R., Sanders, R., Lucas, M., and Statham, P. (2007). The crozet natural iron bloom and export experiment (CROZEX). *Deep Sea Res. Part II: Top. Stud. Oceanog.* 54, 1905–1914. doi: 10.1016/j.dsr2.2007.07.023

Quigg, A., Reinfelder, J. R., and Fisher, N. S. (2006). Copper uptake kinetics in diverse marine phytoplankton. *Limnol. Oceanogr.* 51, 893–899. doi: 10.4319/lo.2006.51.2.0893

Raven, J. A. (1988). The iron and molybdenum use efficiencies of plant growth with different energy, carbon and nitrogen sources. *New Phytol.* 109, 279–287. doi: 10.1111/j.1469-8137.1988.tb04196.x

Rijstenbil, J. W., Derksen, J. W. M., Gerringa, L. J. A., Poortvliet, T. C. W., Sandee, A., van den Berg, M., et al. (1994). Oxidative stress induced by copper: defense and damage in the marine planktonic diatom ditylum brightwellii, grown in continuous cultures with high and low zinc levels. *Mar. Biol.* 119, 583–590. doi: 10.1007/BF00354321

Rinard Hinga, B. D. (2015). *Ring of fire: an encyclopedia of the pacific rim's earthquakes, tsunamis, and volcanoes* (Santa Barbara, California: ABC-CLIO).

Romano, R. L., Liria, C. W., Machini, M. T., Colepicolo, P., and Zambotti-Villela, L. (2017). Cadmium decreases the levels of glutathione and enhances the phytochelatin concentration in the marine dinoflagellate lingulodinium polyedrum. *J. Appl. Phycol* 29, 811–820. doi: 10.1007/s10811-016-0927-z

Rueter, J. G., Hutchins, D. A., Smith, R. W., and Unsworth, N. L. (1992). "Iron nutrition of trichodesmium," in *Marine pelagic cyanobacteria: Trichodesmium and other diazotrophs*. Eds. E. J. Carpenter, D. G. Capone and J. G. Rueter (Netherlands, Dordrecht: Springer), 289–306. doi: 10.1007/978-94-015-7977-3_19

Ruipérez, F., Mujika, J. I., Ugalde, J. M., Exley, C., and Lopez, X. (2012). Pro-oxidant activity of aluminum: Promoting the fenton reaction by reducing Fe(III) to Fe(II). *J. Inorganic Biochem.* 117, 118–123. doi: 10.1016/j.jinorgbio.2012.09.008

Satoh, M., Hirachi, Y., Yoshioka, A., Kobayashi, M., and Oyama, Y. (2002). Determination of cellular levels of nonprotein thiols in phytoplankton and their correlations with susceptibility to mercury. *J. Phycol* 38, 983–990. doi: 10.1046/j.1529-8817.2002.t01-1-01223.x

Satoh, M., Karaki, E., Kakehashi, M., Okazaki, E., Gotoh, T., and Oyama, Y. (1999). Heavy-metal induced changes in nonproteinaceous thiol levels and heavy-metal binding peptide in tetraselmis tetrathele (Prasinophyceae). *J. Phycol* 35, 989–994. doi: 10.1046/j.1529-8817.1999.3550989.x

Scheller, H. V., Huang, B., Hatch, E., and Goldsbrough, P. B. (1987). Phytochelatin synthesis and glutathione levels in response to heavy metals in tomato cells. *Plant Physiol.* 85, 1031–1035. doi: 10.1104/pp.85.4.1031

Schine, C. M. S., Alderkamp, A.-C., van Dijken, G., Gerringa, L. J. A., Sergi, S., Laan, P., et al. (2021). Massive southern ocean phytoplankton bloom fed by iron of possible hydrothermal origin. *Nat. Commun.* 12, 1211. doi: 10.1038/s41467-021-21339-5

Schlitzer, R., Anderson, R. F., Dodas, E. M., Lohan, M., Geibert, W., Tagliabue, A., et al. (2018). The GEOTRACES intermediate data product 2017. *Chem. Geol.* 493, 210–223. doi: 10.1016/j.chemgeo.2018.05.040

Schlosser, C., Klar, J. K., Wake, B. D., Snow, J. T., Honey, D. J., Woodward, E. M. S., et al. (2014). Seasonal ITCZ migration dynamically controls the location of the (sub) tropical Atlantic biogeochemical divide. *Proc. Natl. Acad. Sci. U.S.A.* 111, 1438–1442. doi: 10.1073/pnas.1318670111

Shaked, Y., Kustka, A. B., and Morel, F. M. M. (2005). A general kinetic model for iron acquisition by eukaryotic phytoplankton. *Limnol. Oceanogr.* 50, 872–882. doi: 10.4319/lo.2005.50.3.0872

Stauber, J. L., and Davies, C. M. (2000). Use and limitations of microbial bioassays for assessing copper bioavailability in the aquatic environment. *Environ. Rev.* 8, 255–301. doi: 10.1139/a00-010

Stedmon, C. A., and Bro, R. (2008). Characterizing dissolved organic matter fluorescence with parallel factor analysis: a tutorial: Fluorescence-PARAFAC analysis of DOM. *Limnol. Oceanogr. Methods* 6, 572–579. doi: 10.4319/lom.2008.6.572

Stuart, R. K., Brahamsha, B., Busby, K., and Palenik, B. (2013). Genomic island genes in a coastal marine synechococcus strain confer enhanced tolerance to copper and oxidative stress. *ISME J.* 7, 1139–1149. doi: 10.1038/ismej.2012.175

Stuart, R. K., Dupont, C. L., Johnson, D. A., Paulsen, I. T., and Palenik, B. (2009). Coastal strains of marine *Synechococcus* species exhibit increased tolerance to copper shock and a distinctive transcriptional response relative to those of open-ocean strains. *Appl. Environ. Microbiol.* 75, 5047–5057. doi: 10.1128/AEM.00271-09

Sunda, W. G. (1994). "Trace Metal/Phytoplankton interactions in the Sea," in *Chemistry of aquatic systems: Local and global perspectives*. Eds. G. Bidoglio and W. Stumm (Netherlands, Dordrecht: Springer), 213–247. doi: 10.1007/978-94-017-1024-4_9

Sunda, W. G., and Huntsman, S. A. (1995). Iron uptake and growth limitation in oceanic and coastal phytoplankton. *Mar. Chem.* 50, 189–206. doi: 10.1016/0304-4203(95)00035-P

Sunda, W. G., and Huntsman, S. A. (1998). Interactive effects of external manganese, the toxic metals copper and zinc, and light incontrolling cellular manganese and growth in a coastal diatom. *Limnol. Oceanogr.* 43, 1467–1475. doi: 10.4319/lo.1998.43.7.1467

Tagliabue, A., Bopp, L., Dutay, J.-C., Bowie, A. R., Chever, F., Jean-Baptiste, P., et al. (2010). Hydrothermal contribution to the oceanic dissolved iron inventory. *Nat. Geosci.* 3, 252–256. doi: 10.1038/ngeo818

Tang, D., Hung, C.-C., Warnken, K. W., and Santschi, P. H. (2000). The distribution of biogenic thiols in surface waters of Galveston bay. *Limnol. Oceanogr.* 45, 1289–1297. doi: 10.4319/lo.2000.45.6.1289

F. J. R. Taylor (Ed.) (1987). "The biology of dinoflagellates," in *Botanical monographs* (Oxford ; Boston: Blackwell Scientific Publications).

Tedetti, M., Bigot, L., Turquet, J., Guigue, C., Ferretto, N., Goutx, M., et al. (2020). Influence of freshwater discharges on biogeochemistry and benthic communities of a coral reef ecosystem (La réunion island, Indian ocean). *Front. Mar. Sci.* 7. doi: 10.3389/fmars.2020.596165

Tedetti, M., Marie, L., Röttgers, R., Rodier, M., Van Wambeke, F., Helias, S., et al. (2016). Evolution of dissolved and particulate chromophoric materials during the VAHINE mesocosm experiment in the new caledonian coral lagoon (south-west pacific). *Biogeosciences* 13, 3283–3303. doi: 10.5194/bg-13-3283-2016

Thomas, W. H., Hollibaughl, J. T., Seibertl, D. L. R., and Wallace, G. T. (1980). Toxicity of a mixture of ten metals to phytoplankton. *Mar. Ecol. Prog. Ser.* 2, 213–220. doi: 10.3354/meps002213

Tilliette, C., Taillandier, V., Bouruet-Aubertot, P., Grima, N., Maes, C., Montanes, M., et al. (2022). Dissolved iron patterns impacted by shallow hydrothermal sources along a transect through the Tonga-kermadec arc. *Global Biogeochem. Cycles*. doi: 10.1029/2022GB007363

Timm, C., Bassett, D., Graham, I. J., Leybourne, M. I., de Ronde, C. E. J., Woodhead, J., et al. (2013). Louisville Seamount subduction and its implication on mantle flow beneath the central Tonga–kermadec arc. *Nat. Commun.* 4, 1720. doi: 10.1038/ncomms2702

Uitz, J., Claustre, H., Morel, A., and Hooker, S. B. (2006). Vertical distribution of phytoplankton communities in open ocean: An assessment based on surface chlorophyll. *J. Geophys. Res.: Oceans* 111. doi: 10.1029/2005JC003207

Valsami-Jones, E., Baltatzis, E., Bailey, E. H., Boyce, A. J., Alexander, J. L., Magganas, A., et al. (2005). The geochemistry of fluids from an active shallow submarine hydrothermal system: Milos island, Hellenic volcanic arc. *J. Volcanol. Geothermal Res.* 148, 130–151. doi: 10.1016/j.jvolgeores.2005.03.018

Walker, S. L., and Baker, E. T. (1988). Particle-size distributions within hydrothermal plumes over the Juan de fuca ridge. *Mar. Geol.* 78, 217–226. doi: 10.1016/0025-3227(88)90110-7

Walsh, M. J., Goodnow, S. D., Vezeau, G. E., Richter, L. V., and Ahner, B. A. (2015). Cysteine enhances bioavailability of copper to marine phytoplankton. *Environ. Sci. Technol.* 49, 12145–12152. doi: 10.1021/acs.est.5b02112

Wong, K. H., Obata, H., Kim, T., Wakuta, Y., and Takeda, S. (2019). Distribution and speciation of copper and its relationship with FDOM in the East China Sea. *Mar. Chem.* 212, 96–107. doi: 10.1016/j.marchem.2019.04.005

Worms, I., Simon, D. F., Hassler, C. S., and Wilkinson, K. J. (2006). Bioavailability of trace metals to aquatic microorganisms: importance of chemical, biological and physical processes on biouptake. *Biochimie* 88, 1721–1731. doi: 10.1016/j.biochi.2006.09.008

Wu, Y., and Wang, W.-X. (2011). Accumulation, subcellular distribution and toxicity of inorganic mercury and methylmercury in marine phytoplankton. *Environ. pollut.* 159, 3097–3105. doi: 10.1016/j.envpol.2011.04.012

Wu, Y., and Wang, W.-X. (2012). Thiol compounds induction kinetics in marine phytoplankton during and after mercury exposure. *J. Haz. Mat.* 217–218, 271–278. doi: 10.1016/j.jhazmat.2012.03.024

Zenk, M. H. (1996). Heavy metal detoxification in higher plants - a review. *Gene* 179, 21–30. doi: 10.1016/S0378-1119(96)00422-2

Zhang, Z., Fan, W., Bao, W., Chen, C.-T. A., Liu, S., and Cai, Y. (2020). Recent developments of exploration and detection of shallow-water hydrothermal systems. *Sustainability* 12, 9109. doi: 10.3390/su12219109

frontiers | Frontiers in Marine Science

TYPE Original Research
PUBLISHED 21 August 2023
DOI 10.3389/fmars.2023.1219594

OPEN ACCESS

EDITED BY
Alex J Poulton,
Heriot-Watt University, United Kingdom

REVIEWED BY
Aridane G. Gonzalez,
University of Las Palmas de Gran Canaria, Spain
Martha Gledhill,
Helmholtz Association of German Research Centres (HZ), Germany

*CORRESPONDENCE
Gabriel Dulaquais
gabriel.dulaquais@univ-brest.fr

RECEIVED 09 May 2023
ACCEPTED 26 July 2023
PUBLISHED 21 August 2023

CITATION
Dulaquais G, Fourrier P, Guieu C, Mahieu L, Riso R, Salaun P, Tilliette C and Whitby H (2023) The role of humic-type ligands in the bioavailability and stabilization of dissolved iron in the Western Tropical South Pacific Ocean.
Front. Mar. Sci. 10:1219594.
doi: 10.3389/fmars.2023.1219594

The role of humic-type ligands in the bioavailability and stabilization of dissolved iron in the Western Tropical South Pacific Ocean

Gabriel Dulaquais[1]*, Pierre Fourrier[1], Cécile Guieu[2], Léo Mahieu[3], Ricardo Riso[1], Pascal Salaun[3], Chloé Tilliette[2] and Hannah Whitby[3]

[1]Laboratoire des Sciences de l'Environnement Marin Centre nationale pour la recherche scientifiques (CNRS) UMR 6539, Institut Universitaire Européen de la Mer, Université de Bretagne Occidentale, Plouzané, France, [2]Sorbonne Université, Centre nationale pour la recherche scientifiques (CNRS), Laboratoire d'Océanographie de Villefranche (LOV), Villefranche-sur-Mer, France, [3]Department of Earth, Ocean and Ecological Sciences, School of Environmental Sciences, University of Liverpool, United Kingdom

The high N_2 fixation rate observed in the Lau Basin of the western tropical South Pacific Ocean (WTSP) is fueled by iron (Fe) released from shallow hydrothermal systems. Understanding Fe bioavailability is crucial but the controls on the stability and bioavailability of hydrothermal Fe inputs are still poorly understood. Here, we provide new data on the spatial and vertical distribution of the soluble ubiquitous humic-like ligands (L_{FeHS}) and their associated dissolved Fe (DFe) in the WTSP, including in samples near hydrothermal vents. Our data show that L_{FeHS} are heterogenous ligands with binding sites of both strong and intermediate strengths. These ligands are primarily produced in surface waters and partially mineralized in mesopelagic waters. A substantial fraction of DFe was complexed by L_{FeHS} (mean ~30%). The DFe complexed by L_{FeHS} is likely bioavailable to phytoplankton and L_{FeHS} stabilized Fe released by the mineralization of sinking biomass. However, unsaturation of L_{FeHS} by Fe suggest that part of DFe is not available for complexation with L_{FeHS}. Possible reasons are competition between DFe and other metals, such as dissolved copper, or the inability of L_{FeHS} to access colloidal DFe. The study of two volcanic sites indicates that L_{FeHS} were not produced in these hydrothermal systems. At the active site (DFe ~50 nmol L^{-1}), L_{FeHS} can only partially solubilize the hydrothermal DFe released in this area (1~5.5% of the total DFe). We performed controlled laboratory experiments which show that the observed low solubilization yield result from the inability of L_{FeHS} to solubilize aged Fe oxyhydroxides (FeOx - a kinetically mediated process) and to form stable complexes with Fe(II) species. Our study provides new understanding of the role of L_{FeHS} on the bioavailability and stabilization of hydrothermal DFe.

KEYWORDS

iron, organic complexation, humic substances, hydrothermal vents, Pacific Ocean

1 Introduction

Iron (Fe) bioavailability is crucial for marine life and across a large part of the ocean, primary producers are Fe limited or co-limited (Moore et al., 2013). In seawater, dissolved Fe (DFe) geochemistry is governed by complex redox chemistry limiting the solubility of inorganic DFe at subnanomolar levels (e.g., Sung and Morgan, 1980; Millero et al., 1987; Martin and Fitzwater, 1988; Martin and Gordon, 1988; Martin et al., 1989; Martin et al., 1991; Byrne et al., 2000; Rose and Waite, 2003a; Santana-Casiano et al., 2005; Croot and Heller, 2012). Large-scale measurements of oceanic DFe concentrations conducted in the context of the GEOTRACES program (Schlitzer et al., 2018) evidenced that DFe can be found at higher concentrations than the subnanomolar solubility limit predicted by Liu and Millero (2002). These observations indicate that other processes are involved in controlling Fe solubility in the dissolved phase: organic complexation and colloidal precipitation. Colloidal DFe (0.02 µm< cFe< 0.450 µM) represents a significant fraction (up to > 50%) of oceanic total DFe and has a pivotal role in DFe dynamics (Nishioka et al., 2001; Wu et al., 2001; Boye et al., 2010; Fitzsimmons and Boyle, 2014; Kunde et al., 2019). Chelation with organic ligands enhances Fe solubility and almost all DFe is thought to be complexed by natural ligands in seawater (Gledhill and van den Berg, 1994; Rue and Bruland, 1995; van den Berg, 1995; Wu and Luther, 1995) including in the colloidal phase (Boye et al., 2010; Fitzsimmons et al., 2015). The sources, distributions, chemical functions and reactivity of these ligands need to be assessed to improve our understanding of DFe biogeochemistry (Macrellis et al., 2001; Hunter and Boyd, 2007; Benner, 2011; Gledhill and Buck, 2012; Bundy et al., 2015; Hassler et al., 2017). Organic iron-binding ligands (L_{Fe}) are themselves part of the dissolved organic carbon (DOC) pool, the largest organic carbon pool in the ocean (Guo et al., 1995), but the wide variety of ligand types is a barrier for detailed characterization of these organic compounds. Discrimination of ligand classes using cathodic stripping voltammetry with competing ligand exchange (CLE-CSV) is the most commonly used method to quantify L_{Fe} (Gledhill and Buck, 2012). CLE-CSV methods permit an operational classification of ligands depending on their binding strength. According to the Gledhill and Buck (2012) classification, there are the strong (L_1, log $K_{Fe'L1}$ > 12), the intermediate (L_2, 11 ≤ log $K_{Fe'L2}$ ≤ 12) and the weak classes (L_3, log $K_{Fe'L3<}$ 11). Another weaker class (L_4 log $K_{Fe'L3<}$ 10) can even be introduced for L_{Fe} of very low strength. Nevertheless, CLE-CSV have methodological caveats (Gerringa et al., 2021) and the presence of non-labile DFe species for complexation with the competing ligand can lead to over- and underestimations of L_{Fe}. Futhermore, relying solely on Log $K_{Fe'L}$ for the classification of L_{Fe} may yield inaccurate results due to the heterogeneity of ligand binding sites. It may be more relevant to consider reactivity coefficients (αFeL(Fe′)= log $K_{Fe'L}$ *.LFe′), as suggested by Gledhill and Gerringa (2017). Reactivity coefficients express the probability that any added metal will be complexed by the ambient free ligands. Advances in mass spectrometry open perspectives for the study of siderophores, a class of strong ligands (Gledhill, 2001; McCormack et al., 2003; Mawji et al., 2008; Boiteau and Repeta, 2015). Environmental studies have shown that siderophore compounds are present at picomolar levels in seawater (Bundy et al., 2018; Hawco et al., 2021), far lower than nanomolar ambient L_{Fe} concentrations recorded in seawater (Buck et al., 2018). Thereby, efforts must be conducted to study other ligand types such as polyphenol compounds, extracellular polymeric substances (EPS) and humic substances (HS). In this work we will focus on the role of HS in the stabilization and bioavailability of DFe.

Maillard (1912) described the chemistry of HS for the first time, and this terminology encompasses several definitions, depending on the type of measurement applied to the particulate or dissolved fraction (Davies and Ghabbour, 2003; Riso et al., 2021). HS can be operationally separated into their soluble (fulvic acids) and insoluble (humic acids) parts under acidic conditions (MacCarthy et al., 1979; Thurman and Malcolm, 1981; De Paolis and Kukkonen, 1997). Marine HS are believed to originate from the decomposition of (macro)biomolecules (derived from phytoplankton) microbially-degraded in the ocean interior (Hedges et al., 1992; Tranvik, 1993; Hertkorn et al., 2006). The importance of HS in the stabilization of trace metals in the dissolved phase is known since the early 80's (Boggs et al., 1985) but the difficulties to isolate HS from seawater prevented the study of these compounds and their interactions with Fe for decades.

Recent studies demonstrate the ubiquity of HS in the ocean accounting for more than half of the DOC oceanic concentrations (Zigah et al., 2017; Fourrier et al., 2022). Among the different compounds contributing to HS, some are "electroactive" (called eHS) and able to complex trace elements. The electroactivity is a property of HS measurable by electrochemical methods (Whitby and van den Berg, 2015; Dulaquais et al., 2018a; Sukekava et al., 2018). Electroactivity of HS is representative of the density of the functional groups involved in metal complexation. For Fe and other metals such as copper (Cu), the latter seem to be oxygen-containing functional groups such as carboxyl and phenol moieties (Blazevic et al., 2016). Electroactivity can be converted into concentration of iron-binding ligand of humic nature (L_{FeHS}) providing a quantification of this ligand class. Field measurements show that electroactivity strongly decreases from fresh to marine waters (Riso et al., 2021) and from subsurface to deep waters in the ocean (Dulaquais et al., 2018a; Fourrier et al., 2022). *In situ* experiments conducted by Whitby et al. (2020a) showed that microbial degradation results in a release of eHS, but at high POC degradation rate, there was also concurrent eHS removal. As a result, the impacts of biogeochemical processes (e.g. mineralization, photobleaching) on this property (e.g. electroactivity) remain unclear. In regard to CLE-CSV data, L_{FeHS} are mainly assigned to the intermediate class of ligand (e.g. L_2; Laglera and van den Berg, 2009; Gledhill and Buck, 2012) but this complex mixture possibly includes components of other classes (Perdue and Lytle, 1983; Laglera et al., 2019; Gledhill et al., 2022). Field observations (Buck et al., 2018) and numerical simulations (Misumi et al., 2013) suggest that L_2 type ligands regulate the DFe distribution as well as its residence time in the deep ocean (Hunter and Boyd, 2007). Interactions between Fe and L_{FeHS} were previously investigated by measuring both parameters independently (Laglera and van den Berg, 2009; Batchelli et al., 2010; Bundy et al., 2014; Bundy et al.,

2015; Krachler et al., 2015; Slagter et al., 2017; Dulaquais et al., 2018a) raising ever more questions on the links between the biogeochemistry of both parameters. Considering the occurrence of L_{FeHS} throughout the water column (Dulaquais et al., 2018a; Laglera et al., 2019; Whitby et al., 2020b; Fourrier et al., 2022), the role of L_{FeHS} in the Fe marine biogeochemistry needs to be further considered.

Thanks to the optimization of electrochemical methods, there is now the possibility to quantify the effective amount of Fe complexed by L_{FeHS} (DFe-HS) in a natural sample (Sukekava et al., 2018). The first application of this methodology on samples from the Arctic Ocean evidenced that DFe-HS represents ~80% of total DFe in this basin impacted by riverine inputs (Laglera et al., 2019). This has large implications for our understanding of DFe export from the surface Arctic to the deep Atlantic and encourages the scientific community to extend these kinds of measurements to other oceanic basins submitted to different forcing. Indeed, to confirm the importance of L_{FeHS} in Fe biogeochemistry, we need new data from contrasting environments such as deep environments where data are still scarce (Whitby et al., 2020b). In particular, studies of hydrothermal systems – that provide a large amount of DFe to the deep ocean (e.g. Tagliabue et al., 2010; Resing et al., 2015) – have so far not established a link between L_{FeHS} and DFe. In these extreme environments with low pH and low O_2, a significant large fraction of DFe can can exist in its reduced form as Fe(II) (González-Santana et al., 2021; González-Santana et al., 2023). It has been observed that humic type DOM catalyse the oxidation of Fe(II) (Santana-Casiano et al., 2022) and that some polyphenols reduce Fe(III) into Fe(II) (González et al., 2019; Pérez-Almeida et al., 2022). However, the capacity of L_{FeHS} to form stable complexes with Fe(II) in marine waters remains poorly explored.

In this context, we explored the spatial distributions of L_{FeHS} and DFe-HS in the oligotrophic waters of the Western Tropical South Pacific Ocean (WTSP). With the aim to shed light on the role of L_{FeHS} in the stabilization of hydrothermal DFe, samples were collected along a 6100 km transect partly impacted by shallow hydrothermal vents (TONGA GEOTRACES GPr14 expedition; https://doi.org/10.17600/18000884). As Fe oxyhydroxides (FeOx) can be massively released by hydrothermal systems and can persist under colloidal form in the distal plume (Fitzsimmons et al., 2017; Lough et al., 2019), we conducted complementary kinetic experiments to shed light on the capacity of L_{FeHS} to solubilize FeOx in seawater.

2 Materials and methods

2.1 Sampling strategy and collection of samples

Samples were collected during the TONGA GEOTRACES GPpr14 expedition onboard the R/V *L'Atalante* in November 2019 (20°S – 24°S; -166°W – 165°W). This 6100 km-long transect encountered three biogeochemical zones (Figure 1). As described in Tilliette et al. (2022), two types of stations were sampled during the expedition: eight short-duration stations (SD 2, 3, 4, 6, 7, 8, 11, and

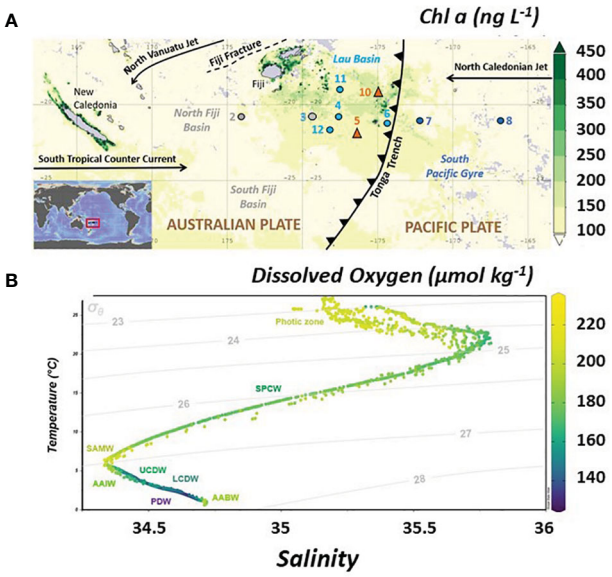

FIGURE 1
(A) Location of the TONGA GPpr14 expedition superimposed on a time average map of chlorophyll a concentrations from satellite data (ng L^{-1}; 8-daily 4-km over 2019-11-09 – 2019-12-09) in the Western Tropical South Pacific Ocean (WTSP). Figure generated using Giovanni (giovanni.gsfc.nasa.gov). Numbers represent sampled stations. Grey dot indicates the station sampled in the Melanesian waters (SD 2 and 3), light blue dots the stations sampled in the Lau Basin (stations SD 4, 11 and, 12) and dark blue dots for the stations of the South Pacific Gyre (SD6, 7 and 8). Orange triangles show the location of the two volcanic sites identified (LD 5 and 10). Main surface currents are indicated by black arrows which also mark the Tonga Trench. **(B)** Temperature-Salinity diagram of the study area with the color corresponding to associated dissolved oxygen concentrations (O_2 expressed in µmol kg^{-1}). Grey lines indicate the potential densities (referenced to a pressure of 0 dbar). Water masses defined on T-S diagrams are indicated (see text for abbreviations). Figure generated using ODV software (Schlitzer, 2022).

12) and two long-duration stations (LD 5 and 10), the latter two dedicated to the study of the dispersion of hydrothermal fluids. These two LD stations included 5 (for LD 5) and 4 (for LD 10) subcasts, named from T5 to T1, with T5 being the closest to the hydrothermal source. Hydrothermal sources were detected from the acoustic anomalies (Bonnet et al., 2023) using a multibeam echosounder (hull-mounted EM-710 echosounder of R/V *L'Atalante*), operating at a frequency of 70–100 kHz for depths shallower than 1000 m. As described in Tilliette et al. (2022), the T5 substations were positioned where the highest acoustic anomalies were recorded at 200 and 300 m for LD 5 and 10, respectively. At both LD 5 and 10, the other substations (T1, T2, T3, T4 for LD 5 and T1, T2, T3 for LD 10) were positioned west of "T5" according to the main surface current direction in order to investigate the longitudinal impact of hydrothermal fluids released from T5 (see Supporting informations in Tilliette et al., 2022 for further details of positions). At LD 10, an additional substation called "Proxnov" (i.e., Metis Shoal; 19.18°S, 174.87°W) located further north of this site (15 km from LD 10-T5) was sampled to capture the eruption of the Late'iki submarine volcano that occurred one month prior to the expedition (Plank et al., 2020).

Sampling was operated using a trace metal clean polyurethane powder-coated aluminum frame rosette (TMR) equipped with twenty-four 12 L Teflon-lined GO-FLO bottles (General Oceanics) and attached to a Kevlar® wire. Potential temperature (θ), salinity (S) and dissolved oxygen (O_2) were retrieved from the conductivity–temperature–depth (CTD) sensors (SBE9+) deployed on the TMR. The cleaning protocols of all the sampling equipment followed the guidelines of the GEOTRACES Cookbook (http://www.geotraces.org). After recovery, the TMR was directly transferred into a clean container equipped with a class 100 laminar flow hood. Samples were then taken from the filtrate of particulate samples (collected on acid-cleaned polyethersulfone filters, 0.45 µm supor). For L_{FeHS}, L_{Fe} and DOC, the filtrate was collected into acid-cleaned and sample-rinsed high density polyethylene (HDPE) 125 mL bottles. Immediately after collection, samples were double-bagged and stored at -20°C until analysis in a shore-based laboratory. For DFe, the filtrate was collected into acid-cleaned and sample-rinsed 60 mL HDPE Nalgene bottles, acidified to pH ~1.7 with Ultrapure HCl (0.2% v/v, Supelco®) within 24 h of collection and stored double-bagged pending analysis at Laboratoire d'Océanographie de Villefranche (full protocol and data in Tilliette et al., 2022).

2.2 Reagents

All aqueous solutions and cleaning procedures used ultrapure water (resistivity > 18.2 MΩ.cm^{-1}, MilliQ Element, Millipore®). An acidic solution (hydrochloric acid, HCl, 0.01 M, Suprapur®, >99%) of 1.24 µmol L^{-1} Fe (III) was prepared daily from a stock solution (1 g L^{-1}, VWR, Prolabo, France). The borate buffer (H_3BO_3, 1M, Suprapur®, Merck, Germany, 99.8%) was prepared in 0.4 M ammonium solution (NH_4OH, Ultrapure normatom, VWR Chemical, USA, 20-22%). The potassium bromate solution ($KBrO_3$, 0.3 M, VWR Chemical, USA, ≥ 99.8%) was prepared in ultrapure water. *Suwannee River Fulvic Acids* (SRFA, 1S101F) were purchased at the International Humic Substances Society (IHSS). The SRFA standard stock solution (22.86 mg SFRA L^{-1}) was prepared in ultrapure water and saturated with iron according to its iron binding capacity in seawater determined by Sukekava et al. (2018). Saturated SRFA solution was equilibrated overnight before its use. Exact concentration of the SRFA stock solution was determined by size exclusion chromatography analysis (Dulaquais et al., 2018b). A 10^{-3} M Gallic Acid (GA) stock solution (Sigma-Aldrich) was prepared in HPLC grade methanol, as described in González et al. (2019). The second GA stock solution (10^{-6} M) was prepared in ultrapure water. The second stock solution of GA was divided into two portions, with one portion saturated with Fe (final concentration of 5 10^{-6} M Fe). Following an overnight equilibration, the Fe-saturated solution was filtered through a 0.02 µm filter to remove any excess iron that precipitated as FeOx.

FeOx dissolution experiments. Artificial seawater (Salinity = 35; pH = 8.2 ± 0.05) was prepared by dissolving sodium chloride (NaCl, 6.563 g, ChemaLab NV, Belgium, 99.8%), potassium chloride (KCl, 0.185 g, Merck, Germany, 99.999%), calcium chloride ($CaCl_2$, 0.245 g, Prolabo, France, > 99.5%), magnesium chloride ($MgCl_2$, 1.520 g, Merck, Germany, 99-101%), magnesium sulfate ($MgSO_4$, 1.006 g, Sigma-Aldrich, USA, ≥99%) and sodium bicarbonate ($NaHCO_3$, 0.057 g, ChemaLab NV, Belgium, >99.7%) in ultrapure water (250 mL). Artificial seawater was then UV irradiated for 2 hours in order to remove all traces of organic compounds.The UV system consisted of a 125-W mercury vapor lamp with 4 30-mL PTFE-capped quartz tubes (http://pcwww.liv.ac.uk/~sn35/Site/UV_digestion_apparatus.html).

2.3 Analysis of iron-binding ligands of humic type and of dissolved iron-humic concentrations

The determination of L_{FeHS} was performed on 213 samples from the eight SD and on the two LD stations, including all LD substations, with half the depth resolution. L_{FeHS} is based on the determination of electroactive humic substances (eHS). Analyses were operated by cathodic stripping voltammetry (CSV) using a polarographic Methrom 663VA stand connected to a potentiostat/galvanostat (µautolab 2, Methrom®) and to an interface (IME 663, Methrom®). Data acquisition was done using the NOVA software (version 10.1). The method used in this study was initially developed by Laglera et al. (2007) and adapted by Sukekava et al. (2018). The method is based on the adsorption at pH 8 of a Fe-humic complex at the surface of a mercury drop electrode under a potential fixed at -0.1 V (vs Ag/AgCl) and its reduction during linear stripping of potentials (0.1 to 0.8 V). In the presence of 30 mmol L^{-1} bromate, the reduction of the Fe-humic complex provides a quantitative peak at -0.5 V (vs Ag/AgCl) with an intensity proportional to the concentration. In this study, the samples were defrosted at 4°C and 100 mL were poured in a 250 mL Teflon® bottle. pH was then set to 8.00 ± 0.05 by addition of a borate buffer (final concentration = 10 mM) and adjusted by small additions of an ammonia solution. A first aliquot of the sample was poured into Teflon® vials (Savillex®) in order to detect the natural iron-humic complex (Sukekava et al., 2018). The sample (remaining in the 250 mL Teflon® bottle) was then spiked with 10 nmol L^{-1} of Fe to saturate all eHS (and others L_{Fe}) in the initial sample. After equilibration (1h), 3 others aliquots (15 mL) of the sample were placed into 3 Teflon® vials (Savillex®). Among them, two were spiked with a SRFA standard (1S101F; standard additions of 50 and 100 µg L^{-1}, respectively) and left for overnight equilibration. After equilibration, the 4 aliquots of samples (1 without Fe, 1 with Fe and 2 with Fe and SRFA additions)were successively placed into a Teflon® voltammetric cell and analyzed by linear sweep voltammetry as described above after 180 s of nitrogen (N_2) purge (Alphagaz®, Air liquide) and a 90 s deposition step at –0.1V. The absence of quantitative signals in MilliQ water ensured no contamination along the entire analytical process. Peak heights were extracted to determine the electroactive humic concentrations (determined in µg eq-SRFA L^{-1}). Errors of these measurements were determined using a least-squares fit function. We converted eHS

concentrations into L_{FeHS}, as described by Sukekava et al. (2018), using the binding capacity of the model humic-type ligand SRFA used (1S101F) for DFe in seawater (14.6 ± 0.7 nmol Fe mgSRFA^{-1}; Sukekava et al., 2018). Similar conversions have been previously used in the recent literature (Dulaquais et al., 2018a; Laglera et al., 2019; Whitby et al., 2020b; Fourrier et al., 2022). The limit of detection (LOD) for 90 s of deposition time was calculated as three times the mean standard deviation of all samples analyzed (n = 213). LOD was estimated at 0.11 nmol eq-Fe L^{-1}. After data treatment, 12 samples were below the calculated LOD. These samples were mostly within the 200-1000 m depth range where L_{FeHS} displays their minimal concentrations (Figure 2). They were discarded from the dataset resulting in 201 datapoints for L_{FeHS}.

Voltammetric peaks of the first (i0, pH adjusted sample) and second (i1, pH adjusted and Fe saturated) aliquots permits the determination of the initial amount of DFe bound to humic-type ligands in the sample. This was determined according to equation (1), first introduced by Sukekava et al., 2018.

$$[DFe - HS]_{sample} = i0/i1 \times L_{FeHs\ sample} \quad (1)$$

As no DFe-HS blank signal can be determined (several samples with no i0 signal), the LOD was defined as three times the standard deviation of the lowest DFe-HS concentration ([DFe-HS]) measured (0.01 ± 0.01 nmol eqFe L^{-1}) and was estimated to be 0.03 nmol eq-Fe L^{-1}. After data treatment, 14 samples had a [DFe-HS] below the calculated LOD; they were removed from the dataset resulting in 187 datapoints for DFe-HS.

Further discussion about the the relevance of the methodology to determine L_{FeHS} can be found in the Supplementary Information.

2.4 Dissolution of iron oxyhydroxide by L_{FeHS}

Experimental dissolutions of FeOx by humic-type ligands were carried out as a function of time and age of FeOx. 250 mL of UV irradiated artificial seawater was spiked with 100 nmol L^{-1} Fe. In the absence of organic ligands, the limit of solubility of DFe is subnanomolar (Liu and Millero, 2002), thereby DFe would rapidly form Fe oxyhydroxides (Rose and Waite, 2003b). Fe-spiked artificial seawater was then placed on an agitation table (320 rpm, IKA®KS basic) all along the duration of the experiment. After intense shaking by hand (10 s), a single aliquot (1.5 mL) of Fe-spiked artificial seawater was sampled at 1 min, 1 h, 6 h and every day over the course of one week and then at two weeks after FeOx initial formation. Aliquots of the FeOx solution were directly transferred to 13.5 mL of a SRFA solution (buffered pH = 8.00 ± 0.05, final concentration 0.5 mg-SRFA L^{-1} in UV irradiated artificial seawater) in a Teflon voltammetric cell. After an initial N_2 purge of 180 s, the dissolution kinetic of FeOx by SRFA was followed by CSV during 30 cycles using the same voltametric conditions as described in section 2.3 with N_2 purge and deposition times set at 15 s and 90 s, respectively. The experiment was run in duplicate and was reproducible ensuring reproducibility of the experiment. Measurement of pH at the end of the experiment indicated no significant variation, confirming the stability of the pH within the voltammetric cell throughout the duration of the experiment (1 hour).

2.5 Competition between natural humic-type ligands with gallic acid for iron complexation

The Fe-binding strength of natural humic-type ligands was determined by ligand competition experiments between natural samples and gallic acid (GA). Experiments were conducted on (1) surface seawater collected at 25 m at station 6 (outside the Lau Basin). The experiment (see design of experiment in supplementary information) is based on the measurement of the FeHS voltammetric signal in the same sample that has undergone different additions of DFe and/or GA. The binding properties of GA for Fe (III) used are those described in González et al. (2019) (L_{FeGA} = 2.75 nmol Fe nmol GA^{-1}; $LogK_{FeGa}$ = 9.1).

The competition for Fe' is based on the equilibrium between DFe and L_{FeHS} (equation 2) and between DFe and GA (equation 3).

$$K_{FeHS} = \frac{[DFeHS]}{[LFeHS'] * [Fe']} \quad (2)$$

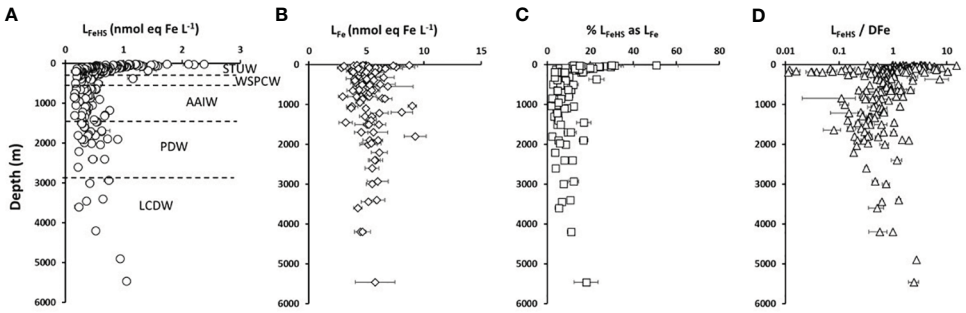

FIGURE 2
Vertical distribution with depth of **(A)** humic type ligands (circles, L_{FeHS}, n = 203), **(B)** Iron binding ligands (diamonds, LFe, n = 103) and **(C)** % L_{Fe} of humic nature (squares,n = 103) measured along the water column during the TONGA expedition. **(D)** L_{FeHS} over DFe ratio (triangles, L_{FeHS}/DFen = 203). Water masses identified by multiparametric optimal analysis and their associated depths are indicated in **(A)** see text for water masses acronyms.

10.3389/fmars.2023.1219594

$$K_{FeGA} = \frac{[DFeGA]}{[GA']*[Fe']} \quad (3)$$

$$DFe = DFeHS + DFeGA + Fe' \quad (4)$$

With K_{FeHS} and $K_{FeGA,}$ the conditional stability constants of natural humic-type ligands and of gallic acid for DFe, respectively, [DFeHS]; the concentration of Fe bound to natural humic type ligands calculated using the binding capacity of SFRA, $[L_{FeHS}]'$; the unsaturated humic-type ligand concentration; [Fe]′, the inorganic Fe species; [DFeGA], the concentration of Fe bound to gallic acid and [GA]′, the concentration of unsaturated Gallic acid ligands.

When the two ligands are in competition, the conditional stability constant of the natural humic-type ligands can be calculated according to equation 4.

$$K_{FeHS} = \frac{[DFeHS]*[GA']}{[DFeGA]*[LFeHS']} * K_{FeGA} \quad (5)$$

The FeHS voltametric signal increasing linearly with Fe, the Fe concentration complexed by humic-type ligands can be determined as the ratio between the FeHS signal for a given experimental condition and the FeHS signal of the samples when saturated with dFe (L_{FeHS}) multiplied by the binding capacity of the sample (see equation 1). Assuming that eHS only complex with Fe, the free humic-type ligands can be then determined using equation 6.

$$[L_{FeHS}'] = [DFeHS] - L_{FeHS\ sample} \quad (6)$$

Assuming that Fe" is negligible over DFe, the concentration of FeGA complex can be estimated using equation 7.

$$[DFeGA] \sim DFe - [DFeHS] \quad (7)$$

Assuming that GA only complex Fe, when GA is added with a known concentration in a sample, [GA′] can be calculated from the total concentration of added GA ($L_{FeGA\ sample}$) according to equation 8.

$$[GA'] = L_{FeGA\ sample} - [DFeGA] \quad (8)$$

2.6 Dissolved iron analysis

DFe concentrations were measured by flow injection and chemiluminescence detection (FIA-CL) in a clean room at the Laboratoire d'Océanographie de Villefranche. The method, data and analytical performance are fully presented in Tilliette et al. (2022). The DFe-rich samples were diluted in DFe-depleted seawater collected at SD 8. The final concentration of those diluted samples did not exceed 5 nmol L^{-1} and a 0-5 nmol L^{-1} calibration curve was used in that case. Each sample was analyzed in triplicate. The mean analytical blank was 21 ± 22 pM and the detection limit was 16 ± 7 pM. Method accuracy was evaluated daily by analyzing the GEOTRACES Surface (GS) seawater (DFe = 0.510 ± 0.046 nmol L^{-1}; n = 24) which compares well with community consensus concentrations of 0.546 ± 0.046 nmol L^{-1}.

2.7 Analysis of dissolved organic carbon concentrations

Dissolved organic carbon concentrations were determined by size exclusion chromatography with multi-detectors according to the methodology described in Fourrier et al. (2022). Accuracy of measurements were checked by analyzing deep sea reference samples (DSR, Hansell lab, Florida) each set of ten samples.

2.8 Analysis of iron-binding ligands

Iron-binding ligands (L_{Fe}) were determined for 103 samples by Mahieu et al. (this issue) using competitive ligand exchange with adsorptive cathodic stripping voltametry (CLE-ACSV). The theory of the CLE-ACSV is presented with great detail in the literature (e.g. Gledhill and van den Berg, 1994; Rue and Bruland, 1995; Abualhaija and van den Berg, 2014; Gerringa et al., 2014; Pižeta et al., 2015). For acquisition of L_{Fe} data, samples were buffered at pH of 8.2 (1 M boric acid, in 0.35 M ammonia) and separated in 16 aliquots. Then natural ligands were left to equilibrate with DFe levels of 0, 0, 0.75, 1.5, 2.25, 3, 3.5, 4, 4.5, 5, 6, 7, 8, 10, 12 and 15 nmol.L^{-1} in the 16 aliquots. The artificial ligand added was salycilaldoxime (SA; 98%; Acros Organics™) at final concentration of 25 µmol.L^{-1} resulting to a detection window (D) of 79 (Buck et al., 2007). Analyses were operated on a 663 VA stand (Metrohm™) under a laminar flow hood (class-100), supplied with nitrogen and equipped with a mercury drop electrode (MDE, Metrohm™), a glassy carbon counter electrode and a silver/silver chloride reference electrode (3M KCl) in a Teflon voltametric cell. During the voltammetric measurement, the sample was kept oxygenated by a constant air-flow at the surface and the nitrogen gas flow from the 663 VA stand above the sample was stopped. Detailed procedure can be found in Mahieu et al. (this issue).

2.9 Statistics

A Shapiro-Wilk test was used to verify that the data follows a normal distribution, and the homogeneity of variances was assessed by conducting a Levene's test. Significance in linear regression analysis was determined using the Pearson test. In cases of normally distributed datasets, the significance of differences between data was examined using t-tests. For non-normally distributed datasets, a non-parametric Wilcoxon-Mann Whitney test was utilized to evaluate the significance of differences. A probability value (p) less than 0.05 was considered statistically significant for all analyses.

10.3389/fmars.2023.1219594

3 Results

3.1 Hydrography and hydrothermal context

Three distinct basins were crossed and sampled during the TONGA expedition (Figure 1A). The Melanesian waters (grey dots, SD2 and 3), the Lau Basin (average depth shallower than 2000 m) (Figure 1A, clear blue dots and orange triangles, SD4, 11 and 12, LD5 and 10) and the South Pacific Gyre, east of the Tonga Kermadec Arc (dark blue dots, SD 6, 7 and 8). In the Lau Basin, two shallow volcanic systems hosting hydrothermal sites were studied (Figure 1, orange triangles), referred to LD 5 and LD 10. The hydrothermal system at LD 5 was active and marked by high DFe concentrations, up to 50 nmol L^{-1}, close to the vent (Tilliette et al., 2022). In contrast, the activity at LD 10 had likely been considerably slowed down at time of sampling, possibly due to the eruption of the nearby *Late'iki* volcano (Plank et al., 2020). Nevertheless, LD 10 water composition was probably impacted, at least for DFe, by the volcanic activity of the shallow hydrothermal site in the upper 300 m and of *Metis* at depths deeper than 1000 m (Tilliette et al., 2022; Tilliette et al., sub.).

Low surface chlorophyll *a* concentrations (< 0.2 mg m^{-3} derived from satellite data, MODIS-Aqua MODISA simulations, Figure 1A) and extremely low nutrient concentrations (NO_3^- and PO_4^{3-}< 50nmol L^{-1}, https://www.seanoe.org/data/00770/88169/) reflect the ultra-oligotrophy of the North Fiji basin and South Pacific Gyre at the time of sampling. The Lau Basin was marked by higher surface chlorophyll *a* concentrations than the subtropical gyre (Figure 1) indicating that primary production was enhanced in this area. Bonnet et al. (accepted) have shown the causal link between this increased productivity due to diazotrophic organisms whose iron needs are very important and the shallow hydrothermal sources that bring the necessary iron to the surface.

The water masses along the transect area were extensively studied in Tilliette et al. (2022) using hydrographic properties collected during the TONGA expedition as well as a multiparametric optimal analysis (OMP). The main thermocline (200-700 m) includes the Surface Tropical Underwater (STUW) and the Western South Pacific Central Water (WSPCW). The STUW originates from the subduction of high salinity waters from the equatorial part of the subtropical gyre and is associated with a shallow salinity maximum. Created by subduction and diapycnal mixing, the WSPCW exhibits a linear relationship between temperature and salinity over a wide range up to the intermediate layer. The intermediate layer (700-1300 m) was composed solely of AAIW, a low salinity water mass originating from the sea surface at sub-Antarctic latitudes and characterized by a minimum salinity reached at 700 m. AAIW circulates around the subtropical gyre from the south-east Pacific, spreading north-westwards as tongues of low-salinity, high-oxygen water, and enters the tropics in the western Pacific. The deep layer (> 1300 m) contains the Pacific Deep Water (PDW) and the Lower Circumpolar Deep Water (LCDW). The PDW originates from the equatorial Pacific and flows southwards. It is formed in the interior of the Pacific from upwelling of Antarctic Bottom Water (AABW). PDW is characterized by low oxygen content and well-mixed temperature and salinity. LCDW originates from the Southern Ocean and overlaps the depth and density ranges of PDW. However, it differs from the PDW by a maximum of salinity and oxygen. The OMP results revealed a uniform distribution of water masses along the transect, except the two deep water masses, PDW and LCDW, for which differences could be observed in their distribution west and east of the Tonga Arc. STUW is mainly present at depths between 150 and 300 m, followed by WSPCW which is predominantly present between 300 and 500 m. AAIW dominated the entire transect over a wide depth range from 500 to 1300 m. A major contribution from PDW was found west of the Tonga Arc from 1300 m to the seafloor, while PDW only occupied depths between 1300 and 3000 m east of the arc. Below 3000 m LCDW dominated (Tilliette et al., 2022). It is worth noting that Upper Circumpolar Deep Water (UCDW) and AABW were detected according to their salinity and Temperature (Figure 1) however the OMP operated by Tilliette et al. (2022) revealed a zero contribution from these water masses along the transect.

3.2 Vertical distribution of iron-binding ligands of humic-type

Along the TONGA section, concentrations of L_{FeHS} ranged from 0.15 ± 0.05 to 2.38 ± 0.05 nmol eq-Fe L^{-1} (n = 201; Figures 2A–4A). The lowest concentration was measured at station 6 at 920 m and the highest concentration was detected at station 8 at 25 m in the South Pacific Gyre. At each station, the vertical distribution was similar (Figure 2A) with high concentration (> 1 nmol eq-Fe L^{-1}) in the upper 55 m (Figure 2A) decreasing with depth in the mesopelagic waters to a relative minimum (L_{FeHS}< 0.2 nmol eq-Fe L^{-1}) generally observed between 500 and 1500 m. In the abyssal waters, L_{FeHS} increased, reaching concentrations close to 0.5 nM eq-Fe (Figure 2A). The interval of concentration and the vertical distribution we report in this work are in good agreement with previous studies reporting humic-type ligand concentrations, including those from the southwestern Pacific (Cabanes et al., 2020). L_{FeHS} concentrations in the different water masses identified by the OMP are presented Table 1. AAIW was the most depleted ($mean_{AAIW}$ = 0.33 ± 0.16 nmol eq-Fe L^{-1} n = 41) and LCDW the most enriched ($mean_{LCDW}$ = 0.55 ± 0.31 nmol eq-Fe L^{-1} n = 9) in L_{FeHS}. Titration of iron-binding ligands (L_{Fe}) over 103 samples provide the complexing capacity of dissolved organic matter for Fe (Figure 2B). L_{Fe} ranged from 2.8 ± 0.4 to 9.3 ± 1.0 nmol eq-Fe.L^{-1} with a mean concentration of 5.2 ± 1.2 nmol eq-Fe.L^{-1}. The distribution of L_{Fe} was relatively homogenous along the water column (Figure 2B). The contribution of L_{FeHS} to L_{Fe} was calculated as the ratio between both parameters. Among the 103 samples investigated, L_{FeHS} contributed to between 2% and 51% of L_{Fe} (Figure 2C) with a mean of 11 ± 8%. The ratio of LFeHS over DFe (Figure 2D) exhibited a wide range of values, spanning from<0.1 to 15.4, with an average of 1.3 ± 1.8. Half of the samples had a ratio below 1, indicating that the organic complexation of DFe by L_{FeHS} cannot explain alone the observed ambient DFe concentrations along the section. Lower values were observed in the LD5 samples and in

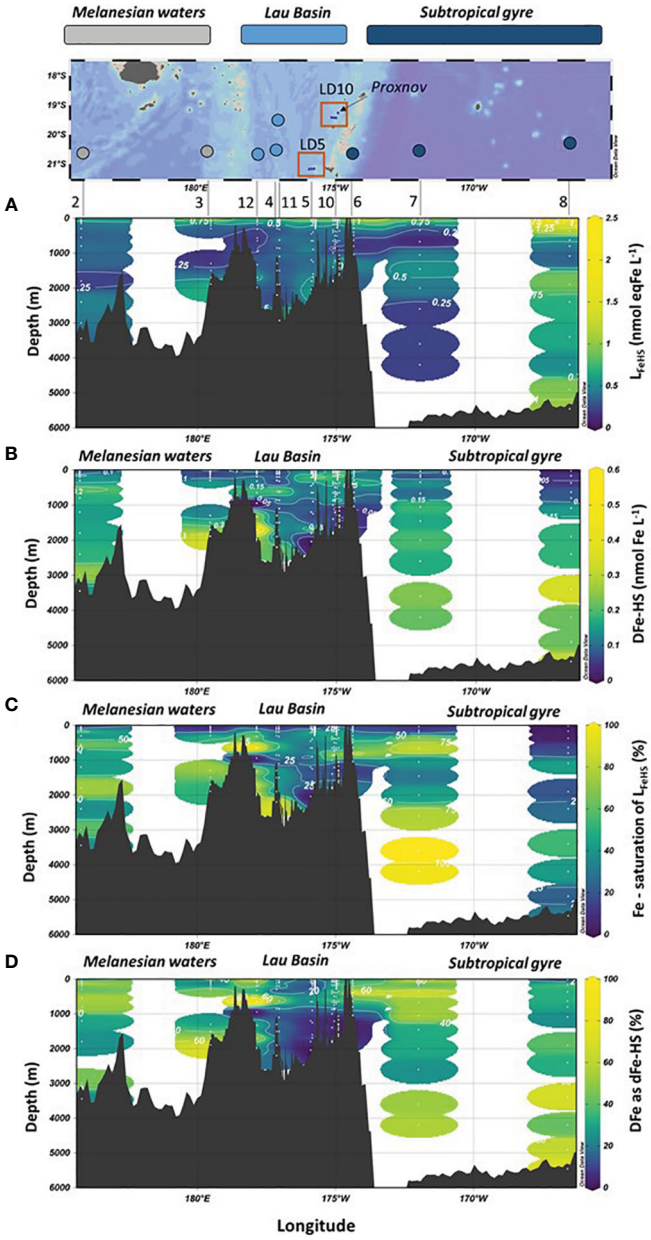

FIGURE 3
Vertical distribution of **(A)** Iron binding ligands of humic nature (L_{FeHS}); **(B)** dissolved iron (DFe) effectively complexed by L_{FeHS} (DFe-HS); **(C)** L_{FeHS} saturation state (%); **(D)** Percentage of DFe under DFe-HS (%) with longitude during the TONGA expeditione (GEOTRACES GPpr14). Map of the expedition and the three distinct biogeochemical domains crossed are indicated.

the samples collected in the PDW, while higher values were observed in the surface samples and in the LCDW.

3.3 Iron associated with L_{FeHS} and L_{FeHS} saturation state

The concentration of Fe complexed by L_{FeHS} was estimated by considering the saturation state of L_{FeHS} and the binding capacity (BC) of the external standard used (SRFA 1S101F; BC_{SRFA} = 14.6 nmol Fe. mg $SRFA^{-1}$, Sukekava et al., 2018). Despite the uncertainty of this methodology (see section 2.3), it provides information regarding the amount of DFe associated to L_{FeHS}. The average calculated DFe-HS was 0.15 ± 0.10 nmol Fe L^{-1} (n = 192) and ranged between 0.03 ± 0.02 nmol Fe L^{-1} to 0.56 ± 0.04 nmol Fe L^{-1}. The mean contribution of DFe-HS to DFe was 30 ± 23%. The lowest concentrations were found between depths at depths between 60 and 120 m for four stations (Figures 3C, 4). The highest

10.3389/fmars.2023.1219594

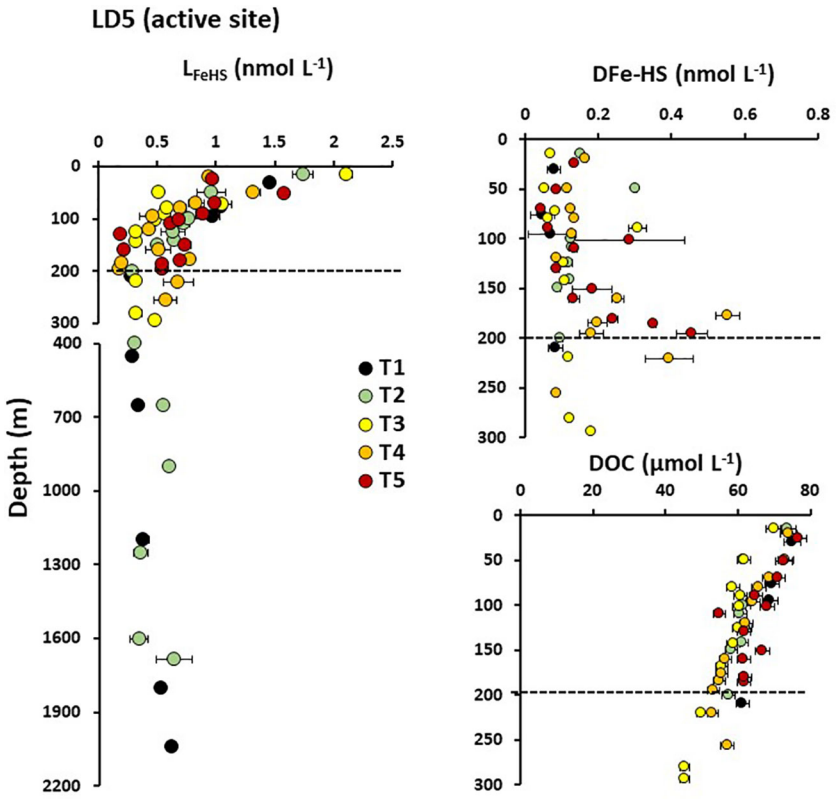

FIGURE 4
Vertical distribution of humic-type ligand concentrations (L_{FeHS}) above and in the vicinity of LD 5 hydrothermal site. Dashed lines indicate the approximate depth of the hydrothermal plume at LD 5-T5 (~190 m). Associated concentrations of dissolved iron complexed by L_{FeHS} (DFe-HS) and of dissolved organic concentrations (DOC) are presented for the upper 300 m.

concentration was recorded at 175 m of substation T4 of LD5 in the vicinity of the hydrothermal plume of LD 5 (Figure 4A). In this latter sample, a DFe peak (~10 nM) associated with hydrothermal activity was recorded by Tilliette et al. (2022) and DFe-HS contributing for 5.5% of total DFe. DFe-HS concentrations were generally lower than 0.2 nmol L^{-1} in the upper 200 m, with the exception of LD 5 and LD 10 (Figure 4), and higher than 0.2 nmol L^{-1} in the intermediate and deep waters (deeper than 1000 m, Figure 3). The local minima of DFe-HS were generally observed at the depth of the local Chlorophyll maxima (see section 4.4). At these depths DFe-HS accounted for 21 ± 15% of total DFe. The saturation of L_{FeHS} by Fe is presented in Figure 3D. With the exception of one datapoint at 3500 m at station 7, ambient L_{FeHS} were not saturated by Fe. The mean saturation state was 37 ± 26% (n = 192), ranging from 3 ± 5% at 25 m at station 8 to up to 102 ± 4% at 3600 m at station 7. Lowest saturation states (< 10%) were found in the upper water, associated with low DFe concentrations (SD 3, 7, 8). This was expected considering the low DFe concentrations (Tilliette et al., 2022) and the high L_{FeHS} concentrations (Figure 3A). In the Lau Basin, relatively low saturation states of L_{FeHS} (< 30%, Figure 3D) were observed between 1000 and 1400 m depth. Deeper than 1000 m depth, the saturation of L_{FeHS} was generally higher than 40% in the Melanesian waters and the south Pacific subtropical gyre. Our results indicate that a large fraction of L_{FeHS} were not saturated by Fe. These free L_{FeHS} should be able to support Fe complexation and its

TABLE 1 Mean concentration of iron binding ligands of humic nature (L_{FeHS}) and associated variability (SD) measured in the water masses encountered during the TONGA expedition.

	STUW	WSPCW	AAIW	PDW	LCDW
Depth range (m)	[100-300]	[300-500]	[500-1300]	[1300-3000]	> 3000
Mean L_{FeHS} (nmol eq-Fe L^{-1})	0.48	0.37	0.33	0.42	0.55
SD (nmol eq-Fe L^{-1})	0.24	0.22	0.16	0.19	0.31
n	60	18	41	34	9

See text for abbreviations of water masses.

stabilization in the dissolved phase if Fe is added to the system by volcanic or hydrothermal activity.

3.4 L_{FeHS} and DFe-HS in a hydrothermal system of the Tonga arc

The impact of the hydrothermal activity along the Tonga arc on L_{FeHS} concentrations and DFe associated with these ligands (DFe-HS) was studied at LD 5 and LD 10. Five and four subcasts were operated at LD 5 and LD 10, respectively, to capture the dispersion of the hydrothermal plume. We focus here on the active site LD5 (Figure 4) where high DFe concentrations (up to 50 nmol L^{-1}) were measured close to the vent (Tilliette et al., 2022). At the subcasts close to the vent (T5 and T4), L_{FeHS} and DOC concentrations did not show any significant enrichment at depths where the hydrothermal plume was located (~195 m; Figure 4). Similarly, there was no L_{FeHS} or DOC enrichment at LD 10 (see Supplementary Information). These results indicate that these hydrothermal systems were not a source of L_{FeHS} or DOC. In contrast, DFe-HS did show an enrichment at depths where the hydrothermal plume was located (Figure 4B). At T5, the concentration of DFe-HS increased while the saturation of L_{FeHS} decreased with increasing proximity to the vent, from 0.06 nmol L^{-1} (8% saturated with Fe) at 70 m to 0.46 nmol L^{-1} (83% saturation) at 195 m depth, nearest the vent. Due to the much higher DFe concentration in the deeper sample (DFe ~50 nmol L^{-1} at 195m), only ~1% of DFe was complexed by L_{FeHS} at this depth. The highest DFe-HS concentration was measured at 175 m depth of T4 (0.56 nmol L^{-1}) where DFe was ~10 nmol L^{-1} with ~5.5% of DFe was present under DFe-HS. Unsaturation of L_{FeHS} at 195 m of T5 despite the high DFe concentration (~ 50 nmol L^{-1}) suggests that this hydrothermal DFe was present under a chemical form not fully accessible for complexation by L_{FeHS}. The increase in DFe-HS concentration during plume dispersion between T5 and T4 (Figure 4B) indicates that complexation of DFe by L_{FeHS} begins at the onset of hydrothermal mixing and proceeds further during plume dispersion. Our data thus indicate that the complexation of hydrothermal DFe by L_{FeHS} is a kinetically controlled process.

3.5 Iron oxyhydroxide dissolution by humic-type ligands: from lability to inertness

Hydrothermal systems release large amounts of FeOx to the ocean, thereby we studied the ability of L_{FeHS} to solubilize FeOx in seawater. For this purpose, a dissolution experiment of FeOx in the presence of a model L_{FeHS} (SRFA) was carried out (Figure 5A). The experiment consisted of monitoring the formation of the DFe-HS as a function of time and as a function of age of FeOx. Results show that immediately after FeOx formation, amorphous Fe(III) is accessible to L_{FeHS} generating a quantifiable signal. Within an hour, 40% of initially-formed FeOx were dissolved, demonstrating that L_{FeHS} can solubilize FeOx with a kinetic rate constant (k) of at least 1.2 10^6 mol^{-1} L min^{-1}.

Age of FeOx was however a strong controlling parameter on the dissolution rate. A dramatic linear decrease of k with time (k = 1.25 10^6 M^{-1} - 0.18 * t(d), R^2 = 0.99, n = 10) was observed (Figure 5B). After 2 days only 2.5 nmol L^{-1} over 10 nmol L^{-1} of FeOx can be dissolved by SRFA after 1 hour of experiment. After a week of ageing, there was no quantifiable signal after 1 hour experiment (Figure 5A). Additional experiments were carried out two weeks after FeOx formation and no measurable signal was observed (data not shown).

4 Discussion

4.1 L_{FeHS} cycling in the WTSP

The high concentrations and surface maxima of L_{FeHS} observed in this area not impacted by continental inputs indicate a marine origin of L_{FeHS} in these subtropical waters. Direct excretion by phytoplankton is a possible source of L_{FeHS} (Stedmon and Cory,

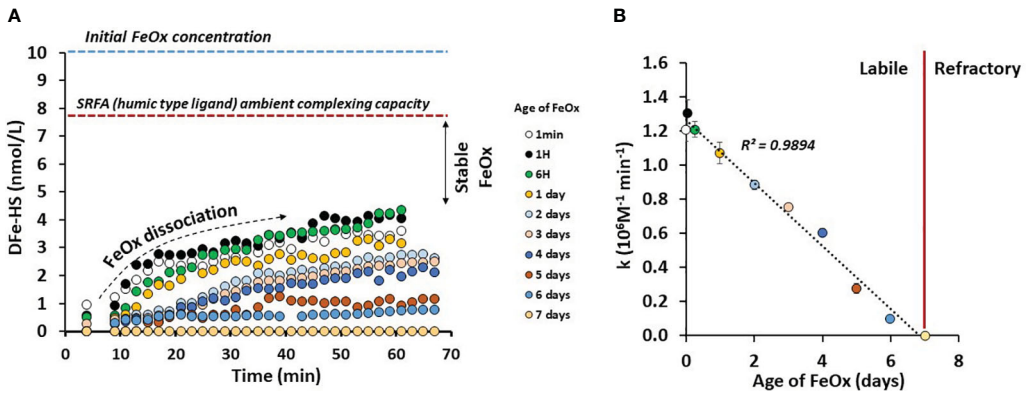

FIGURE 5
(A) [Fe] (nmol kg^{-1}) bound by a humic-type ligand (SRFA 1S101F) as a function of time (min) and age of iron oxyhydroxide (FeOx) in artificial seawater. **(B)** Dissolution rate constant of FeOx (k in μM^{-1} min^{-1}) as a function of FeOx ageing. See text for explanations.

2014), however chlorophyll *a* (derived from CTD fluorescence sensor) and L_{FeHS} discrete maxima were not observed at the same depth (see section 4.4). The absence of a significant correlation between chlorophyll *a* and L_{FeHS} in the upper 200 m ($R^2 < 0.1$; $p > 0.75$, n = 91) suggest an indirect pathway for the production of these ligands. The release of DOM during the degradation of phytoplankton material (cell lysis, grazing) in the first hundred meters combined with its microbial and chemical processing (Obernosterer et al., 1999) are the most probable pathway of production for these ligands. This proposed production pathway is in agreement with *in situ* experiments from Whitby et al. (2020a) who showed a release of humic-type ligands during microbial respiration of biogenic particulate organic carbon originating from the oligotrophic Mediterranean waters and from the high nutrient low chlorophyll Southern Ocean waters.

The vertical decrease of L_{FeHS} in the mesopelagic zone (Figures 2A, 3A) reveals the partial degradation of L_{FeHS} during microbial mineralization of DOM. Direct consumption of humics by heterotrophic bacteria reported in several studies (Cottrell and Kirchman, 2000; Coates et al., 2002; Rosenstock et al., 2005) support our observations. The persistence of L_{FeHS} in the deep PDW ($mean_{PDW}$ = 0.43 ± 0.19 nmol eq-Fe L^{-1} n = 34) indicate that part of L_{FeHS}, however, escapes microbial degradation and is refractory. To monitor the effect of microbial mineralization process on L_{FeHS}, we calculated the apparent oxygen utilization (AOU) based on dissolved oxygen concentrations, S, T (all derived from CTD sensors) using Benson and Krause (1984) formula. AOU is the integrated oxygen consumption by heterotrophic bacteria in the breakdown of organic matter. In the study area, mineralization of labile, semi-labile and semi-refractory DOM can be tracked by the linear decrease of DOC concentration (i.e. proxy of DOM) with increasing AOU down to ~100 µM ($R^2 > 0.57$; $p < 0.05$; n = 133; Figure 6B). At AOU > 100 µmol O_2 kg^{-1}, DOC concentrations were relatively homogenous (~ 37 µM) indicating that DOC was mostly refractory to microbial respiration. A plot of L_{FeHS} against AOU also reveals a decrease of humic-type ligand concentration during the mineralization process (Figure 6B). Down to an AOU of 100 µmol O_2 kg^{-1} the decrease of L_{FeHS} was likely driven by a power law ($R^2 > 0.42$; $p < 0.05$; n =133) rather than by direct linear regression. At AOU > 100 µmol O_2 kg^{-1}, L_{FeHS} seems to increase with increasing AOU (Figure 6A) but the correlation was not significant ($R^2 < 0.05$; p > 0.05; n = 75). A weak but significant correlation between L_{FeHS} and DOC for AOU > 100 µmol O_2 kg^{-1} (Figure 6C; $R^2 > 0.25$; $p < 0.05$; n = 133) was observed indicating that L_{FeHS} cannot be modeled accurately through an empirical equation based on DOC. The weak correlation between L_{FeHS} and DOC was expected due to the intrinsec difference between both parameters. On the one hand,DOC consists of a broad pool of molecules that undergo both respiration-driven losses and gradual conversion into refractory compounds (Figure 6B). On the other hand, L_{FeHS} represents a more specific property (binding sites) of DOM that is primarily lost through microbial turnover (Fourrier et al., 2022).

The contribution of L_{FeHS} to L_{Fe} in our study (2% to 51%, Figure 2) is lower compared to the findings of Whitby et al. (2020b) (23-58%) in the North Atlantic Ocean. This disparity can be attributed to both geographical and methodological differences. Whitby et al. (2020b) studied samples from the North Atlantic Ocean, where the presence of terrestrial influence (and the associated humic substances) could potentially lead to high concentrations of L_{FeHS}. In contrast, the study area of the WTSP lacks terrestrial influence, resulting in the absence of a terrigenous component and lower concentrations of L_{FeHS} than in the Atlantic. Furthermore, our study used SA as the competing ligand for L_{Fe} titration, while Whitby et al. (2020b) used 2-(2-Thiazolylazo)-p-cresol (TAC). It is important to note that TAC may not fully capture the contribution of humic-type ligands (as highlighted by Laglera

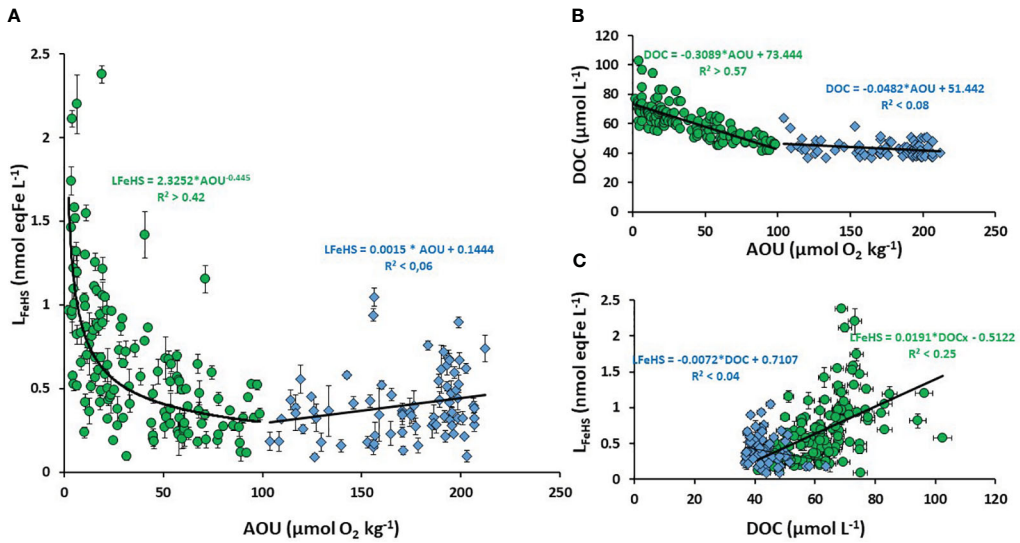

FIGURE 6
Scatter plot of **(A)** Humic type ligand (L_{FeHS}) versus apparent oxygen utilization (AOU); **(B)** Dissolved organic carbon (DOC) versus AOU; **(C)** L_{FeHS} versus DOC. The dataset was separated between low AOU (< 100 µmol O2 kg^{-1}, green dots) and high AOU (> 100 µmol O2 kg^{-1}, blue triangles). Associated correlations are indicated.

et al., 2011 and Slagter et al., 2019). Therefore, the values reported by Whitby et al. (2020b) might represent the minimum concentration of the ligand pool, underestimating the actual presence of humic substances. These factors account for the higher L_{FeHS} contribution reported by Whitby et al. (2020b) in the North Atlantic compared to our study.

4.2 Classification of L_{FeHS} and iron speciation within L_{FeHS} in the western Pacific Ocean

The L_{FeHS} concentrations measured during this study were lower than the total iron binding ligand (L_{Fe}) concentration measured by CLE-CSV (Figure 2). Over the 103 common samples analyzed by CLE-CSV and L_{FeHS}, the mean log $K^{cond}_{FeL,Fe'}$ was 11.6 ± 0.4 ranging from 10.5 ± 0.2 to 12.7 ± 0.3. According to the classification defined by Gledhill and Buck (2012), 84% of samples fall in the L_2 class, 13% in the L_1 class, and 4% in the L_3 class (Mahieu et al., this issue). This result clearly indicate that intermediate class ligands (L_2) dominated the pool of L_{Fe} all along the water column in our study area. This is in agreement with the previous datasets reported by Buck et al. (2018) and Cabanes et al. (2020) in the oligotrophic South Pacific Ocean. Cabanes et al. (2020) also measured L_{FeHS}, and showed that the weakest class of ligand (log $K^{cond}_{FeL,Fe'}$ < 11) observed was associated with the lowest humic-type ligand concentration. All these observations indicate that the L_{FeHS} measured here are ligands of intermediate strength (L_2 type). However, classifying based on log $K^{cond}_{FeL,Fe'}$ does not capture the heterogeneity of binding sites for non-discrete ligands like L_{FeHS}. To mitigate biases introduced by CLE-CSV, it is preferable to use αFeL(Fe') (reactivity coefficients) for studying the nature of LFe (Gledhill and Gerringa, 2017).

To study the nature in term of strength of L_{FeHS}, we conducted competitive ligand experiments for Fe complexation between ambient natural ligand including L_{FeHS} and Gallic Acid (GA) to study the mobility of Fe and its speciation within the Fe-humic complex. According to the only available published data from González et al. (2019), GA in seawater is a weak Fe ligand (log K_{FeGA} = 9.1) with a binding capacity of 2.75 nmol eq-Fe nmol GA^{-1}. We choose this ligand for two reasons. Firstly, GA is a polyphenolic compound with a carboxylate moiety. Phenolic and carboxylates are thought to be the moieties involved in the formation of the Fe-humic complex (Garnier et al., 2004; Hassler et al., 2019). GA is thus a good candidate to compare the affinity of Fe for humic substances with these moieties. Secondly, GA reduces Fe(III) into Fe(II) with time (González et al., 2019; Pérez-Almeida et al., 2022). The affinity of marine humic type ligand for Fe(II) can then be studied after i) the saturation of GA with Fe, ii) equilibrium to allow the reduction of Fe(III) into Fe(II) by GA, and competition ligand experiment.

The sample used for this experiment has an initial DFe concentration of 0.45 ± 0.01 nmol L^{-1}; L_{Fe} was 4.8 ± 0.5 nmol eq-Fe L^{-1} with an associated log $K^{cond}_{FeL,Fe'}$ of 11.8 ± 0.4 (Mahieu et al., this issue). L_{FeHS} was estimated at 1.52 ± 0.02 nmol eq-Fe L^{-1}, 32% of L_{Fe}. The initial DFe-HS was 0.18 nmol L^{-1}. If we consider all DFe to be labile for organic complexation, the initial conditions of the experiment can be described as follows: (i) L_{Fe}' and L_{FeHS}' were respectively 4.3 and 1.34 nmol eq-Fe L^{-1}, (ii) 0.27 nmol L^{-1} DFe were complexed by non-humic L_{Fe} and (iii) the log αFeL(Fe′) (e.g. side reaction coefficient) was 3.4. A first experiment consisted of the addition of 1.6 nmol L^{-1} of Fe to the sample. After 20 h of equilibration, DFe-HS reached 1.50 ± 0.05 nmol L^{-1} thereby L_{FeHS} were at saturation. Considering the ambient L_{Fe} concentration of the sample, determined by CLE-ASV, our results demonstrate that the Fe added went primarily into L_{FeHS}. CLE-ACSV analysis only provides an average lo $K^{cond}_{FeL,Fe'}$ g of the ligand pool (captured by the detection window of the method) but the L_{Fe} pool is composed of a wide variety of organic compounds with different log $K^{cond}_{FeL,Fe'}$ (Town and Filella, 2000). The log $K^{cond}_{FeL,Fe'}$ of 11.8 ± 0.4 measured for the sample studied is an average of the ligand pool that is composed of ligands and binding sites with both higher and lower strength than this average value.

Considering the initial conditions, it can be inferred that approximately 0.43 nmol eq-Fe L^{-1} of the L_{Fe} pool, including 0.18 nmol eq-Fe L^{-1} of L_{FeHS}, have log αFeL(Fe') values higher than 3.4, indicating the potential presence of L_1 type binding sites (estimated mean log $K^{cond}_{FeL,Fe'} \geq 12.8$). Since the addition of DFe initially fills the remaining free sites of L_{FeHS}, our results suggest that the log αFeL_{FeHS}(Fe') values for the binding sites in L_{FeHS} that were not initially filled with DFe are at least equal to 3.4 (estimated mean log $K^{cond}_{FeL,Fe'} \geq 12.3$). Based on the initial conditions and the results of our experiment, a distribution of binding site density within the L_{FeHS} pool can be inferred. L_{FeHS} comprises a small portion (12%) of sites with high affinity (L_1 type) that can outcompete strong discrete ligands, while the majority (88%) of sites fall into the L_2 type category, likely at the higher end of the strength scale associated with L_2 type sites. The remaining 3 nmol eq-Fe L^{-1} of the L_{Fe} pool may be considered as weaker ligands compared to L_{FeHS}. Our findings are consistent with the results reported by Gledhill et al., 2022, who demonstrated that the heterogeneity of binding sites in humic-like DOM enables humic substances to outcompete siderophores at low iron concentrations.

In a second experiment, Fe-free GA was added but the response of DFe-HS was unchanged, showing that the Fe cannot be dissociated from the Fe-humic complex by 2 nmol L^{-1} of GA (L_{FeGA} = 5.5 nmol eq-Fe.L^{-1}) at a pH of 8.0 (Figure 7). This demonstrate that the affinity of L_{FeHS} for Fe is higher than $10^{9.1}$ and that polyphenolic and carboxylate moieties of GA cannot outcompete those involved in the complexation of Fe in L_{FeHS} even at higher GA ligand concentration. This experiment confirms that surface L_{FeHS} in the WTSP are, at least, ligands of intermediate strength.

In a third experiment, 2 nmol L^{-1} of GA saturated with Fe were put in contact with unsaturated L_{FeHS} (Figure 7). After 20 h of equilibration, L_{FeHS} were able to dissociate partly Fe from the Fe-GA complex. However L_{FeHS} but did not reach saturation even with an addition of 5.5 nM of DFe bound to GA (e.g. 5.5 nmol eq Fe L^{-1} for 2 nmol L^{-1} GA; González et al., 2019). Using equations (2) to (8), this scenario allows to calculate the apparent stability constant of L_{FeHS} in the condition of the experiment (20°C, pH = 8, 20h of competition). A value of $\log K_{LFeHS}$ = 8.5 ± 0.2 was obtained, much

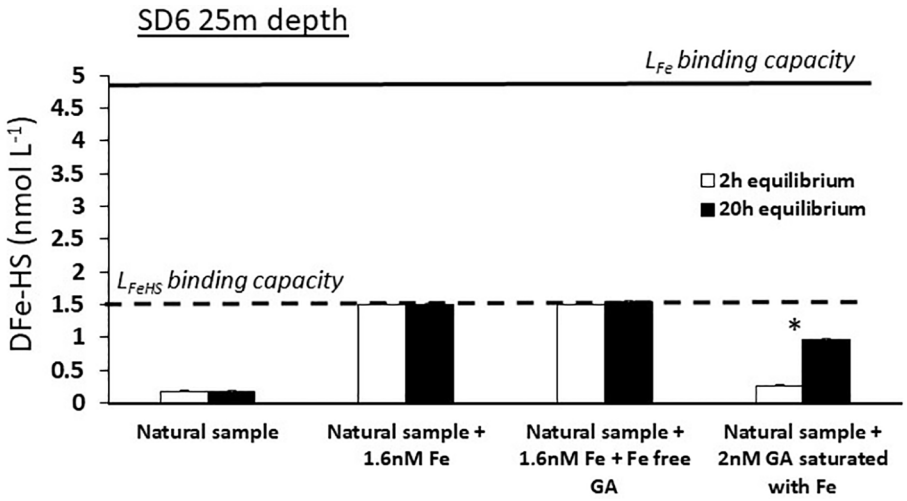

FIGURE 7
Monitoring of dissolved iron complexed by humic type ligand concentration (DFe-HS) before (white bars) and after(dark bars) overnight equilibration between natural ambient iron-binding ligands (L_{Fe}), humic-type ligands (L_{FeHS}) and Gallic Acid (GA) for a surface sample with oligotrophic conditions (SD 6, 25 m depth). Solid and dashed line indicate the iron binding capacity of the ambient L_{Fe} and L_{FeHS}. * indicates a significant difference between initial and final DFe-HS concentrations. Absence of iron saturation of L_{FeHS} in experiments c and c' and no changes in DFe-HS in experiments d and d' indicate the instability of Fe(II)-humic ligand complexes and that Fe(III)-humic complexes are of higher stability than Fe-GA complexes. See text for explanation.

lower than expected from the first two experiments. There are various possibilities to explain these apparent differences:

i) the third experiment was not at equilibrium and the reaction need to be longer than 20h; this hypothesis was disproved by running a similar experiment but with 36h equilibration time; same results were obtained. ii) The Fe-humic complex is metastable and cannot be dissociated even by a stronger ligand; this is unlikely from previous experiments conducted by Laglera et al. (2019) who demonstrated that desferrioxamine B (strong ligand) and EDTA (weak ligand) can both dissociate Fe from a natural Fe-humic complex when their concentrations are sufficiently high. iii) GA partially reduced Fe(III) to Fe(II), because the latter has higher affinity for GA and non-humic L_{Fe} than Fe(III) has for L_{FeHS}, resulting in an apparent lower log $K'^{cond}_{FeL,Fe}$. The pH dependence of the Fe-humic reduction peak potential (increasing peak potential E_{peak} with decreasing pH) observed by Laglera et al. (2007) provide further perspectives for interpretation iii). Their observations indicate that the stability of the Fe-humic complex decreases with decreasing pH. An increasing proportion of Fe(II) at lower pH can explain this shift of E_{peak} with pH, since Fe (II)-humic complexes have lower stabilities compared to Fe(III)-humic complexes (Rose and Waite, 2003a; Blazevic et al., 2016). Based on our experiments and the studies mentioned above, we suggest here that a Fe-humic complex is only stable in seawater with Fe(III). It can be further hypothesized that to form an Fe-GA complex stable in seawater, Fe should be under Fe(II) in the Fe-GA complex. These conclusions have broader implications for the fate of Fe in environments with low pH and changing redox conditions, such as low oxygenated margins and hydrothermal environments (as observed at LD5 T5, Figure S4), or where photoreduction of Fe is enhanced (e.g. clear subtropical waters).

4.3 The role of L_{FeHS} in the stabilization of hydrothermal DFe

The kinetic monitoring of FeOx dissolution by L_{FeHS} demonstrates that the age of FeOx is a main factor controlling their dissolution rate (Figure 5). The experiment we conducted shows that recently formed FeOx are very labile but become gradually refractory to dissolution by L_{FeHS} with time; the studied model humic-type ligand was not able to solubilize FeOx aged one week or more (Figure 5). A similar effect of ageing on the solubilization of FeOx was observed for desferoxiamine B (Rose and Waite, 2003b) with a nearly 50 times decrease of the dissolution rate constant after a week of FeOx maturation. Our results are also in line with those of Krachler et al. (2015) who observed a rapid dissolution of newly formed FeOx by a set of L_{FeHS} and experiments by Tani et al. (2003) that correlated the solubilization of newly formed FeOx with humic-like fluorescence in seawater. In contrast, Kuma et al. (1996) did not see such a strong effect of age on FeOx solubility probably due to inherent differences in methodologies. They added FeOx in natural seawater and followed their solubility over time, which is equivalent to studying the stability of organically complexed DFe originating from the dissolution of newly formed FeOx.

In hydrothermal environments, most DFe is released under the form of soluble Fe(II). The fraction of DFe that escapes precipitation of sulfide minerals (e.g. pyrite, chalcopyrite) is then gradually oxidized and forms insoluble Fe (III) oxyhydroxides species (FeOx) both under colloidal and particulate form (Lough et al., 2019; Cotte et al., 2020; Hoffman et al., 2020). Recent studies highlight the high proportion of colloidal DFe in hydrothermal plume at dozens to hundreds of kilometers from the vent (Tagliabue

et al., 2022; Lough et al., 2023). However the persistence of DFe plumes at great distances from deep vents is often explained by its initial stabilization under an organic form (Sander and Koschinsky, 2011; Hawkes et al., 2013; Wang et al., 2021; Wang et al., 2022). In the first stage of hydrothermal mixing, DFe occurs essentially as Fe (II) species (Waeles et al., 2017). With Fe(II) having low affinity for L_{FeHS}, (Figure 7; Rose and Waite, 2003a), the pathway of Fe-HS formation in hydrothermal plumes requires the oxidation of Fe(II) to Fe(III), through the formation of colloidal Fe oxides species that may be partly dissolved by L_{FeHS}. Our experiments strongly suggest that dissolution of FeOx by humic-type ligands is only possible during the first hours or days after precipitation (Figure 5). Ligand concentration is not the only factor controlling the solubility of FeOx as shown by our lab experiments and field observations (unsaturated L_{FeHS} in the presence of high DFe concentrations, Figure 4). Therefore, the kinetics of the plume dispersion must be taken into account when studying the organic complexation of hydrothermal Fe. The persistence within the DFe fraction of colloidal FeOx observed in the widespread hydrothermal plume of the Pacific Equatorial Ridge (Fitzsimmons et al., 2017) is in agreement with our observations and support our conclusions. It is worth noting that our dissolution experiments were achieved in UV digested artificial seawater, neglecting key parameters of the hydrothermal environment (e.g. pH, O_2, pressure, temperature, DOC, sulfide, other trace metals) that may impact the nature, concentrations, kinetics of formation, stability and transport of these Fe colloidal species. For instance, the composition of the fluid, dissolved O_2 concentrations, pH, temperature and local currents driving plume dilution are parameters to be considered for Fe oxidation and mineral formation (Byrne et al., 2000; Field and Sherrell, 2000; Shaw et al., 2021; Tilliette et al., 2022). Although not representative of the natural hydrothermal system, our dissolution kinetics experiments provide valuable insights into the processes involved.

At LD5, we observed that L_{FeHS} stabilized a very small fraction of the DFe released by the hydrothermal vent (Figure 4) keeping unsaturated L_{FeHS} in the presence of high DFe (~50 nmol L^{-1}). This inability of L_{FeHS} to complex DFe released at LD5-T5 might be due to the low pH (< 6.5) and low O_2 (< 160 µM) values at this site, resulting in a seawater relatively acidic and suboxic (Tilliette et al., 2022; Figure S4). Under these conditions, a significant fraction of Fe (II) may persist which has low affinity for L_{FeHS}. In addition, the fraction of DFe stabilized by L_{FeHS} increased from 1 to 5.5% between substations T5 and T4 while a majority (78%) of the DFe released precipitated in the first 600 m (Tilliette et al., 2022). During its dispersion in shallow waters, the plume is rapidly diluted with more alkaline, more oxygenated and warmer seawater that will favor the formation of FeOx species (Figure S4). This newly formed FeOx may be dissolved by L_{FeHS} (Figure 5) at a rate that is at least dependent on the age of these FeOx as well as the concentration of Fe-free L_{FeHS} (Figure 5) and certainly on many other parameters (concentration of particles, concentration of other dissolved metals, DOC, plume dispersion, etc). It is worth noting that pH and temperature play crucial roles in iron organic complexation and FeOx formation (Byrne et al., 2020; Ye et al., 2020; Zhu et al., 2021). Considering the significant variations in these parameters within hydrothermal environments (Figure S4), it is recommended to design further experiments to gain a better understanding of the impact of pH and temperature on the dissolution of FeOx by L_{FeHS}.

4.4 Bioavailability of DFe-HS and stabilization of DFe by L_{FeHS} in intermediate and deep waters of the WTSP

For data interpretation, samples with DFe concentrations exceeding 2 nnmol L^{-1} were identified as being influenced by the hydrothermal system and were subsequently excluded from the depth horizons discussed in the following sections. In the first 50 m of the water column, above the deep chlorophyll maximum (Above DCM, Chl *a*< 0.075µg L^{-1}), L_{FeHS} was high ($mean_{Above\ DCM}$ L_{FeHS} > 1.2 ± nmol eq-Fe L^{-1} n = 18; Figure 8A) and DFe-HS concentrations were relatively low ($mean_{Above\ DCM}$ DFe-HS = 0.18 ± 0.12 nmol L^{-1} n = 18; Figure 8B) resulting in a low saturation of L_{FeHS} (17 ± 10%, n = 18 Figure 8C). The non-accumulation of DFe in the presence of high L_{FeHS} is in stark contrast with what was observed in the Mediterranean Sea (Dulaquais et al., 2018a) and in the Arctic waters (Laglera et al., 2019). This observation suggests that, in the surface water of the WTSP, DFe can be dissociated from the humic complex, becoming available for surface reaction (e.g. scavenging) or biological uptake. It is not clear from our data if DFe is directly removed from the humic complex or if photoreduction of Fe within the complex via ligand-to-metal charge transfer leads to the production of Fe(II) with low affinity for L_{FeHS} (Figure 5; Barbeau, 2006; Blazevic et al., 2016). An additional process explaining the non-accumulation of DFe within L_{FeHS} in surface could be the presence of DFe under a colloidal fraction that is not available for complexation with L_{FeHS}. Colloidal DFe can represent a large fraction of DFe in surface waters of the Pacific ocean (Wu et al., 2001). It is considered poorly bioavailable (Rich and Morel, 1990; Chen and Wang, 2001; Wang and Dei, 2003) but prone to scavenging, limiting its accumulation in surface waters (Kunde et al., 2019). Below 50 m depth, a clear and significant (p< 0.05) depletion of DFe-HS in the deep chlorophyll maximum (DCM, Chl *a* > 0.1 µg L^{-1}) over the entire section was observed ($mean_{DCM}$ DFe-HS = 0.11 ± 0.08 nmol L^{-1} n = 49; Figure 8). These very low DFe-HS concentrations clearly indicate that when complexed to L_{FeHS}, DFe is bioavailable for phytoplankton. However, it is unclear if phytoplankton cells can directly uptake Fe from the humic complex, if phytoplankton species produce specific ligands to outcompete L_{FeHS} (e.g. EPS, siderophores) or if Fe uptake by the cell is due to remineralisation of the humic-complex (Figure 8). Hassler et al. (2019) classify the model L_{FeHS} SRFA as a source of bioavailable Fe for a set of phytoplankton species but this has not yet been shown, and laboratory culture experiments should be designed to address these questions of DFe-HS bioavailability that could also arise from the dissociation of DFe-HS, as inorganic DFe is continuously assimilated.

Below the DCM (Below DCM, Chl *a*< 0.075 µg L^{-1}; depth > 100m), DFe-HS concentrations was stable ($mean_{Below\ DCM}$ DFe-HS = 0.15 ± 0.12 nmol L^{-1} n = 38; Figure 8B) and significant (p< 0.05)

10.3389/fmars.2023.1219594

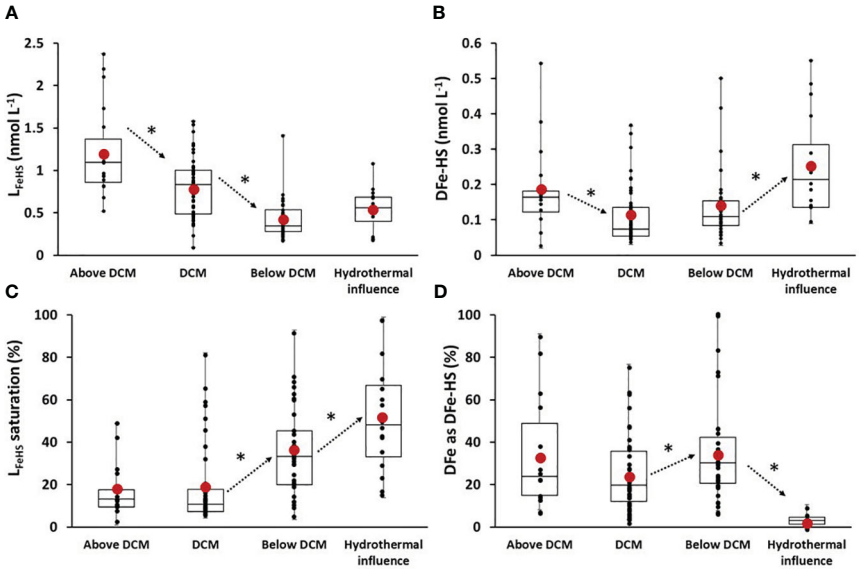

FIGURE 8
Box and whisker plot of **(A)** associated iron binding ligands of humic nature (L_{FeHS} in nmol eq-Fe L^{-1}); **(B)** iron effectively associated with L_{FeHS} (DFe-HS in nmol eq-Fe L^{-1}); **(C)** L_{FeHS} saturation state (%); **(D)** Percentage of DFe under DFe-HS (%) along the section for 4 specific depths clusters of sample: above the deep chlorophyll maximum (above DCM), the deep Chlorophyll maximum (DCM), below the deep chlorophyll maximum and for samples influenced by hydrothermalism. Black dots represent discrete data. Red dots indicate the mean value of data. * and arrows indicate significance and way of variation between two close depth horizons. Significance were tested using Wilcoxon-Mann Whtiney tests and set for 95% of confidence ($p < 0.05$) determined by Wilcoxon-Mann Whtiney test.

increase of L_{FeHS} saturation index (Figure 8C) indicate a stabilization of DFe by L_{FeHS} after the remineralization of sinking biomass. The contribution of DFe-HS to DFe also increase at these depths (Figure 8D), with the exception of LD5-T5 and T4 due to high DFe, further showing an increased stabilisation of DFe by L_{FeHS}. It suggests that Fe binding sites of L_{FeHS} can outcompete Fe adsorption during the mineralization of particulate Fe (e.g. scavenging). This observation is in line with the work of Whitby et al. (2020b) that suggest L_{FeHS} concentration as the upper limit on how much remineralized Fe can be stabilized in the dissolved fraction. As discussed previously in Section 5.3, samples impacted by hydrothermalism exhibit notably higher DFe-HS concentrations ($mean_{hydrothermal\ influence}$ = 0.25 ± 0.11 n = 16) and L_{FeHS} saturation levels ($mean_{hydrothermal\ influence}$ = 52 ± 27% n = 16). However, due to the elevated DFe concentrations, the contribution of DFe-HS to total DFe decreases significantly (5 ± 3%, n = 16), and no significant difference in L_{FeHS} was observed between samples below the DCM and those influenced by hydrothermalism ($p > 0.05$).

Deeper, DFe-HS increased gradually to reach 0.35 nmol L^{-1} in the PDW composite with DFe-HS accounting for 56% of the total DFe in the abyssal waters (deeper than 2000 m; Figure 3). These results show for the first time that a significant part of DFe is complexed by humic type ligands throughout the water column of the oligotrophic Pacific Ocean and lead to new interpretations for Fe-humic interactions.

Rather constant concentrations of DFe-HS in the deep waters (0.2-0.35 nmol L^{-1} deeper than 1500 m, n = 27) suggest that DFe complexed by L_{FeHS} is stable. In the deep ocean, L_{FeHS} protect DFe from scavenging and contribute to increasing DFe residence time, as previously suggested for L_2 type ligands (Hunter and Boyd, 2007). The water-masses encountered at these depths (Figure 1) fill the entire Pacific Ocean. It can be further hypothesized that this deep, stable pool of DFe-HS can fertilize the euphotic layer with bioavailable DFe when it is upwelled to the surface by mesoscale structures in the equatorial area (Hawco et al., 2021) or by deep-ocean ventilation (Tagliabue et al., 2010) in high nutrient low chlorophyll zones.

The co-existence of unsaturated L_{FeHS} and of a DFe pool not complexed to these ligands (Figure 3) indicates that part of DFe escapes L_{FeHS} complexation. At least three hypotheses can be suggested: i) stronger binding sites than those of L_{FeHS} exist within L_{Fe} pool (L_1 type binding sites); ii) other metals fill the binding sites of humic-type ligands (e.g. copper) or/and iii) Fe is in a chemical form (speciation) unavailable for L_{FeHS} complexation. CLE-CSV analyses of 103 samples (Figure 2B) reveal that L_2 type ligands were detected in 84% of the samples (Mahieu et al., this issue). Moreover, experiments conducted in this work likely indicate that L_{FeHS} are in the higher range of Fe-binding strengths for L_2 ligands (see section 4.2) but initial DFe only partly filled L_{FeHS} possibly indicating that strong binding sites co-exist with weak sites in the apparent L_2 pool. Therefore, it is unlikely that high concentrations of L_1 outcompete L_{FeHS} for DFe complexation. However, the presence of L_1-type binding sites at sub-nanomolar concentrations within the diverse pool of heterogeneous ligands can be considered. Humic-type ligands can bind many other metals including dissolved copper (DCu); humics can have similar binding strength for DFe and DCu in seawater leading to competition for humic complexation between these two elements (Abualhaija et al., 2015). Because DCu is accumulated in the deep Pacific Ocean (Ruacho et al., 2020) at higher concentrations than DFe (Buck et al.,

2018), competition probably takes place,promoting the complexation of DCu over DFe by humic-type ligands in this basin.

The speciation of Fe could also partly explain the apparent undersaturation of humic ligands. A recent study conducted by González-Santana et al. (2023) brought attention to the potential underestimation of Fe(II) and its contribution to the dissolved iron (DFe) pool, suggesting that it may account for around 20% of the total DFe. The unsaturation of L_{FeHS} could be attributed to the limited ability of these ligands to form stable complexes with Fe(II). In addition several studies have shown that a significant fraction (up to 50%) of oceanic DFe is present under colloidal form (cFe > 0.02 µm; Nishioka et al., 2001; Wu et al., 2001; Boye et al., 2010; Fitzsimmons and Boyle, 2014; Kunde et al., 2019). Existence of aged colloidal FeOx (Von der Heyden et al., 2012) refractory to L_{FeHS} complexation (Figure 5) is likely to explain the inability of L_{FeHS} to access to DFe. Nevertheless, the evidence for L_{Fe} exceeding cFe (Boye et al., 2010; Fitzsimmons et al., 2015) suggest that cFe is predominantly organic in open ocean waters. The size fractionation becomes a relevant question since marine humic type substances are of low molecular weight (< 10 kDa; Batchelli et al., 2010; Dulaquais et al., 2020; Fourrier et al., 2022) and can pass through the 0.02 µm membrane usually used to operationally separate DFe into the soluble and the colloidal fractions. Because marine soluble ligands have a similar or higher binding strength than colloidal ones (Boye et al., 2010; Fitzsimmons et al., 2015), the occurrence of unsaturated L_{FeHS} we observed can be interpreted as a physical limitation of this ligand type to access colloidal DFe of high molecular weight (0.02-0.45 µm).

5 Conclusions

This study confirms that L_{FeHS} are heterogenous ligands. The Fe binding strength of L_{FeHS} was not directly measured but lab experiments suggest a distribution of binding sites comprising 10% of L_1 type (log $K^{cond}_{FeL,Fe'}$ > 12.8) and 90% of L_2 type site that are in the higher range of the log $K^{cond}_{FeL,Fe'}$ values recognised for L_2 type site (up to 12). L_{FeHS} are primarily produced in the euphotic layer and mineralized during water mass ageing, encompassing partial recalcitrance throughout the water column. These characteristics lead to a complexation of ~30% of total DFe over the transect studied (n = 186) with a higher percentage of complexation in the deepest waters of the Pacific Ocean (~56% of DFe complexed by humic ligands at depths deeper than 2000 m). In this study, we provided field data evidencing the bioavailability of Fe under Fe-HS form in the deep Chlorophyll maximum. Our data also demonstrate the stabilization of Fe in the dissolved phase by L_{FeHS} after biomass remineralization in the mesopelagic waters. We however observed that part of DFe is not accessible to $L_{FeHS,}$ which remain unsaturated. This may result from the inability of L_{FeHS}, predominantly found in the soluble fraction, to access colloidal DFe. In the vicinity of the active shallow hydrothermal sources studied, the low stabilization yield (1 to 5.5% of total DFe) and the presence of unsaturated L_{FeHS} concomitant with high DFe concentrations (~50 nmol L^{-1}) lead to the assumption of an inaccessibility of Fe(II) and FeOx species to L_{FeHS}. To support this hypothesis, complexation with Fe(II) and dissolution experiments of FeOx were conducted. We conclude Fe(II) has low affinity for L_{FeHS} and that only one week is necessary to make FeOx totally refractory to L_{FeHS} dissolution. Our work suggests inorganic Fe speciation and the kinetics of shallow hydrothermal plume dispersion must be considered in future studies attempting to close the hydrothermal Fe budget.

Data availability statement

The raw data supporting the conclusions of this article will be made available by the authors, without undue reservation.

Author contributions

GD: Conceptualization, Methodology, Investigation, Data curation, Formal Analysis, Data visualization, Writing – original draft, Writing – review & editing, Supervision, Project administration; PF: Data acquisition, Methodology, Data visualization, Writing – original draft, Writing – review & editing. CG: Project administration, Writing – review & editing; LM: Data acquisition, Writing – review & editing; RR: Writing – review & editing; CT: Data acquisition, Writing – review & editing; PS: Writing – review & editing; HW: Writing – review & editing. All authors contributed to the article and approved the submitted version.

Funding

This work is a part of the BioDOMPO project (Biogeochemistry of dissolved organic matter in the Pacific Ocean, PI GD) funded by CNRS LEFE-CYBER, ISBlue and Région Bretagne and funded by the TGIRFlotte Océanographique Française, the A-MIDeX of the Aix-Marseille University, the LEFE-CYBER and GMMC program and the ANR.

Acknowledgments

This work was performed in the framework of the TONGA project (TONGA expedition GEOTRACES GPpr14 November2019, https://doi.org/10.17600/18000884) managed by the LOV(C. Guieu) and the MIO (S. Bonnet). Figures were made using ODV (Schlitzer, 2016). We warmly thank the captain, and the crew of the R/V L'Atalante andall the scientists for their cooperative work at sea during theTONGA expedition.

Conflict of interest

The authors declare that the research was conducted in the absence of any commercial or financial relationships that could be construed as a potential conflict of interest.

Publisher's note

All claims expressed in this article are solely those of the authors and do not necessarily represent those of their affiliated organizations, or those of the publisher, the editors and the reviewers. Any product that may be evaluated in this article, or claim that may be made by its manufacturer, is not guaranteed or endorsed by the publisher.

Supplementary material

The Supplementary Material for this article can be found online at: https://www.frontiersin.org/articles/10.3389/fmars.2023.1219594/full#supplementary-material

References

Abualhaija, M. M., and van den Berg, C. M. (2014). Chemical speciation of iron in seawater using catalytic cathodic stripping voltammetry with ligand competition against salicylaldoxime. *Mar. Chem.* 164, 60–74. doi: 10.1016/j.marchem.2014.06.005

Abualhaija, M. M., Whitby, H., and van den Berg, C. M. (2015). Competition between copper and iron for humic ligands in estuarine waters. *Mar. Chem.* 172, 46–56. doi: 10.1016/j.marchem.2015.03.010

Barbeau, K. (2006). Photochemistry of organic iron (III) complexing ligands in oceanic systems. *Photochem. Photobiol.* 82 (6), 1505–1516. doi: 10.1111/j.1751-1097.2006.tb09806.x

Batchelli, S., Muller, F. L., Chang, K. C., and Lee, C. L. (2010). Evidence for strong but dynamic iron– humic colloidal associations in humic-rich coastal waters. *Environ. Sci. Technol.* 44 (22), 8485–8490. doi: 10.1021/es101081c

Benner, R. (2011). Loose ligands and available iron in the ocean. *Proc. Natl. Acad. Sci.* 108 (3), 893–894. doi: 10.1073/pnas.1018163108

Benson, B. B., and Krause, D.Jr. (1984). The concentration and isotopic fractionation of oxygen dissolved in freshwater and seawater in equilibrium with the atmosphere 1. *Limnol. Oceanogr.* 29 (3), 620–632. doi: 10.4319/lo.1984.29.3.0620

Blazevic, A., Orlowska, E., Kandioller, W., Jirsa, F., Keppler, B. K., Tafili-Kryeziu, M., et al. (2016). Photoreduction of terrigenous Fe-humic substances leads to bioavailable iron in oceans. *Angew. Chem.* 128 (22), 6527–6532. doi: 10.1002/ange.201600852

Boggs, S. Jr., Livermore, D., and Seitz, M. G. (1985). *Humic substances in natural waters and their complexation with trace metals and radionuclides: a review [129 references].* United States. doi: 10.2172/5569909

Boiteau, R. M., and Repeta, D. J. (2015). An extended siderophore suite from synechococcus sp. PCC 7002 revealed by LC-ICPMS-ESIMS. *Metallomics* 7 (5), 877–884. doi: 10.1039/c5mt00005j

Bonnet, S., Guieu, C., Taillandier, V., Boulart, C., Bouruet-Aubertot, P., Gazeau, F., et al. (2023). Natural iron fertilization by shallow hydrothermal sources fuels diazotroph blooms in the ocean. *Science* 380, 812-817. doi: 10.1126/science.abq4654

Boye, M., Nishioka, J., Croot, P., Laan, P., Timmermans, K. R., Strass, V. H., et al. (2010). Significant portion of dissolved organic Fe complexes in fact is Fe colloids. *Mar. Chem.* 122 (1-4), 20–27. doi: 10.1016/j.marchem.2010.09.001

Buck, K. N., Lohan, M. C., Berger, C. J., and Bruland, K. W. (2007). Dissolved iron speciation in two distinct river plumes and an estuary: Implications for riverine iron supply. *Limnol. Oceanogr.* 52 (2), 843–855. doi: 10.4319/lo.2007.52.2.0843

Buck, K. N., Sedwick, P. N., Sohst, B., and Carlson, C. A. (2018). Organic complexation of iron in the eastern tropical South Pacific: results from US GEOTRACES Eastern Pacific Zonal Transect (GEOTRACES cruise GP16). *Mar. Chem.* 201, 229–241. doi: 10.1016/j.marchem.2017.11.007

Bundy, R. M., Abdulla, H. A., Hatcher, P. G., Biller, D. V., Buck, K. N., and Barbeau, K. A. (2015). Iron-binding ligands and humic substances in the San Francisco Bay estuary and estuarine-influenced shelf regions of coastal California. *Mar. Chem.* 173, 183–194. doi: 10.1016/j.marchem.2014.11.005

Bundy, R. M., Biller, D. V., Buck, K. N., Bruland, K. W., and Barbeau, K. A. (2014). Distinct pools of dissolved iron-binding ligands in the surface and benthic boundary layer of the California Current. *Limnol. Oceanogr.* 59 (3), 769–787. doi: 10.4319/lo.2014.59.3.0769

Bundy, R. M., Boiteau, R. M., McLean, C., Turk-Kubo, K. A., McIlvin, M. R., Saito, M. A., et al. (2018). Distinct siderophores contribute to iron cycling in the mesopelagic at station ALOHA. *Front. Mar. Sci.* 5. doi: 10.3389/fmars.2018.00061

Byrne, R. H., Luo, Y. R., and Young, R. W. (2000). Iron hydrolysis and solubility revisited: observations and comments on iron hydrolysis characterizations. *Mar. Chem.* 70 (1-3), 23–35. doi: 10.1016/S0304-4203(00)00012-8

Cabanes, D. J., Norman, L., Bowie, A. R., Strmečki, S., and Hassler, C. S. (2020). Electrochemical evaluation of iron-binding ligands along the Australian GEOTRACES southwestern Pacific section (GP13). *Mar. Chem.* 219, 103736. doi: 10.1016/j.marchem.2019.103736

Chen, M., and Wang, W. X. (2001). Bioavailability of natural colloid-bound iron to marine plankton: Influences of colloidal size and aging. *Limnol. Oceanogr.* 46 (8), 1956–1967. doi: 10.4319/lo.2001.46.8.1956

Coates, J. D., Cole, K. A., Chakraborty, R., O'Connor, S. M., and Achenbach, L. A. (2002). Diversity and ubiquity of bacteria capable of utilizing humic substances as electron donors for anaerobic respiration. *Appl. Environ. Microbiol.* 68 (5), 2445–2452. doi: 10.1128/AEM.68.5.2445-2452.2002

Cotte, L., Chavagnac, V., Pelleter, E., Laës-Huon, A., Cathalot, C., Dulaquais, G., et al. (2020). Metal partitioning after *in situ* filtration at deep-sea vents of the Lucky Strike hydrothermal field (EMSO-Azores, Mid-Atlantic Ridge, 37° N). *Deep Sea Res. Part I: Oceanogr. Res. Papers* 157, 103204. doi: 10.1016/j.dsr.2019.103204

Cottrell, M. T., and Kirchman, D. L. (2000). Natural assemblages of marine proteobacteria and members of the Cytophaga-Flavobacter cluster consuming low- and high-molecular-weight dissolved organic matter. *Appl. Environ. Microbiol.* 66 (4), 1692–1697. doi: 10.1128/AEM.66.4.1692-1697.2000

Croot, P. L., and Heller, M. I. (2012). The importance of kinetics and redox in the biogeochemical cycling of iron in the surface ocean. *Front. Microbiol.* 3. doi: 10.3389/fmicb.2012.00219

Davies, G., and Ghabbour, E. (2003). *Humic substances: Nature's most versatile materials* (New York, USA: Taylor & Francis). doi: 10.4324/9780203487600

De Paolis, F., and Kukkonen, J. (1997). Binding of organic pollutants to humic and fulvic acids: influence of pH and the structure of humic material. *Chemosphere* 34 (8), 1693–1704. doi: 10.1016/S0045-6535(97)00026-X

Dulaquais, G., Breitenstein, J., Waeles, M., Marsac, R., and Riso, R. (2018b). Measuring dissolved organic matter in estuarine and marine waters: size-exclusion chromatography with various detection methods. *Environ. Chem.* 15 (7), 436–449. doi: 10.1071/EN18108

Dulaquais, G., Waeles, M., Breitenstein, J., Knoery, J., and Riso, R. (2020). Links between size fractionation, chemical speciation of dissolved copper and chemical speciation of dissolved organic matter in the Loire estuary. *Environ. Chem.* 17 (5), 385–399. doi: 10.1071/EN19137

Dulaquais, G., Waeles, M., Gerringa, L. J., Middag, R., Rijkenberg, M. J., and Riso, R. (2018a). The biogeochemistry of electroactive humic substances and its connection to iron chemistry in the North East Atlantic and the Western Mediterranean Sea. *J. Geophys. Res.: Oceans* 123 (8), 5481–5499. doi: 10.1029/2018JC014211

Field, M. P., and Sherrell, R. M. (2000). Dissolved and particulate Fe in a hydrothermal plume at 9 45′ N, East Pacific Rise:: Slow Fe (II) oxidation kinetics in Pacific plumes. *Geochim. Cosmochim. Acta* 64 (4), 619–628. doi: 10.1016/S0016-7037(99)00333-6

Fitzsimmons, J. N., and Boyle, E. A. (2014). Both soluble and colloidal iron phases control dissolved iron variability in the tropical North Atlantic Ocean. *Geochim. Cosmochim. Acta* 125, 539–550. doi: 10.1016/j.gca.2013.10.032

Fitzsimmons, J. N., Bundy, R. M., Al-Subiai, S. N., Barbeau, K. A., and Boyle, E. A. (2015). The composition of dissolved iron in the dusty surface ocean: An exploration using size-fractionated iron-binding ligands. *Mar. Chem.* 173, 125–135. doi: 10.1016/j.marchem.2014.09.002

Fitzsimmons, J. N., John, S. G., Marsay, C. M., Hoffman, C. L., Nicholas, S. L., Toner, B. M., et al. (2017). Iron persistence in a distal hydrothermal plume supported by dissolved–particulate exchange. *Nat. Geosci.* 10 (3), 195–201. doi: 10.1038/ngeo2900

Fourrier, P., Dulaquais, G., Guigue, C., Giamarchi, P., Sarthou, G., Whitby, H., et al. (2022). Characterization of the vertical size distribution, composition and chemical properties of dissolved organic matter in the (ultra) oligotrophic Pacific Ocean through a multi-detection approach. *Mar. Chem.* 240, 104068. doi: 10.1016/j.marchem.2021.104068

Garnier, C., Pižeta, I., Mounier, S., Benaım, J. Y., and Branica, M. (2004). Influence of the type of titration and of data treatment methods on metal complexing parameters determination of single and multi-ligand systems measured by stripping voltammetry. *Analytica Chimica Acta* 505 (2), 263–275. doi: 10.1016/j.aca.2003.10.066

Gerringa, L. J., Gledhill, M., Ardiningsih, I., Muntjewerf, N., and Laglera, L. M. (2021). Comparing CLE-AdCSV applications using SA and TAC to determine the fe-binding characteristics of model ligands in seawater. *Biogeosciences* 18 (19), 5265–5289. doi: 10.5194/bg-18-5265-2021

Gerringa, L. J., Rijkenberg, M. J., Thuróczy, C. E., and Maas, L. R. (2014). A critical look at the calculation of the binding characteristics and concentration of iron complexing ligands in seawater with suggested improvements. *Environ. Chem.* 11 (2), 114–136. doi: 10.1071/EN13072

Gledhill, M. (2001). Electrospray ionisation-mass spectrometry of hydroxamate siderophores. *Analyst* 126, 1359–1362. doi: 10.1039/B101268L

Gledhill, M., and Buck, K. N. (2012). The organic complexation of iron in the marine environment: a review. *Front. Microbiol.* 3. doi: 10.3389/fmicb.2012.00069

Gledhill, M., and Gerringa, L. J. A. (2017). The effect of metal concentration on the parameters derived from complexometric titrations of trace elements in seawater—a model study. *Front. Mar. Sci.* 4. doi: 10.3389/fmars.2017.00254

Gledhill, M., and van den Berg, C. M. (1994). Determination of complexation of iron (III) with natural organic complexing ligands in seawater using cathodic stripping voltammetry. *Mar. Chem.* 47 (1), 41–54. doi: 10.1016/0304-4203(94)90012-4

Gledhill, M., Zhu, K., Rusiecka, D., and Achterberg, E. P. (2022). Competitive interactions between microbial siderophores and humic-like binding sites in European shelf sea waters. *Front. Mar. Sci.* 9. doi: 10.3389/FMARS.2022.855009

González, A. G., Cadena-Aizaga, M. I., Sarthou, G., González-Dávila, M., and Santana-Casiano, J. M. (2019). Iron complexation by phenolic ligands in seawater. *Chem. Geol.* 511, 380–388. doi: 10.1016/j.chemgeo.2018.10.017

González-Santana, D., González-Dávila, M., Lohan, M. C., Artigue, L., Planquette, H., Sarthou, G., et al. (2021). Variability in iron (II) oxidation kinetics across diverse hydrothermal sites on the northern Mid Atlantic Ridge. *Geochim. Cosmochim. Acta* 297, 143–157. doi: 10.1016/j.gca.2021.01.013

González-Santana, D., Lough, A. J., Planquette, H., Sarthou, G., Tagliabue, A., and Lohan, M. C. (2023). The unaccounted dissolved iron (II) sink: Insights from dFe (II) concentrations in the deep Atlantic Ocean. *Sci. Total Environ.* 862, 161179. doi: 10.1016/j.scitotenv.2022.161179

Guo, L., Santschi, P. H., and Warnken, K. W. (1995). Dynamics of dissolved organic carbon (DOC) in oceanic environments. *Limnol. Oceanogr.* 40 (8), 1392–1403. doi: 10.4319/lo.1995.40.8.1392

Hassler, C. S., van den Berg, C. M., and Boyd, P. W. (2017). Toward a regional classification to provide a more inclusive examination of the ocean biogeochemistry of iron-binding ligands. *Front. Mar. Sci.* 4. doi: 10.3389/fmars.2017.00019

Hassler, C., Cabanes, D., Blanco-Ameijeiras, S., Sander, S. G., and Benner, R. (2019). Importance of refractory ligands and their photodegradation for iron oceanic inventories and cycling. *Mar. Freshw. Res.* 71 (3), 311–320. doi: 10.1071/MF19213

Hawco, N. J., Barone, B., Church, M. J., Babcock-Adams, L., Repeta, D. J., Wear, E. K., et al. (2021). Iron depletion in the deep chlorophyll maximum: mesoscale eddies as natural iron fertilization experiments. *Global Biogeochem. Cycles* 35 (12), e2021GB007112. doi: 10.1029/2021GB007112

Hawkes, J. A., Connelly, D. P., Gledhill, M., and Achterberg, E. P. (2013). The stabilisation and transportation of dissolved iron from high temperature hydrothermal vent systems. *Earth Planet. Sci. Lett.* 375, 280–290. doi: 10.1016/j.epsl.2013.05.047

Hedges, J. I., Hatcher, P. G., Ertel, J. R., and Meyers-Schulte, K. J. (1992). A comparison of dissolved humic substances from seawater with Amazon River counterparts by 13C-NMR spectrometry. *Geochim. Cosmochim. Acta* 56 (4), 1753–1757. doi: 10.1016/0016-7037(92)90241-A

Hertkorn, N., Benner, R., Frommberger, M., Schmitt-Kopplin, P., Witt, M., Kaiser, K., et al. (2006). Characterization of a major refractory component of marine dissolved organic matter. *Geochim. Cosmochim. Acta* 70 (12), 2990–3010. doi: 10.1016/j.gca.2006.03.021

Hoffman, C. L., Schladweiler, C. S., Seaton, N. C., Nicholas, S. L., Fitzsimmons, J. N., Sherrell, R. M., et al. (2020). Diagnostic morphology and solid-state chemical speciation of hydrothermally derived particulate Fe in a long-range dispersing plume. *ACS Earth Space Chem.* 4 (10), 1831–1842. doi: 10.1021/acsearthspacechem.0c00067

Hunter, K. A., and Boyd, P. W. (2007). Iron-binding ligands and their role in the ocean biogeochemistry of iron. *Environ. Chem.* 4 (4), 221–232. doi: 10.1071/EN07012

Krachler, R., Krachler, R. F., Wallner, G., Hann, S., Laux, M., Recalde, M. F. C., et al. (2015). River-derived humic substances as iron chelators in seawater. *Mar. Chem.* 174, 85–93. doi: 10.1016/j.marchem.2015.05.009

Kuma, K., Nishioka, J., and Matsunaga, K. (1996). Controls on iron (III) hydroxide solubility in seawater: the influence of pH and natural organic chelators. *Limnol. Oceanogr.* 41 (3), 396–407. doi: 10.4319/lo.1996.41.3.0396

Kunde, K., Wyatt, N. J., González-Santana, D., Tagliabue, A., Mahaffey, C., and Lohan, M. C. (2019). Iron distribution in the subtropical North Atlantic: The pivotal role of colloidal iron. *Global Biogeochem. Cycles* 33 (12), 1532–1547. doi: 10.1029/2019GB006326

Laglera, L. M., Battaglia, G., and van den Berg, C. M. (2007). Determination of humic substances in natural waters by cathodic stripping voltammetry of their complexes with iron. *Anal. Chim. Acta* 599 (1), 58–66. doi: 10.1016/j.aca.2007.07.059

Laglera, L. M., Battaglia, G., and van den Berg, C. M. (2011). Effect of humic substances on the iron speciation in natural waters by CLE/CSV. *Mar. Chem.* 127 (1-4), 134–143. doi: 10.1016/j.marchem.2011.09.003

Laglera, L. M., Sukekava, C., Slagter, H. A., Downes, J., Aparicio-Gonzalez, A., and Gerringa, L. J. (2019). First quantification of the controlling role of humic substances in the transport of iron across the surface of the Arctic Ocean. *Environ. Sci. Technol.* 53 (22), 13136–13145. doi: 10.1021/acs.est.9b04240

Laglera, L. M., and van den Berg, C. M. (2009). Evidence for geochemical control of iron by humic substances in seawater. *Limnol. Oceanogr.* 54 (2), 610–619. doi: 10.4319/lo.2009.54.2.0610

Liu, X., and Millero, F. J. (2002). The solubility of iron in seawater. *Mar. Chem.* 77 (1), 43–54. doi: 10.1016/S0304-4203(01)00074-3

Lough, A. J. M., Homoky, W. B., Connelly, D. P., Comer-Warner, S. A., Nakamura, K., Abyaneh, M. K., et al. (2019). Soluble iron conservation and colloidal iron dynamics in a hydrothermal plume. *Chem. Geol.* 511, 225–237. doi: 10.1016/j.chemgeo.2019.01.001

Lough, A. J., Tagliabue, A., Demasy, C., Resing, J. A., Mellett, T., Wyatt, N. J., et al. (2023). Tracing differences in iron supply to the Mid-Atlantic Ridge valley between hydrothermal vent sites: implications for the addition of iron to the deep ocean. *Biogeosciences* 20 (2), 405–420. doi: 10.5194/bg-20-405-2023

MacCarthy, P., Peterson, M. J., Malcolm, R. L., and Thurman, E. M. (1979). Separation of humic substances by pH gradient desorption from a hydrophobic resin. *Anal. Chem.* 51 (12), 2041–2043. doi: 10.1021/ac50048a036

Macrellis, H. M., Trick, C. G., Rue, E. L., Smith, G., and Bruland, K. W. (2001). Collection and detection of natural iron-binding ligands from seawater. *Mar. Chem.* 76 (3), 175–187. doi: 10.1016/S0304-4203(01)00061-5

Maillard, L. C. (1912). Action des acides aminés sur les sucres; formation des mélanoïdines par voie méthodique. *CR Acad. Sci. Paris* 154, 66–68. Available at: https://gallica.bnf.fr/ark:/12148/bpt6k31070/f72.tableDesMatieres.

Martin, J. H., and Fitzwater, S. E. (1988). Iron deficiency limits phytoplankton growth in the north-east Pacific subarctic. *Nature* 331 (6154), 341–343. doi: 10.1038/331341a0

Martin, J. H., and Gordon, R. M. (1988). Northeast Pacific iron distributions in relation to phytoplankton productivity. *Deep Sea Res. Part A. Oceanogr. Res. Papers* 35 (2), 177–196. doi: 10.1016/0198-0149(88)90035-0

Martin, J. H., Gordon, M., and Fitzwater, S. E. (1991). The case for iron. *Limnol. Oceanogr.* 36 (8), 1793–1802. doi: 10.4319/lo.1991.36.8.1793

Martin, J. H., Gordon, R. M., Fitzwater, S., and Broenkow, W. W. (1989). Vertex: phytoplankton/iron studies in the Gulf of Alaska. *Deep Sea Res. Part A. Oceanogr. Res. Papers* 36 (5), 649–680. doi: 10.1016/0198-0149(89)90144-1

Mawji, E., Gledhill, M., Milton, J. A., Tarran, G. A., Ussher, S., Thompson, A., et al. (2008). Hydroxamate siderophores: Occurrence and importance in the Atlantic Ocean. *Environ. Sci. Technol.* 42, 8675–8680. doi: 10.1021/es801884r

McCormack, P., Worsfold, P. J., and Gledhill, M. (2003). Separation and detection of siderophores produced by marine bacterioplankton using high-performance liquid chromatography with electrospray ionization mass spectrometry. *Anal. Chem.* 75, 2647–2652. doi: 10.1021/ac0340105

Millero, F. J., Sotolongo, S., and Izaguirre, M. (1987). The oxidation kinetics of Fe (II) in seawater. *Geochim. Cosmochim. Acta* 51 (4), 793–801. doi: 10.1016/0016-7037(87)90093-7

Misumi, K., Lindsay, K., Moore, J. K., Doney, S. C., Tsumune, D., and Yoshida, Y. (2013). Humic substances may control dissolved iron distributions in the global ocean: Implications from numerical simulations. *Global Biogeochem. Cycles* 27 (2), 450–462. doi: 10.1002/gbc.20039

Moore, C. M., Mills, M. M., Arrigo, K. R., Berman-Frank, I., Bopp, L., Boyd, P. W., et al. (2013). Processes and patterns of oceanic nutrient limitation. *Nat. Geosci.* 6 (9), 701–710. doi: 10.1038/ngeo1765

Nishioka, J., Takeda, S., Wong, C. S., and Johnson, W. K. (2001). Size-fractionated iron concentrations in the northeast Pacific Ocean: distribution of soluble and small colloidal iron. *Mar. Chem.* 74 (2-3), 157–179. doi: 10.1016/S0304-4203(01)00013-5

Obernosterer, I., Reitner, B., and Herndl, G. J. (1999). Contrasting effects of solar radiation on dissolved organic matter and its bioavailability to marine bacterioplankton. *Limnol. Oceanogr.* 44 (7), 1645–1654. doi: 10.4319/lo.1999.44.7.1645

Perdue, E. M., and Lytle, C. R. (1983). A distribution model for binding of protons and metal ions by humic substances. *Environ. Sci. Technol.* 17 (11), 654–660. doi: 10.1021/es00117a006

Pérez-Almeida, N., González, A. G., Santana-Casiano, J. M., and González-Dávila, M. (2022). Ocean acidification effect on the iron-gallic acid redox interaction in seawater. *Front. Mar. Sci.* 9. doi: 10.3389/fmars.2022.837363

Pižeta, I., Sander, S. G., Hudson, R. J. M., Omanović, D., Baars, O., Barbeau, K. A., et al. (2015). Interpretation of complexometric titration data: An intercomparison of methods for estimating models of trace metal complexation by natural organic ligands. *Mar. Chem.* 173, 3–24. doi: 10.1016/j.marchem.2015.03.006

Plank, S., Marchese, F., Genzano, N., Nolde, M., and Martinis, S. (2020). The short life of the volcanic island New Late'iki (Tonga) analyzed by multi-sensor remote sensing data. *Sci. Rep.* 10 (1), 1–15. doi: 10.1038/s41598-020-79261-7

Resing, J. A., Sedwick, P. N., German, C. R., Jenkins, W. J., Moffett, J. W., Sohst, B. M., et al. (2015). Basin-scale transport of hydrothermal dissolved metals across the South Pacific Ocean. *Nature* 523 (7559), 200–203. doi: 10.1038/nature14577

Rich, H. W., and Morel, F. M. (1990). Availability of well-defined iron colloids to the marine diatom Thalassiosira weissflogii. *Limnol. Oceanogr.* 35 (3), 652–662. doi: 10.4319/lo.1990.35.3.0652

Riso, R., Mastin, M., Aschehoug, A., Davy, R., Devesa, J., Laës-Huon, A., et al. (2021). Distribution, speciation and composition of humic substances in a macro-tidal temperate estuary. *Estuarine Coast. Shelf Sci.* 255, 107360. doi: 10.1016/j.ecss.2021.107360

Rose, A. L., and Waite, T. D. (2003a). Kinetics of iron complexation by dissolved natural organic matter in coastal waters. *Mar. Chem.* 84 (1-2), 85–103. doi: 10.1016/S0304-4203(03)00113-0

Rose, A. L., and Waite, T. D. (2003b). Kinetics of hydrolysis and precipitation of ferric iron in seawater. *Environ. Sci. Technol.* 37 (17), 3897–3903. doi: 10.1021/es034102b

Rosenstock, B., Zwisler, W., and Simon, M. (2005). Bacterial consumption of humic and non-humic low and high molecular weight DOM and the effect of solar irradiation on the turnover of labile DOM in the Southern Ocean. *Microb. Ecol.* 50 (1), 90–101. doi: 10.1007/s00248-004-0116-5

Ruacho, A., Bundy, R. M., Till, C. P., Roshan, S., Wu, J., and Barbeau, K. A. (2020). Organic dissolved copper speciation across the US GEOTRACES equatorial Pacific zonal transect GP16. *Mar. Chem.* 225, 103841. doi: 10.1016/j.marchem.2020.103841

Rue, E. L., and Bruland, K. W. (1995). Complexation of iron (III) by natural organic ligands in the Central North Pacific as determined by a new competitive ligand equilibration/adsorptive cathodic stripping voltammetric method. *Mar. Chem.* 50 (1-4), 117–138. doi: 10.1016/0304-4203(95)00031-L

Sander, S. G., and Koschinsky, A. (2011). Metal flux from hydrothermal vents increased by organic complexation. *Nat. Geosci.* 4 (3), 145–150. doi: 10.1038/ngeo1088

Santana-Casiano, J. M., González-Dávila, M., and Millero, F. J. (2005). Oxidation of nanomolar levels of Fe (II) with oxygen in natural waters. *Environ. Sci. Technol.* 39 (7), 2073–2079. doi: 10.1021/es049748y

Santana-Casiano, J. M., González-Santana, D., Devresse, Q., Hepach, H., Santana-González, C., Quack, B., et al. (2022). Exploring the effects of organic matter characteristics on Fe (II) oxidation kinetics in coastal seawater. *Environ. Sci. Technol.* 56 (4), 2718–2728. doi: 10.1021/acs.est.1c04512

Schlitzer, R., Anderson, R. F., Dodas, E. M., Lohan, M., Geibert, W., Tagliabue, A., et al. (2018). The GEOTRACES intermediate data product 2017. *Chem. Geol.* 493, 210–223. doi: 10.1016/j.chemgeo.2018.05.040

Schlitzer, R. (2022) *Ocean data view*. Available at: https://odv.awi.de/.

Shaw, T. J., Luther, G. W.III, Rosas, R., Oldham, V. E., Coffey, N. R., Dias, D. M. C., et al. (2021). Fe-catalyzed sulfide oxidation in hydrothermal plumes is a source of reactive oxygen species to the ocean. *PNAS* 118 (40). doi: 10.1073/pnas.2026654118

Slagter, H. A., Laglera, L. M., Sukekava, C., and Gerringa, L. J. (2019). Fe-binding organic ligands in the humic-rich TransPolar Drift in the surface Arctic Ocean using multiple voltammetric methods. *J. Geophys. Res.: Oceans* 124 (3), 1491–1508. doi: 10.1029/2018JC014576

Slagter, H. A., Reader, H. E., Rijkenberg, M. J. A., van der Loeff, M. R., De Baar, H. J. W., and Gerringa, L. J. A. (2017). Organic Fe speciation in the Eurasian Basins of the Arctic Ocean and its relation to terrestrial DOM. *Mar. Chem.* 197, 11–25. doi: 10.1016/j.marchem.2017.10.005

Stedmon, C. A., and Cory, R. M. (2014). Biological origins and fate of fluorescent dissolved organic matter in aquatic environments. *Aquat. Organic Matter Fluorescence*, 278–299. doi: 10.1017/CBO9781139045452.013

Sukekava, C., Downes, J., Slagter, H. A., Gerringa, L. J., and Laglera, L. M. (2018). Determination of the contribution of humic substances to iron complexation in seawater by catalytic cathodic stripping voltammetry. *Talanta* 189, 359–364. doi: 10.1016/j.talanta.2018.07.021

Sung, W., and Morgan, J. J. (1980). Kinetics and product of ferrous iron oxygenation in aqueous systems. *Environ. Sci. Technol.* 14 (5), 561–568. doi: 10.1021/es60165a006

Tagliabue, A., Bopp, L., Dutay, J. C., Bowie, A. R., Chever, F., Jean-Baptiste, P., et al. (2010). Hydrothermal contribution to the oceanic dissolved iron inventory. *Nat. Geosci.* 3 (4), 252–256. doi: 10.1038/ngeo818

Tagliabue, A., Lough, A. J., Vic, C., Roussenov, V., Gula, J., Lohan, M. C., et al. (2022). Mechanisms driving the dispersal of hydrothermal iron from the northern Mid Atlantic Ridge. *Geophys. Res. Lett.* 49 (22), e2022GL100615. doi: 10.1029/2022GL100615

Tani, H., Nishioka, J., Kuma, K., Takata, H., Yamashita, Y., Tanoue, E., et al. (2003). Iron (III) hydroxide solubility and humic-type fluorescent organic matter in the deep water column of the Okhotsk Sea and the northwestern North Pacific Ocean. *Deep Sea Res. Part I: Oceanogr. Res. Papers* 50 (9), 1063–1078. doi: 10.1016/S0967-0637(03)00098-0

Thurman, E. M., and Malcolm, R. L. (1981). Preparative isolation of aquatic humic substances. *Environ. Sci. Technol.* 15 (4), 463–466. doi: 10.1021/es00086a012

Tilliette, C., Taillandier, V., Bouruet-Aubertot, P., Grima, N., Maes, C., Montanes, M., et al. (2022). Dissolved iron patterns impacted by shallow hydrothermal sources along a transect through the Tonga-Kermadec arc. *Global Biogeochemical Cycle* 36 (7), e2022GB007363. doi: 10.1029/2022GB007363

Town, R. M., and Filella, M. (2000). Dispelling the myths: Is the existence of L1 and L2 ligands necessary to explain metal ion speciation in natural waters? *Limnol. Oceanogr.* 45 (6), 1341–1357. doi: 10.4319/lo.2000.45.6.1341

Tranvik, L. J. (1993). Microbial transformation of labile dissolved organic matter into humic-like matter in seawater. *FEMS Microbiol. Ecol.* 12 (3), 177–183. doi: 10.1111/j.1574-6941.1993.tb00030.x

van den Berg, C. M. (1995). Evidence for organic complexation of iron in seawater. *Mar. Chem.* 50 (1-4), 139–157. doi: 10.1016/0304-4203(95)00032-M

Von der Heyden, B. P., Roychoudhury, A. N., Mtshali, T. N., Tyliszczak, T., and Myneni, S. C. B. (2012). Chemically and geographically distinct solid-phase iron pools in the Southern Ocean. *Science* 338 (6111), 1199–1201. doi: 10.1126/science.1227504

Waeles, M., Cotte, L., Pernet-Coudrier, B., Chavagnac, V., Cathalot, C., Leleu, T., et al. (2017). On the early fate of hydrothermal iron at deep-sea vents: A reassessment after *in situ* filtration. *Geophysical Res. Lett.* 44 (9), 4233–4240. doi: 10.1002/2017GL073315

Wang, W. X., and Dei, R. C. (2003). Bioavailability of iron complexed with organic colloids to the cyanobacteria Synechococcus and Trichodesmium. *Aquat. Microb. Ecol.* 33 (3), 247–259. doi: 10.3354/ame033247

Wang, H., Resing, J. A., Yan, Q., Buck, N. J., Michael, S. M., Zhou, H., et al. (2021). The characteristics of Fe speciation and Fe-binding ligands in the Mariana back-arc hydrothermal plumes. *Geochim. Cosmochim. Acta* 292, 24–36. doi: 10.1016/j.gca.2020.09.016

Wang, H., Wang, W., Liu, M., Zhou, H., Ellwood, M. J., Butterfield, D. A., et al. (2022). Iron ligands and isotopes in hydrothermal plumes over backarc volcanoes in the Northeast Lau Basin, Southwest Pacific Ocean. *Geochim. Cosmochim. Acta* 336, 341–352. doi: 10.1016/j.gca.2022.09.026

Whitby, H., Bressac, M., Sarthou, G., Ellwood, M. J., Guieu, C., and Boyd, P. W. (2020a). Contribution of electroactive humic substances to the iron-binding ligands released during microbial remineralization of sinking particles. *Geophys. Res. Lett.* 47 (7). doi: 10.1029/2019GL086685

Whitby, H., Planquette, H., Cassar, N., Bucciarelli, E., Osburn, C. L., Janssen, D. J., et al. (2020b). A call for refining the role of humic-like substances in the oceanic iron cycle. *Sci. Rep.* 10 (1), 1–12. doi: 10.1038/s41598-020-62266-7

Whitby, H., and van den Berg, C. M. (2015). Evidence for copper-binding humic substances in seawater. *Mar. Chem.* 173, 282–290. doi: 10.1016/j.marchem.2014.09.011

Wu, J., Boyle, E., Sunda, W., and Wen, L. S. (2001). Soluble and colloidal iron in the oligotrophic North Atlantic and North Pacific. *Science* 293 (5531), 847–849. doi: 10.1126/science.1059251

Wu, J., and Luther, G. W.III (1995). Complexation of Fe (III) by natural organic ligands in the Northwest Atlantic Ocean by a competitive ligand equilibration method and a kinetic approach. *Mar. Chem.* 50 (1-4), 159–177. doi: 10.1016/0304-4203(95)00033-N

Ye, Y., Völker, C., and Gledhill, M. (2020). Exploring the iron-binding potential of the ocean using a combined pH and DOC parameterization. *Global Biogeochem. Cycles* 34 (6), e2019GB006425. doi: 10.1029/2019GB006425

Zhu, K., Birchill, A. J., Milne, A., Ussher, S., Humphreys, M. P., Carr, N., et al. (2021). Equilibrium calculations of iron speciation and apparent iron solubility in the Celtic Sea at ambient seawater pH using the NICA-Donnan model. *Mar. Chem.* 237, 104038. doi: 10.1016/j.marchem.2021.104038

Zigah, P. K., McNichol, A. P., Xu, L., Johnson, C., Santinelli, C., Karl, D. M., et al. (2017). Allochthonous sources and dynamic cycling of ocean dissolved organic carbon revealed by carbon isotopes. *Geophys. Res. Lett.* 44 (5), 2407–2415. doi: 10.1002/2016GL071348

frontiers | Frontiers in Marine Science

TYPE Original Research
PUBLISHED 04 October 2023
DOI 10.3389/fmars.2023.1232923

OPEN ACCESS

EDITED BY
Alex J. Poulton,
Heriot-Watt University, United States

REVIEWED BY
Casey Schine,
National Aeronautics and Space Administration, United States
Thomas James Ryan-Keogh,
Southern Ocean Carbon and Climate Observatory (SOCCO), South Africa

*CORRESPONDENCE
Zoé Mériguet
zoe.meriguet@imev-mer.fr
Fabien Lombard
fabien.lombard@imev-mer.fr

RECEIVED 01 June 2023
ACCEPTED 21 August 2023
PUBLISHED 04 October 2023

CITATION
Mériguet Z, Vilain M, Baudena A, Tilliette C, Habasque J, Lebourges-Dhaussy A, Bhairy N, Guieu C, Bonnet S and Lombard F (2023) Plankton community structure in response to hydrothermal iron inputs along the Tonga-Kermadec arc. *Front. Mar. Sci.* 10:1232923. doi: 10.3389/fmars.2023.1232923

Plankton community structure in response to hydrothermal iron inputs along the Tonga-Kermadec arc

Zoé Mériguet[1]*, Marion Vilain[2], Alberto Baudena[1], Chloé Tilliette[1], Jérémie Habasque[3], Anne Lebourges-Dhaussy[3], Nagib Bhairy[4], Cécile Guieu[1], Sophie Bonnet[4] and Fabien Lombard[1]*

[1]Laboratoire d'Océanographie de Villefranche, Sorbonne Université, CNRS, Villefranche sur mer, France, [2]Unité Biologie des Organismes et Ecosystèmes Aquatiques, Muséum National d'Histoire Naturelle, Sorbonne Université, CNRS, IRD, Paris, France, [3]LEMAR, UBO, CNRS, IRD, Ifremer, Plouzané, France, [4]Mediterranean Institute of Oceanography, Aix Marseille Univ., Université de Toulon, CNRS, IRD, Marseille, France

The Western Tropical South Pacific (WTSP) basin has been identified as a hotspot of atmospheric dinitrogen fixation due to the high dissolved iron ([DFe]) concentrations (up to 66 nM) in the photic layer linked with the release of shallow hydrothermal fluids along the Tonga-Kermadec arc. Yet, the effect of such hydrothermal fluids in structuring the plankton community remains poorly studied. During the TONGA cruise (November-December 2019), we collected micro- (20-200 µm) and meso-plankton (>200 µm) samples in the photic layer (0-200 m) along a west to east zonal transect crossing the Tonga volcanic arc, in particular two volcanoes associated with shallow hydrothermal vents (< 500 m) in the Lau Basin, and both sides of the arc represented by Melanesian waters and the South Pacific Gyre. Samples were analyzed by quantitative imaging (FlowCam and ZooScan) and then coupled with acoustic observations, allowing us to study the potential transfer of phytoplankton blooms to higher planktonic trophic levels. We show that micro- and meso-plankton exhibit high abundances and biomasses in the Lau Basin and, to some extent, in Melanesian waters, suggesting that shallow hydrothermal inputs sustain the planktonic food web, creating productive waters in this otherwise oligotrophic region. In terms of planktonic community structure, we identified major changes with high [DFe] inputs, promoting the development of a low diversity planktonic community dominated by diazotrophic cyanobacteria. Furthermore, in order to quantify the effect of the shallow hydrothermal vents on chlorophyll *a* concentrations, we used Lagrangian dispersal models. We show that chlorophyll *a* concentrations were significantly higher inside the Lagrangian plume, which came into contact with the two hydrothermal sites, confirming the profound impact of shallow hydrothermal vents on plankton production.

KEYWORDS

plankton imaging, diazotrophic cyanobacteria, iron fertilization, nutrient limitation, WTSP

1 Introduction

The Western Tropical South Pacific (WTSP) is one of the least studied ocean basins notably in terms of the planktonic food web. In surface, it is characterized by oligotrophic conditions, with high stratification accompanied by a virtual absence of destratification periods, limiting nutrient inputs from the deep ocean (Ustick et al., 2021). However, the WTSP has been recognized as a hotspot of dinitrogen (N_2) fixation organisms (Bonnet et al., 2017; Bonnet et al., 2018), contributing ~21% of global fixed N inputs (Bonnet et al., 2017). These N_2-fixation organisms are called diazotrophs and play an essential role in the ocean, as they are responsible for the supply of new nitrogen (N) bio-available at the ocean surface. Diazotrophs alleviate N limitation in 60% of our oceans, helping to maintain ocean primary productivity that in turn, support the food web, organic carbon export and sequestration to the deep ocean (Zehr and Capone, 2020; Bonnet et al., 2023). However, their growth is hampered by the high iron (Fe) demand of their nitrogenase enzyme while Fe bioavailability in the ocean is often limited.

In the WTPS, two biogeochemical subregions, separated by the Tonga-Kermadec arc have been described: (i) in the east, the South Pacific Gyre is characterized by ultra-oligotrophic waters with a deep chlorophyll maximum (DCM) located at ~150 m, and low N_2 fixation rates (~85 µmol N m^{-2} d^{-1}; Bonnet et al., 2018) despite sufficient phosphate concentrations (0.11 µmol L^{-1}; Moutin et al., 2008; Moutin et al., 2018), and (ii) in the west, the Melanesian waters and the Lau Basin are characterized by less oligotrophic waters (DCM located at ~70 m), very high N_2 fixation rates (~631 µmol N m^{-2} d^{-1}; Bonnet et al., 2018), i.e. far above typical rates generally measured in the (sub) tropical ocean (10-100 µmol N m^{-2} d^{-1}) and phosphate concentrations close to detection limit (Moutin et al., 2018). In this latter subregion, such high N_2 fixation rates have been attributed to the release of high dissolved iron ([DFe]) concentrations by shallow hydrothermal vents along the Tonga volcanic arc (Bonnet et al., 2023) (~2,6 vents/100 km; Massoth et al., 2007; German et al., 2016), that can reach up to 66 nM in the euphotic layer (Guieu et al., 2018).

The vast majority of studies conducted in the WTSP have thus focused on the interactions between trace metals and the first levels of the planktonic food web. They mostly focused on the biogeographical distribution of picoplankton (Campbell et al., 2005; Buitenhuis et al., 2012; Bock et al., 2018), diatoms (Leblanc et al., 2018), and diazotrophs (Bonnet et al., 2015; Bonnet et al., 2017; Bonnet et al., 2018; Stenegren et al., 2018; Lory et al., 2022). They associated the DFe-fertilized region of the Melanesian and Lau Basin waters with an increase of *Synechococcus* abundances relative to *Prochlorococcus* in the pico-plankton population (Bock et al., 2018), a large dominance of pennates and diatom-diazotroph associations (DDAs) in the diatom community (Leblanc et al., 2018) and an important bloom of diazotroph *Trichodesmium* while ultra-oligotrophic waters of the South Pacific Gyre were associated with small unicellular diazotroph UCYN-B. *Trichodesmium* and the UCYN-B have been described to dominate the diazotroph community composition (>80%) in the WTSP (Stenegren et al., 2018). Yet, higher trophic levels have been poorly explored. It is still not clear how the bloom-forming diazotrophs influence overall phytoplankton community composition, food webs and trophic transfer in the open sea (Suikkanen et al., 2021). In particular, the role of diazotroph blooms in structuring the planktonic food web in this region is poorly understood (Le Borgne et al., 2011), although several authors have reported that diazotroph-derived nitrogen is efficiently transferred to meso-zooplankton communities (> 200 µm) (Caffin et al., 2018; Carlotti et al., 2018). Moreover, the precise role of DFe inputs on zooplankton communities remains unknown in this region, despite resulting in significant changes in the planktonic community composition in other regions (Caputi et al., 2019).

During the TONGA cruise (Guieu and Bonnet, 2019), we collected plankton samples in the photic layer (0-200 m) along a west to east zonal transect crossing the Tonga volcanic arc, in particular above two volcanoes associated with shallow hydrothermal vents (< 500 m) in the Lau Basin, and both sides of the arc represented oligotrophic Melanesian waters and the ultra-oligotrophic South Pacific Gyre. The objective of this study is to explore the effect of DFe-rich shallow hydrothermal fluids on a large range of planktonic communities (size > 20 µm) including micro-phytoplankton to macro-zooplankton in the photic layer (0-200 m). We highlight that all the size range of plankton communities harbor high abundances and biomasses in the Lau Basin located close to the Tonga volcanic arc. In this study, we uncovered a spatial structuring of the micro-planktonic community by diazotrophic organisms, which in turn, support meso- and macro-planktonic production.

2 Materials and methods

2.1 Sampling methods

This study was conducted as part of the TONGA expedition (GEOTRACES GPpr14; Guieu and Bonnet, 2019; https://doi.org/10.17600/18000884), which took place in the WTSP Ocean from 31/10/2019 to 05/12/2019 (35 days), onboard the R/V L'Atalante, along a transect extending from New Caledonia to the western end of the South Pacific Gyre (Figure 1). Two types of stations were sampled: (i) nine short-duration (SD) stations (SD 01, 02, 03, 04, 06, 07, 08, 11 and 12; Figure 1) were dedicated to biogeochemical sampling through water column vertical casts and (ii) two long-duration (LD) stations (LD 05 and 10; Figure 1B) were dedicated to study the impacts of hydrothermal fluids from two shallow sources along a ~17 km transect. Each of these transects included 5 substations, named from T1 to T5, with T5 being the closest to the hydrothermal source. The strategy used for the detection of hydrothermal sources is detailed in Bonnet et al. (2023) and Tilliette et al. (2022). A west to east transect allowed to characterize the different biogeochemical subregions crossed (Figure 1B).

Plankton was sampled during the day with WP2 nets of 200 µm and 35 µm mesh size, towed vertically from 0 to 200 m during simultaneous deployments. The 35 µm net was not deployed at SD 01 and both nets were not deployed at SD 09. Within the LD stations, plankton nets were deployed for substations LD 05-T1, -T2, and -T4, and LD 10-T1, -T3 and -T5. As the nets were not

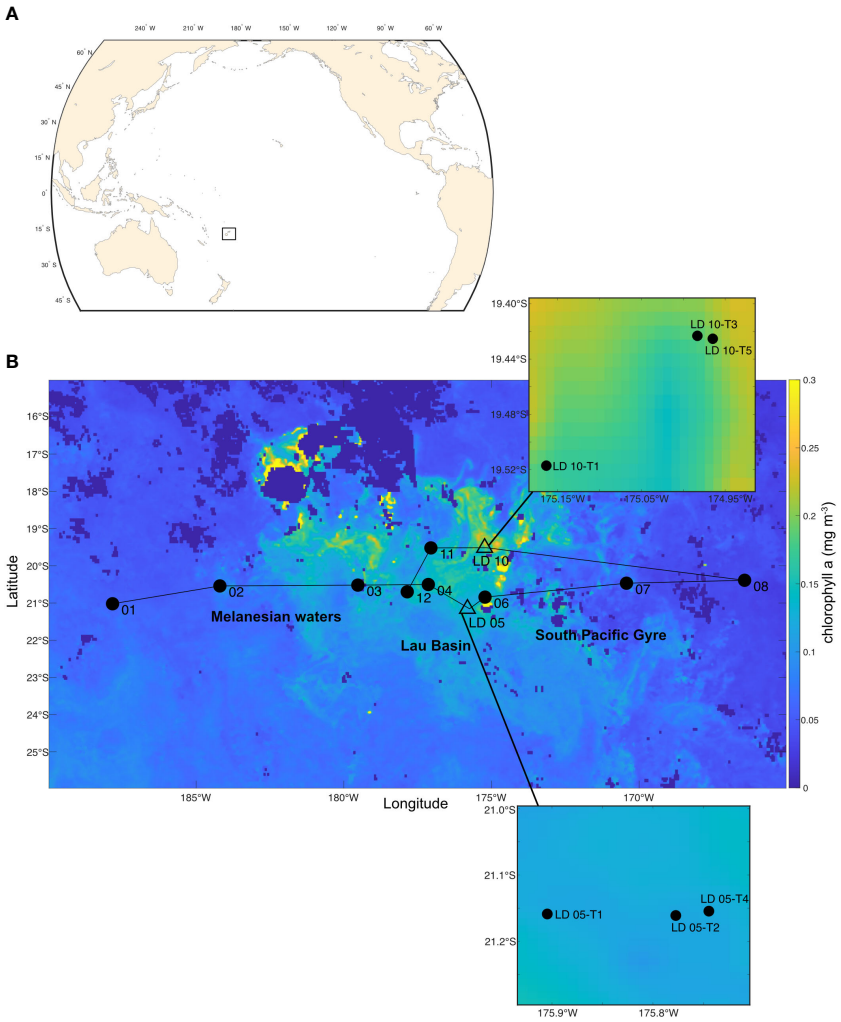

FIGURE 1
(A) Map of the Pacific Ocean showing the position of the Tonga Kermadec arc area by the black square. **(B)** Sampling map of the TONGA campaign superposed on the average chlorophyll *a* concentration ([Chl *a*]; mg m^{-3}) of November 2019 (data from MODIS-Aqua resolution of 4 km). Different oceanic regions were occupied during the cruise: Melanesian waters including short duration (SD) stations 01, 02 and 03, Lau Basin including SD 04, 11 and 12 as well as long duration (LD) stations 05 and 10, and the South Pacific Gyre including SD 06, 07 and 08. Zooms were performed on the substations with plankton sampling of the LD stations: LD 05-T1, -T2, and -T4 and LD 10-T1, -T3 and -T5.

equipped with flowmeters, the filtered volumes were estimated by multiplying the net opening area (0.25 m^2) by the length of cable unwound for each deployment (i.e. 200 m). This calculation potentially leads to an overestimation of the sampled volume since the possible backflow is not corrected (Heron, 1968). Samples from the 200 µm nets were directly concentrated onboard using a 100 µm sieve and preserved in a 4% formaldehyde solution. Samples from the 35 µm nets were separated into 5 subsamples for different analyses: the fraction intended for the present analysis was concentrated using a 20 µm sieve, preserved in acidic lugol solution and stored in opaque bottles. The 35 µm net sample from SD 02 was identified as potentially biased (abundance and size structure different by several orders of magnitude, symptomatic of an inconsistency in the sample subdivision strategy after collection) and was therefore excluded from our analysis.

2.2 Acquisition and treatment of plankton imaging data

2.2.1 FlowCam

The FlowCam analyzer imaging instrument (Fluid Imaging Technologies; Sieracki et al., 1998) equipped with a ×4 objective was used to study the micro-plankton samples (size range of 20-200 µm) from the 35 µm net at the Quantitative Imaging Platform (PIQv) of the Institut de la Mer de Villefranche. This instrument is an automated microscope taking digital images while microscopic particles are pumped through a capillary imaging chamber. Each sample was previously passed through a sieve of 200 µm to remove large objects which could clog the FlowCam imaging cell. Samples were then diluted or concentrated to achieve optimal object flow, and were run through a 300 µm deep glass cell. The auto-image mode was used to image the particles in the focal plane at a constant rate.

2.2.2 ZooScan

The ZooScan imaging instrument (Gorsky et al., 2010) was used to study the meso-plankton (> 200 µm). Samples from the 200 µm nets were gently filtered through 1000 µm and 100 µm mesh and transferred to filtered seawater. They were separated into two size classes: 200-1000 µm and > 1000 µm. Fractions were then split using a Motoda box (Motoda, 1959) to reach a concentration of approximately 1000 objects per subsample and scanned using the ZooScan. This sampling strategy allowed to consider correctly both the numerous small organisms and the large ones, which could be under-sampled if subsampled together by the Motoda box.

2.2.3 Image annotation

For both instruments, the full methodology used is displayed in their respective manual (https://sites.google.com/view/piqv/piqv-manuals/instruments-manuals). Briefly, images generated by the FlowCam and ZooScan were processed using the ZooProcess software (Gorsky et al., 2010) that extract segmented objects as vignettes, with a series of morphometric measurements that were imported into the EcoTaxa web platform (Picheral et al., 2017) for taxonomic classification. Using image recognition algorithms, predicted taxonomic categories were validated or corrected by a trained taxonomist. Overall, 51 406 vignettes were classified into 149 taxa for the ZooScan analyses, and 109 185 vignettes were classified into 124 taxa for the FlowCam analyses. For the majority, the taxonomic classification effort was possible up to the genus and only in rare cases up to the species. A number of organisms could not be reliably identified due to a lack of identification criteria and were therefore grouped into temporary categories (t00x) following similar morphological criteria.

2.2.4 Diazotrophs images

On the FlowCam vignettes, different morphologies of cyanobacteria were identified as diazotrophs, with sizes ranging between 20 and 200 µm. Among them were identified the cyanobacteria *Katagnymene spiralis*, free-living *Richelia* but also in symbiosis within Rhizosolenids diatoms (category Rhizosolenids inter-Richelia) and colonies of unicellular cyanobacteria (UCYN, allowing a sufficient size for detection by FlowCam imagery), likely corresponding to colonies of UCYN-B very abundant in this region (Bonnet et al., 2018; Stenegren et al., 2018). As the identification criteria are insufficient to reliably associate morphologies to genus, we grouped these cyanobacterial morphologies into morphotype categories named cyano a, cyano b and "t005_F". On an identification basis of Tenório et al. (2018), the cyano a category could correspond to some *Katagnymene* species while cyano b could correspond to *Trichodesmium* but we chose to keep morpho groups as other authors, such as Lundgren et al. (2005), consider both morphotypes as *Trichodesmium*. We were also able to identify diazotrophic cyanobacteria on ZooScan vignettes (organisms > 200 µm): the cyanobacterium *Katagnymene spiralis* and a morphology group "cyanobacteria" probably corresponding to *Trichodesmium* species. Examples illustrating these diazotrophs vignettes and morphologies can be found in Figure 2 or directly in the open access project EcoTaxa: https://ecotaxa.obs-vlfr.fr/prj/2841 for the FlowCam and https://ecotaxa.obs-vlfr.fr/prj/2832 for the ZooScan.

2.3 Numerical and statistical analysis

Using a custom-made processing tool (https://github.com/ecotaxa/ecotaxatoolbox), the data were structured in two distinct databases (ZooScan and FlowCam). Major and minor axes of the best ellipsoidal approximation were used to estimate the biovolume (mm^3 m^{-3}) of each object according to the recommendation of Vandromme et al. (2012). Size was expressed as equivalent spherical diameter (ESD, µm). The individual biovolumes of the organisms were arranged in Normalized Biomass Size Spectra (NBSS) as described by Platt (1978) along a harmonic range of biovolume so that the minimal and maximal biovolumes of each class be linked by: $Bv_{max} = 2^{0.25} Bv_{min}$. The NBSS was obtained by dividing the total biovolume of each size class by its biovolume interval ($Bv_{range}=Bv_{max}-Bv_{min}$). The NBSS was representative of the number of organisms (abundance within one factor) per size class. This can provides insight into ecosystem structure and function through the "size spectra" approach, which generalizes Elton's pyramid of numbers (Elton, 1927). For each database, considering the volumes of water filtered by the nets, plankton concentration in individu per m^{-3} (ind m^{-3}) and biovolume were calculated for each taxonomic annotation and for several levels of

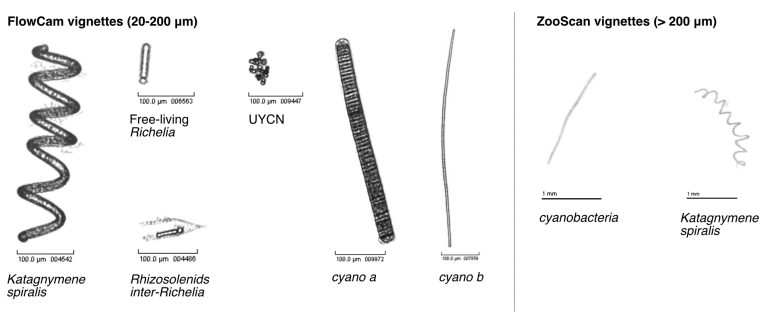

FIGURE 2
Examples of vignettes (FlowCam and ZooScan vignettes) for each category of organisms identified as diazotrophs. All of these categories were grouped into the functional plankton group 'cyanobacteria' for the 3rd analysis (see part 2.3 and 3.4).

grouping: living or non-living, and a functional group annotation. Fifteen planktonic functional groups were defined. The full list of functional group annotations linked with their EcoTaxa taxonomic label can be found in Supplementary Table 1. Diversity was calculated with the Shannon Index (H).

Hierarchical clustering analyses (HAC; descriptive complete link method, Hellinger distance; Legendre and Legendre, 2012) were performed on the relative abundance to group stations with similar planktonic compositions. Principal component analysis (PCA) was performed on the relative abundance (Hellinger transformation; Legendre and Legendre, 2012) of all taxonomic annotations. To link both analyses, the groupings obtained in the HAC analysis were reprojected into the PCA space. The addition of environmental data (temperature, salinity, oxygen, nitrite: NO_2, nitrate: NO_3^-, ammonium: NH_4, phosphate: PO_4^{3-}, dissolved iron: DFe, particulate iron: Pfe, silicate: $Si(OH)_4$, manganese: Mn, aluminum: Al and fluorescence; see part 2.4) as supplementary data was performed in the PCA, allowing to cross-link the environmental influence with the taxonomic composition of the station. Spearman correlation tests were performed between different variables (alpha risk set at 0.05%).

2.4 Plankton adjustment and assembling

In order to study the whole community (all planktonic organisms > 20 µm), we merged the two databases (FlowCam and ZooScan) into one single cross-calibrated database. In its lowest size range, each dataset from FlowCam and ZooScan displayed an undersampling which is symptomatic of either incorrect detection of objects due to optical limitation of device or undersampling of net by mesh extrusion of organisms (Figure 3A; Lombard et al., 2019). Therefore, all parts of the NBSS below the maximal abundance of each device were discarded (Figure 3B). For the highest size range of each dataset, very large organisms were associated with a presence-absence signal rather than a quantitative concentration due to insufficient sampling effort, and were disregarded (Figure 3B). We chose as an objective criterion to discard every NBSS size bin separated by more than five empty size bins. A clear difference of intercepts between NBSS spectra of the two instruments was detected (Figure 3B). Using the ZooScan as a reference, we used overlapping observations between the two instruments (for overlapping observations of size classes 1 to *i*) at a given station *j* to produce a cross-size classes average correction coefficient at the station scale such as: $NBSS_{FlowCam\ adjusted\ j} = NBSS_{FlowCam\ j} \times \text{mean}(NBSS_{FlowCam\ ij}/NBSS_{ZooScan\ ij})$. Results of this correction are shown in Figure 3C.

Finally, to have a unique dataset in the overlapping size range, an average between the values of $NBSS_{FlowCam\ adjusted\ i,j}$ and $NBSS_{ZooScan\ i,j}$ was performed for each station at the functional and trophic group levels. From these unique NBSS spectra, concentrations and biovolumes were calculated. A non-negligible risk to duplicate counts of organisms exists at the original taxonomic identification level, which may differ in taxonomical resolutions between instruments. For example, while different morphotypes of cyanobacteria can be identified with the FlowCam, they are only identified at the level of the phylum cyanobacteria with the ZooScan. To avoid this, assembly at the initial taxonomic identification level was not used, and was only done at functional and trophic levels. We performed a HAC on the normalized biovolume (square root transformation) to group together stations with similar functional planktonic groups. PCA was performed on the normalized biovolume of functional planktonic groups. To link the two analyses, the groupings obtained in the HAC analysis were reprojected into the PCA space. The association with the environment was tested by adding environmental variables as supplementary variables in the analysis and evaluating their correlations to the PCA components. For all linear relationships, we used a robust linear fit which is less sensitive to potential outliers (Greco et al., 2019).

2.5 Environmental data

Temperature, conductivity (salinity), pressure (depth) and dissolved oxygen vertical profiles were obtained using a rosette-mounted CTD SBE 9 plus sensor (data available on SEANOE: https://doi.org/10.17882/88169). At each station, conventional CTD casts were conducted to sample inorganic nutrients using a rosette equipped with 24 Niskin bottles (12 L) and Trace-Metal clean Rosette (TMR) casts were performed for dissolved and particulate trace metal sampling. Seawater samples were collected according to the GEOTRACES guidelines using a Titanium rosette equipped with 24 Teflon-coated 12-L Go-Flos bottles (General Oceanics) and operated along a Kevlar cable. The cleaning protocols for sampling bottles and equipment also followed the GEOTRACES Cookbook (Cutter et al., 2017). CTD and TMC profiles showed a difference in calibration for the O_2 sensors. A linear regression was performed using a robust method (Greco et al., 2019) to adjust the TMC profiles to the quality controlled CTD profiles.

2.5.1 Dfe data

[DFe] was measured from TMR casts by flow injection with online preconcentration and chemiluminescence detection. Each sample was analyzed in triplicate and following GEOTRACES recommendations for validation. Full protocol and dataset can be found in Tilliette et al. (2022).

2.5.2 Nutrients

Inorganic nutrients (NO_2, NO_3^-, PO_4^{3-} and $Si(OH)_4$) were measured as detailed in Bonnet et al. (2018): 20 mL of filtered water samples were collected into High Density PolyEthylene (HDPE) flasks. Filtration by gravity was done through a Sartobrand cartridge from each CTD niskin. NO_2, NO_3^- and PO_4^{3-} samples were frozen at -20°C while $Si(OH)_4$ samples were only refrigerated pending analysis. For ammonium (NH_4), 20 mL samples were collected into PC 60 mL Nalgene Oak Ridge bottles. Analysis was performed on board using a Fluorimeter TD-700 Turner Designs using Holmes et al. (1999) method.

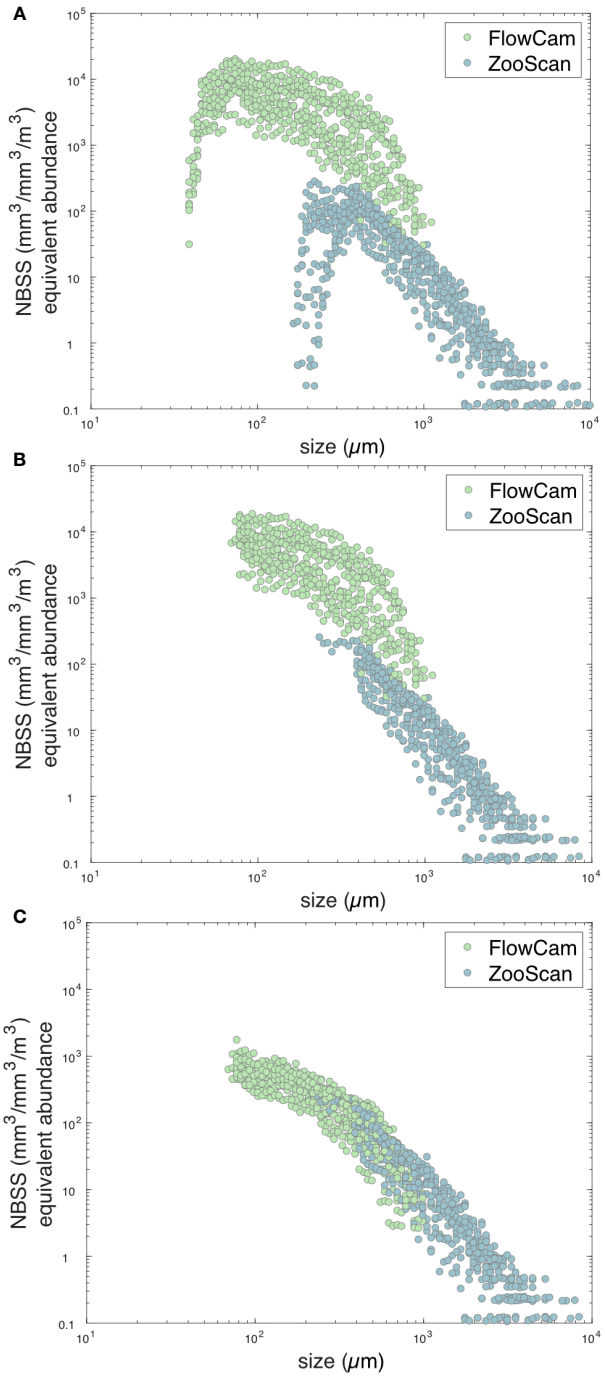

FIGURE 3
Normalized Biovolume Size Spectra (NBSS) in mm^{-3} m^{-3} representative of the number of living organisms per size class (µm) imaged with the two different quantitative imaging devices: FlowCam and ZooScan. **(A)** NBSS representation of the raw data before the correction methods. **(B)** NBSS representation of the intermediate data with the correction of the undersampling in the lowest and largest class size. **(C)** NBSS representation of the adjusted data with the application of the cross-size class average correction coefficient (ZooScan was used as a reference).

2.5.3 Particulate trace elements

Trace element measurements were carried out within 12 months of collection by a SF-HR-ICP-MS Element XR instrument (Thermo Fisher, Bremen, Germany), at Pôle Spectrométrie Océan (IFREMER, France). The method employed was similar to that of Planquette and Sherrell (2012). Particulate Mn (pMn), pFe and pAl were used as proxies to trace hydrothermal inputs.

2.5.4 Interpolation of environmental data

Data were interpolated on the vertical dimension to have a regular depth step (one value every meter from 0 to 200 m) and thus

make the dataset homogeneous to reduce the sampling bias. Macronutrients (NH_4, NO_3^-, PO_4^{3-} and $Si(OH)_4$), DFe and pTM data were polynomially interpolated with a fourth order polynomial function (1), while NO_2 data were interpolated following the Gaussian Model (2):

$$f(x) \ : \ x^4p1 + x^3p2 + x^2p3 + x^1p4 \ + \ p5 \quad (1)$$

$$f(x) = \ a1 \ \times \ e^{-((x-b1)/c1)^2} \quad (2)$$

Because macronutrients, DFe and pTM were generally not collected above 10 m, the surface reference depth was set at 10 m. This also avoids much of the strong variability due to the diurnal cycle in the upper ocean. For all interpolation with a fourth order polynomial function, an upper bound was imposed by setting the deepest concentration value to 200 m. For each station, the Mixed Layer Depth (MLD) has been calculated as the depth where $\theta = \theta_{10m} \pm 0{,}2°C$ (de Boyer Montégut, 2004). The MLD ranged from minimum 17 m (SD 07) to maximum 71 m (SD 03). Two values were finally calculated per environmental parameter by averaging the interpolated data from the surface to the MLD (data "up") and then from the MLD to 200 m (data "down"). The DCM was estimated as the depth at which fluorescence (proxy for Chl *a*) is maximum, according to Sauzède et al. (2015).

2.6 Acoustic data: indicator of macro-zooplankton biomass and density

Continuous acoustic measurements were made with a calibrated (Foote, 1987) Simrad EK60 echosounder operating at two frequencies: 38 and 200 kHz. To focus on the acoustic scattering in the photic layer, we only used the 200 kHz frequency, with a maximum acquisition range of 120 m. Power and pulse length were 45 W and 1024 µs, respectively. Data used in this study were acquired with an average ping interval of 7 s when the vessel speed was higher than 2 knots. Acoustic data were scrutinized, corrected and analyzed using the "Movies3D" software developed at the Institut Français de Recherche pour l'Exploitation de la Mer (Ifremer; Trenkel et al., 2009) combined with the French open-source tool "Matecho" (Perrot et al., 2018) from the Institut de Recherche pour le Développement (IRD). Noise from the surface was removed (from 3 m below the transducer, i.e. 8 m depth from the surface), the bottom ghost echoes were excluded, and the bottom line was corrected. Single-ping interferences from electrical noise or other acoustic instruments, and periods with either noise or attenuated signal due to inclement weather were removed using the filters described by Ryan et al. (2015). Background noise was estimated and subtracted using methods described by de Robertis and Higginbottom (2007). The nautical area scattering coefficient (NASC in m^2 nmi^{-2}), an indicator of marine organism biomass, and the volume backscattering strength (Sv in dB re 1 m^{-1}), an indicator of the marine organism density, were calculated. Acoustic symbols and units used here follow Maclennan (2002). Data were echo-integrated into 1 m high layers over a 0.1 nm giving one ESU (Elementary Sampling Unit) with a -100 dB threshold from 8 m down to 120 m depth. Diel vertical migration (DVM) is a common behavior for zooplankton and micro-nekton that can be observed at almost all spatial scales (Haury et al., 1978). Acoustic data were thus split into day, night and crepuscular periods (dawn and dusk). Day and night periods were defined based on the solar elevation angle: daytime when the solar elevation is higher than 18° and night when the solar elevation is lower than 18°, as described in Lehodey et al. (2015).

2.7 Lagrangian analysis

2.7.1 Velocity currents and trajectories calculation

Horizontal current velocities were provided by the Copernicus Marine Environment Monitoring Service (CMEMS, http://marine.copernicus.eu/). These are considered representative of the velocities in the first ~50 m of the water column, include a geostrophic and Ekman components, and have a daily resolution and 1/25° spatial resolution (product SEALEVEL_GLO_PHY_L4_REP_OBSERVATIONS_008_047). Trajectories were calculated with a 3 hours time step, using a Runge-Kutta scheme of order 4.

2.7.2 Chlorophyll a data

Chlorophyll [CHL a] data were obtained from the OCEANCOLOUR_GLO_BGC_L4_MY_009_104-TDS product which was provided by CMEMS platform (product version cmems_obs-oc_glo_bgc-plankton_my_l4-gapfree-multi-4km_P1D). This is satellite product of level 4 with 4 km spatial resolution and is provided daily. Daily fields of [CHL *a*] for the month of November 2019 were averaged together, providing the mean [CHL *a*] of our region of interest during the campaign period.

2.7.3 Detection of the lagrangian plume stemming from the 2 target volcanoes

In order to quantify the effect of the Tonga Arc on phytoplankton concentration, we analyzed whether water parcels displaying enhanced [Chl *a*] had been in contact with the two shallow hydrothermal vents. To achieve this, a regular grid of 0.1° cell-size (~11 km) covering the study region was created. Each point, considered representative of a water parcel, was advected backward in time from a day t_0 until t_0-150 days. Then, for each water parcel, we identified how many days before it eventually passed over one of the two volcanoes (considered as a disk of 0.5° (~55 km) radius). This metric, hereafter the *Lagrangian plume*, was calculated using the 1st of November 2019 as t_0. This operation was repeated for each day between the 1st and the 30th of November 2019, and the 30 Lagrangian plume fields were averaged together. Points that did not come into contact with either volcano were excluded from the average. The two volcanoes were considered in correspondence with LD 10-T5 and LD 05-T4, which were the closest stations to the hydrothermal vents. This approach has already been validated to study the island mass effect, and has made it possible to reproduce the Kerguelen and Crozet blooms (Sanial et al., 2014; d'Ovidio et al., 2015; Sanial et al., 2015) or, more recently, the phytoplankton bloom stemming from seamounts in the Southern Ocean (Sergi et al., 2020).

2.7.4 Bootstrap test

A bootstrap test was performed to test whether water parcels which came into contact with the volcanoes, and the water parcels which did not, presented different [CHL *a*] values. For this purpose, firstly we calculated the [Chl *a*] value for each point of the regular grid (using the mean [Chl *a*] of November 2019). Secondly, we divided the grid points into two groups: those which have been in contact with volcanoes, less than τ days before, and those who did not. The statistical independence of the two groups was tested with a Mann-Whytney or U test. Finally, a bootstrap analysis was applied following the methodologies in Baudena et al. (2021). As τ, we tested different values, ranging from 5 to 150 days. We selected a tau of 115 days because it was the greatest value for which the difference between the two groups was significant.

3 Results

3.1 Environmental characteristics

The Melanesian waters and the South Pacific Gyre were characterized by oligotrophic waters ([Chl *a*]< 0.15 mg m^{-3}; Figure 1; DCM: 100-180 m). In contrast, the Lau Basin was characterized by mesotrophic waters in the vicinity of the Tonga arc ([Chl *a*] > 0.15 mg m^{-3}; Figure 1; DCM: 70-90 m). NO_3^- concentrations at the surface (0-50 m) were consistently close or below the detection limit (0.05 µmol L^{-1}) throughout the transect, while PO_4^{3-} concentrations were typically 0.1 µmol L^{-1} in oligotrophic zones and depleted down to detection limit (0.05 µmol L^{-1}) in the mesotrophic zone (i.e. Lau Basin). Concerning the dFe values (Tilliette et al., 2022), stations furthest from the Tonga-Kermadec arc in the South Pacific Gyre (i.e., SD 7 and 8) were characterized by low [dFe] in the photic layer (< 0.2 nmol kg^{-1}). The station SD 6, closest to the arc was slightly different from the other stations of the gyre. Although [dFe] remain low throughout the whole water column (< 0.3-0.4 nmol kg^{-1}, [dFe] were higher than those at SD 7 and 8 in the surface layer. Melanesian waters were characterized by a dFe enrichment in the photic layer compared to the waters of the South Pacific gyre with [dFe] as high as 0.4-0.5 nmol kg^{-1}. In the Lau Basin, we observed higher [dFe] than in the South Pacific gyre as well as in Melanesian waters for all stations. SD 11 had the highest [dFe] of the SD in the Lau Basin in the photic layer (0.4-0.6 nmol kg^{-1}). SD 12 presented the least enriched photic layer, with [dFe] similar to those observed to the east (~0.2 nmol kg^{-1}). Sea surface temperature (SST) ranged from 24.3°C (SD 01) to 27.3°C (LD 10-T3) above the MLD.

3.2 Description of the micro-plankton community (20-200 µm)

3.2.1 Quantification

The highest micro-plankton concentrations were found at stations west of the Tonga arc, reaching a maximum at SD 11 (8.60 10^4 ind m^{-3}), LD 10-T5 and LD 10-T3, followed by LD 05-T1 and LD 05-T2 (Figure 4A). The minimum of micro-plankton abundance was found in SD 06 (8.75 10^3 ind m^{-3}) located right to the east of the Tonga Arc. The average concentration of micro-plankton in the Lau Basin was 4.33 10^4 ind m^{-3}. Micro-plankton concentrations in the South Pacific Gyre were 2.28 times lower on average (1.90 10^4 ind m^{-3}).

3.2.2 Community composition

In terms of community composition, diazotrophic cyanobacteria clearly dominated, notably cyano a and b, UCYN colonies and t005_F, accounting for 69% on average of the total micro-planktonic concentration (total: 5.00 10^5 ind m^{-3}), with a maximum at SD 11 (80% of the total community). This dominance was confirmed by the linear regression between cyanobacteria and total micro-plankton concentration (R2 = 0.92). Furthermore, a significant negative correlation was found between the micro-plankton concentration and the Shannon diversity Index (data not shown; y = 1.72 10^{-5} x + 3.17; R^2 = -0.72, p = 0.007). The majority of the variance in the PCA (Figure 4B; PC1; 59% of variance) showed that the diazotroph dominance correlated with water rich in DFe, Chl *a* and pTM (pAl and pMn), and low salinity and PO_4^{3-} concentrations. Changes in community correlated to [DFe] were observed. First, a community dominated by cyano b (probably genus *Trichodesmium*) correlated to high [DFe] was found. Secondly, cyano a and t005_F (probably genus *Katagnymene* for both) were associated to UCYN. Then, a cyanobacteria-poor community was correlated with low [DFe]. Diazotrophic cyanobacteria-poor stations had a more diverse micro-plankton community, such as at SD 08 in the South Pacific Gyre which differed strongly from other stations. Even if this difference represents a few percentages of variance (Figure 4B; PC2; 15%), different cyanobacteria distribution was found in the Lau Basin notably between the two LD stations. More cyano a and t005_F (*Katagnymene*) were found at LD 10 while more cyano b (*Trichodesmium*) were measured at LD 05. This can also be seen on the cluster map (Figure 4C), with stations close to the Tonga arc showing clusters characterized by cyanobacteria dominance, except for LD 10-T1 which is associated with SD 07 in the South Pacific Gyre.

3.3 Description of the meso-plankton community (>200 µm)

3.3.1 Quantification

The highest meso-plankton concentrations (Figure 5A) were found in the Lau Basin at LD 10-T5 (510.6 ind m^{-3}), followed by LD 10-T3 station (446.0 ind m^{-3}) then by LD 05 sub-stations and at SD 11 and 12. The average concentration in the Lau Basin was 328.9 ind m^{-3}. In contrast, low concentrations were found in the oligotrophic zone of the South Pacific Gyre, with SD 07 (78.6 ind m^{-3}) and SD 08 (112.7 ind m^{-3}). The mean concentration in the South Pacific Gyre was 132.8 ind m^{-3}, while Melanesian waters showed an intermediate mean meso-plankton concentration of 232.6 ind m^{-3}. Contrary to the micro-plankton where the concentration was negatively correlated to the diversity (cyanobacteria dominance opposed to a diverse community), no significant correlation was found between meso-plankton concentration and the Shannon

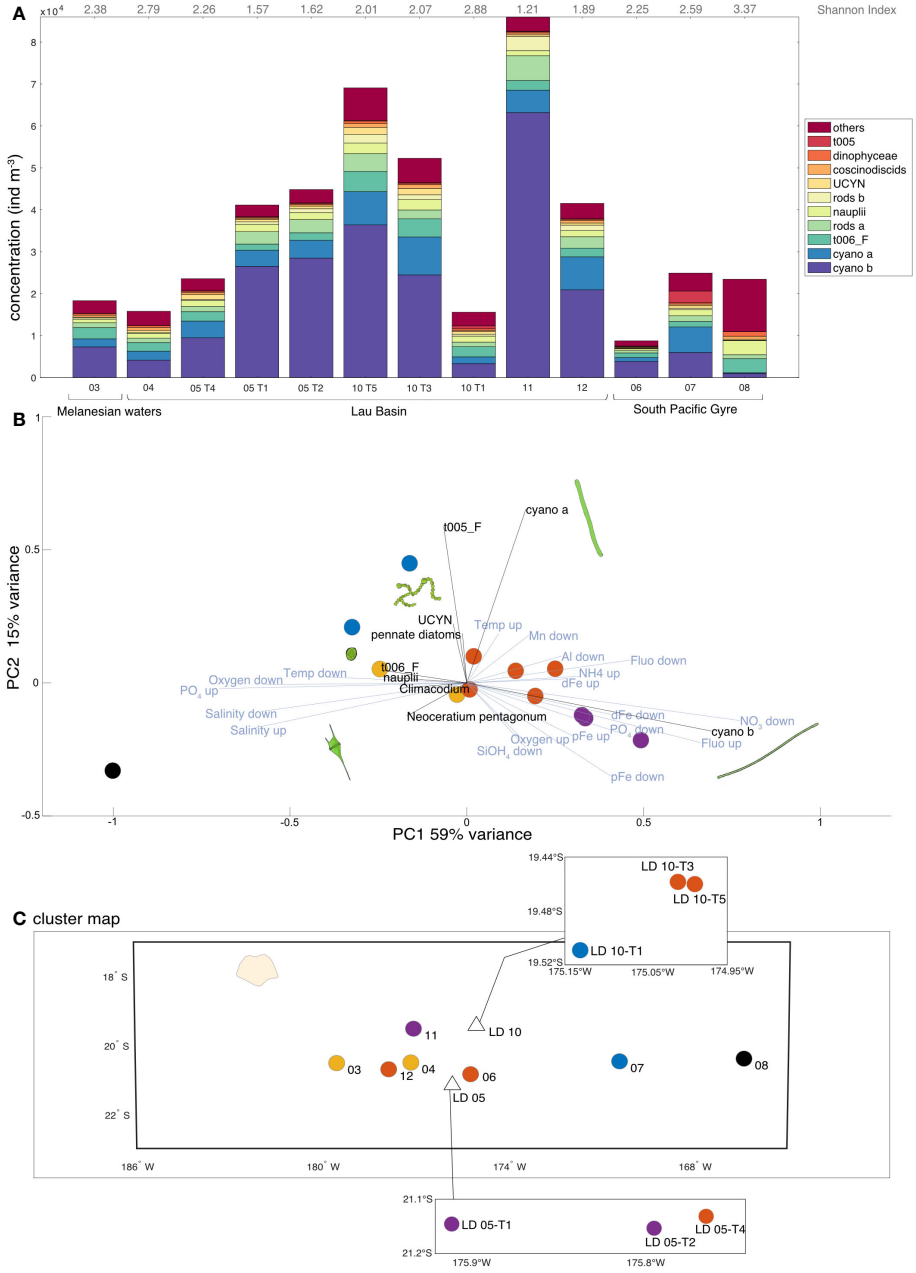

FIGURE 4
(A) Micro-plankton concentration (ind m^{-3}) and composition of the 10 most abundant taxa (representing about 88% of the dataset). The rest of the micro-planktonic organisms (114 taxa) were grouped within the category "others". Values of the Shannon diversity Index are indicated in grey. **(B)** Principal Component Analysis (PCA) on relative abundances of micro-plankton (Hellinger-transformed data). Only environmental data (in blue) with a contribution greater than 0.25 and taxonomic data (in black) with a contribution greater than 0.18 are shown for ease of reading. The environmental variables are the averages of interpolated data from the surface to the MLD (up) and then from the MLD to 200 m (down). The colors correspond to the five characteristic clusters determined via an independent hierarchical analysis (HAC) with Euclidean distance. **(C)** Projection of the clusters determined by HAC on the transect map with the corresponding station numbers. Credit plankton illustration: Tohora Ereere.

diversity Index (data not shown; y = - 8.20 x 10-4 + 3.12; R2 = 0.51; p = 0.06). The relative abundances underlined a shift from copepod dominance to co-dominance of cyanobacteria and copepods (or over-dominance of cyanobacteria in some cases) west of the Tonga arc as one approaches the arc.

3.3.2 Community composition

PCA coupled with cluster analysis (Figures 5B, C) showed a very strong signal on meso-planktonic community change. The maximum of the variance (PC1: 56% of variance; Figure 5B) showed a clear gradient, with (i) the more diverse communities dominated

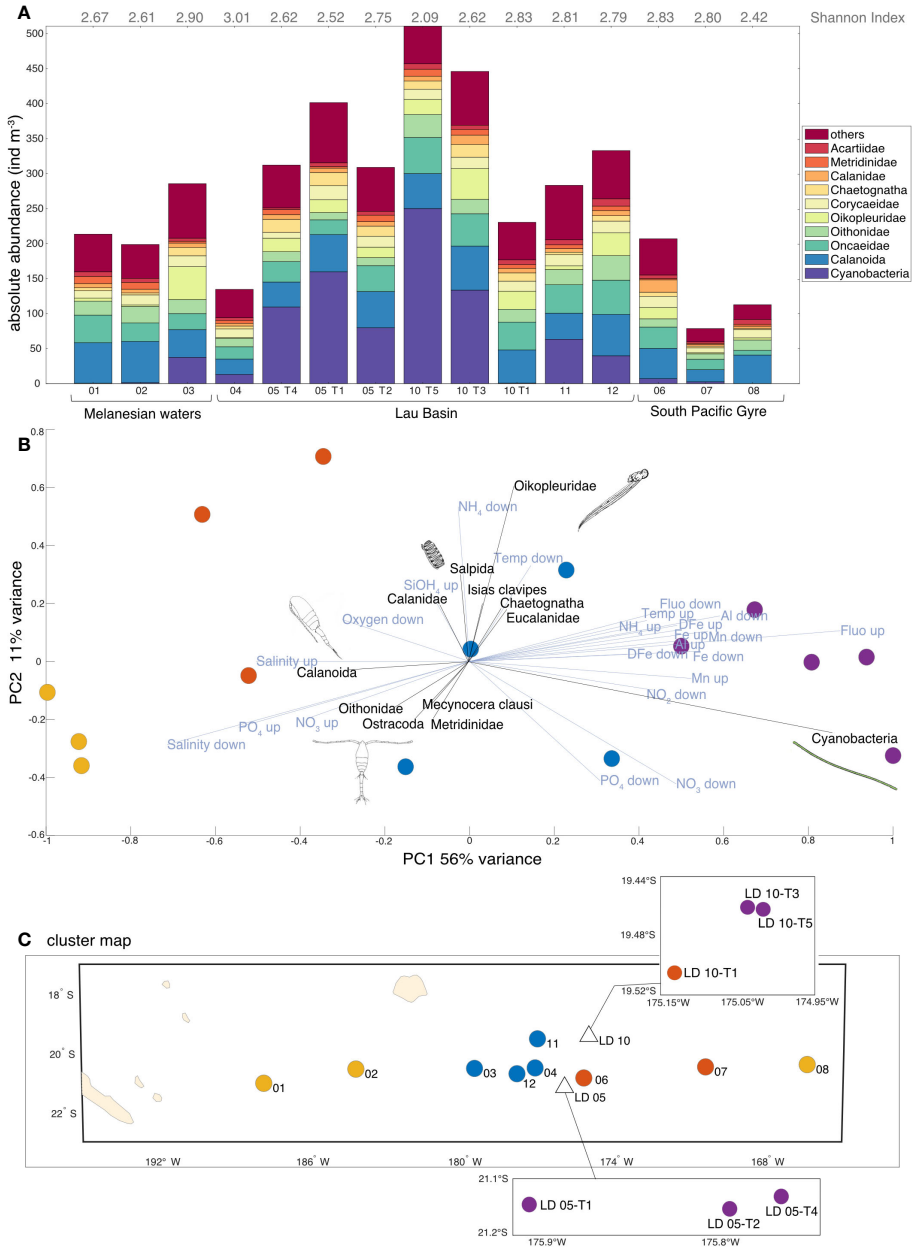

FIGURE 5
(A) Meso-plankton concentration and composition of the 10 most abundant groups (representing about 79% of the dataset). The rest of the planktonic organisms (139 taxa) are grouped within the category "others". Values of the Shannon Index diversity are indicated in grey. **(B)** Principal Component Analysis (PCA) on relative abundances of meso-plankton (Hellinger-transformed data). Only environmental data (in blue) with a contribution greater than 0.25 and taxonomic data (in black) with a contribution greater than 0.17 are shown for ease of reading. The colors correspond to the four characteristic clusters determined via an independent hierarchical analysis (HAC) with Euclidean distance. The environmental variables are the averages of interpolated data from the surface to the MLD (up) and then from the MLD to 200 m (down). **(C)** Projection of the clusters determined by HAC on the transect map with the corresponding station numbers. Credit plankton illustration: Tohora Ereere.

by different copepod genus within SD far from the Tonga Arc (SD 08, 01, 02); (ii) distinctive communities in SD 06, 07 and LD 10-T1, (iii) communities with a rather gelatinous composition (i.e. salpida, oikopleura, chaetognatha, generally filter-feeding and detritivorous organisms) at most SD of the Lau Basin, and (iv) cyanobacteria-dominated communities at LD sub-stations close to the Tonga Arc. Cyanobacteria-dominated sub-stations were correlated with waters rich in DFe, Chl *a* and pTM (pAl and pMn), but with low salinity and PO_4^{3-}.

3.4 Description of the plankton community as a whole

3.4.1 Quantification

To consider both micro- and meso-plankton equally, we considered their biovolume (proxy for biomass) rather than their concentration. An increase in plankton biovolume (Figure 6A) was observed in the Lau Basin with the highest biovolumes observed at LD 10-T3 and LD 05-T1 (i.e. 100.15 and 94.98 mm^3 m^{-3},

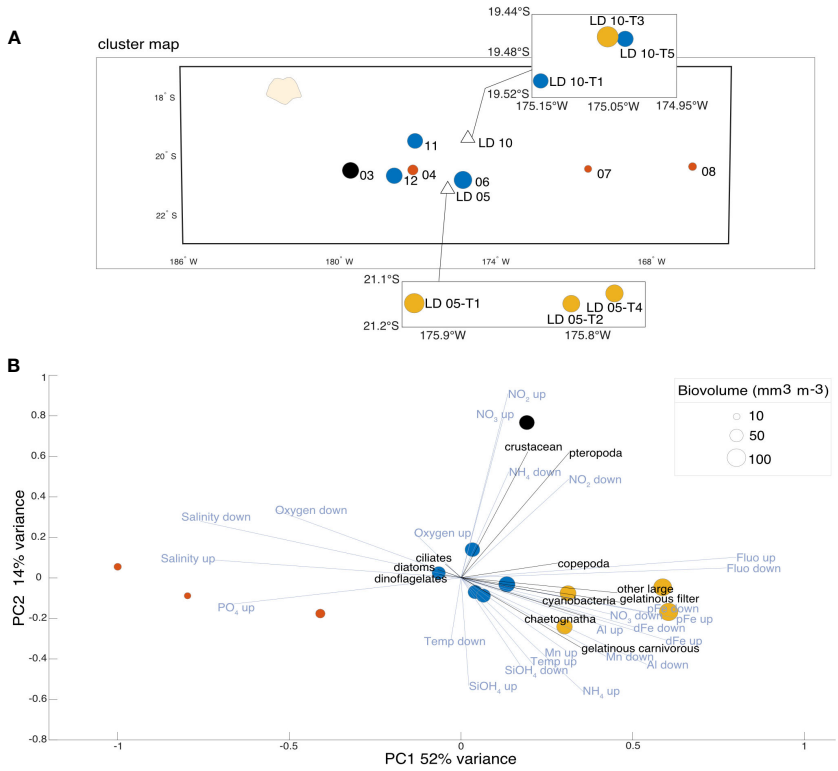

FIGURE 6
(A) Projection of the clusters determined by hierarchical analysis (HAC) on the transect map with the corresponding station numbers, points size corresponding to biovolume. **(B)** PCA on normalized biovolume (equivalent to biomass) of the plankton functional types (pft; in black). Only environmental data (in blue) with a contribution greater than 0.25 are shown for ease of reading. The environmental variables are the averages of interpolated data from the surface to the MLD (up) and then from the MLD to 200 m (down). The size corresponds to the plankton biovolume (mm^3 mm^{-3}) at each station. The colors correspond to the four characteristic clusters determined via the hierarchical analysis (HAC) with Euclidean distance.

respectively). The mean biovolume in the Lau Basin was 66.44 mm^3 m^{-3} while the mean biovolume in the South Pacific Gyre was 35.64 mm^3 m^{-3}. The lowest planktonic biovolumes were found in these oligotrophic waters, especially at SD 07 and 08 where biovolumes reached values of 13.32 and 16.32 mm^3 m^{-3}, respectively.

3.4.2 Community composition

The planktonic community identified at SD 04, in the Lau Basin, was similar to those measured in the stations in the gyre, reaching a low biovolume (26.31 mm^3 m^{-3}; Figures 6A, B). The PCA (Figure 6B) described a plankton community dominated by cyanobacteria associated with gelatinous organisms (pft: filter feeders, carnivores and chaetognatha) and directly correlated with waters rich in DFe, Chl *a* and pTM (pAl and pMn) but with low salinity and PO_4^{3-}. The cyanobacteria-dominated community, associated in previous analyses with LD stations, appears from this analysis to be more representative of LD 05. Indeed, two of the three LD 10 substations were associated with the more diverse planktonic communities in the Lau Basin by the clustering analysis. SD 03, located in the Melanesian waters, is distinguished from the other stations by its high crustacean and pteropod biovolume correlated with high surface NO_3^- concentrations. The oligotrophic zone of the South Pacific Gyre is composed of a community dominated by small autotrophs (pft: ciliates, diatoms, and dinoflagellates).

3.5 Impact on the higher food web (macro-zooplankton and fish) with acoustic detection

Acoustic detection analysis was carried out to gain an overview of the upper food web, mainly meso- and macro-zooplankton. To this end, we represented the results of acoustic detection during the cruise trajectory, with an indicator of the density of these organisms (Sv) in Figure 7A and an indicator of their biomass (NASC) in Figure 7B. The oligotrophic waters of the South Pacific Gyre were identified as poor in biomass and density of meso-plankton and fish (i.e minimum NASC of 5.60 m^2 nmi^{-2} at 167°W in the South Pacific Gyre; Figure 7B). A clear progressive increase in biomass towards the Lau Basin was observed. A biomass peak (up to NASC of 7.40 m^2 nmi^{-2} at 177°W; Figure 7B) was observed in the Lau Basin near the Tonga Arc where the maximum plankton biomass was also observed (see sections 3.2, 3.3 and 3.4). A slight decrease in biomass (NASC average of 6.52 ± 3.32 m^2 nmi^{-2} from 180°W to 193°W; Figure 7B) was visible in the Melanesian waters compared to the Lau Basin,

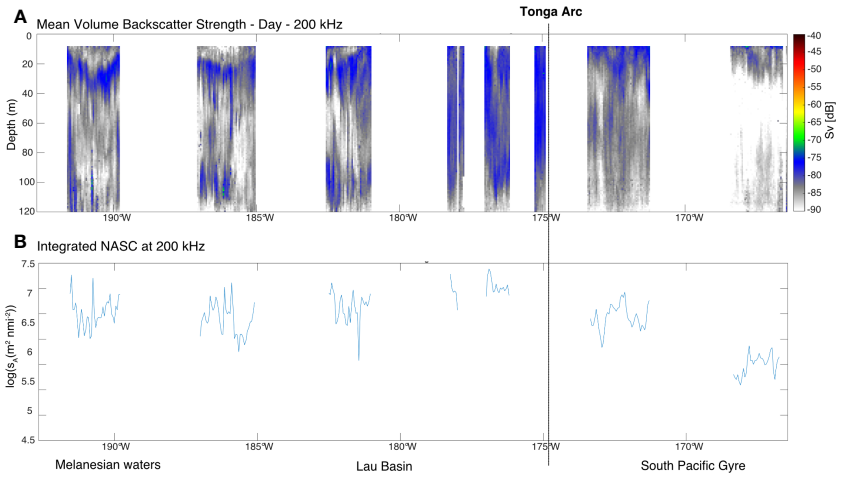

FIGURE 7
(A) Synthetic averaged acoustic density (Sv) echogram at 200 kHz from 8 to 120 **m** during the day. Color bar indicates Sv in dB re 1 m^{-1}. The organisms observed by these acoustic methods are mainly macro-zooplankton and fish. **(B)** Integrated acoustic biomass (nautical area scattering coefficient NASC in $\log(s_A(m^2\ nmi^{-2}))$ at 200 m. The Sv and NASC are averaged on a 0.05° longitude step grid. For **(A)** and **(B)**, the approximate position (Ruellan and Lagabrielle, 2005) of the Tonga arc is represented by a black dotted line.

although it was still higher than the biomass observed in the South Pacific Gyre.

3.6 Lagrangian dispersion around the two target hydrothermal vents of the Tonga Arc

The Lagrangian plume, averaged over the month of November 2019, reveals a global dispersion towards the southeast (Figure 8A). The water parcels sampled at SD 06 (i.e. South Pacific Gyre), 11, 12 and 04 (i.e. Lau Basin) passed above the hydrothermal vents 35, 106, 114, and 103 days before the sampling, respectively. Conversely, water parcels sampled in the western oligotrophic Gyre (SD 08 and 09) and Melanesian waters (SD 01, 02 and 03) did not pass above the hydrothermal vents in the previous 115 days (see 2.7). To determine whether the hydrothermal vents affected the primary productivity of the region, the Lagrangian plume contour at 115 days was superposed on the mean [Chl *a*] of November 2019, finding a remarkable agreement (Figure 8B). For instance, a meander at around 22°S, 167°W characterized by an enhanced [Chl *a*] concentration, passed over the vents ~100 days before. To quantify whether the observed differences in Chl *a* content inside and outside the Lagrangian plume contour were significant, we performed a bootstrap test (Figure 8C) over the whole region. The test revealed that the [Chl *a*] was significantly higher inside the Lagragian plume (0.1044 mg m^{-3}) than outside (0.0738 mg m^{-3}; Figure 8C). Notably, we obtained a significant decrease in [Chl *a*] content as a function of the amount of time since the water parcel passed over the volcanoes (R^2 = 0.49, p< 0.05, slope: -0.0027 mg m^{-3} d^{-1}; see Supplementary Figure 1). In other words, as water parcels moved away from the hydrothermal vents, their [Chl *a*] content decreased. The area of the 115-day Lagrangian influence patch is equal to 412 770 km^2 (white dashed surface air: Figures 8A, B). Complementing our results, previous and subsequent years (averaged over the month of November 2017, 2018, 2020 and 2021, see Supplementary Figure 2) also show an overall southeastward dispersion of Chl *a*, similar with our study year.

4 Discussion

The main goal of the TONGA project was to evaluate the potential impact of shallow hydrothermal inputs in the vicinity of the Tonga volcanic arc on planktonic communities and organic carbon export to the deep ocean (Bonnet et al., 2023). This study highlights that plankton communities, from micro- to macro-plankton, harbor high abundances and biomasses in the Lau Basin located close to the Tonga volcanic arc and, to a lesser extent, in Melanesian waters located west of the arc (Figure 9). These high abundances and biomasses were correlated with the environmental signatures indicative of the hydrothermal vents, as indicated by Guieu et al. (2018) and Bonnet et al. (2023): waters rich in DFe, Chl *a* and particulate trace element (pAl and pMn) but low in salinity and PO_4^{3-} (see PCA Figures 4–6). Therefore, they are associated with these hydrothermal vents in a good agreement with Bonnet et al. (2023) who demonstrated that Fe-rich fluids released close to the shallow volcano represent a significant Fe source for planktonic communities in surface waters.

4.1 Major impact of DFe-rich hydrothermal inputs on the diazotrophic micro-phytoplankton community

4.1.1 Clear dominance of diazotrophs

The highest concentrations of micro-plankton were observed west of the Tonga Arc in the Lau Basin, reaching maximums at stations near the Arc, while the minimums of micro-plankton

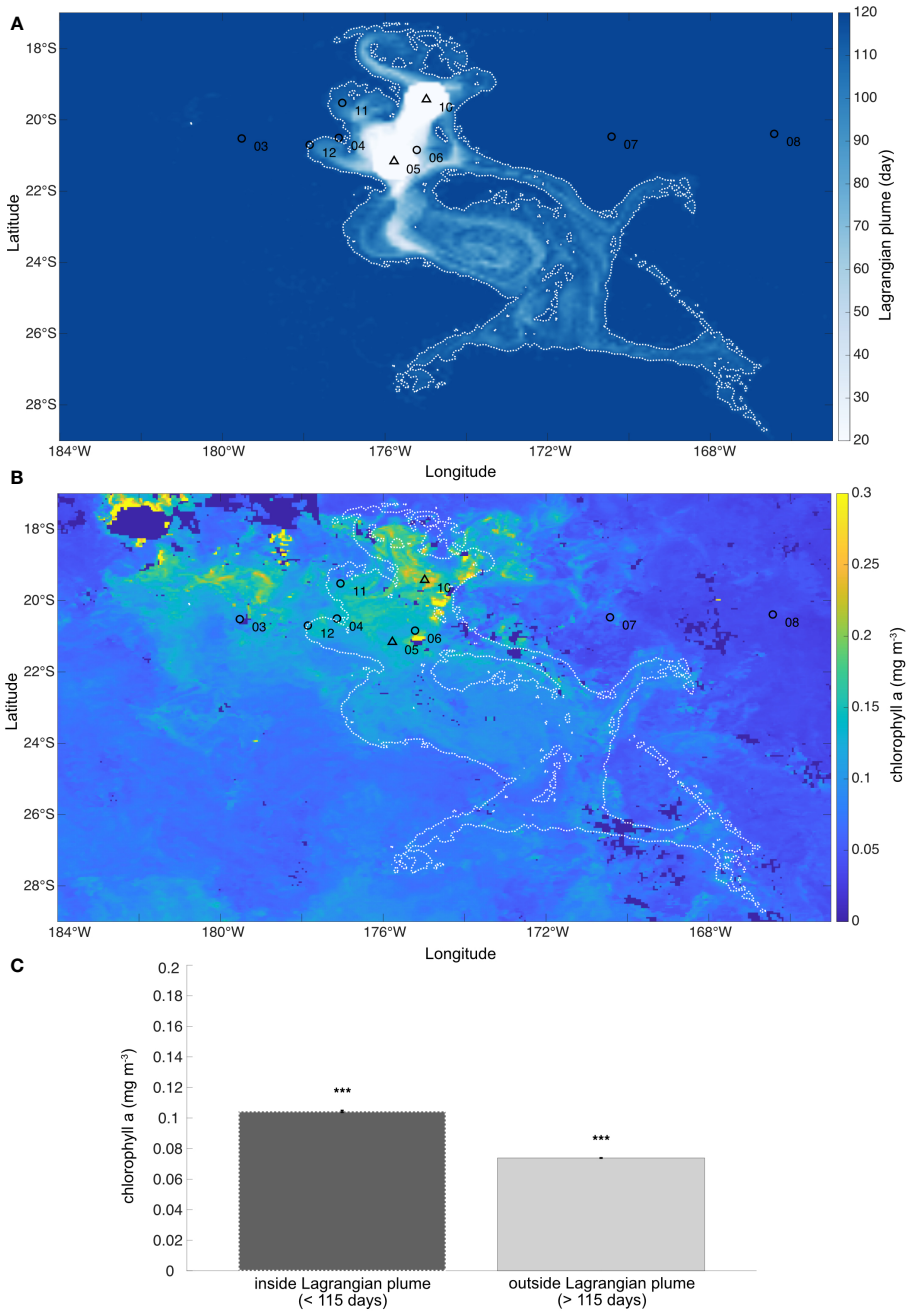

FIGURE 8
(A) Average Lagrangian plume for November 2019 in the WTSP region. The color of each point indicates how many days before the corresponding water parcel came into contact with one of the two target hydrothermal vents (black triangles). White dashed lines show the contours of the Lagrangian plume at 115 days. **(B)** Average chlorophyll *a* concentration ([Chl *a*]; mg m^{-3}) observed in November 2019 (monthly-mean composite image, data from MODIS-Aqua at 4 km resolution). White dashed lines show the contours of the Lagrangian plume at 115 days reported in panel **(A)**. **(C)** Bootstrap results. The dark gray column shows the average [Chl *a*] inside the Lagrangian plume, i.e. at the locations showing a Lagrangian plume value less than 115 days, considered under the effect of the hydrothermal sources. Conversely, the light gray column shows the average [Chl *a*] outside the Lagrangian plume, i.e. at the locations showing a Lagrangian plume value greater than 115 days, considered as not affected by hydrothermalism. Error bars indicate the standard deviation. The three stars indicate the significance of the bootstrap test ($p < 0.001$) between the [Chl *a*] values inside and outside the Lagrangian plume.

concentration were observed east of the Tonga Arc in the South Pacific Gyre (Figure 4A). The high micro-plankton concentration was dominated by diazotrophs in the Lau Basin, accounting for up to 80% of the micro-plankton community near hydrothermal vents (Figure 4A). This strong dominance of the community by diazotrophs has also been demonstrated in Lory et al. (2022) and Bonnet et al. (2023) through quantitative PCR (qPCR) during the TONGA cruise, and in Leblanc et al. (2018) through Sedgewick-rafter chamber during OUTPACE cruise. Globally, this is in good agreement with the characterization of the WTSP as an N_2 fixation

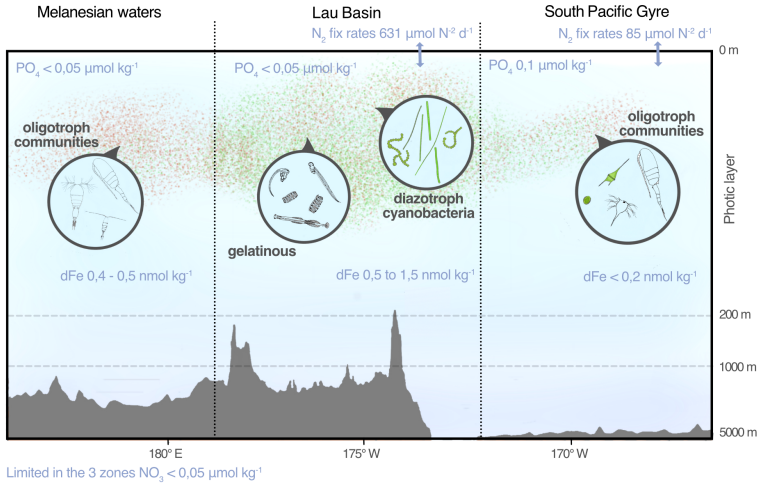

FIGURE 9
Summary diagram of the study results. The green and pink clouds represent the order of magnitude of the abundances of micro-plankton and meso-plankton, respectively (see Figures 3 and 4). Zooms show an overview of the plankton communities found. N_2 fixation rates (N_2 fix rates) are from Bonnet et al. (2017) and dissolved iron concentrations ([DFe]) are from Tilliette et al. (2022). Credit illustration: Tohora Ereere.

hotspot, particularly for the Lau Basin and Melanesian waters, which exhibit very high N_2 fixation rates of ~631 µmol N m^{-2} d^{-1} due to diazotrophs (Bonnet et al., 2018). Our results demonstrate a spatial correlation between high diazotroph concentrations and high DFe inputs from hydrothermal vents into the photic layer (DFe_{up} in the PCA; Figure 4B). This is confirmed by Bonnet et al. (2018) and Bonnet et al. (2023), who demonstrate a significantly positive correlation between N_2 fixation and [DFe] in this region. Planktonic diazotrophs play a crucial role in supplying new available nitrogen as they are capable of assimilating atmospheric N_2, thus overcoming N deficiency. However, besides phosphorus requirements, diazotrophs also have high iron demands due to the iron-rich enzyme involved in the N_2 fixation process (Zehr, 2011). Therefore, the high concentrations of diazotrophs observed in the Lau Basin can be attributed to nitrate limitation (surface [NO_3^-] close to or below the detection limit of 0.05 µmol L^{-1}; see 3.1) and to the DFe input from hydrothermal vents into the photic layer ([DFe] of 66 nM: Guieu et al., 2018; [DFe] of 47 nM: Tilliette et al., 2022). Additionally, our analysis of the variance in PCA Figure 4B revealed that the dominant presence of diazotrophs correlated with low concentrations of [PO_4^{3-}] (depleted to the detection limit of 0.05 µmol L^{-1}; see 3.1), which aligns with the consumption of [PO_4^{3-}] by diazotrophs. Conversely, in the Gyre, the low concentration of diazotrophs resulting from DFe limitation allows for the accumulation of PO_4^{3-}, which explains the high [PO_4^{3-}] measurements in the South Pacific Gyre (0.1 µmol L-1; see 3.1).

4.1.2 Diazotroph composition along the transect

In terms of diazotroph composition, we observed a community mostly composed of cyano a (probably *Katagnymene)*, cyano b (probably *Trichodesmium*), UCYN-B colonies and t005_F (probably *Katagnymene)*. Additionally, we identified the presence of *Katagnymene spiralis, Richelia* alone or in DDAs (*Rhizosolenids inter-Richelia*). Leblanc et al. (2018) also described this diazotrophic composition in plankton nets during the OUTPACE cruise, highlighting the dominance of *Trichodesmium*, *Richelia intracellularis* (alone or in DDAs), UCYN-B and other filamentous cyanobacteria such as *Katagnymene*. Our results demonstrate a distribution of the diazotrophic community along a [DFe] gradient. In the Lau Basin, west of the Tonga Arc, we observed a cyano b-dominated community (*Trichodesmium*) associated with the highest [DFe]. As we move towards lower [DFe], there is a transition to a community dominated by cyano a, t005_F (probably *Katagnymene* for both), and UCYN-B (Figure 4). The t005_F category appears to correspond to the mucilaginous sheath of *Katagnymene* and may indicate the transition to an ultra-oligotrophic zone in the South Pacific Gyre, where DFe is too scarce to support the growth of these diazotrophs.

However, it's important to note that the quantitative imaging used in this study has a limitation in the size range observed, only capturing diazotrophs larger than 20 µm. In complement to this, qPCR analyses were performed during the OUTPACE and TONGA cruises, allowing the detection of the main diazotroph groups (Stenegren et al., 2018; Lory et al., 2022; Bonnet et al., 2023) in the micro (>10 µm), nano- (2-10 µm), and pico-planktonic (0.2-2 µm) fractions. The distribution of diazotrophs observed in our study (> 20 µm) aligns with the findings described by Stenegren et al. (2018) during the OUTPACE cruise, who reported a surface diazotrophic community dominated by *Trichodesmium* and UCYN-B, with *Trichodesmium* primarily associated with oligotrophic waters in the Melanesian and Lau Basin, and UCYN-B predominant in the ultra-oligotrophic waters of the South Pacific Gyre. However, contrasting results were obtained from the TONGA omics analysis (Lory et al., in prep; qPCR of nifH gene, a biomarker used to study the diversity and fixation of diazotrophs). They revealed that surface diazotrophic communities were mainly dominated by UCYN-A (on average, 63% of stations sampled in the photic layer. UCYN-A was not detectable using our imaging methods as it falls below the size threshold of 20 µm. *Trichodesmium* accounted for 27% (average over stations sampled

in the photic layer), while UCYN-B represented approximately 9% (average over stations sampled in the photic layer). This contrast could be potentially explained on the one hand by the different target size range between the methods. It has also been shown that taxonomic assignments between the two omics/imaging data sources are not always comparable as they each present different methodological biases, although they are complementary and could derive mutual benefits (da Silva, 2022). However, in terms of distribution, these qPCR data from the TONGA cruise further confirmed that *Trichodesmium* dominates near the Tonga Arc, while UCYN-B concentrations are highest in the vicinity of hydrothermal vents and within the oligotrophic gyre. These findings also provided additional insights into UCYN-A, which was found to be most abundant away from hydrothermal vents, including in certain areas of the Lau Basin and Melanesian waters.

4.2 Propagation through the plankton food web

4.2.1 To the non-diazotrophic micro-plankton community

Diazotrophic micro-plankton clearly dominate in the Lau Basin and Melanesian waters stations. Indeed, the micro-plankton communities near hydrothermal vents exhibit significantly low Shannon diversity Index (Figure 4A). In comparison, the absolute abundance of non-diazotrophic micro-phytoplankton in the Lau Basin averages at 1.31 x 10^4 ind.m^{-3}, representing approximately 30% of the total micro-phytoplankton abundance in the Lau Basin. In the Melanesian waters, the absolute abundance of non-diazotrophic micro-phytoplankton is 8.78 x 10^3 ind.m^{-3}, accounting for approximately 48% of the total micro-phytoplankton abundance in Melanesian waters. In the oligotrophic Gyre, the average absolute abundance of non-diazotrophic micro-phytoplankton is comparable to the Lau Basin, at 1.27 x 10^4. Thus, these findings do not suggest a significant increase in the concentration of non-diazotrophic micro-plankton across the studied areas. However, in such nitrogen-limited waters, high N_2 fixation may be a main source of new N to surface waters (Gruber, 2008) and may allow the development of non-diazotrophic phytoplankton. An increasing number of studies has demonstrated that dinitrogen fixed by diazotrophs is rapidly transferred to non-diazotrophic plankton, particularly in this region by Adam et al. (2016); Bonnet et al. (2016); Berthelot et al. (2016); Caffin et al. (2018). Several studies have proposed a link between *Trichodesmium* blooms and subsequent increases in non-diazotrophic phytoplankton (Mulholland et al., 2004; Lee Chen et al., 2011). It is possible that our sampling occurred during the *Trichodesmium* bloom, which could potentially explain the absence of a signal indicating an increase in non-diazotrophic micro-phytoplankton. Indeed, Tilliette et al. (2023) performed an 9-day experiment in 300 L reactors onboard the TONGA cruise, to examine the effects of hydrothermal fluids on the succession of natural plankton communities. They showed a growth of the non-diazotrophic species occurred at days 2-4 after the *Trichodesmium* bloom, when phosphate and nitrate concentrations were nearly depleted. Nitrogen was made available to non-diazotrophic phytoplankton through N_2 fixation and the use of rather abundant DOP as an alternative P-source may have allowed their growth (Tilliette et al., 2022). Additionally, another potential hypothesis to consider, which complements the other, is the possibility of top-down control by grazing meso-zooplankton. We show that these organisms exhibit high abundance and biomass near the Tonga Arc (Figures 5 and 6) and thus, may consume directly non-diazotrophic plankton more readily and rapidly than *Trichodesmium* which, according to Capone et al. (1997), remains largely unconsumed. Therefore, the combination of these two hypotheses potentially helps to explain why we do not obtain a significant increase in non-diazotrophic micro-phytoplankton concentration.

4.2.2 To the meso-zooplankton community

The role of diazotroph blooms in structuring higher trophic levels of the planktonic food web have been poorly explored (Le Borgne et al., 2011). Cyanobacteria such as *Trichodesmium* are one of the groups with potential direct and indirect effects on herbivorous zooplankton, therefore affecting the trophic transfer efficiency (Suikannen et al., 2021). Molecular techniques are available to detect diazotrophs in the gut contents of zooplankton (i.e Hunt et al., 2016). Such analyses were not carried out as part of TONGA, and we limit our discussion to the correlations observed between the distribution and increase in abundance of zooplankton species and diazotroph bloom.

In this study, we uncovered a spatial structuring of the micro-planktonic community by diazotrophic organisms, which could, in turn, support meso-planktonic production. We observed important meso-planktonic concentrations (reaching up to 510.6 ind m^{-3} near the hydrothermal vents; Figure 5) and overall high plankton biovolume in the Lau Basin (averaging 67.8 mm^3 m^{-3}; Figure 6). Regarding composition, our findings demonstrate a clear spatial correlation between the meso-planktonic community and its proximity to the hydrothermal vents. Diverse communities dominated by various copepod genera were found further away from the Tonga Arc, contrasting with communities dominated by cyanobacteria and primarily associated with gelatinous organisms (e.g., filter feeders and carnivores) near the Tonga Arc (Figures 5, 6).

Our distribution of the meso-zooplankton community aligns well with the findings of Carlotti et al. (2018) during the OUTPACE cruise in the same region. They observed a similar decreasing trend in meso-zooplankton abundance and biomass from east to west, with a distinct decline in the South Pacific Gyre, which corresponds to the increased contribution of copepods to the meso-zooplankton as we also observed (Figure 5). These results can suggest that gelatinous organisms, primarily filter-feeding organisms, likely feed on pico- or nano-cyanobacteria such as the abundant UCYN-A and -B species highlighted by Lory et al. (qPCR data from the cruise; see section 4.1, in prep.). Gelatinous organisms also contribute to marine snow, providing a food source for detritivorous organisms that can also consume the large *Trichodesmium* species (Koski and Lombard, 2022). These filter feeders and detritus feeders are, in turn, likely consumed by carnivorous meso-zooplankton, which exhibit relatively high

abundances in our study (Figure 6: gelatinous carnivores, chaetognatha, copepoda, and other larger species).

4.2.3 Potential consumption of zooplankton on diazotrophs

Recent studies have provided evidence of zooplankton species feeding on various types of diazotrophs, particularly in this region (during the OUTPACE cruise: Caffin et al., 2018; Carlotti et al., 2018). This is consistent with several studies that have demonstrated the efficient transfer of diazotroph-derived nitrogen to meso-zooplankton communities (> 200 µm; Caffin et al., 2018; Carlotti et al., 2018). Carlotti et al. (2018), based on ^{15}N isotopic data, have established a link between zooplankton abundances and *Trichodesmium* blooms. They found that about 50-95% of the zooplankton N content originates from N_2 fixation in the western part of the Tonga Arc. Caffin et al. (2018) employed nanometre-scale secondary ion mass spectrometry (nanoSIMS) in combination with $^{15}N_2$ isotopic labeling and flow cytometry cell sorting to quantify the transfer of diazotroph-derived nitrogen (DDN) to meso-zooplankton. They suggest that the transfer of DDN to meso-zooplankton is higher with UCYN-B than with *Trichodesmium*, as UCYN-B can be directly grazed due to its small size (2-3 µm), as mentioned by Hunt et al. (2016). This finding can align with one of hypothesis of a high abundance of filter-feeding gelatinous organisms likely feeding on pico- or nano-cyanobacteria. It supports the idea of a direct transfer of DDN from UCYN-B to meso-zooplankton by a direct consumption of meso-zooplankton to UCYN-B. An complementary hypothesis is also the direct consumption of *Trichodesmium* and *Katagnymene* species by meso-zooplankton. *Trichodesmium* has been considered as a food source for zooplankton species, particularly harpacticoid copepods (O'Neil and Roman, 1994; O'Neil, 1998; Koski and Lombard, 2022). In contrast to our results and with previous studies by Carlotti et al. (2018) and Caffin et al. (2018); Turner (2014) have shown that high cyanobacteria biomass does not necessarily lead to an increase in zooplankton biomass, as *Trichodesmium* can be toxic or inedible. It may even cause a decline in the zooplankton community due to *Trichodesmium*-derived compounds that weaken organisms and facilitate the spread of viral infections (Guo and Tester, 1994). The direct via zooplankton grazing, has been considered limited due to cyanobacteria possessing cyanotoxins (Guo and Tester, 1994), large cell size in the case of filamentous cyanobacteria such as *Trichodesmium* and poor nutritional quality (O'Neil and Roman, 1992). However, in the case of the WTSP, our studies have revealed a diazotrophic community supported by DFe inputs from hydrothermal vents, which in turn supports meso-planktonic production.

4.2.4 Complementarity of acoustic data: to the meso- and macro-zooplankton community

The complementary use of acoustic data has provided us with an overview of the transfer to trophic levels higher than meso-zooplankton. These tools allow for the simultaneous assessment of macro-plankton and fish organism density and biomass, but they cannot differentiate between organism types or accurately assess their biomass (Lombard et al., 2019). Our results demonstrate a signal indicative of a zone with low macro-zooplankton density and biomass in the oligotrophic Gyre as we show with imaging data (Figure 5). In a similar way to imaging results too, a signal representative of a rich zone was observed in the Lau Basin and Melanesian waters. Vertical integration of acoustic energy analysis at 200 kHz and the Sv -80 dB signal provide density (Figure 7A) and biomass (Figure 7B) estimates of macro-zooplankton, specifically gelatinous organisms such as siphonophorae and jellyfish, according to Benoit-Bird and Lawson (2016), which aligns directly with the gelatinous signal observed in our imaging methods (Figures 5 and 6). Therefore, these additional analyses confirm and support our conclusion that diazotrophic communities support the production of higher trophic levels (meso- and macro-zooplankton) in the planktonic food web.

4.3 Lagrangian plume effect

By calculating the Lagrangian plume stemming from the position of the two hydrothermal vents, it was possible to reconstruct remarkably well the chlorophyll bloom during November 2019 (Figure 8). Hydrothermally-influenced waters (i.e. those coming in contact with hydrothermal vents) showed [Chl *a*] significantly higher than waters which did not come in contact with the volcanoes. In addition, the [Chl *a*] content in the hydrothermally-influenced waters gradually decreased a few months after their passage through the zone of hydrothermal influence. These observations were associated with a 4.2-fold increase in micro-plankton abundance in the Lau basin (Figure 4). This process is consistent with other types of natural Fe fertilization such as island mass effect (Gove et al., 2016). From a spatial point of view, the influence of these potential iron inputs was calculated to be approximately 412 770 km^2 (for 115-day Lagrangian influence zone; see 3.6). In a very consistent approach, Bonnet et al. (2023), calculated a fluid bloom area of 360,000 km^2 (taking the satellite image of the expedition period, an isoline 0.9 µg/l and a reference to gyre station ST8; see details in Bonnet et al. (2023). Such a geographical range is much larger than those reported in previous studies on the Island Mass Effect (up to about 30 km from the shore in Gove et al., 2016, and about 45 000 km^2 in Blain et al., 2008). This highlighted the major role of such shallow hydrothermal emissions on the primary productivity of the region which impact the entire planktonic food web. Although our study focused on the impact of two hydrothermal sources on the biology, it is important to note that this observed bloom is probably the result of the impact from a multitude of sources localized along the Tonga Arc (Massoth et al., 2007).

4.4 Conclusion on the biogeochemical impact

Our study has revealed a response of the entire ecosystem's trophic structure to shallow hydrothermal DFe inputs, ranging from micro-phytoplankton to macro-zooplankton (covering a broad size spectrum from 20 µm to a few cm). These findings further strengthen the notion of diazotroph dominance in response to DFe inputs from the Tonga hydrothermal vents. The specific role

of DFe inputs on zooplankton communities in this region has remained largely unknown, despite significant planktonic community composition changes observed in other regions (Caputi et al., 2019). Our study has demonstrated the support provided by the diazotrophic community to higher trophic levels, such as meso- and macro-zooplankton production in the Lau Basin zone, particularly highlighting the presence of abundant gelatinous organisms. Indeed, it is well-known that phytoplankton drives the trophic structures of ecosystems (Iverson, 1990; Frederiksen et al., 2006; Boersma et al., 2014; Block et al., 2011) and contributes to the increase in meso-zooplankton. In the Lau Basin, the increase was found to be 2.4 times more abundant on average compared to the oligotrophic Gyre. Meso-zooplankton, as secondary producers in the food web, play in turn a significant role in material flux to higher trophic levels and ultimately to the deep ocean. They contribute to carbon export through fecal production and their diel vertical migrations (Steinberg and Landry, 2017). Thus, this study reaffirms the importance of nutrient regulation in shaping plankton communities and demonstrates that disturbances caused by shallow hydrothermal sources along the Tonga Arc have a profound impact on the entire planktonic food web, affecting the ecosystem as a whole and the biogeochemical context of the region.

Data availability statement

The original contributions presented in the study are included in the article/Supplementary Material, further inquiries can be directed to the corresponding author/s.

Author contributions

ZM: wrote the manuscript, carried out the analysis (in the PIQv platform, taxonomical annotation and statistical analysis). MV: help on the analysis (in the PIQv platform and taxonomical annotation), revisited the manuscript. AB: Lagrangian analysis, revisited the manuscript. CT: provide DFe data, revisited the manuscript. JH and AL-D: provide acoustic data, revisited the manuscript. NB: sampling on board, revisited the manuscript. CG and SB: supervises the study, sampling on board, revisited the manuscript. FL: supervises the study, help on statical analysis, revisited the manuscript. All authors contributed to the article and approved the submitted version.

Funding

TONGA cruise https://doi.org/10.17600/18000884) funded by the Agence Nationale de la Recherche (grant TONGA ANR-18-CE01-0016 and grant CINNAMON ANR-17-CE2-0014-01), the LEFE-CyBER program (CNRS-INSU), the A-Midex foundation, the Institut de Recherche pour le Développement (IRD).

Acknowledgments

This research is a contribution of the TONGA project (Shallow hydrothermal source of trace elements: potential impacts on biological productivity and the bioloGicAl carbon pump. The authors warmly thank the crew of the R/V L'Atalante for outstanding shipboard operations, the DT-INSU, the PIQv team of the Villefranche-sur-Mer laboratory for their help in the analysis of the imaging samples. We also thank the Belmont Forum project "World Wibe Web of Plankton Image Curation" (WWWPIC, grant No ANR-18-BELM-003).

Conflict of interest

The authors declare that the research was conducted in the absence of any commercial or financial relationships that could be construed as a potential conflict of interest.

Publisher's note

Supplementary material

The Supplementary Material for this article can be found online at: https://www.frontiersin.org/articles/10.3389/fmars.2023.1232923/full#supplementary-material

SUPPLEMENTARY FIGURE 1
Average [Chl *a*] (mg m^{-3}; *y*-axis) as a function of the Lagrangian plume, i.e. the time of passage above the volcanoes (*x*-axis). The time of passage was averaged over 5-day bins, from 0 to 115 days (dark gray columns). Lagrangian plume values larger than 115 days were considered as a unique time bin (light gray column). Error bars indicate the standard deviation. Locations with a Lagrangian plume lower than 115 days are considered as affected by the hydrothermal sources, while those showing a Lagrangian plume value greater than 115 days are considered as not affected by hydrothermalism. The black dotted line represents the linear fit between the chlorophyll *a* concentration and the time of passage above the sources, which was statistically significant (R^2 = 0.49, p< 0.05 and slope = -0.0027).

SUPPLEMENTARY FIGURE 2
Map of the average chlorophyll a concentration ([Chl a]; mg m^{-3}) of November 2017, 2018, 2020 and 2021 (data from MODIS-Aqua resolution of 4 km). The two target hydrothermal vents are represented by black triangles.

SUPPLEMENTARY TABLE 1
Taxonomic content of the micro- and macro- planktonic taxo-functional groups annotation (pft) defined for the analyses of surface structure.

References

Adam, B., Klawonn, I., Svedén, J. B., Bergkvist, J., Nahar, N., Walve, J., et al. (2016). N2-fixation, ammonium release and N-transfer to the microbial and classical food web within a plankton community. *ISME J.* 10, 450–459. doi: 10.1038/ismej.2015.126

Baudena, A., Ser-Giacomi, E., D'Onofrio, D., Capet, X., Cotté, C., Cherel, Y., et al. (2021). Fine-scale structures as spots of increased fish concentration in the open ocean. *Sci. Rep.* 11, 15805. doi: 10.1038/s41598-021-94368-1

Benoit-Bird, K. J., and Lawson, G. L. (2016). Ecological insights from pelagic habitats acquired using active acoustic techniques. *Annu. Rev. Mar. Sci.* 8, 463–490. doi: 10.1146/annurev-marine-122414-034001

Berthelot, H., Bonnet, S., Grosso, O., Cornet, V., and Barani, A.. (2016). Transfer of diazotroph-derived nitrogen towards non-diazotrophicplanktonic communities: a comparative study between Trichodesmium erythraeum Crocosphaera watsonii and Cyanothece sp. *Biogeosciences* 13, 4005–4021. doi: 10.5194/bg-13-4005-2016

Blain, S., Sarthou, G., and Laan, P. (2008). Distribution of dissolved iron during the natural iron-fertilization experiment KEOPS (Kerguelen Plateau, Southern Ocean). *Deep Sea Res. Part II: Topical Stud. Oceanography* 55, 594–605. doi: 10.1016/j.dsr2.2007.12.028

Block, B. A., Jonsen, I. D, Jorgensen, S. J, Winship, A. J., Shaffer, S. A, Bograd, S. J., et al. (2011). Tracking apex marine predator movements in a dynamic ocean. *Nature* 475, 86–90. doi: 10.1038/nature10082

Bock, N., Van Wambeke, F., Dion, M., and Duhamel, S. (2018). Microbial community structure in the western tropical South Pacific. *Biogeosciences* 15, 3909–3925. doi: 10.5194/bg-15-3909-2018

Boersma, K. S., Bogan, M. T., Henrichs, B. A., and Lytle, D. A. (2014). Top predator removals have consistent effects on large species despite high environmental variability. *Oikos* 123, 807–816. doi: 10.1111/oik.00925

Bonnet, S., Benavides, M., Le Moigne, F. A. C., Camps, M., Torremocha, A., Grosso, O., et al. (2023). Diazotrophs are overlooked contributors to carbon and nitrogen export to the deep ocean. *ISME J.* 17, 47–58. doi: 10.1038/s41396-022-01319-3

Bonnet, S., Berthelot, H., Turk-Kubo, K., Fawcett, S., Rahav, E., L'Helguen, S., et al. (2016). Dynamics of N2 fixation and fate of diazotroph-derived nitrogen in a low-nutrient, low-chlorophyll ecosystem: results from the VAHINE mesocosm experiment (New Caledonia). *Biogeosciences* 13, 2653–2673. doi: 10.5194/bg-13-2653-2016

Bonnet, S., Caffin, M., Berthelot, H., Grosso, O., Benavides, M., Helias-Nunige, S., et al. (2018). In-depth characterization of diazotroph activity across the western tropical South Pacific hotspot of N2 fixation (OUTPACE cruise). *Biogeosciences* 15, 4215–4232. doi: 10.5194/bg-15-4215-2018

Bonnet, S., Caffin, M., Berthelot, H., and Moutin, T. (2017). Hot spot of N_2 fixation in the western tropical South Pacific pleads for a spatial decoupling between N_2 fixation and denitrification. *Proc. Natl. Acad. Sci. U.S.A.* 114. doi: 10.1073/pnas.1619514114

Bonnet, S., Rodier, M., Turk-Kubo, K. A., Germineaud, C., Menkes, C., Ganachaud, A., et al. (2015). Contrasted geographical distribution of N_2 fixation rates and *nif* H phylotypes in the Coral and Solomon Seas (southwestern Pacific) during austral winter conditions: N_2 FIXATION AND DIVERSITY IN THE PACIFIC. *Global Biogeochem. Cycles* 29, 1874–1892. doi: 10.1002/2015GB005117

Buitenhuis, E. T., Li, W. K. W., Vaulot, D., Lomas, M. W., Landry, M. R., Partensky, F., et al. (2012). Picophytoplankton biomass distribution in the global ocean. *Earth Syst. Sci. Data* 4, 37–46. doi: 10.5194/essd-4-37-2012

Caffin, M., Berthelot, H., Cornet-Barthaux, V., Barani, A., and Bonnet, S. (2018). Transfer of diazotroph-derived nitrogen to the planktonic food web across gradients of N2 fixation activity and diversity in the western tropical South Pacific Ocean. *Biogeosciences* 15, 3795–3810. doi: 10.5194/bg-15-3795-2018

Campbell, L., Carpenter, E. J., and Montoya, J. (2005). *Picoplankton community structure within and outside a Trichodesmium bloom in the southwestern Pacific Ocean*. Vie et Milieu 55 (3), 185–195.

Capone, D. G., Zehr, J. P., Paerl, H. W., Bergman, B., and Carpenter, E. J. (1997). *Trichodesmium* , a globally significant marine cyanobacterium. *Science* 276, 1221–1229. doi: 10.1126/science.276.5316.1221

Caputi, L., Carradec, Q., Eveillard, D., Kirilovsky, A., Pelletier, E., Pierella Karlusich, J. J., et al. (2019). Community-level responses to iron availability in open ocean plankton ecosystems. *Global Biogeochem. Cycles* 33, 391–419. doi: 10.1029/2018GB006022

Carlotti, F., Pagano, M., Guilloux, L., Donoso, K., Valdés, V., Grosso, O., et al. (2018). Meso-zooplankton structure and functioning in the western tropical South Pacific along the 20th parallel south during the OUTPACE survey (February–April 2015). *Biogeosciences* 15, 7273–7297. doi: 10.5194/bg-15-7273-2018

Cutter, G., Casciotti, K., Croot, P., Geibert, W., Heimbürger, L.-E., Lohan, M., et al. (2017). *Sampling and sample-handling protocols for GEOTRACES cruises. Version 3* (Ocean Best Practices: GEOTRACES International Project Office). doi: 10.25607/OBP-2

da Silva, O. (2022). *Structure de l'écosystème planctonique: apport des données à haut débit de séquençage et d'imagerie*. theses HAL Sciences.

de Boyer Montégut, C. (2004). Mixed layer depth over the global ocean: An examination of profile data and a profile-based climatology. *J. Geophys. Res.* 109, C12003. doi: 10.1029/2004JC002378

de Robertis, A., and Higginbottom, I. (2007). A post-processing technique to estimate the signal-to-noise ratio and remove echosounder background noise. *ICES J. Mar. Sci.* 64, 1282–1291. doi: 10.1093/icesjms/fsm112

d'Ovidio, F., Della Penna, A., Trull, T. W., Nencioli, F., Pujol, I., Rio, M. H., et al. (2015). The biogeochemical structuring role of horizontal stirring: Lagrangian perspectives on iron delivery downstream of the Kerguelen plateau. *Biogeochemistry: Open Ocean*. doi: 10.5194/bgd-12-779-2015

Elton, C. (1927). *Animal ecology*. 207 pp. Sidgwick Jackson LTD Lond.

Foote, K. G. (1987). *Fish target strengths for use in echo integrator surveys*. Bergen Norway: Institute of Marine Research.

Frederiksen, M., Edwards, M., Richardson, A. J., Halliday, N. C., and Wanless, S. (2006). From plankton to top predators: bottom-up control of a marine food web across four trophic levels. *J. Anim. Ecol.* 75, 1259–1268. doi: 10.1111/j.1365-2656.2006.01148.x

German, C. R., Casciotti, K. A., Dutay, J.-C., Heimbürger, L. E., Jenkins, W. J., Measures, C. I., et al. (2016). Hydrothermal impacts on trace element and isotope ocean biogeochemistry. *Phil. Trans. R. Soc A.* 374, 20160035. doi: 10.1098/rsta.2016.0035

Gorsky, G., Ohman, M. D., Picheral, M., Gasparini, S., Stemmann, L., Romagnan, J.-B., et al. (2010). Digital zooplankton image analysis using the ZooScan integrated system. *J. Plankton Res.* 32, 285–303. doi: 10.1093/plankt/fbp124

Gove, J. M., McManus, M. A., Neuheimer, A. B., Polovina, J. J., Drazen, J. C., Smith, C. R., et al. (2016). Near-island biological hotspots in barren ocean basins. *Nat. Commun.* 7, 10581. doi: 10.1038/ncomms10581

Greco, L., Luta, G., Krzywinski, M., and Altman, N. (2019). Analyzing outliers: robust methods to the rescue. *Nat. Methods* 16, 275–276. doi: 10.1038/s41592-019-0369-z

Gruber, N. (2008). "The marine nitrogen cycle: Overview and challenges", in *Nitrogen in the Marine Environment* Eds.D. G. Capone, D. A. Bronk, M. R. Mulholland and E. J. Carpenter. (Academic, San Diego), 1–50.

Guieu, C., and Bonnet, S. (2019). *cruise,L'Atalante R/V*, TONGA 2019. doi: 10.17600/18000884

Guieu, C., Bonnet, S., Petrenko, A., Menkes, C., Chavagnac, V., Desboeufs, K., et al. (2018). Iron from a submarine source impacts the productive layer of the Western Tropical South Pacific (WTSP). *Sci. Rep.* 8, 9075. doi: 10.1038/s41598-018-27407-z

Guo, C., and Tester, P. A. (1994). Toxic effect of the bloom-formingTrichodesmium sp. (cyanophyta) to the copepodAcartia tonsa. *Nat. Toxins* 2, 222–227. doi: 10.1002/nt.2620020411

Haury, L. R., McGowan, J. A., and Wiebe, P. H. (1978). "Patterns and Processes in the Time-Space Scales of Plankton Distributions", in *NATO Conference Series book series* (MARS, volume 3) 277–327.

Heron (1979). *Zooplankton sampling. 3. impr.* (Paris: Unesco).

Holmes, R. M., Aminot, A., Kérouel, R., Hooker, B. A., and Peterson, B. J. (1999). A simple and precise method for measuring ammonium in marine and freshwater ecosystems. *Can. J. Fish. Aquat. Sci.* 56, 1801–1808. doi: 10.1139/f99-128

Hunt, B. P. V., Bonnet, S., Berthelot, H., Conroy, B. J., Foster, R. A., and Pagano, M. (2016). Contribution and pathways of diazotroph-derived nitrogen to zooplankton during the VAHINE mesocosm experiment in the oligotrophic New Caledonia lagoon. *Biogeosciences* 13, 3131–3145. doi: 10.5194/bg-13-3131-2016

Iverson, R. L. (1990). Control of marine fish production. *Limnol. Oceanogr.* 35, 1593–1604. doi: 10.4319/lo.1990.35.7.1593

Koski, M., and Lombard, F. (2022). Functional responses of aggregate-colonizing copepods. *Limnology Oceanography* 67, 2059–2072. doi: 10.1002/lno.12187

Leblanc, K., Cornet, V., Rimmelin-Maury, P., Grosso, O., Hélias-Nunige, S., Brunet, C., et al. (2018). Silicon cycle in the tropical South Pacific: contribution to the global Si cycle and evidence for an active pico-sized siliceous plankton. *Biogeosciences* 15, 5595–5620. doi: 10.5194/bg-15-5595-2018

Le Borgne, R., Allain, V., and Matear, V. (2011). "Vulnerability of open ocean food webs in the tropical Pacific to climate change," in *Vulnerability of Fisheries and Aquaculture in the Tropical Pacific to Climate Change* New-York. United State of America: Academic Press.

Lee Chen, Y., Tuo, S., and Chen, H. (2011). Co-occurrence and transfer of fixed nitrogen from Trichodesmium spp. to diatoms in the low-latitude Kuroshio Current in the NW Pacific. *Mar. Ecol. Prog. Ser.* 421, 25–38. doi: 10.3354/meps08908

Legendre, P., and Legendre, L. (2012). *Numerical ecology. 3rd ed.* (Amsterdam: Elsevier).

Lehodey, P., Conchon, A., Senina, I., Domokos, R., Calmettes, B., Jouanno, J., et al. (2015). Optimization of a micronekton model with acoustic data. *ICES J. Mar. Sci.* 72, 1399–1412. doi: 10.1093/icesjms/fsu233

Lombard, F., Boss, E., Waite, A. M., Vogt, M., Uitz, J., Stemmann, L., et al. (2019). Globally consistent quantitative observations of planktonic ecosystems. *Front. Mar. Sci.* 6. doi: 10.3389/fmars.2019.00196

Lory, C., Van Wambeke, F., Fourquez, M., Barani, A., Guieu, C., Tilliette, C., et al. (2022). Assessing the contribution of diazotrophs to microbial Fe uptake using a group specific approach in the Western Tropical South Pacific Ocean. *ISME Commun.* 2, 41. doi: 10.1038/s43705-022-00122-7

Lundgren, P., Janson, S., Jonasson, S., Singer, A., and Bergman, B. (2005). Unveiling of Novel Radiations within *Trichodesmium* Cluster by *hetR* Gene Sequence Analysis. *Appl. Environ. Microbiol.* 71, 190–196. doi: 10.1128/AEM.71.1.190-196.2005

Maclennan, D. (2002). A consistent approach to definitions and symbols in fisheries acoustics. *ICES J. Mar. Sci.* 59, 365–369. doi: 10.1006/jmsc.2001.1158

Massoth, G., Baker, E., Worthington, T., Lupton, J., de Ronde, C., Arculus, R., et al. (2007). Multiple hydrothermal sources along the south Tonga arc and Valu Fa Ridge: Hydrothermal Venting. *Geochem. Geophys. Geosyst.* 8, n/a–n/a. doi: 10.1029/2007GC001675

Motoda, S. (1959). *Devices of simple plankton apparatus*. Memoirs of the Faculty of Fisheries, Hokkaido University. 7 (1959), 73–94

Moutin, T., Karl, D. M., Duhamel, S., Rimmelin, P., Raimbault, P., Van Mooy, B. A. S., et al. (2008). Phosphate availability and the ultimate control of new nitrogen input by nitrogen fixation in the tropical Pacific Ocean. *Biogeosciences* 5, 95–109. doi: 10.5194/bg-5-95-2008

Moutin, T., Wagener, T., Caffin, M., Fumenia, A., Gimenez, A., Baklouti, M., et al. (2018). Nutrient availability and the ultimate control of the biological carbon pump in the western tropical South Pacific Ocean. *Biogeosciences* 15, 2961–2989. doi: 10.5194/bg-15-2961-2018

Mulholland, M. R., Bronk, D., and Heil, C. A. (2004). *Does nitrogen regeneration from the N2 fixing cyanobacteria Trichodesmium spp. fuel Karenia brevis blooms in the Gulf of Mexico*. Harmful Algae 2002.

O'Neil, J. M. (1998). The colonial cyanobacterium *Trichodesmium* as a physical and nutritional substrate for the harpacticoid copepod *Macrosetella gracilis*. *J. Plankton Res.* 20, 43–59. doi: 10.1093/plankt/20.1.43

O'Neil, J. M., and ROman, M. R. (1992). "Marine Pelagic Cyanobacteria: Trichodesmium and other diazotrophs," in *NATO ASI Series book series*, vol. 362 (Springer).

O'Neil, J. M., and ROman, M. R. (1994). *Ingestion of the Trichodesmium spp. by pelagic harpacticoid copepods Macrosetella, Miracia and Oculosetella* (Springer).

Perrot, Y., Brehmer, P., Habasque, J., Roudaut, G., Nolwenn, B., Sarré, A., et al. (2018). *Matecho: an open-source tool for processing fisheries acoustics data to facilitate collaborative development*. Available at: https://horizon.documentation.ird.fr/exl-doc/pleins_textes/divers20-05/010078279.pdf.

Picheral, M., Colin, S., and Irisson, J. O. (2017). *EcoTaxa, a tool for the taxonomic classification of images*. Available at: https://ecotaxa.obs-vlfr.fr.

Planquette, H., and Sherrell, R. M. (2012). Sampling for particulate trace element determination using water sampling bottles: methodology and comparison to *in situ* pumps: Particulate trace element sampling. *Limnol. Oceanogr. Methods* 10, 367–388. doi: 10.4319/lom.2012.10.367

Platt, T. (1978). "Spectral analysis of spatial structure in phytoplankton populations," in *Spatial Pattern In Plankton Communities*. Ed. J. H. Steele (Boston, MA: Springer US), 73–84. doi: 10.1007/978-1-4899-2195-6_4

Ryan, T. E., Downie, R. A., Kloser, R. J., and Keith, G. (2015). Reducing bias due to noise and attenuation in open-ocean echo integration data. *ICES J. Mar. Sci.* 72, 2482–2493. doi: 10.1093/icesjms/fsv121

Ruellan, E., and Lagabrielle, Y. (2005). Subductions et ouvertures océaniques dans le Sud-Ouest Pacifique. *geomorphologie* 11, 121–142. doi: 10.4000/geomorphologie.307

Sanial, V., van Beek, P., Lansard, B., d'Ovidio, F., Kestenare, E., Souhaut, M., et al. (2014). Study of the phytoplankton plume dynamics off the Crozet Islands (Southern Ocean): A geochemical-physical coupled approach. *J. Geophys. Res. Oceans* 119, 2227–2237. doi: 10.1002/2013JC009305

Sanial, V., van Beek, P., Lansard, B., Souhaut, M., Kestenare, E., d'Ovidio, F., et al. (2015). Use of Ra isotopes to deduce rapid transfer of sediment-derived inputs off Kerguelen. *Biogeosciences* 12, 1415–1430. doi: 10.5194/bg-12-1415-2015

Sauzède, R., Lavigne, Héloise, Claustre, Hervé, Uitz, J., Schmechtig, C., D'Ortenzio, F., et al. (2015). Global data product of chlorophyll a concentration and phytoplankton community composition (microphytoplankton, nanophytoplankton and picophytoplankton) computed from *in situ* fluorescence profiles, supplement to: Sauzède, Raphaëlle; Lavigne, Héloise; Claustre, Hervé; Uitz, Julia; Schmechtig, Catherine; D'Ortenzio, Fabrizio; Guinet, Christophe; Pesant, Stephane, (2015): Vertical distribution of chlorophyll a concentration and phytoplankton community composition from *in situ* fluorescence profiles: a first database for the global ocean. *Earth System Sci. Data* 7 (2), 261–273.397. doi: 10.1594/PANGAEA.844485

Sergi, S., Baudena, A., Cotté, C., Ardyna, M., Blain, S., and d'Ovidio, F. (2020). Interaction of the antarctic circumpolar current with seamounts fuels moderate blooms but vast foraging grounds for multiple marine predators. *Front. Mar. Sci.* 7. doi: 10.3389/fmars.2020.00416

Sieracki, C., Sieracki, M., and Yentsch, C. (1998). An imaging-in-flow system for automated analysis of marine microplankton. *Mar. Ecol. Prog. Ser.* 168, 285–296. doi: 10.3354/meps168285

Steinberg, D. K., and Landry, M. R. (2017). Zooplankton and the ocean carbon cycle. *Annu. Rev. Mar. Sci.* 9, 413–444. doi: 10.1146/annurev-marine-010814-015924

Stenegren, M., Caputo, A., Berg, C., Bonnet, S., and Foster, R. A. (2018). Distribution and drivers of symbiotic and free-living diazotrophic cyanobacteria in the western tropical South Pacific. *Biogeosciences* 15, 1559–1578. doi: 10.5194/bg-15-1559-2018

Suikkanen, S., Uusitalo, L., Lehtinen, S., Lehtiniemi, M., Kauppila, P., Mäkinen, K., et al. (2021). Diazotrophic cyanobacteria in planktonic food webs. *Food Webs* 28, e00202. doi: 10.1016/j.fooweb.2021.e00202

Tenório, B., Dupouy, C., Rodier, M., and Neveux, J. (2018). Trichodesmium and other planktonic cyanobacteria in New Caledonian waters (SW tropical Pacific) during an El Niño episode. *Aquat. Microb. Ecol.* 81, 219–241. doi: 10.3354/ame01873

Tilliette, C., Gazeau, F., Portlock, G., Benavides, M., Bonnet, S., Guigue, C., et al. (2023). Influence of shallow hydrothermal fluid release on the functioning of phytoplankton communities. *Front. Mar. Sci.* 10. doi: 10.3389/fmars.2023.1082077

Tilliette, C., Taillandier, V., Bouruet-Aubertot, P., Grima, N., Maes, C., Montanes, M., et al. (2022). DFe patterns impacted by shallow hydrothermal sources along a transect through the Tonga-Kermadec arc. *Oceanography*. doi: 10.1002/essoar.10510604.1

Trenkel, V. M., Berger, L., Bourguignon, S., Doray, M., Fablet, R., Massé, J., et al. (2009). Overview of recent progress in fisheries acoustics made by Ifremer with examples from the Bay of Biscay. *Aquat. Living Resour.* 22, 433–445. doi: 10.1051/alr/2009027

Turner, J. T. (2014). Planktonic marine copepods and harmful algae. *Harmful Algae* 32, 81–93. doi: 10.1016/j.hal.2013.12.001

Ustick, L. J., Larkin, A. A., Garcia, C. A., Garcia, N. S., Brock, M. L., Lee, J. A., et al. (2021). Metagenomic analysis reveals global-scale patterns of ocean nutrient limitation. *Science* 372, 287–291. doi: 10.1126/science.abe6301

Vandromme, P., Stemmann, L., Garcìa-Comas, C., Berline, L., Sun, X., and Gorsky, G. (2012). Assessing biases in computing size spectra of automatically classified zooplankton from imaging systems: A case study with the ZooScan integrated system. *Methods Oceanogr.* 1–2, 3–21. doi: 10.1016/j.mio.2012.06.001

Zehr, J. P. (2011). Nitrogen fixation by marine cyanobacteria. *Trends Microbiol.* 19, 162–173. doi: 10.1016/j.tim.2010.12.004

Zehr, J. P., and Capone, D. G. (2020). Changing perspectives in marine nitrogen fixation. *Science* 368, eaay9514. doi: 10.1126/science.aay9514

frontiers | Frontiers in Marine Science

TYPE Original Research
PUBLISHED 27 October 2023
DOI 10.3389/fmars.2023.1249115

OPEN ACCESS

EDITED BY
Margarita Fernández Tejedor,
Institute of Agrifood Research and Technology (IRTA), Spain

REVIEWED BY
Dengzhou Gao,
East China Normal University, China
Annie Bourbonnais,
University of South Carolina, United States

*CORRESPONDENCE
Heather J. Forrer
hforrer@fsu.edu

RECEIVED 28 June 2023
ACCEPTED 12 October 2023
PUBLISHED 27 October 2023

CITATION
Forrer HJ, Bonnet S, Thomas RK, Grosso O, Guieu C and Knapp AN (2023) Quantifying N_2 fixation and its contribution to export production near the Tonga-Kermadec Arc using nitrogen isotope budgets. *Front. Mar. Sci.* 10:1249115. doi: 10.3389/fmars.2023.1249115

Quantifying N_2 fixation and its contribution to export production near the Tonga-Kermadec Arc using nitrogen isotope budgets

Heather J. Forrer[1]*, Sophie Bonnet[2], Rachel K. Thomas[1], Olivier Grosso[2], Cecile Guieu[3] and Angela N. Knapp[1]

[1]Earth, Ocean, and Atmospheric Science Department, Florida State University, Tallahassee, FL, United States, [2]Aix Marseille University, Université de Toulon, CNRS, IRD, MIO Marseille, France, [3]Laboratoire d'Oceanographie de Villefranche, CNRS, Sorbonne University, Villefranche-sur-mer, France

The spatial distribution of marine di-nitrogen (N_2) fixation informs our understanding of the sensitivities of this process as well as the potential for this new nitrogen (N) source to drive export production, influencing the global carbon (C) cycle and climate. Using geochemically-derived $\delta^{15}N$ budgets, we quantified rates of N_2 fixation and its importance for supporting export production at stations sampled near the southwest Pacific Tonga-Kermadec Arc. Recent observations indicate that shallow (<300 m) hydrothermal vents located along the arc provide significant dissolved iron to the euphotic zone, stimulating N_2 fixation. Here we compare measurements of water column $\delta^{15}N_{NO3+NO2}$ with sinking particulate $\delta^{15}N$ collected by short-term sediment traps deployed at 170 m and 270 m at stations in close proximity to subsurface hydrothermal activity, and the $\delta^{15}N$ of N_2 fixation. Results from the $\delta^{15}N$ budgets yield high geochemically-based N_2 fixation rates (282 to 638 μmol N m^{-2} d^{-1}) at stations impacted by hydrothermal activity, supporting 64 to 92% of export production in late spring. These results are consistent with contemporaneous $^{15}N_2$ uptake rate estimates and molecular work describing high *Trichodesmium* spp. and other diazotroph abundances associated with elevated N_2 fixation rates. Further, the $\delta^{15}N$ of sinking particulate N collected at 1000 m over an annual cycle revealed sinking fluxes peaked in the summer and coincided with the lowest $\delta^{15}N$, while lower winter sinking fluxes had the highest $\delta^{15}N$, indicating isotopically distinct N sources supporting export seasonally, and aligning with observations from most other $\delta^{15}N$ budgets in oligotrophic regions. Consequently, the significant regional N_2 fixation input to the late spring/summer Western Tropical South Pacific results in the accumulation of low-$\delta^{15}N_{NO3+NO2}$ in the upper thermocline that works to lower the elevated $\delta^{15}N_{NO3+NO2}$ generated in the oxygen deficient zones in the Eastern Tropical South Pacific.

KEYWORDS

N_2 fixation, nitrate d15N, Tonga Arc, South Pacific, hydrothermal vents, d15N budget

1 Introduction

The biological fixation of dinitrogen (N_2) gas, mediated primarily by marine prokaryotes ("diazotrophs"), is the largest source of newly fixed nitrogen (N) to the global ocean (Gruber, 2004; Landolfi et al., 2018), fertilizing primary productivity and supporting carbon (C) export (Dugdale and Goering, 1967; Karl et al., 1997; Capone, 2001; Capone et al., 2005). The global rate and distribution of marine N_2 fixation remains uncertain, although geochemical and biological observations indicate significant N_2 fixation rates occur in both the Tropical Atlantic (Gruber, 2004; Capone et al., 2005; Mahaffey, 2005; Marconi et al., 2017) as well as the Western Tropical South Pacific (WTSP) (Berthelot et al., 2017; Bonnet et al., 2017; Caffin et al., 2018; Knapp et al., 2018). These high rates of N_2 fixation in the Tropical Atlantic are consistent with locations of elevated rates of atmospheric dust deposition (Jickells et al., 2005; Mahowald et al., 2005; Conway and John, 2014; Xu and Weber, 2021), while emerging evidence in the WTSP describes the significance of hydrothermally sourced iron (Fe) (Guieu et al., 2018; Bonnet et al., 2023b) meet the high Fe requirements of diazotrophs (Berman-Frank et al., 2001; Kustka et al., 2003) in the region. Indeed, Fe and phosphorus availability are thought to primarily influence the spatial distribution of marine N_2 fixation (Moore et al., 2009; Monteiro et al., 2011; Dutkiewicz et al., 2012; Weber and Deutsch, 2014).

A long-standing goal of marine N_2 fixation research is to better characterize the marine diazotroph community and their sensitivity to environmental fluctuations, while relating these to their regional distributions and consequential N_2 fixation fluxes (Mahaffey, 2005; Moisander et al., 2010; Sohm et al., 2011). Diazotrophs are identified by the nitrogenase (*nifH*) gene that encodes for the Fe binding protein of the *nifH* operon (Zehr et al., 1998; Zehr and Turner, 2001; Turk-Kubo et al., 2012). Common marine proteobacterial (e.g., alpha-, beta- gamma-, delta-) and cyanobacterial diazotroph types include: 1) non-heterocystous filamentous (e.g., *Trichodesmium* spp.), 2) heterocystous filamentous (e.g., *Richelia*), and 3) unicellular (e.g., *Crocosphaera* spp.) (Capone et al., 1997; Luo et al., 2012; Moisander et al., 2014). Historically, high rates of N_2 fixation by these and other diazotrophs have been associated with warm (>25 °C), nitrate (NO_3^-)- and ammonium (NH_4^+)-depleted, Fe-rich surface waters (Kustka et al., 2003; Staal et al., 2003; Bonnet et al., 2009). The impact Fe has on the intra-basin distribution of N_2 fixation rates is particularly evident in the South Pacific, with low Fe supply associated with low rates of N_2 fixation in the Eastern Tropical South Pacific (ETSP) (Dekaezemacker et al., 2013; Knapp et al., 2016a). While historically atmospheric deposition has been considered the primary source of Fe fueling marine diazotrophy, the WTSP surface waters appear relatively unique, with the primary Fe supply thought to originate from shallow (≤300 m) hydrothermal vents, particularly in the Lau Basin (Guieu et al., 2018; Tilliette et al., 2022; Bonnet et al., 2023b).

Biological tools have been used to calculate short-term N_2 fixation rates (e.g., Montoya et al., 2004; Capone et al., 2005; Mulholland et al., 2019) and identify marine diazotrophic potential (Turk-Kubo et al., 2012; Stenegren et al., 2018; Meiler et al., 2022). However, the contribution of N_2 fixation to export production is primarily estimated using a geochemically-derived "$\delta^{15}N$" budget over short timescales (Casciotti et al., 2008; Bourbonnais et al., 2009; White et al., 2013) as well as annual cycles (Böttjer et al., 2017). The "$\delta^{15}N$" budget uses a two end-member mixing model to compare the isotopic composition ($\delta^{15}N$) of exported particulate organic matter captured in a sediment trap (PN_{sink}) to the $\delta^{15}N$ of N_2 fixation inputs (-1‰) (Hoering and Ford, 1960; Minagawa and Wada, 1986; Carpenter et al., 1997) and subsurface NO_3^- (measured at each location, where $\delta^{15}N$ (‰ vs. air) = $[(({}^{15}N/{}^{14}N)_{sample}/({}^{15}N/{}^{14}N)_{AIR})-1]x1000$) (Altabet, 1988; Karl et al., 1997; Dore et al., 2002; Casciotti et al., 2008; Bourbonnais et al., 2009; White et al., 2013). Most prior $\delta^{15}N$ budgets indicate that N_2 fixation supports <20% of export production in oligotrophic regions. In the North Pacific and ETSP, ≤25% of export production is estimated to be supported by N_2 fixation (Casciotti et al., 2008; Knapp et al., 2016a; Böttjer et al., 2017), although that 25% is likely not equally distributed over an annual cycle. Specifically, summertime stratification is believed to promote N_2 fixation-supported export, while the deepening of the wintertime mixed layer promotes NO_3^-supported export production (Casciotti et al., 2008; Böttjer et al., 2017). In contrast to other $\delta^{15}N$ budgets from oligotrophic regions, a recent study from the WTSP describes particularly large contributions of N_2 fixation to export production (>50%) during the late summer and early autumn (Knapp et al., 2018). However, it remains unclear whether N_2 fixation supports a meaningful fraction of N export in the WTSP annually. Here we apply a $\delta^{15}N$ budget to samples collected in shallow (170 m and 270 m), short-term drifting sediment traps to evaluate the importance of N_2 fixation-supported export production during the late spring. Additionally, we use sinking material collected over the course of a year in a deep (1000 m), moored sediment trap to evaluate seasonal trends in the $\delta^{15}N$ of exported particulate organic matter relative to the $\delta^{15}N$ for sources of new N to surface waters. We compare the geochemically-derived N_2 fixation rates from the short-term $\delta^{15}N$ budgets with ${}^{15}N_2$ incubation-based rates and estimates of diazotroph abundance, and evaluate these results in the context of previous regional and global N_2 fixation rate estimates, as well as seasonal trends extracted from the deep, moored trap.

2 Methods

2.1 Sample collection

Sample collection was conducted as part of the GEOTRACES TONGA (shallow hydroThermal sOurces of trace elemeNts: potential impacts on biological productivity and the bioloGicAl carbon pump) research cruises (doi.org/10.17600/18000884) aboard the *R/V L'Atalante* in November 2019 and *R/V Alis* in

October 2020, with both cruises leaving from and returning to Nouméa, New Caledonia. The 2019 primary cruise collected samples at 13 stations along a roughly zonal transect at ~20° S, sampling Melanesian waters (MW), the Lau Basin (LB), and crossing the Tonga-Kermadec Arc into the deeper South Pacific Gyre (SPG). In 2020, samples were collected at four stations in MW and the LB (Figure 1). On both cruises, water column samples (n=200) for nitrate + nitrite ($[NO_3^-+NO_2^-]$) concentration and $\delta^{15}N$ analysis were collected from Niskin or GoFlo bottles deployed on conductivity, temperature, and depth (CTD), TOW (small, classical CTD with 12 Niskin bottles), or trace metal clean (TMC) rosettes equipped with sensors. At discrete depths from each of the casts, 60 mL of 0.2 µm filtered seawater were collected in duplicate and stored in acid and deionized water-washed, sample-rinsed (three times) high-density polyethylene bottles. These samples were then immediately frozen at -20° C and subsequently sent to Florida State University for post cruise analysis.

Short-term Particle Interceptor Traps [PIT, collecting area of 0.0085 m^2, aspect ratio of 6.7, and filled with 0.2 µm filtered seawater with added formaldehyde brine (5% formaldehyde, final concentration) buffered with sodium tetraborate (pH 8)] were deployed on a drifting mooring in close proximity to the hydrothermal vents at 170 m and 270 m at station 5a-2019 for five days and at 270 m at station 10a-2019 for four days during the 2019 cruise, collecting sinking particulate N ("PN_{sink}"). Additionally, a long-term Technicap PPS5 trap (1 m^2 collecting area, aspect ratio of 5.3) was deployed (containing the same buffered formaldehyde brine solution described above) at station 12-2019/4-2020 at 1000 m, collecting samples every 14 days (bimonthly) for 12 months from November 2019 to October 2020. Although sediment traps are a standard tool used to capture sinking particles, uncertainties remain in their collection efficiency within the water column and between trap designs (Buesseler et al., 2007; Baker et al., 2020; Tilliette et al., 2023).

2.2 $NO_3^-+NO_2^-$ concentration and $\delta^{15}N$ analysis

For the 2019 samples, $[NO_3^-+NO_2^-]$ was determined using colorimetric analysis (Aminot and Kerouel, 2007) with a detection limit of 0.05 µM and a standard deviation (S.D.) of ± 0.1 µM. Furthermore, the $[NO_3^-+NO_2^-]$ for the 2020 samples was measured by chemiluminescence (Braman and Hendrix, 1989) using a Thermo 42i NO_x analyzer at Florida State University. Briefly, samples were injected into a heated, acidic vanadium (III) solution that reduces $NO_3^-+NO_2^-$ quantitatively to nitric oxide gas ($NO_{(g)}$). The $NO_{(g)}$ then reacts with ozone inside the analyzer to produce light, the intensity of which is quantitatively related to the amount of $NO_{(g)}$ in the sample and thus the original $[NO_3^-+NO_2^-]$. The range of detection of the instrument was adjusted according to the concentrations of the samples. Sample $[NO_3^-+NO_2^-]$ was calibrated using a standard curve that bracketed the range of samples with a lower reporting limit of 0.1 µM and an average S.D. of ± 0.1 µM.

The nitrogen (N) isotopic composition of $NO_3^-+NO_2^-$ ($\delta^{15}N_{NO3+NO2}$) was determined using the "denitrifier" method (Sigman et al., 2001; Casciotti et al., 2002; McIlvin and Casciotti, 2011; Weigand et al., 2016). This analysis was performed when sample $[NO_3^-+NO_2^-] \geq 0.3$ µM. The $\delta^{15}N_{NO3+NO2}$ values were reported when the standard deviation of replicate analyses was <0.5‰. Samples were calibrated with IAEA N3 and USGS 34 as described in McIlvin and Casciotti (2011).

2.3 Sinking particulate N flux and $\delta^{15}N$ measurements

The bulk PN_{sink} mass flux, and its associated isotopic composition, "$\delta^{15}N_{PNsink}$", collected by the sediment traps, was

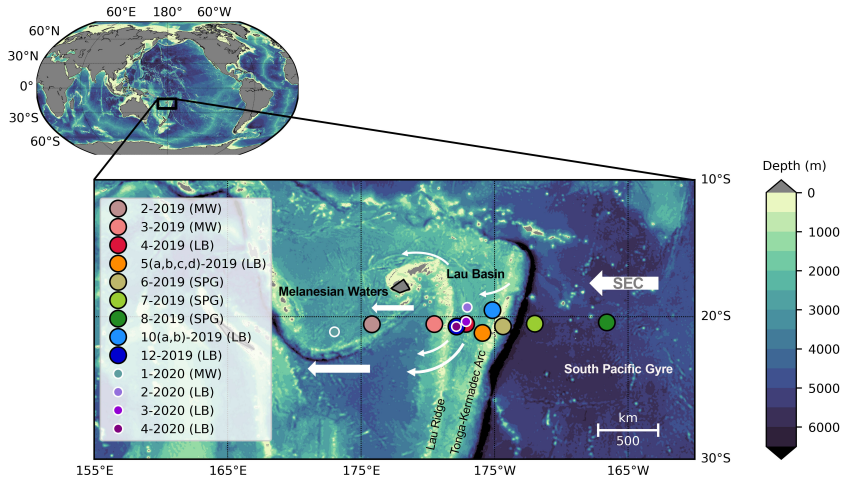

FIGURE 1
Bathymetry of the southwest Pacific region with stations from the TONGA research cruises shown in larger filled circles with black outlines (2019), and smaller filled circles with white outlines (2020); gray represents areas above sea-level. Stations 2-2019, 3-2019 and 1-2020 were sampled in Melanesian waters (MW), stations 4-2019, 5-2019, 10-2019, 12-2019, 2-2020, 3-2020, and 4-2020 were sampled in the Lau Basin (LB), and stations 6-2019, 7-2019, and 8-2019 were sampled in the South Pacific Gyre (SPG). Stations 5 (a, b, c, d)-2019 and 10 (a, b)-2019 were proximal to the shallow hydrothermal vents 'Panamax' and 'Simone', respectively. The South Equatorial Current (SEC) and branches thereof are indicated by the white arrows.

measured using an Elementar Analyser - Isotope Ratio Mass Spectrometer (EA-IRMS) at the Mediterranean Institute of Oceanography (SERCON INTEGRA 2). The Quantification Limit was 7 µg N and the precision was between ± 0.3‰ for highest masses and ± 3.5‰ for masses close to Quantification Limit (k = 2).

2.4 $\delta^{15}N$ budget calculations

A two end-member mixing model was used to evaluate the $\delta^{15}N$ budgets. This model assumes two quantitatively important "new" N sources to surface waters, subsurface $NO_3^-+NO_2^-$ and biological N_2 fixation, as well as one loss term, PN_{sink}. The isotopic composition of N_2 fixation inputs, "$\delta^{15}N_{N2\ fix}$" was assumed to be -1‰ (Hoering and Ford, 1960; Minagawa and Wada, 1986; Carpenter et al., 1997), while the $\delta^{15}N$ of subsurface $NO_3^-+NO_2^-$ and PN_{sink} were measured. The relative contribution of N_2 fixation to export production, "f_{nfix}", is calculated by the following (Knapp et al., 2018):

$$\delta^{15}N_{PNsink} = f_{nfix}(-1\%) + (1 - f_{nfix})(\delta^{15}N_{NO3+NO2}) \quad (1)$$

which can be rearranged to solve for f_{nfix}:

$$f_{nfix} = \frac{\left[(\delta^{15}N_{NO3+NO2}) - (\delta^{15}N_{PNsink})\right]}{\left[1 + (\delta^{15}N_{NO3+NO2})\right]} \quad (2)$$

The depth from which subsurface $NO_3^-+NO_2^-$ is sourced likely varies and is difficult to constrain; therefore, the short-term $\delta^{15}N$ budgets are evaluated over a range of subsurface $\delta^{15}N_{NO3+NO2}$ source values. These values include the shallowest $\delta^{15}N_{NO3+NO2}$ minima and the $\delta^{15}N_{NO3+NO2}$ of the sample collected immediately below the minima (Knapp et al., 2021). The long-term $\delta^{15}N$ budgets are evaluated using the shallowest average $\delta^{15}N_{NO3+NO2}$ minima at station 12-2019/station 4-2020 as well as the average $\delta^{15}N_{NO3+NO2}$ of South Pacific Sub-tropical Under Water (SPSTUW, 150m – 250 m depth) at station 4-2020. Note, sampling resolution at station 12-2019 did not include SPSTUW. These $\delta^{15}N_{NO3+NO2}$ end-members for the moored trap $\delta^{15}N$ bugdet were chosen to encompass the range of $NO_3^-+NO_2^-$ likely entrained to surface waters over an annual cycle (Moutin et al., 2018). This seasonality is also observed at the station ALOHA, Hawaii (Casciotti et al., 2008; Böttjer et al., 2017). Once the fraction of export supported by N_2 fixation is calculated, an N_2 fixation rate, "R_{nfix}" can be calculated by multiplying f_{nfix} by the PN_{sink} mass flux, yielding a geochemically-derived N_2 fixation rate.

2.5 Bathymetric data

Bathymetric data from the sampling region were considered to better understand the bathymetric-induced current steering as well as the proximity of the stations to the shallow hydrothermal vents. These bathymetric data were downloaded from NOAA's National Centers for Environmental Information page (https://www.ngdc.noaa.gov/mgg/global/). The ETOPO1 Global Relief Model was used with the grid version ETOPO1 Bedrock.

3 Hydrography

Water masses along the TONGA transect were identified using temperature, salinity, and potential density (σ_θ) (Figure 2) and align with those reported in Tilliette et al. (2022). Plots of the water column profiles in temperature-salinity space indicate that all stations were largely influenced by the same water masses (Figure 2), reflecting the dominance of the westward flowing SEC, which impacts waters from 400 to 1000 m across this region (Figure 1) (Talley et al., 2011; Guieu et al., 2018; Tilliette et al., 2022). The SEC divides into branches, particularly in the LB, due to the bathymetric blocking by islands and deep-sea ridges (Webb, 2000; Tilliette et al., 2022). Many of these branches in the LB are observed to have an overall southwestern trajectory before returning to a western trajectory over the center of the LB and maintaining this westward trajectory in MW (Figure 1) (Tilliette et al., 2022). Additionally, the Tonga-Kermadec Arc acts as a physical barrier to deep water masses entering the LB from the SPG, influencing circulation downstream (Tilliette et al., 2022). Surface waters across this transect were turbulent down to ~150 m with a σ_θ of 23.7 ± 0.2, temperature of 24.4 ± 0.6°C, and salinity of 35.4 ± 0.5, aligning with previous studies (Table 1) (Tilliette et al., 2022). Below that, in the thermocline and extending to ~700 m, two major water masses were present: SPSTUW and Western South Pacific Central Water (WSPCW) (Talley et al., 2011; Lehmann et al., 2018; Tilliette et al., 2022) (Figure 2) (Table 1). Across the transect, SPSTUW had an average (± 1 S.D.) σ_θ of 25.0 ± 0.2, temperature of 22.5 ± 0.8°C and was further recognized by its characteristic salinity maximum of 35.7 ± 0.1 (Talley et al., 2011; Lehmann et al., 2018; Tilliette et al., 2022) between 150 and 250 m (Table 1). Between 250 and 500 m, WSPCW was identified by a linear temperature-salinity relationship, with an average (± 1 S.D.) σ_θ of 26.4 ± 0.2, temperature of 12.6 ± 0.9°C and salinity of 34.9 ± 0.2, comparable to values reported by Lehmann et al. (2018) and Tilliette et al. (2022). Notably, between 380 and 400 m South Pacific Subtropical Mode Water (SPSTMW), a subsidiary of WSPCW, was identified by its characteristic σ_θ of 26.0 (Talley et al., 2011), with an average (± 1 S.D.) temperature of 14.9 ± 0.5°C and salinity of 35.2 ± 0.1 (Table 1). Finally, deep water masses were observed in the SPG east of the Tonga-Kermadec Arc. In particular, Antarctic Intermediate Water (AAIW) was observed at station 8-2019 and station 2-2020 between 630 and 700 m where a σ_θ of 26.9 ± 0.1 temperature of 6.5 ± 0.1°C and salinity of 34.4 ± 0.0, aligning with previous studies (Table 1) (Talley et al., 2011; Tilliette et al., 2022).

4 Results

4.1 $NO_3^-+NO_2^-$ concentration and $\delta^{15}N$

The $[NO_3^-+NO_2^-]$ in the upper 100 m of the WTSP was ≤0.1 µM except at stations influenced by the hydrothermal vents, i.e., stations 5-2019 and 10-2019, where the $[NO_3^-+NO_2^-]$ was 0.2 ± 0.0 µM to 0.7 ±

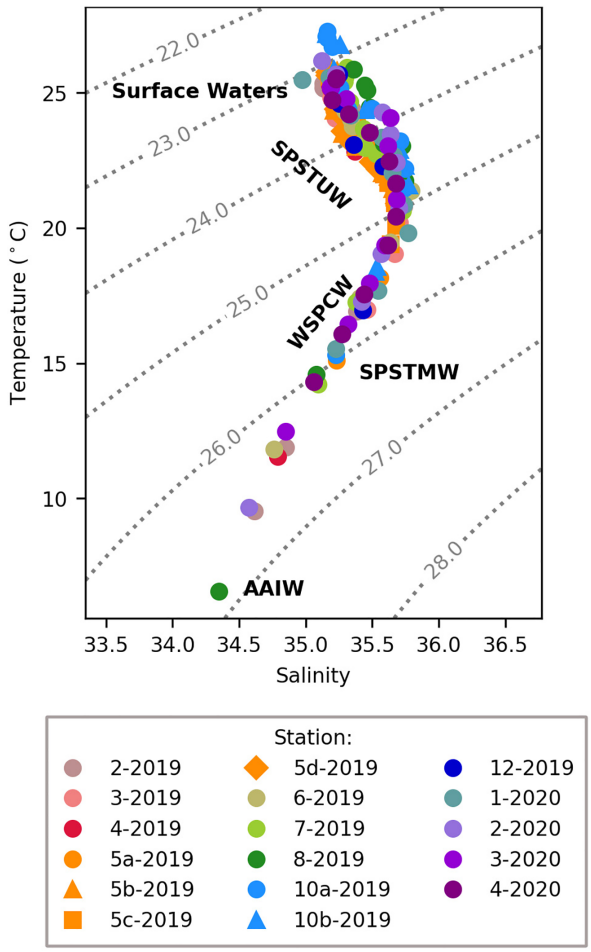

FIGURE 2
Temperature-salinity plot of samples from the 2019 and 2020 TONGA cruises as well as the prevalent water masses across the transect. The dotted grey lines indicate potential density (σ_θ) isopycnals. The water masses include surface waters, South Pacific Subtropical Under Water (SPSTUW), Western South Pacific Central Water (WSPCW), South Pacific Subtropical Mode Water (SPSTMW), a subsidiary of WSPCW and Antarctic Intermediate Water (AAIW).

0.0 µM (average ±1 S.D.) between 60 m and 100 m (Figures 3A, C). At 400 m, the $[NO_3^-+NO_2^-]$ increased to between 10 and 15 µM, corresponding to $\delta^{15}N_{NO3+NO2}$ ranging from 6 to 8‰ (Figures 3B, D). This is consistent with the presence of WSPCW (Tilliette et al., 2022) and more particularly, SPSTMW (Lehmann et al., 2018) and aligns with other studies in the region (Knapp et al., 2018). At station 8-2019, the $[NO_3^-+NO_2^-]$ increased to 26.7 µM at 630 m with a corresponding $\delta^{15}N_{NO3+NO2}$ of 6.9 ± 0.1‰ (Figures 3A, C), consistent with AAIW (Talley et al., 2011; Lehmann et al., 2018; Tilliette et al., 2022). The majority of stations within MW and the LB (i.e., stations 1-2019 to 5-2019, 10-2019, and 12-2019) had $\delta^{15}N_{NO3+NO2}$ ranging from 4 to 6‰ at 200 m, decreasing shallower in the water column to 2 to 4‰ at 150 m associated with the transition between SPSTUW and surface waters (Figures 3B, D). The SPG stations (stations 6-2019, 7-2019 and 8-2019) had an average $\delta^{15}N_{NO3+NO2}$ of 6.8 ± 0.0‰ at ~200 m characteristic of SPSTUW. This $\delta^{15}N_{NO3+NO2}$ was significantly higher than the $\delta^{15}N_{NO3+NO2}$ at 200 m in MW and LB samples, where the average $\delta^{15}N_{NO3+NO2}$ at 200 m was 5.0 ± 0.6‰ and 5.1 ± 0.6‰, respectively ($p<0.5$ and $p<0.01$, respectively, evaluated with the Kruskal-Wallis test; Kruskal and Wallis, 1952). Furthermore, the elevated $\delta^{15}N_{NO3+NO2}$ in SPG SPSTUW corresponded to significantly lower $[NO_3^-+NO_2^-]$ at 200 m (2.4 ± 0.8 µM) compared to the LB, where the average $[NO_3^-+NO_2^-]$ at 200 m was 3.3 ± 0.6 µM ($p<0.01$, Kruskal and Wallis, 1952) (Figures 3A, C). Within the surface waters (upper 150 m), the $\delta^{15}N_{NO3+NO2}$ at hydrothermal station 5-2019 was significantly lower between the four casts (5a – d), 1.8 ± 0.9‰, compared to the average $\delta^{15}N_{NO3+NO2}$ in the upper 150 m at hydrothermal station 10 (10 a, b), 4.4 ± 0.6‰ ($p<0.01$, Kruskal and Wallis, 1952) (Figures 3B, D). The lowest $\delta^{15}N_{NO3+NO2}$, 0.7 ± 0.1‰, was observed at station 5c-2019 at 100 m, above which $\delta^{15}N_{NO3+NO2}$ increased to 1.0 ± 0.0‰ at 95 m (Figures 3A, C). The $\delta^{15}N_{NO3+NO2}$ reported here for the TONGA study are publicly available (Knapp and Forrer, 2023).

4.2 PN_{sink} flux and δ15N

The PN_{sink} flux collected in the shallow short-term drifting traps was calculated to be 350 µmol N m^{-2} d^{-1} (170 m, station 5a-2019), 436 µmol N m^{-2} d^{-1} (270 m, station 5a-2019), and 693 µmol N m^{-2} d^{-1} (270 m, station 10a-2019) (Table 2). Further, the average (± 1 S.D.) $\delta^{15}N_{PNsink}$ was -0.5 ± 3.5‰ and -0.2 ± 1.9‰ at 170 m and 270 m at station 5a-2019, respectively, and -0.6 ± 2.3‰ at 270 m at station 10a-2019 (Table 2) (Figure 4). In comparison, the annual average PN_{sink} flux collected in the long-term 1000 m PPS5 moored trap at station 12-2019/4-2020 was an order of magnitude lower, 16.5 ± 14.3 µmol N m^{-2} d^{-1}, and had a higher annual mass-weighted average (± 1 S.D.) $\delta^{15}N_{PNsink}$, 3.4 ± 1.9‰, compared to the shallower, short-term traps (Table 2) (Figure 4).

The seasonal average (± 1 S.D.) PN_{sink} fluxes collected in the deep, moored trap were higher in the austral summer and autumn, at 30.9 ± 11.0 µmol N m^{-2} d^{-1} and 17.0 ± 15.4 µmol N m^{-2} d^{-1}, respectively, compared to the average austral winter and spring PN_{sink} fluxes of 8.0 ± 9.0 µmol N m^{-2} d^{-1} and 8.5 ± 8.5 µmol N m^{-2} d^{-1}, respectively (Table 2) (Figure 4). The average, mass-weighted (± 1 S.D.) summer $\delta^{15}N_{PNsink}$ from the 1000 m PPS5 moored trap, 1.5 ± 0.7‰, was lower than the wintertime average of 5.9 ± 1.1‰, while the average (± 1 S.D.) spring and autumn mass-weighted $\delta^{15}N_{PNsink}$, 2.9 ± 0.5‰ and 3.3 ± 1.7‰, respectively, were intermediate between summer and winter values.

4.3 Results of the $\delta^{15}N$ budget

The $\delta^{15}N$ budget described above compares the $\delta^{15}N$ of the primary form of N exported from the euphotic zone, $\delta^{15}N_{PNsink}$, with the $\delta^{15}N$ of the two input terms, subsurface $NO_3^-+NO_2^-$ and N_2 fixation. This provides a geochemically-derived estimate of the fractional contribution of N_2 fixation to export production (f_{nfix}) as well as rate of N_2 fixation (R_{nfix}). Given that the subsurface $\delta^{15}N_{NO3+NO2}$ source is difficult to constrain, we evaluate the shallow $\delta^{15}N$ budgets using the shallowest subsurface $\delta^{15}N_{NO3+NO2}$ minima as well as the sample immediately below the minima (Knapp et al., 2021), while the $\delta^{15}N$ budget using the deep trap PN_{sink} flux uses the average subsurface

TABLE 1 Water masses identified from the 2019 and 2020 TONGA cruises and their average (± 1 S.D.) hydrographic and NO_3^-+NO_2^- properties and number (n) of samples from each water mass.

Water Mass	Depth (m)	Temperature (°C)	Salinity	σ_θ	$[NO_3^-+NO_2^-]$ µM	$\delta^{15}N_{NO3+NO2}$ (‰ vs. N_2 in air)
Surface waters (97)	0 – 150	24.4 ± 0.6[1]	35.4 ± 0.5[1]	23.7 ± 0.2	0.2 ± 0.2[1]	2.4 ± 1.5[4] 4.3 ± 1.7[5]
SPSTUW (38)	150 – 250	22.5 ± 0.8[1,3]	35.7 ± 0.1[1,3]	25.0 ± 0.2	2.4 ± 0.8	4.9 ± 1.4
WSPCW (30)	250 – 550	12.6 ± 0.9[1,2]	34.9 ± 0.2[1,2]	26.4 ± 0.2[2]	7.8 ± 2.5[1]	7.0 ± 0.7[2]
SPSTMW (4)	380 – 400	14.9 ± 0.5[3]	35.2 ± 0.1[3]	26.0 ± 0.0[3]	9.0 ± 0.5	7.4 ± 0.4
AAIW (2)	> 600	6.5 ± 0.1	34.4 ± 0.0[1,3]	26.9 ± 0.1[2,3]	26.7 ± 1.2[1]*	6.9 ± 0.1[2]*

[1]Tilliette et al., 2022
[2]Lehmann et al., 2018
[3]Talley et al., 2011
[4] Average for hydrothermal vent stations only (station 5-2019 and station 10-2019).
[5] Average for all non-hydrothermal vent stations (i.e., all stations except station 5-2019 and station 10-2019).
*n = 1 for this measurement.
These data align with the studies indicated in superscript.

$\delta^{15}N_{NO3+NO2}$ minima at station 12-2019/4-2020 and the average SPSTUW $\delta^{15}N_{NO3+NO2}$ at station 4-2020. At the shallow trap stations in close proximity to the hydrothermal vents, the subsurface $\delta^{15}N_{NO3+NO2}$ ranged from 1.2 to 2.2‰ and 3.6 to 4.7‰ at stations 5-2019 and 10-2019, respectively, while at the deep mooring (station 12-2019/4-2020) the average subsurface $\delta^{15}N_{NO3+NO2}$ minima and SPSTUW $\delta^{15}N_{NO3+NO2}$ were 2.4‰ and 4.6‰, respectively (Table 2). Additional uncertainty in the $\delta^{15}N$ budgets includes the standard deviation of the $\delta^{15}N_{PNsink}$ analysis (Table 2). The $\delta^{15}N$ value for N_2 fixation, ($\delta^{15}N_{Nfix}$) of -1‰ is based on literature reports of diazotrophic

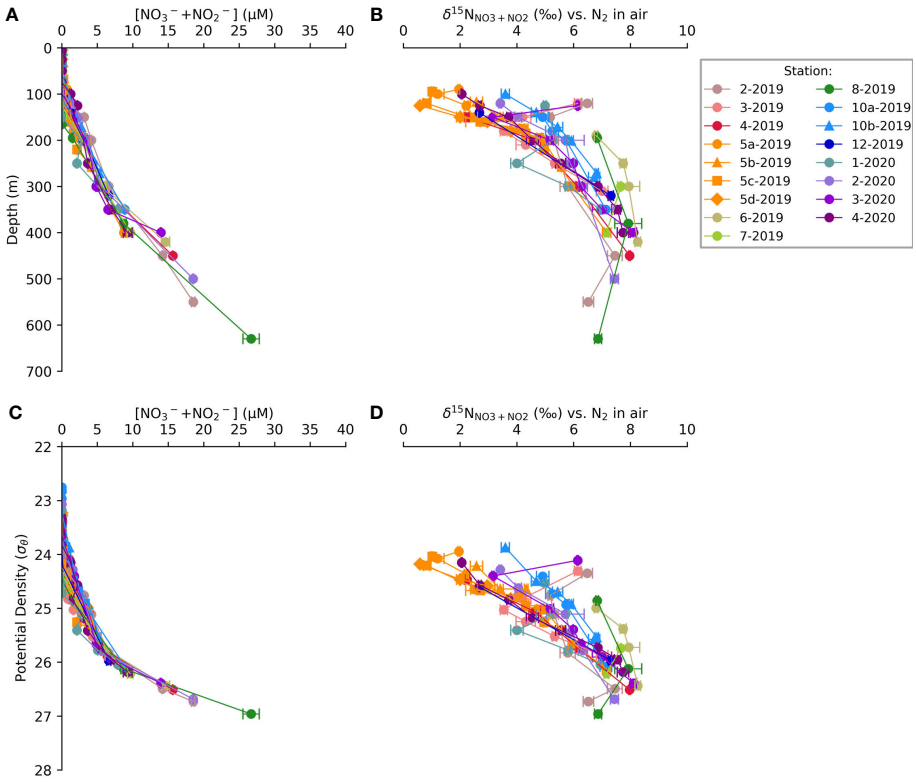

FIGURE 3
Water column profiles of $[NO_3^-+NO_2^-]$ and $\delta^{15}N_{NO3+NO2}$ vs. depth of samples from the 2019 and 2020 TONGA cruises **(A, B)** and vs. potential density **(C, D)**. Error bars represent ±1 S.D. and are often smaller than the symbol size.

biomass $\delta^{15}N$ (Hoering and Ford, 1960; Minagawa and Wada, 1986; Carpenter et al., 1997) (Table 2). Comparing these values with the $\delta^{15}N_{PNsink}$, we calculate that at station 5-2019, the f_{nfix} ranged from 77 to 84 ± 159% for the 170 m trap, while the f_{nfix} ranged from 64 to 76 ± 86% at the 270 m trap (Table 2). At station 10-2019, the f_{nfix} at the 270 m trap ranged from 90 to 92 ± 50% (Table 2). We further calculate a geochemically derived R_{nfix} of 282 ± 550 μmol N m^{-2} d^{-1} and 331 ± 375 μmol N m^{-2} d^{-1} for the 170 m and 270 m traps deployed at station 5-2019, respectively, and 638 ± 347 μmol N m^{-2} d^{-1} for the 270 m trap deployed at station 10-2019 (Table 2). The $\delta^{15}N$ budget calculated for the moored trap at station 12-2019/4-2020 (note that the trap is deeper, i.e. 1000 m instead of 170 – 270 m for the drifting ones) yielded a mass-weighted f_{nfix} of 12 to 64 ± 29% (average = 42 ± 13%) for the summer, while the spring and autumn had similar but lower mass-weighted f_{nfix} of 0 to 37 ± 21% (average = 0 ± 29%) and 0 to 43 ± 69% (average = 12 ± 36%), respectively, and winter had a mass-weighted f_{nfix} of 0 ± 18%.

TABLE 2 The mass and isotopic composition of the sinking particulate N (PN_{sink}) flux captured in the short-term PIT and long-term PPS5 traps, and results of the $\delta^{15}N$ budgets.

	Stn.	Lon.	Trap depth (m)	Time (days)*	Season[1]	Av. PN_{sink} flux (μmol N m^{-2} d^{-1})[2]	Av. $\delta^{15}N_{PNsink}$[2] (‰)	$\delta^{15}N_{NO3+NO2}$ end-member range[3] (‰)	f_{nfix}[4] (%)	R_{nfix}[4] (μmol N m^{-2} d^{-1})	Bottle-based av. N_2 fix rate[2] (μmol N m^{-2} d^{-1})
TONGA (this study)	5-2019 (LB)	175.9° W	170	5	Late Spring	350	-0.5 ± 3.5	1.2 – 2.2	77 to 84 ± 159	282 ± 550	1942 ± 1212[6]
	5-2019 (LB)	175.9° W	270	5	Late Spring	436	-0.2 ± 1.9	1.2 – 2.2	64 to 76 ± 86	331 ± 375	1942 ± 1212[6]
	10-2019 (LB)	175.2° W	270	4	Late Spring	693	-0.6 ± 2.3	3.6 – 4.7	90 to 92 ± 50	638 ± 347	2047 ± 566[6]
	12-2019/4-2020[5] (LB)	177.9° W	1000	360	Spring	8.5 ± 8.5	2.9 ± 0.5[9]	2.4[7] – 4.6[8]	0 to 37 ± 21[9]	-[10]	-[10]
					Summer	30.9 ± 11.0	1.5 ± 0.7[9]		12 to 64 ± 29[9]	-[10]	-[10]
					Autumn	17.0 ± 15.4	3.3 ± 1.7[9]		0 to 43 ± 69[9]	-[10]	-[10]
					Winter	8.0 ± 9.0	5.9 ± 1.1[9]		0 ± 18[9]	-[10]	-[10]
OUTPACE (Knapp et al., 2018)	A (MW)	163.6 °E	150	5	Late summer	303	0.6 ± 1	7.0 – 8.4	80 to 83 ± 13	254 ± 50	593 ± 5[11]
	B (SPG)	170.7° W	150	5	Autumn	30	3.1 ± 1	7.2 – 8.3	50 to 56 ± 12	16 ± 6	706 ± 302[11]
	C (SPG)	165.8° W	150	5	Autumn	47	7.7 ± 1	7.0 – 8.4	0 to 8 ± 11	5 ± 5	59 ± 16[11]

[1] Austral seasons divided into: Spring (September, October, November), Summer (December, January, February), Autumn (March, April, May), Winter (June, July, August).
[2] average ± 1 S.D.
[3] Subsurface $\delta^{15}N_{NO3+NO2}$.
[4] See Methods section 2.6.
[5] Samples collected bimonthly, then seasonally averaged.
[6] Lory et al., 2023.
[7] Shallow subsurface $\delta^{15}N_{NO3+NO2}$ minima end-member for station 12-2019 and 4-2020.
[8] Average SPSTUW $\delta^{15}N_{NO3+NO2}$ end-member at station 4-2020. Note, sampling resolution at station 12-2019 did not include SPSTUW.
[9] Mass-weighted average values for each season.
[10] No data.
[11] Caffin et al., 2018

The table includes the range in the $\delta^{15}N_{NO3+NO2}$ end-member, fraction of export production supported by N_2 fixation ("f_{nfix}") and N_2 fixation rate determined by multiplying the PN_{sink} flux by f_{nfix} for the TONGA (this study) and OUTPACE (Knapp et al., 2018) projects. Uncertainty in f_{nfix} and R_{nfix} reflects both the range in $\delta^{15}N_{NO3+NO2}$ end-member as well as the standard deviation of the PN_{sink} $\delta^{15}N$ measurements.
*Trap deployment time.

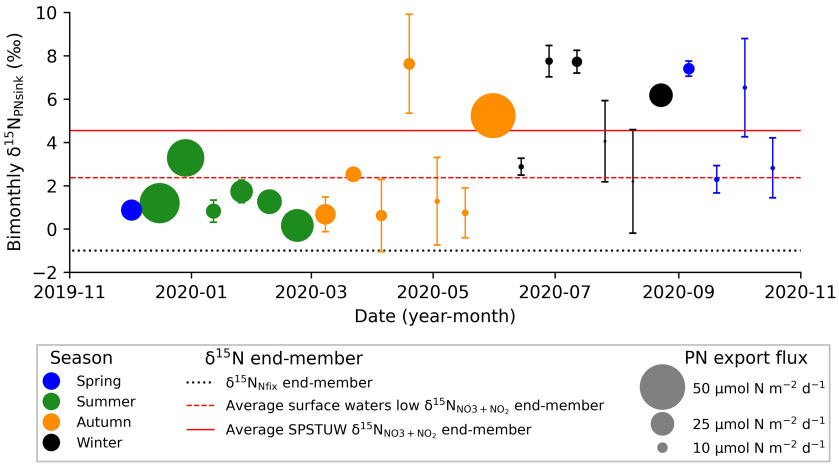

FIGURE 4
Bimonthly measurements of PN_{sink} flux and $\delta^{15}N_{PNsink}$ from the 1000 m trap deployed at station 12-2019/station 4-2020 between November 2019 to October 2020. Circle color corresponds to the season when the majority of the PN_{sink} was collected over bimonthly sampling intervals and circle size corresponds to PN_{sink} flux magnitude (µmol N m^{-2} d^{-1}). Each measurement is plotted at the end date of the two-week sampling interval. The $\delta^{15}N_{Nfix}$ end-member (-1‰) is represented by the dotted black line and the low $\delta^{15}N_{NO3+NO2}$ end-member at station 12-2019 and 4-2020 (2.4‰) and average SPSTUW $\delta^{15}N_{NO3+NO2}$ end-member at station 4-2020 (4.6‰) are represented by the dashed and solid lines, respectively. Data available in Supplementary Table S1.

These f_{nfix} values indicate that the highest contribution of N_2 fixation to export production collected at 1000 m was during the summer, followed by autumn and spring. Due to significant PN_{sink} flux attenuation with depth (Martin et al., 1987), we do not calculate a R_{nfix} for the moored trap data.

5 Discussion

5.1 TONGA $\delta^{15}N$ budgets reflect high rates of N_2 fixation in the WTSP

The results of the short-term $\delta^{15}N$ budgets suggest that N_2 fixation rates were high (282 to 638 µmol N m^{-2} d^{-1}) near the hydrothermal vents at the time of the 2019 cruise. While there are notable differences in the magnitude of these geochemically-derived N_2 fixation rates and the bottle-based $^{15}N_2$ uptake rates reported by Lory et al., 2023, we consider these results to be broadly consistent with one another, as well as consistent with estimates of diazotroph abundance measured contemporaneously (Bonnet et al., 2023b). Specifically, bottle-based $^{15}N_2$ uptake rates were 3 to 7 times higher than the R_{nfix} estimated from the $\delta^{15}N$ budget (Table 2); however, both rate estimates are at the upper-end typically reported by each technique (Gruber, 2004; Capone et al., 2005; Casciotti et al., 2008; Luo et al., 2012; Knapp et al., 2016a) and align with previous work from the region (Montoya et al., 2004; Berthelot et al., 2017; Bonnet et al., 2017; Knapp et al., 2018; Shao et al., 2023). Prior work investigating N_2 fixation's contribution to export production has attributed discrepancies between these two metrics to potential sediment trap under collection of exported material (Knapp et al., 2016a; Böttjer et al., 2017, Knapp et al., 2018), alternate sources of fixed N to the euphotic zone including horizontal advection (Böttjer et al., 2017), phytoplankton bloom stage as well as temporal delay between organic matter formation and capture by the sediment trap (de Verneil et al., 2017; Caffin et al., 2018; Knapp et al., 2018), and bottle-based $^{15}N_2$ incubations with their associated methodological considerations (i.e., bottle effects) (White et al., 2020). Additionally, our $\delta^{15}N$ budgets should be considered a lower bound for estimated N_2 fixation rates because of the mixing-model's inherent assumption that the only fate of newly fixed N is to be balanced by the sinking flux, and that no newly fixed N is released to the dissolved pool, which is likley unrealistic (Capone et al., 1994; Glibert & Bronk, 1994; Mulholland and Capone, 2004; Bonnet et al., 2016; Knapp et al., 2016b). Further, the trap depth used here, 170 m, is below the base of the mixed layer, and thus underestimates new/export production. While euphotic zone nitrification is a source of low-$\delta^{15}N_{NO3}$ that could lead to an overestimation of N_2 fixation supported export production, rates of euphotic zone nitrification from this and other similar oligotrophic regions are low (<10 nmol L^{-1} d^{-1}) (Smith et al., 2014; Raes et al., 2020) compared to the very high rates of N_2 fixation using multiple metrics in this study. This therefore suggests that N_2 fixation is the dominant mechanism generating the low-$\delta^{15}N_{PNSink}$ signal observed.

Regardless of the mechanism(s) driving these discrepancies, both the $\delta^{15}N$ budget and $^{15}N_2$ uptake rate estimates are also consistent with the elevated diazotroph abundances (Bonnet et al., 2023a; Lory et al., 2023) observed on the 2019 TONGA cruise (Figure 5). Here we compare averages of biological and geochemical metrics associated with N_2 fixation for the three hydrographic regions, MW, the LB, and the SPG (defined in Section 2.1). While results from the qPCR analysis targeting *nifH* genes indicate that *Trichodesmium* spp. and UCYN-A dominated the diazotroph assemblage in the upper 50 m across the TONGA transect, *Trichodesmium* spp. were most abundant in the LB near the hydrothermal vents (average 1.0x10^7 gene copies L^{-1}), followed by UCYN-A (average 3.0x10^6 gene copies L^{-1}) (Figures 5A, B). These

exceptionally high abundances of *Trichodesmium* spp. and UCYN-A were on the order of one to four times higher than previous studies (e.g., Zehr & Turner, 2001; Moisander et al., 2010; Turk-Kubo et al., 2012; Moisander et al., 2014; Benavides et al., 2018; Benavides et al., 2020; Confesor et al., 2022). Notably, the highest regionally-averaged, trapezoidally-integrated upper 50 m $^{15}N_2$ uptake rates were found in the LB (1038 ± 600 μmol N m^{-2} d^{-1}), where *Trichodesmium* spp. were most abundant and where the lowest regionally-averaged $\delta^{15}N_{NO3+NO2}$ subsurface minima of 2.8 ± 1.5‰ (Figure 5F) was observed between 100 and 200 m. This underscores the potential significance of *Trichodesmium* spp. supporting N_2 fixation near the hydrothermal vents. UCYN-A was the dominant diazotroph in the upper 50 m in MW and the SPG, with regional averages of 2.5x10^8 gene copies L^{-1} and 3.1x10^8 gene copies L^{-1}, respectively, followed by *Trichodesmium* spp., with regional averages of 3.0x10^5 and 3.7x10^5 gene copies L^{-1}, respectively. Average abundances of UCYN-B (2.6x10^4 to 3.2x10^5 gene copies L^{-1}), UCYN-C (4.3x10^1 to 1.7x10^2 gene copies L^{-1}) and Gamma proteobacteria (5.4x10^3 to 9.9x10^3 gene copies L^{-1}) remained comparatively low across the transect (Figures 5C–E), but were similar in magnitude to previous studies in the region (Moisander et al., 2014; Benavides et al., 2018; Benavides et al., 2020). Although UCYN-A have extremely high gene abundances and dominate the upper 50 m in MW and the SPG, the trapezoidally-integrated upper 50 m $^{15}N_2$ uptake rates were lower than in the LB, 713 ± 691 and 537 ± 629 μmol N m^{-2} d^{-1}, respectively, and were associated with a higher regional average $\delta^{15}N_{NO3+NO2}$ subsurface minima of 4.4 ± 1.2‰ and 5.5 ± 1.9‰, respectively, observed between 100 to 200 m (Figure 5F). While care should be taken when relating *nifH* gene copies to diazotroph biomass, these gene copy abundances broadly correspond to elevated diazotroph abundances (Meiler et al., 2022) and confirm the significance of diazotrophy in the region.

5.2 N_2 fixation is an important source of N supporting export production in the WTSP

The agreement between the geochemically-derived N_2 fixation rates, $^{15}N_2$ uptake rates and diazotroph abundances together indicate that export production in the WTSP at the time of this study was driven by N_2 fixation (Bonnet et al., 2023b). This is in contrast to prior work in other oligotrophic regions where the majority of export was supported by subsurface NO_3^-, even when N_2 fixation inputs were high (Casciotti et al., 2008; Bourbonnais et al., 2009; White et al., 2013; Böttjer et al., 2017). The shallow sediment traps deployed for the TONGA project indicate that N_2 fixation supports a majority of export production (f_{nfix} = 64 to 92%) near the hydrothermal vents, at least in the late spring (Table 2; Figures 6A, B). These f_{nfix} values are similar to those calculated from the previous OUTPACE campaign during the late summer/early autumn in MW (station A, 80 to 83 ± 13%), and near the Tonga-

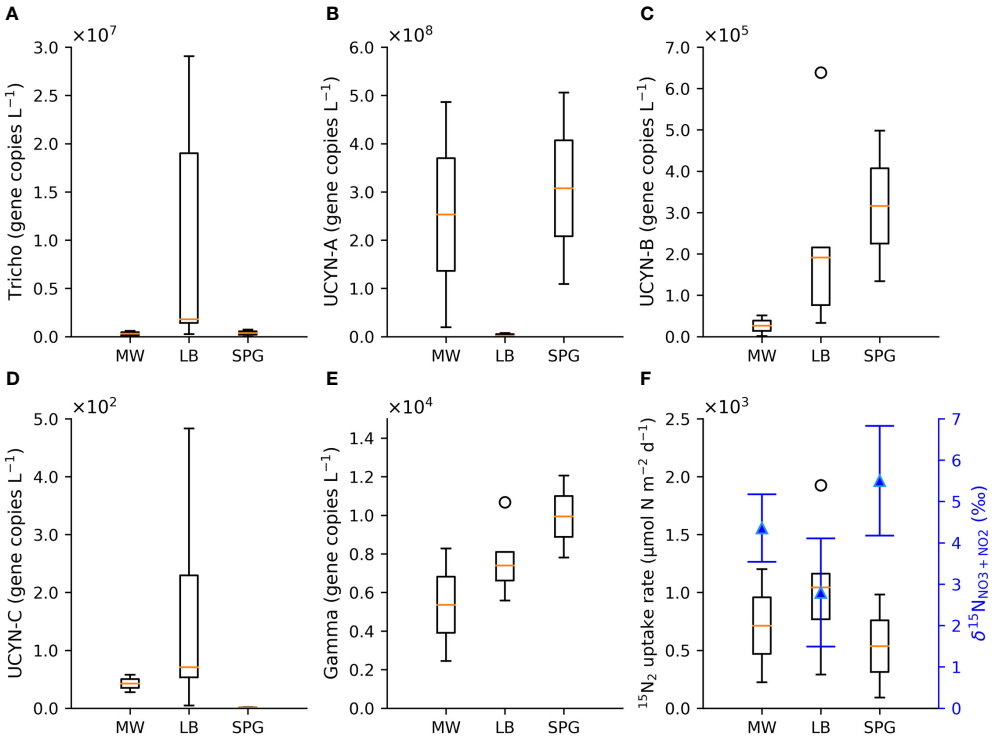

FIGURE 5
Box plots of the upper 50 m *nifH* gene abundances (gene copies L^{-1}) from Bonnet et al., 2023a and Lory et al., 2023 for the hydrographic regions of MW, the LB and the SPG for **(A)** *Trichodesmium* spp., **(B)** UCYN-A, **(C)** UCYN-B, **(D)** UCYN-C, and **(E)** Gamma proteobacteria, as well as (F) box plots of the regional average, trapezoidally-integrated upper 50 m $^{15}N_2$ fixation rates from Lory et al., 2023, with the corresponding regional average 90 to 195 m $\delta^{15}N_{NO3+NO2}$ (blue triangles). The open circles associated with the box plots indicate outliers.

Kermadec Arc (station B, 50 to 56 ± 12%) (Table 2; Figure 6C) (Knapp et al., 2018). The high f_{nfix} values reported here from the short-term traps deployed at TONGA Stations 5 and 10 replicate a geochemical signature that has not been observed outside of the WTSP, underscoring the significance of N_2 fixation regionally (Bonnet et al., 2023b). We also emphasize the potential for the f_{nfix} from our $\delta^{15}N$ budgets to underestimate the importance of N_2 fixation to export due to the mixing-model's inherent assumption that the only fate of newly fixed N is the PN_{sink} flux captured by the sediment traps, as opposed to being released and persisting as dissolved organic nitrogen (Capone et al., 1994; Glibert and Bronk, 1994).

While the results of the short-term $\delta^{15}N$ budgets from both the TONGA and OUTPACE campaigns found that N_2 fixation supports the majority of export production in the late spring, late summer, and early autumn in the LB and MW, we also consider the $\delta^{15}N_{PNsink}$ collected in the deep, moored trap at station 12-2019/4-2020 in the LB to evaluate this trend over an annual cycle (Figure 4). Unsurprisingly, the mass flux collected in the shallower, short-term PIT traps was higher and the $\delta^{15}N_{PNsink}$ was lower than that collected in the deeper, moored trap. However, we note that the moored trap was deployed ~200 km west of the shallow traps and hydrothermal vents (Table 2) (Figures 1, 4), and the conical shape of the PPS5 has been observed to undersample (Baker et al., 2020; Tilliette et al., 2023). The $\delta^{15}N_{PNsink}$ in the shallow PIT traps collected in the late spring at stations 5-2019 and 10-2019 ranged from -0.2 to -0.6‰ compared to a seasonal average $\delta^{15}N_{PNsink}$ of 2.9 ± 0.5‰ and 1.5 ± 0.7‰ observed in the moored PPS5 trap during the spring and summer, respectively. We expect that the higher $\delta^{15}N_{PNsink}$ found in the deeper moored trap likely resulted from the collection of PN_{sink} from a larger surface area than the shallow short-term traps, where export production may have been supported by a mixture of N sources with higher $\delta^{15}N$ (Siegel and Deuser, 1997; Siegel et al., 2008). Additionally, horizontal advection of particles generated at locations not impacted by the shallow hydrothermal vents potentially decouples the euphotic zone diazotrophic abundance and/or importance from the PN collected in the moored trap (Waniek et al., 2000). Indeed, the exported material in the deep trap was observed to be compositionally different from that captured in the shallow, short-term traps, where the hydrothermal signature of the particles was less evident due to organic matter remineralization while being transported to depth (Tilliette et al., 2023). The associated distance and time components of sinking PN to the deep trap potentially underestimates the importance of N_2 fixation to export production. Similar flux and isotopic composition offsets have been observed between shallow and deep sediment traps in the ETSP (Berelson et al., 2015; Knapp et al., 2016a; Tilliette et al., 2023).

Since aerosol inputs to this region are minimal (Guieu et al., 2018), we expect that the seasonal variability of $\delta^{15}N_{PNsink}$ in the deep, moored trap reflects shifts in the importance of N_2 fixation and subsurface NO_3^- for supporting export production over seasonal timescales. In the deep trap, annual PN_{sink} fluxes peaked in the summer (30.9 ± 11.0 µmol N m^{-2} d^{-1}), coinciding with the lowest average mass-weighted $\delta^{15}N_{PNsink}$, 1.5 ± 0.7‰, while the lowest PN_{sink} fluxes were observed in the winter (8.0 ± 9.0 µmol N m^{-2} d^{-1}) and coincided with the highest average mass-weighted $\delta^{15}N_{PNsink}$, 5.9 ± 1.1‰, indicating that isotopically distinct N sources support export seasonally. Since there are steep gradients in both $[NO_3^-+NO_2^-]$ and $\delta^{15}N_{NO3+NO2}$ with depth (Figures 3, 6), a higher winter $\delta^{15}N_{PNsink}$ may reflect entrainment of a deeper $NO_3^-+NO_2^-$ source (likely SPSTUW) with a higher $\delta^{15}N_{NO3+NO2}$ due to winter mixing (Moutin et al., 2018). The net effect of a higher subsurface $\delta^{15}N_{NO3+NO2}$ end-member would be to raise the estimated f_{nfix} (Table 2) (Böttjer et al., 2017). As a result, the mass-weighted seasonal f_{nfix} values for the deep trap range from 12 to 64 ± 29% in the summer and 0 ± 18% in the winter, describing a largely N_2 fixation supported export system in the summer. Further, since the majority of annual export is focused in the summer, and was supported by low-$\delta^{15}N$ N sources, we attribute an important fraction of annual export production and deep (>1000 m) long-term C sequestration to N_2 fixation at station 12-2019/4-2020 (Figure 4; Table 2).

Considering the elevated chlorophyll *a* concentrations observed over a large area in this region ranging up to 360,000 km^2 (Bonnet et al., 2023b), and given the high R_{nfix} and f_{nfix} values estimated at station 5a-2019 and 10a-2019, along with the large fraction of N_2 fixation supported export production at station 12-2019/4-2020 over an annual timescale, the otherwise oligotrophic WTSP appears to be biogeochemically unique where N_2 fixation supports a large fraction of annual export production as a result of the influence of shallow hydrothermal vents. The significance of these regional N_2 fixation inputs in the WTSP are further pronounced in the gradients of water column $\delta^{15}N_{NO3+NO2}$ both zonally as well as with depth (Figures 3, 6). In particular, $\delta^{15}N_{NO3+NO2}$ between 150 and 400 m decreases from east to west (SPG to MW) across the zonal transect, and also decreases from ~400 m to shallower depths. These isotopic gradients reflect the accumulation of low-$\delta^{15}N$ N inputs in the upper thermocline to the west along this transect that are presumably associated with the remineralization of diazotrophic inputs (Casciotti et al., 2008; Knapp et al., 2008). This accumulation of low-$\delta^{15}N_{NO3+NO2}$ in the upper 400 m of the WTSP erodes the elevated $\delta^{15}N_{NO3+NO2}$ originating from dissimilatory NO_3^- reduction occurring in the oxygen deficient zones of the ETSP (Bourbonnais et al., 2015; Peters et al., 2018; Casciotti et al., 2013), a geochemical signature that reflects basin-scale compensation of N losses in the east with N inputs in the west that is consistent with peloceanographic records (Brandes and Devol, 2002; Deutsch et al., 2004; Weber and Deutsch, 2014; Knapp et al., 2018).

6 Conclusions

Here we report results of $\delta^{15}N$ budgets that compare subsurface $\delta^{15}N_{NO3+NO2}$ with the $\delta^{15}N_{PNsink}$ captured in short-term, shallow (170 and 270 m) PIT deployed near the hydrothermal vents of the Tonga-Kermadec Arc and long-term, deep (1000 m) moored PPS5 sediment

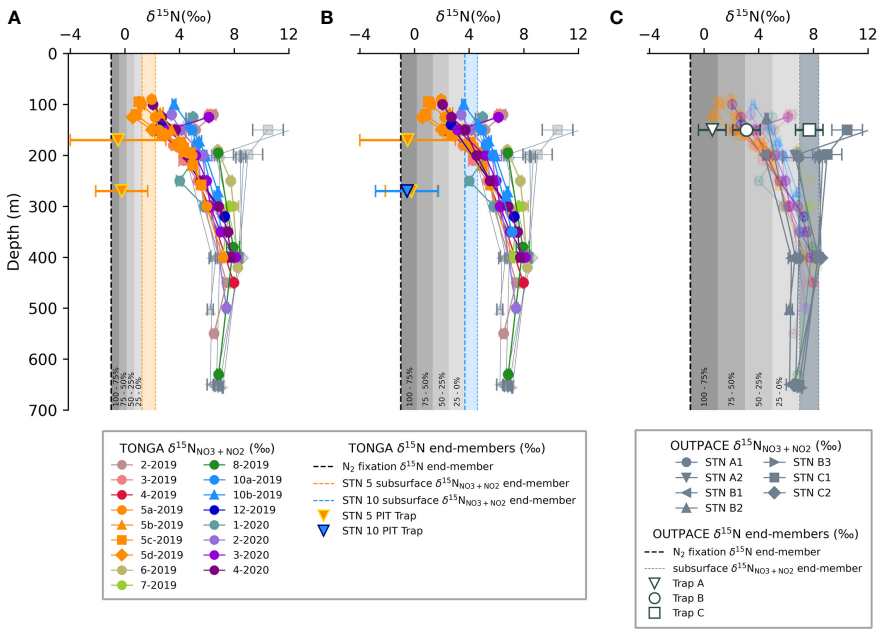

FIGURE 6
The fraction of N_2 fixation-supported export production in the austral spring at **(A)** TONGA station 5-2019, and, **(B)** TONGA station 10-2019, compared with **(C)** results from the austral late summer/early autumn at OUTPACE stations(**A-C**) Each panel includes water column profiles of $\delta^{15}N_{NO3+NO2}$ for samples from the 2019 and 2020 TONGA cruises in color and the OUTPACE cruise in grey and the associated $\delta^{15}N$ budget terms, including the sediment trap $\delta^{15}N_{PNsink}$ (inverted triangles and open circle and square), the $\delta^{15}N_{Nfix}$ (vertical dashed line) and ranges in subsurface $\delta^{15}N_{NO3+NO2,}$ which are represented by the orange shaded region in **(A)**, blue shaded region in **(B)**, and steel-grey shaded region in **(C)** (Table 2). The fractional contribution of N_2 fixation to export production is indicated by the grey shading and the corresponding fraction is indicated along the bottom of each panel.

traps deployed ~200 km west of the Arc. These results are evaluated in the context of $^{15}N_2$ uptake rates (Lory et al., 2023) and *nifH* gene abundances (Bonnet et al., 2023b) collected contemporaneously, as well as with prior work from the region (Knapp et al., 2018). Results from the short-term, shallow $\delta^{15}N$ budgets indicate that N_2 fixation supports the majority, 64 to 92%, of export in late spring in the Lau Basin, while the mass-weighted, seasonally-averaged $\delta^{15}N$ budgets from deeper traps suggest that N_2 fixation supports 12 to 64% of export production and thus long-term C sequestration in the summer when the highest PN_{sink} fluxes are observed. As the seasons progress into winter, export production becomes increasingly supported by subsurface NO_3^-. The observations from this cruise as well as from the OUTPACE study (Knapp et al., 2018) are in contrast to other regions explored so far, where even significant N_2 fixation inputs do not support the majority of export (Casciotti et al., 2008; Bourbonnais et al., 2009; Böttjer et al., 2017), underscoring the significance of diazotrophy in the WTSP. While diazotroph abundance was high across the transect, *Trichodesmium* spp. *nifH* gene copies were highest in the vicinity of the hydrothermal vents, which appear shallow enough to meet the considerable Fe demands of primary productivity in general (Tilliette et al., 2022), and N_2 fixation in particular, in the region (Bonnet et al., 2023b), highlighting the sensitivity of N_2 fixation to Fe availability. These results suggest that the significant N_2 fixation inputs to the WTSP in the late spring, summer, and early autumn work to lower the elevated upper thermocline $\delta^{15}N_{NO3+NO2}$ originating from dissimilatory NO_3^- reduction in the oxygen deficient zones of the Eastern Tropical South Pacific.

Data availability statement

The datasets presented in this study can be found in online repositories. The names of the repository/repositories and accession number(s) can be found in the article/Supplementary Material.

Author contributions

SB, CG, and AK designed the study. SB and CG carried out the sampling. HF and RT carried out the $\delta^{15}N_{NO3+NO2}$ sample analysis and data aqusition. SB and OG carried out the $\delta^{15}N_{PNsink}$ sample analysis and data aqusition. HF and AK wrote the first manuscript draft, which was then revised by all authors. All authors contributed to the article and approved the submitted version.

Funding

The author(s) declare financial support was received for the research, authorship, and/or publication of this article. This research is a contribution to the TONGA project (Shallow hydroThermal sOurces of trace elemeNts: potential impacts on biological productivity and the biological carbon pump; TONGA cruise https://doi.org/10.17600/18000884) funded by the Agence Nationale de la Recherche (grant TONGA ANR-18- CE01-0016), the LEFE-CyBER

program (CNRS-INSU), the A-Midex foundation, the TGIR Flotte océanographique française, the Institut de Recherche pour le Développement (IRD). HF acknowledges funding from the Winchester Fund at Florida State University's EOAS Department. AK acknowledges NSF OCE-1829797 for supporting the nitrate isotopic analyses.

Acknowledgments

The authors warmly thank the captain and crew of the R/V L'Atalante and R/V Alis (both TGIR Flotte, operated by IFREMER) for outstanding shipboard operations. Vincent Taillandier and Nagib Bhairy are thanked for the CTD rosettes management, and data processing, Sandra Nunige for nutrient analyses of the 2019 samples, Mary Dennis for her assistance with the 'denitrifier method' at Florida State University, Caroline Lory for her assistance with the $^{15}N_2$ fixation experiments and data aqusition and Nathalie Leblond (Cellule Piège INSU) for the treatment/splitting of the moored trap.

Conflict of interest

The authors declare that the research was conducted in the absence of any commercial or financial relationships that could be construed as a potential conflict of interest.

Publisher's note

All claims expressed in this article are solely those of the authors and do not necessarily represent those of their affiliated organizations, or those of the publisher, the editors and the reviewers. Any product that may be evaluated in this article, or claim that may be made by its manufacturer, is not guaranteed or endorsed by the publisher.

Supplementary material

The Supplementary Material for this article can be found online at: https://www.frontiersin.org/articles/10.3389/fmars.2023.1249115/full#supplementary-material

References

Altabet, M. A. (1988). Variations in nitrogen isotopic composition between sinking and suspended particles: implications for nitrogen cycling and particle transformation in the open ocean', Deep Sea Research Part A. *Oceanographic Res. Papers* 35.4), 535–554. doi: 10.1016/0198-0149(88)90130-6

Aminot, A., and Kerouel, R. (2007). Dosage automatique des nutriments dans les eaux marines: méthodes en flux continu, Ifremer, Plouzané.

Baker, C. A., Estapa, M. L., Iversen, M., and Lampitt Buesseler, R. K. (2020). Are all sediment traps created equal? An intercomparison study of carbon export methodologies at the PAP-SO site. *Prog. Oceanography* 184, 102317. doi: 10.1016/j.pocean.2020.102317

Benavides, M., Martias, C., Elifantz, H., Berman-Frank, I., Dupouy, C., and Bonnet, S. (2018). Dissolved organic matter influences N2 fixation in the New Caledonian lagoon (Western tropical south pacific). *Front. Mar. Sci.* 5, 89. doi: 10.3389/fmars.2018.00089

Benavides, M., Duhamel, S., Van Wambeke, F., Shoemaker, K. M., Moisander, P. H., Salamon, E., et al. (2020). Dissolved organic matter stimulates N2 fixation and *nifH* gene expression in *Trichodesmium*. *FEMS Microbiol. Lett.* 367 (4), fnaa034. doi: 10.1093/femsle/fnaa034

Berelson, W. M., Haskell, W. Z., Prokopenko, M., Knapp, A. N., Hammond, D. E., Rollins, N., et al. (2015). Biogenic particle flux and benthic remineralization in the Eastern Tropical South Pacific. *Deep Sea Res. Part I: Oceanographic Res. Papers* 99, 23–34. doi: 10.1016/j.dsr.2014.12.006

Berman-Frank, I., Cullen, J. T., Shaked, Y., Sherrell, R. M., and Falkowski, P. G. (2001). Iron availability, cellular iron quotas, and nitrogen fixation in *Trichodesmium*. *Limnology Oceanography* 46 (6), 1249–1260. doi: 10.4319/lo.2001.46.6.1249

Berthelot, H., Benavides, M., Moisander, P. H., Grosso, O., and Bonnet, S. (2017). High-nitrogen fixation rates in the particulate and dissolved pools in the Western Tropical Pacific (Solomon and Bismarck Seas). *Geophysical Res. Lett.* 44 (16), 8414–8423. doi: 10.1002/2017GL073856

Bonnet, S., Biegala, I. C., Dutrieux, P., Slemons, L. O., and Capone, D. G. (2009). Nitrogen fixation in the western equatorial Pacific: Rates, diazotrophic cyanobacterial size class distribution, and biogeochemical significance: N_2 FIXATION IN THE EQUATORIAL PACIFIC. *Global Biogeochemical Cycles* 23 (3). doi: 10.1029/2008GB003439

Bonnet, S., Berthelot, H., Turk-Kubo, K., Fawcett, S., Rahav, E., L'Helguen, S., et al. (2016). Dynamics of N_2 fixation and fate of diazotroph-derived nitrogen in a low-nutrient, low-chlorophyll ecosystem: results from the VAHINE mesocosm experiment (New Caledonia). *Biogeosciences* 13 (9), 2653–2673. doi: 10.5194/bg-13-2653-2016

Bonnet, S., Caffin, M., Berthelot, H., and Moutin, T. (2017). Hot spot of N_2 fixation in the western tropical South Pacific pleads for a spatial decoupling between N_2 fixation and denitrification. *Proc. Natl. Acad. Sci.* 114 (14). doi: 10.1073/pnas.1619514114

Bonnet, S., Benavides, M., Le Moigne, F. A. C., Camps, M., Torremocha, A., Grosso, O., et al. (2023a). Diazotrophs are overlooked contributors to carbon and nitrogen export to the deep ocean. *ISME J.* 17 (1), 47–58. doi: 10.1038/s41396-022-01319-3

Bonnet, S., Guieu, C., Taillandier, V., Boulart, C., Bouruet-Aubertot, P., Gazeau, F., et al. (2023b). Natural iron fertilization by shallow hydrothermal sources fuels diazotroph blooms in the ocean. *Science* 380 (6647), 812–817. doi: 10.1126/science.abq4654

Böttjer, D., Dore, J. E., Karl, D. M., Letelier, R. M., Mahaffey, C., Wilson, S. T., et al. (2017). Temporal variability of nitrogen fixation and particulate nitrogen export at Station ALOHA. *Limnology Oceanography* 62 (1), 200–216. doi: 10.1002/lno.10386

Bourbonnais, A., Lehmann, M. F., Waniek, J. J., and Schulz-Bull, D. E. (2009). Nitrate isotope anomalies reflect N_2 fixation in the Azores Front region (subtropical NE Atlantic). *J. Geophysical Res.* 114 (C3), C03003. doi: 10.1029/2007JC004617

Bourbonnais, A., Altabet, M. A., Charoenpong, C. N., Larkum, J., Hu, H., Bange, H. W., et al. (2015). N-loss isotope effects in the Peru oxygen minimum zone studied using a mesoscale eddy as a natural tracer experiment: N-LOSS ISOTOPE EFFECTS IN AN EDDY. *Global Biogeochemical Cycles* 29 (6), 793–811. doi: 10.1002/2014GB005001

Braman, R. S., and Hendrix, S. A. (1989). Nanogram nitrite and nitrate determination in environmental and biological materials by vanadium(III) reduction with chemiluminescence detection. *Analytical Chem.* 61 (24), 2715–2718. doi: 10.1021/ac00199a007

Brandes, J. A., and Devol, A. H. (2002). A global marine-fixed nitrogen isotopic budget: Implications for Holocene nitrogen cycling: NITROGEN ISOTOPIC BUDGET. *Global Biogeochemical Cycles* 16 (4), 67-1-67–14. doi: 10.1029/2001GB001856

Buesseler, K. O., Antia, A. N., Chen, M., Fowler, S. W., Gardner, W. D., Gustafsson, O., et al. (2007). An assessment of the use of sediment traps for estimating upper ocean particle fluxes. *J. Mar. Res.* 65 (3), 345–416. doi: 10.1357/002224007781567621

Caffin, M., Moutin, T., Foster, R.A., Bouruet-Aubertot, P., Doglioli, A.M., Berthelot, H., et al. (2018). N_2 fixation as a dominant new N source in the western tropical South Pacific Ocean (OUTPACE cruise). *Biogeosciences* 15 (8), 2565–2585. doi: 10.5194/bg-15-2565-2018

Capone, D. G. (2001). Marine nitrogen fixation: what's the fuss? *Curr. Opin. Microbiol.* 4 (3), 341–348. doi: 10.1016/S1369-5274(00)00215-0

Capone, D. G., Zehr, J. P., Paerl, H. W., Bergman, B., and Carpenter, E. J. (1997). *Trichodesmium* , a globally significant marine cyanobacterium. *Science* 276 (5316), 1221–1229. doi: 10.1126/science.276.5316.1221

Capone, D. G., Burns, J. A., Montoya, J. P., Subramaniam, A., Mahaffey, C., Gunderson, T., et al. (2005). Nitrogen fixation by *Trichodesmium* spp.: An important source of new nitrogen to the tropical and subtropical North Atlantic Ocean: NITROGEN FIXATION IN THE NORTH ATLANTIC. *Global Biogeochemical Cycles* 19 (2). doi: 10.1029/2004GB002331

Capone, D. G., Ferrier, M. D., and Carpenter, E. J. (1994). Amino acid cycling in colonies of the planktonic marine cyanobacterium *trichodesmium thiebautii*. *Appl. Environ. Microbiol.* 60 (11), 3989–3995. doi: 10.1128/aem.60.11.3989-3995.1994

Carpenter, E. J., Harvey, H. R., Fry, B., and Capone, D. G. (1997). Biogeochemical tracers of the marine cyanobacterium Trichodesmium. *Deep Sea Res. Part I: Oceanographic Res. Papers* 44 (1), 27–38. doi: 10.1016/S0967-0637(96)00091-X

Casciotti, K. L., Buchwald, C., and McIlvin, M. (2013). Implications of nitrate and nitrite isotopic measurements for the mechanisms of nitrogen cycling in the Peru oxygen deficient zone. *Deep Sea Res. Part I: Oceanographic Res. Papers* 80, 78–93. doi: 10.1016/j.dsr.2013.05.017

Casciotti, K. L., Sigman, D. M., Böhlke, J.K., and Hilkert, A. (2002). Measurement of the oxygen isotopic composition of nitrate in seawater and freshwater using the denitrifier method. *Analytical Chem.* 74 (19), 4905–4912. doi: 10.1021/ac020113w

Casciotti, K. L., Trull, T. W., Glover, D. M., and Davies, D. (2008). Constraints on nitrogen cycling at the subtropical North Pacific Station ALOHA from isotopic measurements of nitrate and particulate nitrogen. *Deep Sea Res. Part II: Topical Stud. Oceanography* 55 (14–15), 1661–1672. doi: 10.1016/j.dsr2.2008.04.017

Confesor, K. A., Selden, C. R., Powell, K. E., Donahue, L. A., Mellett, T., Caprara, S., et al. (2022). Defining the realized niche of the two major clades of trichodesmium: A study on the west florida shelf. *Front. Mar. Sci.* 9, 821655. doi: 10.3389/fmars.2022.821655

Conway, T. M., and John, S. G. (2014). Quantification of dissolved iron sources to the North Atlantic Ocean. *Nature* 511 (7508), 212–215. doi: 10.1038/nature13482

Dekaezemacker, J., Bonnet, S., Grosso, O., Moutin, T., Bressac, M., and Capone, D. G. (2013). Evidence of active dinitrogen fixation in surface waters of the eastern tropical South Pacific during El Niño and La Niña events and evaluation of its potential nutrient controls: N $_2$ FIXATION IN THE ETSP. *Global Biogeochemical Cycles* 27 (3), 768–779. doi: 10.1002/gbc.20063

Deutsch, C., Sigman, D. M., Thunell, R. C., Meckler, A. N., and Haug, G. H. (2004). Isotopic constraints on glacial/interglacial changes in the oceanic nitrogen budget: GLACIAL/INTERGLACIAL NITROGEN BUDGET. *Global Biogeochemical Cycles* 18 (4). doi: 10.1029/2003GB002189

de Verneil, A., Rousselet, L., Doglioli, A. M., Petrenko, A. A., and Moutin, T. (2017). The fate of a southwest Pacific bloom: gauging the impact of submesoscale vs. mesoscale circulation on biological gradients in the subtropics. *Biogeosciences* 14 (14), 3471–3486. doi: 10.5194/bg-14-3471-2017

Dore, J. E., Brum, J. R., Tupas, L. M., and Karl, D. M. (2002). Seasonal and interannual variability in sources of nitrogen supporting export in the oligotrophic subtropical North Pacific Ocean. *Limnology Oceanography* 47 (6), 1595–1607. doi: 10.4319/lo.2002.47.6.1595

Dugdale, R. C., and Goering, J. J. (1967). Uptake of new and regenerated forms of nitrogen in primary productivity1: uptake of nitrogen in primary productivity. *Limnology Oceanography* 12 (2), 196–206. doi: 10.4319/lo.1967.12.2.0196

Dutkiewicz, S., Ward, B. A., Monteiro, F., and Follows, M. J. (2012). Interconnection of nitrogen fixers and iron in the Pacific Ocean: Theory and numerical simulations: MARINE NITROGEN FIXERS AND IRON. *Global Biogeochemical Cycles* 26 (1). doi: 10.1029/2011GB004039

Glibert, P. M., and Bronk, D. A. (1994). Release of dissolved organic nitrogen by marine diazotrophic cyanobacteria, trichodesmium spp.t. *Appl. Environ. Microbiol.* 60, 3996–4000. doi: 10.1128/aem.60.11.3996-4000.1994

Gruber, N. (2004). "The dynamics of the marine nitrogen cycle and its influence on atmospheric CO2 variations," in *The ocean carbon cycle and climate*. Eds. M. Follows and T. Oguz (Dordrecht: Springer Netherlands), 97–148. doi: 10.1007/978-1-4020-2087-2_4

Guieu, C., Bonnet, S., Petrenko, A., Menkes, C., Chavagnac, V., Desboeufs, K., et al. (2018). Iron from a submarine source impacts the productive layer of the Western Tropical South Pacific (WTSP). *Sci. Rep.* 8 (1), 9075. doi: 10.1038/s41598-018-27407-z

Hoering, T. C., and Ford, H. T. (1960). The isotope effect in the fixation of nitrogen by azotobacter. *J. Am. Chem. Soc.* 82 (2), 376–378. doi: 10.1021/ja01487a031

Jickells, T. D., An, Z. S., Andersen, K. K., Baker, A. R., Bergametti, G., Brooks, N., et al. (2005). Global iron connections between desert dust, ocean biogeochemistry, and climate. *Science* 308 (5718), 67–71. doi: 10.1126/science.1105959

Karl, D., Letelier, R., Tupas, L., Dore, J., Christian, J., and Hebel, D. (1997). The role of nitrogen fixation in biogeochemical cycling in the subtropical North Pacific Ocean. *Nature* 388 (6642), 533–538. doi: 10.1038/41474

Knapp, A. N., DiFiore, P. J., Deutsch, C., Sigman, D. M., and Lipschultz, F. (2008). Nitrate isotopic composition between Bermuda and Puerto Rico: Implications for N $_2$ fixation in the Atlantic Ocean: SARGASSO SEA NITRATE ISOTOPES. *Global Biogeochemical Cycles* 22 (3). doi: 10.1029/2007GB003107

Knapp, A. N., Casciotti, K. L., Berelson, W. M., Prokopenko, M. G., and Capone, D. G. (2016a). Low rates of nitrogen fixation in eastern tropical South Pacific surface waters. *Proc. Natl. Acad. Sci.* 113 (16), 4398–4403. doi: 10.1073/pnas.1515641113

Knapp, A. N., Fawcett, S.E., Martínez-Garcia, A., Leblond, N., Moutin, T., and Bonnet, S. (2016b). Nitrogen isotopic evidence for a shift from nitrate- to diazotroph-fueled export production in the VAHINE mesocosm experiments. *Biogeosciences* 13 (16), 4645–4657. doi: 10.5194/bg-13-4645-2016

Knapp, A. N., McCabe, K.M., Grosso, O., Leblond, N., Moutin, T., and Bonnet, S. (2018). Distribution and rates of nitrogen fixation in the western tropical South Pacific Ocean constrained by nitrogen isotope budgets. *Biogeosciences* 15 (9), 2619–2628. doi: 10.5194/bg-15-2619-2018

Knapp, A. N., Thomas, R. K., Stukel, M.R., Kelly, T.B., Landry, M.R., Selph, K.E., et al. (2021). Constraining the sources of nitrogen fueling export production in the Gulf of Mexico using nitrogen isotope budgets. *J. Plankton Res.* 44 (5), 692–710. doi: 10.1093/plankt/fbab049

Knapp, A. N., and Forrer, H. J. (2023). Water column nitrate plus nitrite d15N measurements from seawater collected in November 2019 and November 2020 in the Western Tropical South Pacific. *Biol. Chem. Oceanography Data Manage. Office (BCO-DMO)*. doi: 10.26008/1912/bco-dmo.869963.2

Kruskal, W. H., and Wallis, W. A. (1952). Use of ranks in one-criterion variance analysis. *J. Am. Stat. Assoc.* 47, 583–621. 40. doi: 10.1080/01621459.1952.10483441

Kustka, A., Saudo-Wilhelmy, S., Carpenter, E. J., Capone, D. G., and Raven, J. A. (2003). A revised estimate of the iron use efficiency of nitrogen fixation, with special reference to the marine cyanobacterium *trichodesmium* spp. (cyanophyta) [1]. *J. Phycology* 39 (1), 12–25. doi: 10.1046/j.1529-8817.2003.01156.x

Landolfi, A., Kähler, P., Koeve, W., and Oschlies, A. (2018). Global marine N2 fixation estimates: from observations to models. *Front. Microbiol.* 9, 2112. doi: 10.3389/fmicb.2018.02112

Lehmann, N., Granger, J., Kienast, M., Brown, K. S., Rafter, P. A., Martínez-Méndez, G., et al. (2018). Isotopic evidence for the evolution of subsurface nitrate in the western equatorial pacific. *J. Geophysical Research: Oceans* 123 (3), 1684–1707. doi: 10.1002/2017JC013527

Lory, C., Guieu, C., Rodier, M., Planquette, H., Gonzales Santana, D., Sarthou, G., et al. Environmental drivers of diazotrophs biogeography in the subtropical South Pacific Ocean. *Front Mar Sci* (2023). Available at: https://campagnes.flotteoceanographique.fr/campagnes/18000884/.

Luo, Y.-W., Doney, S. C., Anderson, L. A., Benavides, M., Berman-Frank, I., Bode, A., et al. (2012). Database of diazotrophs in global ocean: abundance, biomass and nitrogen fixation rates. *Earth System Sci. Data* 4 (1), 47–73. doi: 10.5194/essd-4-47-2012

Mahaffey, C. (2005). The conundrum of marine N2 fixation. *Am. J. Sci.* 305 (6–8), 546–595. doi: 10.2475/ajs.305.6-8.546

Mahowald, N. M., Baker, A. R., Bergametti, G., Brooks, N., Duce, R. A., Jickells, T. D., et al. (2005). Atmospheric global dust cycle and iron inputs to the ocean: ATMOSPHERIC IRON DEPOSITION. *Global Biogeochemical Cycles* 19 (4). doi: 10.1029/2004GB002402

Marconi, D., Sigman, D. M., Casciotti, K. L., Campbell, E. C., Alexandra Weigand, M., et al. (2017). Tropical dominance of N $_2$ fixation in the north atlantic ocean: tropical lead of atlantic N $_2$ fixation. *Global Biogeochemical Cycles* 31 (10), 1608–1623. doi: 10.1002/2016GB005613

Martin, J. H., Knauer, G. A., Karl, D. M., and Broenkow, W. W. (1987). VERTEX: carbon cycling in the northeast Pacific. *Deep Sea Res. Part A. Oceanographic Res. Papers* 34 (2), 267–285. doi: 10.1016/0198-0149(87)90086-0

McIlvin, M. R., and Casciotti, K. L. (2011). Technical updates to the bacterial method for nitrate isotopic analyses. *Analytical Chem.* 83 (5), 1850–1856. doi: 10.1021/ac1028984

Meiler, S., Britten, G. L., Dutkiewicz, S., Gradoville, M. R., Moisander, P. H., Jahn, O., et al. (2022). Constraining uncertainties of diazotroph biogeography from *nifH* gene abundance. *Limnology Oceanography* 67 (4), 816–829. doi: 10.1002/lno.12036

Minagawa, M., and Wada, E. (1986). Nitrogen isotope ratios of red tide organisms in the East China Sea: A characterization of biological nitrogen fixation. *Marine Chem.* 19 (3), 245–259. doi: 10.1016/0304-4203(86)90026-5

Moisander, P. H., Beinart, R.A., Hewson, I., White, A. E., Johnson, K. S., Carlson, C. A., et al. (2010). Unicellular cyanobacterial distributions broaden the oceanic N $_2$ fixation domain. *Science* 327 (5972), 1512–1514. doi: 10.1126/science.1185468

Moisander, P. H., Serros, T., Paerl, R. W., Beinart, R. A., and Zehr, J. P. (2014). Gammaproteobacterial diazotrophs and nifH gene expression in surface waters of the South Pacific Ocean. *ISME J.* 8 (10), 1962–1973. doi: 10.1038/ismej.2014.49

Monteiro, F. M., Dutkiewicz, S., and Follows, M. J. (2011). Biogeographical controls on the marine nitrogen fixers: CONTROLS ON MARINE NITROGEN FIXERS. *Global Biogeochemical Cycles* 25 (2). doi: 10.1029/2010GB003902

Montoya, J. P., Holl, C. M., Zehr, J. P., Hansen, A., Villareal, T. A., and Capone, D. G. (2004). High rates of N2 fixation by unicellular diazotrophs in the oligotrophic Pacific Ocean. *Nature* 430 (7003), 1027–1031. doi: 10.1038/nature02824

Moore Mills, M. M., Achterberg, E. P., Geider, R. J., LaRoche, J., Lucas, M. I., McDonagh, E. L., et al. (2009). Large-scale distribution of Atlantic nitrogen fixation controlled by iron availability. *Nat. Geosci.* 2 (12), 867–871. doi: 10.1038/ngeo667

Moutin, T., Wagener, T., Caffin, M., Fumenia, A., Gimenez, A., Baklouti, M., et al. (2018). Nutrient availability and the ultimate control of the biological carbon pump in the western tropical South Pacific Ocean. *Biogeosciences* 15, 2961–2989. doi: 10.5194/bg-2017-565

Mulholland, B., and Capone, D. (2004). Dinitrogen fixation and release of ammonium and dissolved organic nitrogen by Trichodesmium IMS101. *Aquat. Microbial Ecol.* 37, 85–94. doi: 10.3354/ame037085

Mulholland, M. R., Bernhardt, P. W., Widner, B. N., Selden, C. R., Chappell, P. D., Clayton, S., et al. (2019). High rates of N $_2$ fixation in temperate, western north atlantic coastal waters expand the realm of marine diazotrophy. *Global Biogeochemical Cycles* 33 (7), 826–840. doi: 10.1029/2018GB006130

Peters, B., Horak, R., Devol, A., Fuchsman, C., Forbes, M., Mordy, C. W., et al. (2018). Estimating fixed nitrogen loss and associated isotope effects using concentration and isotope measurements of NO3–, NO2–, and N2 from the Eastern Tropical South Pacific oxygen deficient zone. *Deep Sea Res. Part II: Topical Stud. Oceanography* 156, 121–136. doi: 10.1016/j.dsr2.2018.02.011

Raes, E. J., van de Kamp, J., Bodrossy, L., Fong, A. A., Riekenberg, J., Holmes, B. H., et al. (2020). N2 fixation and new insights into nitrification from the ice-edge to the equator in the south pacific ocean. *Front. Mar. Sci.* 7, 389. doi: 10.3389/fmars.2020.00389

Shao, Z., Xu, Y., Wang, H., Luo, W., Wang, L., Huang, Y., et al. (2023). Global oceanic diazotroph database version 2 and elevated estimate of global oceanic N2 fixation. *Earth System Science Data* 15 (8), 3673–3709. doi: 10.5194/essd-15-3673-2023

Siegel, D. A., and Deuser, W. G. (1997). Trajectories of sinking particles in the Sargasso Sea: modeling of statistical funnels above deep-ocean sediment traps. *Deep Sea Res. Part I: Oceanographic Res. Papers* 44 (9–10), 1519–1541. doi: 10.1016/S0967-0637(97)00028-9

Siegel, D. A., Fields, E., and Buesseler, K. O. (2008). A bottom-up view of the biological pump: Modeling source funnels above ocean sediment traps. *Deep Sea Res. Part I: Oceanographic Res. Papers* 55 (1), 108–127. doi: 10.1016/j.dsr.2007.10.006

Sigman, D. M., Casciotti, K. L., Andreani, M., Barford, C., Galanter, M., and Böhlke, J. K. (2001). A bacterial method for the nitrogen isotopic analysis of nitrate in seawater and freshwater. *Anal. Chem.* 73 (17), 4145–4153. doi: 10.1021/ac010088e

Smith, J. M., Chavez, F. P., and Francis, C. A. (2014). Ammonium uptake by phytoplankton regulates nitrification in the sunlit ocean. *PloS One* 9 (9), e108173. doi: 10.1371/journal.pone.0108173

Sohm, J. A., Webb, E. A., and Capone, D. G. (2011). Emerging patterns of marine nitrogen fixation. *Nat. Rev. Microbiol.* 9 (7), 499–508. doi: 10.1038/nrmicro2594

Staal, M., Meysman, F. J. R., and Stal, L. J. (2003). Temperature excludes N2-fixing heterocystous cyanobacteria in the tropical oceans. *Nature* 425 (6957), 504–507. doi: 10.1038/nature01999

Stenegren, M., Caputo, A., Berg, C., Bonnet, S., and Foster, R. A. (2018). Distribution and drivers of symbiotic and free-living diazotrophic cyanobacteria in the western tropical South Pacific. *Biogeosciences* 15 (5), 1559–1578. doi: 10.5194/bg-15-1559-2018

Talley, L. D., Pickard, G. L., Emery, W. J., and Swift, J. H. (2011). *Descriptive physical oceanography: an introduction. 6th ed* (Amsterdam ; Boston: Academic Press).

Tilliette, C., Gazeau, F., Chavagnac, V., Leblond, N., Montanes, M., Leblanc, K., et al. (2023). Temporal and spatial variability in the hydrothermal signature of sinking particles and sediments in the Western Tropical South Pacific Ocean. *ESS Open Archive*. doi: 10.22541/essoar.167898492.26733124/v1

Tilliette, C., Taillandier, V., BouruetAubertot, P., Grima, N., Maes, C., Montanes, M., et al. (2022). Dissolved iron patterns impacted by shallow hydrothermal sources along a transect through the Tonga-kermadec arc. *Global Biogeochemical Cycles* 36, e2022GB007363. doi: 10.1029/2022GB007363

Turk-Kubo, K. A., Achilles, K. M., Serros, T. R. C., Ochiai, M., Montoya, J. P., Zehr, J. P., et al. (2012). Nitrogenase (nifH) gene expression in diazotrophic cyanobacteria in the Tropical North Atlantic in response to nutrient amendments. *Front. Microbiol.* 3. doi: 10.3389/fmicb.2012.00386

Waniek, J., Koeve, W., and Prien, R. D. (2000). Trajectories of sinking particles and the catchment areas above sediment traps in the northeast Atlantic. *J. Mar. Res.* 58 (6), 983–1006. doi: 10.1357/002224000763485773

Webb, D. J. (2000). Evidence for shallow zonal jets in the south equatorial current region of the southwest pacific. *J. Phys. Oceanography* 30, 15. doi: 10.1175/1520-0485(2000)030<0706:EFSZJI>2.0.CO;2

Weber, T., and Deutsch, C. (2014). Local versus basin-scale limitation of marine nitrogen fixation. *Proc. Natl. Acad. Sci.* 111 (24), 8741–8746. doi: 10.1073/pnas.1317193111

Weigand, M. A., Foriel, J., Barnett, B., Oleynik, S., and Sigman, D. M. (2016). Updates to instrumentation and protocols for isotopic analysis of nitrate by the denitrifier method. *Rapid Commun. Mass Spectrometry* 30 (12), 1365–1383. doi: 10.1002/rcm.7570

White, A. E., Foster, R. A., Benitez-Nelson, C. R., Masqué, P., Verdeny, E., Popp, B. N., et al. (2013). Nitrogen fixation in the gulf of california and the eastern tropical north pacific. *Prog. Oceanography* 109, 1–17. doi: 10.1016/j.pocean.2012.09.002

White, A. E., Granger, J., Selden, C., Gradoville, M.R., Potts, L., Bourbonnais, A., et al. (2020). A critical review of the $^{15}N_2$ tracer method to measure diazotrophic production in pelagic ecosystems. *Limnology Oceanography: Methods* 18 (4), 129–147. doi: 10.1002/lom3.10353

Xu, H., and Weber, T. (2021). Ocean dust deposition rates constrained in a data-assimilation model of the marine aluminum cycle. *Global Biogeochemical Cycles* 35 (9). doi: 10.1029/2021GB007049

Zehr, J. P., Mellon, M. T., and Zani, S. (1998). New nitrogen-fixing microorganisms detected in oligotrophic oceans by amplification of nitrogenase (nifH) genes. *Appl. Environ. Microbiol.* 64 (9), 3444–3450. doi: 10.1128/AEM.64.9.3444-3450.1998

Zehr, J. P., and Turner, (2001) *Nitrogen fixation: Nitrogenase genes and gene expression - ScienceDirect*. Available at: https://www.sciencedirect.com/science/article/abs/pii/S0580951701300491?via%3Dihub (Accessed 14 February 2023).

frontiers | Frontiers in Marine Science

TYPE Original Research
PUBLISHED 30 January 2024
DOI 10.3389/fmars.2023.1290625

OPEN ACCESS

EDITED BY
Hiroaki Saito,
The University of Tokyo, Japan

REVIEWED BY
Fuminori Hashihama,
Tokyo University of Marine Science and Technology, Japan
Wokil Bam,
Woods Hole Oceanographic Institution, United States

*CORRESPONDENCE
Sophie Bonnet
sophie.bonnet@mio.osupytheas.fr
Frédéric A. C. Le Moigne
flemoigne1@univ-brest.fr

RECEIVED 07 September 2023
ACCEPTED 26 December 2023
PUBLISHED 30 January 2024

CITATION
Ababou F-E, Le Moigne FAC, Cornet-Barthaux V, Taillandier V and Bonnet S (2024) Composition of the sinking particle flux in a hot spot of dinitrogen fixation revealed through polyacrylamide gel traps.
Front. Mar. Sci. 10:1290625.
doi: 10.3389/fmars.2023.1290625

Composition of the sinking particle flux in a hot spot of dinitrogen fixation revealed through polyacrylamide gel traps

Fatima-Ezzahra Ababou[1], Frédéric A. C. Le Moigne[1,2*], Véronique Cornet-Barthaux[1], Vincent Taillandier[3] and Sophie Bonnet[1*]

[1]Aix Marseille University, Université de Toulon, Centre National de Recherche Scientifique (CNRS), Institut de Recherche pour le Développement (IRD), MIO Marseille, France, [2]Centre National de Recherche Scientifique (CNRS), Univ Brest, Institut de Recherche pour le Développement (IRD), Institut Français de Recherche pour l'Exploitation de la mer (Ifremer), UMR 6539, Laboratoire des sciences de l'Environnement Marin (LEMAR), Plouzané, France, [3]Laboratoire d'Océanographie de Villefranche (LOV), Centre National de Recherche Scientifique (CNRS), Sorbonne Université, Villefranche-sur-Mer, France

Diazotrophs regulate marine productivity in the oligotrophic ocean by alleviating nitrogen limitation, contributing to particulate organic carbon (POC) export to the deep ocean. Yet, the characterization of particles composing the sinking POC flux has never been explored in such ecosystems. Moreover, the contribution of the direct gravitational export of diazotrophs to the overall flux is seldom assessed. Here we explore the composition of the sinking POC flux in a hot spot of N_2 fixation (the western sub-tropical South Pacific) using polyacrylamide gel-filled traps deployed at two stations (S05M and S10M) and three depths (170 m, 270 m, 1000 m) during the TONGA expedition (November-December 2019). Image analyses of particles collected in the gels was used to classify them into 5 categories (fecal aggregates, phytodetrital aggregates, mixed aggregates, cylindrical fecal pellets, and zooplankton carcasses). Fecal aggregates were the most abundant at both stations and all depths and dominated the flux (average of 56 $\pm$ 28% of the POC flux), followed by zooplankton carcasses (24 $\pm$ 19%), cylindrical fecal pellets (15 $\pm$ 14%) and mixed aggregates (5 $\pm$ 4%), whereas phytodetrital aggregates contributed less (<1%). Since N isotope budgets show that export is mainly supported by diazotrophy at these stations, these results suggest that the diazotroph-derived N has been efficiently transferred to the foodweb up to zooplankton and fecal pellets before being exported, pleading for an indirect export of diazotrophy. However, random confocal microscopy examination performed on sinking particles revealed that diazotrophs were present in several categories of exported particles, suggesting that diazotrophs are also directly exported, with a potential contribution to overall POC fluxes increasing with depth. Our results provide the first characterization of particle categories composing the sinking flux and their contribution to the overall flux in a hot spot of N_2 fixation.

KEYWORDS

biological carbon pump, carbon export, export efficiency, transfer efficiency, diazotrophs

Introduction

The oceans play a critical role in regulating atmospheric CO_2 concentrations by sequestering a fraction of the photosynthetically fixed carbon [called primary production (PP)] to the deep ocean over geological time scales (Eppley and Peterson, 1979). Long-term sequestration of this PP requires the organic matter to be exported to the deep ocean through a myriad of processes collectively referred to as the biological carbon pump (BCP) (Eppley and Peterson, 1979). The global range of organic carbon export is very large and estimated at 5–21 Gt C yr^{-1} (Laws et al., 2000; Henson et al., 2011; Siegel et al., 2014; Wang et al., 2023). The pathways for carbon export from the surface to the deep ocean by the BCP are multiple (Boyd et al., 2019; Le Moigne, 2019). They mainly include the biological gravitational pump (BGP), that exports aggregated organic matter out of the euphotic zone (~0-100 m) via sinking marine snow (Burd and Jackson, 2009; Boyd et al., 2019; Le Moigne, 2019; Iversen, 2023), and the particle injection pumps (Omand et al., 2015; Dall'Olmo et al., 2016; Boyd et al., 2019) recently defined by Boyd et al. (2019). The latters can be separated into three physical subduction pumps (Levy et al., 2013; Omand et al., 2015; Dall'Olmo et al., 2016; Stukel et al., 2017) including: (1) the mixed-layer pump (shallow export ~10 m and short-term sequestration), (2) the eddy-subduction pump (~100 km export and hundreds of years scales) and (3) the large-scale subduction pump (1,000 km and 1,000 years scales). Besides, two pumps associated with zooplankton migration (Bianchi et al., 2013; Steinberg and Landry, 2017) are at work, with organisms feeding at night in surface waters and defecating deeper into the mesopelagic zone during the day, termed the migration pump (Stukel et al., 2017; Aumont et al., 2018), and zooplankton hibernation at depth during winter at high latitudes, termed the seasonal lipid pump (Steinberg et al., 2008; Jónasdóttir et al., 2015; Steinberg and Landry, 2017; Iversen, 2023). Finally, the fraction of particulate organic carbon (POC) flux exported out of the euphotic zone relative to PP, referred to as the export efficiency (Buesseler et al., 1992), and the fraction of the exported POC flux relative to the deep (>1000 m) POC flux, referred to as the transfer efficiency (Francois et al., 2002), are both widely used to determine the strength of the BGP. The export efficiency depends on the sinking velocity of particles and their remineralization rate (De La Rocha and Passow, 2007; Bach et al., 2019), as well as on the lateral advection and the time lag between PP and organic matter export (Stange et al., 2017; Laws and Maiti, 2019). The export efficiency is generally high in polar waters (0.1-1.3) (Le Moigne et al., 2015) compared to temperate (0.05-0.65) (Buesseler et al., 1998; Haskell II et al., 2017) and (sub)-tropical oligotrophic waters (0.01-0.2) (Quay et al., 2010; Henson et al., 2012; Maiti et al., 2016; Buesseler et al., 2020; Karl et al., 2021). In fact, in Low Nutrient Low Chlorophyll (LNLC) ecosystems, the export efficiency is deemed to be weak because of low nutrient inputs and high recycling processes in the surface pelagic food web (Buesseler et al., 2008; Buesseler and Boyd, 2009). Therefore, these ecosystems have received less attention than mid/high latitudes ones with respect to the BGP, although they account for ~60% of the global ocean surface.

In these vast LNLC ecosystems, atmospheric dinitrogen (N_2) fixing organisms, called diazotrophs, provide new bioavailable N to non-diazotrophic organisms, support >50% of new PP (Berthelot et al., 2015; Bonnet et al., 2015; Bonnet et al., 2016b; Caffin et al., 2018b), and the export of organic matter through the N_2-primed prokaryotic carbon pump (Karl et al., 2003). Geochemical $\partial^{15}N$ budgets reported that N_2 fixation contributes to ~25-50% of export production in the subtropical North Pacific (ALOHA, Hawaii) (Karl et al., 1998; Böttjer et al., 2017), ~10% in the subtropical North Atlantic (BATS) (Knapp et al., 2005), and 50-80% in the subtropical South Pacific (Knapp et al., 2018; Bonnet et al., 2023b). N_2 fixation is now recognized to indirectly support the BGP through the use of the diazotrophic-derived N (DDN) by non-diazotrophic plankton that get finally exported (Berthelot et al., 2016; Bonnet et al., 2016b; Caffin et al., 2018b). Alternatively, diazotrophs can also be directly exported down to >1000 m (Agusti et al., 2015; Pabortsava et al., 2017; Caffin et al., 2018a; Poff et al., 2021; Benavides et al., 2022) and account for a significant part of the export flux (Bonnet et al., 2023a). The mechanisms involved in the gravitational export of diazotrophs has recently been experimentally investigated by Ababou et al. (2023) who showed that both filamentous and unicellular diazotrophs sink at velocities of ~100 to 400 meters per day through the formation of large (7,000–32,014 µm) aggregates. However, these studies are still at their infancy, and the role of diazotrophs in the BGP, in particular the relative contribution of the direct export of diazotrophs versus the indirect export pathways after transfer of the DDN to the food web, remains to be elucidated. Therefore, determining the composition of the sinking flux and the contribution of different particle types (including diazotrophs) to the overall flux is crucial to understand the underlying mechanisms that control the magnitude and efficiency of the BCP in these LNLC ecosystems.

Sinking particles are heterogenous. Capturing their diversity and determining who constitute and drive the flux in a given region is therefore challenging. Sediment traps allow to collect particles and to assess the relationship between PP, particle export and attenuation in the mesopelagic zone (Buesseler and Boyd, 2009; Baker et al., 2020; Baumas and Bizic, 2023). Polyacrylamide gels mounted on sediment traps enable the composition of the sinking flux to be estimated by collecting and preserving and preservation of their morphological characteristics during deposition in the gel (Jannasch et al., 1980; Lundsgaard, 1995; Waite et al., 2000). Studies in different regions have found either fecal pellets (Wassmann et al., 2000; Turner, 2002; Ebersbach and Trull, 2008; Laurenceau-Cornec et al., 2015; Durkin et al., 2021) or large organic aggregates (Alldredge and Gotschalk, 1988; De La Rocha and Passow, 2007; Burd and Jackson, 2009) to be the main drivers of the particle flux. However, this kind of gel traps have repeatedly been deployed in temperate and polar regions, but have never been used to assess the sinking flux in LNLC ecosystems in which primary, secondary and export productions are primarily supported by N_2 fixation.

Here we deployed gel traps in the western subtropical South Pacific (WTSP), a LNLC ecosystem recognized as a hot spot of N_2 fixation activity, with an estimated contribution of ~21% to 40% to the global fixed N input and average fluxes >600 µmol N m^{-2} d^{-1} (Bonnet et al., 2017; Shao et al., 2023). This hot spot has been attributed, among other factors, to the Fe fertilization by shallow hydrothermal sources along the Tonga-Kermadec arc (Bonnet et al., 2023b), resulting in dissolved Fe concentrations up to ~10 nmol L^{-1}

in the euphotic layer (Tilliette et al., 2022). Here we used a gel traps approach to characterize the composition of the sinking flux and estimate the contribution of each particle category to the overall POC fluxes inside of this hot spot of N_2 fixation. We also explored the interior of sinking particles using confocal microscopy to detect the possible presence of diazotrophs and evaluate their potential contribution to the overall POC flux.

Material and methods

Sinking particle collection

Samples were collected during TONGA expedition (GEOTRACES GPpr14, https://doi.org/10.17600/18000884) onboard the R/V L'Atalante from November 1st to December 5th of 2019 (beginning of austral summer) in the WTSP (Figure 1). A surface-tethered mooring line (~1000 m) equipped with sediment traps was deployed at 2 stations: S05M (21.157°S; 175.153°W) and S10M (19.423°S; 175.133°W) (Figure 1) for 5 and 3.8 days respectively and at 3 depths: 170 m (below the base of the euphotic layer), 270 m and 1000 m. Each trap was made up of four particle interceptor tubes (PITs) of a collecting area of 0.0085 m^2 (aspect ratio of 6.7) that were attached to a cross frame (KC Denmark®). At each depth, tubes were dedicated to either optical (gel traps), biogeochemical, microbiological or molecular analyses (Benavides et al., 2022; Bonnet et al., 2023a). In this study, the optical tubes containing polyacrylamide gels were used to collect intact sinking particles: gels provide a slow deceleration of particles, isolate them in their original forms and therefore provide a direct 'picture' of the sinking flux (Ebersbach and Trull, 2008). The biogeochemical tubes were used to measure bulk carbon fluxes, and the microbiological tubes were used to visualize phycoerythrin-containing organisms by confocal microscopy (see details below).

Polyacrylamide gels were prepared as described in Ebersbach and Trull (2008) and Laurenceau-Cornec et al. (2015) and poured into a transparent cups. Prior to deployments of the mooring line, polyacrylamide gel cups were fixed to the bottom of the tube. Brine (salinity of ~50 g L^{-1}) with formalin (2%) was carefully added to the surface of the gel to decelerate the sinking velocity of particles and prevent them from breaking on contact with the gel. The tube was then entirely filled with 0.2 µm filtered seawater. Immediately after recovery of the mooring line, the seawater covering the gels was removed using a peristaltic pump and the gel cups were recovered, carefully covered with parafilm and stored at 4°C until laboratory optical analysis back in the laboratory.

For the biogeochemical tube, the density gradient was visually inspected immediately after removal of the mooring line. The tubes were stabilized for two hours before the supernatant seawater was gently removed using a peristaltic pump. The sinking material in the remaining water was transferred to a hydrochloric acid-washed container, while being sieved with a 500 µm mesh to remove zooplankton that actively entered the traps (swimmers). After homogenization with a magnetic stir bar, a triplicate set of aliquots were filtered onto 25-mm diameter combusted (4h, 450° C) glass microfiber filters (Whatman GF/F), dried for 24 h at 60°C, pelleted and analyzed for POC and PON by EA-IRMS (Elemental Analyzer-Isotope Ratio Mass Spectrometry) using an Integra 2 (Sercon) mass spectrometer (Bonnet et al., 2018).

Polyacrylamide gel imaging

Polyacrylamide gels were visualized under a binocular magnifier and imaged using a Leica 165C camera (Figure 2). Particles were lit by placing a cold light illuminated plate below the gel cups, then images were captured at a 6.5 magnification to visualize particles. The whole gel cup surface area was imaged

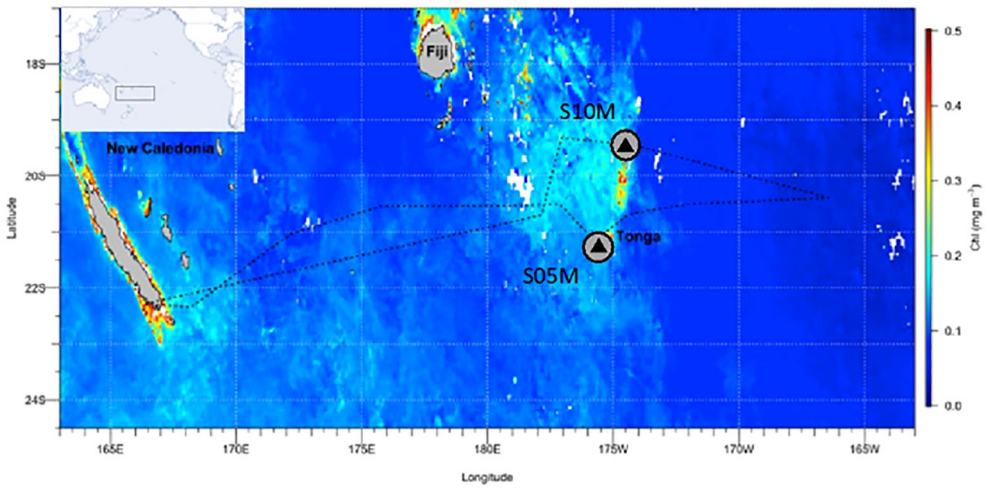

FIGURE 1
|Transect of the TONGA GPpr14 cruise. Satellite-derived surface chlorophyll *a* concentrations during the cruise (1 November-5 December 2019) (MODIS Aqua, 4 km, 8-days composite, level 3 product). Black triangles correspond to stations where surface-tethered sediment traps were deployed (170 m, 270 m, 1000 m).

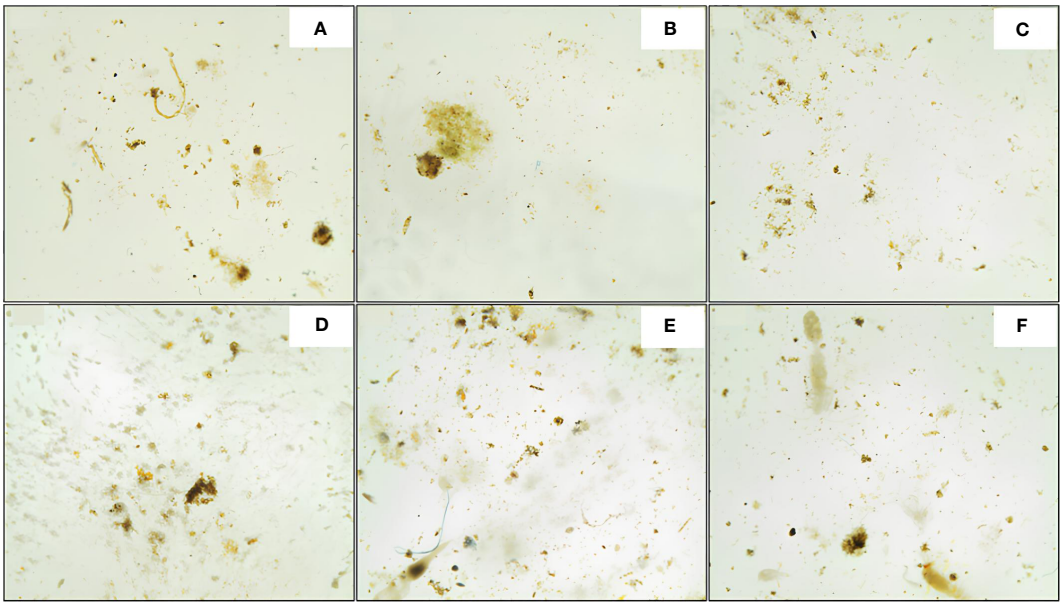

FIGURE 2
Images of sinking particles embedded in polyacrylamide gels, collected at station S05M at 170 m **(A)**, 270 m **(B)** and 1000 m **(C)**, and station S10M **(D–F)** at the same depths respectively. Image analysis of particles collected at 170 m at S10M was not possible due to the damaged aspect of the gel, this depth was thus excluded from this study.

following horizontal transects. Approximately 24 to 26 images in a single focal plan were obtained for each gel at each depth. Images of incomplete grid cells were removed from the analysis to avoid bias. The average surface analyzed per gel was 0.0035 ± 0.0004 m^2, corresponding to 41 ± 5% of the gel collection area (0.0085 m^2). Images were analyzed using the FIJI software (the US National Institutes of Health's free software ImageJ) (Schindelin et al., 2015) that allows the measurement of particles shape descriptors (area, angle, circularity, perimeter, fit ellipse and aspect ratio among others). In each processed image, the particles were delineated and numbered, and then individually identified according to their typical shapes and colors, thus indicating the category where they will be classified. Particles were classified into five categories: fecal aggregates (hereafter FA), phytodetrital aggregates (hereafter PA), mixed aggregates (hereafter Mix, which are aggregates containing both PA and FA or FA and zooplankton carcasses), cylindrical fecal pellets (hereafter CFP) and zooplankton carcasses (hereafter zoo carcasses). Routine one-to-one particle identification was applied on 125 images in total.

With the sinking particle projected areas obtained with FIJI, we first identified their size spectra and then their number and volume flux spectra. Finally, we estimated the number, volume and carbon fluxes associated with each particle category (described below).

Particles shape descriptors

The projected areas of sinking particles provided by FIJI (Figure 3) enabled to calculate their Equivalent Spherical Diameter (ESD) by assuming spheres (Equation 1).

$$ESD = \frac{2\sqrt{projected\ \ area}}{\pi} \quad (1)$$

Where the projected area is the surface area occupied by a particle in mm^2.

The ESD allowed to determine the size spectra of the sinking particles by binning them into 9 logarithmically spaced size classes (Table 1) (Laurenceau-Cornec et al., 2015) that cover the whole size range of particles detected in our gels (0.1-1.7 mm). All particle shape descriptors and fluxes considered in this study and their units are reported in Table 1. A cut-off of particles with projected areas<0.009 mm^2 (equivalent to 0.1 mm ESD) was applied to exclude small and spurious particles arising from gel imperfections, and to avoid misidentification as their size did not allow to identify them correctly. This cut-off removed hundreds of particles at both stations but represents an average loss of 25 ± 5% of the total projected area of particles at S05M and 25 ± 0.2% at S10M.

Particle number ($m^{-2}\ d^{-1}\ mm^{-1}$) (Equation 2) (Figure 4, left) and volume flux spectra ($mm^3\ m^{-2}\ d^{-1}\ mm^{-1}$) (Equation 3) (Figure 4, right) allowed to determine the abundance of particles and their corresponding volumes in each size class. The particle number flux spectra was calculated as follows:

$$Particle\ \ number\ \ flux\ \ spectra = \frac{\frac{\sum particle\ \ number}{surface\ \ area}}{\frac{trap\ \ deployment\ \ duration}{size\ \ of\ \ the\ \ size\ \ class}} \quad (2)$$

Where Σparticle number is the sum of particles within a size class, the surface area is the total imaged surface area of the gel in m^2, the trap deployment duration in days (5 for S05M and 3.8 for S10M) and the size of the size class is the difference between upper and lower limits ESD in mm.

10.3389/fmars.2023.1290625

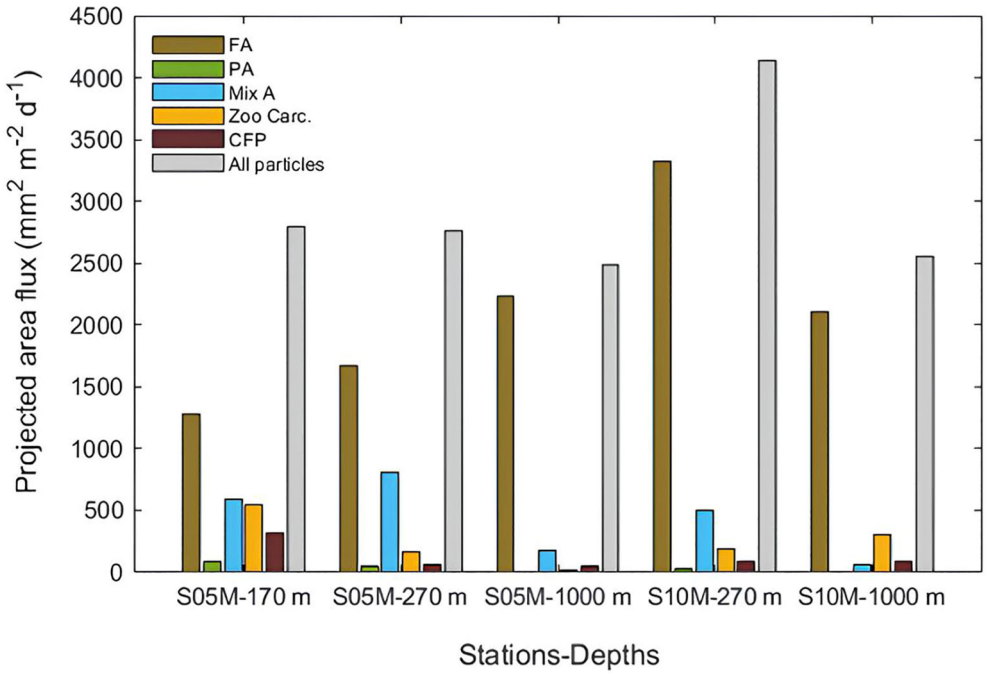

FIGURE 3
Projected area flux of sinking particles reconstructed from image analysis at each station and depth (mm^2 m^{-2} d^{-1}). FA, fecal aggregates; PA, phytodetrital aggregates; Mix A, mixed aggregates; CFP, cylindrical fecal pellets; Zoo Carc., zooplankton carcasses.

TABLE 1 Units and definitions of particle shape descriptors and calculated fluxes (upper table), and size classes (ESD, mm) (lower table) of particle categories: phytodetrital aggregates, fecal aggregates, mixed aggregates, cylindrical fecal pellets and zooplankton carcasses.

Shape descriptors and fluxes	Unit	Description
Projected area	mm^2	Surface area occupied by a particle
Volume	mm^3	Volume of a theoretical spherical particle calculated from its projected area
Equivalent spherical diameter (ESD)	mm	Diameter of a theoretical spherical particle calculated from its projected area
Number flux	m^{-2} d^{-1}	Number flux of sinking particles
Volume flux	mm^3 m^{-2} d^{-1}	Volume flux of sinking particles
Carbon flux	mg C m^{-2} d^{-1}	Organic carbon flux by sinking particles
Number flux spectrum	m^{-2} d^{-1} mm^{-1}	Number flux per unit ESD size interval
Volume flux spectrum	mm^3 m^{-2} d^{-1} mm^{-1}	Volume flux per unit ESD size interval
Number, volume and carbon fractional contributions	%	Proportion of number, volume and carbon fluxes of particle categories as a percentage of total

Size classes	**1**	**2**	**3**	**4**	**5**	**6**	**7**	**8**	**9**
Lower Limit	0.102	0.145	0.207	0.296	0.422	0.603	0.86	1.228	1.752
Upper Limit	0.145	0.207	0.296	0.422	0.603	0.86	1.228	1.752	–
Center	0.124	0.176	0.252	0.359	0.513	0.732	1.044	1.49	–

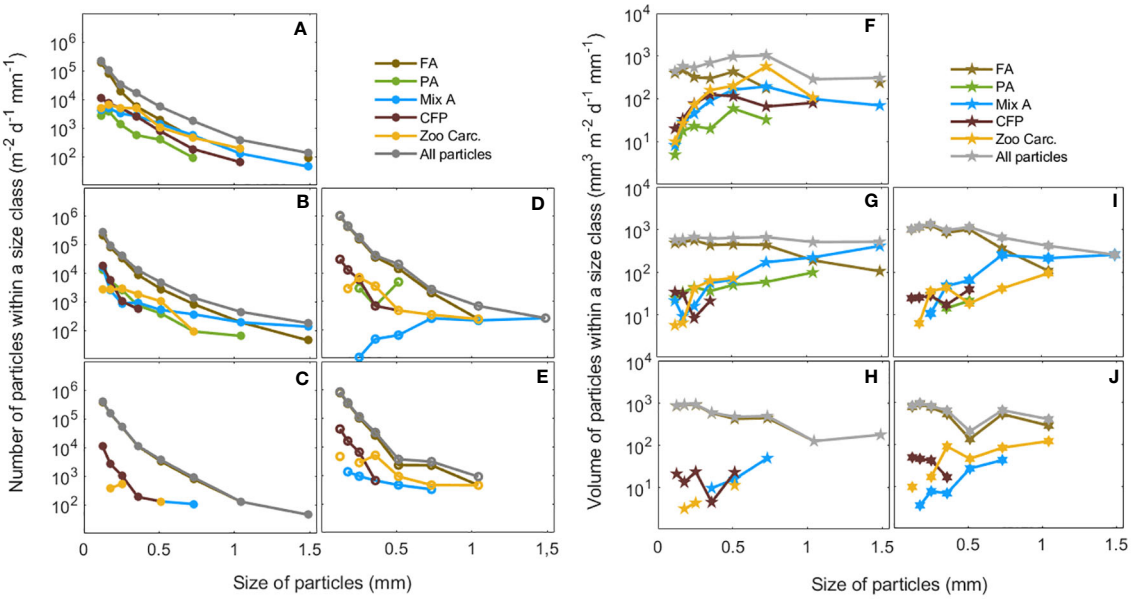

FIGURE 4
Total number (m^{-2} d^{-1} mm^{-1}) and volume fluxes (mm^3 m^{-2} d^{-1} mm^{-1}) of particles binned in 9 size classes (Table 1). Number flux spectra are shown at **(A)** S05M-170 m, **(B)** S05M-270 m, **(C)** S05M-1000 m, **(D)** S10M-270 m, **(E)** S10M-1000 m, and volume flux spectra at **(F)** S05M-170 m, **(G)** S05M-270 m, **(H)** S05M-1000 m, **(I)** S10M-270 m, **(J)** S10M-1000 m, for each category of particles FA, fecal aggregates; PA, phytodetrital aggregates; Mix A, mixed aggregates; CFP, cylindrical fecal pellets; Zoo Carc., zooplankton carcasses.

The volume flux spectra (mm^3 m^{-2} d^{-1} mm^{-1}) was calculated as for the number flux spectra as follows:

$$Particle\ \ volume\ \ flux\ \ spectra = \frac{\frac{\sum particle\ \ volume}{surface\ \ area}}{\frac{trap\ \ deployment\ \ duration}{size\ \ of\ \ the\ \ size\ \ class}} \quad (3)$$

Where ∑particle volume is the sum of volumes within a size class in mm^3, the surface area is the total imaged surface area of the gel in m^2, the trap deployment duration in days (5 for S05M and 3.8 for S10M) and the size of the size class is the difference between upper and lower limits ESD in mm.

Estimation of particle carbon fluxes in the polyacrylamide gel traps

The particles projected areas were first converted into volumes according to geometric assumptions as in Ebersbach and Trull (2008) and Laurenceau-Cornec et al. (2015). Fecal and phytodetrital aggregates were considered spherical, mixed aggregates, zooplankton carcasses as ellipsoids and cylindrical fecal pellets as cylinders. Volumes were then converted to carbon content by using relationships provided in the literature for each particle type (Equation 4): carbon content of fecal aggregates was obtained using fecal marine snow power relationship (Alldredge, 1998):

$$POC\ (\mu g) = 1.05 \times V\ (mm^3)^{0.51} \quad (4)$$

Where POC is the carbon content of fecal aggregates in µg and V is their corresponding volumes in mm^3.

POC content of phytodetrital aggregates was obtained using diatom marine snow relationship (Equation 5) (Alldredge, 1998):

$$POC\ (\mu g) = 0.97 \times V(mm^3)^{0.56} \quad (5)$$

Where POC is the carbon content of phytodetrital aggregates in µg and V is their corresponding volumes in mm^3.

Carbon content of cylindrical fecal pellets was obtained from their volumes using a value of 0.057 mg C mm^{-3} (Gonzalez and Smetacek, 1994). For zooplankton carcasses, we first estimated their dry weight using the correlation (r^2 = 0.967) of subtropical copepods with a size range of body area of 0.1-8.3 mm^2 (Lehette and Hernández-León, 2009) (Equation 6), as follows:

$$dry\ \ weight\ (\mu g) = 45.25 \times projected\ \ area^{1.59} \quad (6)$$

Where projected area is the surface area occupied by the zooplankton carcasses in mm^2.

Then, carbon content of zooplankton carcasses was thus calculated as 45% of the estimated dry weight (Billones et al., 1999). Only identifiable particles and zooplankton carcasses were considered in estimates of POC flux. Unidentified particles and healthy-looking swimmers accidentally caught in the gel (not carcasses) were excluded from the data set. All relationships used in volume and POC conversions are listed in Table 2.

Number, (Figure 4, left), volume (Figure 4, right) and carbon fluxes (Figure 5) of particles were estimated at each station and depth by dividing their respective total counted particles number, volume (mm^3) or carbon (mg) by the analyzed surface area of the gel (m^2) and the trap collection duration (days). Contributions of each particle category in number, volume and carbon fluxes were calculated as a percentage of a total and are presented in Table 3.

TABLE 2 Relationships used to estimate volumes and carbon contents of sinking particles according to their shapes. Lengths and widths used corresponds to major and minor lengths provided by FIJI.

Cat.	Shapes	Volumes (mm^3)	POC (µg)	Reference
FA	Spherical	$\frac{4}{3} \times \pi \times \left(\frac{ESD}{2}\right)^3$	$1.05 \times V(mm^3)^{0.51}$	(Laurenceau-Cornec et al., 2015)
PA	Spherical	$\frac{4}{3} \times \pi \times \left(\frac{ESD}{2}\right)^3$	$0.97 \times V(mm^3)^{0.56}$	(Laurenceau-Cornec et al., 2015)
Mixed A	Ellipsoid	$\frac{4}{3} \times \pi \times \left(\frac{length}{2}\right) \times \left(\frac{width}{2}\right)^2$	$0.99 \times V(mm^3)^{0.52}$	(Ebersbach and Trull, 2008)
CFP	Cylindrical	$length \times \pi \times \left(\frac{width}{2}\right)^2$	$0.057\ mg\ C\ mm^{-3}$	(Ebersbach and Trull, 2008)
Zoo carcasses	Ellipsoid	$\frac{4}{3} \times \pi \times \left(\frac{length}{2}\right) \times \left(\frac{width}{2}\right)^2$	$45\ \% \times (45.25 \times projected\ area^{1.59}$	(Billones et al., 1999; Lehette and Hernández-León, 2009; Dai et al., 2016)

Evaluation of the presence of diazotrophs within aggregates

The presence of diazotrophs within the sinking aggregates was evaluated at only one station (S05M) as both stations were quite similar in composition and because such method is time consuming. For that, the interior of the aggregates collected in tubes dedicated to microbiological analyses was visualized using confocal microscopy. 250 mL of the traps material were filtered onboard onto 0.8 µm polycarbonate filters and fixed with 4% paraformaldehyde. Filters obtained were then carefully inverted onto clean transparent glass slides and freezed using a cooling spray to instantly transfer all the traps material from the filter to the glass slide. The filter was then carefully removed and inspected to ensure that no particles remained after transfer. Without covering the slides to avoid flattening the aggregates, they were directly placed under the microscope and visualized at a x10 magnification using the microscope lasers. The visualized aggregates here were from several categories, i.e. either fecal, mixed or phytodetrical aggregates and we were not able to clearly discriminate them with this method. Organic matter was visualized with ultraviolet (UV, wavelength= 405 nm) and phycoerythrin was used as a relative indictor of cyanobacterial diazotrophs as *Trichodesmium* spp., unicellular diazotrophic cyanobacteria from Group B (UCYN-B) and C (UCYN-C) and endosymbiotic nitrogen fixers possess this accessory pigment (Grabowski et al., 2008; White et al., 2018; Bonnet et al., 2023a) (phycoerythrin, wavelength= 455 nm), while UCYN-A do not (Zehr et al., 2008). Twelve focal plans with evenly distributed aggregates were randomly selected from each depth. Before starting the imaging, parameters (slices thickness, pinhole diameter, gain and contrasts) of the images were set using the microscope software. The two lasers used enabled the excitation of the aggregates organic matter in blue color and the phycoerythrin pigments in red/pink color. An average of 15 images (slices) with a thickness of 5.9 µm per focal plan

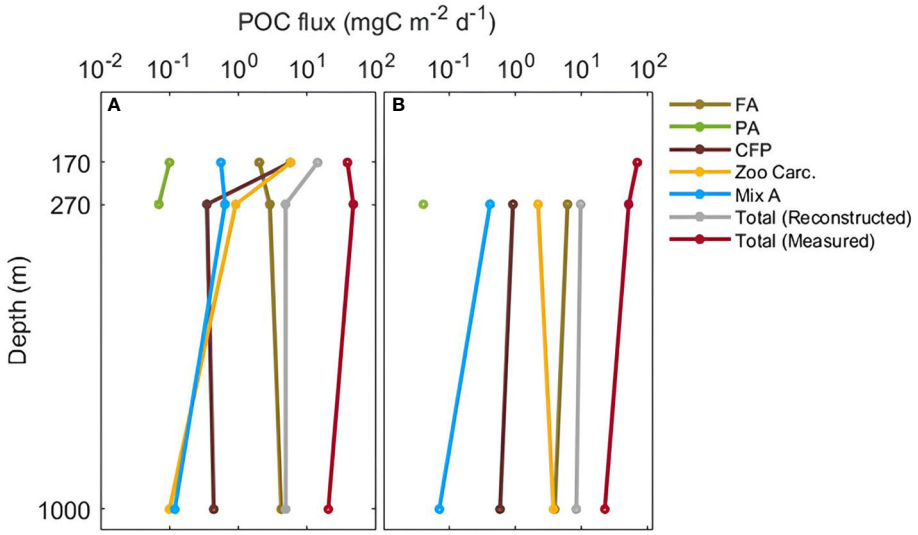

FIGURE 5
Reconstructed POC fluxes of FA= fecal aggregates, PA= phytodetrital aggregates, Mix A= mixed aggregates, CFP= cylindrical fecal pellets, and Zoo Carc.= zooplankton carcasses, total reconstructed and measured POC fluxes at 170 m, 270 m and 1000 m. POC fluxes are presented in mg C m^{-2} d^{-1} at S05M **(A)** and S10M **(B)**.

10.3389/fmars.2023.1290625

TABLE 3 Number, volume and POC fluxes reconstructed from polyacrylamide gel traps with fractional contributions of each category of particle.

Site	Depth (m)	Number flux (m^{-2} d^{-1}) Total	Fractional contributions (%)					Volume flux (mm^3 m^{-2} d^{-1})	Fractional contributions (%)					POC flux (mg C m^{-2} d^{-1})	Fractional contributions (%)				
			FA	PA	MIX	CFP	Z	Total	FA	PA	MIX	CFP	Z	Total	FA	PA	MIX	CFP	Z
S05M	170	48,513	72.2	2.8	7.2	8.6	9.2	917	45	3	25	11	17	**14.14**	14	1	4	40	41
	270	53,000	82.1	2.2	6.1	5.6	4.1	**1108**	42	2	53	1	3	4.84	59	1	13	7	19
	1000	**76,368**	96.7	0	7.4	2	0.6	592	80	0	18	1	0.5	4.86	86	0	2.5	9	2
S10M	270	**105,532**	94.7	0.4	0.9	2.7	1.3	**1104**	65	1	26	1	7	**9.63**	74	0.5	5	11	10
	1000	75,107	92.6	0	0.6	4.7	2.1	597	82	0	3	2	14	8.28	47	0	1	7	45

Maximum fluxes are indicated in bold. FA, fecal aggregates; PA, phytodetrital aggregates; MIX, mixed aggregates; CFP, cylindrical fecal pellets; Z, zooplankton carcasses.

(Figure 6) was needed to explore the aggregate's interior (total of 180 images per depth at S05M). The high resolution of images allowed the reconstruction of the aggregates (Figure 6) and the quantification of the phycoerythrin proportion area in these aggregates (Table 4). With many marine diazotrophs being cyanobacteria (although not all cyanobacteria are diazotrophs), phycoerythrin was used as a relative indicator of the cyanobacterial diazotrophs in the sinking material. Two potential pitfalls of this method are that 1/other (non-diazotrophic) cyanobacteria, notably *Synechococcus* spp., also contain phycoerythrin. However, the morphology of *Synechococcus* and cyanobacterial diazotrophs is very different: *Synechococcus* spp. are picoplantonic in size (~1 µm), while *Trichodesmium* spp. are long filaments or colonies (>100 µm), and unicellular diazotrophs (UCYN) are spherical/ovoid (5-8 µm). According to our observations in the exported material, *Synechococcus* spp. were in the minority compared with diazotrophs. Moreover, because of their small size, their carbon content is 10-100 times lower than that of diazotrophs. We therefore considered the phycoerythrin zones reported below to be a relative indicator of diazotrophs, but the results reported below may be slightly overestimated. 2/UCYN-A do not contain pigments and cannot be visualized with this method, which may on the opposite underestimate the contribution of cyanobacterial diazotrophs to export. This method was compared in the discussion to another method based on quantitative PCR.

Estimation of the contribution of diazotrophs to the sinking flux

The confocal images were analyzed using FIJI (Figure 6). First, each group of focal images (slices) was combined to be analyzed as a stack. Then, the contrast of the images stack was adjusted for a better visualization of the aggregates before selecting and measuring each fluorescent area separately (blue for organic matter and red/pink for phycoerythrin-containing organisms) using the color threshold function of FIJI.

Total projected areas of each fluorescence were obtained. This allowed to measure the proportion of phycoerythrin-containing organisms in the sinking material over the total fluorescent projected area (blue+pink) as follows (Table 4) (Equation 7):

$$phyco.\ area\ proportion = \frac{total\ phyco.\ area}{total\ fluorescent\ area} \times 100 \quad (7)$$

where phycoerythrin area proportion is the area mostly occupied by cyanobacteria (essentially attributed to cyanobacterial diazotrophs, see above) over the total fluorescent area in percentage (%).The diazotroph projected area fluxes were obtained by summing the projected areas of diazotrophs in all slices of the twelve images analyzed and by converting them into fluxes in mm^2 m^{-2} d^{-1}.

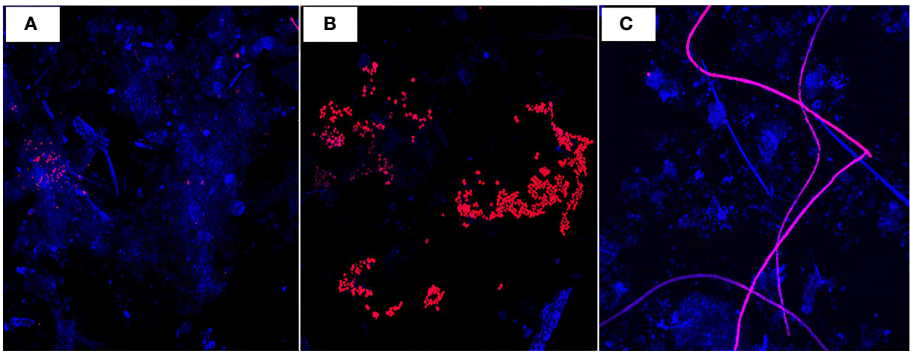

FIGURE 6
Confocal microscopy images of random aggregates (blue, wavelength= 405 nm) (S05M) with diazotrophs and phycoeryhtrin-containing organisms (pink/red, wavelength= 555 nm) visualized at x10 magnification, at 170 m **(A)**, 270 m **(B)** showing UCYN-like aggregates and 1000 m **(C)** showing *Trichodesmium* filaments.

10.3389/fmars.2023.1290625

TABLE 4 Diazotroph projected area and specific reconstructed POC fluxes at S05M.

Depth (m)	Total Projected area flux[a]	Diazotroph projected area flux[b]	Diazotroph proportion in the total area flux[c]	Total Measured POC flux[d]	Diazotroph POC flux[e]	Diazotroph Contribution to the POC flux[f]
170	2800	373.4	13.3	38.3	2.6	6.7
270	2761.4	1440.9	52.2	46.6	15.7	33.7
1000	2484.2	1111.1	44.7	20.2	10.4	51.4

[a]total projected area flux obtained using gel image analysis in $mm^2\ m^{-2}\ d^{-1}$ (see material methods section).
[b]projected area occupied by diazotrophs in $mm^2\ m^{-2}\ d^{-1}$.
[c]proportion of diazotroph area flux from the total area flux in percentage (%).
[d]total POC flux measured using the biogeochemical tubes in mg C $m^{-2}\ d^{-1}$.
[e]POC flux of diazotrophs in mg C $m^{-2}\ d^{-1}$.
[f]proportion of diazotroph POC flux from the total POC flux in percentage (%).

The contribution of diazotrophs to the POC flux was roughly estimated by calculating the volumes (μm^3) from their projected areas (mm^2) assuming spheres by using the ESD (Eq. 1) cited above. Further, we estimated the POC content (pg) of diazotrophs by plotting the volumes and carbon contents provided in Goebel et al. (2008) and Luo et al. (2012) and those measured in Dron et al. (2012) (Supplementary Table, Supplementary Figure 1).

Surface chlorophyll and primary production

Surface Chlorophyll a concentrations were assessed by satellite (MODIS Aqua, 4 442 km, 8-days composite, level 3 product) (http://oceancolor.gsfc.nasa.gov). Primary production was measured in triplicates at the locations of the traps deployments (S05M and S10M) as described in Lory et al. (In prep.).

Results

Sinking particle characteristics and statistics

Figure 2 shows the different categories of sinking particles identified in this study. Fecal aggregates are compact and dark brown, whereas phytodetrital aggregates are diffuse and green. Mixed aggregates are relatively large in size with irregular colors i.e. brownish with some green inclusions when they are made of fecal and phytodetrital materials; and shapes i.e. spherical to elongated when zooplankton carcasses are attached to the fecal aggregates. Cylindrical fecal pellets are brown and long with a relatively high aspect ratio (i.e. length over width ratio >2) with rounded or conical edges.

At S05M, the total number flux spectra, corresponding to the sum of all particle categories within all the size classes (ESD), was $8.16\ 10^5\ m^{-2}\ d^{-1}\ mm^{-1}$ at 170 m, $9.53\ 10^5\ m^{-2}\ d^{-1}\ mm^{-1}$ at 270 m and $1.38\ 10^6 \pm 2\ 10^4\ mm^3\ m^{-2}\ d^{-1}\ mm^{-1}$ at 1000 m (Figure 4). At S10M, no data are available at 170 m because the gel was not exploitable (see Figure 2). The number flux spectra at 270 m was higher ($1.75\ 10^6\ m^{-2}\ d^{-1}\ mm^{-1}$) compared to S05M, and almost similar to S05M at 1000 m (Figure 4).

Most of the number flux spectra at all depths and both stations was dominated by fecal aggregates, in particular of small and medium size (0.1-1 mm ESD), which contribution was close to the total number flux spectra, especially at 1000 m at both stations (Figure 4). Cylindrical fecal pellets were the second most numerous particles at all depths at both stations averaged, with a maximum flux of $6.64\ 10^4\ m^{-2}\ d^{-1}\ mm^{-1}$ of particles (0.1-0.4 mm ESD) observed at S10M at 1000 m. Zooplankton carcasses were the third most numerous particles at all depths at both stations averaged, except at S05M at 270 m, where phytodetrital and mixed aggregates were the more numerous. No phytodetrital aggregates were observed at 1000 m at any station (Figure 4). Aggregates were rather mixed at this depth, with values ranging from 1.3 to $3.7\ 10^3\ m^{-2}\ d^{-1}\ mm^{-1}$ at S05M and S10M respectively. Overall, particles with a size range 0.1-0.5 mm ESD were the most numerous at both stations and their number increased progressively with depth (Figure 4), likely due to fragmentation, leading to smaller but more numerous aggregates.

At S05M, the total volume flux spectra, corresponding to the sum of volumes of all particle categories within all the size classes (ESD), was $4880\ mm^3\ m^{-2}\ d^{-1}\ mm^{-1}$ at 170 m and $4752\ mm^3\ m^{-2}\ d^{-1}\ mm^{-1}$ at 270 m (Figure 4). At S10M, no data are available at 170 m (see Figure 2). However, as for the total number flux spectra, the total volume flux spectra at this station was higher ($6949\ mm^3\ m^{-2}\ d^{-1}\ mm^{-1}$) at 270 m and almost similar ($4532 \pm 20\ mm^3\ m^{-2}\ d^{-1}\ mm^{-1}$) at 1000 m at both stations. Overall, the total volume flux spectra decreased with depth at both stations. However, the decrease was more pronounced between 270 and 1000 m at S10M than at S05M (Figure 4).

As for the number flux spectra, most of the volume flux spectra at all depths and both stations was carried out by fecal aggregates, especially those between 0.1 and 0.7 mm ESD (Figure 4). Fecal aggregates of size range 0.1-1 mm ESD were the most voluminous particles, with volumes almost equivalent to the total volume flux spectra at all depths of both stations. This is due to their higher abundance compared to larger fecal aggregates (>1 mm) and to other particle categories.

Particle number, projected area and volume fluxes

Particle number and projected area fluxes of all depths averaged were higher at S10M ($90320\ m^{-2}\ d^{-1}$ and $3342\ mm^2\ m^{-2}\ d^{-1}$, respectively) than at S05M ($59294\ m^{-2}\ d^{-1}$ and $2682\ mm^2\ m^{-2}\ d^{-1}$,

10.3389/fmars.2023.1290625

respectively) (Table 3; Figure 3). Volumes fluxes were almost similar at both stations in an average stations and depths of 861 ± 15 mm^3 m^{-2} d^{-1} (Table 3).

Fecal aggregates were the most numerous and voluminous particle category at the three depths at both stations. They represented 88 ± 10% of the total number flux, 72 ± 18% of the total projected area flux and 63 ± 19% of the total volume flux (stations and depths averaged) (Table 3; Figures 4, 3). Mixed aggregates were the second contributors to the projected area (14 ± 11% of the total, stations and depths averaged) and volume fluxes (25 ± 18% of the total) despite their low abundance. The remaining fraction is distributed among the other particle categories, the lowest contribution to the fluxes being for phytodetrital aggregates that contributed for 1.1 ± 1.3% to the total number flux, 1.2 ± 1.4% of the total projected area and 1.2 ± 1.3% of the total volume flux (Table 3; Figures 4, 3).

Reconstruction of POC flux from images analysis

Fecal aggregates dominated the total reconstructed POC flux at 270 and 1000 m at both stations, with 67 ± 17% of the total POC flux (Table 3; Figure 5). At S05M, zooplankton carcasses and cylindrical fecal pellets drove the reconstructed POC flux at 170 m with a similar contribution of 40% each, whereas no data are available for S10M at this depth (see Figure 2). Phytodetrital and mixed aggregates contribution to the total POC flux was low at both stations and all depths with an average of 0.5 ± 0.5% and 5 ± 1%, respectively (Table 3; Figure 5).

The total reconstructed POC flux was higher at S10M than at S05M (Figure 5). At S05M, reconstructed POC fluxes decreased by 65.8% between 170 and 270 m and remained constant between 270 and 1000 m (Table 3; Figure 5). This is mainly due to the decrease of cylindrical fecal pellets and zooplankton carcasses fluxes by 94 and 84% respectively between these two depths, while other particle category fluxes remained constant. However, at 1000 m, phytodetrital and mixed aggregates fluxes were almost zero and fecal aggregate fluxes increased by 32%, while other particle category fluxes remained constant. This led to a constant total reconstructed POC fluxes between 270 and 1000 m (Table 3; Figure 5). At S10M, all particle category fluxes decreased between 270 and 1000 m, by 84% for mixed aggregates fluxes and by 36% for cylindrical fecal pellets and fecal aggregate fluxes, whereas fluxes attributed to zooplankton carcasses almost doubled between these two depths (Table 3; Figure 5).

The total POC flux measured in the biogeochemical tubes was generally higher at S10M compared to S05M at all depths (Figure 5). The total measured POC flux was almost twice as much at S10M (69.6 mg C m^{-2} d^{-1}) than at S05M (38.4 mg C m^{-2} d^{-1}) at 170 m. However, it decreases more intensely at S10M (67.78%) than at S05M (47.22%) between 170 and 1000 m. Overall, our reconstructed POC fluxes were 3 to 9-fold lower than the measured POC flux at both stations (Figure 5).

Particle export and transfer efficiencies

Particle export efficiencies (*Eeff*), estimated using gel image analysis, were 0.03 at 170 m at S05M and were similar (0.01) at 270 and 1000 m at both stations (Table 5). However, the *Eeff* measured using the biogeochemical tubes, were systematically higher than estimated ones and were comparable between both stations and depths (Table 5).

Particle transfer efficiencies (*Teff*), estimated using gel image analysis, were similar between 270 and 1000 m at both stations (average of 0.95 ± 0.07) (Table 5). *Teff* measured using the biogeochemical tubes, were higher at S05M compared to S10M between 170 and 1000 m and between 170 and 270 m, whereas they were similar at both stations between 270 and 1000 m (0.4). Overall, *Eeff* were comparable at both stations but a more efficient transfer of C to depth occurred at S05M compared to S10M (Table 5).

Phycoerythrin projected area and estimation of POC fluxes potentially associated with diazotroph

Phycoerythrin occupied 13%, 52% and 45% at 170, 270 and 1000 m respectively of the total projected area flux at S05M (Table 4). Despite approximations (see Method section), we considered phycoerythrin as a relative indicator of diazotrophs in this study. The POC fluxes attributable to diazotrophs were

TABLE 5 Comparison of total estimated and measured export (*Eeff*) and particle transfer efficiencies (*Teff*) at the two stations (S05M and S10M).

Depths (m)	*Eeff*				*Teff*			
	S05M		S10M		S05M		S10M	
	Estim.[a]	Measur.[b]	Estim.[a]	Measur.[b]	Estim.[c]	Measur.[d]	Estim.[c]	Measur.[d]
170	0.03	0.08	-	0.09	0.3	0.5	-	0.3
270	0.01	0.1	0.01	0.07	0.3	1.2	–	0.7
1000	0.01	0.04	0.01	0.03	1	0.4	0.9	0.4

[a]estimated = total POC fluxes estimated of each particle category (mg C m^{-2} d^{-1})/Net PP flux (mg C m^{-2} d^{-1}, integration euphotic zone).
[b]measured = total POC flux in the biogeochemical tube (mg C m^{-2} d^{-1})/Net PP flux (mg C m^{-2} d^{-1}, integration euphotic zone).
[c]estimated = total POC fluxes reconstructed of each particle category (mg C m^{-2} d^{-1}) at the deepest depth/total reconstructed POC fluxes (mg C m^{-2} d^{-1}) at the shallowest depth.
[d]measured= total POC flux in the biogeochemical tube (mg C m^{-2} d^{-1}) measured at the deepest depth/total POC flux measured (mg C m^{-2} d^{-1}) at the shallowest depth. At 170 m=Teff between 170 and 1000 m, at 270 m=Teff between 170 and 270 m and at 1000 m=Teff between 270 and 1000 m.

relatively low (2.6 mg C m^{-2} d^{-1}) at the shallowest depth (170 m), increased by 6-fold at 270 m (15.7 mg C m^{-2} d^{-1}), then decreased at 1000 m (10.39 mg C m^{-2} d^{-1}) (Table 4). However, due to the attenuation of total POC fluxes with depth, the evaluated contribution of diazotrophs to this flux increased with depth, potentially accounting for 7% at 170 m, 34% at 270 m and 51% to the overall POC flux at 1000 m (Table 4).

Discussion

LNLC ecosystems are deemed to be poorly efficient at exporting C due to intense recycling of PP in surface waters (Buesseler et al., 2008; Buesseler and Boyd, 2009). Past studies using delta ^{15}N budgets revealed that N_2 fixation supports 50-80% of export production in the WTSP (Knapp et al., 2018), which has been recently confirmed during the TONGA cruise at our two studied stations on the same traps (64-76 ± 86% and 90-92 ± 50% at stations S05M and S10M, respectively, Bonnet et al., 2023b). Yet, the precise pathways by which diazotrophs are exported in this hot spot are poorly understood. Diazotrophs may be exported to the deep ocean through two major pathways: the direct gravitational sinking of diazotrophic organisms (Benavides et al., 2022; Bonnet et al., 2023a) and/or the transfer of their DDN to non-diazotrophic phytoplankton, zooplankton, and bacteria (Berthelot et al., 2016; Bonnet et al., 2016a; Caffin et al., 2018a), which are subsequently exported to the deep ocean as aggregates or fecal pellets (Siegel et al., 2016; Le Moigne, 2019). Consequently, the nature of organic matter derived from diazotrophy may be diazotrophs themselves, phytoplankton and/or zooplankton that have consumed DDN, detritus, fecal pellets, or a mixture of these.

Composition of the sinking fluxes in the WTSP

Here we show that the POC fluxes were primarily driven by zooplankton derived particles (fecal pellets and aggregates, and zooplankton carcasses), with fecal aggregates dominating at 1000 m, while cylindrical fecal pellets and zooplankton carcasses dominated at 170 m (Table 3; Figure 5). The dominance of zooplankton derived particles is in line with the plankton community composition present in surface waters during the same expedition (Mériguet et al., 2023). This latter study reports that grazers, dominated by gelatinous carnivores, chaetognatha, copepoda, and other larger species, account for 34% (average abundance of 329 ind. m^{-3}) of the total mesozooplankton community (>200 µm) between 0 and 200 m depth. The high POC fluxes derived from zooplankton particles suggest that the Fe-rich hydrothermal inputs from the Tonga arc have stimulated N_2 fixation (Bonnet et al., 2023b), that in turn stimulated primary and secondary productions in this LNLC ecosystem. Mériguet et al. (2023) showed that diazotrophs dominated the microplankton (20-200 µm) community in the area of trap deployment (69% of the total community abundance of 5.10^5 ind.m^{-3}) and that >80% of diazotrophs were *Trichodesmium* spp. In this ecosystem, diazotrophy supports >80% of export production (Bonnet et al., 2023b). The high POC flux derived from zooplankton particles suggest that the DDN has been efficiently transferred to the food web up to zooplankton and fecal pellets before being exported, pleading for an indirect export of diazotrophs. Previous studies based on ^{15}N isotopic measurements on zooplankton reported that the DDN contribution to zooplankton biomass was estimated at ~25% in the Southern Baltic Sea (Wannicke et al., 2013), 30-40% in the tropical Atlantic (Montoya et al., 2002; Loick-Wilde et al., 2016), and 67-75% in the WTSP (Carlotti et al., 2018). Other studies based on direct observations, grazing experiments, or *nifH* detection in full-gut copepods, report that several copepod species graze on diverse diazotrophs such as *Trichodesmium* (O'Neil et al., 1996; O'Neil, 1999; Koski and Lombard, 2022), UCYN from groups A, B and C (Scavotto et al., 2015; Hunt et al., 2016; Conroy et al., 2017), *Richelia* (Hunt et al., 2016; Conroy et al., 2017), and *Aphanizomenon* (Wannicke et al., 2013; Koski and Lombard, 2022). Finally, ^{15}N-labelling experiments revealed that diazotrophs can be a direct source of N supporting the metabolism of zooplankton (Loick-Wilde et al., 2012; Wannicke et al., 2013; Adam et al., 2016; Hunt et al., 2016; Caffin et al., 2018a). Altogether, these studies suggest that the pool of DDN can be efficiently transferred to zooplankton, which seems to be the case in the WTSP.

POC fluxes reconstructed in this study through the image analyses and conversion factors were 3 to 9-fold lower than those actually measured in the replicate biogeochemical tubes (Figure 6). We propose two main hypotheses to explain such differences. First, the volume-to-carbon conversion factors used here were originally determined for diatoms or fecal marine snow collected in temperate regions (Alldredge, 1998). However, because the composition of sinking particles varies across coastal, open ocean, temperate and subtropical environments (Durkin et al., 2021), carbon contents of particles -relative to their volumes- originating from different environments may also vary. Moreover, similar volume-to-carbon ratios are generally used to determine the carbon content of cylindrical fecal pellets. This likely did not accurately represent the diversity of cylindrical fecal pellets identified in our study, especially that it is highly dependent on the feeding behavior of zooplankton species and on ecosystem structure (Cavan et al., 2017). Durkin et al. (2021) showed that carbon contents obtained using the classical Alldredge's conversion factors (Alldredge, 1998) and those they optimized were comparable for aggregates of sizes up to 709 µm ESD. This may suggest that our POC fluxes are coherent, as most of particles analyzed in our study have sizes between 120 and 700 µm ESD (Figure 4). Second, the cut-off we applied in one-to-one particle identification removed hundreds of small particles (<0.009 mm^2). This cutoff has probably underestimated the small particle flux and, by extension, the total reconstructed flux. However, single particle identification is less biased than other approaches, such as automated identification, although it is time consuming and labor intensive. It allows to accurately identify sinking particles by visualizing them one by one.

Equations 4 to 6 are used for converting a given particle volume (mm^3) into POC content (g). In our study, we used three different

equations to take into account the variability of carbon content relative to size in three different categories of particles, namely, fecal aggregates, phytodetrital aggregates and cylindrical fecal pellets. These equations were taken from previous literature looking at particles carbon content, mainly from the two following references (Alldredge, 1998; Lehette and Hernández-León, 2009). The few previous papers looking at particles imaging and attempting to reconstruct POC flux from imaging (Ebersbach and Trull, 2008; Ebersbach et al., 2011; Laurenceau-Cornec et al., 2015) have used a similar set of equations. Likewise, Durkin et al., 2015 have used simpler approach by using a single equation directly relating carbon content to particle volume without no further distinction between particle types.

Such equations do not provide uncertainties unfortunately bacause they are empirically defined. They are based on field measurements that do not allow sufficient reproducibility to provide robust uncertainties. Collecting intact particles at sea is a challenge because large particles (which can be clearly identified as certain category and are the main contributor to the overall POC flux) are scarce and very fragile. For instance, defining uncertainties on such equations would require to have a several contiguous cohorts of particles of similar size (for example: 10 fecal pellets of exactly 300 µm, 10 fecal pellets of exactly 500 µm, 10 fecal pellets of exactly 1000 µm and so on) and measure their individual carbon content. In the field, particles size spectra are more complex than that, and the sampling strategy described in the sentence above is simply not possible to find. Currently, the sampling capacity of intact particles (enabling sizing and POC content measurement) is very limited to a few particles at the time suing the Marine Snow Catcher for instance (Riley et al., 2012). Therefore, uncertainties cannot be assessed at present.

Evolution of the POC flux with depth at the two stations

The total reconstructed and measured POC fluxes decreased with depth by 66 and 47% at S05M and by 67% of the measured POC fluxes at S10M (Table 3; Figure 5). This is consistent with the decrease of POC by 46 and 55% between 150 and 500 m at station ALOHA assessed using neutrally buoyant sediment traps (Lamborg et al., 2008). In our study, the decrease of the total reconstructed POC flux was mainly due to the decrease of cylindrical fecal pellets and zooplankton carcasses fluxes by 94 and 84%, respectively between 170 and 270 m, while the particle flux of the categories of particles remained constant or even increased for fecal aggregates at S05M (Table 3; Figure 5). This suggests that a fragmentation of fecal material occurred at shallow depths, likely by bacterial activity or zooplankton coprorhexy (Lampitt et al., 1990; Suzuki et al., 2003; Iversen and Poulsen, 2007), followed by a reaggregation at depth by physical processes. For physical aggregation to occur, high particle concentrations are required (Jackson, 1990). Thus, the high fecal pellet flux at 170 m and its decrease at depth suggest that sufficient fragmented particles were released to allow a reaggregation into fecal aggregates at depth.

In addition, both estimated and measured export efficiencies (*Eeff*)(Table 5) were within the range of those reported in LNLC ecosystems (0.02-0.2) (Henson et al., 2019) but lower than those reported in the WTSP (0.2-0.4) using a mesocosm experiments (Berthelot et al., 2015), likely due to shallow depth of the mesocosms (15 m). Estimated *Eeff* and transfer efficiencies (*Teff*) were similar at both stations at 1000 m, whereas measured ones showed a more efficient export and transfer of POC at shallower depths at S05M and similar at 1000 m (Table 5). The similarities between the two stations may be explained by their geographical proximity and their belonging to the same biogeochemical province i.e. both are Fe fertilized by the shallow hydrothermal sources along the Tonga-Kermadec arc (Figure 1) (Bonnet et al., 2023b).

Evaluation of the potential direct export of diazotrophs

In addition to export pathways mediated by zooplankton partly sustained by DDN, our results also emphasize that diazotrophs gravitationally sink to the deep ocean as they are retrieved in sediment traps. With our method based on confocal microscopy, we were not able to accurately determine in which type of aggregates they were embedded, but the aggregates containing recognizable diazotrophs often looked fecal or mixed aggregates, with the exception of *Trichodesmium* colonies, which were often present as single filaments or entire colonies and were thus likely phytodetrital aggregates. We attempted to estimate the potential contribution of diazotrophs to the total POC export flux, and estimated that they could contribute from 7 to 51%, with a potential contribution increasing with depth. Although our method includes biases associated with the use of phycoerythrin as a relative indicator of the presence of diazotrophs (see details in method section) and the use of conversion factors, the trend obtained here is comparable with that obtained in a parallel study carried out in the same traps during the same campaign using quantitative PCR (Bonnet et al., 2023a). In the latter study, the authors estimated that the direct export of diazotrophs would contribute ~1% (at 170 m) to 85% (at 1000 m) of total PON export, and thus also report this trend of increasing contribution with depth, mostly due to the presence at 1000 m of large amounts of intact *Trichodesmium* spp. filaments and colonies having high carbon and nitrogen contents due to their large size (this study, Bonnet et al., 2023a). Finally, we also used nitrogen isotope budget to infer the contribution of N_2 fixation to export production in the same traps (Bonnet et al., 2023b; Forrer et al., 2023). This approach reports that N_2 fixation supports 77 to 84 ± 159% and 64 to 76 ± 86% of exported production at 170 and 270 m, respectively at the same station (S05M) (no data were available at 1000 m). These estimates are therefore comparable to those based on confocal microscopy (this study) and quantitative PCR (Bonnet et al.,

2023a study), but are higher at the two shallowest depths. This seems logical as the approach based on nitrogen isotopes do not discriminate the direct export of diazotrophs, to the export of non-diazotrophic organisms which growth was supported by N_2 fixation in surface waters (indirect export), and give the sum of both. In all, these three independant approaches indicate that diazotrophs leave the euphotic layer and are exported up to 1000 m depth, thus contributing to carbon export fluxes to the deep ocean.

The increasing contribution of diazotroph to the POC fluxes with depth may be explained by a temporal decoupling between surface production and export. MODIS satellite estimates of surface chlorophyll concentrations during the TONGA expedition (Supplementary Figure 2) indicate that the peak of chlorophyll occurred approximately two weeks before the traps deployment at this station (S05M). Thus, considering sinking velocities of filamentous and UCYN diazotroph aggregates (100 and 400 m d^{-1} respectively) measured in the laboratory by Ababou et al. (2023), they would reach the depth of 270 m within 0.67 to 3 days, and the depth of 1000 m within 2 to 10 days, which supports our hypothesis. Another hypothesis that could explain the higher contribution of diazotrophs to POC fluxes at 1000 m compared to that at is the high abundance of zooplankton carcasses (Table 3) at 170 m (thus increasing total POC, and decreasing the contribution of POC associated with diazotrophs) and gelatinous organisms (329 ind m^{-3}) in shallow (0-200 m) waters (Mériguet et al., 2023). This suggests that these organisms may have ingested diazotrophs between 0 and 200 m, consequently decreasing their export flux at 170 m. *Trichodesmium* spp. has traditionally been considered as a food source for only few zooplankton species, mainly harpacticoid copepods (O'Neil and Roman, 1994) due to its toxicity (O'Neil, 1998), but recent studies suggest that they are grazed by other zooplankton species (Hunt et al., 2016; Koski and Lombard, 2022), although *Trichodesmium* spp. produces sulfuric compounds repulsive to grazers in Fe deficiency conditions (Bucciarelli et al., 2013). Because Fe was highly available in this area (Tilliette et al., 2022; Bonnet et al., 2023b) and *Trichodesmium* spp. has an efficient Fe uptake system (Lory et al., 2022), the hypothesis that *Trichodesmium* spp. would escape grazing by releasing zooplankton repulsive compounds is unlikely.

Conclusion

This study explored for the first time the composition of the sinking flux in the oligotrophic ocean. It was conducted in a hot spot of N_2 fixation, in which diazotrophy supports the majority of export based on nitrogen isotopic budgets (Knapp et al., 2018; Bonnet et al., 2023b). Here we explored pathways though which diazotrophs support the export of organic matter. We reveal that fecal aggregates dominated the particles flux between 170 and 1000 m, suggesting that the DDN in the euphotic layer has been efficiently transferred to the food web up to zooplankton and fecal pellets before being exported, pleading for an indirect export of diazotrophs. Additionally, our study report that diazotrophic cells, filaments and colonies are present embedded in different categories of particles, mostly fecal and mixed aggregates, and account for a direct i.e. gravitational export pathways of diazotrophs. This indicates that diazotroph biomass can escape short-term sub-surface and mesopelagic remineralization and reach the deep ocean, where a fraction will be sequestered for long time scales. Additional investigation is needed in other oligotrophic regions to determine the contribution of diazotrophs to export fluxes at larger scales, and eventually integrate direct and indirect export pathways in biogeochemical models.

Data availability statement

The datasets presented in this study can be found in online repositories. The names of the repository/repositories and accession number(s) can be found below: http://www.obs-vlfr.fr/proof/php/TONGA/tonga.php.

Author contributions

F-EA: Formal Analysis, Investigation, Methodology, Software, Writing – original draft, Writing – review & editing. FM: Conceptualization, Investigation, Methodology, Software, Supervision, Writing – review & editing. VC-B: Methodology, Software. VT: Conceptualization, Data curation, Investigation, Software. SB: Conceptualization, Data curation, Funding acquisition, Investigation, Methodology, Project administration, Resources, Supervision, Validation, Writing – review & editing.

Funding

The author(s) declare financial support was received for the research, authorship, and/or publication of this article. This work was performed in the framework of the TONGA project (TONGA cruise GEOTRACES GPpr14, November 2019, https://doi.org/10.17600/18000884) managed by the M.I.O (SB) and LOV (Cécile Guieu). The project was funded by the TGIR Flotte Océanographique Française, the A-MIDeX of Aix-Marseille University, the LEFE-CYBER and GMMC program and the Agence Nationale de Recherche (ANR-18-CE01-0016).

Acknowledgments

We warmly thank all the scientists, the captain, and the crew of the R/V L'Atalante for their cooperative work at sea during the TONGA cruise.

Conflict of interest

The authors declare that the research was conducted in the absence of any commercial or financial relationships that could be construed as a potential conflict of interest.

Publisher's note

All claims expressed in this article are solely those of the authors and do not necessarily represent those of their affiliated organizations, or those of the publisher, the editors and the reviewers. Any product that may be evaluated in this article, or claim that may be made by its manufacturer, is not guaranteed or endorsed by the publisher.

Supplementary material

The Supplementary Material for this article can be found online at: https://www.frontiersin.org/articles/10.3389/fmars.2023.1290625/full#supplementary-material

References

Ababou, F., Le Moigne, F. A. C., Grosso, O., Guigue, C., Nunige, S., Camps, M., et al. (2023). Mechanistic understanding of diazotroph aggregation and sinking: "A rolling tank approach. *Limnol. Oceanogr.* 68 (3), 666–677. doi: 10.1002/lno.12301

Adam, B., Klawonn, I., Svedén, J. B., Bergkvist, J., Nahar, N., Walve, J., et al. (2016). N2-fixation, ammonium release and N-transfer to the microbial and classical food web within a plankton community. *ISME J.* 10, 450–459. doi: 10.1038/ismej.2015.126

Agusti, S., González-Gordillo, J. I., Vaqué, D., Estrada, M., Cerezo, M. I., Salazar, G., et al. (2015). Ubiquitous healthy diatoms in the deep sea confirm deep carbon injection by the biological pump. *Nat. Commun.* 6, 7608. doi: 10.1038/ncomms8608

Alldredge, A. (1998). The carbon, nitrogen and mass content of marine snow as a function of aggregate size. *Deep Sea Res. Part Oceanogr. Res. Pap.* 45, 529–541. doi: 10.1016/S0967-0637(97)00048-4

Alldredge, A. L., and Gotschalk, C. (1988). *In situ* settling behavior of marine snow1: Sinking rates of marine snow. *Limnol. Oceanogr.* 33, 339–351. doi: 10.4319/lo.1988.33.3.0339

Aumont, O., Maury, O., Lefort, S., and Bopp, L. (2018). Evaluating the potential impacts of the diurnal vertical migration by marine organisms on marine biogeochemistry. *Glob. Biogeochem. Cycles* 32, 1622–1643. doi: 10.1029/2018GB005886

Bach, L. T., Stange, P., Taucher, J., Achterberg, E. P., Algueró-Muñiz, M., Horn, H., et al. (2019). The influence of plankton community structure on sinking velocity and remineralization rate of marine aggregates. *Glob. Biogeochem. Cycles* 33, 971–994. doi: 10.1029/2019GB006256

Baker, C. A., Estapa, M. L., Iversen, M., Lampitt, R., and Buesseler, K. (2020). Are all sediment traps created equal? An intercomparison study of carbon export methodologies at the PAP-SO site. *Prog. Oceanogr.* 184, 102317. doi: 10.1016/j.pocean.2020.102317

Baumas, C., and Bizic, M. (2023). Did you say marine snow? Zooming into different types of organic matter particles and their importance in the open ocean carbon cycle. EarthArXiv. *doi: 10.31223/X5RM1T*

Benavides, M., Bonnet, S., Le Moigne, F. A. C., Armin, G., Inomura, K., Hallstrøm, S., et al. (2022). Sinking Trichodesmium fixes nitrogen in the dark ocean. *ISME J.* 16, 2398–2405. doi: 10.1038/s41396-022-01289-6

Berthelot, H., Bonnet, S., Grosso, O., Cornet, V., and Barani, A. (2016). Transfer of diazotroph-derived nitrogen towards non-diazotrophic planktonic communities: a comparative study between *Trichodesmium erythraeum*, *Crocosphaera watsonii* and Cyanothece sp. *Biogeosciences* 13, 4005–4021. doi: 10.5194/bg-13-4005-2016

Berthelot, H., Moutin, T., L'Helguen, S., Leblanc, K., Hélias, S., and Grosso, O.. (2015). Dinitrogen fixation and dissolved organic nitrogen fueled primary production and particulate export during the VAHINE mesocosm experiment (New Caledonia lagoon). *Biogeosciences* 12, 4099–4112. doi: 10.5194/bg-12-4099-2015

Bianchi, D., Stock, C., Galbraith, E. D., and Sarmiento, J. L. (2013). Diel vertical migration: Ecological controls and impacts on the biological pump in a one-dimensional ocean model. *Glob. Biogeochem. Cycles* 27, 478–491. doi: 10.1002/gbc.20031

Billones, R. G., Tackx, M. L. M., Flachier, A. T., Zhu, L., and Daro, M. H. (1999). Image analysis as a tool for measuring particulate matter concentrations and gut content, body size, and clearance rates of estuarine copepods: validation and application. *J. Mar. Syst.* 22, 179–194. doi: 10.1016/S0924-7963(99)00040-8

Bonnet, S., Berthelot, H., Turk-Kubo, K., Cornet-Barthaux, W., Fawcett, S., Berman-Frank, I., et al. (2016a). Diazotroph derived nitrogen supports diatom growth in the South West Pacific: A quantitative study using nanoSIMS. *Limnol. Oceanogr.* 61, 1549–1562. doi: 10.1002/lno.10300

Bonnet, S., Berthelot, H., Turk-Kubo, K., Fawcett, S., Rahav, E., L'Helguen, S., et al. (2016b). Dynamics of N_2 fixation and fate of diazotroph-derived nitrogen in a low-nutrient, low-chlorophyll ecosystem: results from the VAHINE mesocosm experiment (New Caledonia). *Biogeosciences* 13, 2653–2673. doi: 10.5194/bg-13-2653-2016

Bonnet, S., Caffin, M., Berthelot, H., Grosso, O., Benavides, M., Helias-Nunige, S., et al. (2018). In-depth characterization of diazotroph activity across the western tropical South Pacific hotspot of N 2 fixation (OUTPACE cruise). *Biogeosciences* 15, 4215–4232. doi: 10.5194/bg-15-4215-2018

Bonnet, S., Caffin, M., Berthelot, H., and Moutin, T. (2017). Hot spot of N_2 fixation in the western tropical South Pacific pleads for a spatial decoupling between N_2 fixation and denitrification. *Proc. Natl. Acad. Sci.* 114 (14), E2800–E2801. doi: 10.1073/pnas.1619514114

Bonnet, S., Benavides, M., Le Moigne, F. A. C., Camps, M., Torremocha, A., and Grosso, O. (2023a). Diazotrophs are overlooked contributors to carbon and nitrogen export to the deep ocean. *ISME J.* 17, 47–58. doi: 10.1038/s41396-022-01319-3

Bonnet, S., Guieu, C., Taillandier, V., Boulart, C., Bouruet-Aubertot, P., and Gazeau, F. (2023b). Natural iron fertilization by shallow hydrothermal sources fuels diazotroph blooms in the ocean. *Science* 380, 812–817. doi: 10.1126/science.abq4654

Bonnet, S., Rodier, M., Turk-Kubo, K. A., Germineaud, C., Menkes, C., and Ganachaud, A. (2015). Contrasted geographical distribution of N2 fixation rates and nifH phylotypes in the Coral and Solomon Seas (southwestern Pacific) during austral winter conditions. *Glob. Biogeochem. Cycles* 29, 1874–1892. doi: 10.1002/2015GB005117

Böttjer, D., Dore, J. E., Karl, D. M., Letelier, R. M., Mahaffey, C., Wilson, S. T., et al. (2017). Temporal variability of nitrogen fixation and particulate nitrogen export at Station ALOHA. *Limnol. Oceanogr.* 62, 200–216. doi: 10.1002/lno.10386

Boyd, P. W., Claustre, H., Levy, M., Siegel, D. A., and Weber, T. (2019). Multi-faceted particle pumps drive carbon sequestration in the ocean. *Nature* 568, 327–335. doi: 10.1038/s41586-019-1098-2

Bucciarelli, E., Ridame, C., Sunda, W. G., Dimier-Hugueney, C., Cheize, M., and Belviso, S. (2013). Increased intracellular concentrations of DMSP and DMSO in iron-limited oceanic phytoplankton *Thalassiosira oceanica* and *Trichodesmium erythraeum*. Limnol. *Oceanogr.* 58, 1667–1679. doi: 10.4319/lo.2013.58.5.1667

Buesseler, K. O., Bacon, M. P., Cochran, J. K., and Livingston, H. D. (1992). Carbon and nitrogen export during the JGOFS North Atlantic Bloom Experiment estimated from 234Th: 238U disequilibria. *Deep Sea Res. Part Oceanogr. Res. Pap.* 39, 1115–1137. doi: 10.1016/0198-0149(92)90060-7

Buesseler, K., Ball, L., Andrews, J., Benitez-Nelson, C., Belastock, R., Chai, F., et al. (1998). Upper ocean export of particulate organic carbon in the Arabian Sea derived from thorium-234. *Deep Sea Res. Part II Top. Stud. Oceanogr.* 45, 2461–2487. doi: 10.1016/S0967-0645(98)80022-2

Buesseler, K. O., and Boyd, P. W. (2009). Shedding light on processes that control particle export and flux attenuation in the twilight zone of the open ocean. *Limnol. Oceanogr.* 54, 1210–1232. doi: 10.4319/lo.2009.54.4.1210

Buesseler, K. O., Boyd, P. W., Black, E. E., and Siegel, D. A. (2020). Metrics that matter for assessing the ocean biological carbon pump. *Proc. Natl. Acad. Sci.* 117, 9679–9687. doi: 10.1073/pnas.1918114117

Buesseler, K. O., Trull, T. W., Steinberg, D. K., Silver, M. W., Siegel, D. A., and Saitoh, S.-I. (2008). VERTIGO (VERtical Transport In the Global Ocean): A study of particle sources and flux attenuation in the North Pacific. Deep Sea Res. Part II Top. Stud. *Oceanogr.* 55, 1522–1539. doi: 10.1016/j.dsr2.2008.04.024

Burd, A. B., and Jackson, G. A. (2009). Particle aggregation. *Annu. Rev. Mar. Sci.* 1, 65–90. doi: 10.1146/annurev.marine.010908.163904

Caffin, M., Berthelot, H., Cornet-Barthaux, V., Barani, A., and Bonnet, S. (2018b). Transfer of diazotroph-derived nitrogen to the planktonic food web across gradients of N_2 fixation activity and diversity in the western tropical South Pacific Ocean. *Biogeosciences* 15, 3795–3810. doi: 10.5194/bg-15-3795-2018

Caffin, M., Moutin, T., Foster, R. A., Bouruet-Aubertot, P., Doglioli, A. M., and Berthelot, H. (2018a). N_2 fixation as a dominant new N source in the western tropical South Pacific Ocean (OUTPACE cruise). *Biogeosciences* 15, 2565–2585. doi: 10.5194/bg-15-2565-2018

Carlotti, F., Pagano, M., Guilloux, L., Donoso, K., Valdés, V., Grosso, O., et al. (2018). Meso-zooplankton structure and functioning in the western tropical South Pacific along the 20th parallel south during the OUTPACE survey (February–April 2015). *Biogeosciences* 15, 7273–7297. doi: 10.5194/bg-15-7273-2018

Cavan, E. L., Henson, S. A., Belcher, A., and Sanders, R. (2017). Role of zooplankton in determining the efficiency of the biological carbon pump. *Biogeosciences* 14, 177–186. doi: 10.5194/bg-14-177-2017

Conroy, B. J., Steinberg, D. K., Song, B., Kalmbach, A., Carpenter, E. J., and Foster, R. A. (2017). Mesozooplankton graze on cyanobacteria in the Amazon River plume and western tropical North Atlantic. *Front. Microbiol.* 8. doi: 10.3389/fmicb.2017.01436

Dai, L., Li, C., Yang, G., and Sun, X. (2016). Zooplankton abundance, biovolume and size spectra at western boundary currents in the subtropical North Pacific during winter 2012. *J. Mar. Syst.* 155, 73–83. doi: 10.1016/j.jmarsys.2015.11.004

Dall'Olmo, G., Dingle, J., Polimene, L., Brewin, R. J. W., and Claustre, H. (2016). Substantial energy input to the mesopelagic ecosystem from the seasonal mixed-layer pump. *Nat. Geosci.* 9, 820–823. doi: 10.1038/ngeo2818

De La Rocha, C. L., and Passow, U. (2007). Factors influencing the sinking of POC and the efficiency of the biological carbon pump. *Deep Sea Res. Part II Top. Stud. Oceanogr.* 54, 639–658. doi: 10.1016/j.dsr2.2007.01.004

Dron, A., Rabouille, S., Claquin, P., Chang, P., Raimbault, V., Talec, A., et al. (2012). Light:dark (12:12 h) quantification of carbohydrate fluxes in Crocosphaera watsonii. *Aquat. Microb. Ecol.* 68, 43–55. doi: 10.3354/ame01600

Durkin, C. A., Buesseler, K. O., Cetinić, I., Estapa, M. L., Kelly, R. P., and Omand, M. (2021). A visual tour of carbon export by sinking particles. *Glob. Biogeochem. Cycles* 35, e2021GB006985. doi: 10.1029/2021GB006985

Durkin, C. A., Margaret, L. E., and Buesseler, K. O. (2015). Observations of carbon export by small sinking particles in the upper mesopelagic. *Mar. Chem.* 175, 72–81. doi: 10.1016/j.marchem.2015.02.011

Ebersbach, F., and Trull, T. W. (2008). Sinking particle properties from polyacrylamide gels during the KErguelen Ocean and Plateau compared Study (KEOPS): Zooplankton control of carbon export in an area of persistent natural iron inputs in the Southern Ocean. *Limnol. Oceanogr.* 53, 212–224. doi: 10.4319/lo.2008.53.1.0212

Ebersbach, F., Trull, T. W., Davies, D. M., and Bray, S. G. (2011). Controls on mesopelagic particle fluxes in the Sub-Antarctic and Polar Frontal Zones in the Southern Ocean south of Australia in summer—Perspectives from free-drifting sediment traps. *Deep Sea Res. Part II: Topical Stud. Oceanography* 58 (21-22), 2260–2276. doi: 10.1016/j.dsr2.2011.05.025

Eppley, R. W., and Peterson, B. J. (1979). Particulate organic matter flux and planktonic new production in the deep ocean. *Nature* 282, 677–680. doi: 10.1038/282677a0

Forrer, H. J., Bonnet, S., Thomas, R. K., Grosso, O., Guieu, C., and Knapp, A. N. (2023). Quantifying N2 fixation and its contribution to export production near the Tonga-Kermadec Arc using nitrogen isotope budgets. *Front. Mar. Sci.* 10. doi: 10.3389/fmars.2023.1249115

Francois, R., Honjo, S., Krishfield, R., and Manganini, S. (2002). Factors controlling the flux of organic carbon to the bathypelagic zone of the ocean: FACTORS CONTROLLING ORGANIC CARBON FLUX. *Glob. Biogeochem. Cycles* 16, 34-1-34–20. doi: 10.1029/2001GB001722

Goebel, N. L., Edwards, C. A., Carter, B. J., Achilles, K. M., and Zehr, J. P. (2008). GROWTH AND CARBON CONTENT OF THREE DIFFERENT-SIZED DIAZOTROPHIC CYANOBACTERIA OBSERVED IN THE SUBTROPICAL NORTH PACIFIC 1. *J. Phycol.* 44, 1212–1220. doi: 10.1111/j.1529-8817.2008.00581.x

Gonzalez, H. E., and Smetacek, V. (1994). The possible role of the cyclopoid copepod Oithona in retarding vertical flux of zooplankton faecal material. *Mar. Ecol. Prog. Ser.* 113, 233–246. doi: 10.3354/meps113233

Grabowski, M. N. W., Church, M. J., and Karl, D. M. (2008). Nitrogen fixation rates and controls at Stn ALOHA. *Aquat Microb. Ecol.* 52, 175–183. doi: 10.3354/ame01209

Haskell, W. Z. II, Prokopenko, M. G., Hammond, D. E., Stanley, R. H. R., and Sandwith, Z. O. (2017). Annual cyclicity in export efficiency in the inner Southern California Bight. *Glob. Biogeochem. Cycles* 31, 357–376. doi: 10.1002/2016GB005561

Henson, S., Le Moigne, F., and Giering, S. (2019). Drivers of carbon export efficiency in the global ocean. *Glob. Biogeochem. Cycles* 33, 891–903. doi: 10.1029/2018GB006158

Henson, S. A., Sanders, R., and Madsen, E. (2012). Global patterns in efficiency of particulate organic carbon export and transfer to the deep ocean: EXPORT AND TRANSFER EFFICIENCY. *Glob. Biogeochem. Cycles* 26. doi: 10.1029/2011GB004099

Henson, S. A., Sanders, R., Madsen, E., Morris, P. J., Le Moigne, F., and Quartly, G. D. (2011). A reduced estimate of the strength of the ocean's biological carbon pump. *Geophys. Res. Lett.* 38. doi: 10.1029/2011GL046735

Hunt, B. P. V., Bonnet, S., Berthelot, H., Conroy, B. J., Foster, R. A., and Pagano, M. (2016). Contribution and pathways of diazotroph-derived nitrogen to zooplankton during the VAHINE mesocosm experiment in the oligotrophic New Caledonia lagoon. *Biogeosciences* 13, 3131–3145. doi: 10.5194/bg-13-3131-2016

Iversen, M. H. (2023). Carbon export in the ocean: A biologist's perspective. *Annu. Rev. Mar. Sci.* 15, 357–381. doi: 10.1146/annurev-marine-032122-035153

Iversen, M. H., and Poulsen, L. K. (2007). Coprorhexy, coprophagy, and coprochaly in the copepods Calanus helgolandicus, Pseudocalanus elongatus, and Oithona similis. *Mar. Ecol. Prog. Ser.* 350, 79–89. doi: 10.3354/meps07095

Jackson, G. A. (1990). A model of the formation of marine algal flocs by physical coagulation processes. *Deep Sea Res. Part Oceanogr. Res. Pap.* 37, 1197–1211. doi: 10.1016/0198-0149(90)90038-W

Jannasch, H. W., Zafiriou, O. C., and Farrington, J. W. (1980). A sequencing sediment trap for time-series studies of fragile particles 1, 2. *Limnol. Oceanogr.* 25, 939–943. doi: 10.4319/lo.1980.25.5.0939

Jónasdóttir, S. H., Visser, A. W., Richardson, K., and Heath, M. R. (2015). Seasonal copepod lipid pump promotes carbon sequestration in the deep North Atlantic. *Proc. Natl. Acad. Sci.* 112, 12122–12126. doi: 10.1073/pnas.1512110112

Karl, D. M., Bates, N. R., Emerson, S., Harrison, P. J., Jeandel, C., and Llinás, O. (2003). "Temporal studies of biogeochemical processes determined from ocean time-series observations during the JGOFS era," in *Ocean biogeochemistry*. Ed. M. J. R. Fasham (Ocean Biogeochemistry: Springer Berlin Heidelberg), 239–267. doi: 10.1007/978-3-642-55844-3_11

Karl, D. M., Hebel, D. V., Björkman, K., and Letelier, R. M. (1998). The role of dissolved organic matter release in the productivity of the oligotrophic North Pacific Ocean. *Limnol. Oceanogr.* 43, 1270–1286. doi: 10.4319/lo.1998.43.6.1270

Karl, D. M., Letelier, R. M., Bidigare, R. R., Björkman, K. M., Church, M. J., Dore, J. E., et al. (2021). Seasonal-to-decadal scale variability in primary production and particulate matter export at Station ALOHA. *Prog. Oceanogr.* 195, 102563. doi: 10.1016/j.pocean.2021.102563

Knapp, A. N., McCabe, K. M., Grosso, O., Leblond, N., Moutin, T., and Bonnet, S. (2018). Distribution and rates of nitrogen fixation in the western tropical South Pacific Ocean constrained by nitrogen isotope budgets. *Biogeosciences* 15, 2619–2628. doi: 10.5194/bg-15-2619-2018

Knapp, A. N., Sigman, D. M., and Lipschultz, F. (2005). N isotopic composition of dissolved organic nitrogen and nitrate at the Bermuda Atlantic Time-series Study site: N ISOTOPES OF DON AND NITRATE AT BATS. *Glob. Biogeochem. Cycles* 19. doi: 10.1029/2004GB002320

Koski, M., and Lombard, F. (2022). Functional responses of aggregate-colonizing copepods. *Limnol. Oceanogr.* 67, 2059–2072. doi: 10.1002/lno.12187

Lamborg, C. H., Buesseler, K. O., Valdes, J., Bertrand, C. H., Bidigare, R., and Manganini, S. (2008). The flux of bio-and lithogenic material associated with sinking particles in the mesopelagic "twilight zone" of the northwest and North Central Pacific Ocean. *Deep Sea Res. Part II Top. Stud. Oceanogr.* 55, 1540–1563. doi: 10.1016/j.dsr2.2008.04.011

Lampitt, R. S., Noji, T., and Von Bodungen, B. (1990). What happens to zooplankton faecal pellets? Implications for material flux. *Mar. Biol.* 104, 15–23. doi: 10.1007/BF01313152

Laurenceau-Cornec, E. C., Trull, T. W., Davies, D. M., Bray, S. G., Doran, J., and Planchon, F. (2015). The relative importance of phytoplankton aggregates and zooplankton fecal pellets to carbon export: insights from free-drifting sediment trap deployments in naturally iron-fertilised waters near the Kerguelen Plateau. *Biogeosciences* 12, 1007–1027. doi: 10.5194/bg-12-1007-2015

Laws, E. A., Falkowski, P. G., Smith, W. O. Jr., Ducklow, H., and McCarthy, J. J. (2000). Temperature effects on export production in the open ocean. *Glob. Biogeochem. Cycles* 14, 1231–1246. doi: 10.1029/1999GB001229

Laws, E. A., and Maiti, K. (2019). The relationship between primary production and export production in the ocean: Effects of time lags and temporal variability. *Deep Sea Res. Part Oceanogr. Res. Pap.* 148, 100–107. doi: 10.1016/j.dsr.2019.05.006

Lehette, P., and Hernández-León, S. (2009). Zooplankton biomass estimation from digitized images: a comparison between subtropical and Antarctic organisms. *Limnol. Oceanogr. Methods* 7, 304–308. doi: 10.4319/lom.2009.7.304

Le Moigne, F. A. C. (2019). Pathways of organic carbon downward transport by the oceanic biological carbon pump. *Front. Mar. Sci.* 6. doi: 10.3389/fmars.2019.00634

Le Moigne, F. A., Poulton, A. J., Henson, S. A., Daniels, C. J., Fragoso, G. M., and Mitchell, E. (2015). Carbon export efficiency and phytoplankton community composition in the A tlantic sector of the Arctic Ocean. *J. Geophys. Res. Oceans* 120, 3896–3912. doi: 10.1002/2015JC010700

Levy, M., Bopp, L., Karleskind, P., Resplandy, L., Ethe, C., and Pinsard, F. (2013). Physical pathways for carbon transfers between the surface mixed layer and the ocean interior: PHYSICAL CARBON FLUXES. *Glob. Biogeochem. Cycles* 27, 1001–1012. doi: 10.1002/gbc.20092

Loick-Wilde, N., Dutz, J., Miltner, A., Gehre, M., Montoya, J. P., and Voss, M. (2012). Incorporation of nitrogen from N2 fixation into amino acids of zooplankton. *Limnol. Oceanogr.* 57, 199–210. doi: 10.4319/lo.2012.57.1.0199

Loick-Wilde, N., Weber, S. C., Conroy, B. J., Capone, D. G., Coles, V. J., Medeiros, P. M., et al. (2016). Nitrogen sources and net growth efficiency of zooplankton in three A mazon River plume food webs. *Limnol. Oceanogr.* 61, 460–481. doi: 10.1002/lno.10227

Lory, C., Van Wambeke, F., Fourquez, M., Barani, A., Guieu, C., and Tilliette, C. (2022). Assessing the contribution of diazotrophs to microbial Fe uptake using a group

specific approach in the Western Tropical South Pacific Ocean. *ISME Commun.* 2, 41. doi: 10.1038/s43705-022-00122-7

Lundsgaard, C. (1995). *Use of a high viscosity medium in studies of aggregates, in Sediment trap studies in the Nordic countries 3. Proceedings of the Symposium on Seasonal Dynamics of Planktonic Ecosystems and Sedimentation in Coastal Nordic Waters*. Eds. S. Floderus, A. S. Heisakanen, M. Oleson and P. Wassman (Helsinki: Finnish Environment Agency), 141–152.

Luo, Y.-W., Doney, S. C., Anderson, L. A., et al. (2012). Database of diazotrophs in global ocean: abundance, biomass and nitrogen fixation rates. *Earth Syst. Sci. Data* 4, 47–73. doi: 10.5194/essd-4-47-2012

Maiti, K., Bosu, S., D'sa, E. J., Adhikari, P. L., Sutor, M., and Longnecker, K. (2016). Export fluxes in northern Gulf of Mexico-Comparative evaluation of direct, indirect and satellite-based estimates. *Mar. Chem.* 184, 60–77. doi: 10.1016/j.marchem.2016.06.001

Mériguet, Z., Vilain, M., Baudena, A., Tilliette, C., Habasque, J., and Lebourges-Dhaussy, A. (2023). Plankton community structure in response to hydrothermal iron inputs along the Tonga-Kermadec arc. *Front. Mar. Sci.* 10. doi: 10.3389/fmars.2023.1232923

Montoya, J. P., Carpenter, E. J., and Capone, D. G. (2002). Nitrogen fixation and nitrogen isotope abundances in zooplankton of the oligotrophic North Atlantic. *Limnol. Oceanogr.* 47, 1617–1628. doi: 10.4319/lo.2002.47.6.1617

Omand, M. M., D'Asaro, E. A., Lee, C. M., Perry, M. J., Briggs, N., Cetinić, I., et al. (2015). Eddy-driven subduction exports particulate organic carbon from the spring bloom. *Science* 348, 222–225. doi: 10.1126/science.1260062

O'Neil, J. M. (1998). The colonial cyanobacterium Trichodesmium as a physical and nutritional substrate for the harpacticoid copepod Macrosetella gracilis. *J. Plankton Res.* 20, 43–59. doi: 10.1093/plankt/20.1.43

O'Neil, J. M. (1999). Grazer interactions with nitrogen-fixing marine Cyanobacteria: adaptation for N-acquisition? *Bull.-Inst. Oceanogr. MONACO-NUMERO Spec.*, 293–318.

O'Neil, J. M., Metzler, P. M., and Glibert, P. M. (1996). Ingestion of 15N2-labelled Trichodesmium spp. and ammonium regeneration by the harpacticoid copepod Macrosetella gracilis. *Mar. Biol.* 125, 89–96. doi: 10.1007/BF00350763

O'Neil, J. M., and Roman, M. R. (1994). Ingestion of the cyanobacterium Trichodesmium spp. by pelagic harpacticoid copepods Macrosetella, Miracia and Oculosetella. *Hydrobiologia* 292, 235–240. doi: 10.1007/BF00229946

Pabortsava, K., Lampitt, R. S., Benson, J., Crowe, C., McLachlan, R., Le Moigne, F. A. C., et al. (2017). Carbon sequestration in the deep Atlantic enhanced by Saharan dust. *Nat. Geosci.* 10, 189–194. doi: 10.1038/ngeo2899

Poff, K. E., Leu, A. O., Eppley, J. M., Karl, D. M., and DeLong, E. F. (2021). Microbial dynamics of elevated carbon flux in the open ocean's abyss. *Proc. Natl. Acad. Sci.* 118, e2018269118. doi: 10.1073/pnas.2018269118

Quay, P. D., Peacock, C., Björkman, K., and Karl, D. M. (2010). Measuring primary production rates in the ocean: Enigmatic results between incubation and non-incubation methods at Station ALOHA. *Glob. Biogeochem. Cycles* 24. doi: 10.1029/2009GB003665

Riley, J. S., Sanders, R., Marsay, C., Le Moigne, F. A. C., Achterberg, E. P., and Poulton, A. J. (2012). The relative contribution of fast and slow sinking particles to ocean carbon export. *Global Biogeochemical Cycles* 26 (1). doi: 10.1029/2011GB004085

Scavotto, R. E., Dziallas, C., Bentzon-Tilia, M., Riemann, L., and Moisander, P. H. (2015). Nitrogen-fixing bacteria associated with copepods in coastal waters of the N orth A tlantic O cean. *Environ. Microbiol.* 17, 3754–3765. doi: 10.1111/1462-2920.12777

Schindelin, J., Rueden, C. T., Hiner, M. C., and Eliceiri, K. W. (2015). The ImageJ ecosystem: An open platform for biomedical image analysis. *Mol. Reprod. Dev.* 82, 518–529. doi: 10.1002/mrd.22489

Shao, Z., Xu, Y., Wang, H., Luo, W., Wang, L., Huang, Y., et al. (2023). Global oceanic diazotroph database version 2 and elevated estimate of global oceanic N_2 fixation. *Earth Syst. Sci. Data* 15 (8 ESSD), 3673–3709. doi: 10.5194/essd-2023-13

Siegel, D. A., Buesseler, K. O., Behrenfeld, M. J., Benitez-Nelson, C. R., Boss, E., Brzezinski, M. A., et al. (2016). Prediction of the export and fate of global ocean net primary production: the EXPORTS science plan. *Front. Mar. Sci.* 3. doi: 10.3389/fmars.2016.00022

Siegel, D. A., Buesseler, K. O., Doney, S. C., Sailley, S. F., Behrenfeld, M. J., and Boyd, P. W. (2014). Global assessment of ocean carbon export by combining satellite observations and food-web models. *Glob. Biogeochem. Cycles* 28, 181–196. doi: 10.1002/2013GB004743

Stange, P., Bach, L. T., Le Moigne, F. A., Taucher, J., Boxhammer, T., and Riebesell, U. (2017). Quantifying the time lag between organic matter production and export in the surface ocean: Implications for estimates of export efficiency. *Geophys. Res. Lett.* 44, 268–276. doi: 10.1002/2016GL070875

Steinberg, D. K., Cope, J. S., Wilson, S. E., and Kobari, T. (2008). A comparison of mesopelagic mesozooplankton community structure in the subtropical and subarctic North Pacific Ocean. *Deep Sea Res. Part II Top. Stud. Oceanogr.* 55, 1615–1635. doi: 10.1016/j.dsr2.2008.04.025

Steinberg, D. K., and Landry, M. R. (2017). Zooplankton and the ocean carbon cycle. *Annu. Rev. Mar. Sci.* 9, 413–444. doi: 10.1146/annurev-marine-010814-015924

Stukel, M. R., Aluwihare, L. I., Barbeau, K. A., Chekalyuk, A. M., Goericke, R., Miller, A. J., et al. (2017). Mesoscale ocean fronts enhance carbon export due to gravitational sinking and subduction. *Proc. Natl. Acad. Sci.* 114, 1252–1257. doi: 10.1073/pnas.1609435114

Suzuki, H., Sasaki, H., and Fukuchi, M. (2003). Loss processes of sinking fecal pellets of zooplankton in the mesopelagic layers of the Antarctic marginal ice zone. *J. Oceanogr.* 59, 809–818. doi: 10.1023/B:JOCE.0000009572.08048.0d

Tilliette, C., Taillandier, V., Bouruet-Aubertot, P., Grima, N., Maes, C., Montanes, M., et al. (2022). Dissolved iron patterns impacted by shallow hydrothermal sources along a transect through the Tonga-Kermadec Arc. *Glob. Biogeochem. Cycles* 36, e2022GB007363. doi: 10.1029/2022GB007363

Turner, J. (2002). Zooplankton fecal pellets, marine snow and sinking phytoplankton blooms. *Aquat. Microb. Ecol.* 27, 57–102. doi: 10.3354/ame027057

Waite, A. M., Safi, K. A., Hall, J. A., and Nodder, S. D. (2000). Mass sedimentation of picoplankton embedded in organic aggregates. *Limnol. Oceanogr.* 45, 87–97. doi: 10.4319/lo.2000.45.1.0087

Wang, W. L., Fu, W., Le Moigne, F. A.C., Letscher, R. T., Liu, Y., Tang, J. -M., et al. (2023). Biological carbon pump estimate based on multidecadal hydrographic data. *Nature* 624, 579–585. doi: 10.1038/s41586-023-06772-4

Wannicke, N., Korth, F., Liskow, I., and Voss, M. (2013). Incorporation of diazotrophic fixed N2 by mesozooplankton—Case studies in the southern Baltic Sea. *J. Mar. Syst.* 117, 1–13. doi: 10.1016/j.marsys.2013.03.005

Wassmann, P., Ypma, J. E., and Tselepides, A. (2000). Vertical flux of faecal pellets and microplankton on the shelf of the oligotrophic Cretan Sea (NE Mediterranean Sea). *Prog. Oceanogr.* 46, 241–258. doi: 10.1016/S0079-6611(00)00021-5

White, A. E., Watkins-Brandt, K. S., and Church, M. J. (2018). Temporal variability of Trichodesmium spp. and diatom-diazotroph assemblages in the North Pacific subtropical gyre. *Front. Mar. Sci.* 5. doi: 10.3389/fmars.2018.00027

Zehr, J. P., Bench, S. R., Carter, B. J., Hewson, I., Niazi, F., Shi, T., et al. (2008). Globally distributed uncultivated oceanic N2-fixing cyanobacteria lack oxygenic photosystem II. *Science* 322 (5904), 1110–1112. doi: 10.1126/science.1165340

frontiers | Frontiers in Marine Science

TYPE Original Research
PUBLISHED 14 February 2024
DOI 10.3389/fmars.2024.1304118

OPEN ACCESS

EDITED BY
Antonio Cobelo-Garcia,
Spanish National Research Council (CSIC), Spain

REVIEWED BY
Aridane G. Gonzalez,
University of Las Palmas de Gran Canaria, Spain
Laramie Jensen,
University of Washington, United States

*CORRESPONDENCE
Léo Mahieu
leo.mahieu@oregonstate.edu;
leo.mahieu@live.fr

RECEIVED 28 September 2023
ACCEPTED 08 January 2024
PUBLISHED 14 February 2024

CITATION
Mahieu L, Whitby H, Dulaquais G, Tilliette C, Guigue C, Tedetti M, Lefevre D, Fourrier P, Bressac M, Sarthou G, Bonnet S, Guieu C and Salaün P (2024) Iron-binding by dissolved organic matter in the Western Tropical South Pacific Ocean (GEOTRACES TONGA cruise GPpr14).
Front. Mar. Sci. 11:1304118.
doi: 10.3389/fmars.2024.1304118

Iron-binding by dissolved organic matter in the Western Tropical South Pacific Ocean (GEOTRACES TONGA cruise GPpr14)

Léo Mahieu[1,2]*, Hannah Whitby[1], Gabriel Dulaquais[3], Chloé Tilliette[4,5], Catherine Guigue[6], Marc Tedetti[6], Dominique Lefevre[6], Pierre Fourrier[7,8], Matthieu Bressac[5], Géraldine Sarthou[3], Sophie Bonnet[6], Cécile Guieu[5] and Pascal Salaün[1]

[1]School of Environmental Sciences, University of Liverpool, Liverpool, United Kingdom, [2]College of Earth, Ocean and Atmospheric Sciences, Oregon State University, Corvallis, OR, United States, [3]CNRS, Univ Brest, IRD, Ifremer, LEMAR, Plouzané, France, [4]CNRS, Univ. Littoral Côte d'Opale, UMR 8187 – LOG – Laboratoire d'Océanologie et de Géosciences, Univ. Lille, Lille, France, [5]Laboratoire d'Océanographie de Villefranche, CNRS UMR7093, Sorbonne Université, Villefranche-sur-Mer, France, [6]Aix-Marseille Univ., Universiteé de Toulon, CNRS, IRD, MIO UM 110, Marseille, France, [7]Conservatoire National des Arts et Métiers INTECHMER, Cherbourg, France, [8]Laboratoire des Sciences Appliquées de Cherbourg, Normandie University, UNICAEN, Cherbourg, France

Iron (Fe) is an essential micronutrient for phytoplankton growth, but its scarcity in seawater limits primary productivity across much of the ocean. Most dissolved Fe (DFe) in seawater is complexed with Fe-binding organic ligands, a poorly constrained fraction of dissolved organic matter (DOM), which increase Fe residence time and impact Fe bioavailability. Here, we present the conditional concentration (L_{Fe}) and binding-strength (log $K^{cond}_{Fe'L}$) of Fe-binding ligands in the Western Tropical South Pacific (WTSP) Ocean during the GEOTRACES TONGA cruise (GPpr14). The transect crossed the Lau basin, a region subject to shallow hydrothermal Fe inputs that fuel intense diazotrophic activity, the oligotrophic South Pacific gyre, and the Melanesian basin. Organic speciation was analyzed by competitive ligand exchange adsorptive cathodic stripping voltammetry (CLE-AdCSV) using salicylaldoxime at 25 µM. We found a high mean L_{Fe} of 5.2 ± 1.2 nMeqFe (n = 103) across the entire transect, predominantly consisting of intermediate strength L2 ligands (84%; mean log $K^{cond}_{Fe'L}$ of 11.6 ± 0.4), consistent with humic-like substances. DFe correlated with the humic-like component of the fluorescent DOM (HS-like FDOM), yet the electroactive Fe-binding humic-like substances (L_{FeHS}) accounted for only 20 ± 13% of L_{Fe} in the mixed layer and 8 ± 6% in deep waters. Ligands were in large excess compared to DFe (mean excess ligand eL_{Fe} = 4.6 ± 1.1 nMeqFe), suggesting poor stabilization of DFe inputs. High L_{Fe} (up to 9 nMeqFe) in samples close to hydrothermal sites could be due to detoxification strategies from plankton communities toward hydrothermally-fueled toxic trace metals other than Fe, with an apparent dilution of the DOM from the Lau basin into neighboring regions. We also observed a different peak potential of the Fe salicylaldoxime complex detected by CLE-AdCSV between the Lau and Melanesian basins, and between surface and deep waters. To our knowledge, this change in potential has not previously been

reported; whether this represents a novel detection of specificities in DOM composition merits further investigation. Competition between Fe and competing metals for ligand binding sites could favor DFe oxidation and precipitation near hydrothermal vents and explain the absence of strong Fe stabilization in the WTSP.

KEYWORDS

iron-binding ligands, hydrothermal, diazotroph, remineralization, humic substances, voltammetry, fluorescence

Introduction

Iron (Fe) is an essential micronutrient for phytoplankton growth because of its role in multiple metabolic processes (Twining and Baines, 2013). Biological Fe demand is such that its availability co-limits primary production across around 40% of the ocean (Moore et al., 2013; Browning and Moore, 2023). Fe scarcity is also explained by its very low solubility in seawater (Liu and Millero, 2002). Fe is quickly hydrolyzed and exported as oxyhydroxide aggregates in oxygenated conditions (Liu and Millero, 2002), and as Fe-sulfide (e.g., pyrite) in more anoxic environments such as hydrothermal vents (Rickard and Luther, 2007). However, despite its low solubility and inorganic scavenging, the Fe concentration found in the dissolved fraction (DFe; defined by the filter of 0.2 µm or 0.45 µm pore size) is higher than what is expected from its inorganic speciation (Liu and Millero, 2002). This is partly explained by extensive complexation of DFe by a fraction of the dissolved organic matter (DOM) pool, known as Fe-binding ligands, that enhance Fe solubility and increase its residence time in surface waters, thereby impacting its bioavailability to phytoplankton. It is generally accepted that most DFe (> 99%) is complexed to organic ligands (Gledhill and Buck, 2012). Knowledge of the nature and cycling of these ligands is required to understand and predict Fe distribution and bioavailability in seawater, but obtaining this information is challenging. Characterization of the Fe complexing fraction is difficult because of the sheer chemical diversity of DOM (Mentges et al., 2017; Dittmar et al., 2021) and the relatively low abundance of Fe-binding compounds, only exceeding DFe by around 1 nmol equivalent of Fe per liter (nMeqFe) in the global ocean (Gledhill and Buck, 2012; Boyd and Tagliabue, 2015). Various methods enable measurements of the major individual Fe-binding ligand groups, namely siderophores (Bundy et al., 2018; Boiteau and Repeta, 2022), humic-like substances (HS-like; Laglera and van den Berg, 2009; Pernet-Coudrier et al., 2013; Whitby and van den Berg, 2015; Sukekava et al., 2018), and exopolymeric substances (EPS; Hassler et al., 2011; Hassler et al., 2015; Norman et al., 2015). Those methods, however, have a limited resolution because of the diversity encountered within each group.

The challenge of identifying individual ligands within the range of metal-binding compounds composing DOM is overcome by Competitive Ligand Exchange (CLE). This approach is based on the competition between the natural Fe-binding ligands and an added competitive ligand at increasing DFe concentrations. The titration of the natural Fe-binding ligands is monitored by adsorptive cathodic stripping voltammetry (AdCSV), quantifying the electrons needed to reduce the DFe that formed an electroactive complex with the added ligand. This approach allows the determination of the maximum amount of DFe that can be complexed by the natural DOM present within a sample, defined as the Fe-binding ligand concentration (L_{Fe}), and the averaged conditional stability constant (log $K^{cond}_{Fe'L}$) of the Fe-binding complexes within the detection window ($\alpha_{Fe'AL}$) applied. The detection window is defined as the product of the added ligand concentration ([AL]) forming the electroactive complex $FeAL_n$ and of its binding affinity with DFe ($\beta^{cond}_{Fe'AL}$; $\alpha_{Fe'AL} = [AL]^n * \beta^{cond}_{Fe'AL}$). The log $K^{cond}_{Fe'L}$ values obtained by CLE-AdCSV are commonly divided into classes, with L_1 corresponding to strong Fe-binding ligands (log $K^{cond}_{Fe'L}$ > 12), L_2 to intermediate ligands (10< log $K^{cond}_{Fe'L}$ < 12) and L_3 to weak ligands (log $K^{cond}_{Fe'L}$ < 10; Gledhill and Buck, 2012). These classes roughly correspond to the three major types of ligands identified in the environment, with siderophores falling into the L_1 class, HS into L_2, and EPS into L_3 (Hassler et al., 2017), although classes can overlap and remain a simplistic view of the Fe organic speciation. For example, accumulating evidence suggests HS encompass multiple binding sites across the L_1 and L_2 ligand classes and are able to compete with siderophores (Fourrier et al., 2022; Gledhill et al., 2022; Sukekava et al., 2024). The log $K^{cond}_{Fe'L}$ of specific functional groups has also been determined and their contribution to the pool of Fe-binding ligands highlighted (e.g., Santana-Casiano et al., 2000; González et al., 2019). However, in natural samples, the binding ability of the DOM is a continuum of log $K^{cond}_{Fe'L}$ values rather than a specific value as determined by CLE-AdCSV (Town and Filella, 2000). Indeed, the log $K^{cond}_{Fe'L}$ determined by CLE-AdCSV is an average value of all the titrated ligands, and it is not well understood how the log $K^{cond}_{Fe'L}$ of each compound or functional group is weighted during the titration of a continuum of ligands. In all, while being mindful of limitations, this classification remains a helpful way to interpret and compare Fe-binding ligand data.

Fe-binding ligand distribution is often characterized by high L_{Fe} and $K^{cond}_{Fe'L}$ surface waters with maximum values coinciding with the chlorophyll-a maximum, and progressive decrease from the surface

until the oxycline due to adsorption onto particles (Kondo et al., 2007: Ibisanmi et al., 2011; Gledhill and Buck, 2012; Gerringa et al., 2015; Bundy et al., 2016). Phytoplankton production of L_{Fe} has been widely attested by concomitant L_{Fe} and chlorophyll-a fluorescence (Gledhill and Buck, 2012; Gerringa et al., 2015; Bundy et al., 2016; Hassler et al., 2017). L_{Fe} depletion can sometimes be observed in surface waters due to photochemical breakdown of ligands, but this process is highly variable (Barbeau et al., 2001; Powell and Wilson-Finelli, 2003; Croot et al., 2004), while atmospheric deposition such as dust and rain supply Fe-binding ligands to surface waters (Gerringa et al., 2006; Rijkenberg et al., 2008; Cheize et al., 2012; González et al., 2022). Below the oxycline, L_{Fe} increases through the breakdown of biogenic material by heterotrophic bacteria (Boyd et al., 2010) which produce Fe-binding ligands that are mostly attributed to HS due to their intermediate log $K^{cond}_{Fe'L}$ and relatively homogenous distribution in deep waters (van den Berg, 1995; Witter and Luther, 1998; van den Berg, 2006; Dulaquais et al., 2018; Whitby et al., 2020b). Heterotrophic bacteria produce siderophore compounds, associated with the breakdown of sinking particles (Cordero et al., 2012; Bundy et al., 2016; Velasquez et al., 2016; Hassler et al., 2017) while the resuspension of sediments and hydrothermal activity are important sources of Fe-binding ligands to bottom waters (Jones et al., 2011; Gerringa et al., 2015; Tagliabue and Resing, 2016. Buck et al., 2018; Sukekava et al., 2023).

The classification of binding strength presented by Gledhill and Buck (2012) has been used to compare basin scale datasets of Fe-binding ligand characteristics from samples collected in the West and North Atlantic Oceans (Buck et al., 2015; Gerringa et al., 2015), and in the Tropical Pacific Ocean (Buck et al., 2018). In addition to a general trend of decreasing log $K^{cond}_{Fe'L}$ and increasing L_{Fe} with depth and water mass aging, L_1 has been shown to correlate with increasing DFe concentrations around hydrothermal vents in the Atlantic and Pacific Oceans (Buck et al., 2015; Buck et al., 2018) and with vent communities supplying siderophores specifically (Hoffman et al., 2023). L_1 ligands were also observed in hydrothermal fluid samples collected at the New Hebrides Island arc in the Western Tropical South Pacific (WTSP) Ocean with concentrations reaching the micromolar range for L_{Fe} and DFe (Kleint et al., 2016). These authors also detected weaker L_3 ligands in several WTSP Ocean hydrothermal samples, while intermediate L_2 ligands have been observed in hydrothermal plumes in the Mariana Back Arc of the Western Pacific (Wang et al., 2021) and in the Southern Ocean (Hawkes et al., 2013).

In hydrothermal fluids, concentrations of DFe and Fe-binding ligands can vary from the nM to µM range depending on the initial fluid chemistry (e.g., Hawkes et al., 2013; Resing et al., 2015; Kleint et al., 2016; Tilliette et al., 2022). The chemistry of hydrothermal fluids is geographically diverse and variable over time, and sampling in such dynamic environments is challenging, making hydrothermal Fe-binding ligand chemistry complicated to constrain (Kleint et al., 2019). In terms of DFe, it is well known that the free ionic Fe^{2+} initially found in hot and acidic hydrothermal fluid is quickly oxidized and precipitated during mixing with seawater by the formation of Fe-sulfides and Fe-oxyhydroxide minerals (Millero et al., 1987; Kleint et al., 2017), but it can also be adsorbed on organic matrices or stabilized by Fe-binding ligands (Toner et al., 2009; Sander and Koschinsky, 2011; Kleint et al., 2017; Santana-Casiano et al., 2022). The inorganic transport of DFe as Fe-sulfide nanoparticles and colloidal Fe-oxyhydroxides has also been observed and the accessibility of these fractions to Fe-binding ligands is controversial (Yücel et al., 2011; Yücel et al., 2021). Recent work showed that electroactive humic component of Fe-binding ligands (L_{FeHS}) can solubilize a large fraction of freshly formed Fe-oxyhydroxides, but this decreases rapidly with aging of the inorganic particles. This experiment was performed at constant temperature and pH (Dulaquais et al., 2023) but is yet to be addressed under variable physicochemical conditions such as during the dilution of hydrothermal plumes. The variable interplay between the inorganic and organic processes impacting the amount of DFe stabilized and transported away from hydrothermal sources is an essential aspect to constrain, as vents could account for an estimated 12-22% of the deep-ocean DFe budget (Bennett et al., 2008).

In the WTSP Ocean, the subduction of the Pacific Plate beneath the Australian Plate has formed the Tonga volcanic arc, one of the most seismically active subduction zones which consequently hosts a high density of submarine volcanoes and associated hydrothermal vents (German et al., 2006; Timm et al., 2013). The submarine hydrothermal activity fuels the area with DFe (Guieu et al., 2018; Tilliette et al., 2022), supporting the growth of nitrogen fixers (diazotroph). Some of the highest rates of dinitrogen (N_2) fixation ever observed in open ocean have been measured in the area (Bonnet et al., 2017; Bonnet et al., 2018), specifically in the Lau basin, but the mechanistic link between shallow hydrothermal Fe inputs and intense N_2 fixation has only been recently demonstrated (Bonnet et al., 2023b). The possibility to investigate the connection between hydrothermal sourcing of trace metals and the fueling of diazotroph activity motivated the GEOTRACES process cruise GPpr14 (TONGA cruise; Guieu and Bonnet, 2019, https://doi.org/10.17600/18000884), which crossed the Melanesian basin, the Lau basin, and the western part of the South Pacific gyre between October 31st and December 5th, 2019.

The TONGA transect presented the opportunity to quantify, for the first time in this region, L_{Fe} and log $K^{cond}_{Fe'L}$, and to explore the relation between Fe-binding ligands and DFe distribution in the area. Several complementary analyses targeting specific fractions of the DOM pool were also conducted, notably regarding HS-like material. HS are of specific interest as they have been estimated to represent around 50% of the DOM (Zigah et al., 2017; Fourrier et al., 2022) with a smaller fraction, around 5% of DOC, able to bind with Fe (Laglera and van den Berg, 2009; Fourrier et al., 2022). The diversity of the HS-like material is responsible for various properties, notably in terms of electroactivity and photo-reactivity, the latter in terms of absorbance and fluorescence (CDOM and FDOM, respectively). It has been shown that electroactive Fe-HS complexes (L_{FeHS}) are able to control Fe solubility in a variety of systems (Dulaquais et al., 2018; Sukekava et al., 2018; Laglera et al., 2019; Whitby et al., 2020b; Fourrier et al., 2022). Similarly, the HS-like fluorescent component of the DOM (HS-like FDOM) often correlates with DFe distributions (Tani et al., 2003; Ohno et al., 2008; Hioki et al., 2014; Jia et al., 2021).

The complementarity and/or overlapping of these two different operationally defined fractions of HS is, however, not well constrained. While covariation of L_{FeHS} and HS-like FDOM is observed in estuarine waters (Lee et al., 2023), opposite trends are observed in open ocean surface waters, suggesting that the microbial aerobic respiration of the DOM increases the fluorescent yields and lowers the electroactivity of the HS fraction of the DOM with depth (Fourrier et al., 2022).

We present here the results obtained for Fe-binding ligand characteristics during the TONGA cruise using the same competitive ligand method that was used in both the Equatorial Pacific (Buck et al., 2018) and the North Atlantic Oceans (Buck et al., 2015). We relate the distribution observed in L_{Fe} and log K'^{cond}_{FeL} to other parameters such as DFe, apparent oxygen utilization (AOU), dissolved organic carbon (DOC), L_{FeHS} and HS-like FDOM to identify the processes impacting Fe-binding ligands and HS-like compounds, and to constrain their impact on DFe distribution in the WTSP Ocean.

Material and methods

Sampling strategy during the TONGA cruise

Samples were collected during the TONGA GEOTRACES process study in the WTSP Ocean (GPpr14). The section presented here is composed of 8 main stations between the Melanesian basin and the South Pacific gyre (Figure 1), with additional casts performed around two known hydrothermal sites, LD 5 and LD 10, identified by acoustic detection (Bonnet et al., 2023b). Here, we present data for one of the hydrothermal stations, LD10, for which stations LD 10-T1, T2 and T3 were sampled at 15, 8, and 2 km from the hydrothermal source, respectively. The western part of the Lau basin was sampled at stations 4, 11 and 12. Stations 2 and 3 were located in the Melanesian basin, on the western side of the transect. Stations 6, 7 and 8 were located in the South Pacific gyre for comparison with oligotrophic conditions. Station 6 was located East of the Tonga arc, but on the western side of the Tonga trench, where the topography is expected to limit water exchange between the Lau basin and the South Pacific gyre (Talley et al., 2011).

Sample collection and storage

The seawater samples for DFe and Fe-binding ligand analyses were collected using GO-FLO bottles mounted on a Trace Metal Clean Rosette (TMR; General Oceanics Inc., Model 1,018 Intelligent Rosette) transferred into a trace metal clean van (class-100) and pressurized with 0.2 µm-filtered nitrogen (Air Liquide) for sub-sampling. GO-FLO bottles and all the sampling material were cleaned before the cruise following the GEOTRACES cookbook (Cutter et al., 2017). Dissolved fractions for the analysis of DFe and Fe-binding ligands were sampled through 0.45 µm acid-cleaned polyethersulfone filters (Supor). For DFe, the cleaning procedure of the bottles used for seawater collection, sample storage, handling and analyses are detailed in Tilliette et al. (2022).

For Fe-binding ligands, 250 mL low-density polyethylene (LDPE; Nalgene) bottles were left to soak for one week in a 2% surfactant bath (Decon), one week in a 1 M HCl bath (laboratory reagent grade 32%, FisherScientific) and one week in a 0.1 M HCl bath, before being left to dry in a laminar flow hood (Class-100) and double-bagged. Between each step, the bottles were rinsed 5-times with Milli-Q water (resistivity > 18.2 MΩ.cm). The samples were collected after rinsing the bottles 3 times with around 20 mL of filtered sample and frozen to -20°C immediately after sampling. Samples were thawed at room temperature in the dark and swirled before analysis.

The seawater samples for dissolved oxygen (O_2), DOC and FDOM analyses were collected in glass bottles from a classical rosette equipped with twenty-four 12 L Niskin bottles. The samples were immediately filtered under low vacuum (< 50 mm Hg) through pre-combusted 25-mm fiberglass filters (GF/F, size pore: ~0.7 µm, Whatman) using glass filtration apparatus. For DOC analyses, filtered samples were transferred into 10 mL glass ampoules and acidified with 20 µL of sulfuric acid (H_2SO_4, 95-98%, Sigma-Aldrich). Ampoules were then flame-sealed and stored in the dark at 4°C pending analysis. For FDOM measurements, filtered samples were

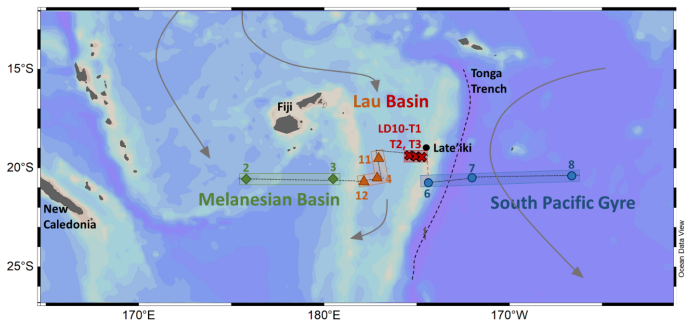

FIGURE 1
Map of the studied area, cruise transect and sampling stations for Fe-binding ligand characteristics during the TONGA cruise (GPpr14; Guieu and Bonnet, 2019, https://doi.org/10.17600/18000884). The small-dashed black line corresponds to the transect drawn to present the data. Colors, symbols and shapes correspond to the splitting of the dataset for presentation and interpretation. Geographic features (in black) include the main islands, the Tonga trench and the location of the Late'iki site.

transferred into 100 mL amber glass bottles with clean Teflon-lined caps and stored at -20°C in the dark before analysis. Before use, all glassware was left to soak for 24 h in a 1 M HCl bath, rinsed thoroughly with Milli-Q water, then combusted at 450°C for 6 h, and finally rinsed three times with the respective sample before filling.

Analyses

Detailed description of the analysis and interpretation for L_{FeHS}, CDOM/FDOM and DFe can be found in connected papers (Tilliette et al., 2022; Dulaquais et al., 2023; Tedetti et al., in prep.[1]). For L_{FeHS}, CDOM/FDOM, DFe, dissolved organic carbon and Fe-binding ligands, the seawater was filtered in-line using an acid-cleaned 0.45 µm polyethersulfone filter (Supor).

Dissolved oxygen

O_2 concentration was measured following the Winkler method (Winkler, 1888) modified by Carpenter (1965) and Carritt and Carpenter (1966), with potentiometric endpoint detection using a Titrino 716 DMS (Metrohm; Oudot et al., 1988). The recommendations from Langdon (2010) were followed for sampling, reagent preparation and analysis. The thiosulfate solution was calibrated by titrating it against a potassium iodate certified standard solution of 0.0100 N (CSK standard solution; WAKO). The reproducibility, expressed as the standard deviation of replicate samples, was 0.8 µM (n = 15, mean = 195.4 µmol kg^{-1}. Apparent Oxygen Utilization (AOU, in µM) was calculated from the difference between O_2 solubility concentration (at P = 0 dbar) estimated with the Benson and Krause coefficients (Garcia and Gordon, 1992) and *in-situ* O_2.

Dissolved organic carbon

DOC concentration was measured in two ampoule replicates on a Shimadzu TOC-V analyzer according to Sohrin and Sempéré (2005) and Fourrier et al. (2022). Before injection, the GF/F-filtered and acidified samples were bubbled for 2 min with CO_2-free air to purge inorganic carbon. The accuracy and system blank of the instrument were determined by the analysis of certified water references (batch 19, lot #03–19, Hansell Laboratory, Miami, USA). The nominal precision of the analysis procedure was within 2%.

Iron-binding ligands

The theory of the CLE-AdCSV approach has been thoroughly detailed in previous work (e.g., Gledhill and van den Berg, 1994; Rue and Bruland, 1995; Abualhaija and van den Berg, 2014; Gerringa et al., 2014; Pižeta et al., 2015; Mahieu, 2023). We used the added ligand salicylaldoxime (SA; 98% Acros Organics) at 25 µM following the procedure described in Mahieu (2023). For data interpretation the side reaction coefficient (β_{FeSA_2}) of 11.1 leading to $\alpha_{Fe'AL}$ of 79 was used, as in previous basin scale work (Buck et al., 2007; Buck et al., 2015; Buck et al., 2018). A borate buffer (boric acid, analytical reagent grade, Fisher Scientific) at 1 M in 0.35 M of ammonia (NH_4OH; 29% Laporte) was used at 10 mM for a final pH of 8.2 in the sample (Rue and Bruland, 1995; Buck et al., 2007; Abualhaija and van den Berg, 2014; Buck et al., 2015; Buck et al., 2018; Mahieu, 2023). The following equilibration procedure was applied: natural ligands were left to equilibrate with increasing additions of DFe in buffered samples for a minimum of 2 h, with SA added at least 15 min before the start of the analysis. The titrations were performed with 16 aliquots, with DFe additions of 0, 0, 0.75, 1.5, 2.25, 3, 3.5, 4, 4.5, 5, 6, 7, 8, 10, 12 and 15 nM. The DFe additions were adjusted from Buck et al. (2018) after preliminary tests showing emergence of the $FeSA_2$ reduction current around 3 nM of DFe added (nMeqFe). The sensitivity was estimated using the three last linear additions of the titration of the seawater sample. The apparatus and procedures for the conditioning of cells and tubes (Trace Metal Free, Labcon) are described in Mahieu (2023) and Mahieu et al. (2024), along with a detailed description of the set up and data treatment.

Statistical treatments

The variables considered in this study did not follow a normal distribution, and were inter-dependent and non-linear, calling for the application of non-parametric statistical methods. The significance of the difference between water masses and regions was tested using the Wilcoxon-Mann-Whitney test, using the Python function 'scipy.stats.mannwhitneyu'. The difference between two samples is defined by p values< 0.05. Full p value matrices can be found in Supplementary Information 2, 3. The Spearman rank correlation (ρ; Spearman, 1904) analysis was chosen to compare the Fe-binding characteristics and the other parameters described hereafter as it has been previously used for the investigation of Fe-binding ligands and FDOM (e.g., Heller et al., 2013; Genovese et al., 2018). The calculation was performed using the Python function 'scipy.stats.spearmanr' (version 3.9). For the Spearman test, ρ from 0.00 to 0.19 were attributed to very weak correlation, ρ from 0.20 to 0.39 to weak correlation, ρ from 0.40 to 0.59 to moderate correlation, ρ from 0.60 to 0.79 to strong correlation, and ρ from 0.80 to 0.99 to very strong correlation (ρ = 1.00 being a perfectly monotonic correlation). We considered the correlation to be significant for p< 0.0001, at least one order of magnitude lower than in other studies discussing Spearman correlation matrices including Fe-binding ligands data to ensure a strong level of confidence in the interpretation of the dataset (e.g., Heller et al., 2013; Genovese et al., 2018; bold values in Table 1).

Results

Hydrography

The water mass composition and circulation have been thoroughly described by Tilliette et al. (2022). We present here a simplistic description of the water column based on O_2 fluctuations (Figures 2, 3A). During the TONGA transect, surface waters were characterized by high O_2 due to primary production and

1 Tedetti, M., Guigue, C., Mahieu, L., Fourrier, P., Dulaquais, G., Benavides, M., et al. Chromophoric and fluorescent dissolved organic matter in the Western Tropical South Pacific.

TABLE 1 Mean values for DFe, L_{Fe}, L_{FeHS}, DOC and HS-like FDOM for the mixed layer and deep waters.

Considered data	DFe (nM)	L_{Fe}	L_{FeHS}		DOC (µgC L^{-1})	HS-like FDOM (QSU)
		(nMeqFe)	(nMeqFe)	(µgeqC L^{-1})		
Mixed layer	0.45 ± 0.50	5.3 ± 1.4	1.3 ± 0.7	40.2 ± 23.1	883 ± 53	1.7 ± 0.5
	n = 60	n = 24	n = 31		n = 40	n = 36
Deep waters	0.51 ± 0.30	5.2 ± 1.1	0.5 ± 0.3	12.5 ± 10.1	580 ± 126	2.5 ± 0.7
	n = 178	n = 79	n = 75		n = 129	n = 94

Estimates of Fe-binding equivalent concentrations for L_{FeHS} were calculated using 16.4 nmolFe.mgFA^{-1} from Sukekava et al. (2018). Estimates of carbon equivalent were calculated using the official value of 0.5244% gC/gSRFA (International Humic Substances Society).

atmospheric exchange enhanced by physical mixing in the mixed layer, which ranged from 70 to 140 m deep during the cruise. The water mass below the mixed layer corresponds to the Subtropical Underwater (STUW) in the South Pacific gyre and Lau basin, and to the Western South Pacific Central Water (WSPCW) in the Melanesian and Lau basins. Both STUW and WSPCW are characterized by a maximum of salinity (S) and minimum of O_2 around 200 m, the latter being due to microbial respiration (e.g., remineralization). Below these two water masses is the Antarctic Intermediate Water (AAIW), with a S minimum and an O_2 maximum (Figure 2) also corresponding to the thermocline at around 650 m depth (Kawabe and Fujio, 2010; Talley et al., 2011). Below the AAIW, S increases and temperature decreases. O_2 concentrations below 150 µmol kg^{-1} is characteristic of the Pacific Deep Water (PDW), originating from the upwelling of Antarctic Bottom Water (AABW) in the middle of the Pacific Ocean, mixing with the O_2 depleted waters from the Pacific oxygen minimum zone and with the deep waters from the oxygen minimum zone off Chile in the Eastern South Pacific Ocean (Silva et al., 2009). AAIW and PDW supposedly reach the Lau and Melanesian basins from a branch of the South Pacific gyre flowing from the North of the Lau basin following south-westward currents (Summers and Watling, 2021; Tilliette et al., 2022). However, the circulation in and between the Lau and Melanesian basins is variable, and northeast currents have been observed in the Melanesian basin (Komaki and Kawabe, 2007). In the South Pacific gyre, deeper than 3500 m, O_2 increases to around 190 µmol kg^{-1} due to the intrusion of Lower Circumpolar Deep Water (LCDW) from the southeast (Kawabe and Fujio, 2010). Over the whole transect, O_2 concentrations range from 121 µmol kg^{-1} in the PDW of the Lau basin, to 211 µmol kg^{-1} in the AAIW of the South Pacific gyre (Figure 3A).

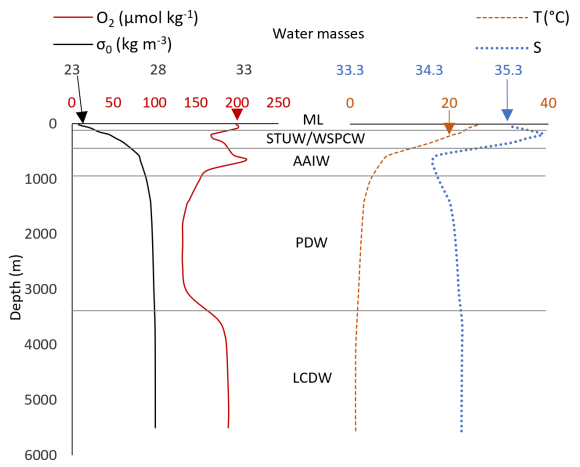

FIGURE 2
Profile of σ_0 (black full line), O_2 (red full line, diamond), T (temperature, orange dash line), and S (salinity, blue dot line) at station 7 with the water mass separations applied in this study, namely the mixed layer (ML), the Subtropical Underwater (STUW), the Western South Pacific Central Water (WSPCW), the Antarctic Intermediate Water (AAIW), the Pacific Deep Water (PDW) and the Lower Circumpolar Deep Water (LCDW). The WSPCW, not present at ST7, is also mentioned to not omit any water mass investigated in this work.

DOC

The distribution and range of DOC concentrations measured in this study are typical to what has been previously reported in the Tropical South Pacific Ocean (e.g., Buck et al., 2018; Fourrier et al., 2022). DOC concentrations ranged from 35 to 80 µM (Figure 3B), with the highest values observed in the mixed layer typical of primary production, ranging from 60 to 80 µM. DOC concentrations decreased with depth due to microbial remineralization to reach typical deep-water values, ranging from 35 to 45 µM in the PDW (and LCDW at stations 7 and 8). Typical deep values are reached within the STUW/WSPCW in line with microbial aerobic respiration at most stations (Figures 2, 3), except at stations 3, 4 and 7, where the concentrations gradient reaches depths of up to 1000 m.

DFe

DFe distribution has been thoroughly described in Tilliette et al. (2022). For the dataset considered in this work, DFe concentrations ranged from 0.13 nM in the mixed layer of the Western Lau basin to 3.13 nM in the mixed layer of the Eastern Lau basin (Figure 4A). Higher DFe concentrations, up to 50 nM, were observed at another location (station 5; Tilliette et al., 2022), however, no data is available for Fe-binding ligand characteristics at this station. The Melanesian basin and the South Pacific gyre show DFe depletion in surface waters attributed to predominant removal processes and limited supply

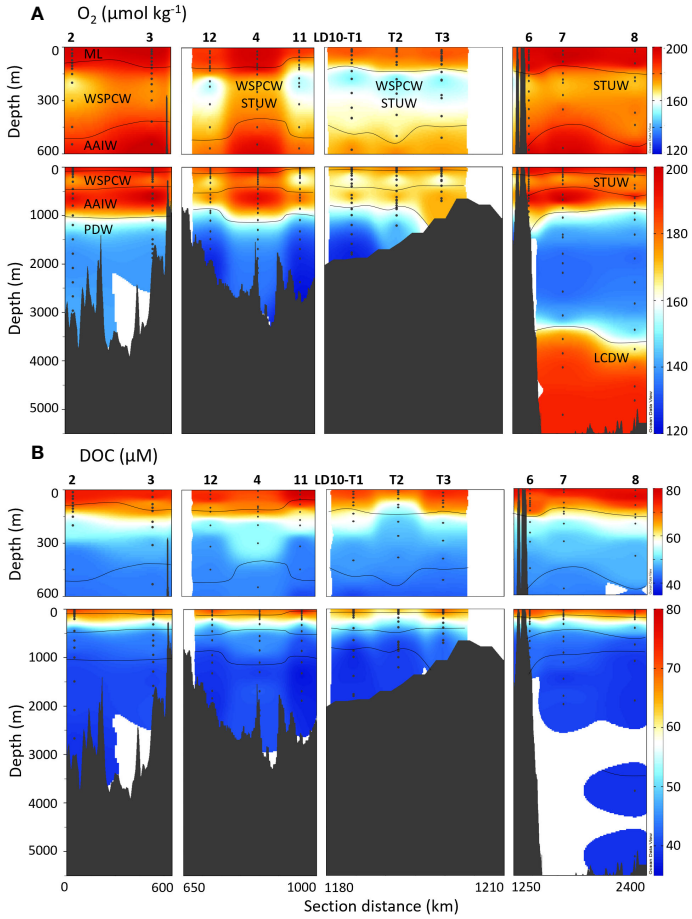

FIGURE 3
Top 600 m and full depth distribution of **(A)** O_2 and **(B)** DOC concentrations for the TONGA cruise (GEOTRACES GPpr14). The approximative water mass boundaries are defined by O_2 (see Figure 2). The section is separated in four segments with, from left to right, the Melanesian basin (stations 2 and 3), the Western Lau basin (stations 12, 4 and 11), the Eastern Lau basin (stations LD10-T1, LD10-T2 and LD10-T3) and the South Pacific gyre (stations 6, 7, and 8). See Figure 1 for more details on the sampling locations.

(Tilliette et al., 2022), and an increase at depth with mineralization in the range of previously reported open-ocean values (e.g., Tagliabue et al., 2012; Resing et al., 2015; Tonnard et al., 2020). The Western Lau basin shows similar DFe depletion in subsurface waters except for an enhancement at station 11 in the WSPCW. Another strong DFe enhancement is observed in the mixed layer of the Eastern Lau basin. The highest values observed in this study are considered to be solely hydrothermal, while deep waters of the Eastern and Western Lau basin show anomalies of DFe enrichment related to either remineralization, island effect, benthic fluxes and/or hydrothermal activity (up to 1.5 nM; Tilliette et al., 2022). Similar concentrations were previously reported for bottom enrichment related to hydrothermal and shelf inputs (e.g. Klunder et al., 2011; Klunder et al., 2012; Resing et al., 2015; Tonnard et al., 2020).

HS-like FDOM

The HS-like FDOM component identified here through EEM/PARAFAC (λ_{Ex1}, $\lambda_{Ex2}/\lambda_{Em}$: 235, 315/436 nm), which are referred to as peaks A + M/C (Coble, 1996; Hudson et al., 2007; Coble et al., 2014) or component 3 (Ishii and Boyer, 2012) in different DOM fluorophore classifications, has been reported in various coastal and marine environments (Ferretto et al., 2017; Tedetti et al., 2020). HS-like FDOM content ranged from 1 QSU in the mixed layer of the Western Lau basin to 4 QSU in the PDW of the Melanesian basin (Figure 4B). HS-like FDOM systematically increased with depth, reflecting its loss by photobleaching or extinction of its fluorescence in the photic layer, and its production in deep waters through the remineralization of organic matter (Nelson et al., 2010; Heller et al., 2013; Yamashita et al., 2017). The depth profiles of HS-like FDOM along the transect (i.e., lower values in surface waters, higher at depth) were thus opposite to those of DOC, a phenomenon already reported for the Atlantic and North Pacific Oceans, as well as at our station 8 in the South Pacific gyre (Omori et al., 2010; Stedmon and Álvarez-Salgado, 2011; Yamashita et al., 2017; Cao et al., 2020; Fourrier et al., 2022). High HS-like FDOM signals were observed in the deep waters at stations 2, 3, 4, LD10-T1, LD10-T2, the highest signal being observed at station 8.

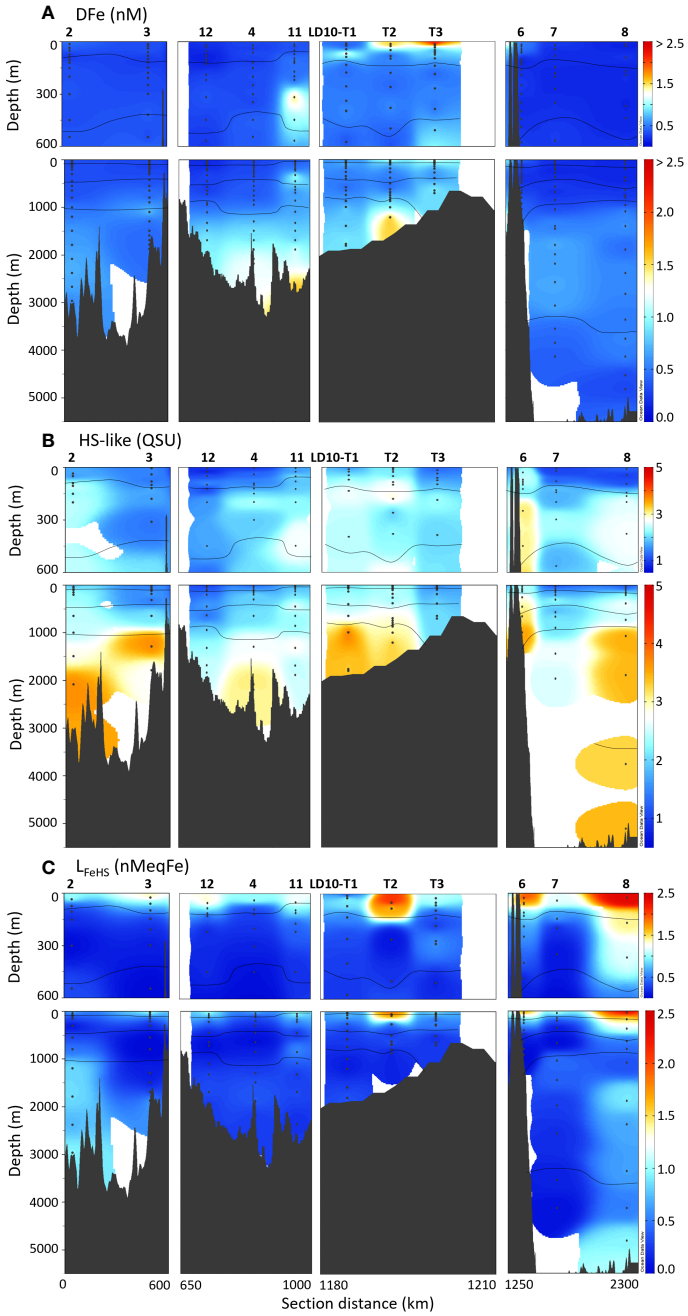

FIGURE 4
Top 600 m and full depth distribution of **(A)** DFe, **(B)** HS-like FDOM and **(C)** L_{FeHS} for the TONGA cruise (GEOTRACES GPpr14). The approximative water mass boundaries are defined by O_2 (see Figures 2, 3A). The section is separated following the description of the studied area (Figure 1).

L_{FeHS}

Details on the distribution and determination of electroactive HS (eHS) in the area during the same cruise are fully described elsewhere (Dulaquais et al., 2023). We show here the eHS determined by complexation with Fe (Dulaquais et al., 2023), referred to as L_{FeHS}, for comparison with HS-like FDOM and Fe-binding ligands (Figure 4C). L_{FeHS} are expressed in nMeqFe following the estimated Fe binding capacity of the fulvic acid standard used (16.4 nmolFe mgFA^{-1}; Sukekava et al., 2018). For the dataset considered in this work, L_{FeHS} concentrations ranged from 0.2 to 2.4 nMeqFe with a mean value of 0.6 ± 0.5 nMeqFe (n = 106). The highest values were observed in the mixed layer at all stations and concentrations decreased with depth down to relative minima (between 0.2 and 0.4 nMeqFe) in intermediate waters. Below, in the abyssal waters, concentrations increased again to values higher than 0.6 nMeqFe. Comparatively, high L_{FeHS} concentrations were detected through the entire water column in the oligotrophic waters of the South Pacific gyre collected at station 8 (Fourrier et al., 2022).

Fe-binding ligands

A single class of Fe-binding ligand was detected in all samples, with a mean L_{Fe} of 5.2 ± 1.2 nMeqFe and mean log $K^{cond}_{Fe'L}$ of 11.6 ± 0.4 (n = 103; Figures 5A, C, respectively). Log $K^{cond}_{Fe'L}$ ranged from 10.5 ± 0.2 in the AAIW of the Melanesian basin (station 2) to 12.7 ± 0.3 in the PDW of the Western Lau basin (station 11), encompassing the three ligand classes defined by Gledhill and Buck (2012). As such, 84% of our samples fall in the L_2 class, 13% in the L_1 class, and 4% in the L_3 class. L_{Fe} ranged from 2.8 ± 0.4 nMeqFe in the mixed layer of the Melanesian basin (station 2) to 9.3 ± 1.0 nMeqFe in the PDW of the Melanesian basin (also station 2). The co-occurrence of the maximal and minimal values at the same station illustrates the variability of the processes impacting the DOM in the area, discussed hereafter. High values of L_{Fe} reaching up to 9.0 nMeqFe were observed at two other locations, in the AAIW above the Tonga ridge in the South Pacific gyre (station 6), and in the mixed layer in the Lau basin (station LD 10-T3). At stations 2 and 6, higher L_{Fe} coincided with increased HS-like FDOM (Figure 4B).

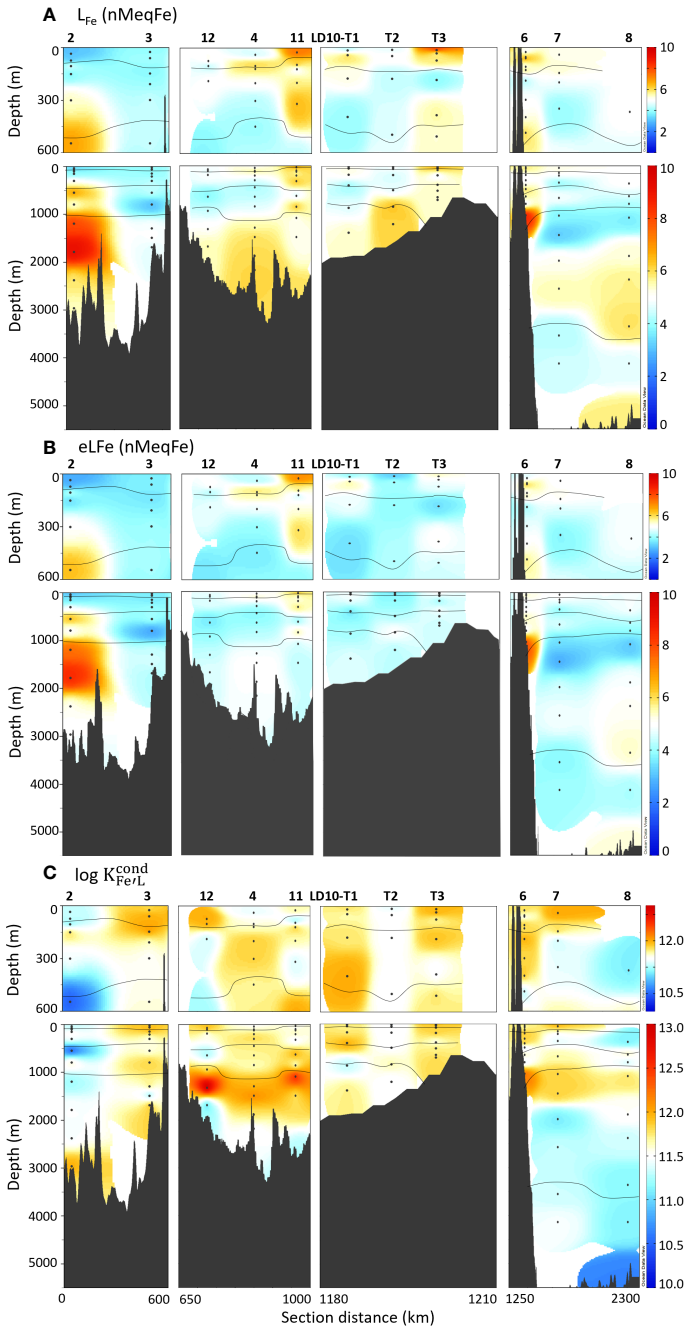

FIGURE 5
Top 600 m and full depth distribution of **(A)** L_{Fe}, **(B)** eL_{Fe} and **(C)** log $K^{cond}_{Fe'L}$ for the TONGA cruise (GEOTRACES GPpr14). The approximative water mass boundaries are defined by O_2 (see Figures 2, 3A). The section is separated following the description of the studied area (Figure 1).

10.3389/fmars.2024.1304118

In all samples, L_{Fe} was present in unusually large excess compared to DFe, with excess ligand (eL_{Fe} = L_{Fe} - DFe) ranging from 2.6 to 8.6 nMeqFe (Figure 5B) and a mean eL_{Fe} of 4.6 ± 1.1 nMeqFe (n = 103).

Fe-binding ligands show relatively constant L_{Fe} and log $K^{cond}_{Fe'L}$ values along water masses and regions over the whole transect (Figure 6), but a few significant differences were observed (Mann-Whitney test, $p< 0.05$; Supplementary Material 2, 3). The significant differences for L_{Fe} were observed between the low values of the mixed layer of the Melanesian basin and the other regions, and between the high values of the PDW and both the mixed layer and the STUW/WSPCW in the Melanesian basin. Log $K^{cond}_{Fe'L}$ was significantly lower in the LCDW in the South Pacific gyre and all other water masses, suggesting specific Fe-binding characteristics of the DOM in this deep water mass.

Discussion

L_{Fe} and log $K^{cond}_{Fe'L}$ distribution in the WTSP

Our eL_{Fe} values (mean = 4.6 ± 1.1 nMeqFe) are c.a. 2.5 times higher than the average reported in the Eastern and Central Tropical South Pacific Oceans (Buck et al., 2018) using exactly the same experimental procedure. The large fraction of eL_{Fe} belonging to the L_2 class throughout the water column suggests a rather homogenous Fe-binding ability of the DOM, while the decreasing DOC concentration along the water column infers a refractory nature of the binding sites and an increase in binding site density with depth. We find that the ligand pool is dominated by L_2 ligands even though we use a high detection window, which can favor detection of the strongest ligands and miss contributions from weaker ligands. In comparison, it was found in the Eastern and Central Tropical South Pacific Oceans that L_1 ligands were generally in excess compared to DFe in the first 1000 m, while excess L_2 and L_3 increased in deeper waters (Buck et al., 2018). The ligand distribution observed in these environments reflects the biological production of strong L_1 in upper waters, and the loss and saturation of these L_1 ligands as DOM is remineralized, resulting in increasing DFe and weaker L_2 and L_3 ligand concentrations in deep waters. In our study, a decrease in log $K^{cond}_{Fe'L}$ with depth was observed in the South Pacific gyre, but without change of ligand class, and no change in log $K^{cond}_{Fe'L}$ in the Melanesian and Lau basins (Figures 5, 6).

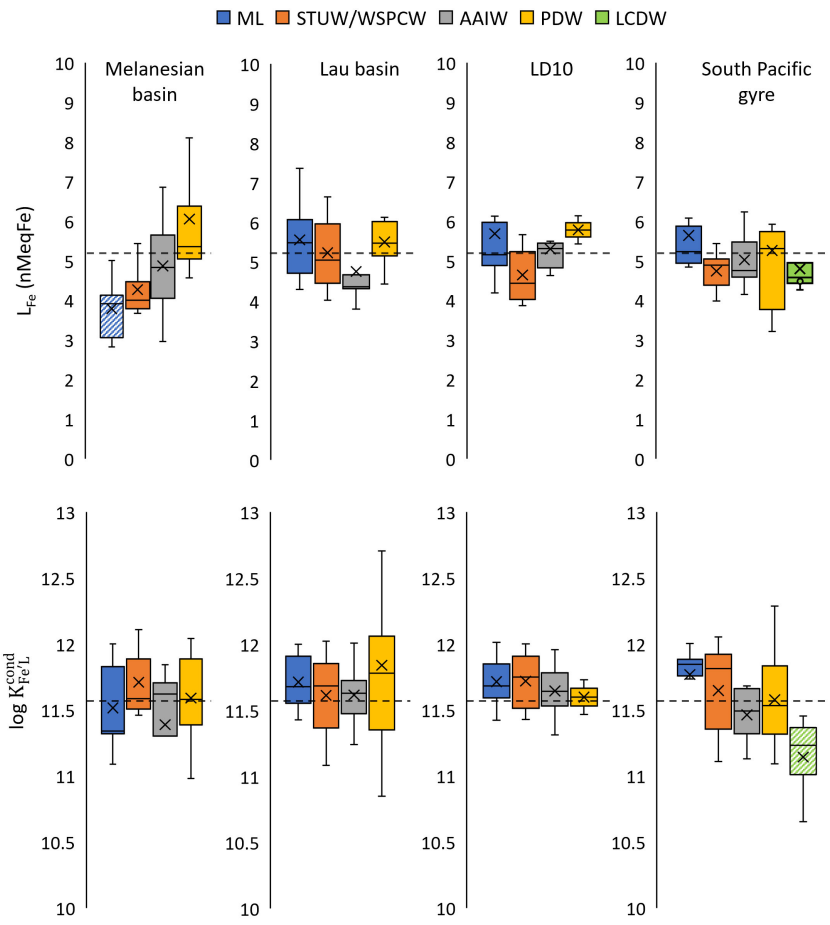

FIGURE 6
Box and Whiskers plots of L_{Fe} and log $K^{cond}_{Fe'L}$ split by the regions and water masses. The mean values of the entire dataset are represented by black dot lines. The hatched boxes correspond to water mass being significantly different compared to the same water mass in other regions (Wilcoxon-Mann-Whitney test, $p < 0.05$). Water mass acronyms can be found in Figures 2, 3A.

The progressive decrease in log $K^{cond}_{Fe'L}$ with increasing depth and increasing distance from the Lau basin gives the impression of a dilution gradient from stronger to weaker ligands into the South Pacific gyre and within the mixed layer of the Melanesian basin (Figures 5, 6, Supplementary Information 3), even though the South Pacific gyre is largely isolated from the Lau basin waters by the Tonga ridge, as seen in DFe and diazotroph abundance (Lory et al., 2022; Tilliette et al., 2022; Figure 4A). Assuming that the DOM produced in the Lau basin has specific Fe-binding ligand properties and it disperses into the Melanesian basin and the South Pacific gyre, it would have to be decoupled from diazotrophic activity and DFe dispersion. This would be in line with previous studies suggesting faster turnover of DFe than Fe-binding ligands, the latter having a much longer residence time (Gerringa et al., 2015; Tagliabue et al., 2023). However, higher resolution is needed to better constrain the spreading of the DOM thought to originate from the recycling of the diazotroph that are thriving in the Lau basin (Bonnet et al., 2023a).

L_{Fe} production for trace metal detoxification

A strong production of L_{Fe} was observed in the surface waters at LD10-T3, related to a hydrothermal input of DFe (Tilliette et al., 2022; Figures 4A, 5B; Table 2). Interestingly, the L_{Fe} enhancement was only detected at the maximum DFe value and did not follow the linear dilution pattern showed by DFe with distance from the hydrothermal vent, suggesting that the amount of hydrothermally-sourced trace metals reached a concentration threshold triggering the production of Fe-binding ligands. The DFe enhancement did not reach toxic levels, therefore, the Fe-binding ligands detected could have been produced by the local plankton communities, including abundant diazotrophs, to neutralize toxic elements and not be Fe-specific/specifically produced to bind Fe. While HS can bind a range of metals, L_{FeHS} and HS-like FDOM did not increase at LD10-T3 (Table 2), and siderophores alone cannot be responsible for the increase in L_{Fe} and DFe since they are usually found at pM concentrations and have higher log $K^{cond}_{Fe'L}$ (Mawji et al., 2008; Bundy et al., 2018; Boiteau et al., 2019). On the other hand, bacterial production of EPS by species collected near hydrothermal vents has been reported as a mechanism for slowing the diffusion of toxic elements into the organism and participating in the scavenging of toxic trace metals (Rougeaux et al., 1996; Nichols et al., 2005; Moppert et al., 2009; Deschatre et al., 2013). Production of EPS showing Fe binding properties was also observed for the nitrogen fixer *Crocosphaera watsonii* collected during the TONGA cruise (C. Lory, unpublished). Our results call for further consideration of the potential implication of EPS for regulating the distribution of the hydrothermally-sourced Fe and other toxic elements in the surface waters of the WTSP Ocean. One must also keep in mind the possible implication of small inorganic forms of Fe to explain the short-distance transport of the DFe enhancement, as highlighted by Dulaquais et al. (2023) and Tagliabue et al. (2023), as well as enhanced scavenging and precipitation in hydrothermally-influenced waters, which may result in ligand unsaturation (Gerringa et al., 2015; Thuroczy et al., 2011).

Both the Melanesian basin and the South Pacific gyre show strong L_{Fe} production in several deep-water samples (Figures 5A, B). On the eastern side of the Tonga ridge, L_{Fe} production coincides with relatively high log $K^{cond}_{Fe'L}$ (Figure 5), high HS-like FDOM (Figure 4) and high tryptophan-like FDOM (Tedetti et al., in prep), while no change in L_{FeHS} nor DFe is apparent (Figure 4). In the Melanesian basin (particularly at station 2), increased L_{Fe} coincides with relatively low log $K^{cond}_{Fe'L}$ (Figure 5), high HS-like FDOM (Figure 4) and high thiol-like compounds (Portlock et al., this issue[2]) and increased L_{FeHS} and DFe (Figure 4). The increased L_{Fe}, thiol-like compounds and tryptophan-like FDOM could be related to the toxicity of hydrothermally sourced metals. Indeed, the production of thiol-like compounds was recently associated with the detoxification of hydrothermal fluid in a ship-board incubation experiment performed with WTSP waters (Tilliette et al., 2023). Regarding the tryptophan-like signal, abiotic processes can lead to the production of tryptophan in hydrothermal systems (Ménez et al., 2018), and benthic interaction could also be involved. More information is required to disentangle the sources of Fe-binding ligands and tryptophan-like FDOM at this location, and efforts should focus on identifying the metals preferentially bound by the DOM associated with hydrothermal activity.

TABLE 2 Values in surface samples (depth < 20 m) with distance from the hydrothermal site.

	LD10-T1 – 15 km	LD10-T2 – 8 km	LD10-T3 – 2 km
DFe (nM)	0.38	1.52	3.20
L_{Fe} (nMeqFe)	4.2 ± 0.6	4.7 ± 0.9	8.8 ± 0.7
log K^{cond}_{FeL}	11.8 ± 0.2	11.4 ± 0.3	11.9 ± 0.2
L_{FeHS} (nMeqFe)	1.2	2.2	1.1
HS-like FDOM (QSU)	1.8	2.1	1.3

Humic contribution to DFe stabilization and to the Fe-binding ligand pool

Previous studies have also found L_2 ligands to dominate the water column in the South Tropical Pacific (e.g., Buck et al., 2018; Cabanes et al., 2020). The L_2 ligand class is often considered to be humic-like (Gledhill and Buck, 2012; Hassler et al., 2017), and our averaged log $K^{cond}_{Fe'L}$ of 11.6 ± 0.4 corresponds to log $K^{cond}_{Fe'L}$ values reported for Suwannee River humic-acid standards (SRHA; 11.1-11.6; Laglera and van den Berg, 2009; Abualhaija and van den Berg, 2014; Abualhaija et al., 2015). While there was no correlation of Fe-

2 Portlock, G., Tilliette, C., Bonnet, S., Guieu, C., Whitby, H., and Salaun, P. Distribution and behaviour of reduced sulphur substances in the oligotrophic and hydrothermal waters of the Western South Tropical Pacific.

binding ligands with any parameters considered in this study, DFe showed the strongest correlation with HS-like FDOM (Table 3). Both DFe and HS-like FDOM increased in deep waters, with DFe being possibly complexed by HS-like FDOM as Fe(II) and/or Fe (III). Indeed, HS-like FDOM have been reported in hydrothermal fluids and are potentially capable of stabilizing Fe(II) (Yang et al., 2012; Sarma et al., 2018). However, it is not possible to estimate the proportion of L_{Fe} represented by the HS-like FDOM; for this, fluorescence quenching experiments, consisting of titrating the fluorophore with DFe, could be considered in future studies (Chen et al., 1994; Ohno et al., 2008).

The fluorescent and electroactive components of HS are thought to overlap, but the electroactive fraction of humic material, L_{FeHS} which comprises around 5% of the DOC in deep waters (Laglera and van den Berg, 2009; Dulaquais et al., 2018; Fourrier et al., 2022; Dulaquais et al., 2023), is thought to represent the metal-binding fraction specifically and can be compared to ligand concentrations directly. LFeHS have been shown to compose a large fraction of the Fe-binding ligands supplied during remineralisation (Whitby et al. 2020a). DFe has been shown to correlate with L_{FeHS} in some oceanic regions (Dulaquais et al., 2018; Laglera et al., 2019; Whitby et al., 2020b), and with AOU and HS-like FDOM in the Arctic and North Pacific Oceans (Tani et al., 2003; Hioki et al., 2014; Yamashita et al., 2017; Cao et al., 2020). On the other hand, DFe, L_{Fe}, L_{FeHS} and HS-like FDOM tend not to correlate in the Atlantic Ocean (Heller et al., 2013; Whitby et al., 2020b). The electroactive and fluorescent properties of HS have been thoroughly investigated at station 8 of the TONGA cruise (Fourrier et al., 2022), but in hydrothermal systems, the contribution of L_{FeHS} and HS-like FDOM to the Fe-binding ligand pool and DFe transport is currently unknown.

Here, L_{FeHS} represented 20 ± 13% of L_{Fe} in the mixed layer, and 8 ± 6% in deep waters (Table 1; error calculated with L_{FeHS} standard deviation); therefore, while the average log $K^{cond}_{Fe'L}$ across the samples is consistent with humic complexation, and DFe correlates well with humic-like FDOM, electroactive L_{FeHS} specifically do not dominate the Fe-binding ligand pool. While this may seem unexpected, this % contribution to L_{Fe} is similar to previous studies in the Pacific (2-51%; Cabanes et al., 2020; Whitby et al., 2020b), which tends to have a lower contribution of L_{FeHS} to the total ligand pool than in other ocean basins [e.g. L_{FeHS} comprise ~20-60% of the ligand pool in the Atlantic and Mediterranean (Dulaquais et al., 2018; Whitby et al., 2020b) and almost all of the ligand pool in parts of the Arctic Ocean (Slagter et al., 2017)]. While a large fraction of the ligand pool is not associated with electroactive HS, the L_{FeHS} that are present play an important role in Fe complexation, actively complexing around 30% of the DFe in these samples (Dulaquais et al., 2023).

Comparing the carbon content of the FA standard to DOC concentrations, L_{FeHS} represented 4.6 ± 2.6% of the DOC in the mixed layer (n = 17), and 2.2 ± 1.7% in deep waters (n = 60), similar to previously reported ranges (2 to 5%; Laglera and van den Berg, 2009; Dulaquais et al., 2018). While other, non-humic ligand groups may be contributing to the high L_{Fe}, the low correlation of L_{FeHS} with DFe, DOC, and AOU could be an indication of intense *in-situ* production of non-electroactive HS, corroborated by the low negative correlation between L_{FeHS} and HS-like FDOM (Table 3), characteristic of microbial respiration (Fourrier et al., 2022). Other metals can compete with Fe for L_{FeHS} complexation (e.g., Yang and van den Berg, 2009; Abualhaija and van den Berg, 2014; Whitby and van den Berg, 2015) and can also impact the HS-like FDOM (Zhao and Nelson, 2005). Non-specific ligands which contribute to L_{Fe} but can complex other metals could explain the unsaturation of the Fe-binding ligands produced in the Lau basin. The effect of competitive metals on Fe-binding ability of ligands, L_{FeHS} and HS-like FDOM would need to be investigated to better understand their potential impact on Fe speciation and cycling in hydrothermal environments.

Suggestions for future CLE-AdCSV studies

Toward tracing DOM characteristics with the reduction potential of the $FeSA_2$ complex

During AdCSV analyses, a variation in the peak potential of the reduction of the Fe-added ligand complex ($FeSA_2$) was

TABLE 3 Table of the Spearman rank correlation (ρ) of investigated parameters in this study.

	AOU (µM)	DOC (µM)	DFe (µM)	eL_{Fe} (nMeqFe)	log $K^{cond}_{Fe''L}$	L_{FeHS} (nMeqFe)
DOC (µM)	**-0.93 n = 161**					
DFe (µM)	**0.52 n = 238**	**-0.50 n = 151**				
eL_{Fe} (nMeqFe)	0.07 n = 103	0.00 n = 66	0.09 n = 103			
log $K^{cond}_{Fe'L}$	-0.18 n = 103	0.12 n = 66	-0.08 n = 103	-0.18 n = 103		
L_{FeHS} (nMeqFe)	-0.47 n = 120	0.46 n = 79	-0.23 n = 119	-0.05 n = 94	0.11 n = 94	
HS-like FDOM (QSU)	**0.71 n = 130**	**-0.73 n = 124**	**0.45 n = 116**	-0.03 n = 50	-0.17 n = 50	-0.26 n = 61

Blue corresponds to negative correlation, red to positive correlation, and white to absence of correlation. The intensity of the color is proportional to the strength of the correlation. Bold values correspond to p< 0.0001.

observed along the water column. The $FeSA_2$ peak potential ranged from -413 mV to -445 mV within the first 200 m (well-oxygenated mixed layer and most of the STUW/WSPCW), then decreased with depth to 1200 m where it reached a stable mean value of -473 mV down to the most abyssal waters (Figure 7). Also, in the mixed layer, the peak potential was significantly different between the Melanesian basin, the Lau basin, and the South Pacific gyre (Mann-Whitney test, $p< 0.05$; Supplementary Information 3). We hypothesize that the shift in reduction potential was due to an electroactive fraction of the DOM produced in the surface waters in the area. Indeed, the reduction of the metal complexed by the added ligand during AdCSV analysis happens at a specific potential following the Nernst equation (Nernst, 1889). The value of this potential is driven by i) the conditions of temperature, pH, and salinity, ii) the activity of the redox species, iii) the experimental conditions such as stripping scan rate, pulse time and pulse amplitude and iv) the adsorbed layer of organics accumulated on the electrode surface during the deposition step. Here, the temperature in the laboratory was controlled, the pH fixed by the addition of a buffer, and no correlation was found between the reduction potential and the salinity. The experimental measuring conditions were kept the same. The CLE-AdCSV method using SA takes advantage of a catalytic loop involving the reduction of the dissolved O_2 to hydrogen peroxide which immediately re-oxidize Fe(II) back into Fe(III), allowing for multiple reductions of the same ion and enhancing the signal (Laglera et al., 2016; Mahieu, 2023). The samples were equilibrated with air in the voltametric cell, ensuring a constant oxygen concentration (Mahieu, 2023) and a similar catalytic effect, regardless of the sample being analyzed. AdCSV analysis includes an accumulation step at a positive potential where the electroactive complex $FeSA_2$ adsorbs at the electrode surface prior to its stripping. During this stripping, other compounds, organic and inorganic, may adsorb at the electrode surface and may impact the stripping peak potential. The influence of the DOM composition on the peak potential of $FeSA_2$ is yet to be addressed, but the ubiquity of the peak shift suggests similar electroactive DOM in the surface waters of all basins of the WTSP. It will be interesting to assess whether it is possible to identify specific components of DOM by the shift in the peak potential. Overall, this observation could highlight a novel way to identify changes in DOM composition, but it requires further investigation.

Analytical constraints for Fe-binding ligand detection by CLE-AdCSV

There are different CLE-AdCSV methodologies currently in use to evaluate the role of DOM complexation in DFe stabilization and transport. Although all are valuable, they are difficult to compare because of the specificities (e.g. detection window) of each method. Several basin scale investigations have presented Fe organic speciation in the WTSP, but they were obtained using different experimental procedure which might explain some of the observed differences. Using TAC as added ligand, Kondo et al. (2012) reported in most samples a low eL_{Fe} (< 1 nMeqFe) in the L_1 ligand class. In contrast, other studies in the Pacific Ocean using the added ligand SA showed ubiquitous, large eL_{Fe} (> 1 nMeqFe) falling in the L_2 class (Buck et al., 2018; Cabanes et al., 2020; this study). The difference can be explained by the analytical conditions with a higher detection window ($\alpha_{Fe'AL}$) for TAC than for SA, meaning that titrations with TAC focus on fewer Fe-binding ligands of

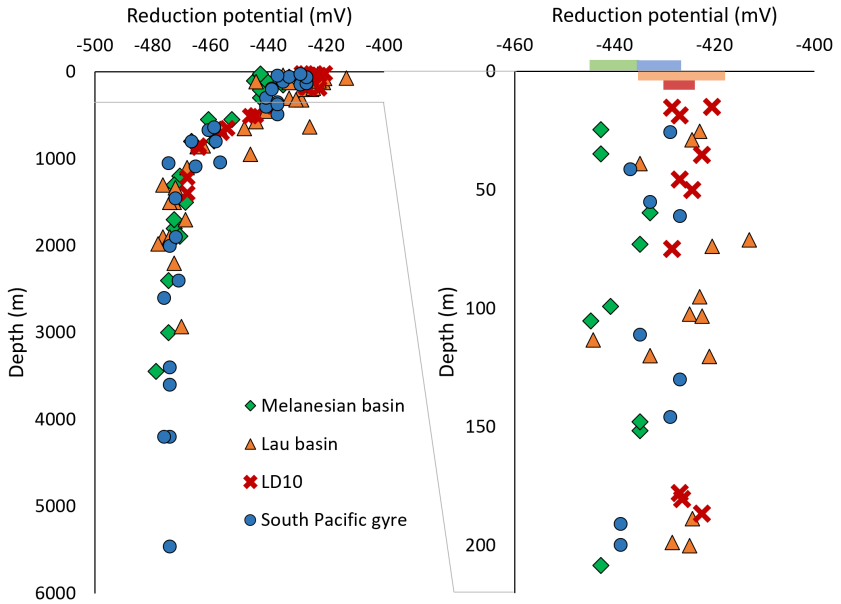

FIGURE 7
Reduction potential of the FeSA peak with depth for the entire water column (left) and the top 200 m (right), with the standard deviation centered on the averaged value for the first 200 m represented by colored bar.

higher log $K^{cond}_{Fe'L}$ than the titrations with SA. The difference in detection window could lead to the underestimation of the HS-like contribution to the ligand pool because of the absence of competition with TAC (Laglera et al., 2011).

The analyses presented in this study were all performed in the dissolved fraction, without discrimination of the soluble and colloidal size fraction. Metal-binding compounds in the soluble Fe fraction (< 0.02 µm) are assumed to be mostly organic, while the colloidal fraction (0.02 to 0.2 µm, or 0.45 µm here) may be composed of a wider mix of organic and inorganic compounds. It was suggested that this colloidal fraction of Fe was essential for DFe transport in the Subarctic Pacific (Kondo et al., 2021). Similarly, knowledge of the size fractionation of DFe, Fe-binding ligands, and HS partitioning in the Lau basin would greatly help better understand DFe speciation in this very dynamic region.

Accurate DFe concentrations are required in the calculation of L_{Fe} and log $K^{cond}_{Fe'L}$. Compared to mid-ocean ridges, volcanic arcs are characterized by higher carbon dioxide (CO_2), sulfur dioxide (SO_2) and hydrogen sulfide (H_2S) enrichments, responsible for increased DFe removal by the formation of Fe-sulfide and Fe-oxyhydroxides along the dilution of hydrothermal plumes (e.g., Field and Sherrell, 2000). Such gas enrichment and DFe removal have been observed at several locations along the Tonga-Kermadec volcanic arc (Massoth et al., 2003; de Ronde et al., 2007; Resing et al., 2011; Neuholz et al., 2020; Kleint et al., 2022). The presence of such inorganic colloidal material can be problematic because DFe may be released under the acidic conditions used for DFe determination while being possibly inert species for CLE-AdCSV, which is performed at natural pH. The net effect is therefore an overestimation of the effective DFe concentration, leading to biased L_{Fe} and log $K^{cond}_{Fe'L}$. It is known for instance that the crystalline structure of some Fe-oxyhydroxides can sterically isolate Fe from metal-binding ligands (Kraemer et al., 2005; Dulaquais et al., 2023) while dissolving in acidic conditions (Liu and Millero, 2002). This effect has been observed in hydrothermal plumes by Kleint et al. (2016). They showed that up to 90% of DFe determined in acidified samples was non-labile to their added ligand in the buoyant plume, but this value was down to 15% in the non-buoyant plume. It is worth noting that the hydrothermal fluids investigated by Kleint et al. (2016) had DFe concentrations in the µM range, so the overestimation of DFe had a considerable impact on L_{Fe} and log $K^{cond}_{Fe'L}$ calculations. In the transect presented here, the most hydrothermally-influenced station was still 2km away from the vent and 90% of DFe concentrations were< 1 nM, which represents no more than 20% of the average L_{Fe} measured for our dataset. Thus, the error related to the potential overestimation of DFe is negligible for most of our samples. Nevertheless, the impact on CLE-AdCSV titrations of sulfides, oxyhydroxides and other aggregate materials filtered and classified as dissolved by the traditional operational definition is not known, and the competition between binding with the added ligand and adsorption/binding with inorganic and colloidal material is unknown.

The increasing number of Fe-binding ligand investigations in hydrothermal systems have encompassed a variety of techniques, each with advantages and disadvantages. Kleint et al. (2016) highlighted the issue related to the accurate definition of DFe concentration with SA within the hydrothermal plume in the Lau basin, and Wang et al. (2022) presented the correlation of the Fe isotopic ratios with the log $K^{cond}_{Fe'L}$ defined by reversed CLE-AdCSV using 1-nitroso-2-napthol (NN). Here, we present the distribution of the Fe-binding ligands in the Lau Basin and adjacent waters using SA. The next step forward in the characterization of hydrothermally derived Fe-binding ligands could be to directly compare the different available electroanalytical methods on the same water samples.

Conclusion

The TONGA transect (GPpr14) revealed intense production and accumulation of Fe-binding ligands predominantly of intermediate log $K^{cond}_{Fe'L}$ at all stations. The high L_{Fe} and eL_{Fe} observed in the area contrast with similar regions and may originate from the unusually high diazotroph activity known to occur in the Lau basin. Limited stabilization of the hydrothermally-sourced DFe is most likely explained by competition from other metals and non-specificity of the ligands being produced, further supported by companion studies that report high levels of reduced sulfur substances and humic-like FDOM that coincide with our high L_{Fe} (in prep.). These non-specific ligands could be a detoxification response to hydrothermal waters, a hypothesis supported by ship-board incubation experiments (Tilliette et al., 2023).

Around 30% of DFe in these samples is within humic complexes (Dulaquais et al., 2023) and good agreement between FDOM and DFe suggest possible stabilization of a fraction of DFe as Fe(II) by HS-like FDOM. However, while the average log $K^{cond}_{Fe'L}$ was consistent with humic complexation across the ligand pool, ligands were in great excess of DFe and electroactive L_{FeHS} accounted for only 20 ± 13% of L_{Fe} in the mixed layer and 8 ± 6% in deep waters. Different trends in L_{FeHS} and HS-like FDOM distributions confirm that HS-like FDOM and L_{FeHS} account for overlapping yet distinct fractions of the humic pool, and that the electroactive fraction of humics may underestimate the role of humic material in metal complexation. We recommend the use of quenching experiments in samples collected in the WTSP to evaluate the role of the HS-like FDOM in DFe transport and in Fe-binding ligand composition in future studies. Other ligands such as EPS and siderophores likely also contributed to Fe complexation, although the average log $K^{cond}_{Fe'L}$ values suggest strong ligands such as siderophores were also not a dominant component of the ligand pool. Our results may also be explained by competition between metals for non-specific ligands, and a multi-metal approach to examine the affinity of the binding sites of humic nature toward hydrothermally sourced trace metals would provide further insight. Ultimately, the partitioning of DFe, Fe-binding ligands, L_{FeHS} and HS-like FDOM should be investigated in both the soluble and colloidal fractions, and include the characterization of EPS, siderophores and other potential ligands.

The Tonga ridge effectively isolates the South Pacific gyre from the Lau basin, and yet there was an apparent dilution gradient from stronger to weaker ligands from the Lau basin into the South Pacific

gyre and within the mixed layer of the Melanesian basin. This gradient was also seen in the electrochemical potential of the $FeSA_2$ peak in the mixed layer, which was highest in the Lau basin and decreased in adjacent surface waters of the Melanesian basin and South Pacific gyre. To our knowledge, this is the first time that a change in peak potential associated with changes in sample composition has been reported. We hypothesize that the peak shift could present a novel way to identify specific components of DOM, but this requires further investigation. In view of the existing studies harnessing a combination of forward and reverse titrations and different added ligands to determine Fe speciation in the WTSP, this region could present an ideal location for further intercomparison efforts to evaluate the ability of CLE-AdCSV in characterizing Fe-binding ligands of hydrothermal origin.

Data availability statement

The original contributions presented in the study are included in the article/Supplementary Material. Further inquiries can be directed to the corresponding author.

Author contributions

LM: Formal Analysis, Investigation, Writing – original draft. HW: Supervision, Writing – review & editing. GD: Formal Analysis, Writing – review & editing. CT: Formal Analysis, Writing – review & editing. CaG: Formal Analysis, Writing – review & editing. MT: Formal Analysis, Writing – review & editing. DL: Formal Analysis, Writing – review & editing. PF: Formal Analysis, Writing – review & editing. MB: Writing – review & editing. GS: Writing – review & editing. SB: Writing – review & editing. CéG: Writing – review & editing. PS: Supervision, Writing – review & editing.

Funding

The author(s) declare financial support was received for the research, authorship, and/or publication of this article. The work contained in this paper was conducted during a PhD study supported by the Natural Environment Research Council (NERC) EAO Doctoral Training Partnership and is fully-funded by NERC whose support is gratefully acknowledged (grant NE/L002469/1). This work is a contribution to the TONGA project (Shallow hydroThermal sOurces of trace elemeNts: potential impacts on biological productivity and the bioloGicAl carbon pump). The TONGA cruise (GEOTRACES GPpr14, November 2019, https://doi.org/10.17600/18000884) was funded by the TGIR Flotte Océanographique Française, the A-MIDeX foundation of the Aix-Marseille University, the LEFE-CYBER and GMMC programs and the ANR (grant TONGA ANR-18- CE01-0016). This work was partially supported by the "PHC Alliance" programme, funded by the UK Department for Business, Energy & Industrial Strategy (now DSIT), the French Ministry for Europe and Foreign Affairs, and the French Ministry of Higher Education, Research and Innovation.

Acknowledgments

We warmly thank all the scientists, the captain, and the crew of the R/V L'Atalante for their cooperative work at sea during the TONGA cruise. We also thank V. Taillander for the CTD acquisition and data treatment, and D. Gonzales-Santana, M-E Vorrath, members of the trace metal sampling team. We also thank K. Buck for the valuable comments and discussion during the preparation of the manuscript.

Conflict of interest

The authors declare that the research was conducted in the absence of any commercial or financial relationships that could be construed as a potential conflict of interest.

Publisher's note

Supplementary material

The Supplementary Material for this article can be found online at: https://www.frontiersin.org/articles/10.3389/fmars.2024.1304118/full#supplementary-material

References

Abualhaija, M. M., and van den Berg, C. M. G. (2014). Chemical speciation of iron in seawater using catalytic cathodic stripping voltammetry with ligand competition against salicylaldoxime. *Mar. Chem.* 164, 60–74. doi: 10.1016/j.marchem.2014.06.005

Abualhaija, M. M., Whitby, H., and van den Berg, C. M. G. (2015). Competition between copper and iron for humic ligands in estuarine waters. *Mar. Chem.* 172, 46–56. doi: 10.1016/j.marchem.2014.06.00510.1016/j.marchem.2015.03.010

Barbeau, K., Rue, E. L., Bruland, K. W., and Butler, A. (2001). Photochemical cycling of iron in the surface ocean mediated by microbial iron(iii)-binding ligands. *Nature* 413, 409–413. doi: 10.1038/35096545

Bennett, S. A., Achterberg, E. P., Connelly, D. P., Statham, P. J., Fones, G. R., and German, C. R. (2008). The distribution and stabilisation of dissolved Fe in deep-sea hydrothermal plumes. *Earth Planetary Sci. Lett.* 270 (3-4,), 157–167. doi: 10.1016/j.epsl.2008.01.048

Boiteau, R. M., and Repeta, D. J. (2022). Slow kinetics of iron binding to marine ligands in seawater measured by isotope exchange liquid chromatography-inductively coupled plasma mass spectrometry. *Environ. Sci. Technol.* 56, 3770–3779. doi: 10.1021/acs.est.1c06922

Boiteau, R. M., Till, C. P., Coale, T. H., Fitzsimmons, J. N., Bruland, K. W., and Repeta, D. J. (2019). Patterns of iron and siderophore distributions across the California Current System. *Limnology Oceanography* 64, 376–389. doi: 10.1002/lno.11046

Bonnet, S., Benavides, M., Le Moigne, F. A. C., Camps, M., Torremocha, A., Grosso, O., et al. (2023a). Diazotrophs are overlooked contributors to carbon and nitrogen export to the deep ocean. *ISME J.* 17, 47–58. doi: 10.1038/s41396-022-01319-3

Bonnet, S., Caffin, M., Berthelot, H., Grosso, O., Benavides, M., Helias-Nunige, S., et al. (2018). In-depth characterization of diazotroph activity across the western tropical South Pacific hotspot of N2 fixation (OUTPACE cruise). *Biogeosciences* 15, 4215–4232. doi: 10.5194/bg-15-4215-2018

Bonnet, S., Caffin, M., Berthelot, H., and Moutin, T. (2017). Hot spot of N2 fixation in the western tropical South Pacific pleads for a spatial decoupling between N2 fixation and denitrification. *Proc. Natl. Acad. Sci.* 114, E2800–E2801. doi: 10.1073/pnas.1619514114

Bonnet, S., Guieu, C., Taillandier, V., Boulart, C., Bouruet-Aubertot, P., Gazeau, F., et al. (2023b). Natural iron fertilization by shallow hydrothermal sources fuels diazotroph blooms in the ocean. *Science* 380, 812–817. doi: 10.1126/science.abq4654

Boyd, P. W., Ibisanmi, E., Sander, S. G., Hunter, K. A., and Jackson, G. A. (2010). Remineralization of upper ocean particles: Implications for iron biogeochemistry. *Limnology Oceanography* 55, 1271–1288. doi: 10.4319/lo.2010.55.3.1271

Boyd, P. W., and Tagliabue, A. (2015). Using the L* concept to explore controls on the relationship between paired ligand and dissolved iron concentrations in the ocean. *Mar. Chem. SCOR WG 139: Organic Ligands A Key Control Trace Metal Biogeochem. Ocean* 173, 52–66. doi: 10.1016/j.marchem.2014.12.003

Browning, T. J., and Moore, C. M. (2023). Global analysis of ocean phytoplankton nutrient limitation reveals high prevalence of co-limitation. *Nat. Commun.* 14, 5014. doi: 10.1038/s41467-023-40774-0

Buck, K. N., Lohan, M. C., Berger, C. J. M., and Bruland, K. W. (2007). Dissolved iron speciation in two distinct river plumes and an estuary: Implications for riverine iron supply. *Limnol. Oceanogr.* 52, 843–855. doi: 10.4319/lo.2007.52.2.0843

Buck, K. N., Sedwick, P. N., Sohst, B., and Carlson, C. A. (2018). Organic complexation of iron in the eastern tropical South Pacific: Results from US GEOTRACES Eastern Pacific Zonal Transect (GEOTRACES cruise GP16). *Mar. Chem. U.S. GEOTRACES Eastern Trop. Pacific Transect (GP16)* 201, 229–241. doi: 10.1016/j.marchem.2017.11.007

Buck, K. N., Sohst, B., and Sedwick, P. N. (2015). The organic complexation of dissolved iron along the U.S. GEOTRACES (GA03) North Atlantic Section. *Deep Sea Res. Part II Top. Stud. Oceanogr.* 116, 152–165. doi: 10.1016/j.dsr2.2014.11.016

Bundy, R. M., Boiteau, R. M., McLean, C., Turk-Kubo, K. A., McIlvin, M. R., Saito, M. A., et al. (2018). Distinct siderophores contribute to iron cycling in the mesopelagic at station ALOHA. *Front. Mar. Sci.* 5. doi: 10.3389/fmars.2018.00061

Bundy, R. M., Jiang, M., Carter, M., and Barbeau, K. A. (2016). Iron-binding ligands in the southern california current system: mechanistic studies. *Front. Mar. Sci.* 3. doi: 10.3389/fmars.2016.00027

Cabanes, D. J. E., Norman, L., Bowie, A. R., Strmečki, S., and Hassler, C. S. (2020). Electrochemical evaluation of iron-binding ligands along the Australian GEOTRACES southwestern Pacific section (GP13). *Mar. Chem.* 219, 103736. doi: 10.1016/j.marchem.2019.103736

Cao, F., Zhu, Y., Kieber, D. J., and Miller, W. L. (2020). Distribution and photoreactivity of chromophoric and fluorescent dissolved organic matter in the Northeastern North Pacific Ocean. *Deep Sea Res. Part Oceanogr. Res. Pap.* 155, 103168. doi: 10.1016/j.dsr.2019.103168

Carpenter, J. H. (1965). The accuracy of the winkler method for dissolved oxygen analysis1. *Limnol. Oceanogr.* 10, 135–140. doi: 10.4319/lo.1965.10.1.0135

Carritt, D. E., and Carpenter, J. H. (1966). Comparison and evaluation of currently employed modifications of the Winkler method for determining dissolved oxygen in sea-water; a NASCO report. *J. Mar. Res.* 24, 286–318.

Cheize, M., Sarthou, G., Croot, P. L., Bucciarelli, E., Baudoux, A.-C., and Baker, A. R. (2012). Iron organic speciation determination in rainwater using cathodic stripping voltammetry. *Analytica Chim. Acta* 736, 45–54. doi: 10.1016/j.aca.2012.05.011

Chen, Y., Jurkevitch, E., Bar-Ness, E., and Hadar, Y. (1994). Stability constants of pseudobactin complexes with transition metals. *Soil Sci. Soc. America J.* 58, 390–396. doi: 10.2136/sssaj1994.03615995005800020021x

Coble, P. G. (1996). Characterization of marine and terrestrial DOM in seawater using excitation-emission matrix spectroscopy. *Mar. Chem.* 51, 325–346. doi: 10.1016/0304-4203(95)00062-3

Coble, P. G., Lead, J., Baker, A., Reynolds, D. M., and Spencer, R. G. M. (2014). *Aquatic Organic Matter Fluorescence* (New York, USA: Cambridge University Press).

Cordero, O. X., Ventouras, L.-A., DeLong, E. F., and Polz, M. F. (2012). Public good dynamics drive evolution of iron acquisition strategies in natural bacterioplankton populations. *Proc. Natl. Acad. Sci.* 109, 20059–20064. doi: 10.1073/pnas.1213344109

Croot, P. L., Andersson, K., Öztürk, M., and Turner, D. R. (2004). The distribution and speciation of iron along 6°E in the Southern Ocean. *Deep Sea Res. Part II: Topical Stud. Oceanography SWEDARP 1997/98 Expedition* 51, 2857–2879. doi: 10.1016/j.dsr2.2003.10.012

Cutter, G. A., Casciotti, K., Croot., P. L., Heimburger, L.-E., Lohan, M., Planquette, H., et al. (2017). *Sampling and sample-handling protocols for GEOTRACES cruises, Version 3.* Available at: https://epic.awi.de/id/eprint/51363/1/Cookbook.pdf.

de Ronde, C. E. J., Baker, E. T., Massoth, G. J., Lupton, J. E., Wright, I. C., Sparks, R. J., et al. (2007). Submarine hydrothermal activity along the mid-Kermadec Arc, New Zealand: Large-scale effects on venting. *Geochem. Geophys. Geosyst.* 8, Q07007. doi: 10.1029/2006GC001495

Deschatre, M., Ghillebaert, F., Guezennec, J., and Colin, C. S. (2013). Sorption of copper(II) and silver(I) by four bacterial exopolysaccharides. *Appl. Biochem. Biotechnol.* 171, 1313–1327. doi: 10.1007/s12010-013-0343-7

Dittmar, T., Lennartz, S. T., Buck-Wiese, H., Hansell, D. A., Santinelli, C., Vanni, C., et al. (2021). Enigmatic persistence of dissolved organic matter in the ocean. *Nat. Rev. Earth Environ.* 2, 570–583. doi: 10.1038/s43017-021-00183-7

Dulaquais, G., Fourrier, P., Guieu, C., Mahieu, L., Riso, R., Salaun, P., et al. (2023). The role of humic type ligands in the bioavailability and stabilization of dissolved iron in the Western Tropical South Pacific Ocean. *Front. Mar. Sci.* 10, 19. doi: 10.3389/fmars.2023.1219594

Dulaquais, G., Waeles, M., Gerringa, L. J. A., Middag, R., Rijkenberg, M. J. A., and Riso, R. (2018). The biogeochemistry of electroactive humic substances and its connection to iron chemistry in the north east atlantic and the western mediterranean sea. *J. Geophys. Res. Oceans* 123, 5481–5499. doi: 10.1029/2018JC014211

Ferretto, N., Tedetti, M., Guigue, C., Mounier, S., Raimbault, P., and Goutx, M. (2017). Spatio-temporal variability of fluorescent dissolved organic matter in the Rhône River delta and the Fos-Marseille marine area (NW Mediterranean Sea, France). *Environ. Sci. Pollut. Res.* 24, 4973–4989. doi: 10.1007/s11356-016-8255-z

Field, M. P., and Sherrell, R. M. (2000). Dissolved and particulate Fe in a hydrothermal plume at 9°45′N, East Pacific Rise:: Slow Fe (II) oxidation kinetics in Pacific plumes. *Geochim. Cosmochim. Acta* 64, 619–628. doi: 10.1016/S0016-7037(99)00333-6

Fourrier, P., Dulaquais, G., Guigue, C., Giamarchi, P., Sarthou, G., Whitby, H., et al. (2022). Characterization of the vertical size distribution, composition and chemical properties of dissolved organic matter in the (ultra)oligotrophic Pacific Ocean through a multi-detection approach. *Mar. Chem.* 240, 104068. doi: 10.1016/j.marchem.2021.104068

Garcia, H. E., and Gordon, L. I. (1992). Oxygen solubility in seawater: Better fitting equations. *Limnol. Oceanogr.* 37, 1307–1312. doi: 10.4319/lo.1992.37.6.1307

Genovese, C., Grotti, M., Pittaluga, J., Ardini, F., Janssens, J., Wuttig, K., et al. (2018). Influence of organic complexation on dissolved iron distribution in East Antarctic pack ice. *Mar. Chem.* 203, 28–37. doi: 10.1016/j.marchem.2018.04.005

German, C. R., Baker, E. T., Connelly, D. P., Lupton, J. E., Resing, J., Prien, R. D., et al. (2006). Hydrothermal exploration of the fonualei rift and spreading center and the northeast lau spreading center. *Geochem. Geophys. Geosyst.* 7 (11). doi: 10.1029/2006GC001324

Gerringa, L. J. A., Rijkenberg, M. J. A., Schoemann, V., Laan, P., and de Baar, H. J. W. (2015). Organic complexation of iron in the West Atlantic Ocean. *Mar. Chem. Cycles Metals Carbon Oceans A Tribute Work Stimulated Hein Baar* 177, 434–446. doi: 10.1016/j.marchem.2015.04.007

Gerringa, L. J. A., Rijkenberg, M. J. A., Thuróczy, C.-E., and Maas, L. R. M. (2014). A critical look at the calculation of the binding characteristics and concentration of iron complexing ligands in seawater with suggested improvements. *Environ. Chem.* 11, 114–136. doi: 10.1071/EN13072

Gerringa, L. J. A., Veldhuis, M. J. W., Timmermans, K. R., Sarthou, G., and de Baar, H. J. W. (2006). Co-variance of dissolved Fe-binding ligands with phytoplankton characteristics in the Canary Basin. *Mar. Chem.* 102, 276–290. doi: 10.1016/j.marchem.2006.05.004

Gledhill, M., and Buck, K. N. (2012). The organic complexation of iron in the marine environment: A review. *Front. Microbiol.* 3. doi: 10.3389/fmicb.2012.00069

Gledhill, M., and van den Berg, C. M. G. (1994). Determination of complexation of iron(III) with natural organic complexing ligands in seawater using cathodic stripping voltammetry. *Mar. Chem.* 47, 41–54. doi: 10.1016/0304-4203(94)90012-4

Gledhill, M., Zhu, K., Rusiecka, D., and Achterberg, E. P. (2022). Competitive interactions between microbial siderophores and humic-like binding sites in european shelf sea waters. *Front. Mar. Sci.* 9. doi: 10.3389/fmars.2022.855009

González, A. G., Bianco, A., Boutorh, J., Cheize, M., Mailhot, G., Delort, A.-M., et al. (2022). Influence of strong iron-binding ligands on cloud water oxidant capacity. *Sci. Total Environ.* 829, 154642. doi: 10.1016/j.scitotenv.2022.154642

González, A. G., Cadena-Aizaga, M. I., Sarthou, G., González-Dávila, M., and Santana-Casiano, J. M. (2019). Iron complexation by phenolic ligands in seawater. *Chem. Geol.* 511, 380–388. doi: 10.1016/j.chemgeo.2018.10.017

Guieu, C., and Bonnet, S. (2019). *TONGA 2019 cruise, L'Atalante R/V*. doi: 10.17600/18000884

Guieu, C., Bonnet, S., Petrenko, A., Menkes, C., Chavagnac, V., Desboeufs, K., et al. (2018). Iron from a submarine source impacts the productive layer of the Western Tropical South Pacific (WTSP). *Sci. Rep.* 8, 9075. doi: 10.1038/s41598-018-27407-z

Hassler, C. S., Berg, V. D., and Boyd, P. W. (2017). Toward a regional classification to provide a more inclusive examination of the ocean biogeochemistry of iron-binding ligands. *Front. Mar. Sci.* 4. doi: 10.3389/fmars.2017.00019

Hassler, C. S., Norman, L., Mancuso Nichols, C. A., Clementson, L. A., Robinson, C., Schoemann, V., et al. (2015). Iron associated with exopolymeric substances is highly bioavailable to oceanic phytoplankton. *Mar. Chem. SCOR WG 139: Organic Ligands A Key Control Trace Metal Biogeochem. Ocean* 173, 136–147. doi: 10.1016/j.marchem.2014.10.002

Hassler, C. S., Schoemann, V., Nichols, C. M., Butler, E. C. V., and Boyd, P. W. (2011). Saccharides enhance iron bioavailability to Southern Ocean phytoplankton. *Proc. Natl. Acad. Sci.* 108, 1076–1081. doi: 10.1073/pnas.1010963108

Hawkes, J. A., Connelly, D. P., Gledhill, M., and Achterberg, E. P. (2013). The stabilisation and transportation of dissolved iron from high temperature hydrothermal vent systems. *Earth Planet Sci. Lett.* 375, 280–290. doi: 10.1016/j.epsl.2013.05.047

Heller, M., Gaiero, D., and Croot, P. (2013). Basin scale survey of marine humic fluorescence in the Atlantic: Relationship to iron solubility and H2O2. *Glob. Biogeochem. Cycles* 27 (1), 88–100. doi: 10.1029/2012GB004427

Hioki, N., Kuma, K., Morita, Y., Sasayama, R., Ooki, A., Kondo, Y., et al. (2014). Laterally spreading iron, humic-like dissolved organic matter and nutrients in cold, dense subsurface water of the Arctic Ocean. *Sci. Rep.* 4, 1–9. doi: 10.1038/srep06775

Hoffman, C. L., Monreal, P. J., Albers, J. B., Lough, A. J., Santoro, A. E., Mellett, T., et al. (2023). Microbial strong organic ligand production is tightly coupled to iron in hydrothermal plumes. *bioRxiv*, 2023–01. doi: 10.1101/2023.01.05.522639

Hudson, N., Baker, A., and Reynolds, D. (2007). Fluorescence analysis of dissolved organic matter in natural, waste and polluted waters—a review. *River Res. Appl.* 23, 631–649. doi: 10.1002/rra.1005

Ibisanmi, E., Sander, S. G., Boyd, P. W., Bowie, A. R., and Hunter, K. A. (2011). Vertical distributions of iron-(III) complexing ligands in the Southern Ocean. *Deep Sea Res. Part II: Topical Stud. Oceanography Biogeochem. Aust. Sector South. Ocean* 58, 2113–2125. doi: 10.1016/j.dsr2.2011.05.028

Ishii, S. K. L., and Boyer, T. H. (2012). Behavior of reoccurring PARAFAC components in fluorescent dissolved organic matter in natural and engineered systems: A critical review. *Environ. Sci. Technol.* 46, 2006–2017. doi: 10.1021/es2043504

Jia, K., Manning, C. C. M., Jollymore, A., and Beckie, R. D. (2021). Technical note: Effects of iron(II) on fluorescence properties of dissolved organic matter at circumneutral pH. *Hydrol. Earth Syst. Sci.* 25, 4983–4993. doi: 10.5194/hess-25-4983-2021

Jones, M. E., Beckler, J. S., and Taillefert, M. (2011). The flux of soluble organic-iron (III) complexes from sediments represents a source of stable iron(III) to estuarine waters and to the continental shelf. *Limnol. Oceanogr.* 56, 1811–1823. doi: 10.4319/lo.2011.56.5.1811

Kawabe, M., and Fujio, S. (2010). Pacific ocean circulation based on observation. *J. Oceanogr.* 66, 389–403. doi: 10.1007/s10872-010-0034-8

Kleint, C., Bach, W., Diehl, A., Fröhberg, N., Garbe-Schönberg, D., Hartmann, J. F., et al. (2019). Geochemical characterization of highly diverse hydrothermal fluids from volcanic vent systems of the Kermadec intraoceanic arc. *Chem. Geol.* 528, 119289. doi: 10.1016/j.chemgeo.2019.119289

Kleint, C., Hawkes, J. A., Sander, S. G., and Koschinsky, A. (2016). Voltammetric investigation of hydrothermal iron speciation. *Front. Mar. Sci.* 3. doi: 10.3389/fmars.2016.00075

Kleint, C., Pichler, T., and Koschinsky, A. (2017). Geochemical characteristics, speciation and size-fractionation of iron (Fe) in two marine shallow-water hydrothermal systems, Dominica, Lesser Antilles. *Chem. Geol.* 454, 44–53. doi: 10.1016/j.chemgeo.2017.02.021

Kleint, C., Zitoun, R., Neuholz, R., Walter, M., Schnetger, B., Klose, L., et al. (2022). Trace metal dynamics in shallow hydrothermal plumes at the kermadec arc. *Front. Mar. Sci.* 8. doi: 10.3389/fmars.2021.782734

Klunder, M. B., Laan, P., Middag, R., Baar, H. J. W., and Bakker, K. (2012). Dissolved iron in the Arctic Ocean: Important role of hydrothermal sources, shelf input and scavenging removal. *J. Geophys. Res. Oceans* 117 (C4). doi: 10.1029/2011JC007135

Klunder, M. B., Laan, P., Middag, R., De Baar, H. J. W., and van Ooijen, J. C. (2011). Dissolved iron in the Southern Ocean (Atlantic sector). *Deep Sea Res. Part II Top. Stud. Oceanogr. Physics Carbon Dioxide Trace Elements Isotopes South. Ocean: Polarstern Expeditions ANT XXIV-3 (2008) ANT XXIII/3 (2006)* 58, 2678–2694. doi: 10.1016/j.dsr2.2010.10.042

Komaki, K., and Kawabe, M. (2007). Structure of the upper deep current in the Melanesian Basin, western North Pacific. *Monthly Energy Review* 45, 15–22.

Kondo, Y., Bamba, R., Obata, H., Nishioka, J., and Takeda, S. (2021). Distinct profiles of size-fractionated iron-binding ligands between the eastern and western subarctic Pacific. *Sci. Rep.* 11, 2053. doi: 10.1038/s41598-021-81536-6

Kondo, Y., Takeda, S., and Furuya, K. (2007). Distribution and speciation of dissolved iron in the Sulu Sea and its adjacent waters. *Deep Sea Res. Part II: Topical Stud. Oceanography Biogeochem. Biodiversity Sulu Sea* 54, 60–80. doi: 10.1016/j.dsr2.2006.08.019

Kondo, Y., Takeda, S., and Furuya, K. (2012). Distinct trends in dissolved Fe speciation between shallow and deep waters in the Pacific Ocean. *Mar. Chem.* 134–135, 18–28. doi: 10.1016/j.marchem.2012.03.002

Kraemer, S. M., Butler, A., Borer, P., and Cervini-Silva, J. (2005). Siderophores and the dissolution of iron-bearing minerals in marine systems. *Rev. Mineral. Geochem.* 59, 53–84. doi: 10.2138/rmg.2005.59.4

Laglera, L. M., Battaglia, G., and van den Berg, C. M. G. (2011). Effect of humic substances on the iron speciation in natural waters by CLE/CSV. *Mar. Chem.* 127, 134–143. doi: 10.1016/j.marchem.2011.09.003

Laglera, L. M., Caprara, S., and Monticelli, D. (2016). Towards a zero-blank, preconcentration-free voltammetric method for iron analysis at picomolar concentrations in unbuffered seawater. *Talanta* 150, 449–454. doi: 10.1016/j.talanta.2015.12.060

Laglera, L. M., Sukekava, C., Slagter, H. A., Downes, J., Aparicio-Gonzalez, A., and Gerringa, L. J. A. (2019). First quantification of the controlling role of humic substances in the transport of iron across the surface of the arctic ocean. *Environ. Sci. Technol.* 53, 13136–13145. doi: 10.1021/acs.est.9b04240

Laglera, L. M., and van den Berg, C. M. G. (2009). Evidence for geochemical control of iron by humic substances in seawater. *Limnol. Oceanogr.* 54, 610–619. doi: 10.4319/lo.2009.54.2.0610

Langdon, C. (2010). Determination of Dissolved Oxygen in Seawater by Winkler Titration Using The Amperometric Technique. In, *The GO-SHIP Repeat Hydrography Manual: A Collection of Expert Reports and Guidelines*. Version 1, (eds E. M. Hood, C. L. Sabine and B. M. Sloyan). 18pp. (IOCCP Report Number 14; ICPO Publication Series Number 134). doi: 10.25607/OBP-1350

Lee, Y. P., Wong, K. H., Obata, H., Nishitani, K., Ogawa, H., Fukuda, H., et al. (2023). Distributions of humic substances in an estuarine region (Otsuchi Bay, Japan) determined using electrochemical and optical methods. *Mar. Chem.* 256, 104301. doi: 10.1016/j.marchem.2023.104301

Liu, X., and Millero, F. J. (2002). The solubility of iron in seawater. *Mar. Chem.* 77, 43–54. doi: 10.1016/S0304-4203(01)00074-3

Lory, C., Van Wambeke, F., Fourquez, M., Barani, A., Guieu, C., Tilliette, C., et al. (2022). Assessing the contribution of diazotrophs to microbial Fe uptake using a group specific approach in the Western Tropical South Pacific Ocean. *ISME Commun.* 2, 1–11. doi: 10.1038/s43705-022-00122-7

Mahieu, L. (2023). *Analytical challenges, development and application of CLE-AdCSV for the determination of the organic speciation of iron in marine waters* (University of Liverpool: Doctoral thesis). Available at: https://livrepository.liverpool.ac.uk/3170548/.

Mahieu, L., Omanović, D., Whitby, H., Buck, K. N., Caprara, S., Salaün, P., et al. (2024). Recommendations for best practice for iron speciation by competitive ligand exchange adsorptive cathodic stripping voltammetry with salicylaldoxime. *Mar. Chem.* 104348.

Massoth, G. J., De Ronde, C. E. J., Lupton, J. E., Feely, R. A., Baker, E. T., Lebon, G. T., et al. (2003). Chemically rich and diverse submarine hydrothermal plumes of the southern Kermadec volcanic arc (New Zealand). *Geol. Soc Lond. Spec. Publ.* 219, 119–139. doi: 10.1144/GSL.SP.2003.219.01.06

Mawji, E., Gledhill, M., Milton, J. A., Tarran, G. A., Ussher, S., Thompson, A., et al. (2008). Hydroxamate siderophores: occurrence and importance in the atlantic ocean. *Environ. Sci. Technol.* 42, 8675–8680. doi: 10.1021/es801884r

Ménez, B., Pisapia, C., Andreani, M., Jamme, F., Vanbellingen, Q. P., Brunelle, A., et al. (2018). Abiotic synthesis of amino acids in the recesses of the oceanic lithosphere. *Nature* 564, 59–63. doi: 10.1038/s41586-018-0684-z

Mentges, A., Feenders, C., Seibt, M., Blasius, B., and Dittmar, T. (2017). Functional molecular diversity of marine dissolved organic matter is reduced during degradation. *Front. Mar. Sci.* 4. doi: 10.3389/fmars.2017.00194

Millero, F. J., Sotolongo, S., and Izaguirre, M. (1987). The oxidation kinetics of Fe(II) in seawater. *Geochim. Cosmochim. Acta* 51, 793–801. doi: 10.1016/0016-7037(87)90093-7

Moore, C. M., Mills, M. M., Arrigo, K. R., Berman-Frank, I., Bopp, L., Boyd, P. W., et al. (2013). Processes and patterns of oceanic nutrient limitation. *Nat. Geosci.* 6, 701–710. doi: 10.1038/ngeo1765

Moppert, X., Le Costaouec, T., Raguenes, G., Courtois, A., Simon-Colin, C., Crassous, P., et al. (2009). Investigations into the uptake of copper, iron and selenium by a highly sulphated bacterial exopolysaccharide isolated from microbial mats. *J. Ind. Microbiol. Biotechnol.* 36, 599–604. doi: 10.1007/s10295-009-0529-8

Nelson, N. B., Siegel, D. A., Carlson, C. A., and Swan, C. M. (2010). Tracing global biogeochemical cycles and meridional overturning circulation using chromophoric dissolved organic matter. *Geophys. Res. Lett.* 37. doi: 10.1029/2009GL042325

Nernst, W. (1889). Die elektromotorische Wirksamkeit der Jonen. *Zeitschrift für Physikalische Chemie* 4U, 129–181. doi: 10.1515/zpch-1889-0412

Neuholz, R., Kleint, C., Schnetger, B., Koschinsky, A., Laan, P., Middag, R., et al. (2020). Submarine hydrothermal discharge and fluxes of dissolved fe and mn, and he isotopes at brothers volcano based on radium isotopes. *Minerals* 10, 969. doi: 10.3390/min10110969

Nichols, C. M., Lardière, S. G., Bowman, J. P., Nichols, P. D., Gibson, A. E., and Guézennec, J. (2005). Chemical characterization of exopolysaccharides from Antarctic marine bacteria. *Microb. Ecol.* 49, 578–589. doi: 10.1007/s00248-004-0093-8

Norman, L., Worms, I. A. M., Angles, E., Bowie, A. R., Nichols, C. M., Ninh Pham, A., et al. (2015). The role of bacterial and algal exopolymeric substances in iron chemistry. *Mar. Chem. SCOR WG 139: Organic Ligands A Key Control Trace Metal Biogeochem. Ocean* 173, 148–161. doi: 10.1016/j.marchem.2015.03.015

Ohno, T., Amirbahman, A., and Bro, R. (2008). Parallel factor analysis of excitation–emission matrix fluorescence spectra of water soluble soil organic matter as basis for the determination of conditional metal binding parameters. *Environ. Sci. Technol.* 42, 186–192. doi: 10.1021/es071855f

Omori, Y., Hama, T., Ishii, M., and Saito, S. (2010). Relationship between the seasonal change in fluorescent dissolved organic matter and mixed layer depth in the subtropical western North Pacific. *J. Geophys. Res. Oceans* 115 (C6). doi: 10.1029/2009JC005526

Oudot, C., Gerard, R., Morin, P., and Gningue, I. (1988). Precise shipboard determination of dissolved oxygen (Winkler procedure) for productivity studies with a commercial system1. *Limnol. Oceanogr.* 33, 146–150. doi: 10.4319/lo.1988.33.1.0146

Pernet-Coudrier, B., Waeles, M., Filella, M., Quentel, F., and Riso, R. D. (2013). Simple and simultaneous determination of glutathione, thioacetamide and refractory organic matter in natural waters by DP-CSV. *Sci. Total Environ.* 463–464, 997–1005. doi: 10.1016/j.scitotenv.2013.06.053

Pižeta, I., Sander, S. G., Hudson, R. J. M., Omanović, D., Baars, O., Barbeau, K. A., et al. (2015). Interpretation of complexometric titration data: An intercomparison of methods for estimating models of trace metal complexation by natural organic ligands. *Mar. Chem. SCOR WG 139: Organic Ligands A Key Control Trace Metal Biogeochem. Ocean* 173, 3–24. doi: 10.1016/j.marchem.2015.03.006

Powell, R. T., and Wilson-Finelli, A. (2003). Photochemical degradation of organic iron complexing ligands in seawater. *Aquat. Sci.* 65, 367–374. doi: 10.1007/s00027-003-0679-0

Resing, J. A., Rubin, K. H., Embley, R. W., Lupton, J. E., Baker, E. T., Dziak, R. P., et al. (2011). Active submarine eruption of boninite in the northeastern Lau Basin. *Nat. Geosci.* 4, 799–806. doi: 10.1038/ngeo1275

Resing, J. A., Sedwick, P. N., German, C. R., Jenkins, W. J., Moffett, J. W., Sohst, B. M., et al. (2015). Basin-scale transport of hydrothermal dissolved metals across the South Pacific Ocean. *Nature* 523, 200–203. doi: 10.1038/nature14577

Rickard, D., and Luther, G. W. (2007). Chemistry of iron sulfides. *Chem. Rev.* 107, 514–562. doi: 10.1021/cr0503658

Rijkenberg, M. J. A., Powell, C. F., Dall'Osto, M., Nielsdottir, M. C., Patey, M. D., Hill, P. G., et al. (2008). Changes in iron speciation following a Saharan dust event in the tropical North Atlantic Ocean. *Mar. Chem.* 110, 56–67. doi: 10.1016/j.marchem.2008.02.006

Rougeaux, H., Pichon, R., Kervarec, N., Raguénès, G. H. C., and Guezennec, J. G. (1996). Novel bacterial exopolysaccharides from deep-sea hydrothermal vents. *Carbohydr. Polymers* 31, 237–242. doi: 10.1016/S0144-8617(96)00079-3

Rue, E. L., and Bruland, K. W. (1995). Complexation of iron(III) by natural organic ligands in the Central North Pacific as determined by a new competitive ligand equilibration/adsorptive cathodic stripping voltammetric method. *Mar. Chem. Chem. Iron Seawater Interaction Phytoplankton* 50, 117–138. doi: 10.1016/0304-4203(95)00031-L

Sander, S. G., and Koschinsky, A. (2011). Metal flux from hydrothermal vents increased by organic complexation. *Nat. Geosci.* 4, 145–150. doi: 10.1038/ngeo1088

Santana-Casiano, J. M., González-Santana, D., Devresse, Q., Hepach, H., Santana-González, C., Quack, B., et al. (2022). Exploring the effects of organic matter characteristics on Fe(II) oxidation kinetics in coastal seawater. *Environ. Sci. Technol.* 56, 2718–2728. doi: 10.1021/acs.est.1c04512

Santana-Casiano, J. M., González-Dávila, M., Rodríguez, M. J., and Millero, F. J. (2000). The effect of organic compounds in the oxidation kinetics of Fe(II). *Marine Chemistry* 70, 211–222. doi: 10.1016/s0304-4203(00)00027-x

Sarma, N. S., Kiran, R., Rama Reddy, M., Iyer, S. D., Peketi, A., Borole, D. V., et al. (2018). Hydrothermal alteration promotes humic acid formation in sediments: A case study of the Central Indian Ocean Basin. *J. Geophys. Res. Oceans* 123, 110–130. doi: 10.1002/2017JC012940

Silva, N., Rojas, N., and Fedele, A. (2009). Water masses in the Humboldt Current System: Properties, distribution, and the nitrate deficit as a chemical water mass tracer for Equatorial Subsurface Water off Chile. *Deep Sea Res. Part II Top. Stud. Oceanogr. Oceanography Eastern South Pacific II: Oxygen Minimum Zone* 56, 1004–1020. doi: 10.1016/j.dsr2.2008.12.013

Slagter, H. A., Reader, H. E., Rijkenberg, M. J. A., van der Loeff, M. R., De Baar, H. J. W., and Gerringa, L. J. A. (2017). Organic Fe speciation in the Eurasian Basins of the Arctic Ocean and its relation to terrestrial DOM. *Mar. Chem.* 197, 11–25. doi: 10.1016/j.marchem.2017.10.005

Sohrin, R., and Sempéré, R. (2005). Seasonal variation in total organic carbon in the northeast Atlantic in 2000–2001. *J. Geophys. Res. Oceans* 110 (C10). doi: 10.1029/2004JC002731

Spearman, C. (1904). The proof and measurement of association between two things. *Am. J. Psychol.* 15, 72–101. doi: 10.2307/1412159

Stedmon, C., and Álvarez-Salgado, X. A. (2011). Shedding light on a black box: UV–Visible spectroscopic characterization of marine dissolved organic matter. *American Association for the Advancement of Science*. doi: 10.1126/science.opms.sb0001

Sukekava, C. F., Andrade, C. F. F., Niencheski, L. F. H., de Souza, M. S., and Laglera, L. M. (2023). Macronutrients, iron and humic substances summer cycling over the extended continental shelf of the South Brazil Bight. *Sci. Total Environ.* 865, 161182. doi: 10.1016/j.scitotenv.2022.161182

Sukekava, C. F., Downes, J., Filella, M., Vilanova, B., and Laglera, L. (2024). Ligand exchange provides new insight into the role of humic substances in the marine iron cycle. *Geochim. Cosmochim. Acta* 366, 17–30. doi: 10.1016/j.gca.2023.12.007

Sukekava, C., Downes, J., Slagter, H. A., Gerringa, L. J. A., and Laglera, L. M. (2018). Determination of the contribution of humic substances to iron complexation in seawater by catalytic cathodic stripping voltammetry. *Talanta* 189, 359–364. doi: 10.1016/j.talanta.2018.07.021

Summers, N., and Watling, L. (2021). Upper Bathyal Pacific Ocean biogeographic provinces from octocoral distributions. *Prog. Oceanogr.* 191, 102509. doi: 10.1016/j.pocean.2020.102509

Tagliabue, A., Buck, K. N., Sofen, L. E., Twining, B. S., Aumont, O., Boyd, P. W., et al. (2023). Authigenic mineral phases as a driver of the upper-ocean iron cycle. *Nature* 620, 104–109. doi: 10.1038/s41586-023-06210-5

Tagliabue, A., Mtshali, T., Aumont, O., Bowie, A. R., Klunder, M. B., Roychoudhury, A. N., et al. (2012). A global compilation of dissolved iron measurements: focus on distributions and processes in the Southern Ocean. *Biogeosciences* 9 (6), 2333–2349. doi: 10.5194/bg-9-2333-2012

Tagliabue, A., and Resing, J. (2016). Impact of hydrothermalism on the ocean iron cycle. *Philos. Trans. R. Soc. A: Mathematical Phys. Eng. Sci.* 374, 20150291. doi: 10.1098/rsta.2015.0291

Talley, L. D., Pickard, G. L., Emery, W. J., and Swift, J. H. (2011). Chapter 10 - Pacific Ocean. *Descriptive Physical Oceanography* (*Sixth* Edition) Eds. L. D. Talley, G. L. Pickard, W. J. Emery and J. H. Swift. (Boston: Academic Press), 303–362. doi: 10.1016/B978-0-7506-4552-2.10010-1

Tani, H., Nishioka, J., Kuma, K., Takata, H., Yamashita, Y., Tanoue, E., et al. (2003). Iron(III) hydroxide solubility and humic-type fluorescent organic matter in the deep water column of the Okhotsk Sea and the northwestern North Pacific Ocean. *Deep Sea Res. Part Oceanogr. Res. Pap.* 50, 1063–1078. doi: 10.1016/S0967-0637(03)00098-0

Tedetti, M., Bigot, L., Turquet, J., Guigue, C., Ferretto, N., Goutx, M., et al. (2020). Influence of freshwater discharges on biogeochemistry and benthic communities of a coral reef ecosystem (La Réunion Island, Indian Ocean). *Front. Mar. Sci.* 7. doi: 10.3389/fmars.2020.596165

Tilliette, C., Gazeau, F., Portlock, G., Benavides, M., Bonnet, S., Guigue, C., et al. (2023). Influence of shallow hydrothermal fluid release on the functioning of phytoplankton communities. *Front. Mar. Sci.* 10. doi: 10.3389/fmars.2023.1082077

Tilliette, C., Taillandier, V., Bouruet-Aubertot, P., Grima, N., Maes, C., Montanes, M., et al. (2022). Dissolved iron patterns impacted by shallow hydrothermal sources along a transect through the Tonga-kermadec arc. *Glob. Biogeochem. Cycles* 36, e2022GB007363. doi: 10.1029/2022GB007363

Timm, C., Bassett, D., Graham, I. J., Leybourne, M. I., de Ronde, C. E. J., Woodhead, J., et al. (2013). Louisville seamount subduction and its implication on mantle flow beneath the central Tonga–Kermadec arc. *Nat Commun* 4, 1720. doi: 10.1038/ncomms2702

Thuróczy, C.-E., Gerringa, L. J. A., Klunder, M., Laan, P., Le Guitton, M., de Baar, H. J. W., et al. (2011). Distinct trends in the speciation of iron between the shallow shelf seas and the deep basins of the Arctic Ocean. *J. Geophys. Res.* 116. doi: 10.1029/2010JC006835

Toner, B. M., Fakra, S. C., Manganini, S. J., Santelli, C. M., Marcus, M. A., Moffett, J. W., et al. (2009). Preservation of iron(II) by carbon-rich matrices in a hydrothermal plume. *Nat. Geosci.* 2, 197–201. doi: 10.1038/ngeo433

Tonnard, M., Planquette, H., Bowie, A. R., van der Merwe, P., Gallinari, M., Desprez de Gésincourt, F., et al. (2020). Dissolved iron in the North Atlantic Ocean and Labrador Sea along the GEOVIDE section (GEOTRACES section GA01). *Biogeosciences* 17, 917–943. doi: 10.5194/bg-17-917-2020

Town, R. M., and Filella, M. (2000). Dispelling the myths: Is the existence of L1 and L2 ligands necessary to explain metal ion speciation in natural waters? *Limnol. Oceanogr.* 45, 1341–1357. doi: 10.4319/lo.2000.45.6.1341

Twining, B. S., and Baines, S. B. (2013). The trace metal composition of marine phytoplankton. *Annu. Rev. Mar. Sci.* 5, 191–215. doi: 10.1146/annurev-marine-121211-172322

van den Berg, C. M. G. (1995). Evidence for organic complexation of iron in seawater. *Mar. Chem. Chem. Iron Seawater Interaction Phytoplankton* 50, 139–157. doi: 10.1016/0304-4203(95)00032-M

van den Berg, C. M. G. (2006). Chemical speciation of iron in seawater by cathodic stripping voltammetry with dihydroxynaphthalene. *Anal. Chem.* 78, 156–163. doi: 10.1021/ac051441

Velasquez, I. B., Ibisanmi, E., Maas, E. W., Boyd, P. W., Nodder, S., and Sander, S. G. (2016). Ferrioxamine Siderophores Detected amongst Iron Binding Ligands Produced during the Remineralization of Marine Particles. *Front. Mar. Sci.* 3. doi: 10.3389/fmars.2016.00172

Wang, H., Resing, J. A., Yan, Q., Buck, N. J., Michael, S. M., Zhou, H., et al. (2021). The characteristics of Fe speciation and Fe-binding ligands in the Mariana back-arc hydrothermal plumes. *Geochim. Cosmochim. Acta* 292, 24–36. doi: 10.1016/j.gca.2020.09.016

Wang, H., Wang, W., Liu, M., Zhou, H., Ellwood, M. J., Butterfield, D. A., et al. (2022). Iron ligands and isotopes in hydrothermal plumes over backarc volcanoes in the Northeast Lau Basin, Southwest Pacific Ocean. *Geochim. Cosmochim. Acta* 336, 341–352. doi: 10.1016/j.gca.2022.09.026

Whitby, H., Bressac, M., Sarthou, G., Ellwood, M. J., Guieu, C., and Boyd, P. W. (2020a). Contribution of electroactive humic substances to the iron-binding ligands released during microbial remineralization of sinking particles. *Geophys. Res. Lett.* 47, e2019GL086685. doi: 10.1029/2019GL086685

Whitby, H., Planquette, H., Cassar, N., Bucciarelli, E., Osburn, C. L., Janssen, D. J., et al. (2020b). A call for refining the role of humic-like substances in the oceanic iron cycle. *Sci. Rep.* 10, 1–12. doi: 10.1038/s41598-020-62266-7

Whitby, H., and van den Berg, C. M. G. (2015). Evidence for copper-binding humic substances in seawater. *Mar. Chem. SCOR WG 139: Organic Ligands A Key Control Trace Metal Biogeochem. Ocean* 173, 282–290. doi: 10.1016/j.marchem.2014.09.011

Winkler, L. W. (1888). Die Bestimmung des im Wasser gelösten Sauerstoffes. Berichte der deutschen chemischen. *Gesellschaft* 21, 2843–2854. doi: 10.1002/cber.188802102122

Witter, A. E., and Luther, G. W. (1998). Variation in Fe-organic complexation with depth in the Northwestern Atlantic Ocean as determined using a kinetic approach. *Mar. Chem.* 62, 241–258. doi: 10.1016/S0304-4203(98)00044-9

Yamashita, Y., Hashihama, F., Saito, H., Fukuda, H., and Ogawa, H. (2017). Factors controlling the geographical distribution of fluorescent dissolved organic matter in the surface waters of the Pacific Ocean. *Limnol. Oceanogr.* 62, 2360–2374. doi: 10.1002/lno.10570

Yang, L., Hong, H., Guo, W., Chen, C.-T. A., Pan, P.-I., and Feng, C.-C. (2012). Absorption and fluorescence of dissolved organic matter in submarine hydrothermal vents off NE Taiwan. *Mar. Chem.* 128–129, 64–71. doi: 10.1016/j.marchem.2011.10.003

Yang, R., and van den Berg, C. M. G. (2009). Metal complexation by humic substances in seawater. *Environ. Sci. Technol.* 43, 7192–7197. doi: 10.1021/es900173w

Yücel, M., Gartman, A., Chan, C. S., and Luther, G. W. (2011). Hydrothermal vents as a kinetically stable source of iron-sulphide-bearing nanoparticles to the ocean. *Nat. Geosci.* 4, 367–371. doi: 10.1038/ngeo1148

Yücel, M., Sevgen, S., and Le Bris, N. (2021). Soluble, colloidal, and particulate iron across the hydrothermal vent mixing zones in broken spur and rainbow, mid-atlantic ridge. *Front. Microbiol.* 12. doi: 10.3389/fmicb.2021.631885

Zhao, J., and Nelson, D. J. (2005). Fluorescence study of the interaction of Suwannee River fulvic acid with metal ions and Al3+-metal ion competition. *J. Inorganic Biochem.* 99, 383–396. doi: 10.1016/j.jinorgbio.2004.10.005

Zigah, P. K., McNichol, A. P., Xu, L., Johnson, C., Santinelli, C., Karl, D. M., et al. (2017). Allochthonous sources and dynamic cycling of ocean dissolved organic carbon revealed by carbon isotopes. *Geophys. Res. Lett.* 44, 2407–2415. doi: 10.1002/2016GL071348

frontiers | Frontiers in Marine Science

TYPE Original Research
PUBLISHED 16 August 2024
DOI 10.3389/fmars.2024.1432122

OPEN ACCESS

EDITED BY
Cecile Guieu,
UMR7093 Laboratoire d'océanographie de Villefranche (LOV), France

REVIEWED BY
Thomas Michael Holmes,
Antarctic Climate and Ecosystems Cooperative Research Centre (ACE CRC), Australia
Cedric Boulart,
UMR7144 Adaptation et diversité en milieu marin (AD2M), France

*CORRESPONDENCE
Oleg Belyaev
o.belyaev@csic.es

RECEIVED 13 May 2024
ACCEPTED 29 July 2024
PUBLISHED 16 August 2024

CITATION
Belyaev O, Huertas IE, Navarro G, Amaya-Vías S, de la Paz M, Sparaventi E, Heredia S, Sukekava CF, Laglera LM and Tovar-Sánchez A (2024) Hydrothermal alteration of seawater biogeochemistry in Deception Island (South Shetland Islands, Antarctica). *Front. Mar. Sci.* 11:1432122. doi: 10.3389/fmars.2024.1432122

Hydrothermal alteration of seawater biogeochemistry in Deception Island (South Shetland Islands, Antarctica)

Oleg Belyaev[1]*, I. Emma Huertas[1], Gabriel Navarro[1], Silvia Amaya-Vías[1], Mercedes de la Paz[2], Erica Sparaventi[1], Sergio Heredia[1], Camila F. Sukekava[3], Luis M. Laglera[3] and Antonio Tovar-Sánchez[1]

[1]Department of Ecology and Coastal Management, Institute of Marine Sciences of Andalusia (CSIC), Puerto Real, Cádiz, Spain, [2]Oceanography Department, Marine Research Institute (CSIC), Vigo, Pontevedra, Spain, [3]Chemistry Department, University of the Balearic Islands (UIB), Mallorca, Spain

Deception Island (DI) is an active volcanic caldera in the South Shetland Islands, Antarctica, with an inner bay, Port Foster, formed by an ancient eruption. The bay's seafloor hydrofracture system contains hydrothermal seeps and submarine vents, which are a source of trace metals (TMs) like Fe, Ni, Co, V, and greenhouse gases (GHGs) such as CO_2 and CH_4. This study presents measurements of TMs and GHGs in Port Foster's surface waters during January-February 2021 to characterize their spatial distribution. TMs concentrations in the northeastern region of the bay, particularly V (74 nM), Fe (361 nM), Co (3.9 nM) and Ni (17.2 nM), were generally higher than in the Southern Ocean, likely due to hydrothermal activity. As some TMs such as Fe are scarce in the SO and limit primary productivity, inputs of these nutrients from DI into surrounding waters may also regionally promote increased primary productivity. Higher surface temperature (ST), elevated partial pressure of CO_2 (pCO_2), and lower salinity were found near submarine fumaroles, with ST positively correlated with pCO_2 and negatively with salinity. Although hydrothermal sites showed localized CO_2 outgassing, the bay overall acted as a CO_2 sink, with a median flux of -2.78 mol m^{-2} yr^{-1} with an interquartile range (IQR) of 3.84 mol m^{-2} yr^{-1}. CH_4 highest concentration levels were found in the southeastern sector. The median concentration was 8.9 nM with an IQR of 1.9 nM, making Port Foster a regional net CH_4 source with a median flux of 9.7 µmol m^{-2} d^{-1} and an IQR of 3.4 µmol m^{-2} d^{-1}. Ultimately, the analysis of spatial patterns of the measured variables suggested that fumaroles of DI may be playing a significant role in the alteration of regional seawater biogeochemistry.

KEYWORDS

Deception Island, trace metals, fumaroles, biogeochemistry, hydrothermal vents, Southern Ocean, greenhouse gases emission

1 Introduction

The cycling of chemical compounds in the Southern Ocean (SO) is a fundamental component of the functioning of Earth. By taking up atmospheric CO_2 via biological and solubility pump processes and by releasing CO_2 from the deep ocean (Gruber et al., 2019), the SO modulates Earth's climate over seasonal-to-millennial timescales. Observational analyses and numerical models both indicate that the SO currently accounts for 40-50% of anthropogenic carbon uptake by the ocean (Terhaar et al., 2021). The biogeochemical cycling of carbon (C) and, in turn, of macronutrients (i.e., nitrate, nitrite, phosphate and silicate) and trace metals (TMs; e.g., iron (Fe), niquel (Ni), cobalt (Co) or vanadium (V), among others) in the SO has strong implications, not only for regional ecosystem functioning but also for primary production and carbon export throughout the world's oceans.

The Southern Ocean exhibits substantial spatial and temporal variability in its biogeochemical processes, particularly between the Antarctic shelves and open ocean regions. This variability spans seasonal to decadal timescales, driven by diverse factors including climate change. The Western Antarctic Peninsula (WAP), for instance, has been significantly affected by climate changes over the last 50 years (Morley et al., 2020), with the continental shelf and surrounding areas such as Deception Island (62°57'S, 60°8'W, Figure 1A) showcasing unique environmental phenomena. In this dynamic context, TMs in the Southern Ocean play a relevant role, where they are primarily found in the dissolved phase, complexed with biological or terrestrial ligands that influence their solubility, reactivity, toxicity, and bioavailability. These metals transition from the water column into particulate forms through adsorption onto organic and inorganic suspended particles, processes that are crucial for functions such as carbon fixation, nutrient uptake, and synthesis of vital biomolecules. However, their concentrations must be carefully evaluated in the marine environment because while some metals, like mercury and lead, are inherently toxic at any concentration, others may become toxic in excess (Da Silva and Williams, 2001; Morel and Price, 2003) or in their ionic form, like Cu^{2+} which in seawater can impede phytoplankton growth (García-Veira et al., 2024). Understanding the roles of TMs in ocean biogeochemistry, particularly in polar regions, remains challenging due to uncertainties about their sources, sinks, and internal cycling. Despite traditionally low estimates of external TM sources to Antarctic waters, recent research indicates that these metals can also reach the ocean through advection of water masses from continental margins, atmospheric deposition, and hydrothermal vent inputs (Xu and Gao, 2014; Janssen et al., 2020). This highlights a more complex and dynamic biogeochemical cycle than previously understood (SCOR Working Group, 2007; Chever et al., 2010; Klunder et al., 2011, 2011). Additionally, locations like Deception Island, part of the South Shetland Islands archipelago, supports large colonies of penguins which are pivotal in local nutrient cycling. These penguins contribute significantly to the biogeochemical cycling of TMs by transferring nutrients from their krill diet into the ecosystem through their excretions. This action enriches the soil and releases substantial amounts of Cu, Fe, Mn, and Zn into the surrounding waters—estimated annually at 28, 521, 4, and 29 tons, respectively (Sparaventi et al., 2021; Belyaev et al., 2023). The role of these TMs in the local biogeochemistry is critical, impacting everything from plant growth to animal health within the ecosystem (Liu et al., 2013; Chu et al., 2019; Castro et al., 2021; Sparaventi et al., 2021; Belyaev et al., 2023).

An intense global effort to quantify marine sources and sinks of greenhouse gases (GHGs) is currently ongoing (Friedlingstein et al., 2020). Nevertheless, there are still certain areas where monitoring is minimal, such as vast regions of the Antarctic basin (Montzka et al., 2011) – leading to a significant lack of accurate measurements in the SO, mainly due to the logistical restrictions of performing oceanographic operations in such areas. In the latest climatology of oceanic CH_4 emissions (Weber et al., 2019) no data were

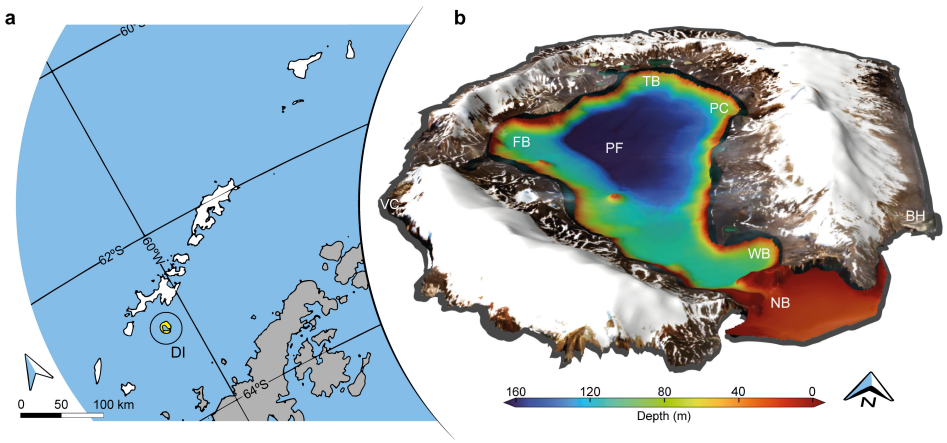

FIGURE 1
South Shetland Islands archipelago and Deception Island close-up view. **(A)** South Shetland Islands (highlighted in white) are located north of the West Antarctic Peninsula, with the Drake Passage in the north and the Bransfield Strait in the south. Deception Island (DI) is highlighted in yellow. **(B)** Sentinel-2 satellite merge with a digital elevation model of DI, displaying Port Foster (PF) bathymetry. VC, Vapor Col; BH, Baily Head; NB, Neptune's Bellows; PC, Pendulum Cove; TB, Telefon Bay; FB, Fumarole Bay; WB, Whalers Bay.

available between 0° and 90°W and south of 70°S, as only a few studies have reported surface distribution of CH_4 in the SO and with contrasting patterns (Lamontagne et al., 1974; Tilbrook and Karl, 1994; Bates et al., 1996; Heeschen et al., 2004; Yoshida et al., 2011; Bui et al., 2018). The paucity of CO_2 and CH_4 observations in the SO and particularly over Antarctic sub-shelves, calls for a better documentation of their distribution. In this sense, DI stands out as a volcanic environment populated by numerous hydrothermal vents, which while being a source of TMs also releases a significant amount of gases. The gas mixture released is predominantly CO_2 (75-90%), hydrogen sulfide (H_2S, 0.3 – 0.9%; Somoza et al., 2004) and methane (CH_4) to surrounding waters, therefore raising special interest as a potentially relevant contributor of these gases to this region of the SO.

We hypothesize that the inundated caldera of DI acted as a source of TMs and GHGs to seawater due to its active volcanic and hydrothermal activity. Therefore, the aim of this work was to characterize the spatial distribution of various trace elements (Fe, V, Co and Ni among others) and CO_2 and CH_4, in surface waters of Port Foster and provide new insights on the role of these geological processes on the occurrence of biogeochemical fertilizers in ocean waters of the SO.

2 Materials and methods

2.1 Study area

Deception Island is one of the most active Antarctic volcanoes, with several sites exhibiting a high geothermal activity, such as Pendulum Cove, Fumarola Bay, Telefon Bay and Whalers Bay (PC, FB, TB and WB respectively in Figure 1B). The island is crossed by three large fault systems (Rey et al., 1995), and many other smaller faults (Maestro et al., 2007). Seismic time series indicate noticeable long events associated to variations in the shallow hydrothermal system, along with earthquakes of a volcano-tectonic origin (Carmona et al., 2012). Port Foster, as the submerged part of the volcano (Figure 1B), experienced eruptive episodes in 1967, 1969 and 1970. During summer, water circulation in Port Foster can be approximated as a two-layers system, which is primarily forced by temperature and cause the upper layer (occupying the first 40-60 m of the water column) to move anticlockwise around the bay. Internal tides originated at the sill of Neptune's Bellows radiate towards the western side of the bay, favoring mixing and leaving the eastern side in a shadow zone. Sea ice melting associated to hydrothermal activity modify local circulation at small scales (~1 km) (Flexas et al., 2017). During winter, surface cooling mixes the water column until fully homogeneous, with temperatures near freezing.

2.2 Sampling design

In-situ measurements of conductivity (further converted to salinity, S) and surface temperature (ST) combined with collection of water samples in the surface layer (50 cm – 1 m in depth) for further chemical analysis, were conducted using a small boat along a transect consisting of 20 sites for Transect 1 (Leg 1) (January, 29 – Figure 2A) and 15 sites for Transect 2 (Leg 2) (February, 19 – Figure 2B), extending from Neptune's Bellows to

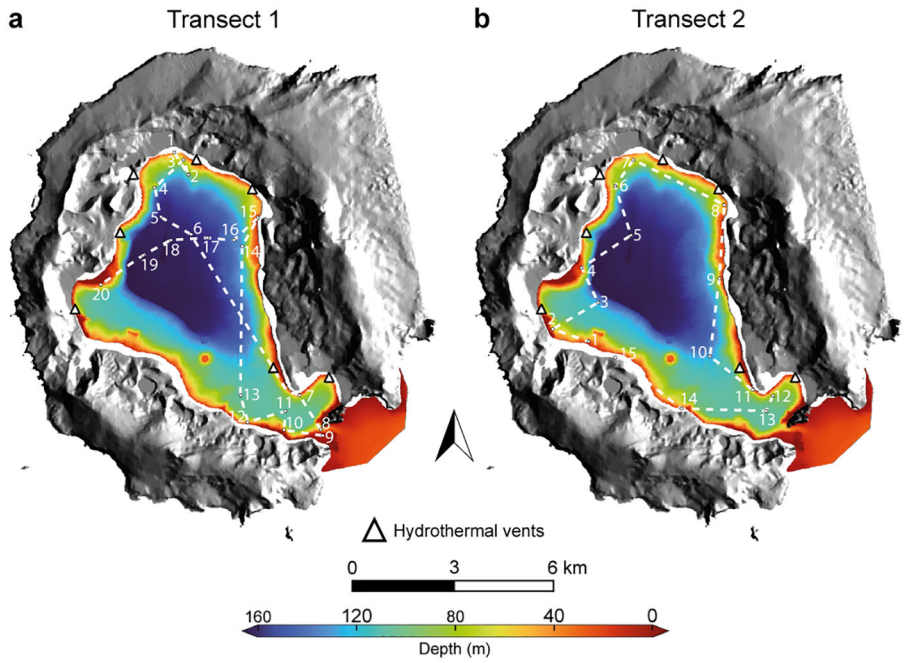

FIGURE 2
Transect 1 **(A)**, with 20 stations, was carried out on January 29, 2021 and Transect 2 **(B)**, with 15 stations was performed on February 19, 2021. Data on common variables was averaged for both samplings.

the northernmost section of Port Foster. Due to meteorological and logistic limitations, data for CO_2 and CH_4 were taken on different sampling days, and with sampling tracks also differing. In selecting our sample sites, we considered that the main CH_4 source at DI is related to fumarolic emissions, which are primarily concentrated near the coastline of the island, and that Port Foster is rich in dissolved oxygen which impedes CH_4 production by methanogenesis within the bay.

Geographic positions of all samples were recorded using a hand-held geographic positioning system (Magellan-Meridian-Platinum GPS, Magellan, USA, ± 5 m). The system was set to track positions at high resolution throughout the sampling campaigns and was later linked to measurement timestamps (care was taken to ensure times were synchronized) using linear interpolation, yielding individual positions for every sample. A single position for each set of vertical water parameter profiles was then derived as the center point of the cloud of positions, allowing factors such as boat drift to be accounted for. Communication with the GPS was facilitated by GPSBabel (https://www.gpsbabel.org).

2.3 Thermohaline properties

At each site conductivity and ST were quickly measured using a hand-held water quality multiprobe [YSI-6920V2, YSI Incorporated, USA (conductivity acc. - ± 0.5% of reading + 0.001 mS/cm; ST acc.: ± 0.15°C)] that was deployed by hand from the boat with the help of a winch.

2.4 Biogeochemical variables

Seawater samples were collected from a pneumatic boat at 50 cm - 1 m below the surface using a peristaltic pumping system equipped with acid-washed C-Flex tubing in the pump head and filtered *in-situ* through an acid-cleaned polypropylene cartridge filter (0.22 µm; MSI, Calyx). Once collected, a sub-sample was immediately transferred to a container where pH was measured (NBS scale), pH had an accuracy of ± 0.002 units and it was converted to pH at total scale (25°C) with the CO2SYS program (Version v3.2.0 for MATLAB) (Van Heuven et al., 2011; Sharp and Byrne, 2020). Conductivity was also converted to S PSU using an instrument specific conversion equation. The rest of the seawater sample was immediately processed for analysis of total alkalinity (TA), ammonium (NH_4^+), nitrite (NO_2^-), nitrate (NO_3^-), orthophosphate (PO_4^{3-}), and silicate (SiO_2) in the laboratory. In particular, samples for TA analysis were collected in 500-ml borosilicate bottles, and poisoned with 100 µl of $HgCl_2$-saturated aqueous solution and stored until measurement onshore within 3 months upon collection. TA was measured by potential titration with a Titroprocessor (model Metrohm 794), with precision and accuracy of measurements being determined from certified reference material (CRMa batch #97 provided by Prof. Andrew Dickson, Scripps Institution of Oceanography, La Jolla, CA, USA) and equivalent to ±0.8 and ±4 µmol kg^{-1} respectively. For inorganic nutrient analysis, samples (5 mL, two replicates) were taken, filtered immediately (Whatman GF/F, 0.7 µm) and stored frozen. Nutrient concentrations were measured with a continuous flow auto-analyzer (Skalar San^{++} System) using standard colorimetric techniques (Hansen and Koroleff, 1999). The accuracy of the analysis was established using Reference Material for Nutrients in Seawater - KANSO CRM (Lot. CP). The recoveries for n=3 were 108 ± 3%, 124 ± 1%, 102 ± 2% and 99 ± 2% for NO_2^-, NO_3^-, PO_4^{3-} and SiO_2 respectively.

Concentrations of Co, Cu, Mo, Ni, Pb, Cd, Fe, V and Zn were analyzed by ICP-MS (iCAP, Thermo) after extraction and preconcentration using the APDC/DDDC organic extraction method (Bruland et al., 1979; Tovar-Sanchez, 2012). The accuracy of the analysis was established using Coastal Seawater References Material for trace metals ERM-CA403 (European Reference Material). The recoveries for n=1 ranged from ~81% for Pb to ~109% for Cd (see Supplementary Table S1 for recoveries). Blanks (acidified ultra-pure water) were preconcentrated following the same method as the samples.

Partial pressure of dissolved CO_2 (pCO2, µatm) was subsequently calculated for each sampling station with the CO2SYS program using TA, pH_{T25}, phosphate and silicate concentrations, S, ST, and P as input parameters. Proper dissociation constants for carbon (Mehrbach et al., 1973; Dickson and Millero, 1987), sulfate (KSO_4) (Dickson et al., 1990) and fluorine (KF) (Perez and Fraga, 1987) were considered, and a borate-salinity ratio (Lee et al., 2010) was also used.

For CH_4 measurements, samples (two replicates) were collected using 120 mL serum vials, sealed with grey-butyl rubber septa and aluminum crimps and preserved with 250 µL of saturated $HgCl_2$ to inhibit microbial activity. Trace gas samples were stored upside down in the dark, until analysis in the laboratory. Dissolved CH_4 was analyzed by static headspace equilibration gas chromatography (GC) according to De La Paz et al. (2015). In summary, the method uses a high-precision automated burette to introduce ultrapure N_2 gas into a sample vial; once equilibrium is achieved overnight, the headspace is injected automatically into the gas chromatograph (Agilent GC 7890-A) which is subsequently separated using a Porapak Q-packed column and detected using a flame ionization detector. Overall, the accuracy of the method (the average coefficient of variation from the analysis of replicates), is assessed to be 5% for CH_4, and the limit of detection is 1.5 parts per billion (ppb).

Chlorophyll-a surface concentrations were obtained from Copernicus Sentinel-2 satellites, where the images of Deception Island taken by Sentinel-2 on December 27, 2020, were acquired (https://scihub.copernicus.eu/ on August 15, 2023) and subsequently processed. This processing used the methodology outlined by Caballero et al. (2022). Originally, the images were in the Top of Atmosphere (TOA) Level 1C format, having undergone radiometric and geometric adjustments. These were then transformed into Bottom-of-Atmosphere (BOA) visuals using ACOLITE, a widely-used software for atmospheric correction. Corrections for sunglint effects were also applied to these images. Further, an OC3 product, essential for biogeochemical analysis, was derived from these images. The OC3 approach is a band ratio algorithm facilitating the assessment of chlorophyll-a levels in

seawater, utilizing three spectral bands in the vicinity of blue, green, and red wavelengths (O'Reilley et al., 2000).

2.5 CH_4 and CO_2 saturation ratios and air-sea fluxes

2.5.1 Methane

Air-sea CH_4 exchange in Port Foster, were calculated across the sampled stations according to the following equation:

$$F = k\ (C_W - C_A) \quad (1)$$

where F is the atmosphere-ocean CH_4 flux (in μmol m^{-2} d^{-1}), k is the gas transfer velocity (in cm h^{-1}), C_w is the CH_4 concentration in water and C_A is the equilibrium concentration of CH_4 in the layer of air above the water. In Equation 1, k was estimated according to (Wanninkhof, 2014):

$$k = a\ \langle U10 \rangle^2 \left(\frac{Sc_{CH4}}{660}\right)^{-0.5} \quad (2)$$

where a is a cost function used for gas transfer coefficient optimization (0.251), U10 is the *in situ* average winds (AEMET, 2021), averaged for 31 days (15 before and 15 after the sample was taken) and corrected for 10m height (m s^{-1}) (Wanninkhof, 2014) and Sc_{CH4} is the Schmidt number adjusted for temperature. The atmospheric equilibrium solubility of CH_4 was derived following Equation 3 (Wiesenburg and Guinasso, 1979):

$$\ln C_a = \ln f_G + A_1 + A_2\left(\frac{100}{T}\right) + A_3 \ln\left(\frac{T}{100}\right) + A_4\left(\frac{T}{100}\right) + S\text{‰}\left[B_1 + B_2\left(\frac{T}{100}\right) + B_3\left(\frac{T}{100}\right)^2\right] \quad (3)$$

where f_G is the molar fraction in dry air for methane (1.82×10^{-6} as of January, 2021 at Palmer Station), T is the temperature in Kelvin and S is the salinity in ppt. A_i and B_i are the constants for calculation of solubilities in nmol L^{-1}: A_1 = -415.2807; A_2 = 596.8104; A_3 = 379.2599; A_4 = -62.0757; B_1 = -0.059160; B_2 = 0.032174; B_3 = -0.0048198 (Wiesenburg and Guinasso, 1979). The fourth temperature dependent parameter [A_4(T/100)] especially accounts for the vapor pressure of water. Additionally, methane saturation ratios expressed as percentage were calculated as $C_W/C_A \times 100$.

2.5.2 Carbon dioxide

Air-sea CO_2 exchange was calculated using the bulk flux equation of (Wanninkhof, 2014):

$$F = kK'(pCO_{2W} - pCO_{2A}) \quad (4)$$

where F is the flux (in mol m^{-2} yr^{-1}), k is the gas transfer velocity (in cm h^{-1}), K' is the CO_2 atmospheric equilibrium solubility from moist air (in mol L^{-1} atm^{-1}) and pCO_{2W} and pCO_{2A} denote the partial pressures of CO_2 (in μatm) in equilibrium with surface water and the overlying air respectively. In the Equation 4, k was calculated as it was for CH_4, using the Equation 2. K' was obtained as:

$$\ln K' = A_1 + A_2\left(\frac{100}{T}\right) + A_3 \ln\left(\frac{T}{100}\right) + A_4\left(\frac{T}{100}\right)^2 + S\text{‰}\left[B_1 + B_2\left(\frac{T}{100}\right) + B_3\left(\frac{T}{100}\right)^2\right] \quad (5)$$

T is the temperature in Kelvin and S is the salinity expressed in ppm. A_i and B_i are the constants (moist air) for calculation of solubilities in mol L^{-1} atm^{-1}: A_1 = -160.7333; A_2 = 215.4152; A_3 = 89.8920; A_4 = -1.47759; B_1 = 0.029941; B_2 = -0.027455; B_3 = 0.0053407 (Weiss and Price, 1980). To account for the CO_2 partial pressure in air, molar fraction surface monthly average data for January 2021 was used in Equation 5, equivalent to 410.5 ppm (NOAA/GML). Finally, CO_2 saturation ratios were calculated as $pCO_{2W}/pCO_{2A} \times 100$.

3 Results

3.1 Hydrothermal venting shapes the biochemical composition of Port Foster

Chemical and physical variables measured in surface waters of Port Foster during both sampling legs (January 29 and February 19, 2021) showed an evident zonal distribution, possibly reflecting the presence of volcanic structures inside the bay (Figure 3). Hydrothermal vents whose inputs are expected to affect surface biogeochemistry in the caldera are mainly restricted to shallow areas of the Port Foster perimeter. Accordingly, special physicochemical features clearly different from those at the center of the bay were indeed found in surface waters located above the hydrothermally active areas of FB, TB, PC and WB (Figure 2). Hydrothermal activity tracers, such as elevated ST (Figure 3A) high pCO2 were observed in these shallow and coastal spots of Port Foster. Computed correlations (Supplementary Figure S1) indicated a direct and statistically significant relationship between ST and pCO_2 levels (*r=0.85, 95% CI, P<.001, n=20*). Temperature was also inversely correlated with salinity (*r=-0.73, 95% CI, P<.001, n=35*), suggesting the presence of freshwater input from the underneath venting activity or coastal melting runoff. Additionally, the spatial distribution of CH_4 sea surface concentrations was consistent with the location of the venting sites (Figure 4A), although significant correlations were not observed with the rest of hydrothermal tracers. Trace metals distribution within Port Foster Bay also revealed zonality associated to the volcanic structures inside the bay. V, Fe, Co and Ni exhibited the highest concentrations in surface waters of PC and TB, as well as slightly increased values near WB, peaking at 74 nM (Leg 1, St. 15), 361 nM (Leg 1, St. 1, white star), 3.9 nM (Leg 1, St. 1, white star) and 17.2 nM (Leg 1, St. 1, white star) respectively (Figures 3C–F).

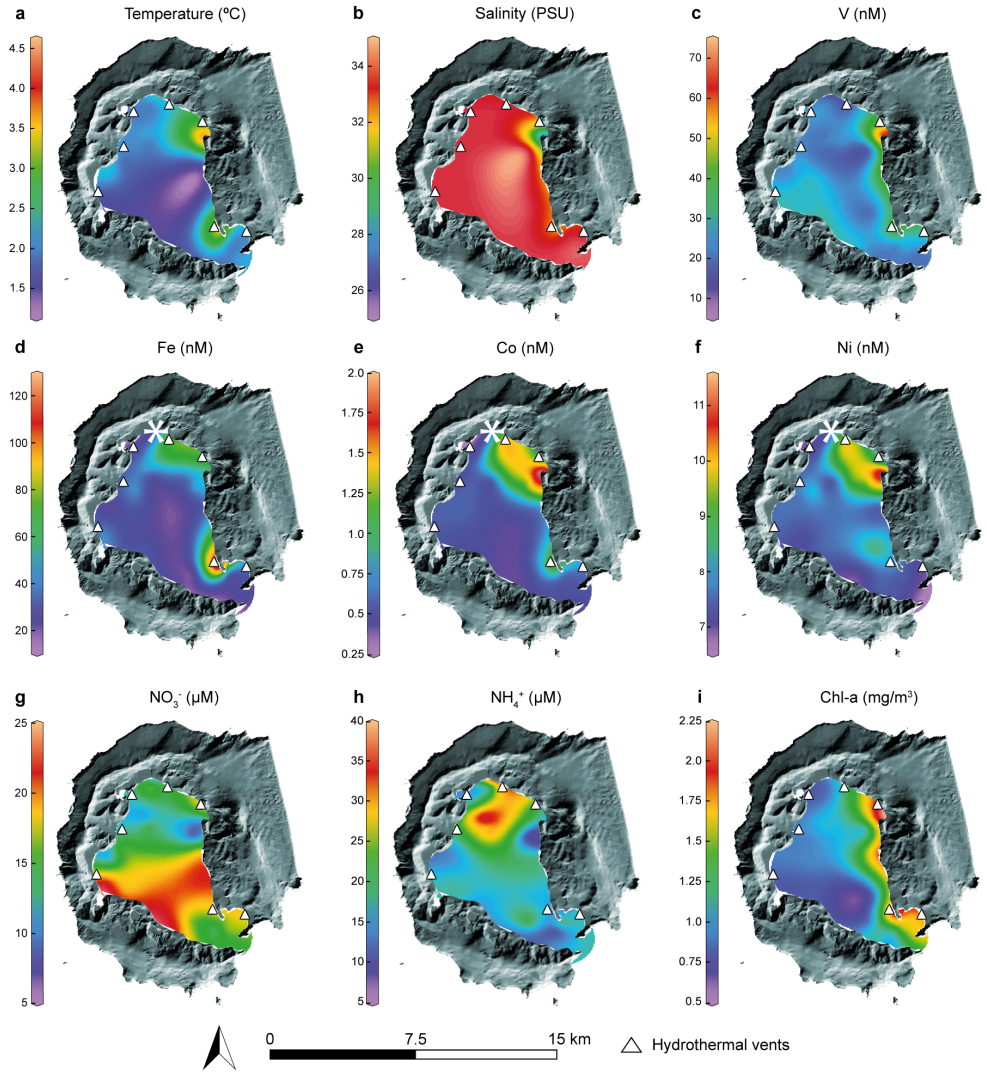

FIGURE 3
Spatial distribution of thermohaline properties **(A, B)**, most relevant TMs **(C, D, E, F)**, nutrients **(G, H)** and chlorophyll-a **(I)** in Port Foster Bay as obtained during the sampling campaigns. White star in Fe **(D)**, Co **(E)** and Ni **(F)** indicates a sampling station (Leg 1, St. 1) where high concentrations of those trace metals were obtained (Fe = 361.13 Nm; Co = 3.89 nM; Ni = 17.19 nM). Concentrations observed at the white star were omitted from the interpolation for better visualization.

3.1.1 Concentrations influenced by hydrothermal venting

Correlations with fumarolic inherent features (Supplementary Figure S1), such as ST, salinity or pCO_2 showed that V was directly correlated with ST (*r=0.47, 95% CI, P=.005, n=35*) and pCO_2 (*r=0.71, 95% CI, P=.001, n=20*), and inversely correlated with salinity (*r= -0.84, 95% CI, P<.001, n=35*), being also present in FB and towards the mouth of the bay. Cobalt and Ni showed very similar behavior, with *r= 0.57, 95% CI, P<.001, n=35*; and *r=0.48, 95% CI, P=.004, n=35* respectively for ST, *r= -0.44, 95% CI, P=.011, n=35*; and *r= -0.37, 95% CI, P=.028, n=35* respectively for salinity and r=0.67 and 0.65 respectively for pCO_2. Averaged chlorophyll surface concentration was characterized by higher levels predominantly on the western side of PF and exhibited direct and statistically significant relationships with ST (r=0.5, *95% CI, P=.002, n=35*) and V (r=0.53, *95% CI, P=.001, n=35*), and an inverse correlation with salinity and surface pCO2 (r=-0.45, *95% CI, P=.006, n=35;* r=0.29, *95% CI, P=.219, n=20*, respectively).

3.1.2 Concentrations not restricted to hydrothermal venting sources

Fe exhibited weaker but still statistically significant relationships with ST (*r=0.37, 95% CI, P=.027, n=35*), but poorer correlation with salinity (*r=-0.17, 95% CI, P=.341, n=35*) and pCO2 (*r=0.36, 95% CI, P=.122, n=20*). In the other hand, TMs like Cd, Zn and Pb correlated inversely to hydrothermal indicators such as ST (r=-0.41, *95% CI, P=.034, n=35*; r=-0.19, *95% CI, P=.048, n=35*; r=-0.42, *95% CI, P=.317, n=13*, respectively) or pCO2 (r=-0.14, *95% CI, P=.559, n=20*; r=-0.17, *95% CI, P=.460, n=20*; r=-0.3, *95% CI, P=.246, n=20*, respectively). Molybdenum exhibited no correlation with ST and pCO2 (r=0.002, *95% CI, P=.99, n=35*; r=0.12, *95% CI, P=.624, n=20*, respectively). In the same way, Cu showed almost no

correlation with ST and pCO_2 (r=0.14, *95% CI, P=.405, n=35*; r=0.1, *95% CI, P=.687, n=20*, respectively). Regarding nutrient occurrence and distribution, an evident zonal pattern was not observed within the bay. The highest concentrations of NO_3^- and PO_4^{3-} were primarily located in the south-western region of PF, peaking 23.0 ± 0.1 (Leg 2, St. 2) and 1.45 ± 0.00 µM (Leg 2, St. 2) respectively (Figure 3G, PO_4^{3-} not shown). High levels of NH_4^+ were found in surface waters located in the northern central section of Port Foster, peaking 37.5 µM in Leg 1, St. 3. This nutrient was not significantly correlated with the hydrothermal tracers, and, as expected, inversely correlated with NO_3^- and PO_4^{3-} (*r=-0.41, 95% CI, P=.0244, n=35; r=-0.45, 95% CI, P=.013, n=35*, respectively).

3.2 Distribution and fluxes of GHGs in Port Foster

The distribution of concentrations of CH_4 found in the surface waters of Port Foster matches the localization of known sources of hydrothermal activity i.e., FB, TB, PC and WB (Figure 4A). The concentrations of CH_4 found in Port Foster range from 6.69 to 15.93 nM (Supplementary Table S2). The highest levels of CH_4 were observed in the vicinity of WB, for Leg 2, St. 13 and 14, with 15.93 and 13.47 nM respectively with the median concentration of CH_4 in the bay resulting in 8.88 nM with an IQR of 1.90 nM. Surface waters of Port Foster were supersaturated with respect to atmospheric CH_4, ranging from ~202% to ~465% (Figure 4C). Air-sea CH_4 exchange in Port Foster presented a median flux of 9.68 µmol m^{-2} d^{-1} and an IQR of 3.43 µmol m^{-2} d^{-1}, with the maximum effluxes of 22.38 and 17.93 µmol m^{-2} d^{-1} being obtained Leg 2, St. 12 and 13 respectively and a minimum flux of 6.36 µmol m^{-2} d^{-1} estimated in Leg 2, St. 11 (Figure 4B) (positive flux values indicating CH_4 flux from water to atmosphere) (See median, Q1-Q3 and histograms in Supplementary Table S3). Hence, the inundated caldera behaved as a net source of CH_4 to the atmosphere during the monitored period, with a regional water to atmosphere methane transport median (Q1-Q3) inequivalent to 0.002 (0.0016 – 0.0023) Gg yr^{-1} (considering a surface for the inner bay of approximately 36 km^2). Despite the limitation of mid-bay data availability, it was considered that the major sources of CH_4 were located in the fumarolic areas distributed in the shoreline of the bay.

An evident spatial pattern of both, the dissolved CO2 levels (Figure 5A) and the air-sea gradient of CO_2 (ΔpCO_2) was observed in Port Foster. Areas with the largest positive ΔpCO_2 (~ 400 µatm) were located on the north-eastern part of the bay, where a marked fumarolic activity in the vicinity of PC has been described. Overall, the CO_2 surface-atmospheric equilibrium seems to be mostly displaced around PC and TB areas, possibly indicating a volcanic source-like nature in this coastal fringe. In contrast, the area with the largest negative ΔpCO_2 was located in the center of the bay, which is characterized by an average depth of ~120m (peaking more than 160m) and lack of near-surface hydrothermal vents. Hence, this central zone acted as a local CO_2 sink. Accordingly, air-water CO_2 fluxes result in outgassing occurring mostly in the PC area, reaching 18.96 mol m^{-2} yr^{-1} in Leg 1, St. 15. Similarly, CO_2 emissions towards the atmosphere were also measured at Leg 1, St. 1, 2, 14 and 16, all of them near the PC area (Figure 5B) where CO_2 oversaturated waters were measured (Figure 5C). In particular, sampling stations of Leg 1, 1, 2, 14, 15 and 16 registered oversaturation values with respect to the atmospheric CO_2 level equivalent to ~135%, ~120%, ~103%, ~221% and ~112% respectively. The median (Q1-Q3) flux across the entire Port Foster extension was calculated to be -2.78 (-3.58 – 0.26) mol m^{-2} yr^{-1}, which correspond to an annual median (Q1-Q3) withdrawal from the atmosphere of 4.41 (5.69 – 0.42) Gg of CO_2 (See Supplementary Table S4 for CO_2 data) (See median, Q1-Q3 and histograms in Supplementary Table S3).

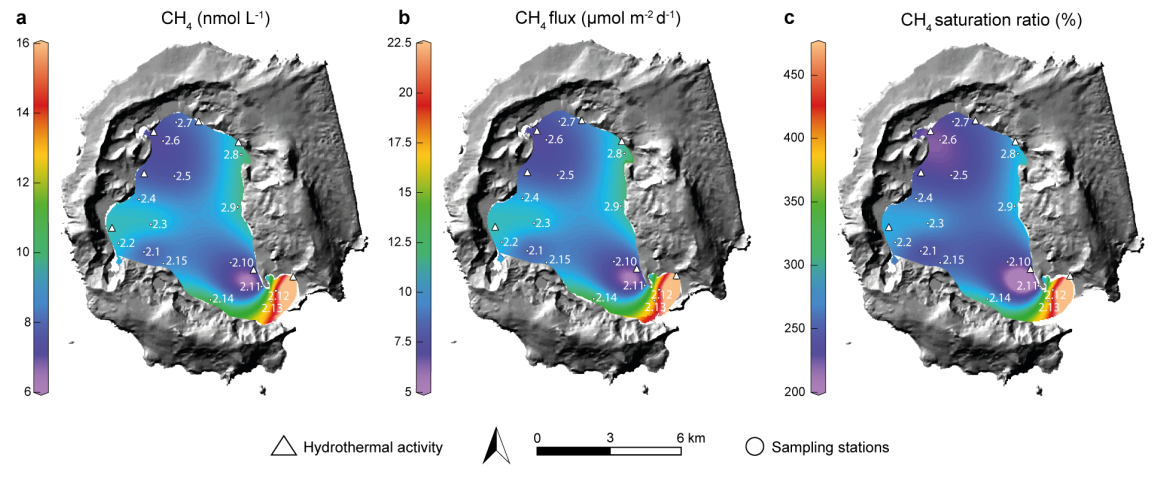

FIGURE 4
Characterization of CH_4 presence and distribution within Port Foster Bay. Station number is indicated within Port Foster as 2.x (Transect 2 – station x). **(A)** Surface CH_4 concentrations in nmol L^{-1} as collected during the second leg, on February 19, 2021. **(B)** Calculated CH_4 sea-air flux expressed in µmol m^{-2} d^{-1} according to local wind speed, salinity and water ST (Weiss, 1970; Wiesenburg and Guinasso, 1979; Wanninkhof, 2014). **(C)** Methane sea-air saturation ratios calculated as $C_W/C_A \times 100$, expressed in %.

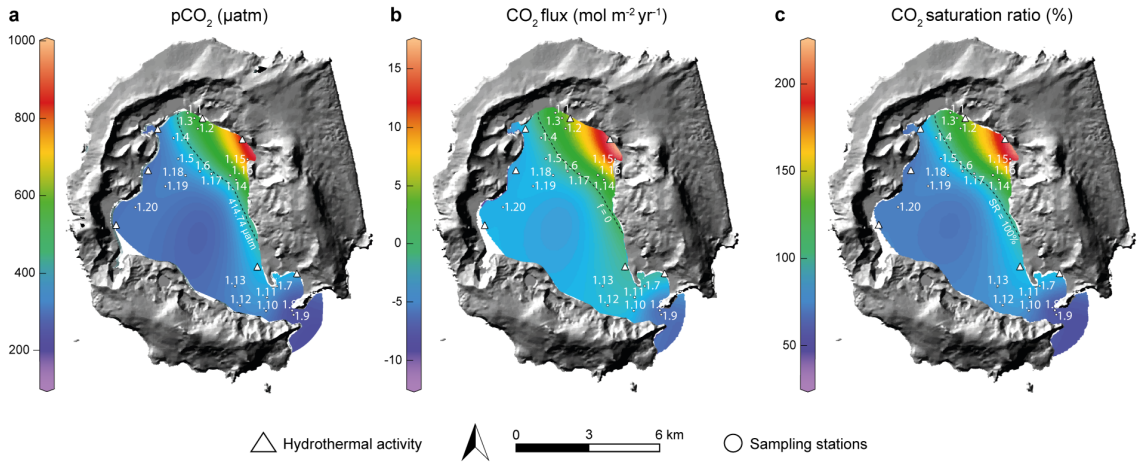

FIGURE 5
Characterization of CO_2 distribution within Port Foster Bay. **(A)** Surface carbon dioxide partial pressures in µatm as collected during the first leg, on January 29, 2021. Black dashed line indicates where pCO_{2W}/pCO_{2A} = 1. **(B)** Calculated carbon dioxide sea-air flux expressed in mol m^{-2} yr^{-1} according to local wind speed, salinity and water ST (Wiesenburg and Guinasso, 1979; Weiss and Price, 1980; Wanninkhof, 2014). Black dashed line indicates where flux = 0. **(C)** Carbon dioxide sea-air saturation ratios calculated as pCO_{2W}/pCO_{2A} × 100, expressed in %. Black dashed line indicates where water saturation = 100%.

4 Discussion

Results presented in this work indicate that the spatial distribution of TMs, CO_2 and CH_4 in Port Foster seems to be related to the distinct geologic characteristics of the fumaroles present in DI. For CH_4, although our studied transect has limited CH_4 measurements at the bay's center, nearby samples reveal a peripheral CH_4 distribution near the shore, coinciding spatially with fumarole presence rather than in Port Foster's center. While the presence of CH_4 in Port Foster's surface waters can also be attributed to biological production and organic matter (OM) degradation, oxygen levels throughout the basin are considerably high within the entire water column (Sturz et al., 2003), which does not favor OM methanogenesis and instead enhances available CH_4 oxidation. While aerobic CH_4 production can occur, it is less prevalent due to the preferential use of oxygen in bacterial respiration. It is still possible however that some CH_4 near the fumaroles could have a mixed origin – hydrothermal and biotic – from small, localized anoxic zones near the coast (due to organic matter accumulation and microbial activity), influencing the biotic/abiotic ratios of methane production. Given the mentioned characteristics of Port Foster, we consider that the majority of CH_4 detected in our study has hydrothermal origin. According to Caselli et al. (2004), PC and WB are considered as water vapor emanating fumaroles, with overall lower temperatures (20-70°C) as compared to the more sulfidic and hotter (90-100°C) FB fumaroles. CH_4 emissions are known to be higher in low-temperature fluid vents (Von Damm and Lilley, 2004), which would explain the spatial distribution of the surface levels of CH_4 observed in Port Foster in our study. In this regard, although mainly large and intense bubbling was observed in the fumarolic area, it is important to note that in shallow vent environments, the intensity of gas bubbling and the size of the gas bubbles may also influence CH_4 concentrations due to variations in microbial oxidation rates. The CH_4 concentrations reported here are consistent with previous early research performed under the RACER program in 1987, which investigated CH_4 enrichments in Port Foster and providing an average concentration of 9.37 nM of CH_4 within the bay, which is particularly high with respect to the levels of this gas found in the surrounding water masses in the Bransfield Strait, whose surface levels averaged 2-3 nM (Tilbrook and Karl, 1993). These low CH_4 concentrations have been more recently confirmed as a mean value of 2.7 nM for the surface Southern Ocean layer (Polonik et al., 2021). Surface concentrations of CH_4 obtained in the inner bay of DI are also considerably higher than the typical CH_4 ranges reported across the Southern Ocean (Ye et al., 2023), which are characterized by a generally CH_4 undersaturated waters. It is worthy to indicate that higher concentrations of CH_4 (up to 10.95 nM) have also been detected in the Bransfield Strait, particularly in the south of the South Shetland Islands archipelago. Even though a more comprehensive assessment is required to fully discriminate the sources and sinks of CH_4 in the SO, our data could be associated to the presence of such high levels of CH_4 in the area close to the Bransfield Strait possibly due to the eastward transport of the gas from Port Foster through the Neptune Bellows (Kholmogorov et al., 2022), largely mediated by the hydrographic regime of the area. These authors report a transect next to DI with the highest levels of dissolved CH_4, reaching 10 nM further east in the Bransfield Strait. Calculated effluxes obtained in our study indicate that Port Foster behaved almost entirely as a CH_4 source for the SO, whose origin could lie on the hydrothermal activity present in the caldera. Although no significant correlation was obtained with other hydrothermal tracers like ST and pCO_2, probably due to the oxidation processes affecting the gas in the water column from

the source, our assessment suggests that Deception Island still plays a role as a contributor to CH_4 SO budgets.

This was not the case for CO_2, as our measurements showed a net uptake of this gas from the bay. Previous research conducted in the Bransfield Strait reveals varying patterns in dissolved CO_2 concentrations across different locations and seasons. For instance, during Macro'95, a survey performed in the Bransfield Strait and Bellingshausen Sea, the western basin of the Bransfield Strait acted as a minor source of CO_2 to the atmosphere, releasing an average of 0.44 mol C m^{-2} yr^{-1}, while the Bellingshausen domain has been characterized by presenting a marked influx of CO_2 equivalent to 7.3 mol C m^{-2} yr^{-1} (Álvarez et al., 2002). In other adjacent regions to DI such as the Gerlache Strait, the annual net sea-air CO_2 flux from 2002 to 2017 averaged 0.45 ± 1.58 mol m^{-2} yr^{-1} (Monteiro et al., 2020). Similarly, Ito et al. (2018) observed between 2008 and 2010 that surface waters in the Bransfield Strait generally acted as a sink of atmospheric CO_2 during the summers, except in 2009 when it became a weak CO_2 source. Rodrigues et al. (2023) also reported that in the spring of 2018, the Bransfield Strait consistently functioned as a CO_2 sink, with an average influx of 0.99 mol m^{-2} yr^{-1}. Although Bransfield Strait presents similar heterogeneous CO_2 flux dynamics than those found here in Port Foster, the drivers behind both systems can be different. In the Strait, CO_2 air-sea exchange is mainly influenced by hydrodynamic factors such as the interaction of various cold and warm water masses from the Weddell Sea shelf and the Bellinghausen sea respectively, while the CO_2 fluxes (mainly strong efflux) observed in Port Foster were primarily associated to active hydrothermal systems present in the perimeter of the bay. Deception Island, being situated in a back-arc system, exhibits a higher concentration of CO_2 in the hydrothermal fluids when compared with other volcanically active geological systems with respect to the surrounding water masses (German and Seyfried, 2014). This is consistent with our measurements displaying higher levels of this gas in the northeastern section of the bay close to the proximities of the fumaroles (Leg 1, St 15 and 16), which clearly diminished towards the deeper center of the caldera where CO_2 undersaturated waters were found. This spatial distribution is in line with earlier studies that revealed a regional variation in CO_2 dynamics caused by localized fumarolic and hydrothermal activity (Shitashima, 1998).

To assess the origin of such gasses in Port Foster, while specific isotopic data about CO_2 and CH_4 was not analyzed in the present study, information is available on isotopic gas composition in DI, that allows to infer the origin of such gases within the bay. For instance, Kusakabe et al. (2009), while not specifically mentioning δ^{13}C-CH_4 values, provide δ^{13}C values for CO_2, which range from -5 to -6‰. These values indicate degassing from a mid-ocean ridge basalt (MORB)-type mantle source, suggesting a similar mantle origin for other carbon-containing gases, including CH_4. Regarding helium isotopes, Kusakabe et al. shows the existence of high ^{3}He/^{4}He ratios and other noble gas data highlight the significant contribution of mantle-derived helium.

The volcanic nature of DI influenced the distribution of some TMs (V, Fe, Co, and Ni) near the active hydrothermal vents in the north-eastern side of Port Foster. However, this was not the case for Cu, Mo, Zn and Cd. It is not clear why the active flux of warmer and less saline water to Port Foster surface waters was enriched in some metals and not in others although coprecipitation to excess iron and biological uptake on the highly productive East half of Port Foster could have played a role. Our results for Fe, Co, V and Ni are in agreement with previous studies evidencing that hydrothermal activity represents a strong driver behind the availability of TMs in the ocean (German and Seyfried, 2014; Resing et al., 2015; Mei et al., 2022). Moreover, sediments in Port Foster have been found to be enriched in many of these TMs (Somoza et al., 2004) suggesting that the hydrothermal venting could contribute to its accumulation in the sea bottom after being released. Given the high concentrations of TMs found in Port Foster in this study relative to regional open ocean concentrations, DI emerges as a potentially important source of TMs to the Bransfield Strait and nearby oceanic regions. In this sense, Measures et al. (2013) showed evidence of transport of TMs from coastal waters of the Antarctic Peninsula into the Antarctic Circumpolar Current. This suggests that TMs from coastal regions, including volcanic islands like DI, are transported into the open ocean, influencing the biogeochemistry of larger oceanic areas. Additionally, reported Fe concentrations in the Weddell Sea show elevated levels particularly near the Antarctic Peninsula (Sañudo-Wilhelmy et al., 2002). The Fe levels (ranging from 4.5 to 31 nM) are attributed to natural processes such as resuspension of benthic sediments, upwelling and, by extension to the present study, hydrothermal activity from volcanic islands like DI. Similarly, a recent study by Sierpinski et al. (2023) also reported 18.9 ± 6.1 nM Fe concentrations in Admiralty Bay, King George Island, concentrations which while being high when compared to surrounding waters of the Bransfield Strait, Bellingshausen (De Jong et al., 2015) Sea or the Atlantic sector of the SO (Klunder et al., 2011), are considerably below the dissolved Fe concentrations found within Port Foster in this research. Other TMs like Co or Al reported by Sañudo-Wilhelmy et al. (2002) in the Bransfield Strait, reflect lower concentrations when compared to those found in DI highlighting the role of hydrothermal emissions in the pool of these elements in the SO. The Bransfield Current, particularly the Transitional Water with Bellingshausen Sea influence (TBW), is characterized by an eastward flow of water in the section where DI is located, possibly influencing the distribution of trace TMs (Measures et al., 2013). Data supports the observation that Chl-a concentrations are greater under the influence of TBW (Gonçalves-Araujo et al., 2015).

Unlike TMs, nutrients measured across Port Foster showed to be rather homogeneous, with slightly higher levels of both NO_3^- and PO_4^{3-} being observed in the mid-southern bay, not restricted to specific areas such as those above the fumaroles, inversely correlated for example to hydrothermal tracers such as pCO_2 or ST (Supplementary Figure S1). This pattern may indicate inputs of open ocean waters from the Bransfield Strait through the Neptune Bellows, according to other studies that provide NO_3^- concentrations ranging from 22.5 to 38 µM in the Bransfield Strait (Polukhin et al., 2021). Similarly, these authors measured

silicate concentrations in the upper layer of the Strait, between 74 to 81 μM, a range that is consistent with our data in Port Foster. As expected, a correlation is found between the nutrients and all indicators of chl-a growth, highlighting their significant role in phytoplankton development, which is also supported by a study conducted by Sturz et al. (2003) further corroborating these values. However, the lack of significance between chl-a and the concentrations of NH_4^+, NO_3^-, and PO_4^{3-} could suggest that the phytoplankton growth is being limited by another nutrient or TM in Port Foster, potentially leaving excess of NH_4^+, NO_3^-, and PO_4^{3-} within the bay. This ultimately gives evidence of the need for contrasting studies in various locations of Port Foster that could provide further insights into the dynamics of phytoplankton growth. It is interesting to note that specifically, in Port Foster, a notably high concentration of NH_4^+ in surface waters was observed, exhibiting a slight negative correlation with *chl-a*, which suggested a possible consumption by phytoplankton. Ammonium production in the euphotic zone is often the result of heterotrophic metabolism, which is later subjected to removal processes including phytoplankton uptake and nitrification. Also, NH_4^+ can be produced via dinitrogen reduction by hydrogen sulfide at moderate temperatures in hydrothermal venting systems (Schoonen and Xu, 2001), however, more data is needed about the distribution of concentrations of hydrogen sulfide within Port Foster to draw any possible correlations. Nevertheless, Sturz et al. (2003) showed that snow and runoff around Port Foster Bay was characterized by NH_4^+ concentrations as high as 90 μM, suggesting that glacier meltwater may be flowing into the bay and in combination with waste from the marine biota (Laglera et al., 2020), would become not limiting for phytoplankton growth. In the Bransfield Strait NH_4^+ levels varying between 1 and 3.8 μM were measured (Polukhin et al., 2021) and Sturz et al. (2003) reported NH_4^+ concentrations in Port Foster's mid bay and peripheral coves, which ranged from 0 to 4 μM. Our statistical analysis does not seem to support the runoff NH_4^+ source, as inverse correlation of NH_4^+ with salinity is not well correlated. Further analysis is thus required to elucidate the origin of the high levels of NH_4^+ found in Port Foster.

5 Conclusion

This study explores the connection between hydrothermal venting, the distribution of metals and inorganic nutrients, and the dynamics of CO_2 and CH_4 exchange in Port Foster. Increases in GHGs in the surface waters above the coastal fumarolic areas were identified, indicating that fumarolic activity plays a relevant role in influencing local GHGs sea-air budgets. This is in contrast to the broader patterns observed in Bransfield Strait, where hydrodynamic factors are more dominant in chemical distributions. These findings suggest that DI acts as both a net source of CH_4 to the atmosphere and a sink of CO_2. The distribution and concentration of certain TMs like V, Ni, Co, and to a lesser extent Fe, chlorophyll, and nutrients (NH_4^+, NO_3^-, PO_4^{3-} and SiO_2) also suggests that hydrothermal inputs enhance biogeochemical processes and primary productivity, which is essential for the marine food web, supporting higher trophic levels, including fish, birds, and mammals. Enhanced primary productivity can also lead to increased biological carbon sequestration, where CO_2 is captured by phytoplankton and transported to the deep ocean through the biological pump, contributing to long-term carbon storage. Overall, this research highlights DI's role as a volcanically active environment influencing local TMs cycling and GHGs emissions, and likely regional biogeochemical conditions in the Bransfield Strait, which has been shown to deliver TMs enriched waters to the typically TM-poor Drake passage.

Data availability statement

Publicly available datasets were analyzed in this study. This data can be found here: https://github.com/obkorolev/Port_Foster_Paper. Further inquiries can be directed to the corresponding author/s.

Author contributions

OB: Conceptualization, Data curation, Formal analysis, Investigation, Methodology, Software, Validation, Visualization, Writing – original draft, Writing – review & editing. IH: Conceptualization, Data curation, Formal analysis, Funding acquisition, Investigation, Methodology, Project administration, Resources, Supervision, Validation, Visualization, Writing – original draft, Writing – review & editing. GN: Conceptualization, Funding acquisition, Project administration, Resources, Supervision, Validation, Writing – review & editing. SA-V: Conceptualization, Data curation, Formal analysis, Investigation, Methodology, Software, Validation, Visualization, Writing – original draft, Writing – review & editing. MD: Conceptualization, Data curation, Formal analysis, Investigation, Methodology, Supervision, Validation, Visualization, Writing – review & editing. ES: Conceptualization, Data curation, Formal analysis, Investigation, Methodology, Validation, Visualization, Writing – review & editing. SH: Data curation, Methodology, Software, Writing – review & editing. CS: Data curation, Investigation, Methodology, Software, Writing – review & editing. LL: Investigation, Methodology, Software, Supervision, Validation, Visualization, Writing – review & editing. AT-S: Conceptualization, Funding acquisition, Investigation, Methodology, Project administration, Resources, Supervision, Validation, Writing – review & editing.

Funding

The author(s) declare that financial support was received for the research, authorship, and/or publication of this article. This research has been funded by the Spanish Government projects PIMETAN (ref. RTI2018-098048-B-I00), DICHOSO (PID2021-125783OB-I00), EQC2018-004275-P and EQC2019-005721-P

funded by MCIN/AEI/10.13039/501100011033 and by "ERDF A way of making Europe". OB is supported by a predoctoral grant PRE2022-103391, SA-V is supported by a pre-doctoral grant FPU19/04338 and ES is supported by a pre-doctoral grant PRE2019-089679, the three from the Spanish Ministry of Science, Innovation and Universities. Copernicus Sentinel data (2021) was obtained from Copernicus SciHub. Permissions to work in the study area were granted by the Spanish Polar Committee. This research is part of the POLARCSIC and TELEDETECT research initiative. CS participated thanks to a grant provided by the Coordenação de Aperfeiçoamento de Pessoal de Nível Superior (CAPES, 88882.182291/2007-01).

Acknowledgments

We thank the military staff of the Spanish Antarctic Base Gabriel de Castilla, the crew of the Sarmiento de Gamboa oceanographic vessel and the Marine Technology Unit (UTM-CSIC) for their logistic support, for making the XXXIV Spanish Antarctic campaign possible. We thank D. Roque for supporting data collecting operations, M. Agulló, I. Carribero and M. Ferrer for analytical assistance in the laboratory and P. Almaraz for advice on statistical analysis.

Conflict of interest

The authors declare that the research was conducted in the absence of any commercial or financial relationships that could be construed as a potential conflict of interest.

The author(s) declared that they were an editorial board member of Frontiers, at the time of submission. This had no impact on the peer review process and the final decision.

Publisher's note

Supplementary material

The Supplementary Material for this article can be found online at: https://www.frontiersin.org/articles/10.3389/fmars.2024.1432122/full#supplementary-material

References

AEMET (2021). *Data from long observation series in Antarctica (at the Juan Carlos I and Gabriel de Castilla bases.*

Álvarez, M., Ríos, A. F., and Rosón, G. (2002). Spatio-temporal variability of air–sea fluxes of carbon dioxide and oxygen in the Bransfield and Gerlache Straits during Austral summer 1995–96. *Deep Sea Res. Part II: Topical Stud. Oceanogr* 49, 643–662. doi: 10.1016/S0967-0645(01)00116-3

Bates, T. S., Kelly, K. C., Johnson, J. E., and Gammon, R. H. (1996). A reevaluation of the open ocean source of methane to the atmosphere. *J. Geophys. Res.* 101, 6953–6961. doi: 10.1029/95JD03348

Belyaev, O., Sparaventi, E., Navarro, G., Rodríguez-Romero, A., and Tovar-Sánchez, A. (2023). The contribution of penguin guano to the Southern Ocean iron pool. Available online at: https://zenodo.org/badge/latestdoi/506643010.

Bruland, K. W., Franks, R. P., Knauer, G. A., and Martin, J. H. (1979). Sampling and analytical methods for the determination of copper, cadmium, zinc, and nickel at the nanogram per liter level in sea water. *Analytica Chim Acta* 105, 233–245. doi: 10.1016/S0003-2670(01)83754-5

Bui, O. T. N., Kameyama, S., Yoshikawa-Inoue, H., Ishii, M., Sasano, D., Uchida, H., et al. (2018). Estimates of methane emissions from the Southern Ocean from quasi-continuous underway measurements of the partial pressure of methane in surface seawater during the 2012/13 austral summer. *Tellus B: Chem. Phys. Meteorol* 70, 1478594. doi: 10.1080/16000889.2018.1478594

Caballero, I., Roca, M., Santos-Echeandía, J., Bernárdez, P., and Navarro, G. (2022). Use of the sentinel-2 and landsat-8 satellites for water quality monitoring: an early warning tool in the mar menor coastal lagoon. *Remote Sens.* 14, 2744. doi: 10.3390/rs14122744

Carmona, E., Almendros, J., Serrano, I., Stich, D., and Ibáñez, J. M. (2012). Results of seismic monitoring surveys of Deception Island volcano, Antarctica, from 1999–2011. *Antarctic Sci.* 24, 485–499. doi: 10.1017/S0954102012000314

Caselli, A. T., Afonso, M. S., and Agusto, M. (2004). *The fumarolic gases at Deception Island (South Shetland Islands, Antarctica). Chemical changes and deposits related to seismic crisis of 1999.*

Castro, M. F., Neves, J. C. L., Francelino, M. R., Schaefer, C. E. G. R., and Oliveira, T. S. (2021). Seabirds enrich Antarctic soil with trace metals in organic fractions. *Sci. Total Environ.* 785, 147271. doi: 10.1016/j.scitotenv.2021.147271

Chever, F., Sarthou, G., Bucciarelli, E., Blain, S., and Bowie, A. R. (2010). An iron budget during the natural iron fertilization experiment KEOPS (Kerguelen Islands, Southern Ocean). *Biogeosciences* 7, 455–468. doi: 10.5194/bg-7-455-2010

Chu, Z., Yang, Z., Wang, Y., Sun, L., Yang, W., Yang, L., et al. (2019). Assessment of heavy metal contamination from penguins and anthropogenic activities on Fildes Peninsula and Ardley Island, Antarctic. *Sci. Total Environ.* 646, 951–957. doi: 10.1016/j.scitotenv.2018.07.152

Da Silva, J. F., and Williams, R. J. P. (2001). *The biological chemistry of the elements: the inorganic chemistry of life* (Oxford University Press, New York).

De Jong, J. T. M., Stammerjohn, S. E., Ackley, S. F., Tison, J.-L., Mattielli, N., and Schoemann, V. (2015). Sources and fluxes of dissolved iron in the Bellingshausen Sea (West Antarctica): The importance of sea ice, icebergs and the continental margin. *Mar. Chem.* 177, 518–535. doi: 10.1016/j.marchem.2015.08.004

De La Paz, M., Huertas, I. E., Flecha, S., Ríos, A. F., and Pérez, F. F. (2015). Nitrous oxide and methane in Atlantic and Mediterranean waters in the Strait of Gibraltar: Air-sea fluxes and inter-basin exchange. *Prog. Oceanogr* 138, 18–31. doi: 10.1016/j.pocean.2015.09.009

Dickson, A. G., and Millero, F. J. (1987). A comparison of the equilibrium constants for the dissociation of carbonic acid in seawater media. *Deep Sea Res. Part A. Oceanogr Res. Papers* 34, 1733–1743. doi: 10.1016/0198-0149(87)90021-5

Dickson, A. G., Wesolowski, D. J., Palmer, D. A., and Mesmer, R. E. (1990). Dissociation constant of bisulfate ion in aqueous sodium chloride solutions to 250. degree. C. *J. Phys. Chem.* 94, 7978–7985. doi: 10.1021/j100383a042

Flexas, M. M., Arias, M. R., and Ojeda, M. A. (2017). Hydrography and dynamics of port foster, deception island, Antarctica. *Antarctic Sci.* 29, 83–93. doi: 10.1017/S0954102016000444

Friedlingstein, P., O'Sullivan, M., Jones, M. W., Andrew, R. M., Hauck, J., Olsen, A., et al. (2020). Global carbon budget 2020. *Earth Syst. Sci. Data* 12, 3269–3340. doi: 10.5194/essd-12-3269-2020

García-Veira, D., Sukekava, C. F., Sparaventi, E., Navarro, G., Huertas, I. E., Tovar-Sánchez, A., et al. (2024). A first estimation of the role of penguin guano on copper cycling and organic speciation in Antarctic coastal waters. *Sci. Total Environ.* 912, 169266. doi: 10.1016/j.scitotenv.2023.169266

German, C. R., and Seyfried, W. E. (2014). *Hydrothermal processes, in: treatise on geochemistry* (Elsevier Science, AE Amsterdam, Netherlands), 131–233.

Gonçalves-Araujo, R., De Souza, M. S., Tavano, V. M., and Garcia, C. A. E. (2015). Influence of oceanographic features on spatial and interannual variability of phytoplankton in the Bransfield Strait, Antarctica. *J. Mar. Syst.* 142, 1–15. doi: 10.1016/j.jmarsys.2014.09.007

Gruber, N., Clement, D., Carter, B. R., Feely, R. A., Van Heuven, S., Hoppema, M., et al. (2019). The oceanic sink for anthropogenic CO_2 from 1994 to 2007. *Science* 363, 1193–1199. doi: 10.1126/science.aau5153

Hansen, H. P., and Koroleff, F. (1999). Determination of nutrients. in: Grasshoff, K., Kremling, K., and Ehrhardt, M. (Eds.), *Methods of Seawater Analysis*. Wiley, pp, 159–228. doi: 10.1002/9783527613984.ch10

Heeschen, K. U., Keir, R. S., Rehder, G., Klatt, O., and Suess, E. (2004). Methane dynamics in the Weddell Sea determined via stable isotope ratios and CFC-11. *Global Biogeochem Cycles* 18, 2003GB002151. doi: 10.1029/2003GB002151

Ito, R. G., Tavano, V. M., Mendes, C. R. B., and Garcia, C. A. E. (2018). Sea-air CO2 fluxes and pCO2 variability in the Northern Antarctic Peninsula during three summer periods, (2008–2010). *Deep Sea Res. Part II: Topical Stud. Oceanogr* 149, 84–98. doi: 10.1016/j.dsr2.2017.09.004

Janssen, D. J., Sieber, M., Ellwood, M. J., Conway, T. M., Barrett, P. M., Chen, X., et al. (2020). Trace metal and nutrient dynamics across broad biogeochemical gradients in the Indian and Pacific sectors of the Southern Ocean. *Mar. Chem.* 221, 103773. doi: 10.1016/j.marchem.2020.103773

Kholmogorov, A., Syrbu, N., and Shakirov, R. (2022). Influence of hydrological factors on the distribution of methane fields in the water column of the bransfield strait: cruise 87 of the R/V "Academik mstislav keldysh", 7 December 2021–5 April 2022. *Water* 14, 3311. doi: 10.3390/w14203311

Klunder, M. B., Laan, P., Middag, R., De Baar, H. J. W., and van Ooijen, J. C. (2011). Dissolved iron in the Southern Ocean (Atlantic sector). *Deep Sea Res. Part II: Topical Stud. Oceanogr* 58, 2678–2694. doi: 10.1016/j.dsr2.2010.10.042

Kusakabe, M., Nagao, K., Ohba, T., Seo, J. H., Park, S.-H., Lee, J. I., et al. (2009). Noble gas and stable isotope geochemistry of thermal fluids from Deception Island, Antarctica. *Antarctic Sci.* 21, 255–267. doi: 10.1017/S0954102009001783

Laglera, L. M., Tovar-Sanchez, A., Sukekava, C. F., Naik, H., Naqvi, S. W. A., and Wolf-Gladrow, D. A. (2020). Iron organic speciation during the LOHAFEX experiment: Iron ligands release under biomass control by copepod grazing. *J. Mar. Syst.* 207, 103151. doi: 10.1016/j.jmarsys.2019.02.002

Lamontagne, R. A., Swinnerton, J. W., and Linnenbom, V. J. (1974). C_1-C_4 hydrocarbons in the north and south pacific[1]. *Tellus A: Dynamic Meteorol Oceanogr* 26, 71. doi: 10.3402/tellusa.v26i1-2.9738

Lee, K., Kim, T.-W., Byrne, R. H., Millero, F. J., Feely, R. A., and Liu, Y.-M. (2010). The universal ratio of boron to chlorinity for the North Pacific and North Atlantic oceans. *Geochim Cosmochim Acta* 74, 1801–1811. doi: 10.1016/j.gca.2009.12.027

Liu, X., Nie, Y., Sun, L., and Emslie, S. D. (2013). Eco-environmental implications of elemental and carbon isotope distributions in ornithogenic sediments from the Ross Sea region, Antarctica. *Geochim Cosmochim Acta* 117, 99–114. doi: 10.1016/j.gca.2013.04.013

Maestro, A., Somoza, L., Rey, J., Martínez-Frías, J., and López-Martínez, J. (2007). Active tectonics, fault patterns, and stress field of Deception Island: A response to oblique convergence between the Pacific and Antarctic plates. *J. South Am. Earth Sci.* 23, 256–268. doi: 10.1016/j.jsames.2006.09.023

Measures, C. I., Brown, M. T., Selph, K. E., Apprill, A., Zhou, M., Hatta, M., et al. (2013). The influence of shelf processes in delivering dissolved iron to the HNLC waters of the Drake Passage, Antarctica. *Deep Sea Res. Part II: Topical Stud. Oceanogr* 90, 77–88. doi: 10.1016/j.dsr2.2012.11.004

Mehrbach, C., Culberson, C. H., Hawley, J. E., and Pytkowicx, R. M. (1973). MEASUREMENT OF THE APPARENT DISSOCIATION CONSTANTS OF CARBONIC ACID IN SEAWATER AT ATMOSPHERIC PRESSURE1. *Limnol Oceanogr* 18, 897–907. doi: 10.4319/lo.1973.18.6.0897

Mei, K., Wang, D., Jiang, Y., Shi, M., Chen, C.-T. A., Zhang, Y., et al. (2022). Transformation, fluxes and impacts of dissolved metals from shallow water hydrothermal vents on nearby ecosystem offshore of kueishantao (NE Taiwan). *Sustainability* 14, 1754. doi: 10.3390/su14031754

Monteiro, T., Kerr, R., and MaChado, E. D. C. (2020). Seasonal variability of net sea-air CO2 fluxes in a coastal region of the northern Antarctic Peninsula. *Sci. Rep.* 10, 14875. doi: 10.1038/s41598-020-71814-0

Montzka, S. A., Dlugokencky, E. J., and Butler, J. H. (2011). Non-CO2 greenhouse gases and climate change. *Nature* 476, 43–50. doi: 10.1038/nature10322

Morel, F. M. M., and Price, N. M. (2003). The biogeochemical cycles of trace metals in the oceans. *Science* 300, 944–947. doi: 10.1126/science.1083545

Morley, S. A., Abele, D., Barnes, D. K. A., Cárdenas, C. A., Cotté, C., Gutt, J., et al. (2020). Global drivers on southern ocean ecosystems: changing physical environments and anthropogenic pressures in an earth system. *Front. Mar. Sci.* 7. doi: 10.3389/fmars.2020.547188

O'Reilley, J. E., Maritorena, S., O'Brien, M. C., Siegel, D. A., Toole, D., Menzies, D., et al. (2000). *Volume 11, SeaWiFS Postlaunch Calibration and Validation Analyses, Part 3*. (NASA Goddard Space Flight Center).

Perez, F. F., and Fraga, F. (1987). Association constant of fluoride and hydrogen ions in seawater. *Mar. Chem.* 21, 161–168. doi: 10.1016/0304-4203(87)90036-3

Polonik, N. S., Ponomareva, A. L., Eskova, A. I., Shakirov, R. B., Obzhirov, A. I., and Morozov, E. G. (2021). Distribution and sources of methane in the water layers of the antarctic straits: bransfield strait and antarctic sound. *Oceanology* 61, 892–898. doi: 10.1134/S0001437021060308

Polukhin, A. A., Morozov, E. G., Tishchenko, P. P., Frey, D. I., Artemiev, V. A., Borisenko, G. V., et al. (2021). Water structure in the bransfield strait (Antarctica) in january 2020: hydrophysical, optical, and hydrochemical features. *Oceanology* 61, 632–644. doi: 10.1134/S0001437021050106

Resing, J. A., Sedwick, P. N., German, C. R., Jenkins, W. J., Moffett, J. W., Sohst, B. M., et al. (2015). Basin-scale transport of hydrothermal dissolved metals across the South Pacific Ocean. *Nature* 523, 200–203. doi: 10.1038/nature14577

Rey, J., Somoza, L., and Martínez-Frías, J. (1995). Tectonic, volcanic, and hydrothermal event sequence on Deception Island (Antarctica). *Geo-Marine Lett.* 15, 1–8. doi: 10.1007/BF01204491

Rodrigues, C. C. F., Santini, M. F., Lima, L. S., Sutil, U. A., Carvalho, J. T., Cabrera, M. J., et al. (2023). Ocean-atmosphere turbulent CO2 fluxes at Drake Passage and Bransfield Strait. *An Acad. Bras. Ciênc* 95, e20220652. doi: 10.1590/0001-3765202320220652

Sañudo-Wilhelmy, S. A., Olsen, K. A., Scelfo, J. M., Foster, T. D., and Flegal, A. R. (2002). Trace metal distributions off the Antarctic Peninsula in the Weddell Sea. *Mar. Chem.* 77, 157–170. doi: 10.1016/S0304-4203(01)00084-6

Schoonen, M. A. A., and Xu, Y. (2001). Nitrogen reduction under hydrothermal vent conditions: implications for the prebiotic synthesis of C-H-O-N compounds. *Astrobiology* 1, 133–142. doi: 10.1089/153110701753198909

SCOR Working Group (2007). GEOTRACES – An international study of the global marine biogeochemical cycles of trace elements and their isotopes. *Geochemistry* 67, 85–131. doi: 10.1016/j.chemer.2007.02.001

Sharp, J. D., and Byrne, R. H. (2020). Interpreting measurements of total alkalinity in marine and estuarine waters in the presence of proton-binding organic matter. *Deep Sea Res. Part I: Oceanogr Res. Papers* 165, 103338. doi: 10.1016/j.dsr.2020.103338

Shitashima, K. (1998). CO2 supply from deep-sea hydrothermal systems. *Waste Manage.* 17, 385–390. doi: 10.1016/S0956-053X(97)10046-0

Sierpinski, S. F. D., Baquer, L. M. L., Martins, C. C., and Grassi, M. T. (2023). Exploratory evaluation of iron and its speciation in surface waters of Admiralty Bay, King George Island, Antarctica. *An Acad. Bras. Ciênc* 95, e20211520. doi: 10.1590/0001-3765202320211520

Somoza, L., Martínez-Frías, J., Smellie, J. L., Rey, J., and Maestro, A. (2004). Evidence for hydrothermal venting and sediment volcanism discharged after recent short-lived volcanic eruptions at Deception Island, Bransfield Strait, Antarctica. *Mar. Geol* 203, 119–140. doi: 10.1016/S0025-3227(03)00285-8

Sparaventi, E., Rodríguez-Romero, A., Barbosa, A., Ramajo, L., and Tovar-Sánchez, A. (2021). Trace elements in Antarctic penguins and the potential role of guano as source of recycled metals in the Southern Ocean. *Chemosphere* 285, 131423. doi: 10.1016/j.chemosphere.2021.131423

Sturz, A. A., Gray, S. C., Dykes, K., King, A., and Radtke, J. (2003). Seasonal changes of dissolved nutrients within and around Port Foster Deception Island, Antarctica. *Deep Sea Res. Part II: Topical Stud. Oceanogr* 50, 1685–1705. doi: 10.1016/S0967-0645(03)00086-9

Terhaar, J., Frölicher, T. L., and Joos, F. (2021). Southern Ocean anthropogenic carbon sink constrained by sea surface salinity. *Sci. Adv.* 7, eabd5964. doi: 10.1126/sciadv.abd5964

Tilbrook, B. D., and Karl, D. M. (1993). RACER: methane enrichments in port foster, deception island. *Antarctic J. United States* 28, 165–166.

Tilbrook, B. D., and Karl, D. M. (1994). Dissolved methane distributions, sources, and sinks in the western Bransfield Strait, Antarctica. *J. Geophys. Res.* 99, 16383–16393. doi: 10.1029/94JC01043

A. Tovar-Sanchez (Ed.) (2012). *Comprehensive sampling and sample preparation: analytical techniques for scientists* (Amsterdam: Elsevier).

Van Heuven, S., Pierrot, D., Rae, J., Lewis, E., and Wallace, D. (2011). *CO2SYS v 1.1, MATLAB program developed for CO2 system calculations. ORNL/CDIAC-105b* (Oak Ridge, TN: Oak Ridge National Laboratory).

Von Damm, K. L., and Lilley, M. D. (2004). "Diffuse flow hydrothermal fluids from 9° 50′ N East Pacific Rise: Origin, evolution and biogeochemical controls," in *Geophysical Monograph Series*. Eds. W. S. D. Wilcock, E. F. DeLong, D. S. Kelley, J. A. Baross and S. Craig Cary (American Geophysical Union, Washington, D. C.), 245–268. doi: 10.1029/144GM16

Wanninkhof, R. (2014). Relationship between wind speed and gas exchange over the ocean revisited. *Limnol Ocean Methods* 12, 351–362. doi: 10.4319/lom.2014.12.351

Weber, T., Wiseman, N. A., and Kock, A. (2019). Global ocean methane emissions dominated by shallow coastal waters. *Nat. Commun.* 10, 4584. doi: 10.1038/s41467-019-12541-7

Weiss, R. F. (1970). The solubility of nitrogen, oxygen and argon in water and seawater. *Deep Sea Res. Oceanogr Abstracts* 17, 721–735. doi: 10.1016/0011-7471(70)90037-9

Weiss, R. F., and Price, B. A. (1980). Nitrous oxide solubility in water and seawater. *Mar. Chem.* 8, 347–359. doi: 10.1016/0304-4203(80)90024-9

Wiesenburg, D. A., and Guinasso, N. L. (1979). Equilibrium solubilities of methane, carbon monoxide, and hydrogen in water and sea water. *J. Chem. Eng Data* 24, 356–360. doi: 10.1021/je60083a006

Xu, G., and Gao, Y. (2014). Atmospheric trace elements in aerosols observed over the Southern Ocean and coastal East Antarctica. *Polar Res.* 33, 23973. doi: 10.3402/polar.v33.23973

Ye, W., Arévalo-Martínez, D. L., Li, Y., Wen, J., He, H., Zhang, J., et al (2023). Significant methane undersaturation during austral summer in the Ross Sea (Southern Ocean). *Limnol. Oceanogr. Letters* 8, 305–312. doi: 10.1002/lol2.10315

Yoshida, O., Inoue, H. Y., Watanabe, S., Suzuki, K., and Noriki, S. (2011). Dissolved methane distribution in the South Pacific and the Southern Ocean in austral summer. *J. Geophys. Res.* 116, 2009JC006089. doi: 10.1029/2009JC006089

frontiers | Frontiers in Microbiology

TYPE Original Research
PUBLISHED 03 October 2024
DOI 10.3389/fmicb.2024.1473822

OPEN ACCESS

EDITED BY
Douglas G. Capone,
University of Southern California, United States

REVIEWED BY
Sujata Dabolkar,
Government College of Arts, Science and Commerce, Quepem, India
Minglei Ren,
Chinese Academy of Sciences (CAS), China

*CORRESPONDENCE
Gunter Wegener
✉ gwegener@marum.de
Massimiliano Molari
✉ mamolari@mpi-bremen.de

†These authors have contributed equally to this work

RECEIVED 31 July 2024
ACCEPTED 11 September 2024
PUBLISHED 03 October 2024

CITATION
Wegener G, Molari M, Purser A, Diehl A, Albers E, Walter M, Mertens C, German CR and Boetius A (2024) Hydrothermal vents supporting persistent plumes and microbial chemoautotrophy at Gakkel Ridge (Arctic Ocean). *Front. Microbiol.* 15:1473822. doi: 10.3389/fmicb.2024.1473822

Hydrothermal vents supporting persistent plumes and microbial chemoautotrophy at Gakkel Ridge (Arctic Ocean)

Gunter Wegener[1,2,3*†], Massimiliano Molari[2,3*†], Autun Purser[3], Alexander Diehl[1,4], Elmar Albers[1,4,5], Maren Walter[1,6], Christian Mertens[6], Christopher R. German[5] and Antje Boetius[1,2,3]

[1]MARUM, Center for Marine Environmental Sciences, University of Bremen, Bremen, Germany, [2]Max Planck Institute for Marine Microbiology, Bremen, Germany, [3]Alfred Wegener Institute, Helmholtz Centre for Polar and Marine Research, Bremerhaven, Germany, [4]Department of Geosciences, University of Bremen, Bremen, Germany, [5]Woods Hole Oceanographic Institution, Woods Hole, MA, United States, [6]Institute of Environmental Physics, University of Bremen, Bremen, Germany

Hydrothermal vents emit hot fluids enriched in energy sources for microbial life. Here, we compare the ecological and biogeochemical effects of hydrothermal venting of two recently discovered volcanic seamounts, Polaris and Aurora of the Gakkel Ridge, in the ice-covered Central Arctic Ocean. At both sites, persistent hydrothermal plumes increased up to 800 m into the deep Arctic Ocean. In the two non-buoyant plumes, rates of microbial carbon fixation were strongly elevated compared to background values of 0.5–1 μmol m^{-3} day^{-1} in the Arctic deep water, which suggests increased chemoautotrophy on vent-derived energy sources. In the Polaris plume, free sulfide and up to 360 nM hydrogen enabled microorganisms to fix up to 46 μmol inorganic carbon (IC) m^{-3} day^{-1}. This energy pulse resulted in a strong increase in the relative abundance of SUP05 by 25% and Candidatus Sulfurimonas pluma by 7% of all bacteria. At Aurora, microorganisms fixed up to 35 μmol IC m^{-3} day^{-1}. Here, metal sulfides limited the bioavailability of reduced sulfur species, and the putative hydrogen oxidizer *Ca.* S. pluma constituted 35% and SUP05 10% of all bacteria. In accordance with this data, transcriptomic analysis showed a high enrichment of hydrogenase-coding transcripts in Aurora and an enrichment of transcripts coding for sulfur oxidation in Polaris. There was neither evidence for methane consumption nor a substantial increase in the abundance of putative methanotrophs or their transcripts in either plume. Together, our results demonstrate the dominance of hydrogen and sulfide as energy sources in Arctic hydrothermal vent plumes.

KEYWORDS

hydrothermal vent, hydrogen oxidation, plume, sulfur oxidation, chemoautotrophy

1 Introduction

The chemistry of hydrothermal fluids differs strongly between and among mid-ocean ridges, back-arc spreading centers, and submarine volcanoes (Beaulieu and Szafranski, 2020; Diehl and Bach, 2020; Früh-Green et al., 2022). Hydrothermal fluids carry highly variable amounts of reduced components such as Fe^{2+}, Mn^{2+}, H_2S, CH_4, and H_2 as well as complex

organic molecules into the water column (Baker and German, 2004; Beaulieu et al., 2013). Upon cooling of hydrothermal fluids, the solubilities of different minerals change, resulting in the formation of metal sulfide and metal oxide deposits. At the seafloor, the chemical energy transported by vent fluids feeds diverse benthic microorganisms and their symbioses with invertebrates (Jannasch, 1985; Petersen et al., 2011). Accordingly, distinct assemblages of microbial taxa are associated with hydrothermal vents, including rock-associated, mat-forming, and invertebrate-hosted chemosynthetic microorganisms at the seafloor (Früh-Green et al., 2022). Some vent fields even host the largest biomasses known in marine environments (Dubilier et al., 2008; Jannasch, 1983; Van Dover et al., 2002). Because of the vigorous emission of hot fluids from some vents, the majority of reduced compounds escape the seafloor communities and form persistent plumes. These plumes may rise hundreds of meters above the seafloor and then spread laterally hundreds of kilometers away from their source (German and Seyfried, 2014; Schultz and Elderfield, 1997). While heat and fluid transports in hydrothermal plumes are relatively well understood, the influence of their variable chemical energy fluxes on the distribution of deep-sea life remains understudied, especially in polar regions (Bennett S. A. et al., 2013; Cathalot et al., 2021; Dick, 2019; Edmonds et al., 2003; McCollom, 2000). The total geothermal heat arising from Gakkel Ridge significantly warms the deep basin waters (Björk and Winsor, 2006), but little is known about the chemistry and microbiology of its hydrothermal vent fields (Edmonds et al., 2003). Thus, this study focuses on the influence of hydrothermal venting on microbial biodiversity associated with persistent plumes in the ice-covered Arctic Ocean.

Gakkel Ridge extends across the Arctic Ocean for a length of 1,800 km from Greenland to the Russian Shelf and has an ultraslow spreading rate of 8–13 mm per year (Cochran et al., 2003). An initial exploratory mission in 2001 discovered approximately 30 hydrothermal plumes along this ridge (Baker et al., 2004; Edmonds et al., 2003; Jokat and Schmidt-Aursch, 2007). This confirmed that hydrothermal venting along ultraslow spreading ridges is more abundant than previously anticipated (Bach et al., 2002; German et al., 1998; German et al., 1996). A combination of seafloor topography and rock sampling, coupled with plume detection, suggested that the majority of hydrothermal sources are associated with volcanic centers (Edmonds et al., 2003; Michael et al., 2003). Their occurrence under year-round ice cover has recently intrigued several international expeditions, including those conducted in conjunction with astrobiology and space science researchers, due to the potential analogy with hydrothermalism under ice on Earth to that possibly occurring on other celestial bodies, such as Saturn's moon Enceladus (Hsu et al., 2015; Ramirez-Llodra et al., 2023; Seewald, 2017; Waite et al., 2017).

In their recent global analysis, Zhou et al., 2023 proposed that sulfur is the major energy substrate shaping the diversity of microorganisms in plumes (Zhou et al., 2023). In an earlier study of the first hydrothermal plume sampling at Gakkel Ridge, we discovered a novel Sulfurimonas type (^{U}*Sulfurimonas pluma*) distinct from previously known microaerophilic types, whose abundance and global distribution in hydrothermal plumes seems to depend on the hydrogen availability (Molari et al., 2023). In contrast, a biogeochemical model suggests that the highly diluted chemical energy in hydrothermal plumes can support only minor chemolithoautotrophic activity (Cathalot et al., 2021). Here, we studied hydrothermal fields at the western and central Gakkel Ridge, and the relationship of energy sources, biogeochemical reactions, and microbial community compositions in their deep-water plumes. We analyzed the role of hydrogen, sulfur, and methane as energy sources available for the composition of the plume-hosted deep-water life, using a combination of *in situ* measurements, shipboard incubations, and sequencing of plume samples (16S rRNA genes and transcriptomes). Specifically, we tested to what extent hydrogen supports microbial life in the studied hydrothermal plumes.

2 Materials and methods

2.1 Bathymetry and maps

The Gakkel Ridge areas investigated here were partially previously mapped during the AMORE cruise in 2001, which used the former Hydrosweep DS-2 system of RV Polarstern (59 beams) and a Seabeam system of Healy (121 beams) (Thiede, 2002). During PS86 and PS101, we added survey tracks to fill up gaps in the AMORE bathymetry grid. RV Polarstern's shipboard deep-sea multibeam echo sounder was an Atlas Hydrosweep DS-3. Its transducer frequency ranged from 13.6 to 16.4 kHz. The individual beam width was approximately 2.3°, which allowed a beam footprint of approximately 160 m at an area depth of 4,000 m. The swath width was set to 150% of the water depth throughout the entire mission. Peripheral sensors connected to the multibeam were a GPS Trimble receiver for positioning, an internal navigation system, and heave sensor system HYDRINS (Inertial Navigation System) for retrieving the ship's roll, pitch, heading angles, and sound velocity keel probe. The acquired data were processed on board using Caris HIPS/SIPS Editor. The data were manually edited, filtered by applying matrix-based median filters, and exported to grids and xyz soundings. The resulting grids were produced at 100 m resolution. These grids were regularly updated as background layers for the real-time mapping tool GlobalMapper, which was used for the navigation and tracking of underwater instruments. All data are available in PANGAEA (links in the cruise reports), as well as further details on the methods reported below (Boetius, 2015; Boetius and Purser, 2017). The event labels are registered in the Earth System database www.pangaea.de and all further station information and data can be retrieved in open access from there.

2.2 OFOS photography transects

The Ocean Floor Observation System OFOS is an underwater camera system towed a few meters above the seafloor and equipped with both a high-resolution photo camera (iSiTEC, CANON EOS 5D Mark III) and a high-definition video camera (iSiTEC, Sony FCB-H11). The cameras are mounted on a steel frame (1,400 mm in length, 920 mm in width, and 1,350 mm in height), together with two strobe lights (iSiTEC UW-Blitz 250, TTL driven) four LED lights, and a USBL positioning system (Posidonia; iXblue) to track the position of the OFOS during deployments. Three laser pointers at a distance of 50 cm from each other were used to estimate the size of seafloor structures (Boetius, 2015). For PS101, the OFOS was upgraded with bathymetry technology to additionally mount side-scan and

forward-looking sonar systems, referred to thereafter as the OFOBS system (Boetius and Purser, 2017; Purser et al., 2019).

2.3 Configuration and operation of the CTD and connected *in situ* pumps

The CTD rosette was operated with sensors recording conductivity as a measure of salinity, temperature, and density. The CTD was equipped with sensors for oxygen, sulfide, turbidity, and highly sensitive redox sensors (courtesy of Koichi Nakamura, National Institute of Advanced Industrial Science and Technology, Japan) and NOAA PMEL. Signals were processed and digitally transmitted to the ship. Additionally, Miniature Autonomous Plume Recorders (MAPR, supplied by the PMEL Earth-Ocean observation program of the National Oceanic and Atmospheric Administration; NOAA) were deployed along the ship's wire and in particular at depths of the *in situ* pumps to enhance the resolution of measurements. Within the target areas, the CTDs were operated as towed yo-yo casts to detect and size plumes. In specific depths of interest (bottom water, below, in, and above the plume as identified by combined changes of temperature, turbidity, and E), the water column was sampled by closing one of the Niskin water samplers.

2.4 *In situ* filtration of seawater for molecular and geochemical analysis

To retrieve larger quantities of biomass and particles from plumes, background and reference water for molecular and trace metal analyses, we used large volume *in situ* pumps (WTS-LV04; McLane) equipped with polycarbonate filters (142 mm diameter; 0.2 µm pore size for molecular analyses) or hydrophilic polyethersulfone filters (HPWP1425; Millipore Express PLUS membrane filters, pore size 0.2 µm). In total, we analyzed the gene expression from 19 samples (Polaris) and 6 samples (Aurora). The filters were washed with trace metal-free solvents according to GEOTRACES protocols (Cutter et al., 2010). The pumps were programmed to operate at a maximum pump rate for 90 min. Pumps were installed on the CTD 10 to 60 meters above the CTD or at specific reference horizons. The pumps were placed in the plume for pumping time by placing the ship and lowering the CTD. Because filters have very small pore sizes, on average only 200 liters of water were filtered. For molecular analysis, pump heads were opened directly after retrieval, the filter was collected and sectioned into four equal pieces, which were shock-frozen in liquid nitrogen and stored at −80°C until analysis in the home laboratory. For trace metal analysis, pump heads were opened and complete filters were percolated with Milli-Q grade water (>18.2 MΩ) by using the *in situ* pumps in the manual operation mode. Filters were dried and stored at −20°C until analysis.

2.5 Determination of noble gas concentrations and isotopic ratios in water column samples

For the analysis of helium and neon isotopic composition, samples were collected in two ways from the Niskin bottles. All samples from the Polaris site and parts of the Aurora samples were collected by flushing a copper tube and closing the ends gas-tight with clamps. In addition, the Aurora site was sampled with an ampoule-based water sampler, where previously evacuated glass ampoules were filled half with the sample, and the headspace was directly available for analysis (Roether et al., 2013b). To compare the two approaches, 13 Niskin bottles were sampled with both methods. Because the background signals for ^{3}He in this area are unknown, samples for CFC/Freon and Tritium analysis were taken around the plume signal to determine tritiugenic ^{3}He as suggested by Roether et al. (2013a). These and the noble gas samples were analyzed and quality controlled in the Bremen Trace Gas Laboratory. After extraction, helium and neon were separated from other gases in cryo-traps at 25 and 14 K. Helium isotopes were analyzed with a high-resolution static mass spectrometer (MAP 215–50). The system is capable of resolving ^{3}He from the mass-3 hydrogen species (HD and H_3) leaking from metal walls. The high stability of the system provides an uncertainty of 0.5% for the ^{3}He/^{4}He ratio (Sültenfuß et al., 2009).

2.6 Determination of methane and hydrogen concentrations of water column samples

To determine methane and hydrogen concentrations of the CTD Niskin bottles, replicates of 40 mL of seawater were headspace-free sampled using a 60 mL syringe. Samples were heated to room temperature, and a 10 mL N_2 headspace was applied. The syringes were vigorously shaken for 1 min to transfer the dissolved gases to the headspace. Methane was detected using gas chromatography coupled with flame ionization detection (Hewlett–Packard HP 5890 Series II Gas Chromatograph). Standard calibration was performed daily using NIST-traceable 100.0 ppm CH_4 in N_2. For hydrogen measurements, a Peak Performer gas chromatograph with a reduced compound photometer (Peak Performer 1, Peak Laboratories) with a 250 µL sampling loop was used and measured against 100 ppm H_2 in air standards. At Polaris, we measured hydrogen and methane concentrations from 56 horizons. At Aurora, methane concentrations were determined from 30 samples.

2.7 Rates of dark CO_2 fixation

Measurements of dark CO_2 fixation (DCF) rates were carried out by applying a modification of the methodology previously described by Herndl et al. (2005) for deep-sea water. Water samples were collected from Niskin bottles using a sterilized silicon tube connected to sterilized 50-mL plastic syringes. Before the collection of the sample, the syringe and tube were washed with HCl (0.1 M), Milli-Q water, and three times with the Niskin seawater. Samples were stored in the dark at *in situ* temperature (−1 to −0.8°C) until the radiotracer injection, which occurred within 30 min after sampling. DCF rates were measured in 40-mL seawater in triplicate, with two formaldehyde-killed blanks supplemented with 40 µL of [^{14}C]bicarbonate (1,380 kBq) and incubated in the dark at *in situ* temperature for 3 to 12 h for plume water and 48 h for background water. For assessing the concentration of added radiotracer, 5 µL of samples were added to

6 mL of scintillation cocktail (Filter Count, Perkin Elmer) and measured with a scintillation counter (TRI-CARB, Perkin Elmer). The incubations were terminated by the addition of formaldehyde (2% final concentration) to the samples. The samples were filtered onto 0.22-µm cellulose nitrate filters (Millipore) and rinsed three times with 10 mL of sterile-filtered seawater. Subsequently, the filters were exposed to fuming HCl (37%) for 2 h. After that, filters were transferred to a scintillation vial containing 6 mL of Filter Count, and the disintegration per minute (DPM) was measured using a scintillation counter. The DCF rates (µmol C m^{-3} d^{-1}) are determined according to Reinthaler et al. (2010) (Equation 1):

$$DCF = \left(DPM_{net} \times 1.05 \times C_{DIC}\right) / \left(SA \times Tr \times V \times T\right) \quad (1)$$

with DPM*net* = DPM*sample* – DPM*blank* (*counts of the sample – counts of killed sample*), C_{DIC} is the dissolved IC in seawater (i.e., 2,100 µmol L^{-1}), SA is the specific activity of [^{14}C]bicarbonate (59 mCi $mmol^{-1}$; Hartmann Analytic, Germany), *Tr* is the concentration of injected tracer measured at the start of incubation, volume V (cubic meter) and the time T (days). The factor 1.05 accounts for the discrimination of the ^{14}C isotope in carbon fixation. A total of 86 samples (Polaris) and 75 samples (Aurora) were analyzed in these assays.

2.8 Time course experiments to determine methane and hydrogen consumption rates

Directly after recovery, we sampled water from dedicated Niskin bottles into multiple serum bottles (256 mL), which were sealed headspace-free with gas-tight rubber stoppers. In each experiment, 9 to 21 replicates were produced and immediately transferred back to *in situ* temperature (−1°C). Because oxygen concentrations were three orders of magnitude higher than that of potential electron donors, we based activity measurements on the consumption of the electron donors, not the oxygen. To measure potential methane and hydrogen consumption in reference and non-buoyant plume water samples, 250 µL of H_2 and CH_4 saturated seawater were added through the stopper to reach approx. 200 nM of both substrates. For other experiments, only hydrogen was added (see Supplementary Figure S3). At each sampling point, three of the replicate bottles were supplied with a headspace of 24.1 mL (1 mmol) synthetic air, in exchange for the same medium volume, which was removed with another syringe. After that, samples were warmed up to room temperature, and bottles were vigorously shaken for 30 s using a vortexer. To measure hydrogen from the headspace, 3 mL of sterile-filtered hydrogen/methane-free medium was injected into the bottle, and in exchange, 3 mL of headspace gas was pressed through connected tubing into the 250-µl sampling loop of the Peak Performer gas chromatograph (see above). For methane concentration measurements, 10 mL of gas phase was collected with a syringe, replacing 10 mL headspace with 10 mL of sterile medium. Methane concentrations were measured using a Hewlett–Packard GC and FID detection as described above. The resulting concentrations in ppmv were converted into nmol per liter seawater (nM). The hydrogen results are based on a total of 148 bottles of incubation (hydrogen), and all measurements were performed in technical replicates.

2.9 Determination of methane oxidation using $^{14}CH_4$ tracer

Methane oxidation rate were determined in incubation experiments. Therefore we filled 156-ml cultivation vials completely with plume water and capped it with headspace-free with butyl rubber stoppers. We injected 20 µL of ^{14}C-methane containing water through the rubber stopper (approx. 1 kBq per sample) and incubated the water at 0°C for 3 days. To stop potential microbial methane turnover, a headspace of 5 mL was supplied to all samples and 1 mL of 50% NaOH was added to the sample. In the home laboratory, concentrations of methane, methane tracer content, and produced ^{14}C IC were determined following the protocol of Treude et al. (2005) Only a few of the incubated water samples showed ^{14}C-IC values that were significantly elevated (>2 × standard deviation) compared to an average of ≥3 killed controls. A total of 46 samples (Polaris) and 107 samples (Aurora) were analyzed in these assays.

2.10 Determination of cell numbers

At sea, 500 mL of seawater was fixed with formaldehyde (2% final concentration) for 8 h at 4\u00B0C and filtered onto a 0.22-µm polycarbonate filter (47 mm diameter, Millipore). The filters were washed with sterile-filtered seawater and with 70% ethanol in MQ-water, and then after drying, they were stored at −20°C until further processing. In the home, laboratory cells were stained with DAPI (4′,6′-diamidino-2-phenylindole; Sigma-Aldrich). For a subset of samples, catalyzed reporter deposition fluorescence in situ hybridization (CARD-FISH) was performed using a specific probe for *Sulfurimonas pluma* (Molari et al., 2023) and the SUP05 cluster (Meier et al., 2016). After that, cells were counter-stained with DAPI. All filters were enumerated under the epifluorescence microscope. For this, at least 1,000–2,000 DAPI-stained cells were counted and numbers were extrapolated for the filter size and seawater volume. A total of 12 samples (Polaris) and 34 samples (Aurora) were analyzed for total cell numbers. In total, 5 samples (Polaris) and 10 samples (Aurora) were analyzed with specific probes specific for *S. pluma* and SUP05, respectively.

2.11 Amplification and sequencing of 16S rRNA genes

Seawater samples for DNA analysis were filtered immediately after the retrieval of Niskin bottles, and the filtration was carried out in a temperature-controlled room (2°C) in the dark and did not exceed 1–1.5 h. At Aurora, 3 L of seawater was filtered onto 0.22-µm polycarbonate filters (47 mm diameter, Millipore) with a vacuum pump (N 022 AN.18; KNF, Freiburg, Germany). At Polaris, 8–10 L of seawater was filtered onto 0.22-µm Sterivex filters (Millipore) with a peristaltic pump (Masterflex; Cole Parmer, Vernon Hills, IL). After the filtration, the filters were stored at −80°C. DNA was extracted from the filter with DNeasy PowerWater Kit (MO BIO Laboratories, Inc., Carlsbad, CA, United States) following the protocol. Extracted DNA was stored at −20°C. Amplicon sequencing was performed at the Center for Biotechnology (CeBiTec laboratory, Bielefeld University). For the 16S rRNA gene amplicon library preparation, we used the bacterial primers 341F (5′-CCTACGGGNGGCWGCAG-3′) and 785R

(5′-GACTACHVGGGTATCTAATCC-3′) (Herlemann et al., 2011), which amplify the 16S rDNA hypervariable region V3–V4 in Bacteria (400–425 bp fragment length). Sequences were obtained on the Illumina MiSeq platform (Illumina, San Diego, CA, United States) in a 2 × 300 bp paired-end run aiming for >50 000 reads per sample at CeBiTec Bielefeld, Germany, following the standard instructions of the 16S Metagenomic Sequencing Library Preparation protocol (Illumina, San Diego, CA, United States). The quality cleaning of the sequences was performed with the following software tools. The primer clipping was performed with the tool cutadapt (v1.9.1; Martin, 2011). Then the TRIMMOMATIC software v0.35 (Bolger et al., 2014) was used to remove low-quality sequences (SLIDINGWINDOW:4:20 MINLEN:300). The merging of forward and reverse reads was performed with the PEAR software (v0.9.6); setting a minimum overlap of 10 bp (Zhang et al., 2014). SWARM algorithm (v2.2.2; Mahé et al., 2014) was applied for clustering the sequences into operational taxonomic units (OTUs; local clustering threshold for operational taxonomic units set d = 1). The taxonomic classification of OTUs was based on the SILVA database, release 132 (Quast et al., 2013). The total number of sequences and OTUs generated in this study are reported in Supplementary Table S7. Sequences were deposited at the European Nucleotide Archive (ENA) under BioProject PRJEB48226 (accession numbers are reported in Supplementary Table S7). The sequences were archived using the brokerage service of the German Federation for Biological Data [GFBio; (Diepenbroek et al., 2014)]. A total of 21 (Polaris) and 16 (Aurora) samples were analyzed for these assays.

2.12 Metatranscriptomic analysis

After the recovery of *in situ* pumps, filters were immediately cut into six pieces, transferred to screw-cap tubes, frozen in liquid nitrogen for 5 min, and then transferred to −80°C. The RNA was extracted from three replicate filter sections using an RNase-free tube and the mirVana mRNA Isolation kit (Ambion GmbH, Germany). For DNA depletion, the extracted nucleic acids were treated with a TURBO DNA-free Kit (Ambion GmbH, Germany), and the RNA was purified and concentrated using RNeasy MinElute Kit (Qiagen GmbH, Germany). The RNA quantification, library preparation, and sequencing were carried out at CeBiTec laboratory (Bielefeld University) as described (Molari et al., 2023). The library was sequenced on a HiSeq1500 platform (Illumina, San Diego, CA), in 1 × 150 bases single-end runs, with a total number of reads per sample > 20 million. The adaptor sequence was removed and a read quality trimming with Q20 was performed using bbduk v34 from the BBMAP package and TRIMMOMATIC software v0.35 (Bolger et al., 2014). The trimmed reads were sorted in ribosomal RNA (rRNA) and non-ribosomal RNA (non-rRNA) using SortMeRNA software v2.0 (Kopylova et al., 2012) with the SILVA rRNA database. Statistics and ENA accession numbers are reported in Supplementary Table S8. The taxonomic classification of rRNA reads (1 million per sample) was assigned with phyloFlash software v3.0 beta 1 (Gruber-Vodicka et al., 2020) based on the SILVA database (release 132).

The non-rRNA reads of the transcriptome were *de novo* assembled using rnaSPAdes (Nurk et al., 2017) The genes were predicted on reconstructed transcripts using Prodigal [v.2.6.3 (Hyatt et al., 2010)], and the genes clustered using MMseq2 [v13.45111; (Steinegger and Söding, 2017) --min-seq-id 1 -c 0.80 --cov-mode 1 --cluster-mode 2]. Genes with length < 150 nucleotides were removed (*ca.* 12% of total genes). Taxonomic affiliation of the contigs was performed with Kaiju [v.1.9.2 (Menzel et al., 2016)] using a non-redundant protein sequences database ("nr") and protein sequences from representative assemblies from NCBI BLAST ("refsed"). The functional annotation of genes was conducted using Pfam [v.35.0; (Mistry et al., 2021)] with hmmsearch HMMER [v.3.3.2; (Wheeler and Eddy, 2013)], NCycDB, a curated database for nitrogen cycling genes (Tu et al., 2019) with diamond v.2.0.15; (Buchfink et al., 2015), iron cycling genes FeGenie's database (Garber et al., 2020) with diamond v.2.0.15, and Greening lab metabolic marker gene databases [Version 3; (Greening, 2021); with diamond v.2.0.15]. The metatranscriptomic reads were mapped to the gene sequences using bwa-mem2 v.2.2.1 (Vasimuddin et al., 2019) and converted in counts per gene with htseq-count script from HTSeq [v.2.0.2;(Putri et al., 2022)]. On average, 71 and 65% of reads from Polaris and Aurora metatranscriptomes, respectively, were retrieved by the catalog of genes (Supplementary Table S9). Gene read counts were divided by the length of each gene in kilobases (RPK) and reported as transcripts per million (TPM). We defined the genes highly transcribed in the plume, as those genes that have a level of transcription with centered log ratio value higher than 2 at PS101/188 (2,645 mbsl) and at PS86/055 (2,958 mbsl). A total of 19 samples (Polaris) and 6 samples (Aurora) were analyzed for these assays.

2.13 Data analysis

Non-parametric multidimensional scaling (NMDS) based on the Bray–Curtis dissimilarity index was used to depict differences in microbial communities based on counts of 16S rRNA genes, rRNA reads, and gene transcripts. All datasets were Hellinger transformed. The significance of differences between sites and seawater types was tested using the analysis of similarity (ANOSIM) (Clarke, 1993). The total effective number of species, exponential Shannon entropy, and inverse Simpson index were used to describe alpha-diversity (Chao et al., 2014) in each seawater type for Aurora and Polaris mounds. Beta-diversity between Aurora and Polaris plumes was quantified by calculating Jaccard dissimilarity based on rarefied (15,427 sequences) counts of 16S rRNA genes presence-absence (PA) transformed.

For the construction of the 16S rRNA phylogenetic tree, the sequences were aligned with MAFFT using the L-INS-i method with default settings (Katoh and Standley, 2014), and the alignment was cleaned with BMGE with default settings (Criscuolo and Gribaldo, 2010). Both programs were used on the Galaxy platform (Afgan et al., 2018). A maximum-likelihood-based tree was constructed using W-IQ-TREE (Trifinopoulos et al., 2016), first searching for the best substitution model (Kalyaanamoorthy et al., 2017), before evaluating branch support using 1,000 ultrafast bootstraps (UFBoot) and SH-aLRT branch test replicates. Phylogenetic trees for NiFe hydrogenase were constructed following the workflow described for the backbone 16S rRNA gene tree, with amino acids as coding sequence and MAFFT alignment method set to 'auto'.

Significant differences in alpha-diversity, total cell counts, and CARD-FISH counts between seawater types and sites were tested by analysis of variance (one-way ANOVA) or by the non-parametric Kruskal–Wallis (KW) test when the ANOVA's assumptions were not satisfied. Differentially abundant OTUs and 16S–18S rRNA reads (cDNA), and differential expressions of reconstructed transcripts were detected using the R package edgeR (Robinson and Smyth, 2007) at a significance threshold of 0.01 for Benjamini–Hochberg adjusted [BH;

(Benjamini and Hochberg, 1995)] *p*-values (see Supplementary Tables S9, S10).

All statistical analyses and plots were conducted in R using the core distribution with the additional packages vegan (Oksanen et al., 2013), ggplot2 (Villanueva and Chen, 2019), and pheatmap (RRID:SCR_016418) (Kolde and Kolde, 2015).

3 Results

3.1 Identification of active vent fields at Gakkel Ridge

After the original detection of hydrothermalism across the ice-covered ultraslow spreading Gakkel Ridge in 2001 with temperature and turbidity sensors (Edmonds et al., 2003), this study had the objective to revisit plumes, assessing for the first time their sources at the seafloor and identifying potential chemoautotrophic life associated with the venting. The "Polaris" vent field was first visited in 2016 in the central part of the Eastern Volcanic Zone (Boetius and Purser, 2017) and "Aurora" in 2014 at the westernmost end of the Western Volcanic Zone (Baker et al., 2004; Boetius, 2015; Edmonds et al., 2003; German et al., 2022). In both areas, year-round full sea-ice coverage had prevented thorough studies of the source of the plumes prior to the RV Polarstern expeditions PS86 and PS101. Our main survey instruments to find the hydrothermal vents were ocean floor observing systems (PS86:OFOS; PS101:OFOBS) for seafloor morphology and geobiology (Purser et al., 2019) and a CTD (conductivity, temperature, depth) rosette that was equipped with highly sensitive redox and turbidity sensors, 24 Niskin bottle samplers, and *in situ* pumps. To survey the vent fields and sample their plumes, the icebreaker Polarstern had to drift with the ice floes across specific locations according to predicted trajectories (Boetius, 2015; Boetius and Purser, 2017).

During PS101, we visited the Eastern Volcanic Zone to investigate the source of a large hydrothermal plume hovering above the NW flank of a previously unnamed seamount discovered 15 years earlier (Baker et al., 2004; Edmonds et al., 2003). We named this structure "Polaris" (86°87.5'N, 55°42.4'E; 3,170 m water depth) (Figure 1A). In OFOBS surveys, we found indications for hydrothermal activity on the NW flank of the mount in the form of small vents with shimmering water. Some of the small vents contain orange precipitates or microbial mats. In the venting area, we detected a higher number of ophiuroids and polychaetes (Supplementary Figures S1A–E; for additional images, see Supplementary Table S1). The temperature sensor mounted on the OFOBS instrument recorded a temperature anomaly up to 1°C close to the seafloor, and high turbidity was visually detected above the seafloor by OFOBS, yet we did not find large chimneys or black smokers in the studied area. At Polaris, 13 CTD casts were performed in tow-yo mode to assess the size and extent of the plumes. The plumes and the surrounding water column were repeatedly sampled with Niskin bottles and high-volume *in situ* pumps.

During PS86, we discovered the Aurora field of black smoker vents at the southwestern flank of the mound (82°53.83'N; 6°15.32'W, in 3900 m water depth) (Figures 1D–F) during the PS86 expedition (Boetius, 2015). Subsequent expeditions (German et al., 2022; Ramirez-Llodra et al., 2023; Schlindwein, 2023) further studied the vent field with its giant, highly active chimneys. The chimneys were black to bright yellow-orange and released substantial amounts of particulate metal sulfides, visible as black smoke. The surroundings of the Aurora vent field showed basalt rocks, populated by glass sponges, amphipods, limpets, and snails of higher density than in the surroundings or at other mounds of this part of Gakkel Ridge (Supplementary Figures S1F–J, for additional images, see Supplementary Table S1; Boetius, 2015). Near the vent field, a number of cracks and fissures with diffuse vents and dead chimneys were discovered, the latter fully overgrown with sponges. The Aurora hydrothermal plume had a relatively strong turbidity signal that we could follow over a distance of approximately 2 km and for more than 800 m vertically (Figures 1D–F). Using OFOS, we were able to link the origin of this plume to the above-described field of black smokers (Supplementary Figure S1F; German et al., 2022). At Aurora, 14 CTD casts were performed, yet due to unpredictable ice flow movements, only approximately half of the casts reached the target area and allowed the sampling of the plume with Niskin bottles and *in situ* pumps.

3.2 Chemical energy in persistent non-buoyant plumes above vent fields

This study analyses the chemistry of large hydrothermal plumes associated with active venting from two volcanic seamounts. The plumes are rising several hundred meters above the rift valley of the Gakkel Ridge and were originally identified in 2001 (Edmonds et al., 2003). The non-buoyant component of the "Polaris" hydrothermal plume assessed by tow-yo CTD showed sharp anomalies in turbidity, redox values, and temperature extending from a depth of >2,800 meters below sea level (mbsl) to *ca.* 2,400 mbsl, i.e., ca 400–800 m above seafloor, with a horizontal stretch of over 1,200 m according to the turbidity signal (Figures 1B,C; Figure 2A). The CTD cast PS101-226 (86° 57.41' N, 55 44.42′ E) intercepted the buoyant part of the plume closer to the seafloor (~2,900 m) with temperature anomalies up to 160 mK above ambient seawater (−0.8°C), suggesting further, more vigorous venting at the NW flank of the mound. Based on the plume rise height and the measured stratification of the water column, we calculate a vent power of 130 MW. At an endmember fluid temperature of maximal 270° C, which is typical for a low H_2:CH_4 ratio observed here (Table 1), this could translate into a water flux of at least 11,600 m^3 per day (for calculation, see Supplementary material). The observed maximal redox anomaly was relatively low with −25 mV, and this redox signal disappeared faster than the turbidity signal (Figures 1B, 2A). The low redox anomaly likely results from the low concentrations of reduced iron and manganese in the plume below the detection limit (Table 1). The Polaris plume was rich in ^{3}He, with δ^3He values of up to 75% compared to atmospheric helium standards, indicating a substantial concentration of mantle-derived gas in the rising fluids (Figure 2B). The seawater samples from the buoyant part of the plume closer to the seafloor contained up to 300 nM CH_4 and 360 nM H_2 (Figures 2C,D). During the closure of Niskin bottles, temperature anomalies of up to 30 mK were measured. Hence, in all plume samples, the fluids were diluted by at least a factor of 1:9000 in the seawater (see Table 1). This suggests that the original vent fluids contained approximately 2.7 mM CH_4 and 3.3 mM H_2. Based on the calculated fluid flux rates, the Polaris vents would feed approximately 51,200 mol hydrogen and 43,200 mol methane per day into the plume.

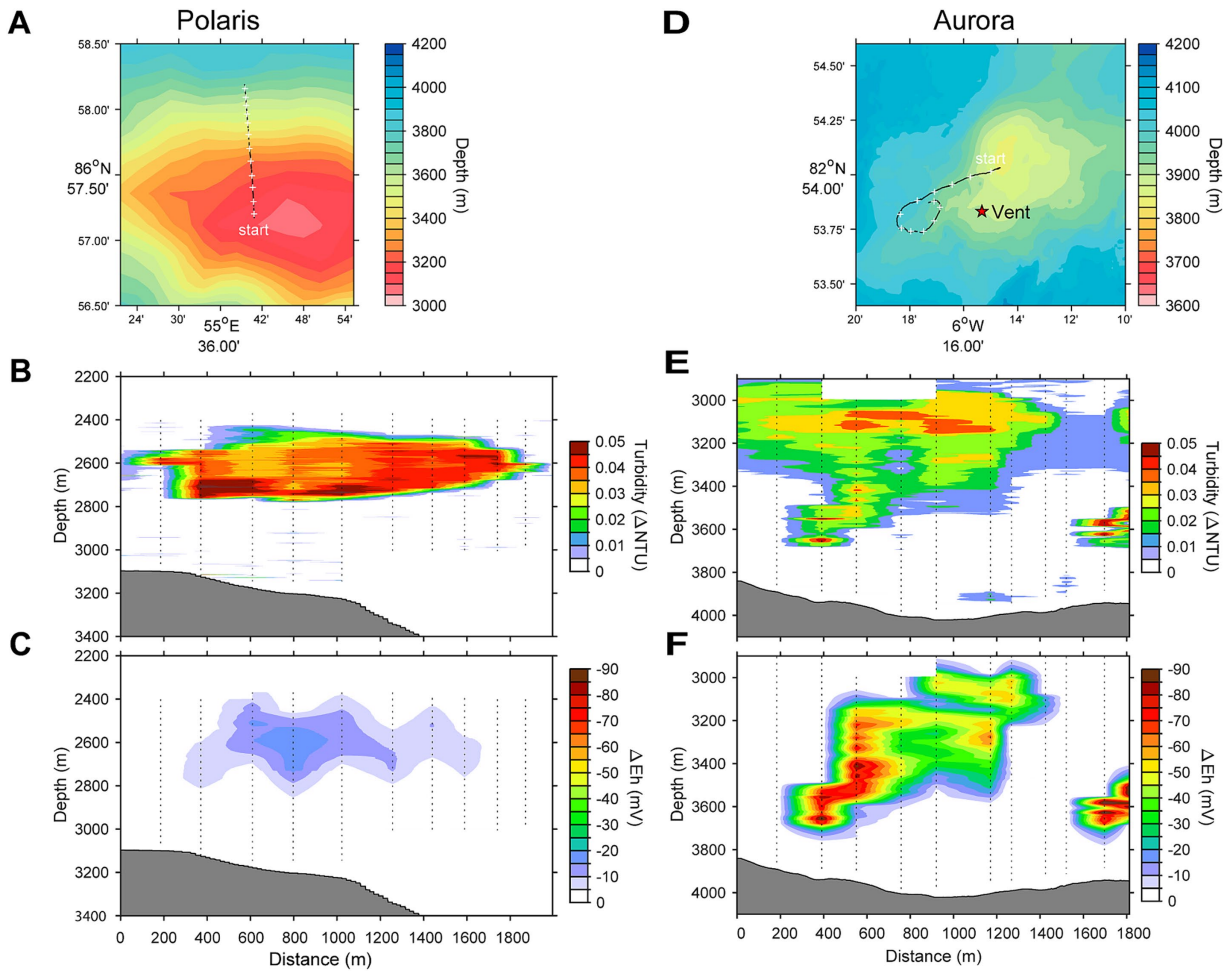

FIGURE 1
Locations and water column profiles of the studied vents. **(A,D)** Bathymetric maps and location of the Polaris and the Aurora vent. The star on the map indicates the position of vents observed by OFOBS. **(B,E)** Water column profiles for turbidity. **(C,F)** Water column profiles for plume-driven anomalies in redox potential (ΔEh).

We detected neither dissolved nor precipitated iron (detection limit between 10 and 50 μM), and sulfide was analytically undetectable in the plume according to the Cline assay (detection limit ~10 μM). However, several plume samples had a noticeable sulfidic smell, which suggests sulfide concentrations greater than 100 nM. Therewith, sulfide total sulfide emissions from the Polaris vents could theoretically be in a similar range as hydrogen and methane emissions (Radford-Knoery et al., 2001).

Based on the observed plume characteristics, we estimate that the vents have a power of at least 24 MW (for calculation see Supplementary material). Endmember fluids of volcanically hosted black smokers at ultraslow spreading ridges typically have temperatures of 370°C (Beaulieu and Szafranski, 2020; Diehl and Bach, 2020; Kumagai et al., 2008; Noowong et al., 2021), which would result in fluid fluxes of 1,400 m^3 per day to feed the observed plume. In all retrieved samples, the temperature anomalies were low (< 8 mK), translating to dilution factors of $\geq 45 \times 10^3$ for all samples. This high dilution of the Aurora plume is consistent with measured small ^{3}He anomalies (δ^3He values ≤10%) (Figure 2G). By contrast, the redox anomaly of the Aurora plume was much greater than that measured in the Polaris plume. The pronounced redox anomaly is consistent with high concentrations of dissolved iron and manganese in the plume, derived from the large black smoker field at Aurora (Figure 2F; German et al., 2022). *In situ* filtration of the water yielded a yellowish residue, suggesting partial precipitation of metal oxides and metal sulfides. The calculated concentrations of metals in the vent fluid endmember (6.8 mM Fe, 0.7 mM Mn) represent a conservative estimate, missing the fraction precipitated from the plume. Dissolved sulfide was not detectable, and the plume waters did not smell sulfidic. The plume contained up to 30 nM methane (German et al., 2022; Figure 2H), which translates to 1.4 mM methane in the fluid endmember. On board of PS86, we were not able to measure hydrogen concentrations. Typically, high-temperature vent fluids have a molar H_2:CH_4 ratio of approximately 10 or higher (Aquino et al., 2022; Charlou et al., 2002; Kumagai et al., 2008). Future studies should measure the endmember compositions. Based on the calculated fluid volume flux rates (see earlier), we estimate corresponding geochemical fluxes from the Aurora vents (Table 1) of approximately 17,000 mol H_2, approximately 1,700 mol CH_4 per day; >8,000 mol Fe per day (168 tons per year), and ≥ 850 mol of Mn per day (17 tons per year).

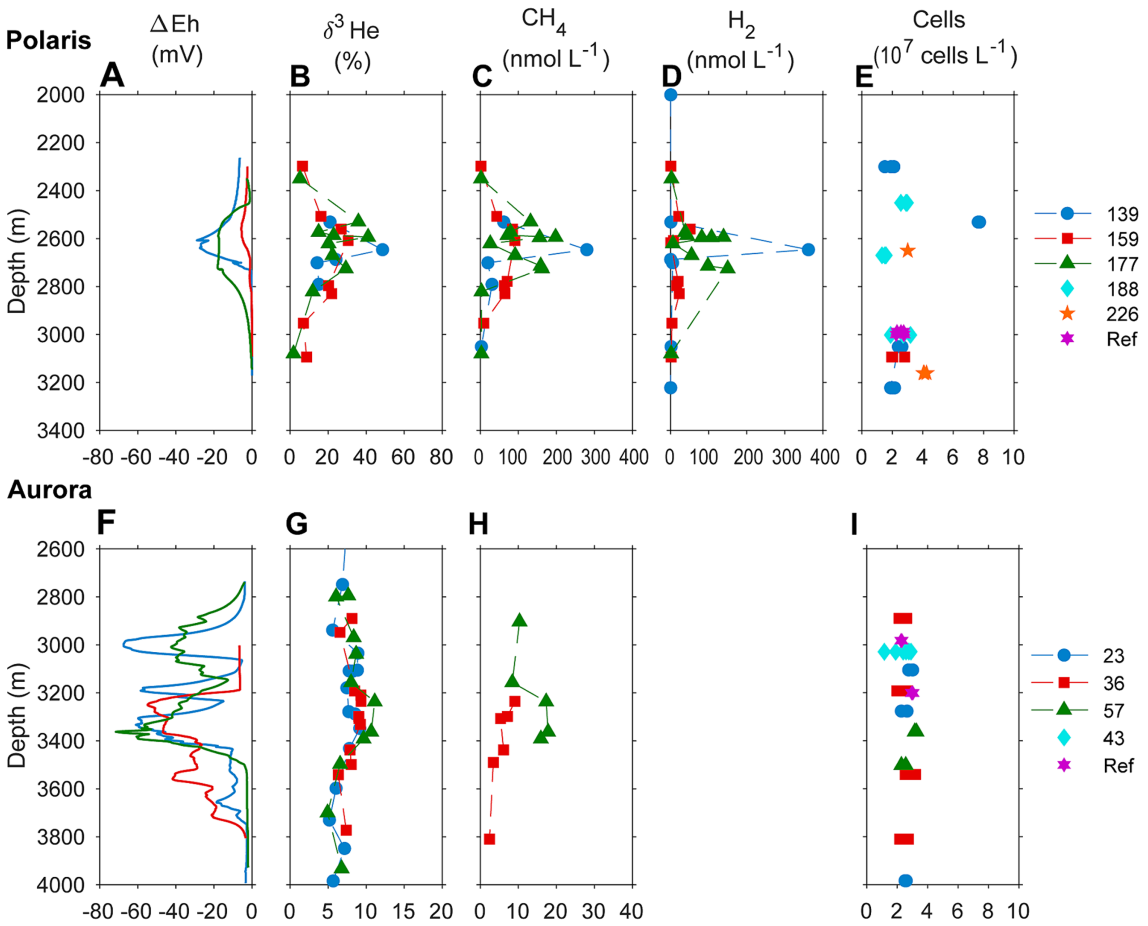

FIGURE 2
Biogeochemical signatures of the water column of **(A–D)** the Aurora and **(F–I)** the Polaris hydrothermal plume. **(A,F)** Redox potential measured as an offset of Eh value from background values; **(B,G)** helium isotopic composition measured as δ^3H (%) against atmospheric helium as standard; **(C,H)** concentrations of methane in the water column; **(D)** hydrogen water column concentrations; and **(E,I)** cell numbers. Samples of different casts through the plume and reference sites are color-coded.

3.3 Hydrogen consumption in the plumes

To quantify the influence of the energy sources on the carbon fixation by the non-buoyant plume microbiota, we collected water samples from the plume and local background waters (above and below each plume) and deep-sea reference water (>five nautical miles from the vents) from both, Polaris ($n = 29$) and the Aurora ($n = 25$) area. We incubated replicate samples of these waters with ^{14}C-bicarbonate at *in situ* temperatures (−1°C) and measured the transfer of the radioisotope into the particulate carbon fraction (Reinthaler et al., 2010). Both reference waters distant from the vent, and local background water samples from above and below the plume, showed carbon fixation rates between 0.5 and 1 µmol C m^{-3} d^{-1} (Polaris $n = 22$ Aurora $n = 15$; Figure 3). These are typical values for dark carbon fixation in the oligotrophic deep ocean, as fueled by anaplerotic activity during heterotrophy and ammonium oxidation (Braun et al., 2021; Reinthaler et al., 2010). In contrast, plume water samples from both sites with notable *in situ* redox anomalies exhibited much higher carbon fixation rates between 5 and 45 µmol m^{-3} d^{-1} (Polaris $n = 6$; Aurora $n = 10$; Figure 3). At a mean carbon fixation of 13 µmol m^{-3} at Polaris, or 14 µmol m^{-3} at Aurora, and a carbon content of 10 fmol per cell (Fukuda et al., 1998), this would allow the growth of approx. 1.35×10^9 autotrophic microorganisms per cubic meter of plume water each day. This translates into a maximal increase of cell mass of 60% per day compared to the background community. This value matches well with the moderately increased cell numbers (Kruskal–Wallis chi-squared = 0.18182, df = 1, p-value = 0.6698). Only one of the plume samples at Polaris (PS101/139) had three times elevated cell numbers compared to the average in the background (Figures 2E,I).

To evaluate the microbial metabolism associated with the non-buoyant plume waters, we compared hydrogen and methane concentrations in the water column and incubated replicate water samples from the hydrothermal plume and reference waters, (hydrogen data only available for Polaris). Within the different plume water samples, the concentrations of methane correlated with the helium isotope ratios, which suggests pure dilution and no consumption of methane during plume dispersion (Bennett B. et al., 2013). In contrast, the hydrogen concentrations dropped faster than the helium isotope ratios (Supplementary Figures S2A,B), indicating the microbial consumption of hydrogen. Consequently, the ratios of H_2/CH_4 dropped from values of 1.35 in the most concentrated plume samples close to the vent (characterized by higher δ^3He values, CH_4 concentrations, and/or temperature anomalies) to ratios near zero in

TABLE 1 Physical–chemical parameters of hydrothermal venting at Polaris and Aurora.

	Polaris	Aurora
Max. values in the hydrothermal plume		
CH_4 (nM)	300	30
H_2 (nM)	360	300[c]
Max. ΔT (mK)	60	8
Dilution factor	9,000	46,250
Vent fluid endmember (calculated)		
Temp (°C)	≤270[a]	370[c]
Mn (mM)	b.d.	0.7
Fe (mM)	b.d.	6.8
CH_4 (mM)	2.7[b]	1.4
H_2 (mM)	3.3[b]	14[f]
Sulfide	>3 mM[c]	<10[c]
Total vent fluxes		
Power (MW)	130[d]	24[d]
Volume (m^3 d^{-1})	11600[d]	1400[d]
Mn (10^3 mol d^{-1})	-	0.85
Fe (10^3 mol d^{-1})	-	8
CH_4 (10^3 mol d^{-1})	43.2	1
H_2 (10^3 mol d^{-1})	51.2	≥17

[a]Typical temperature for observed CH_4:H_2 ratio; [b]calculated based on dilution factors; [c]min. Concentrations based on sulfidic smell and absence of free iron and the calculated dilution factor; [d]calculated based on ocean physics and plume height, see methods; [e]typical black smoker temperature; [f] calculated from H_2:CH_4 ratios of typical black smokers.

more dilute samples (Supplementary Figures S2C–E). At Aurora, the methane: helium ratio is relatively constant, confirming that methane is not consumed (Supplementary Figure S2F).

To further compare the microbial consumption of methane and hydrogen, we incubated replicate bottles of background water (two different sites, 2,542 m; $n = 24$), buoyant plume water, (from one site; 3,010 m water depth; $n = 19$), and non-buoyant plume waters (7 sites, 2,722 m water depth; $n = 90$). We incubated water samples from the Polaris plume with low amounts of hydrogen and methane (for most samples, approx. 200 nM) at *in situ* temperatures of −0.8°C and *in situ* oxygen concentrations of 200 µM (Figure 4; Supplementary Figure S3), to mimic natural availabilities. In the background water (station PS101-175-5), concentrations of added hydrogen (165 nM ± 8) and added methane (31 nM; ±3) remained stable throughout incubation times of up to 5 days, i.e., neither of the energy substrates were consumed by microorganisms. (Figure 4A). Similarly, in the buoyant plume waters, the natural concentrations of hydrogen (323 nM) and methane (272 nM) remained stable (Figure 4B). In contrast, in samples of the non-buoyant plume, concentrations of added hydrogen decreased from 150 nM to 22 nM within only 2 days, whereas concentrations of added methane remained stable for the entire observation period of 5 days (Figure 4C). Four of six additional incubation experiments with non-buoyant plume water show clear hydrogen consumption (Supplementary Figure S3). Aerobic hydrogen oxidizers have growth efficiencies of up to 25% of the reducing equivalents released during hydrogen oxidation (Yu and Lu, 2019). An estimated average hydrogen oxidation rate of 30 µmol m^{-3} day^{-1} from all experiments would translate into the fixation of 7.5 µmol C m^{-3} day^{-1}. This is approximately 50% of the carbon fixed in the plume. This amount might enable the growth of 0.75×10^9 cells m^{-3} day^{-1}.

3.4 Linking plume chemistry with microbial community activity

We investigated methane oxidation rates in the plume samples using highly sensitive ^{14}C-methane radiotracer assays. Methane oxidation was not detectable, neither in the Aurora nor the Polaris plume nor in reference waters (lifetime of environmental methane ≥5 years; see Supplementary Table S2). To our knowledge, similar experimental quantifications of the fate of hydrogen and methane do not exist for any other non-buoyant vent plume to date. However, we were not able to test the influence of nanomolar amounts of reduced metals and sulfide on plume microbiota because of the lack of respective clean lab trace metal equipment and methods to measure low quantities of environmental sulfide at sea. In the Polaris plume, low metal concentrations result in the presence of free sulfide, allowing high microbial sulfur oxidation rates. In the Aurora plume, the excess of metals caused the formation of metal sulfides (black smoke), which will be less bioavailable.

To investigate the influence of the reduced compounds in the plumes on the abundance and activity of microorganisms, we analyzed the 16S rRNA genes and gene transcripts (here referred to as "active members") extracted from plume, local background and reference waters (Polaris $n = 19$; Aurora $n = 6$; Figures 5, 6; Supplementary Figure S3; Supplementary Tables S7, S8). In the Polaris non-buoyant plume characterized by the highest carbon fixing activity, the most abundant taxon was SUP05 with 9% (PS101/139) to 47% (PS101/159) of total 16S rRNA gene sequences (average of 25% across all plume samples). In the background water and at reference stations, this taxon had a much lower relative abundance of 1–9% and 3–4%, respectively. At Polaris, Sulfurimonas contributed 4–19% in the non-buoyant plume compared to <1% in reference samples (Figure 5). Most of the other active fraction of microbial communities was similar in both plumes and in the background waters (Supplementary Figure S3). A difference between the non-buoyant plumes was the fraction of Sulfurimonas, which dominated the microbial communities at Aurora with 16 to 66% (PS86/055; Figure 5) of bacterial 16S rRNA gene sequences and 69 to 79% of all SSU rRNA reads (PS86/055; Figure 5; Supplementary Figure S4). SUP05 reached on average 10 and 8% in the Aurora plume, of total and active community members, respectively (Figure 5; Supplementary Figure S3).

The substantial enrichments of SUP05 and Sulfurimonas (i.e., *U S. pluma*) cells in Arctic hydrothermal plume waters were confirmed by microscopy applying specific oligonucleotide probes, reaching values of 6–12% and SUP05 2–20% Sulfurimonas cells, respectively, in the plume samples (Supplementary Table S3; Kruskal–Wallis chi-squared = 6.6, df = 1, p-value = 0.01). In background waters, Sulfurimonas still accounted for up to 2–10% of all SSU rRNA reads (PS86/074 at 2500 m), and SUP05 was 2%. These numbers—especially for *Sulfurimonas*—appear very high and suggest that Arctic deep-sea waters may be thoroughly mixed with hydrothermal waters from Gakkel Ridge (Edmonds et al., 2003), and that their mortality is very

low. Furthermore, it remains to be investigated, if both taxa can maintain their energy needs by other electron donors.

To assess the impact of venting on the overall microbial community structure, we statistically analyzed the amplified 16S rRNA gene patterns. In both plumes, the increase of specific taxa resulted in a significant decrease of evenness as described by exponential Shannon entropy and inverse Simpson index, while the overall species richness of the water types was not affected (Supplementary Figures S5, S6; Supplementary Table S4). Aurora and Polaris plumes shared on average 36 ± 6% of bacterial 16S rRNA gene sequences with reference seawater, with lowest values at stations PS101/177 (25 ± 2%) and PS86/055 (29 ± 1%; Supplementary Table S5). The two plumes shared on average 32 ± 4% of the 16S rRNA genes, which is slightly lower than the value of 16S rRNA genes shared among the different non-plume waters (40 ± 1%; Supplementary Table S5). As previously reported by Molari et al. (2023), phylogenetic comparison of the Sulfurimonas SSU rRNA gene sequences from both hydrothermal plumes revealed two main distinct but closely related populations that share >99% SSU rRNA nucleotide sequence identity. Similarly, the analysis of the V3 – V4 region of the 16S rRNA gene of SUP05 revealed two related ribotypes (similarity >98%). One ribotype dominates at Polaris, and the other is more dominant at Aurora (Supplementary Table S6). These results were confirmed by the 98–100% identity between dominant OTUs of the 16S rRNA gene amplicons and 16S rRNA gene sequences from three metagenomic assembled genomes obtained from Aurora and Polaris water samples (Scilipoti and Molari, 2024). Based on phylogenetic analysis of their 16S rRNA, one of the two SUP05 strains clusters with SUP05 sequences from Pacific Ocean hydrothermal plumes, and the other species was more similar to SUP05 sequences from the Atlantic and the Pacific oxygen minimum zone (Supplementary Figure S7). In addition, some less abundant taxa show differential abundance. For instance, the Polaris plume was enriched in Oleispira, which include alkane oxidizers from the Arctic Ocean (Yakimov et al., 2003) and methane oxidizers of the Methylococcales cluster Milano-WD1B-03 (Supplementary Figure S4).

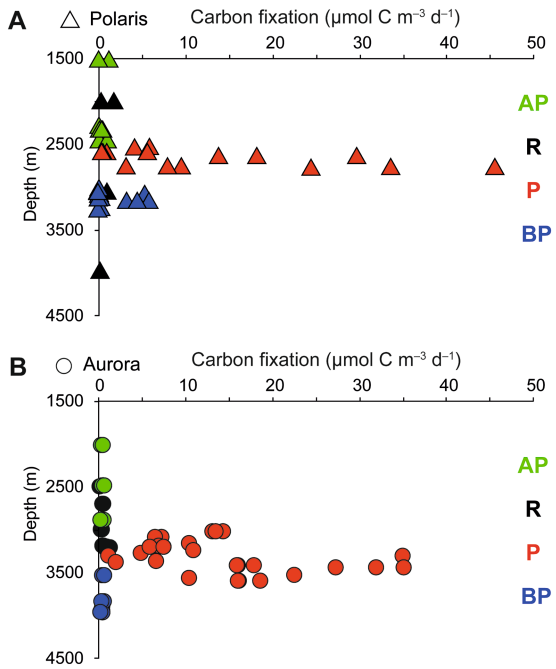

FIGURE 3
Stimulation of carbon fixation in **(A)** the Aurora and **(B)** Polaris plumes. Dark CO_2 fixation (DCF) rates in deep-sea water collected above the plume (AP), in the plume (P), below the plume (BP), and at reference locations (R). Each data point represents a single rate measurement.

To analyze the metabolism of key community members, we analyzed the transcription activity for different functional genes. Transcripts for carbon fixation of Sulfurimonas via the reverse tricarboxylic acid cycle (i.e., *aclA* and *aclB*) are highly enriched at Aurora, whereas SUP05 transcripts for carbon fixation via the ribulose monophosphate pathway (*rbcL*) are more enriched at Polaris. This is in line with the dominance of either *Sulfurimonas* or SUP05 at Aurora and Polaris, respectively.

Genes for hydrogen and sulfur metabolism were highly expressed in the Polaris and the Aurora plumes, but the transcription levels differed between the two plumes and the abundant taxa (Figure 6). In both plumes, the hydrogenase [Ni,Fe]hyd1b assigned to Sulfurimonas was the highest expressed hydrogenase. This is the prototypical oxygen-sensitive hydrogenase of hydrogen oxidizers isolated from hydrothermal vents and other redoxcline environments (Adam and Perner, 2018, Lappan et al., 2023, Molari et al., 2023; Supplementary Figure S7), which supports the hypothesis of a dominant role of hydrogen oxidation at these Arctic vents. The dataset also contains transcripts of the groups 1d and 1 L [NiFe]-hydrogenase

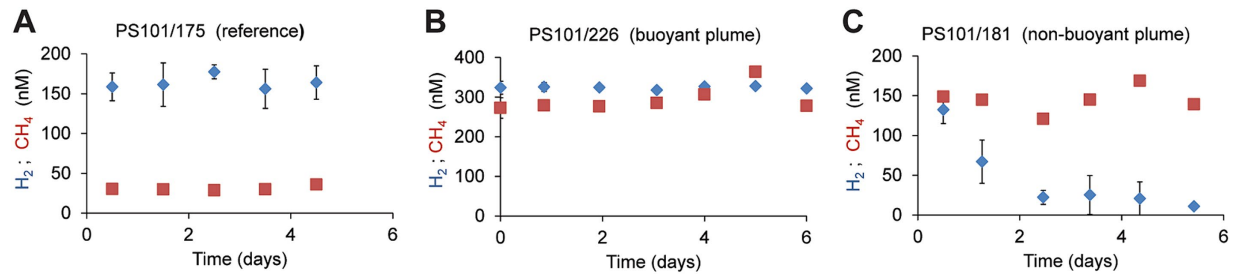

FIGURE 4
Development of hydrogen and methane concentrations in different water types. **(A)** In reference to waters incubated with hydrogen or methane **(B)** in buoyant plume water **(C)** in the outer, non-buoyant plume. In the reference and non-buoyant plume waters, hydrogen, and methane were added as sterile-filtered seawater equilibrated with methane/hydrogen-saturated water. Each symbol is a mean of $n = 3$ biological replicates, and error bars mark standard deviations.

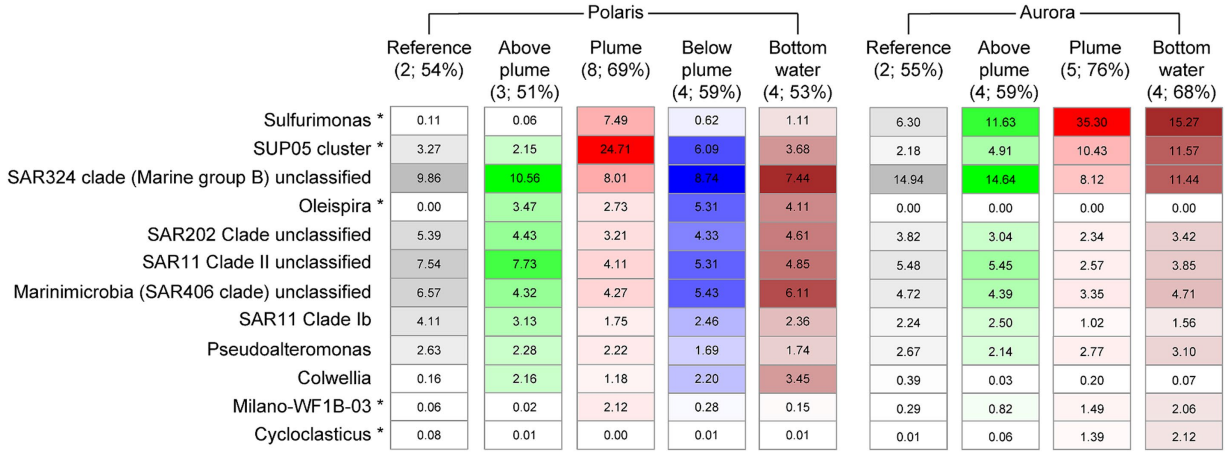

FIGURE 5
Relative abundance of microorganisms of different water masses at Polaris and Aurora based on 16S rRNA amplicon sequences. Relative abundance is calculated from amplified bacteria 16S rRNA genes. Only the 10 most abundant/significantly different abundant genera are shown (in brackets: numbers of samples and the sum of listed 10 taxa).

that belong to SUP05. Group 1d was highly enriched in the Polaris plume, but comparatively depleted in the Aurora plume. In contrast, the [NiFe]-hydrogenases group 1 L was similarly highly expressed in both plumes (Figure 6). These two hydrogenases most likely belong to two different SUP05 strains (Supplementary Figures S7, S8). Group 1d is the canonical enzyme for aerobic hydrogen oxidation, and it catalyzes hydrogen oxidation in the SUP05 symbionts of Bathymodiolus mussels from hydrothermal vents (Petersen et al., 2011). Hence, it is likely that the SUP05 of the Arctic plumes is also capable of growing on hydrogen. Recently, Lappan et al. (2023) reported that 1 L [NiFe]-hydrogenases are widespread in marine microorganisms; however, their function in many of these organisms remains unclear. SUP05 has been shown to grow on reduced sulfur compounds (Shah et al., 2017), and it was suggested that it also utilizes hydrogen (Anantharaman et al., 2013). Yet, not all SUP05 MAGs from hydrothermal plumes code for [NiFe]-hydrogenases (Dede et al., 2022; Zhou et al., 2023). Thus, it remains to be shown how widespread and important hydrogen metabolism is in pelagic SUP05 bacteria (Morris and Spietz, 2022).

At both sites, the transcripts of sulfur metabolism of SUP05 and Sulfurimonas are highly expressed. The highest enrichment of transcripts of the sulfur metabolism is found at Polaris. Here, the transcripts of SUP05 encoding the sulfur oxidation pathway, including sulfur oxidation to sulfate (*dsrA, aprA*) and thiosulfate oxidation to sulfate (*soxA, soxB*), belonged to the most enriched functional gees (Figure 6). In addition, transcripts of sulfur metabolism assigned to Sulfurimonas are substantially expressed, which points toward the potential of *S. pluma* to metabolize and grow on sulfur compounds. However, the dominance of Sulfurimonas in the hydrogen-rich Aurora plume and the dominance of SUP05 in the sulfur-rich Polaris plume combined with the transcriptomic data suggest different substrate affinities of both organisms and therefore potential niche separation as reported for other marine environments (Meier et al., 2017; Rogge et al., 2017).

Puzzled by the lack of evidence for microbial oxidation of methane, we also looked for the transcription of methane monooxygenases (*pmo*). Surprisingly, the pmo expression was relatively high in all water samples, and only in the Polaris plume some subunits were enriched compared to measurements in other water bodies (Figure 6). The relative abundance and activity of potential methanotrophs were low (≤ 2%; Figure 5; Supplementary Figure S4). These findings suggest that methanotrophs do not profit from the elevated methane concentration in the non-buoyant plumes, which has been predicted previously (Reed et al., 2015). This fits to the apparent lack of methane consumption in the plume as determined by the gas ratios and the incubations with ^{14}C methane radiotracer. Moreover, we did not identify enrichment of transcripts related to iron oxidation within the pool of highly transcribed genes at Polaris and Aurora, suggesting minor importance of microbial metal oxidation (Dick, 2019; Zhou et al., 2023). Only some metal-related metabolic genes assigned to *Sulfurimonas* (*cft, arsC*) were highly transcribed in the plumes, matching the physiology of *Sulfurimonas* in their need for particulate metals (Molari et al., 2023).

4 Discussion

Our geobiological surveys of seamounts of the Western and Eastern Volcanic Zones resulted in the identification of persistent hydrothermal activity linked to large non-buoyant plumes in the deep Arctic Ocean. At both sites, i.e., Aurora and Polaris, we detected the plumes at the same sites as described in 2001 (Edmonds et al., 2003), showing significant turbidity and temperature anomalies compared to the background. At the Aurora mound, we tracked down the plume to a typical high-temperature black smoker field, where metals co-precipitate with sulfide. We calculated emissions of 168 tons of iron per year and similar amounts of sulfide from the Aurora field and observed the formation of large chimneys and iron–sulfur precipitates at the seafloor (Supplementary Figures S1F,H). At Polaris, we located the source of the plume at the previously described location at the NW axial volcanic ridge and detected a mound with substantial hydrothermal features. Yet the many small clear-water vent chimneys observed (20–30 cm in height) and the fissures between the rocks are unlikely the source for the large plume rising up to 800 m into the

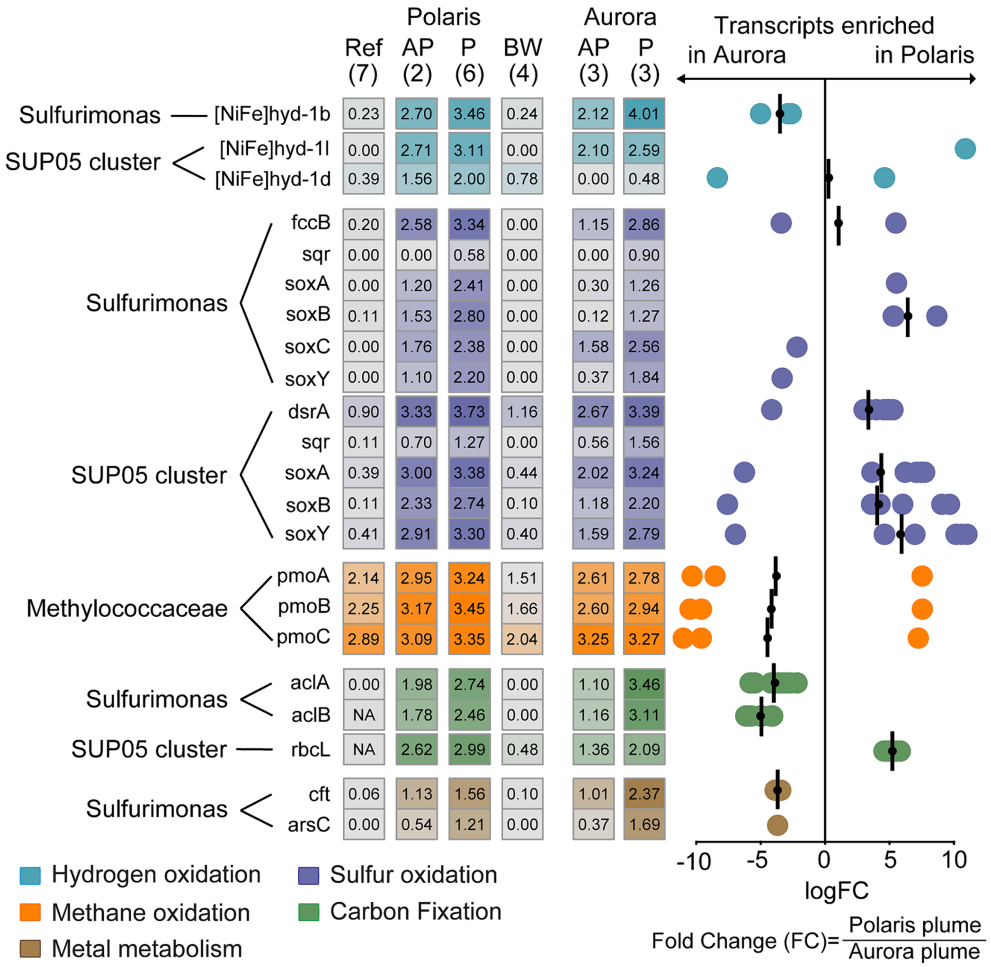

FIGURE 6
Expression of functional genes in different at Polaris and Aurora. Left: Heatmap depicts normalized transcription values at logarithmic scale for key functional genes of the hydrogen, sulfur, and methane metabolism assigned to Sulfurimonas, SUP05, and Methylococcaceae and their key genes for carbon fixation. In addition, the transcription values for metal transporters in Sulfurimonas in different water bodies are shown. In brackets: number of replications. Right: Enrichment of specific gene transcripts in plume samples of Aurora or Polaris, respectively. Each circle represents the fold change in for an individual gene encoding enzymes of a group specified with Pfam v.35.0 (Mistry et al., 2021). These genes do not necessarily belong to the same organism (see Supplementary Table S9 for details). The bars represent the geometric mean of the fold change in transcription for the genes encoding the same enzyme and were assigned to the same taxon. Negative values translate into enrichment in Aurora and positive values enrichment in Polaris. Genes: [NiFe]hyd1b/–l/1d: a large subunit of the different group 1 membrane-bound Ni,Fe hydrogenases; fccB, sulfide dehydrogenase flavoprotein chain; *sqr*, sulfide quinone reductase; *dsrA*, dissimilatory sulfite reductase alpha subunit; *aprA*, adenylylsulfate reductase alpha subunit; *SoxA*, sulfur oxidation protein subunit A; *pmoA*, particulate methane monooxygenase alpha subunit; *acl*A,B; ATP citrate lyase; alpha and beta *cbbL*: Rubisco large subunit. *Cft, arsC*: genes coding for metal metabolism.

water column (Figure 1). The lack of iron in the overlying plume suggests a low-temperature type venting. According to preliminary seafloor observations, the hydrothermal areas hosted a higher number of different invertebrates than the surrounding area (e.g., accumulations of filter feeders, polychaetes, mat-type precipitates, and crustaceans; Supplementary Figure S2), yet it remains to be assessed if any of the different macrofauna species benefit directly or indirectly from microbial chemosynthesis.

Due to the low stratification of the Arctic Ocean's deep waters, the formed hydrothermal plumes increased up to 900 meters in the water column. In the deep buoyant part of the plume, the numbers of potentially autotrophic microorganisms were low, and at Polaris, the water did not show immediate hydrogen oxidation activity. We explain the absence of microbial activity in the buoyant plume with the short rising period of approximately 1 h (Reed et al., 2015). Within this period, the ambient microbial communities are unlikely yet to respond to the presence of hydrogen or other reduced compounds. Moreover, most microorganisms transported from the vent chimney are likely thermo- or mesophilic and not adapted to the plume temperatures of −0.8°C. Thus, the high carbon fixation rates of up to 45 μmol m^{-3} in the non-buoyant hydrothermal plumes are best explained by a specific functional microbial assemblage able to adapt to this extreme niche in the central Arctic Ocean. All samples showing an increased carbon fixation also showed a specific microbial community composition, selecting for chemosynthetic bacteria. The very sluggish tidal current regime of the deep Arctic Ocean can retain the same water mass for relatively long times above the vents.

At Polaris, the most abundant and active taxon is SUP05. SUP05 is widely distributed across different pelagic environments (Canfield et al., 2010; Glaubitz et al., 2013). Recent analyses based on amplified 16S rRNA genes and metagenomic analyses revealed that non-buoyant plumes are generally enriched in globally distributed SUP05 clades,

which are recruited from background waters (Anantharaman et al., 2013; Dede et al., 2022; Dick, 2019; Dick et al., 2013; Lesniewski et al., 2012). Based on their dominance in most studied plumes to date, it was concluded that their specific deep-water niches are low-temperature, high-oxygen waters with low concentrations of reduced sulfur species (Dede et al., 2022; Meier et al., 2017). Hence, the microorganisms were exposed to physiologically relevant concentrations of vent-derived energy sources. Polaris and Aurora represent the coldest habitats of SUP05 so far found in the ocean. Still, their 16S rRNA genes cluster with sequences from strains in the Pacific and South Atlantic deep waters. At Aurora, *Ca. S. pluma* was more dominant. Here, hydrogen was the by far most abundant energy source, suggesting that the availability of hydrogen is a factor selecting for this group. Due to the precipitation of iron sulfide, reduced sulfur phases were only available in minor quantities; hence, the abundance of SUP05 increased only moderately. The use of hydrogen as the main energy source was supported by the highest expression of the hydrogenase in *Ca. S. pluma*, and the presence of *Ca. S. pluma* in other hydrogen- or metal-rich hydrothermal plumes (Molari et al., 2023). All previous cultures of Sulfurimonas showed a preference for suboxic conditions (Han and Perner, 2015). So far, it is not fully resolved how *Ca. S. pluma* thrives in oxygen-saturated Arctic seawater, but modifications in the reductive tricarboxylic acid pathway seem to have a role in this adaption (Molari et al., 2023).

The biogeochemistry of the hydrothermal vent plumes is also largely reflected in the gene expression patterns extracted from the plume waters. In the hydrogen-rich and sulfur-depleted Aurora plume, the hydrogenase of Sulfurimonas is the most expressed gene, suggesting the dominance of hydrogen oxidation by *S. pluma*. However, based on substantially expressed pathways for elemental sulfur oxidation (Sox pathway) and potentially sulfide oxidation (non-canonical flavocytochrome c), *Ca. S. pluma* may also be capable of growing on sulfur compounds. To test this hypothesis, further experiments and cultures are required.

In contrast, at Polaris, the genes of the oxidative sulfur metabolism *dsr, apr,* and the *sox* complex were enriched and linked to the higher bioavailability of sulfur. Interestingly, the sulfide quinone reductase (*sqr*) that encodes the enzyme for the activation of hydrogen sulfide was not strongly enriched. This may indicate that much of the hydrogen sulfide is oxidized chemically, and the Arctic plume microbiota rather thrives on the products, i.e., elemental sulfur and thiosulfate. The highly expressed *dsr*, *apr,* and *sox* genes belong primarily to SUP05, supporting the hypothesis that SUP05 relies on sulfur species as its main substrate (Anderson et al., 2013; Rogge et al., 2017). Because SUP05 also expresses hydrogenases, it might also utilize hydrogen in competition with *Ca. S. pluma*.

Altogether, hydrogen emissions appear responsible for a dominant fraction of microbial biomass production at the Polaris and the Aurora vents, respectively. Sulfur oxidation provides another important energy source in both vent plumes, similar to what is known from temperate vent environments (Zhou et al., 2023). Yet, our results showed that in the Arctic hydrothermal vent plumes, the sulfur-oxidizing community is less diverse than in other hydrothermal plumes (Zhou et al., 2023). Most interestingly, the bacteria selected by the persistent plume environment are represented in the background deep waters, even far away from the vent sites. It remains to be studied how they can survive in the absence of their main electron donors. Our study further confirms that sulfur speciation has a great influence on the bioavailability of sulfur. A co-occurrence with high metal loads in the endmember limits the bioavailability of this energy source.

Methane has been often suggested to play a role as an energy source to plume microorganisms, based on the widespread presence of aerobic methanotrophs, e.g., in 16S rRNA gene surveys as well as based on functional genes (Anantharaman et al., 2016; Lesniewski et al., 2012). However, in the plume waters studied here, the relative numbers of methane oxidizers such as Methylomonaceae were not significantly increased compared to surrounding waters (Figure 5). Despite notable transcription of the *pmo* genes both in the plume and in the background waters, we could not detect methane oxidation (Figure 4; Supplementary Figures S2, S3; Supplementary Table S2). Cultured methanotrophs show relatively high half-saturation constants for methane in the range of 2 to 12 µM (Bender and Conrad, 1992; Knief and Dunfield, 2005). In the plumes, methane rapidly diluted to low nanomolar concentrations, and together with temperatures below 0°C, this may be the reason, why methane-consuming microorganisms do not grow, even though methane oxidation is thermodynamically favorable. We conclude that methanotrophs may not be able to grow fast enough in these icy oceans to exploit the methane enrichments observed. Other vent plumes in warmer waters, such as those of the Juan de Fuca Ridge, show comparatively higher methane consumption (Cowen et al., 2002; de Angelis et al., 1993).

The location and exploration of vents and retrieving endmember fluids of vents in Arctic oceans remains technologically challenging. However, this study shows that relatively few chemical analyses, experiments, and simple community descriptions can already provide insights into the nature of the venting present. Conversely, it is also possible to predict plume community compositions from the fluid endmember chemistry. The vigorous venting found at Aurora and Polaris releases large amounts of geothermal energy, provides a source of rare elements into the deep ocean, and fuels a specific community, apparently hydrogen and sulfur-based microbial growth. Further studies are needed to resolve the extent of venting and its influence on the deep-sea microbiome and fauna across the Gakkel Ridge.

Data availability statement

The datasets presented in this study can be found in online repositories. The data presented in this study have been deposited at the European Nucleotide Archive (ENA) under the project number PRJEB48226. The 16S rRNA gene amplicon data can be found under the accession numbers ERR7132482-ERR7132512. The metatranscriptomic data was deposited under the accession numbers ERR7132513-ERR7132538. Further information can be found in the article/Supplementary material.

Author contributions

GW: Conceptualization, Data curation, Formal analysis, Funding acquisition, Investigation, Methodology, Project administration, Resources, Supervision, Validation, Visualization, Writing – original draft, Writing – review & editing. MM: Conceptualization, Data curation, Formal analysis, Investigation, Resources, Software, Visualization, Writing – original draft, Writing – review & editing. AP: Data curation, Investigation, Writing – review & editing, Formal analysis, Methodology, Software, Visualization. AD: Writing – review & editing, Data curation, Investigation. EA: Methodology, Writing

– review & editing, Investigation. MW: Methodology, Writing – review & editing, Formal analysis, Investigation. CM: Data curation, Writing – review & editing, Investigation, Visualization, Methodology. CG: Conceptualization, Funding acquisition, Supervision, Writing – review & editing, Investigation. AB: Conceptualization, Funding acquisition, Project administration, Writing – review & editing, Methodology, Writing – original draft.

Funding

The author(s) declare that financial support was received for the research, authorship, and/or publication of this article. Leibniz Grant by Deutsche Forschungsgemeinschaft (DFG, German Research Foundation) to AB; funding of material and salaries European Research Council (ERC) Advanced Investigator Grant ABYSS (294757) to AB; funds allowed the purchase of instruments necessary for research. Germany's Excellence Initiative of the Deutsche Forschungsgemeinschaft (DFG, German Research Foundation) through the Clusters of Excellence 'The Ocean in the Earth System' (EXC-309-49926684) and 'The Ocean Floor-Earth's Uncharted Interface' (EXC-2077-390741603) to the University of Bremen; Funding of first author, and instruments. This study was further supported by the Alfred Wegener Institute Helmholtz Center for Polar and Marine Research, Bremerhaven, the Helmholtz Association (HGF), and the Max Planck Society (MPG). Both institutes contributed to the funding of the research expeditions.

Acknowledgments

We thank the captain, crew, and science party of RV Polarstern expeditions PS86 and PS101 for high-precision sampling during the ice-drift. We thank Janna Köhler and Jill McDermott for geophysical and geochemical data acquisition, W. Bach for scientific discussion and equipment, and M. Meiners, W. Stiens, R. Stiens, J. Barz, M. Alisch, F. Schramm, and A. Nordhausen (HGF-MPG Joint Research Group for Deep-Sea Ecology and Technology) for technical support.

Conflict of interest

The authors declare that the research was conducted in the absence of any commercial or financial relationships that could be construed as a potential conflict of interest.

The author(s) declared that they were an editorial board member of Frontiers, at the time of submission. This had no impact on the peer review process and the final decision.

Publisher's note

Supplementary material

The Supplementary material for this article can be found online at: https://www.frontiersin.org/articles/10.3389/fmicb.2024.1473822/full#supplementary-material

References

Adam, N., and Perner, M. (2018). Microbially mediated hydrogen cycling in Deep-Sea hydrothermal vents. *Front. Microbiol.* 9:2873. doi: 10.3389/fmicb.2018.02873

Afgan, E., Baker, D., Batut, B., van den Beek, M., Bouvier, D., Čech, M., et al. (2018). The galaxy platform for accessible, reproducible and collaborative biomedical analyses: 2018 update. *Nucleic Acids Res.* 46, W537–W544. doi: 10.1093/nar/gky379

Anantharaman, K., Breier, J. A., and Dick, G. J. (2016). Metagenomic resolution of microbial functions in deep-sea hydrothermal plumes across the eastern Lau spreading center. *ISME J.* 10, 225–239. doi: 10.1038/ismej.2015.81

Anantharaman, K., Breier, J. A., Sheik, C. S., and Dick, G. J. (2013). Evidence for hydrogen oxidation and metabolic plasticity in widespread deep-sea sulfur-oxidizing bacteria. *Proc. Natl. Acad. Sci.* 110, 330–335. doi: 10.1073/pnas.1215340110

Anderson, R. E., Beltran, M. T., Hallam, S. J., and Baross, J. A. (2013). Microbial community structure across fluid gradients in the Juan de Fuca ridge hydrothermal system. *FEMS Microbiol. Ecol.* 83, 324–339. doi: 10.1111/j.1574-6941.2012.01478.x

Aquino, K. A., Früh-Green, G. L., Rickli, J., Bernasconi, S. M., Lang, S. Q., Lilley, M. D., et al. (2022). Multi-stage evolution of the lost City hydrothermal vent fluids. *Geochim. Cosmochim. Acta* 332, 239–262. doi: 10.1016/j.gca.2022.06.027

Bach, W., Banerjee, N. R., Dick, H. J., and Baker, E. T. (2002). Discovery of ancient and active hydrothermal systems along the ultra-slow spreading southwest Indian ridge 10°–16° E. *Geochem. Geophys. Geosyst.* 3, 1–14. doi: 10.1029/2001GC000279

Baker, E. T., Edmonds, H. N., Michael, P. J., Bach, W., Dick, H. J. B., Snow, J. E., et al. (2004). Hydrothermal venting in magma deserts: the ultraslow-spreading Gakkel and southwest Indian ridges. *Geochem. Geophys. Geosyst.* 5. doi: 10.1029/2004GC000712

Baker, E. T., and German, C. R. (2004). On the global distribution of hydrothermal vent fields. Mid-Ocean ridges: hydrothermal interactions between the lithosphere and oceans. *Geophys. Monogr. Ser* 148, 245–266. doi: 10.1029/148GM10

Beaulieu, S. E., Baker, E. T., German, C. R., and Maffei, A. (2013). An authoritative global database for active submarine hydrothermal vent fields. *Geochem. Geophys. Geosyst.* 14, 4892–4905. doi: 10.1002/2013GC004998

Beaulieu, S. E., and Szafranski, K. (2020). InterRidge global database of active submarine hydrothermal vent fields, Version 3.4. World Wide Web electronic publication. Available online at: http://vents-data.interridge.org

Bender, M., and Conrad, R. (1992). Kinetics of CH4 oxidation in oxic soils exposed to ambient air or high CH4 mixing ratios. *FEMS Microbiol. Lett.* 10, 261–269. doi: 10.1111/j.1574-6941.1992.tb01663.x

Benjamini, Y., and Hochberg, Y. (1995). Controlling the false discovery rate - a practical and powerful approach to multiple testing. *J. R. Stat. Soc. Ser. B Stat. Methodol.* 57, 289–300. doi: 10.1111/j.2517-6161.1995.tb02031.x

Bennett, B., Adams, J. J., Gray, N. D., Sherry, A., Oldenburg, T. B. P., Huang, H., et al. (2013). The controls on the composition of biodegraded oils in the deep subsurface - part 3. The impact of microorganism distribution on petroleum geochemical gradients in biodegraded petroleum reservoirs. *Org. Geochem.* 56, 94–105. doi: 10.1016/j.orggeochem.2012.12.011

Bennett, S. A., Coleman, M., Huber, J. A., Reddington, E., Kinsey, J. C., McIntyre, C., et al. (2013). Trophic regions of a hydrothermal plume dispersing away from an ultramafic-hosted vent-system: Von Damm vent-site, mid-Cayman rise. *Geochem. Geophys. Geosyst.* 14, 317–327. doi: 10.1002/ggge.20063

Björk, G., and Winsor, P. (2006). The deep waters of the Eurasian Basin, Arctic Ocean: geothermal heat flow, mixing and renewal. *Deep-Sea Res. I Oceanogr. Res. Pap.* 53, 1253–1271. doi: 10.1016/j.dsr.2006.05.006

Boetius, A. (2015). The expedition PS86 of the research vessel POLARSTERN to the Arctic Ocean in 2014. Bremerhaven, Germany: Alfred-Wegener-Institut, Helmholtz-Zentrum für Polar- und Meeresforschung;. Report no, 1866–3192.

Boetius, A., and Purser, A. (2017). The expedition PS101 of the research vessel POLARSTERN to the Arctic Ocean in 2016. Bremerhaven, Germany: Alfred-Wegener-Institut, Helmholtz-Zentrum für Polar- und Meeresforschung;. Report no, 1866–3192.

Bolger, A. M., Lohse, M., and Usadel, B. (2014). Trimmomatic: a flexible trimmer for Illumina sequence data. *Bioinformatics* 30, 2114–2120. doi: 10.1093/bioinformatics/btu170

Braun, A., Spona-Friedl, M., Avramov, M., Elsner, M., Baltar, F., Reinthaler, T., et al. (2021). Reviews and syntheses: heterotrophic fixation of inorganic carbon – significant but invisible flux in environmental carbon cycling. *Biogeosciences* 18, 3689–3700. doi: 10.5194/bg-18-3689-2021

Buchfink, B., Xie, C., and Huson, D. H. (2015). Fast and sensitive protein alignment using DIAMOND. *Nat. Methods* 12, 59–60. doi: 10.1038/nmeth.3176

Canfield, D. E., Stewart, F. J., Thamdrup, B., De Brabandere, L., Dalsgaard, T., Delong, E. F., et al. (2010). A cryptic sulfur cycle in oxygen-minimum-zone waters off the Chilean coast. *Science* 330, 1375–1378. doi: 10.1126/science.1196889

Cathalot, C., Roussel, E. G., Perhirin, A., Creff, V., Donval, J.-P., Guyader, V., et al. (2021). Hydrothermal plumes as hotspots for deep-ocean heterotrophic microbial biomass production. *Nat. Commun.* 12:6861. doi: 10.1038/s41467-021-26877-6

Chao, A., Gotelli, N. J., Hsieh, T., Sander, E. L., Ma, K., Colwell, R. K., et al. (2014). Rarefaction and extrapolation with hill numbers: a framework for sampling and estimation in species diversity studies. *Ecol. Monogr.* 84, 45–67. doi: 10.1890/13-0133.1

Charlou, J. L., Donval, J. P., Fouquet, Y., Jean-Baptiste, P., and Holm, N. (2002). Geochemistry of high H2 and CH4 vent fluids issuing from ultramafic rocks at the rainbow hydrothermal field (36°14′N, MAR). *Chem. Geol.* 191, 345–359. doi: 10.1016/S0009-2541(02)00134-1

Clarke, K. R. (1993). Non-parametric multivariate analyses of changes in community structure. *Aust. J. Ecol.* 18, 117–143. doi: 10.1111/j.1442-9993.1993.tb00438.x

Cochran, J. R., Kurras, G. J., Edwards, M. H., and Coakley, B. J. (2003). The Gakkel ridge: bathymetry, gravity anomalies, and crustal accretion at extremely slow spreading rates. *J Geophys Res Solid Earth* 108:2116. doi: 10.1029/2002JB001830

Cowen, J. P., Wen, X., and Popp, B. N. (2002). Methane in aging hydrothermal plumes. *Geochim. Cosmochim. Acta* 66, 3563–3571. doi: 10.1016/S0016-7037(02)00975-4

Criscuolo, A., and Gribaldo, S. (2010). BMGE (block mapping and gathering with entropy): a new software for selection of phylogenetic informative regions from multiple sequence alignments. *BMC Evol. Biol.* 10, 210–221. doi: 10.1186/1471-2148-10-210

Cutter, G., Andersson, P., Codispoti, L., Croot, P., François, R., Lohan, M. C., et al. (2010). Sampling and sample-handling protocols for GEOTRACES cruises.

de Angelis, M. A., Lilley, M. D., and Baross, J. A. (1993). Methane oxidation in deep-sea hydrothermal plumes of the Endeavour segment of the Juan de Fuca ridge. *Deep-Sea Res. I Oceanogr. Res. Pap.* 40, 1169–1186. doi: 10.1016/0967-0637(93)90132-M

Dede, B., Hansen, C. T., Neuholz, R., Schnetger, B., Kleint, C., Walker, S., et al. (2022). Niche differentiation of sulfur-oxidizing bacteria (SUP05) in submarine hydrothermal plumes. *ISME J.* 16, 1479–1490. doi: 10.1038/s41396-022-01195-x

Dick, G. J. (2019). The microbiomes of deep-sea hydrothermal vents: distributed globally, shaped locally. *Nat. Rev. Microbiol.* 17, 271–283. doi: 10.1038/s41579-019-0160-2

Dick, G. J., Anantharaman, K., Baker, B. J., Li, M., Reed, D. C., and Sheik, C. S. (2013). The microbiology of deep-sea hydrothermal vent plumes: ecological and biogeographic linkages to seafloor and water column habitats. *Front. Microbiol.* 4:124. doi: 10.3389/fmicb.2013.00124

Diehl, A., and Bach, W. (2020). MARHYS (MARine HYdrothermal solutions) database: a global compilation of marine hydrothermal vent fluid, end member, and seawater compositions. *Geochem. Geophys. Geosyst.* 21:e2020GC009385. doi: 10.1029/2020GC009385

Diepenbroek, M., Glöckner, F. O., Grobe, P., Güntsch, A., Huber, R., König-Ries, B., et al. (2014). Towards an integrated biodiversity and ecological research data management and archiving platform: the German federation for the curation of biological data (GFBio). *Informatik*.

Dubilier, N., Bergin, C., and Lott, C. (2008). Symbiotic diversity in marine animals: the art of harnessing chemosynthesis. *Nat. Rev. Microbiol.* 6, 725–740. doi: 10.1038/nrmicro1992

Edmonds, H. N., Michael, P. J., Baker, E. T., Connelly, D. P., Snow, J. E., Langmuir, C. H., et al. (2003). Discovery of abundant hydrothermal venting on the ultraslow-spreading Gakkel ridge in the Arctic Ocean. *Nature* 421, 252–256. doi: 10.1038/nature01351

Früh-Green, G. L., Kelley, D. S., Lilley, M. D., Cannat, M., Chavagnac, V., and Baross, J. A. (2022). Diversity of magmatism, hydrothermal processes and microbial interactions at mid-ocean ridges. *Nat. Rev. Earth Environ.* 3, 852–871. doi: 10.1038/s43017-022-00364-y

Fukuda, R., Ogawa, H., Nagata, T., and Koike, I. I. (1998). Direct determination of carbon and nitrogen contents of natural bacterial assemblages in marine environments. *Appl. Environ. Microbiol.* 64, 3352–3358. doi: 10.1128/AEM.64.9.3352-3358.1998

Garber, A. I., Nealson, K. H., Okamoto, A., McAllister, S. M., Chan, C. S., Barco, R. A., et al. (2020). FeGenie: a comprehensive tool for the identification of iron genes and iron gene neighborhoods in genome and metagenome assemblies. *Front. Microbiol.* 11:37. doi: 10.3389/fmicb.2020.00037

German, C. R., Baker, E. T., Mevel, C., and Tamaki, K.the FUJI Science Team (1998). Hydrothermal activity along the southwest Indian ridge. *Nature* 395, 490–493. doi: 10.1038/26730

German, C. R., Parson, L., HEAT Scientific Team, , German, C. R., Parson, L. M., Bougault, H., et al. (1996). Hydrothermal exploration near the Azores triple junction: tectonic control of venting at slow-spreading ridges? *Earth Planet. Sci. Lett.* 138, 93–104. doi: 10.1016/0012-821X(95)00224-Z

German, C. R., Reeves, E. P., Türke, A., Diehl, A., Albers, E., Bach, W., et al. (2022). Volcanically hosted venting with indications of ultramafic influence at Aurora hydrothermal field on Gakkel ridge. *Nat. Commun.* 13:6517. doi: 10.1038/s41467-022-34014-0

German, C., and Seyfried, W. (2014). Treatise on geochemistry. Treatise on Geochemistry. Amsterdam: Elsevier.

Glaubitz, S., Kiesslich, K., Meeske, C., Labrenz, M., and Jurgens, K. (2013). SUP05 dominates the Gammaproteobacterial sulfur oxidizer assemblages in pelagic redoxclines of the Central Baltic and black seas. *Appl. Environ. Microbiol.* 79, 2767–2776. doi: 10.1128/AEM.03777-12

Greening, C. (2021). Greening lab metabolic marker gene databases.

Gruber-Vodicka, H. R., Seah, B. K., and Pruesse, E. (2020). PhyloFlash: Rapid small-subunit rRNA profiling and targeted assembly from metagenomes. *mSystems*. 5:10.1128/msystems.00920-20. doi: 10.1128/msystems.00920-20

Han, Y., and Perner, M. (2015). The globally widespread genus Sulfurimonas: versatile energy metabolisms and adaptations to redox clines. *Front. Microbiol.* 6:989. doi: 10.3389/fmicb.2015.00989

Herlemann, D. P. R., Labrenz, M., Jurgens, K., Bertilsson, S., Waniek, J. J., and Andersson, A. F. (2011). Transitions in bacterial communities along the 2000 km salinity gradient of the Baltic Sea. *ISME J.* 5, 1571–1579. doi: 10.1038/ismej.2011.41

Herndl, G. J., Reinthaler, T., Teira, E., van Aken, H., Veth, C., Pernthaler, A., et al. (2005). Contribution of Archaea to total prokaryotic production in the deep Atlantic Ocean. *Appl. Environ. Microbiol.* 71, 2303–2309. doi: 10.1128/AEM.71.5.2303-2309.2005

Hsu, H.-W., Postberg, F., Sekine, Y., Shibuya, T., Kempf, S., Horányi, M., et al. (2015). Ongoing hydrothermal activities within Enceladus. *Nature* 519, 207–210. doi: 10.1038/nature14262

Hyatt, D., Chen, G.-L., LoCascio, P. F., Land, M. L., Larimer, F. W., and Hauser, L. J. (2010). Prodigal: prokaryotic gene recognition and translation initiation site identification. *BMC Bioinformat.* 11, 1–11. doi: 10.1186/1471-2105-11-119

Jannasch, H. W. (1983). Microbial processes at deep sea hydrothermal vents. Berlin: Springer, 677–709.

Jannasch, H. (1985). Review lecture-the chemosynthetic support of life and the microbial diversity at deep-sea hydrothermal vents. *Proc. Royal Soc. London* 225, 277–297.

Jokat, W., and Schmidt-Aursch, M. C. (2007). Geophysical characteristics of the ultraslow spreading Gakkel ridge, Arctic Ocean. *Geophys. J. Int.* 168, 983–998. doi: 10.1111/j.1365-246X.2006.03278.x

Kalyaanamoorthy, S., Minh, B. Q., Wong, T. K., Von Haeseler, A., and Jermiin, L. S. (2017). ModelFinder: fast model selection for accurate phylogenetic estimates. *Nat. Methods* 14, 587–589. doi: 10.1038/nmeth.4285

Katoh, K., and Standley, D. M. (2014). MAFFT: iterative refinement and additional methods. Berlin: Springer, 131–146.

Knief, C., and Dunfield, P. F. (2005). Response and adaptation of different methanotrophic bacteria to low methane mixing ratios. *Environ. Microbiol.* 7, 1307–1317. doi: 10.1111/j.1462-2920.2005.00814.x

Kolde, R., and Kolde, M. R. (2015). Package 'pheatmap'. *R package* 1:790. doi: 10.32614/CRAN.package.pheatmap

Kopylova, E., Noé, L., and Touzet, H. (2012). SortMeRNA: fast and accurate filtering of ribosomal RNAs in metatranscriptomic data. *Bioinformatics* 28, 3211–3217. doi: 10.1093/bioinformatics/bts611

Kumagai, H., Nakamura, K., Toki, T., Morishita, T., Okino, K., Ishibashi, J. I., et al. (2008). Geological background of the Kairei and Edmond hydrothermal fields along the central Indian ridge: implications of their vent fluids' distinct chemistry. *Geofluids* 8, 239–251. doi: 10.1111/j.1468-8123.2008.00223.x

Lappan, R., Shelley, G., Islam, Z. F., Leung, P. M., Lockwood, S., Nauer, P. A., et al. (2023). Molecular hydrogen in seawater supports growth of diverse marine bacteria. *Nat. Microbiol.* 8, 581–595. doi: 10.1038/s41564-023-01322-0

Lesniewski, R. A., Jain, S., Anantharaman, K., Schloss, P. D., and Dick, G. J. (2012). The metatranscriptome of a deep-sea hydrothermal plume is dominated by water column methanotrophs and lithotrophs. *ISME J.* 6, 2257–2268. doi: 10.1038/ismej.2012.63

Mahé, F., Rognes, T., Quince, C., de Vargas, C., and Dunthorn, M. (2014). Swarm: robust and fast clustering method for amplicon-based studies. *PeerJ* 2:e593. doi: 10.7717/peerj.593

Martin, M. (2011). Cutadapt removes adapter sequences from high-throughput sequencing reads. *EMBnet J.* 17, 10–12. doi: 10.14806/ej.17.1.200

McCollom, T. M. (2000). Geochemical constraints on primary productivity in submarine hydrothermal vent plumes. *Deep-Sea Res. I Oceanogr. Res. Pap.* 47, 85–101. doi: 10.1016/S0967-0637(99)00048-5

Meier, D. V., Bach, W., Girguis, P. R., Gruber-Vodicka, H. R., Reeves, E. P., Richter, M., et al. (2016). Heterotrophic Proteobacteria in the vicinity of diffuse hydrothermal venting. *Environ. Microbiol.* 18, 4348–4368. doi: 10.1111/1462-2920.13304

Meier, D. V., Pjevac, P., Bach, W., Hourdez, S., Girguis, P. R., Vidoudez, C., et al. (2017). Niche partitioning of diverse sulfur-oxidizing bacteria at hydrothermal vents. *ISME J.* 11, 1545–1558. doi: 10.1038/ismej.2017.37

Menzel, P., Ng, K. L., and Krogh, A. (2016). Fast and sensitive taxonomic classification for metagenomics with kaiju. *Nat. Commun.* 7:11257. doi: 10.1038/ncomms11257

Michael, P., Langmuir, C., Dick, H., Snow, J., Goldstein, S., Graham, D., et al. (2003). Magmatic and amagmatic seafloor generation at the ultraslow-spreading Gakkel ridge. *Arctic Ocean. Nature* 423, 956–961. doi: 10.1038/nature01704

Mistry, J., Chuguransky, S., Williams, L., Qureshi, M., Salazar, G. A., Sonnhammer, E. L., et al. (2021). Pfam: the protein families database in 2021. *Nucleic Acids Res.* 49, D412–D419. doi: 10.1093/nar/gkaa913

Molari, M., Hassenrueck, C., Laso-Pérez, R., Wegener, G., Offre, P., Scilipoti, S., et al. (2023). A hydrogenotrophic Sulfurimonas is globally abundant in deep-sea oxygen-saturated hydrothermal plumes. *Nature* 8, 651–665. doi: 10.1038/s41564-023-01342-w

Morris, R. M., and Spietz, R. L. (2022). The physiology and biogeochemistry of SUP05. *Annu. Rev. Mar. Sci.* 14, 261–275. doi: 10.1146/annurev-marine-010419-010814

Noowong, A., Gomez-Saez, G. V., Hansen, C. T., Schwarz-Schampera, U., Koschinsky, A., and Dittmar, T. (2021). Imprint of Kairei and Pelagia deep-sea hydrothermal systems (Indian Ocean) on marine dissolved organic matter. *Org. Geochem.* 152:104141. doi: 10.1016/j.orggeochem.2020.104141

Nurk, S., Meleshko, D., Korobeynikov, A., and Pevzner, P. A. (2017). metaSPAdes: a new versatile metagenomic assembler. *Genome Res.* 27, 824–834. doi: 10.1101/gr.213959.116

Oksanen, J., Blanchet, F. G., Kindt, R., Legendre, P., Minchin, P. R., O'hara, R., et al. (2013). *Package 'vegan'*. Community ecology package, version 2.

Petersen, J. M., Zielinski, F. U., Pape, T., Seifert, R., Moraru, C., Amann, R., et al. (2011). Hydrogen is an energy source for hydrothermal vent symbioses. *Nature* 476, 176–180. doi: 10.1038/nature10325

Purser, A., Marcon, Y., Dreutter, S., Hoge, U., Sablotny, B., Hehemann, L., et al. (2019). Ocean floor observation and bathymetry system (OFOBS): a new towed camera/sonar system for Deep-Sea habitat surveys. *IEEE J. Ocean. Eng.* 44, 87–99. doi: 10.1109/JOE.2018.2794095

Putri, G. H., Anders, S., Pyl, P. T., Pimanda, J. E., and Zanini, F. (2022). Analysing high-throughput sequencing data in Python with HTSeq 2.0. *Bioinformatics* 38, 2943–2945. doi: 10.1093/bioinformatics/btac166

Quast, C., Pruesse, E., Yilmaz, P., Gerken, J., Schweer, T., Yarza, P., et al. (2013). The SILVA ribosomal RNA gene database project: improved data processing and web-based tools. *Nucleic Acids Res.* 41, D590–D596. doi: 10.1093/nar/gks1219

Radford-Knoery, J., German, C. R., Charlou, J.-L., Donval, J.-P., and Fouquet, Y. (2001). Distribution and behavior of dissolved hydrogen sulfide in hydrothermal plumes. *Limnol. Oceanogr.* 46, 461–464. doi: 10.4319/lo.2001.46.2.0461

Ramirez-Llodra, E., Claudio, A., Maria, B., Antje, B., Carolina, C., Håkon, D., et al. (2023). Hot vents beneath an icy ocean - the Aurora vent field, Gakkel Rdige, revealed. *Oceanography* 36, 6–17. doi: 10.5670/oceanog.2023.103

Reed, D. C., Breier, J. A., Jiang, H. S., Anantharaman, K., Klausmeier, C. A., Toner, B. M., et al. (2015). Predicting the response of the deep-ocean microbiome to geochemical perturbations by hydrothermal vents. *ISME J.* 9, 1857–1869. doi: 10.1038/ismej.2015.4

Reinthaler, T., van Aken, H. M., and Herndl, G. J. (2010). Major contribution of autotrophy to microbial carbon cycling in the deep North Atlantic's interior. *Deep-Sea Res. II Top. Stud. Oceanogr.* 57, 1572–1580. doi: 10.1016/j.dsr2.2010.02.023

Robinson, M. D., and Smyth, G. K. (2007). Small-sample estimation of negative binomial dispersion, with applications to SAGE data. *Biostatistics* 9, 321–332. doi: 10.1093/biostatistics/kxm030

Roether, W., Jean-Baptiste, P., Fourré, E., and Sültenfuß, J. (2013a). The transient distributions of nuclear weapon-generated tritium and its decay product 3 He in the Mediterranean Sea, 1952–2011, and their oceanographic potential. *Ocean Sci.* 9, 837–854. doi: 10.5194/os-9-837-2013

Roether, W., Vogt, M., Vogel, S., and Sültenfuß, J. (2013b). Combined sample collection and gas extraction for the measurement of helium isotopes and neon in natural waters. *Deep-Sea Res. I Oceanogr. Res. Pap.* 76, 27–34. doi: 10.1016/j.dsr.2013.02.006

Rogge, A., Vogts, A., Voss, M., Jürgens, K., Jost, G., and Labrenz, M. (2017). Success of chemolithoautotrophic SUP05 and Sulfurimonas GD17 cells in pelagic Baltic Sea redox zones is facilitated by their lifestyles as K-and r-strategists. *Environ. Microbiol.* 19, 2495–2506. doi: 10.1111/1462-2920.13783

Schlindwein, V. (2023). The expedition PS137 of the research vessel POLARSTERN to the Arctic Ocean in 2023 Alfred-Wegener-Institut Helmholtz-Zentrum für polar- und Meeresforschung.

Schultz, A., and Elderfield, H. (1997). Controls on the physics and chemistry of seafloor hydrothermal circulation. Philosophical transactions of the Royal Society of London. *Philos Trans A Math Phys Eng Sci* 355, 387–425. doi: 10.1098/rsta.1997.0014

Scilipoti, S., and Molari, M. (2024). High-quality draft genome of Gammaproteobacterial SUP05 cluster from non-buoyant hydrothermal plumes of ultraslow spreading Gakkel ridge (Central Arctic Ocean). *Microbiol Resour Announc* 13:e0012124. doi: 10.1128/mra.00121-24

Seewald, J. S. (2017). Detecting molecular hydrogen on Enceladus. *Science* 356, 132–133. doi: 10.1126/science.aan0444

Shah, V., Chang, B. X., and Morris, R. M. (2017). Cultivation of a chemoautotroph from the SUP05 clade of marine bacteria that produces nitrite and consumes ammonium. *ISME J.* 11, 263–271. doi: 10.1038/ismej.2016.87

Steinegger, M., and Söding, J. (2017). MMseqs2 enables sensitive protein sequence searching for the analysis of massive data sets. *Nat. Biotechnol.* 35, 1026–1028. doi: 10.1038/nbt.3988

Sültenfuß, J., Roether, W., and Rhein, M. (2009). The Bremen mass spectrometric facility for the measurement of helium isotopes, neon, and tritium in water. *Isot. Environ. Health Stud.* 45, 83–95. doi: 10.1080/10256010902871929

Thiede, J. (2002). Polarstern ARKTIS XVII/2: Cruise Report: AMORE 2001 (Arctic Mid-Ocean Ridge Expedition). Bremerhaven: Alfred Wegener Institute for Polar and Marine Research.

Treude, T., Krueger, M., Boetius, A., and Joergensen, B. (2005). Environmental control on anaerobic oxidation of methane in the gassy sediments of Eckernfoerde Bay (German Baltic). *Limnol. Oceanogr.* 50, 1771–1786. doi: 10.4319/lo.2005.50.6.1771

Trifinopoulos, J., Nguyen, L.-T., von Haeseler, A., and Minh, B. Q. (2016). W-IQ-TREE: a fast online phylogenetic tool for maximum likelihood analysis. *Nucleic Acids Res.* 44, W232–W235. doi: 10.1093/nar/gkw256

Tu, Q., Lin, L., Cheng, L., Deng, Y., and He, Z. (2019). NCycDB: a curated integrative database for fast and accurate metagenomic profiling of nitrogen cycling genes. *Bioinformatics* 35, 1040–1048. doi: 10.1093/bioinformatics/bty741

Van Dover, C. L., German, C., Speer, K. G., Parson, L., and Vrijenhoek, R. (2002). Evolution and biogeography of deep-sea vent and seep invertebrates. *Science* 295, 1253–1257. doi: 10.1126/science.1067361

Vasimuddin, M., Misra, S., Li, H., and Aluru, S. (2019). Efficient architecture-aware acceleration of BWA-MEM for multicore systems. 314–324. 2019 IEEE international parallel and distributed processing symposium (IPDPS): IEEE.

Villanueva, R. A. M., and Chen, Z. J. (2019). ggplot2: Elegant graphics for data analysis. Oxfordshire: Taylor & Francis.

Waite, J. H., Glein, C. R., Perryman, R. S., Teolis, B. D., Magee, B. A., Miller, G., et al. (2017). Cassini finds molecular hydrogen in the Enceladus plume: evidence for hydrothermal processes. *Science* 356, 155–159. doi: 10.1126/science.aai8703

Wheeler, T. J., and Eddy, S. R. (2013). Nhmmer: DNA homology search with profile HMMs. *Bioinformatics* 29, 2487–2489. doi: 10.1093/bioinformatics/btt403

Yakimov, M. M., Giuliano, L., Gentile, G., Crisafi, E., Chernikova, T. N., Abraham, W.-R., et al. (2003). *Oleispira antarctica* gen. Nov., sp. nov., a novel hydrocarbonoclastic marine bacterium isolated from Antarctic coastal sea water. *Int. J. Syst. Evol. Microbiol.* 53, 779–785. doi: 10.1099/ijs.0.02366-0

Yu, J., and Lu, Y. (2019). Carbon dioxide fixation by a hydrogen-oxidizing bacterium: biomass yield, reversal respiratory quotient, stoichiometric equations and bioenergetics. *Biochem. Eng. J.* 152:107369. doi: 10.1016/j.bej.2019.107369

Zhang, J., Kobert, K., Flouri, T., and Stamatakis, A. (2014). PEAR: a fast and accurate Illumina paired-end reAd mergeR. *Bioinformatics* 30, 614–620. doi: 10.1093/bioinformatics/btt593

Zhou, Z., Tran, P. Q., Adams, A. M., Kieft, K., Breier, J. A., Fortunato, C. S., et al. (2023). Sulfur cycling connects microbiomes and biogeochemistry in deep-sea hydrothermal plumes. *ISME J.* 17, 1194–1207. doi: 10.1038/s41396-023-01421-0

frontiers | Frontiers in Marine Science

TYPE Original Research
PUBLISHED 04 November 2024
DOI 10.3389/fmars.2024.1304930

OPEN ACCESS

EDITED BY
Johan Schijf,
University of Maryland, United States

REVIEWED BY
Chen-Feng You,
National Cheng Kung University, Taiwan
Toshihiro Yoshimura,
Japan Agency for Marine-Earth Science and Technology (JAMSTEC), Japan
Di Cai,
Tongji University, China

*CORRESPONDENCE
Valérie Chavagnac
valerie.chavagnac@get.omp.eu

RECEIVED 30 September 2023
ACCEPTED 30 September 2024
PUBLISHED 04 November 2024

CITATION
Chavagnac V, Destrigneville C, Boulart C, Taillandier V, Vigier N, Guieu C and Bonnet S (2024) Impact of submarine volcanic versus hydrothermal activity onto the strontium and lithium isotopic signatures of the water column (TONGA).
Front. Mar. Sci. 11:1304930.
doi: 10.3389/fmars.2024.1304930

Impact of submarine volcanic versus hydrothermal activity onto the strontium and lithium isotopic signatures of the water column (TONGA)

Valérie Chavagnac[1]*, Christine Destrigneville[1], Cédric Boulart[2], Vincent Taillandier[3], Nathalie Vigier[3], Cecile Guieu[3] and Sophie Bonnet[4]

[1]Géosciences Environnement Toulouse, GET UMR5563, CNRS/UPS/IRD/CNES, University of Toulouse, Toulouse, France, [2]Station Biologique de Roscoff, EDYCO – CHIMAR UMR7144, Roscoff, France, [3]Laboratoire d'Océanographie de Villefranche (LOV), Sorbonne Université/CNRS/Institut de la mer de Villefranche, Villefranche-sur-mer, France, [4]Institut Méditerranéen d'Océanologie (MIO), Aix Marseille Université/Université de Toulon/CNRS/IRD, Marseille, France

During the TONGA cruise (2019), seawater samples were collected to assess the effect of volcanic eruption versus submarine hydrothermal system on the water column. For this purpose, two locations were investigated, the first one located directly under the influence of the New Late'iki island (eruption in October 2019), and the second one showing ongoing submarine hydrothermal activity. At both locations, the total strontium (TSr) and lithium (TLi) concentrations vary between 94.4 and 152.3 µmol/L and 13.2 and 203.5 µmol/L, respectively. When combined, TSr and TLi concentrations of all samples in the water column are higher than those of the oligotrophic water. Both volcanic eruption and submarine hydrothermal activity (e.g. volcanic ashes, particles, gas condensate) can deliver substantial amount of TSr and TLi to the water column. The distribution of TSr versus TLi evidences linear trends either with a negative or positive slope. The negative correlation is observed in the water column at both sites, directly under the influence of the eruption and in the vicinity of the volcano with hydrothermal activity. The positive TSr versus TLi correlation is observed at site under submarine hydrothermal influence and is in line with black smokers related hydrothermal plumes. The $^{87}Sr/^{86}Sr$ ratios vary between 0.709147 and 0.709210 and δ^7Li values vary between +10.1 and +37.6 ‰. While 92% of the measured $^{87}Sr/^{86}Sr$ ratios are in line with the mean value of oligotrophic waters, once combined with the δ^7Li values, only 20% of them remains within this field. The wide range of δ^7Li values decreases from sea-surface down to ~140 mbsl, before increasing at greater depth, while defining different linear trend according to the dissolved inorganic carbon concentrations. The variability of δ^7Li values reflect hydrothermal contribution, mineral–seawater interaction and potentially biology–environment interaction. In the particular geological setting of the study, where both hydrothermal and volcanic activities were at play, disentangling both contributions on water column implies a combined use of elemental and isotopic signatures of Sr and Li tracers.

KEYWORDS

lithium isotopes, strontium, hydrothermalism, volcanic eruption, TONGA

1 Introduction

Along the 2,500 km long Tofua-Kermadec Arc in the Western Tropical South Pacific (WTSP), numerous submarine volcanoes have been identified using bathymetric map of the seafloor whereby only a few of them have their summit crossing sea level. This region is magmatically very active with about 77 volcanic eruptions which have been reported since the 18th century along the Tongan section alone (Global Volcanism Program, 2019). A significant number of powerful volcanic eruptions have taken place leading to hazardous phenomena via pyroclastic and explosive eruptions, air pollution of asphyxiant gases, and lava flows, stimulating the scientific communities to better explore and characterize submerged volcanoes and their associated hydrothermal system as well as their potential effect on environmental conditions for human health, ocean ecosystem and climate change (Stewart et al., 2022 among others). Trace elements such as iron, zinc, copper among others, derived from hydrothermal activity, are clearly identified as a main source of micronutrient to the water column with potential impact on the development and thriving of marine ecosystems on a global scale and at different water depth (German et al., 2016 for a review). For example, Bonnet et al. (2017), Guieu et al. (2018) and Tilliette et al. (2022) showed that a shallow submarine hydrothermal source was needed to provide the necessary dissolved iron level to maintain a high N_2-fixation rate, leading to increased primary production and carbon export (Bonnet et al., 2023).

In this area and on 14th October 2019, a powerful surtseyan volcanic eruption started nearby the Vava'u island and lasted until 30th of October. This event led to the formation of 21 000 m^2 New Late'iki island which was eroded by wave action within a few weeks and submerged by 14th December 2019 (Plank et al., 2020). During submarine volcanic event, different sources of material such as volcanic ash particles, hydrothermal fluids, gas condensates and salt precipitates, can be delivered to the hydrosphere modifying at different water depth seawater chemical composition, and therefore the living environment of marine ecosystems. The TONGA cruise which took place aboard the R.V. *L'Atalante* between 31st October and 5th December 2019, provided ideal temporal conditions to better constrain the dispersion of submarine shallow hydrothermal/volcanic supply to the water column. One of the objectives of the cruise was to constrain the impact of shallow hydrothermal supply on biogeochemical cycles, trace element content and dispersion in the water column and planktonic communities. For this purpose, two sites were investigated. The first one is directly under the influence of the New Late'iki island, and the second one (Volcano 1) showed in the early 2000s a significant hydrothermal activity (Stoffers et al., 2003; Massoth et al., 2007) that is still ongoing (Bonnet et al., 2023).

Here, we address the fate of volcanic-related emissions which can impact the water column nearby while we assess the detection and influence of hydrothermal-derived element supply from Volcano 1 on the surrounding seawater environment. The present study is entirely based on the chemical and isotopic signatures of water column samples collected at both sites. We selected two elements of interest, namely Strontium (Sr) and Lithium (Li). We report here total dissolved Sr (TSr) and Li (TLi). Their isotopic signatures are distinct in hydrothermal and marine environments, and they have both been applied in carbonate sedimentary archives to better reconstruct past carbon cycle variations (Misra and Froelich, 2012; Albarède et al., 1981; Palmer and Edmond, 1989; Vance et al., 2009; Millot et al., 2010a,b; Tomascak et al., 2016). Indeed, marine calcifiers form their carbonate shell from seawater-derived element pool which may contain the contribution of external sources, such as volcanic and/or hydrothermal ones. The comparison between the two selected sites may contribute in disentangling and fingerprinting geochemical features associated to each geological process, thus providing ideal isotopic tool to detect both processes in sedimentary archive over the Earth geological time-scale.

2 Materials and methods

2.1 Study area and sample collection

The studied area is located in the WTSP, nearby the Tonga-Kermadec subduction zone, along the Tofua-Kermadec arc (Figure 1A). Sample collection was carried out during the TONGA cruise which took place aboard the R.V. *L'Atalante* between 31st October and 5th December 2019. A 6,100 km long transect has been realized starting from New Caledonia within the Melanesian Waters, crossing the Tonga-Kermadec arc and entering the South Pacific gyre (GEOTRACE GPpr14; Guieu and Bonnet, 2019). The two locations of our study are Simone (19°24'S and 175° 03'W), just 10 nautical miles south from the New Late'iki island and Volcano 1 (21°09'S and 175°45'W) as shown on Figure 1A.

Simone is a submerged volcano, which is barely known about its morphology and lithology, thus far (Figure 1B). Volcano 1 is a stratovolcano located on the southern branch of the Tonga back-arc in the Lau Basin (Figures 1A, C). It has been extensively studied through CTD cast operations and direct observations via remotely operated vehicle dives (Stoffers et al., 2003; 2006; Massoth et al., 2007; Lupton et al., 2008). Volcano 1 displays an oval caldera (7 km long and 4.5 km wide) with a seafloor at 450 mbsl and two well-preserved scoria cones (Stoffers et al., 2003; 2006). At Volcano 1, the water column is strongly affected by submarine hydrothermal emissions as supported by multi-beam echo-sounder image evidencing fluid and gas hydrothermal emission rising up from caldera seafloor up to sub-surface (Figure 1D; Bonnet et al., 2023).

Vertical oceanographic profiles and seawater samples were collected at every station of the TONGA cruise. However, samples of interest for this study were only collected at a few casts located in the vicinity of the two sites (listed in Table 1). For all of these casts, a conventional 12 Niskin bottles rosette frame was deployed together with a Sea-bird SBE 9+ underwater unit equipped with a suite of *in-situ* physico-chemical sensors, namely two turbidimeters (Seapoint Turbidity Meters), one pH sensor (AMT GmBH) and one Eh sensor (AMT GmBH). Raw sensor data were processed into quality-controlled profiles at the vertical resolution of 1 mbsl as detailed in Taillandier et al. (2018). Seawater samples were not filtered aboard the research vessel prior to onshore chemical and isotopic analyses and were kept at 4°C until

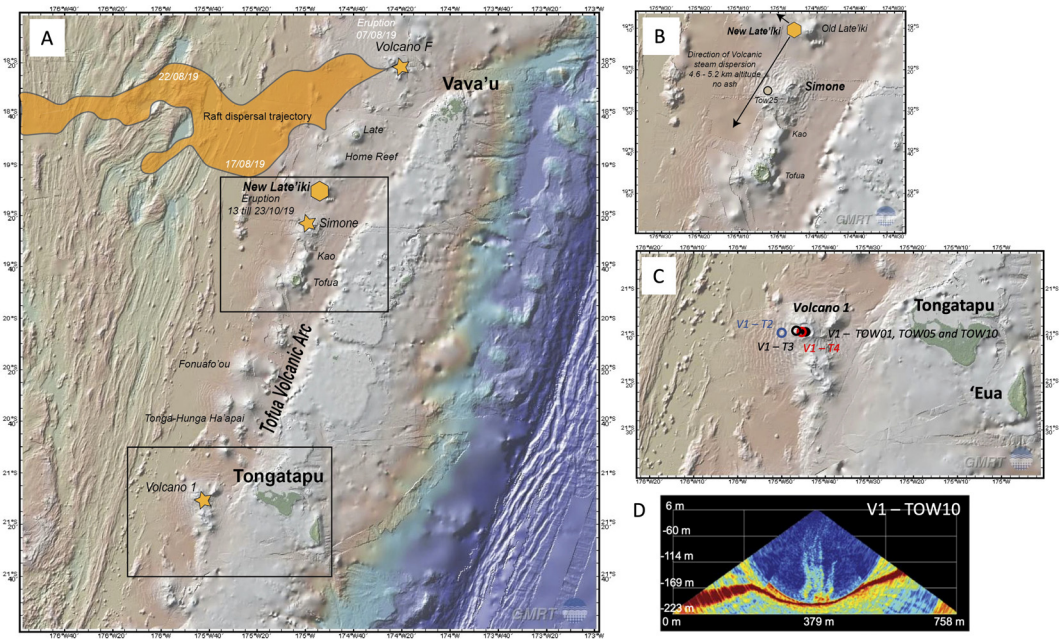

FIGURE 1
(A) Bathymetric map of the studied area in the WTSP (GMRT; Ryan et al., 2009). We report the location of Simone and Volcano 1 sites which are investigated here. The map also reports the locations of submarine volcanoes with their names. Two additional submarine volcanoes erupted recently, namely Volcano F which took place on August 2019 (Brandl et al., 2020) and led to a two-time Manhattan size pumice-raft which drifted away from its source over time, and the Hunga Tonga-Hunga Ha'apai volcano which erupted extremely violently on 15th January 2022 (Bernath et al., 2023). **(B)** Bathymetric map at the Simone location on which we report the location of S – TOW25 cast. We also report the direction of volcanic steam dispersion (Plank et al., 2020). **(C)** Bathymetric map at the Volcano 1 on which we report the location of each cast performed there. **(D)** Multibeam echo-sounder image performed at Volcano 1 just above the hydrothermal emissions at the caldera seafloor (modified from Bonnet et al., 2023).

aliquoting. CTD data were converted and processed using the SBE Data Processing software following Seabird recommendation for data corrections. Data from pH, Eh and turbidity sensors were averaged every 5 sec and outliers were removed using the median absolute deviation. All sensor data were processed using a R-based routine. All CTD casts were performed from onboard operation, without the involvement of submarine vehicle.

At the Simone site, the *in-situ* physico-chemical sensor package detected a turbidity layer below 190 mbsl i.e., seawater column investigation on the western flank of the volcano to the seafloor (~1200 mbsl) (Supplementary Figure S1). However, this feature was not associated to any hydrothermal-related physico-chemical anomalies (pH, Eh, temperature, salinity; Guieu and Bonnet, 2019) although acoustic anomalies likely attributed to hydrothermal activity were recorded. One CTD cast named "TOW25 Volcano2 St10 T2" was carried out enabling the collection of 4 samples (Table 1). During the cruise, the full sample name ensures its reference tracking within any database for analyses results that have been obtained on each sample. For clarity in the following sections, we will label this cast S–TOW25.

At Volcano 1 site, the full package of sensors enabled the detection of hydrothermal contribution to the water column at ~170 mbsl as evidenced by anomalies in temperature, salinity, turbidity, pH and Eh values (Bonnet et al., 2023; Figure 1D; Supplementary Figures S2, S3). This is in line with previous operations at this site by Massoth et al. (2007). For our study, Niskin bottles were fired during upward casts at different water depth in the water column where chemical and physical anomalies were detected. Three CTD casts were performed in the Volcano 1 caldera, namely "Station 5 TOW10 Panamax", "V1 CTD01 TOW01", and "TOW05 Volcano 1" between sea-surface and 200 mbsl collecting 26 seawater samples (Figure 1C). Additionally, three CTD casts (16 samples in total) were carried out along a westward transect covering a 17 km distance i.e., "Station 5 CTD15 V1 - T2", "CTD18 St5 V1 T3" and "St5 V1 TOW14 T4" (Figure 1C). For clarity in the following sections, we will label each cast at Volcano 1 as V1–TOW10, V1–TOW 01, and V1–TOW05 and each cast along a westward transect V1-T2, V1-T3 and V1-T4, respectively. Notwithstanding V1–T2 cast is located the furthest away from Volcano 1 and V1–T4 cast the closest.

2.2 Elemental and isotopic analysis

Water samples for dissolved methane (CH_4) analysis were taken from the Niskin bottles into precleaned and flushed 20 ml headspace glass vials and processed straight after the CTD-rosette was brought back on deck. The method of analysis was based on headspace extraction followed by gas chromatography analysis using a Shimadzu GC-BID coupled to a Shimadzu HS-20 headspace sampler. The detection threshold of this method is 0.2 nmol for dissolved CH_4, and variation between duplicates was 5% (Bonnet et al., 2023).

TABLE 1 Measured TLi and TSr elemental and isotopic signatures of water samples collected during the TONGA cruise.

Station	date	Depth (mbsl)	T (°C)	Salinity (PSU)	Eh (mV)	pH	TSr (µmol/L)	$^{87}Sr/^{86}Sr$	±2sE	TLi (µmol/L)	$\delta^{7}Li+$ (‰)	CH_4 (nmol/L)	DIC (µmol/L)
V1 CTD01 TOW01	09/ 11/ 2019	15	24.88	35.20	358	7.85	109.9	n.d.	n.d.	n.d.	n.d.	3.3	2033
V1 - TOW01		16	24.87	35.20	358	7.85	100.8	0.709178	0.000004	124.9	n.d.	0.5	1929
Latitude : 21.152 S		28	24.87	35.21	350	7.86	111.5	0.709205	0.000004	126.4	10.1	5.6	2119
Longitude : 175.741W		35	24.69	35.22	353	7.86	113.2	0.709205	0.000004	123.4	33.0	n.d.	2247
		45	24.51	35.23	367	7.86	121.3	0.709179	0.000003	107.2	29.3	2.6	2051
		54	24.45	35.24	372	7.86	109.9	0.709170	0.000004	128.6	32.3	1.7	n.d.
		63	24.25	35.26	372	7.86	112.2	0.709172	0.000004	119.8	36.0	23.6	2003
		75	23.93	35.29	385	7.87	99.2	n.d.	n.d.	131.8	n.d.	n.d.	2026
		77	23.92	35.29	381	7.87	126.0	0.709193	0.000004	203.5	27.6	12.0	n.d.
		106	23.02	35.37	441	7.88	120.4	0.709175	0.000004	146.8	n.d.	104.1	2048
		125	22.76	35.42	465	7.89	115.8	0.709168	0.000004	142.1	20.2	6.2	2073
		150	22.50	35.50	513	7.89	109.4	0.709165	0.000004	112.2	31.0	40.7	2296
TOW05 Volcano 1	09/ 11/ 2019	33	24.87	35.21	313	7.83	99.5	0.709166	0.000004	95.7	30.8	5.7	2048
V1 - TOW05		45	24.52	35.23	324	7.83	125.9	0.709171	0.000004	61.3	28.7	1.0	2008
Latitude: 21.155 S		63	24.27	35.25	343	7.84	152.3	0.709185	0.000004	n.d.	36.0	n.d.	2064
Longitude : 175.746W		94	23.30	35.33	417	7.83	109.9	0.709166	0.000004	64.7	n.d.	9.8	2048
		95	23.48	35.32	418	7.83	118.0	0.709183	0.000004	18.8	n.d.	1.9	n.d.
		97	23.37	35.33	424	7.83	113.5	0.709161	0.000004	79.6	28.7	5.7	2010
		105	23.21	35.36	418	7.83	119.0	0.709186	0.000004	n.d.	24.3	n.d.	n.d.
Station 5 TOW10 Panamax	11/ 11/ 2019	14	25.60	35.23	373	7.76	97.9	0.70919	0.000004	26.2	35.0	3.8	2350

(Continued)

10.3389/fmars.2024.1304930

TABLE 1 Continued

Station	date	Depth (mbsl)	T (°C)	Salinity (PSU)	Eh (mV)	pH	TSr (µmol/L)	$^{87}Sr/^{86}Sr$	±2sE	TLi (µmol/L)	$\delta^{7}Li+$ (‰)	CH_4 (nmol/L)	DIC (µmol/L)
V1 - TOW10		66	24.36	35.22	425	7.75	99.1	0.709179	0.000004	n.d.	27.0	9.8	1914
Latitude : 21.154 S		89	23.55	35.27	488	7.73	95.9	0.709189	0.000004	56.1	29.8	26.8	2845
Longitude : 175.745W		118	22.94	35.38	532	7.72	94.4	0.709165	0.000003	n.d.	26.6	3.8	2233
		152	22.07	35.57	591	7.71	118.5	0.709166	0.000004	115.8	32.0	44.5	2162
		177	21.54	35.64	607	7.67	112.2	0.70919	0.000004	45.8	32.2	2.6	2188
		194	21.47	35.65	563	7.63	102.2	0.709147	0.000004	38.7	24.8	16.2	2222
Station5 CTD15 V1-T2	12/ 11/ 2019	150	22.52	35.58	n.m.	n.m.	126.5	0.709199	0.000003	67.8	37.3	9.7	1977
V1 - T2		160	22.22	35.65	n.m.	n.m.	118.9	0.709179	0.000004	46.9	37.6	5.4	2013
Latitude : 21.159 S		178	21.74	35.66	n.m.	n.m.	109.2	0.709186	0.000005	78.2	32.3	2.1	2210
Longitude : 175.842 W		190	21.55	35.68	n.m.	n.m.	125.7	0.709187	0.000004	60.6	24.8	4.8	n.d.
CTD18 St5 V1 T3	13/ 11/ 2019	169	21.79	35.65	n.m.	n.m.	121.0	0.709197	0.000004	44.0	33.1	n.d.	2141
V1 - T3		181	21.58	35.64	n.m.	n.m.	119.5	0.709204	0.000004	55.2	28.6	n.d.	2094
Latitude : 21.155 S		190	21.30	35.66	n.m.	n.m.	116.0	0.709169	0.000004	76.5	n.d.	2.2	2048
Longitude : 175.762W		199	21.07	35.67	n.m.	n.m.	108.4	0.709183	0.000004	45.5	34.6	n.d.	2119
St5 V1 TOW14 T4	13/ 11/ 2019	70	24.14	35.38	450	7.75	99.0	n.d.	n.d.	111.4	n.d.	n.d.	2483
V1 - T4		96	23.62	35.38	454	7.73	103.7	n.d.	n.d.	65.6	n.d.	14.8	2195
Latitude : 21.155 S		161	21.98	35.39	535	7.73	102.4	n.d.	n.d.	72.0	n.d.	1.7	2297
Longitude : 175.751W		174	21.68	35.62	536	7.72	95.3	n.d.	n.d.	77.8	n.d.	5.9	2330

(Continued)

10.3389/fmars.2024.1304930

10.3389/fmars.2024.1304930

TABLE 1 Continued

Station	date	Depth (mbsl)	T (°C)	Salinity (PSU)	Eh (mV)	pH	TSr (µmol/L)	$^{87}Sr/^{86}Sr$	±2sE	TLi (µmol/L)	δ^7Li+ (‰)	CH_4 (nmol/L)	DIC (µmol/L)
		188	21.14	35.66	591	7.72	105.5	n.d.	n.d.	60.7	n.d.	5.5	2564
		195	20.94	35.67	618	7.72	107.0	n.d.	n.d.	47.0	n.d.	11.8	2281
		221	20.08	35.68	690	7.71	113.2	n.d.	n.d.	13.2	n.d.	3.1	2363
		260	19.41	35.64	761	7.71	99.6	n.d.	n.d.	87.0	n.d.	n.d.	2309
TOW25 Volcano2 St10 T2	24/11/2019	180	21.85	35.75	n.m.	n.m.	132.0	0.709158	0.000004	34.6	25.4	n.d.	n.d.
S - TOW25		800	5.31	34.36	n.m.	n.m.	112.7	0.70921	0.000004	53.9	27.0	n.d.	n.d.
Latitude: 19.416 S		870	4.82	34.39	n.m.	n.m.	132.4	0.709189	0.000004	43.8	32.1	n.d.	n.d.
Longitude : 175.052 W		950	4.37	34.40	n.m.	n.m.	140.1	0.709183	0.000004	17.2	n.d.	n.d.	n.d.

Environmental parameters measured *in-situ* i.e., temperature (°C), salinity (PSU), Eh (mV), pH are also reported. Onshore dissolved methane (CH_4, nmol/L) and DIC (µmol/L) concentrations are reported. n.d., not determined; n.m., not measured.

The TSr and TLi concentrations were measured by an inductively coupled plasma atomic emission spectrometer (ICP-AES) Horiba Ultima instrument at the Geosciences Environnement Toulouse laboratory. The instrument was calibrated with IAPSO seawater standard (OSIL Ltd., United Kingdom) doped with a prepared Li and Sr mono-elemental solution following the protocol described in Artigue et al. (2022). The IAPSO calibration curve was composed of one blank solution (Milli-Q water) and 6 solutions corresponding to a concentration range of 0 to 896.1 µmol/L for Li and 0 to 239.3 µmol/L for Sr. For TLi and TSr concentrations, raw seawater samples were doped with the same prepared dissolved Li and Sr mono-elemental solutions of known concentrations and with the same quantity. All samples were void of any particles by visual inspection. For each seawater sample, the TSr and TLi concentrations were quantified by the method of standard addition. The analytical precision was better than 2%. The limit of detection (3*SD) is determined by 10 consecutive analysis of Milli-Q water at 0.3 µmol/L for TLi and 0.01 µmol/L for TSr.

For the isotopic measurements, all seawater samples were treated in clean laboratory at the Geosciences Environnement Toulouse laboratory, to isolate via conventional liquid chromatography the two elements of interest from the heavily charged matrix. TSr was isolated using Sr-Spec resin (Eichrom, United States) using the protocol described in Pin et al. (2014) while TLi was isolated using two back-to-back ion exchange columns made of AGW-X12 200–400 mesh cation resin bed and eluted with 1N HCl based and adapted on the James and Palmer (2000) protocol.

The $^{87}Sr/^{86}Sr$ and $^{7}Li/^{6}Li$ isotopic ratios were measured with a Thermo Fisher Triton +, namely Thermal Ionisation Mass Spectrometer located at the Observatoire Midi-Pyrénées following the protocol described in Artigue et al. (2022). They were determined as the average values of 200 measurements of ion intensities following a static multi-collection mode. After purification in the clean laboratory, the TSr fraction was put back in solution with 1.5 µL mixture of 1/6 HPO_4 0.02N and 5/6 HCl 1N, loaded and dried down on a tungsten filament at 1 A. The $^{87}Sr/^{86}Sr$ ratios were corrected for mass fractionation based on the normalization value of $^{86}Sr/^{88}Sr$ ratio at 0.1194. The repeated measurements of the NBS 987 standard gave a mean value of 0.710260 ± 0.000015 (2SD; n = 8; 2SE = 0.000005). For each sample, the mean measured $^{87}Sr/^{86}Sr$ ratio was adjusted to the recommended value of the NBS 987 at 0.710250 i.e., a correction of -0.000010. Regarding the $^{7}Li/^{6}Li$ isotopic ratios, each purified TLi fraction were taken up in 3 µL of freshly made 0.15 N H_3PO_4, of which 1.5 µL was loaded on a degassed refined rhenium filament together with additional 1 µL of 0.15 N H_3PO_4. The sample was slowly dried down at 0.8 A filament current, then heated up to 2.4 A until phosphoric acid fumes were driven off, and then flashed at 2.8 A. During isotopic measurement, the current of the ionization filament was raised to ~2 A to reach a pyrometer temperature of ~1210–1220°C whereas the evaporation filament was increased to ~0.7–0.9 A until a stable ^{7}Li beam of ~5 V was reached. The repeated measurements of the IRMM-16 standard (Li_2CO_3) gave a mean value of 12.086 ± 0.016 (2SD; n = 42) in line with the reported value of 12.087 ± 0.015 (2SD; n = 33) in Artigue et al. (2022). The $^{7}Li/^{6}Li$ isotopic ratios of all samples are reported as δ^7Li ‰ notation relative to the IRMM-16 standard. The internal and external precision are 0.23 ‰ (2SE; n = 42) and 1.35 ‰

(2SD; n = 42), respectively. Seawater δ^7Li value is obtained using IAPSO seawater standard which is at +30.8 ± 0.1 ‰ (2SE, with external precision ≤ 1 ‰, Rosner et al., 2007).

3 Results

TLi and TSr elemental and isotopic signatures together with environmental parameters measured *in-situ* and dissolved CH_4 concentrations are reported in Table 1 for both sites. TSr and TLi elemental and isotopic signatures are represented as depth profiles in Figure 2 for Volcano 1. No TLi and TSr isotopic signatures are available for V1–T4.

3.1 Environmental parameters at Simone and volcano 1 sites

Depth profile of environmental parameters collected during CTD casts are reported in the Supplementary Materials for both sites (water depth reported as hydrostatic pressure). Complementary data such as trace metal concentrations (dissolved iron i.e., DFe), active acoustic data and turbulence among others are available in Tilliette et al. (2022), Bonnet et al. (2023) and Guieu et al. (2023).

Based on the distribution of the water properties recorded during the TONGA cruise, Tilliette et al. (2022) identified the different water masses present in the vicinity of the two volcanoes, expanding also regionally along the whole transect with roughly same vertical display. At these sites, the surface layer was well mixed in the first 30-50 mbsl and marked by high temperatures progressively decreasing with depth. Just below, a shallow salinity maximum identified the Subtropical Underwater (STUW); it was encountered between 150 and 350 mbsl at the two sites. Underneath, waters that make up the thermocline, so-called the Western South Pacific Central Water (WSPCW), extended down to 600 mbsl. Two water masses were identified at greater depth, the low salinity and high dissolved oxygen Antarctic Intermediate water (AAIW) down to 1300 mbsl, and below, the low dissolved oxygen and high nitrate Pacific Deep Water (PDW). This distribution shapes the water column with marked thermohaline gradients at their interfaces; in particular, the shallow hydrothermal activity encountered at the two sites was located inside STUW and their plume could extend to the surface layer crossing the sharp haline interface at the top of STUW. Internal waves preferentially propagate along this interface, and eventually break as it has been observed in the lee of the Tonga arc during the cruise.

At the Simone volcano site, the *in-situ* physico-chemical sensor package detected a turbidity layer below 190 mbsl (Supplementary Figure S1, not sampled). The sampled station was located downstream on the western flank of the volcano with a seafloor at 1200 mbsl depth (cast labeled S–TOW25 hereinafter). This cast enabled the collection of 4 samples in two turbidity layers (Table 1). A shallow turbidity layer was encountered inside the STUW core between 260 and 310 mbsl. Most likely, this layer corresponds to the extension of the plume observed at the volcano site. A second turbidity layer was encountered deeper, between 830 and 950 mbsl, just below the AIW core. These two features were not associated with any hydrothermal-related physico-chemical anomalies (pH, Eh, T° C, salinity, oxygen, Supplementary Figure S1).

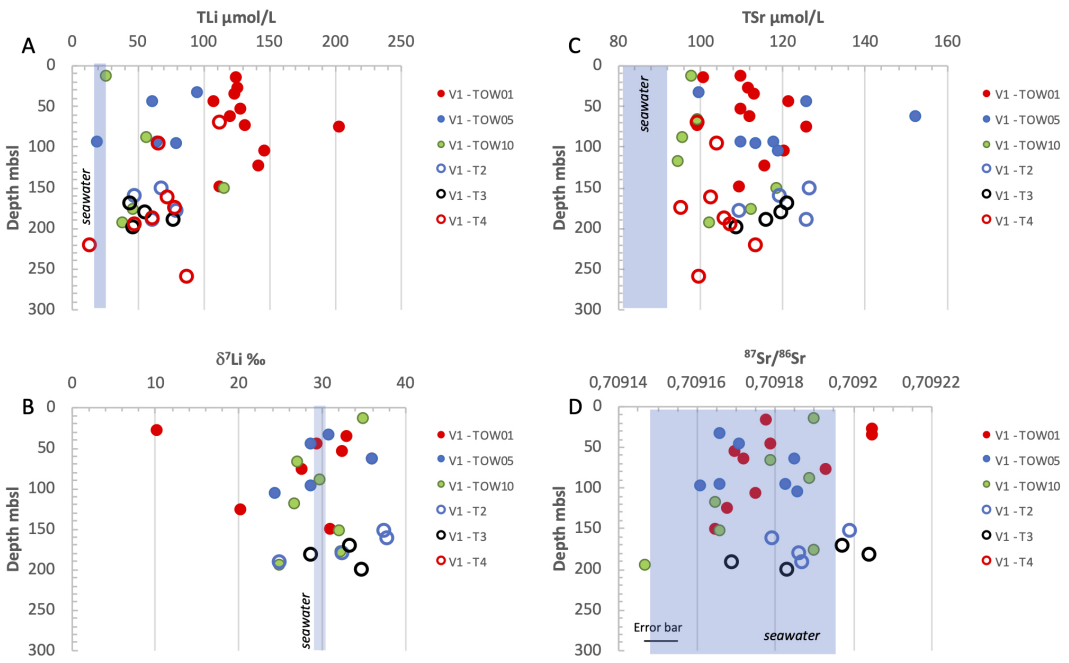

FIGURE 2
Depth profiles of TLi **(A)** and δ^7Li ‰ **(B)**, TSr **(C)** and $^{87}Sr/^{86}Sr$ in **(D)**, for Volcano 1 and transects samples. Blue boxes stand for seawater values (Leleu, 2017; Rosner et al., 2007; El Meknassi et al., 2018).

At Volcano 1, the full package of sensors enabled the detection of hydrothermal contribution to the water column at ~170 mbsl as evidenced by anomalies in temperature, salinity, turbidity, pH and Eh values (Bonnet et al., 2023; Figure 1D; Supplementary Figures S2–S6). This is in line with previous observations at this site by Massoth et al. (2007). The high-resolution transect above the caldera and the western flank of the Volcano 1 revealed a plume strongly maintained vertically below 140 mbsl by the salinity gradient of STUW, and horizontally by the orography of the caldera (reaching 100 mbsl). The extension of the plume on the flanks is limited at the km scale, with a thin turbidity layer centered at 200 mbsl depth (Figure S3). We also provide additional data of dissolved methane concentrations for Volcano 1 and transect casts. The concentrations vary between 0.5 and 104.1 nmol/L i.e., enriched dissolved CH_4 waters throughout the water column (Table 1; Supplementary Material S4-S6).

3.2 TLi elemental and isotopic signatures

TLi concentrations vary between 13.2 and 203.5 µmol/L and 90% of them are above oligotrophic 0.2 µm filtered water values at 24.6 µmol/L (Leleu, 2017) (Figure 2A). Overall, TLi concentrations in and around Volcano 1 cover the full variability range while those at Simone are at the lowest end of Volcano 1 values, reaching a maximum concentration of 53.0 µmol/L at 800 mbsl (Table 1). The three casts within the Volcano 1 caldera are located very close to one another but display strong TLi variability at the same water depth. Even if TLi concentrations at V1–TOW01 are the most enriched of all of them, away from the Volcano 1 caldera and along the transect the water mass between 150 and 200 mbsl is characterized by similar TLi concentrations, ranging between 44.0 and 78.2 µmol/L, but two to three times higher than oligotrophic water values. Nevertheless, we can still observe decreasing TLi concentrations with depth for V1–T4, the nearest cast to Volcano 1 caldera.

The δ^7Li values of all samples at both locations also display a large variability range at values lower, equal or higher than oligotrophic water of ~ +30.0 ‰ (IAPSO value at +30.8 ± 0.1‰, reproducibility <1 ‰; Rosner et al., 2007) i.e., between +10.1 and +37.6 ‰ (Figure 2B; Supplementary Figure S7). For the three casts performed within the submarine Volcano 1 caldera (V1–TOW01; V1–TOW05 and V1–TOW10), the δ^7Li values are progressively decreasing to first order from sea-surface (apart one exception) down to ~140 mbsl, before increasing abruptly at greater depth. At 140 mbsl, a strong shear zone within the water masses have been evidenced (Bonnet et al., 2023). Nevertheless, sea-surface waters can display the lowest δ^7Li value as well as one of the highest i.e., +10.1 ‰ vs. +35.0 ‰ (Table 1). There is no isotopic data for V1–T4. The water mass between 150 and 200 mbsl along the transect exhibits scattered δ^7Li values. At Simone, the δ^7Li values increase with depth from +25.4 up to +32.1 ‰ and fall within the same range as for those of Volcano 1.

3.3 TSr elemental and isotopic signatures

TSr concentrations vary between 94.4 and 152.3 µmol/L (Figure 2C), all above the oligotrophic 0.2 µm filtered water range of 80-90 µmol/L (El Meknassi et al., 2018). At Simone, TSr concentrations are at the higher end of the Volcano 1 ones, and vary between 112.7 and 140.1 µmol/L (Table 1). There, the highest TSr concentration is measured at 950 mbsl. For Volcano 1 caldera, no obvious trend is observed but the maximum concentration of 152.3 µmol/L is measured at ~64 mbsl. Along the westward transect, TSr concentrations vary within the same range as those of Volcano 1 caldera. Nevertheless, we observe increasing TSr concentrations of the water mass when moving westward from V1–T4 to V1–T2 (Figure 2C).

Figure 2D presents the variation of the $^{87}Sr/^{86}Sr$ ratios as depth profiles. The $^{87}Sr/^{86}Sr$ ratios vary between 0.709147 and 0.709210 with a mean value of 0.709181 ± 0.000014 (1SD; 2SE = 0.000006, n = 36) (Supplementary Figure S8). 92% of the measured $^{87}Sr/^{86}Sr$ ratios are within the 95% confidence interval of the average value of oligotrophic waters of 0.709172 ± 0.000023 (2SD; n = 84; El Meknassi et al., 2018). A recent value of seawater Sr isotopic signature highlights an identical average $^{87}Sr/^{86}Sr$ ratio at 0.709172 ± 0.000003 (North Deep Pacific seawater; 2SD, n = 6; Wakaki et al., 2017) but with a much smaller standard deviation. Considering respective numbers of Sr isotopic data in each study, their standard error on the average value are identical at 0.000003 (2SE).

4 Discussion

TSr and TLi are ideal tracers to track down sources contribution and to fingerprint water-rock interaction and processes at play (Huh et al., 1998; Brunskill et al., 2003; Davis et al., 2003; Barker et al., 2008; Vance et al., 2009; Millot et al., 2010b; Araoka et al., 2016; Chavagnac et al., 2018; Artigue et al., 2022). In the present study, the two selected sites are under the influence of different sources, meaning eruptive volcanism for Simone and submarine hydrothermalism for Volcano 1. Before considering both geological contexts, we observe clearly different behaviors between these two tracers based on the variability of their concentrations. Combining both TSr and TLi concentrations in Figure 3 points out that all samples are located outside the range of oligotrophic waters. Moreover, their variability defines a linear trend which has either a negative slope, especially at Simone, or a positive one. It remains to elucidate whether the observed trace element distributions reflect the two different and distinctive geological contexts, involving different processes and elemental sources. However, all transect casts nearby Volcano 1 influence display TSr and TLi concentrations mimicking those at Simone, questioning the dispersion of hydrothermal input in Volcano 1 vicinity.

Indeed at Volcano 1, the water column is strongly affected by submarine hydrothermal emissions as supported by multi-beam echo-sounder image evidencing fluid and gas hydrothermal emission rising up from caldera seafloor up to sub-surface (Figure 1D; Bonnet et al., 2023). At this location, water column environment is suboxic (low dissolved oxygen), slightly acidic (pH down to 6.5; Bonnet et al., 2023), enriched in dissolved methane concentrations (Table 1) and high CO_2 content (high DIC concentrations, Table 1), with extreme and abrupt concentration variation throughout the water column (Supplementary Material S4–S6). Moreover, Tilliette et al. (2022) measured DFe

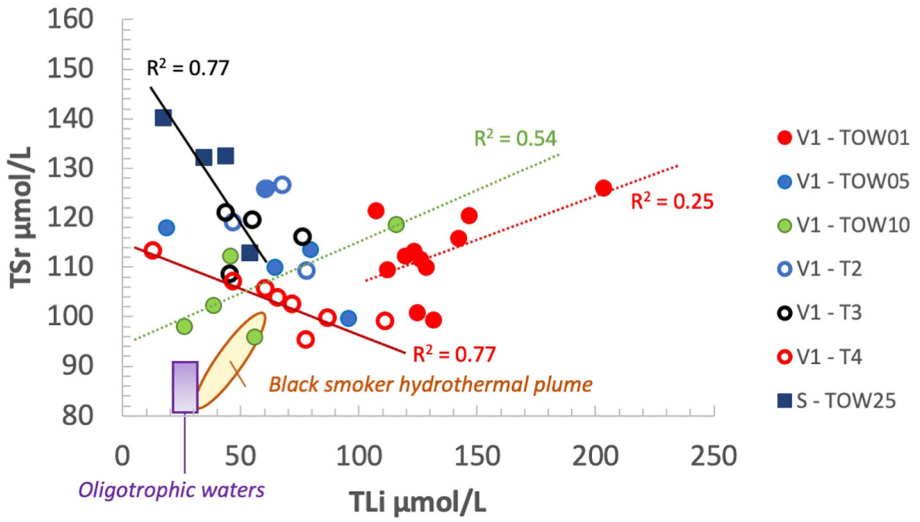

FIGURE 3
TSr vs TLi concentration plot of collected samples in comparison to oligotrophic waters (Leleu, 2017; El Meknassi et al., 2018) and black smoker hydrothermal plume (Artigue et al., 2022). Linear trends with R^2 values are reported for S–TOW25, V1–T4, V1–TOW01 and V1–TOW10.

concentrations of water column samples and found high DFe hydrothermal input from caldera seafloor to sub-surface water (3-5 times higher than typical oligotrophic DFe concentrations). Their datasets argued for a weak hydrothermal plume dispersion, whereby only a few % of initial hydrothermal DFe supply is maintained as dissolved form within the photic zone when moving westward from Volcano 1 caldera. To explain this DFe distribution pattern, three main processes were invoked such as mineral precipitation, trace element scavenging and to a lesser extend biological uptake; all of them potentially affecting the TSr and TLi elemental and isotopic composition distribution studied here.

4.1 Simone site

Simone site is under the direct influence of a volcanic eruption of surtseyan style which is characterized by emission of volcanic plumes rich in water vapor, condensed water and fine volcanic ash and associated water-rock interaction processes. Volcanic material can be transported hundreds of kilometres away from the source either in the marine realm (Newland et al., 2022; Clare et al., 2023) or in the atmosphere as a 4.6 to 5.2 km altitude steam plume has been reported during this volcanic eruption leading to New Late'iki island formation (Global Volcanism Program, 2019). Both processes can deliver volcanic materials supplying additional Li and Sr to the environment, and leading to higher concentrations in water column.

During volcanic eruption, the volcanic plume is strongly enriched in Li because the partition coefficient for alkali element such as Li is well above 1000 during magmatic vapor–magma interaction (Lowenstern et al., 2012). Moreover, the volcanic plume is also enriched in gases mainly composed of CO_2, H_2O, SO_2 among others (Symonds et al., 1994; Aiuppa et al., 2009) and is the place of many processes leading to little acidic droplets formation composed of HCl, HF, H_2SO_4 (Symonds et al., 1988; Zhu et al., 2020) and to salt precipitation on ash surfaces (Rose, 1977; Oppenheimer, 2003; Delmelle et al., 2007, 2018). The occurrence of acidic droplets enables local dissolution of particle ashes in line with a few dissolution holes observed on microscopic images of lithogenic particles collected in the water column at S–TOW25 location (Tilliette et al., 2023a). Indeed, lithogenic particles display essentially angular, clean and smooth surfaces pointing out limited influence of particle dissolution within the water column as well as particle freshness i.e., lack of remobilization and resuspension of old seafloor particle in the water column (Tilliette et al., 2023a). Particles from sea-surface sank progressively vertically and are advected horizontally (Tilliette et al., 2023a). Colombier et al. (2019) characterized that extensive salt precipitation as NaCl and $CaSO_4$ on surface particle occurs during surtseyan volcanic eruption, taking the Hunga Tonga - Hunga Ha'apai tuff cone as a site study (this volcano is part of the Tofua volcanic arc (Figure 1A), just north of Volcano 1). The dissolution of these salts (Stewart et al., 2020) leads to Li and Sr supplies in the water column as Li is known to be highly concentrated in brine (Garcia et al., 2020) and Sr is enriched in $CaSO_4$ e.g., anhydrite such those found at black smoker hydrothermal field (1164 to 2218 ppm; Humphris and Bach, 2005). Thus, this process may explain why the TSr and TLi concentrations measured at Simone are higher than those of oligotrophic waters i.e., by a factor of two (Figure 3). Considering the Na/Li molar ratio of brines at 61 (Garcia et al., 2020), an increase of 25-30 µmol/L of Li in seawater would induce a global salinity (reported here as halite) increase of ~0.1 g/L. In addition, we observe a negative TSr vs. TLi linear trend (Figure 3). Chemical analyses of brine samples collected at the Ethiopian rift under the direct influence of tectonism and volcanism, also evidence negative Sr vs. Li correlation (Bekele and Schmerold, 2020). Even if the dissolution of these salts leads to higher TSr and TLi concentrations,

a different dissolution rate of Sr- and Li-bearing minerals i.e., anhydrite vs. halite, should induce distinctive TSr and TLi supply to the water column. Halite is highly soluble (Alkattan et al., 1997) and its dissolution would deliver Li which will be instantaneously diluted within the water column. Even if the TLi concentrations are similar to that of oligotrophic waters at Simone site, the δ^7Li values are significantly different near the surface from oligotrophic waters i.e., +25.4‰, increase with water depth and reach a value similar to oligotrophic water near the seafloor (Table 1). This δ^7Li shift towards lower value compared to oligotrophic water can potentially reflect the combined effect of brines dissolution and biological uptake. A potential contribution of brine is supported by their low δ^7Li values at +5.9 to +10.3 ‰ (Garcia et al., 2020), meaning that any contribution would lower the δ^7Li value of the solution. The second hypothesis is based on recent scientific outcomes from the studied area evidencing high primary productivity rate estimated up to 145 mmol C m^{-2} yr^{-1} at this location (Tilliette et al., 2023a), together with the increase of organic matter and calcium carbonate within the particle pool collected by sediment trap at 200 mbsl (Tilliette et al., 2023a). Marine carbonate organisms are very diverse. Preliminary studies have showed that mussel/oyster/clam, all having a calcium carbonate shell, are preferentially enriched in ^{7}Li i.e., higher δ^7Li values compared to that of their aqueous environment which shows consequently low δ^7Li values (Thibon et al., 2021). Thibon et al. (2021) showed that these marine carbonate calcifiers tend to accumulate Li proportionally to the Li concentration of their surrounding aqueous environment. Indeed, at the studied area, Vigier et al. (2022) showed that plankton is characterized by very high Li concentrations (10 to 120 µg/g dry weight) compared to any other marine carbonate calcifiers (≤1 µg/g dry weight; Thibon et al., 2021), suggesting therefore that Li concentration of seawater at this location should be very high, as we argue here. In case of mineral–water interaction, ^{6}Li is preferentially adsorbed onto particles (lithogenic particle), leading to isotopic fractionation evidenced by high δ^7Li values for the solution and low δ^7Li values for particle, such as smectite among others (Chan and Hein, 2007; Vigier et al., 2008; Araoka et al., 2016). Here, the δ^7Li values of collected samples are equal and lower to that of seawater within error, reflecting the absence of particle–seawater interaction.

Unlike Li, TSr concentrations are all above the range of oligotrophic waters along depth profile (Table 1). Considering anhydrite with a Sr concentration of 1164 to 2218 ppm (Humphris and Bach, 2005) as the potential source of Sr, a maximum 50 µmol/L increase of TSr in our sample compared to oligotrophic waters (80–90 µmol/L) is thermodynamically possible and would imply the dissolution of 1.9 to 3.7 g/L of anhydrite which is below the solubility of anhydrite in seawater characterized by 4.95 g/L and 25°C (values calculated from PHREEQC). This suggests that anhydrite dissolution is a feasible process in the geological context of Simone. Further investigation on volcanically derived anhydrite is needed to better constrain the dissolved amount of this mineral as the available Sr dataset on anhydrite is solely provided by hydrothermal environment. Nevertheless, the ^{87}Sr/^{86}Sr ratios fall within the range of oligotrophic ones, except at 800 mbsl. The least radiogenic ^{87}Sr/^{86}Sr ratio of 0.709158, is measured at 180 mbsl, and can signify a contribution from the dissolution of basaltic material i.e., ^{87}Sr/^{86}Sr = 0.703–0.704 (Escrig et al., 2012), especially as a dense nephelometric layer was detected between 260 and 310 mbsl (Guieu and Bonnet, 2019). This nephelometric layer can be related to volcanic material delivered to the water column by erosion processes of the New Late'iki island (Plank et al., 2020). Indeed, by 24th November 2019 i.e., date of sample collection at Simone, erosion processes were still in progress delivering a substantial amount of volcanic particles to the water column (Tilliette et al., 2023a). At greater water depth, ^{87}Sr/^{86}Sr ratios are linearly correlated to 1/TSr (R^2 = 0.99) as shown in Supplementary Figure S8, with a trend controlled by the most radiogenic ^{87}Sr/^{86}Sr ratio of 0.709210. The analyzed samples have been sampled within the nephelometric layer as shown in Supplementary Figure S1, indicating the occurrence of particles. Similar radiogenic ratios are also measured at Volcano 1 and along the transect away from Volcano 1. With the present dataset, we cannot propose a potential source for such Sr isotopic signatures (Table 1, Figure 2D).

4.2 Volcano 1 site

The TSr vs. TLi distribution defines two linear tendencies with either negative or positive slope (Figure 3). Away from the Volcano 1 and along the transect, the TSr vs. TLi concentrations show negative linear trends, as that observed at Simone. However, the slope value decreases gradually when getting closer to Volcano 1. Within Volcano 1 caldera, this negative slope is observed for V1–TOW05 but V1–TOW01 and V1–TOW10 casts show a positive linear trend. These observations clearly evidence a heterogeneous and complex environment within a submarine volcano caldera. Indeed, at Volcano 1, active hydrothermal activity has been identified at the caldera seafloor through direct observation of fluid emission in the early 2000s (Stoffers et al., 2006; Massoth et al., 2007). In 2019 during the TONGA cruise, this hydrothermal activity was still ongoing as evidenced by physico-chemical anomalies detected in the water column at similar seafloor location (Bonnet et al., 2023; Supplementary Material S4, Supplementary Material S5-S6). Strong hydrothermal input is also supported by the high dissolved methane concentrations measured at this location, as oligotrophic waters commonly exhibit low methane concentrations of ~0.5 nmol/L (Table 1). A positive linear correlation of TSr vs. TLi was previously evidenced at black smokers of the Lucky Strike hydrothermal field (LSHF, on the Mid-Atlantic ridge) based on the analyses of 0.2 µm filtered seawater samples collected up to 300 m above the seafloor covering the 1 km^2 hydrothermal field (Artigue et al., 2022). Artigue et al. (2022) interpreted this co-variation (similar positive slope as our study), as reflecting a hydrothermal contribution of up to 10% to the water column. At Volcano 1, the hydrothermal contribution would be much more important as the TSr and TLi concentrations are increased by 5–41% and 7–88%, respectively compared to oligotrophic water concentrations. High hydrothermal contribution is also highlighted by very high dissolved methane concentration up to 104.1 µmol/L measured within the Volcano 1 caldera, and to a lesser extend along the transect. The variation of

TSr and TLi concentrations according to their respective isotopic signatures i.e., $^{87}Sr/^{86}Sr$ ratios and δ^7Li values, respectively, do not define any clear linear relationship which would have reflected binary mixing, apart from V1-TOW01. For this cast and without surface seawater samples i.e., <35 mbsl, the Sr elemental and isotopic signatures of samples define a linear trend (R^2 = 0.74) suggesting mixing between oligotrophic water and an unradiogenic Sr isotopic source depleted in Sr compared to seawater (Supplementary Figure S8). Unfortunately, at Volcano 1, the seafloor hydrothermal fluids have not been characterized for their TSr and TLi elemental and isotopic signatures thus far, hindering further calculation to better constrain hydrothermal contribution to the water column. Nevertheless, information can be obtained from worldwide sites exhibiting similar geological setting. At submarine Niuatahi Volcano (174°W and 15.35°S, Tonga rear arc), Falkenberg et al. (2022) report the occurrence of different venting styles displaying acid-sulfate (clear) to black smoker (particle-bearing) hydrothermal fluids and encompassing fluid boiling to magmatic volatile influxes. This study points out the complexity and diversity of hydrothermal venting, unfortunately without Sr and Li dataset on fluids. Wilckens et al. (2019) characterized chemically and isotopically both styles of venting at similar geological setting further north at North Su and DESMOS volcanic back-arc. Unfiltered acid-sulfate hydrothermal fluids display Sr and Li concentrations at 59–87 µmol/L and 21-41 µmol/L for corresponding isotopic signatures at 0.7087 to 0.70902 and +17.2 to +30.1 ‰, respectively (Wilckens et al., 2019). Unlike acid-sulfate fluids, unfiltered black smoker ones from the same location exhibit contrasted and distinctive Sr and Li elemental and isotopic signatures. Indeed, all black smoker fluids are enriched in Sr (151–410 µmol/L) and Li (348–806 µmol/L) for isotopic signatures being closer to substratum values at 0.70444 to 0.70582 and +5.7 to +6.8 ‰, respectively (Wilckens et al., 2019). Furthermore, the 0.2 µm filtered LSHF black smoker fluids are characterized by Sr and Li concentrations at 76–139 µmol/L and 287–398 µmol/L, respectively, and $^{87}Sr/^{86}Sr$ ratios and δ^7Li values at 0.70383 to 0.70436 and +4.8 to +5.9 ‰, respectively (Leleu, 2017; Artigue et al., 2022). Thus, this shows that volcanic-arc hydrothermal systems (Li = 0.23 to 1.3 mmol/kg and δ^7Li = +4.3 to +7.2 ‰; Araoka et al., 2016) have similar chemical features as basalt-hosted black smokers on mid-ocean ridges (Artigue et al., 2022; Wilckens et al., 2019; among others). Taking these elemental and isotopic signatures into account, the $^{87}Sr/^{86}Sr$ vs. (1/TSr) trend observed for V01–TOW01 can potentially reflect the contribution of an acid-sulfate hydrothermal fluid but alone this source cannot explain the large variability observed here for all casts performed at and away from Volcano 1.

In Figure 4, we report the $^{87}Sr/^{86}Sr$ ratios vs. δ^7Li values for collected samples together with the domains of that ratio in the literature for oligotrophic waters, acid-sulfate fluids and black smokers. While 92% of the measured $^{87}Sr/^{86}Sr$ ratios are in line with the mean value of oligotrophic waters of 0.709172 ± 0.000023 (2SD; n = 84; El Meknassi et al., 2018), the δ^7Li values display a large variability at values lower, equal or higher than oligotrophic water at +30.8 ± 0.1 ‰ (Rosner et al., 2007) i.e., between +10.1 and +37.6 ‰. Once combined, only 20% of measured samples fit within the field of oligotrophic water signatures (Figure 4). Sr and Li isotope systematics are key tracers of source, and Li isotopes provide additional information on processes related to mineral–seawater interaction (Chan and Hein, 2007; Artigue et al., 2022) and biology–aqueous environment interaction (Vigier et al., 2015; Thibon et al., 2021; Vigier et al., 2022; Poet et al., 2023; Chen et al., 2023). In Figure 4, we observe the combined effects of sources and processes. Four samples exhibit $^{87}Sr/^{86}Sr$ ratios more radiogenic than oligotrophic waters. Previous studies such as Nonell et al. (2005) report $^{87}Sr/^{86}Sr$ ratios ranging between 0.7049 and 0.71008 on volcanic gas condensates at Vulcano Island (Italy). Thus, it is possible that a substantial amount of gas condensate with radiogenic Sr isotopic signatures is produced in Volcano 1 caldera, increasing $^{87}Sr/^{86}Sr$ ratios towards more radiogenic signatures than oligotrophic waters. The main feature of the remaining samples relies on the δ^7Li values and their variability. Lower ones (32% of all samples) compared to oligotrophic waters are in line with hydrothermal contribution while higher ones (52% of all samples) can fingerprint either mineral–seawater interaction or biology-seawater interaction as DFe distribution in the water column suggests mineral precipitation, trace element scavenging and biological uptake (Tilliette et al., 2022).

In Figure 5, we report the measured δ^7Li values according to the DIC concentrations acquired on the same water samples. For comparison we also report the measured values on foraminifera shells collected after culture experiments in solution at different DIC concentrations (Vigier et al., 2015). DIC concentration in seawater is ~2400 µmol/L. Three putative trends can be proposed. Trend 1 delineates decreasing DIC concentrations for higher δ^7Li values compared to seawater features i.e., samples collected along transect casts and sub-surface Volcano 1 samples (0-50 mbsl). This feature can signify either the effect of mineral–seawater interaction, as ^6Li is preferentially adsorbed on mineral surfaces (Chan and Hein, 2007; Vigier et al., 2008), leading to ^7Li enrichment in the water column (Artigue et al., 2022) or the phytoplankton–seawater interactions, as Vigier et al. (2022) showed that plankton at this location exhibit lower δ^7Li values than seawater, leading to high δ^7Li values in solution. Trend 2 is defined by decreasing DIC concentrations concomitantly to lower δ^7Li values compared to seawater. This is evidenced by samples of Volcano 1 collected between 50 and 150 mbsl. Seawater sampled at depths greater than 50 mbsl is enriched in dissolved iron concentrations by several orders of magnitude compared to oligotrophic waters [Figure 3 in Tilliette et al. (2022)] as well as in dissolved methane concentrations (Table 1), in line with submarine hydrothermal contribution. The latter is further supported by lower δ^7Li values compared to oligotrophic water, as any hydrothermal contribution whether of acid-sulfate or black smoker type would lower δ^7Li values of seawater, based on the reported δ^7Li values of Wilckens et al. (2019). Trend 3 displays lower DIC concentrations and δ^7Li values compared to oligotrophic waters, mimicking trend 2 but with a much steeper slope i.e., narrower range of DIC variability. While submarine hydrothermal source can provide substantial amount of macronutrient up to the euphotic zone to stimulate phytoplankton development, hence carbon export, modification of seawater chemical composition can at first stress phytoplankton community, inhibiting biological activity until aqueous environments return to more favorable

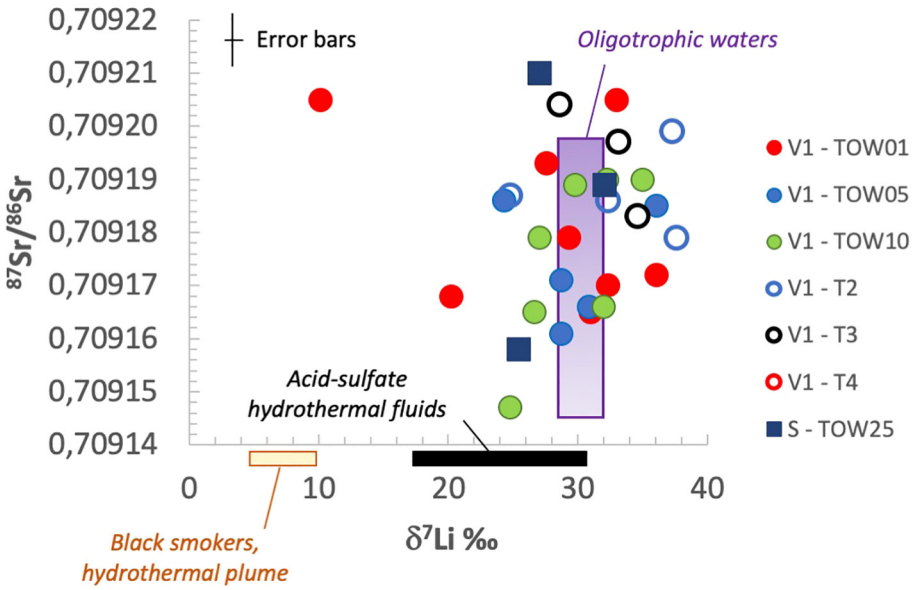

FIGURE 4
Binary diagram of δ^7Li values and $^{87}Sr/^{86}Sr$ ratios for collected samples in comparison to oligotrophic waters (Rosner et al., 2007), acid-sulfate hydrothermal fluids (Wilckens et al., 2019) and black smoker hydrothermal plume signatures (Artigue et al., 2022).

conditions. Using experimental minicosms operated during the TONGA cruise, Tilliette et al. (2023b) showed that production of thiol ligand by *Synechococcus* ecotypes enables binding of trace metals such as Cu, Cd, and Hg, leading to detoxification of the environment. As a consequence, phytoplankton growth i.e., enabling carbon export, can be delayed by several days, depending on the detoxification of the environment. Due to limited DIC and δ^7Li values, further scientific research is needed to assess the effect of biological activity onto Li elemental and isotope behavior in a context of high hydrothermal contribution. Overall, it is unfortunate that drifting conical sediment trap deployed at 200 mbsl within the caldera of Volcano 1 did not operate (Tilliette et al., 2023a), which would have helped us in characterizing particle chemistry and mineralogy as well as composition of the biogenic fraction. Meanwhile, the surtseyan volcanic eruption as well as hydrothermal systems can generate strong currents in the water column as a consequence of important heat supply in a cold environment (Dutay et al., 2004). Bonnet et al. (2023) identified a high-salinity water mass below surface waters, at the top of the permanent thermocline, which may have impacted the distribution of δ^7Li values according to depth (Figure 2B).

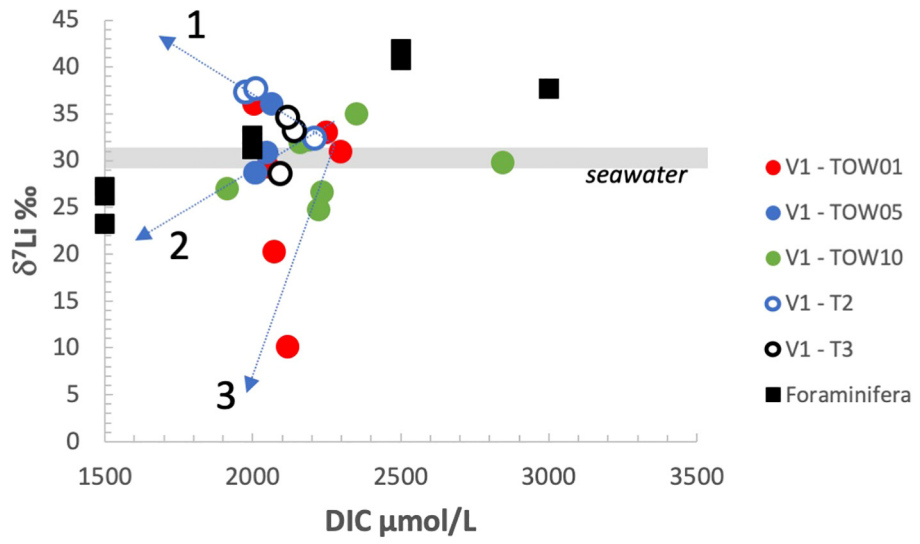

FIGURE 5
Binary diagram of Replacement TextLi values and DIC concentrations for collected samples. Measured δ^7Li values of foraminifera cultured in solution of various DIC concentrations are reported for comparison (Vigier et al., 2015). See the text for explanation of the three trends.

4.3 Effects of volcanic vs. hydrothermal contribution on water column

The effect of volcanism and hydrothermalism is evidenced by higher TSr and TLi concentrations of the water column compared to oligotrophic water ones. The volcanic contribution is expressed by high TSr and TLi concentrations due to the dissolution of different salts coating ash particles i.e., halite enriched in Li and anhydrite enriched in Sr. These supplies are directly linked to the eruptive style of volcanism. We observe this process at Simone site, directly under the influence of the New Late'iki eruption, and along the transect casts located ~150 km southwest of Simone. There, TSr concentrations decrease as TLi increases concomitantly. Unlike volcanic eruption, hydrothermalism provokes mutual increases of TSr and TLi in the water column. We observe this process in the Volcano 1 caldera at two out of three casts. When applying TSr and TLi isotopic systematics, the $^{87}Sr/^{86}Sr$ ratios vs. δ^7Li values point to different inputs as well as processes involving seawater interaction with particles and biological activity. In particular, this is evidenced by high δ^7Li values compared to oligotrophic waters at Volcano 1. Nonetheless, particles can be of different origin i.e., volcanic eruption ejects ashes while hydrothermalism leads to mineral formation within the mixing gradient between hydrothermal fluid and surrounding seawater. While processes can be similar, the minerals involved are distinctive in composition. They are either lithogenic in volcanic context, or polymetallic sulfides and oxyhydroxides in the case of hydrothermalism, leading to different isotopic fractionation when interacting with seawater. Alternatively, marine organisms rely on macro-nutrient supply to thrive. Submarine hydrothermal source provides a substantial amount of trace elements to seawater, among which some of them can stimulate primary productivity i.e., dissolved iron, while others, such as Hg or Cu can provoke the opposite, by inhibiting their development once their dissolved concentrations are too elevated. As a consequence, marine carbon export can be affected. Vigier et al. (2022) showed that plankton collected at hydrothermal setting is characterized by very high Li concentrations together with low δ^7Li values compared to seawater. In this particular setting where both volcanic and hydrothermal activities were at play, disentangling both contributions on water column required the combined use of elemental and isotopic signatures of several tracers, here Sr and Li.

5 Conclusion

The present study based on the TSr and TLi elemental and isotopic signatures of water column samples collected at Simone and Volcano 1 sites, reveals the contributions of volcanic and hydrothermal products to the surrounding environment. This is clearly evidenced by TSr and TLi concentrations higher than oligotrophic waters. Both volcanic eruption and submarine hydrothermal activity e.g., volcanic ashes, particles, gas condensate, etc., can deliver substantial amount of TSr and TLi to the water column.

On one side, volcanic eruption of surtseyan style is characterized by emission of volcanic plumes rich in water vapor, condensed water and fine volcanic ash and associated water-rock interaction processes. We observe a negative correlation between TSr and TLi in the water column at Simone and close to Volcano 1 that we propose to reflect differential dissolution rates of salt-coated ejected ashes since Sr and Li are associated to different minerals, anhydrite and halite respectively. Further analyses of ashes and Ca, sulphate and chloride concentrations in the water column need to be conducted to support this hypothesis. On the other side, hydrothermal supply at Volcano 1 leads to a positive TSr vs. TLi correlation, in line with black smoker related hydrothermal plume (Artigue et al., 2022).

When applying TSr and TLi isotopic systematics, the $^{87}Sr/^{86}Sr$ ratios vs. δ^7Li values point to different sources as well as processes involving seawater interaction with particles and/or biology. While 92% of the measured $^{87}Sr/^{86}Sr$ ratios are in line with the mean value of oligotrophic waters, only 20% of them remain within the field once combined with δ^7Li values. The δ^7Li values display a large variability i.e., between +10.1 and +37.6 ‰, decreasing linearly to first order from sea-surface down to 140 mbsl i.e., depth of water mass shear zone. The different linear trends defined between δ^7Li values and DIC concentrations highlight particle–seawater interaction, hydrothermal contribution and biology–seawater interaction.

When considering geological sedimentary archive, disentangling volcanic vs. hydrothermal contribution relies on combining different tracers among which one tracks down sources and another fingerprints water-rock interaction processes.

Data availability statement

The original contributions presented in the study are included in the article/Supplementary Material. Further inquiries can be directed to the corresponding author.

Author contributions

VC: Conceptualization, Formal analysis, Methodology, Validation, Writing – original draft, Writing – review & editing. CD: Writing – original draft, Writing – review & editing. CB: Data curation, Writing – original draft, Writing – review & editing. VT: Data curation, Formal analysis, Writing – review & editing. NV: Writing – original draft, Writing – review & editing. CG: Funding acquisition, Writing – original draft, Writing – review & editing. SB: Funding acquisition, Writing – original draft, Writing – review & editing.

Funding

The author(s) declare financial support was received for the research, authorship, and/or publication of this article. The ANR

-TONGA (ANR-18-CE01-0016) provided funding for all authors. In addition, the TONGA project and cruise was funded by the IR* Flotte Océanographique Française, the A-MIDeX of Aix-Marseille University, the LEFE-CYBER and GMMC program.

Acknowledgments

We are grateful to the IR* French Oceanographic Fleet and the crew of the R.V. L'Atalante which provided the technical support to carry out sample collection at sea during the oceanographic cruise TONGA. We acknowledge constructive comments from five reviewers and Johan Schijf.

Conflict of interest

The authors declare that the research was conducted in the absence of any commercial or financial relationships that could be construed as a potential conflict of interest.

Generative AI statement

The author(s) declare that no Generative AI was used in the creation of this manuscript.

Publisher's note

Supplementary material

The Supplementary Material for this article can be found online at: https://www.frontiersin.org/articles/10.3389/fmars.2024.1304930/full#supplementary-material

References

Aiuppa, A., Baker, D. R., and Webster, J. D. (2009). Halogens in volcanic systems. *Chem. Geology* 263, 1–18. doi: 10.1016/j.chemgeo.2008.10.005

Albarède, F., Michard, A., Minster, J. F., and Michard, G. (1981). $^{87}Sr/^{86}Sr$ ratios in hydrothermal waters and deposits from the East Pacific Rise at 21°N. *Earth Planetary Sci. Lett.* 55, 229–236. doi: 10.1016/0012-821X(81)90102-3

Alkattan, M., Oelkers, E. H., Dandurand, J.-L., and Schott, J. (1997). Experimental studies of halite dissolution kinetics, 1 The effect of saturation state and the presence of trace metals. *Chem. Geology* 137, 201–219. doi: 10.1016/S0009-2541(96)00164-7

Araoka, D., Nishio, Y., Gamo, T., Yamaoka, K., and Kawahata, H. (2016). Lithium isotopic systematics of submarine vent fluids from arc and back-arc hydrothermal systems in the western Pacific. *Geochemistry Geophysics Geosystems* 17, 3835–3853. doi: 10.1002/2016GC006355

Artigue, L., Chavagnac, V., Destrigneville, C., Ferron, B., and Cathalot, C. (2022). Tracking the lithium and strontium isotope signature of hydrothermal plume in the water column: A case study at the EMSO-azores deep-sea observatory. *Front. Environ. Chem.* 3. doi: 10.3389/fenvc.2022.784385

Barker, A. K., Coogan, L. A., Gillis, K. M., and Weis, D. (2008). Strontium Isotope Constraints on Fluid Flow in the Sheeted dike Complex of Fast Spreading Crust: Pervasive Fluid Flow at Pito Deep. *Geochemistry Geophysics. Geosystems* 9, 1–19. doi: 10.1029/2007gc001901

Bekele, A., and Schmerold, R. (2020). Characterization of brines and evaporite deposits for their lithium contents in the northern part of the Danakil Depression and in some selected areas of the Main Ethiopian Rift Lakes. *J. Afr. Earth Sci.* 170, 103904. doi: 10.1016/j.jafrearsci.2020.103904

Bernath, P., Boone, C., Pastorek, A., Cameron, D., and Lecours, M. (2023). Satellite characterization of global stratospheric sulfate aerosols released by Tonga volcano. *J. Quantitative Spectrosc. Radiative Transfer* 299, 108520. doi: 10.1016/j.jqsrt.2023.108520

Bonnet, S., Caffin, M., Berthelot, H., and Moutin, T. (2017). Hot spot of N_2 fixation in the western tropical South Pacific pleads for a spatial decoupling between N_2 fixation and denitrification. *Proc. Natl. Acad. Sci.* 114, 14 E2800–E2801. doi: 10.1073/pnas.1619514114

Bonnet, S., Guieu, C., Taillandier, V., Boulart, C., Bouruet-Aubertot, P., Gazeau, F., et al. (2023). Natural iron fertilization by shallow hydrothermal sources fuels diazotroph blooms in the ocean. *Science* 380, 812–817. doi: 10.1126/science.abq4654

Brandl, P. A., Schmid, F., Augustin, N., Grevemeyer, I., Arculus, R. J., Devey, C. W., et al. (2020). The 6–8 aug 2019 eruption of 'Volcano F' in the tofua arc, Tonga. *J. Volcanology Geothermal Res.* 390, 106695. doi: 10.1016/j.jvolgeores.2019.106695

Brunskill, G. J., Zagorskis, I., and Pfitzner, J. (2003). Geochemical mass balance for lithium, boron, and strontium in the gulf of papua, papua new Guinea (Project TROPICS). *Geochimica Cosmochimica Acta* 67, 3365–3383. doi: 10.1016/S0016-7037(02)01410-2

Chan, L.-H., and Hein, J. R. (2007). Lithium contents and isotopic compositions of ferromanganese deposits from the global ocean. *Deep Sea Res. Part II: Topical Stud. Oceanography* 54, 1147–1162. doi: 10.1016/j.TSr2.2007.04.003

Chavagnac, V., Leleu, T., Fontaine, F., Cannat, M., Ceuleneer, G., and Castillo, A. (2018a). Spatial variations in vent chemistry at the lucky strike hydrothermal field, mid-atlantic ridge (37°N): updates for subseafloor flow geometry from the newly discovered capelinhos vent. *Geochemistry Geophysics Geosystems* 19, 4444–4458. doi: 10.1029/2018GC007765

Chen, D., Thibon, F., Felbacq, A., Weppe, L., Metian, M., and Vigier, N. (2023). Coupled survey of lithium isotopes and Li/Ca in biogenic and inorganic carbonates. *Earth Sci. Rev.* 244, 104500. doi: 10.1016/j.earscirev.2023.104500

Clare, M. A., Yeo1, I. A., Watson, S., Wysoczanski, R., Seabrook, S., Mackay, K., et al. (2023). Fast and destructive density currents created by ocean-entering volcanic eruptions. *Science* 381, 1085–1092. doi: 10.1126/science.adi3038

Colombier, M., Mueller, S. B., Kueppers, U., Scheu, B., Delmelle, P., Cimarelli, C., et al. (2019). Diversity of soluble salt concentrations on volcanic ash aggregates from a variety of eruption types and deposits. *Bull. Volcanology* 81, 39. doi: 10.1007/s00445-019-1302-0

Davis, A. C., Bickle, M. J., and Teagle, D. A. H. (2003). Imbalance in the oceanic strontium budget. *Earth Planetary Sci. Lett.* 211, 173–187. doi: 10.1016/S0012-821X(03)00191-2

Delmelle, P., Lambert, M., Dufrêne, Y., Gerin, P., and Óskarsson, N. (2007). Gas/aerosol–ash interaction in volcanic plumes: New insights from surface analyses of fine ash particles. *Earth Planetary Sci. Lett.* 259, 159–170. doi: 10.1016/j.epsl.2007.04.052

Delmelle, P., Wadsworth, F. B., Maters, E. C., and Ayris, P. M. (2018). High temperature reactions between gases and ash particles in volcanic eruption plumes. *Rev. Mineralogy Geochemistry* 84, 285–308. doi: 10.2138/rmg.2018.84.8

Dutay, J.-C., Jean-Baptiste, P., Campin, J.-M., Ishida, A., Maier-Reimer, E., Matear, R. J., et al. (2004). Evaluation of OCMIP-2 ocean models' deep circulation with mantle helium-3. *J. Mar. Syst.* 48, 15–36. doi: 10.1016/j.jmarsys.2003.05.010

El Meknassi, S., Dera, G., Cardone, T., De Rafélis, M., Brahmi, C., and Chavagnac, V. (2018). isotope ratios of modern carbonate shells: Good and bad news for chemostratigraphy. *Geology* 46, 1003–1006. doi: 10.1130/G45380.1

Escrig, S., Bézos, A., Langmuir, C. H., Michael, P. J., and Arculus, R. (2012). Characterizing the effect of mantle source, subduction input and melting in the Fonualei Spreading Center, Lau Basin: Constraints on the origin of the boninitic signature of the back-arc lavas. *Geochemistry Geophysics Geosystems* 13, 10. doi: 10.1029/2012GC004130

Falkenberg, J. J., Keith, M., Haase, K. M., Sporer, C., Bach, W., Klemd, R., et al. (2022). Spatial variations in magmatic volatile influx and fluid boiling in the submarine hydrothermal systems of niuatahi caldera, Tonga rear-arc. *Geochemistry Geophysics Geosystems* 23, e2021GC010259. doi: 10.1029/2021GC010259

Garcia, M. G., Borda, L. G., Godfrey, L. V., López Steinmetz, R. L., and Losada-Calderon, A. (2020). Characterization of lithium cycling in the Salar De Olaroz, Central Andes, using a geochemical and isotopic approach. *Chem. Geology* 531, 119340. doi: 10.1016/j.chemgeo.2019.119340

German, C. R., Casciotti, K. A., Dutay, J., Heimbürger, L. E., Jenkins, W. J., Measures, C. I., et al. (2016). Hydrothermal impacts on trace element and isotope ocean biogeochemistry. *Philos. Trans. R. Soc. A.* 374, 20160035. doi: 10.1098/rsta.2016.0035

Global Volcanism Program (2019). "Report on lateiki (Tonga)," in *Weekly volcanic activity report, 9 october-15 october 2019*. Ed. S. K. Sennert (Washington DC: Smithsonian Institution and US Geological Surve). Available at: https://volcano.si.edu/showreport.cfm?wvar=GVP.WVAR20191009-243070.

Guieu, C., and Bonnet, S. (2019). TONGA 2019 cruise report, L'Atalante R/V. *SEANOE*. 74. doi: 10.17600/18000884

Guieu, C., Bonnet, S., Petrenko, A., Menkes, C., Chavagnac, V., Desboeufs, K., et al. (2018). Iron from a submarine source impacts the productive layer of the Western Tropical South Pacific (WTSP). *Sci. Rep.* 8, 9075. doi: 10.1038/s41598-018-27407-z

Guieu, C., Bonnet, S., Abadou, F., Alliouane, S., Arnaud-Haond, S., Arnone, V., et al. (2023). *Biogeochemical dataset collected during the TONGA cruise* (SEANOE). doi: 10.17882/88169

Huh, Y., Chan, L.-H., Zhang, L., and Edmond, J. M. (1998). Lithium and its isotopes in major world rivers: implications for weathering and the oceanic budget. *Geochimica Cosmochimica Acta* 62, 2039–2051. doi: 10.1016/S0016-7037(98)00126-4

Humphris, S. E., and Bach, W. (2005). On the Sr isotope and REE compositions of anhydrites from the TAG seafloor hydrothermal system. *Geochimica Cosmochimica Acta* 69, 1511–1525. doi: 10.1016/j.gca.2004.10.004

James, R. H., and Palmer, M. R. (2000). The lithium isotope composition of international rock standards. *Chem. Geology* 166, 319–326. doi: 10.1016/S0009-2541(99)00217-X

Leleu, T. (2017). *Variabilitè spatio-temporelle de la composition des fluides hydrothermaux (observatoire fond de mer EMSO-Açores, Lucky Strike): Traçage de la circulation hydrothermale et quantification des flux chimiques associés. Ph.D. Thesis, University of Toulouse III Paul Sabatier*. (Toulouse: University of Toulouse III Paul Sabatier).

Lowenstern, J. B., Bleick, H., Vazquez, J. A., Castro, J. M., and Larson, P. B. (2012). Degassing of Cl, F, Li, and Be during extrusion and crystallization of the rhyolite dome at Volcán Chaitén, Chile during 2008 and 2009. *Bull. Volcanology* 74, 2303–2319. doi: 10.1007/s00445-012-0663-4

Lupton, J., Lilley, M., Butterfield, D., Evans, L., Embley, R., Massoth, G., et al. (2008). Venting of a separate CO_2 -rich gas phase from submarine arc volcanoes: Examples from the Mariana and Tonga-Kermadec arcs. *J. Geophysical Res.* 113, B8. doi: 10.1029/2007JB005467

Massoth, G., Baker, E., Worthington, T., Lupton, J., De Ronde, C., Arculus, R., et al. (2007). Multiple hydrothermal sources along the south Tonga arc and Valu Fa Ridge. . *Geochemistry Geophysics Geosystems* 8, 11. doi: 10.1029/2007GC001675

Millot, R., Petelet-Giraud, E., Guerrot, C., and Négrel, P. (2010a). Multi-isotopic composition (δ^7Li–δ^{11}B–δD–δ^{18}O) of rainwaters in France: Origin and spatio-temporal characterization. *Appl. Geochemistry* 25, 1510–1524. doi: 10.1016/j.apgeochem.2010.08.002

Millot, R., Scaillet, B., and Sanjuan, B. (2010b). Lithium isotopes in island arc geothermal systems: Guadeloupe, Martinique (French West Indies) and experimental approach. *Geochimica Cosmochimica Acta* 74, 1852–1871. doi: 10.1016/j.gca.2009.12.007

Misra, S., and Froelich, P. N. (2012). Lithium isotope history of Cenozoic seawater: changes in silicate weathering and reverse weathering. *Science* 335, 818–823. doi: 10.1126/science.1214697

Newland, E. L., Mingotti, N., and Woods, A. W. (2022). Dynamics of deep-submarine volcanic eruptions. *Sci. Rep.* 12, 3276. doi: 10.1038/s41598-022-07351-9

Nonell, A., Toutain, J.-P., Polvé, M., Munoz, M., and Berger, G. (2005). First coupled Sr and Pb isotopic measurements in volcanic gas condensates and groundwaters of Vulcano Island (Italy). *Geochemistry Geophysics Geosystems* 6, 11. doi: 10.1029/2005GC000980

Oppenheimer, C. (2003). "Volcanic degassing," in *The crust. Treatise in geochemistry*, vol. 3 . Ed. R. L. Rudnick (Elsevier), 123–166.

Palmer, M. R., and Edmond, J. M. (1989). The strontium isotope budget of the modern ocean. *Earth Planetary Sci. Lett.* 92, 11–26. doi: 10.1016/0012-821X(89)90017-4

Pin, C., Gannoun, A., and Dupont, A. (2014). Rapid, simultaneous separation of Sr, Pb, and Nd by extraction chromatography prior to isotope ratios determination by TIMS and MC-ICP-MS. *J. Analytical Atomic Spectrometry* 29, 1858–1870. doi: 10.1039/C4JA00169A

Plank, S., Marchese, F., Genzano, N., Nolde, M., and Martinis, S. (2020). The short life of the volcanic island New Late'iki (Tonga) analyzed by multi-sensor remote sensing data. *Sci. Rep.* 10, 22293. doi: 10.1038/s41598-020-79261-7

Poet, M., Vigier, N., Bouret, Y., Jarretou, G., Gautier, R., Bendahhou, S., et al. (2023). Biological fractionation of lithium isotopes by cellular Na^+/H^+ exchangers unravels fundamental transport mechanisms. *iScience* 26, 106887. doi: 10.1016/j.isci.2023.106887

Rose, W. I. (1977). Scavenging of volcanic aerosol by ash: atmospheric and volcanologic implications. *Geology* 5, 621–624. doi: 10.1130/0091-7613(1977)5<621:SOVABA>2.0.CO;2

Rosner, M., Ball, L., Peucker-Ehrenbrink, B., Blusztajn, J., Bach, W., and Erzinger, J. (2007). A simplified, accurate and fast method for lithium isotope analysis of rocks and fluids, and δ^7Li values of seawater and rock reference materials. *Geostandards Geoanalytical Res.* 31, 77–88. doi: 10.1111/j.1751-908X.2007.00843.x

Ryan, W. B. F., Carbotte, S. M., Coplan, J. O., O'Hara, S., Melkonian, A., Arko, R., et al. (2009). Global multi-resolution topography synthesis. *Geochemistry Geophysics Geosystems* 10, 3. doi: 10.1029/2008GC002332

Stewart, C., Damby, D. E., Horwell, C. J., Elias, T., Ilyinskaya, E., Tomašek, I., et al. (2022). Volcanic air pollution and human health: recent advances and future directions. *Bull. Volcanology* 84, 11. doi: 10.1007/s00445-021-01513-9

Stewart, C., Damby, D. E., Tomašek, I., Horwell, C. J., Plumlee, G. S., Armienta, M. A., et al. (2020). Assessment of leachable elements in volcanic ashfall: a review and evaluation of a standardized protocol for ash hazard characterization. *J. Volcanology Geothermal Res.* 392, 106756. doi: 10.1016/j.jvolgeores.2019.106756

Stoffers, P., Worthington, T. J., Schwarz-Schampera, U., Hannington, M. D., Massoth, G. J., Hekinian, R., et al. (2006). Submarine volcanoes and high-temperature hydrothermal venting on the Tonga arc, southwest Pacific. *Geology* 34, 453. doi: 10.1130/G22227.1

Stoffers, P., Worthington, T., Shipboard Scientific Party (2003). "Cruise report SONNE 167, louisville," in *Louisville Ridge: Dynamics and magmatism of a mantle plume and its influence on the Tonga-Kermadec Subduction System* (Kiel Christian-Albrechts-Universität, Suva, Fiji – Wellington, New Zealand), 276, ISBN: .

Symonds, R. B., Rose, W. I., Bluth, G. J., and Gerlach, T. M. (1994). Volcanic-gas studies: Methods, results, and applications. *Mineralogical Soc. America* 30, 1–66.

Symonds, R. B., Rose, W. I., and Reed, M. H. (1988). Contribution of C1- and F-bearing gases to the atmosphere by volcanoes. *Nature* 334, 415–418. doi: 10.1038/334415a0

Taillandier, V., Wagener, T., D'Ortenzio, F., Mayot, N., Legoff, H., Ras, J., et al. (2018). Hydrography and biogeochemistry dedicated to the Mediterranean BGC-Argo network during a cruise with RV Tethys 2 in May 2015. *Earth System Sci. Data* 10, 627–641. doi: 10.5194/essd-10-627-2018

Thibon, F., Metian, M., Oberhänsli, F., Montanes, M., Vassileva, E., Orani, A. M., et al. (2021). Bioaccumulation of lithium isotopes in mussel soft tissues and implications for coastal environments. *ACS Earth Space Chem.* 5, 1407–1417. doi: 10.1021/acsearthspacechem.1c00045

Tilliette, C., Gazeau, F., Chavagnac, V., Leblond, N., Montanes, M., Leblanc, K., et al. (2023a). Temporal and spatial variability in the hydrothermal signature of sinking particles and sediments in the Western Tropical South Pacific Ocean. *J. Geophysical Res. – Oceans* 128, e2023JC019828. doi: 10.1029/2023JC019828

Tilliette, C., Gazeau, F., Portlock, G., Benavides, M., Bonnet, S., Guigue, C., et al. (2023b). Influence of shallow hydrothermal fluid release on the functioning of phytoplankton communities. *Front. Mar. Sci.* 10. doi: 10.3389/fmars.2023.1082077

Tilliette, C., Taillandier, V., Bouruet-Aubertot, P., Grima, N., Maes, C., Montanes, M., et al. (2022). Dissolved iron patterns impacted by shallow hydrothermal sources along a transect through the Tonga-kermadec arc. *Global Biogeochemical Cycles* 36, e2022GB007363. doi: 10.1029/2022GB007363

Tomascak, P. B., Magna, T., and Dohmen, R. (2016). *Advances in lithium isotope geochemistry, advances in isotope geochemistry* (Springer International Publishing). doi: 10.1007/978-3-319-01430-2

Vance, D., Teagle, D. A. H., and Foster, G. L. (2009). Variable Quaternary chemical weathering fluxes and imbalances in marine geochemical budgets. *Nature* 458, 493–496. doi: 10.1038/nature07828

Vigier, N., Decarreau, A., Millot, R., Carignan, J., Petit, S., and France-Lanord, C. (2008). Quantifying li isotope fractionation during smectite formation and implications for the li cycle. *Geochimica Cosmochimica Acta* 72, 780–792. doi: 10.1016/j.gca.2007.11.011

Vigier, N., Rollion-Bard, C., Levenson, Y., and Erez, J. (2015). Lithium isotopes in foraminifera shells as novel proxy for the ocean dissolved inorganic carbon (DIC). *Comptes Rendu Geosci.* 347, 43–51. doi: 10.1016/j.crte.2014.12.001

Vigier, N., Weppe, L., Tilliette, C., Chavagnac, V., Boulart, C., Thibon, F., et al. (2022). "Impact of shallow hydrothermalism on lithium content and lithium isotope composition of marine plankton," in *Goldschmidt Conference*. doi: 10.46427/gold2022.11142

Wakaki, S., Obata, H., Tazoe, H., and Ishikawa, T. (2017). Precise and accurate analysis of deep and surface seawater Sr stable isotopic composition by double-spike thermal ionization mass spectrometry. *Geochemical J.* 51, 227–239. doi: 10.2343/geochemj.2.0461

Wilckens, F. K., Reeves, E. P., Bach, W., Seewald, J. S., and Kasemann, S. A. (2019). Application of B, mg, li and sr isotopes in acid-sulfate vent fluids and volcanic rocks as tracers for fluid-rock interaction in back-arc hydrothermal systems. *Geochemistry Geophysics Geosystems* 20, 5849–5866. doi: 10.1029/2019GC008694

Zhu, Y., Toon, O. B., Jensen, E. J., Bardeen, C. G., Mills, M. J., Tolbert, M. A., et al. (2020). Persisting volcanic ash particles impact stratospheric SO_2 lifetime and aerosol optical properties. *Nat. Communication* 11, 4526. doi: 10.1038/s41467-020-18352-5

frontiers | Frontiers in Marine Science

TYPE Original Research
PUBLISHED 13 November 2024
DOI 10.3389/fmars.2024.1426906

OPEN ACCESS

EDITED BY
Douglas G Capone,
University of Southern California,
United States

REVIEWED BY
Peter Leslie Croot,
University of Galway, Ireland
Randelle M Bundy,
University of Washington, United States

*CORRESPONDENCE
Gemma Portlock
g.l.portlock@soton.ac.uk
Pascal Salaün
salaun@liverpool.ac.uk

RECEIVED 02 May 2024
ACCEPTED 11 September 2024
PUBLISHED 13 November 2024

CITATION
Portlock G, Whitby H and Salaün P (2024) Distribution and behaviour of reduced sulfur substances in the oligotrophic and hydrothermal waters of the Western Tropical South Pacific.
Front. Mar. Sci. 11:1426906.
doi: 10.3389/fmars.2024.1426906

Distribution and behaviour of reduced sulfur substances in the oligotrophic and hydrothermal waters of the Western Tropical South Pacific

Gemma Portlock[1,2*], Hannah Whitby[2] and Pascal Salaün[2*]

[1]School of Ocean and Earth Science, National Oceanography Centre Southampton, University of Southampton, Southampton, United Kingdom, [2]Department of Earth, Ocean and Ecological Sciences, School of Environmental Sciences, University of Liverpool, Liverpool, United Kingdom

Reduced sulfur species (RSS) are involved in essential biological and chemical processes, including metal complexation, yet little is known about their occurrence and behaviour in marine systems. Here, we present a quantitative and qualitative data set of species-specific RSS in open ocean samples collected during the GEOTRACES Tonga GPpr14 cruise. The cruise traversed differing biogeochemical provinces, from the mesotrophic Melanesian waters and the North Fiji Basin, through the hydrothermally active Lau Basin, eastward to the oligotrophic South Pacific Gyre. Using cathodic stripping voltammetry in acidified samples (pH 2), we measured the concentration of two RSS, with peak potentials of -0.18 and -0.09 V in equivalents of thioacetamide (TA) and glutathione (GSH) respectively. GSH-like compounds were only present in the upper 200 m at concentrations up to 6.2 nM eq. GSH, consistent with other cathodic stripping voltammetry as well as chromatography-based studies. In contrast, $RSS^{2}_{-0.18\ V}$ compounds were detected at all depths at concentrations ranging from 48 nM to 980 nM eq. TA. Both $RSS^{2}_{-0.18\ V}$ and GSH-like compounds were present at higher levels in the hydrothermally-impacted region of the Lau Basin relative to other stations. The highest levels, along with high sulfide concentrations, were detected in a hydrothermal plume sample, indicating that hydrothermal vents are a direct or indirect source of these compounds. Elevated levels of $RSS^{2}_{-0.18\ V}$ compounds were detected throughout almost the entire water column at a station located in the North Fiji Basin. We also employed the qualitative technique of cathodic pseudopolarography on unbuffered samples (pH ~ 8.5). Pseudopolarograms of marine RSS were compared to sulfide, GSH and TA standards. Pseudopolarography supports the presence of GSH in marine samples. However, while a compound that is electrochemically similar to TA is often detected in marine samples, TA itself is not thought to be naturally present. This is supported by our pseudopolarograms of $RSS^{8.5}_{-0.52\ V}$ which often lacked the characteristic TA reduction wave but suggested the presence of other unidentified RSS compounds.

KEYWORDS

reduced sulfur substances, thioacetamide, glutathione, sulfide, hydrothermal fluids, Western Tropical South Pacific, pseudopolarography

1 Introduction

The Western Tropical South Pacific (WTSP) is a vast oceanic region that extends from Australia to the western boundary of the South Pacific Gyre. Within the WTSP is the Tonga-Kermadec Arc where the Pacific plate subducts under the Australian plate, causing a region of extensive hydrothermal activity (Baker et al., 2019; German et al., 2006). Hydrothermal vents release both metal and non-metal chemicals, including sulfur, iron, carbon dioxide and methane (Feely et al., 1996; Klinhammer et al., 1977; Klinkhammer et al., 1983; Resing et al., 2015) which play an important role in ocean chemistry. These inputs can influence the biogeochemical cycles of surrounding waters, affecting primary production and nutrient availability (Ardyna et al., 2019; Schine et al., 2021). Recently, attention has been focused on the importance of shallow (<200 m) hydrothermal vents (Guieu et al., 2018; Tilliette et al., 2022) as the buoyant hydrothermal plumes are able to reach surface waters (Zhang et al., 2020) providing the surface communities with an abundance of elements that can either be beneficial (Bonnet et al., 2023a) or detrimental to their physiology (Tilliette et al., 2023). The shallow hydrothermal vents in the WTSP release high concentrations of metals, including iron (Guieu et al., 2018; Tilliette et al., 2022; Wang et al., 2022); a lack of this critical micronutrient often limits marine productivity, particularly to nitrogen fixers in nitrogen-depleted waters, as they have a high iron requirement (Moore et al., 2013, 2001; Morel and Price, 2003). Iron inputs from shallow hydrothermal origin coupled with the >25°C sea surface temperature and phosphorus-rich waters of the WTSP (Bonnet et al., 2018; Caffin et al., 2018), had been hypothesized to lead to extensive blooms of diazotrophs, causing the area to be a global hotspot for nitrogen fixation (Bonnet et al., 2018, 2017; Shao et al., 2023). Recently, the link between shallow hydrothermal inputs, diazotroph blooms and enhanced carbon sequestration has been established in this region (Bonnet et al., 2023b).

It is important to understand the controls on bioactive metals in seawater, as they can profoundly affect biogeochemical cycles. Reduced sulfur substances (RSS) play an important role in trace metal complexation and thus on their availability, but little is known regarding their distribution in marine systems. RSS encompass a wide range of sulfur-containing molecules, including thiols, thioureas, thioamides and hydrogen sulfide. They can complex with metals, which can either inhibit metal toxicity or help with uptake (Dupont and Ahner, 2005; Huang et al., 2018; Mironov and Tsvelodub, 1996; Navarrete et al., 2019; Rea et al., 2004; Steffens, 1990; Walsh et al., 2015). Phytoplankton, plants and fungi have been shown to produce various RSS as a result of elevated metal exposure (Ahner et al., 2002; Bjørklund et al., 2019; Kumar et al., 2021; Pál et al., 2018). Leal and van den Berg (1998) showed that RSS can stabilise Cu as Cu^{+}, limiting concentrations of the more toxic Cu^{2+} (Leal and van den Berg, 1998). In environments with low trace metal concentrations, microbes have also been found to produce RSS to help with metal uptake (Huang et al., 2018; Walsh et al., 2015). RSS also act as antioxidants against reactive oxygen species (ROS) (Apel and Hirt, 2004; Madkour, 2020a, 2020b; Morris et al., 2022; Schieber and Chandel, 2014; Ulrich and Jakob, 2019). They are able to remove ROS by accepting their unpaired electron (McLeay et al., 2017; Morelli and Scarano, 2004), preventing tissue damage and injury (Baba and Bhatnagar, 2018; Dupont et al., 2004; Rijstenbil, 2002).

RSS can enter the marine environment through biological processes (Al-Farawati and van den Berg, 2001; Carfagna et al., 2016; Ciglenečki and Ćosović, 1996; Moran and Durham, 2019; Swarr et al., 2016), decomposition (Treude et al., 2009), sediments (Kiene, 1991; Kiene et al., 1990), cell leakage (Bluhm et al., 2010) and hydrothermal activity (McCollom and Seewald, 2007). They can be found throughout the marine environment, from estuaries to open ocean waters, and from the surface to the deep ocean. RSS can be removed from the marine environment through various sink processes. These include biological uptake by microorganisms (Moran and Durham, 2019) and photochemical processes (Chu et al., 2017; Laglera and van den Berg, 2006). In oxic seawater, RSS are typically present at nanomolar concentrations (Dupont et al., 2006; Gao and Guéguen, 2018; Swarr et al., 2016; Tang et al., 2000) while in anoxic environments, their concentrations can be much higher (Gomez-Saez et al., 2021; Mopper and Kieber, 1991); however, there are few studies focusing on their distributions and biogeochemical cycling.

Analytical detection and identification of RSS compounds in seawater, typically using chromatography or electrochemical techniques, is challenging due to the wide diversity of compounds and their relatively low concentrations (nM and below). Using high performance liquid chromatography (HPLC), only a few biogenic RSS compounds have been identified in seawater including glutathione, cysteine, γ-glutamate-cysteine and dipeptides such as arginine-cysteine or glutamine-cysteine (Dupont et al., 2006; Kawakami et al., 2006; Swarr et al., 2016). However, chromatograms also revealed the presence of a significant amount of other unidentified compounds, which are probably RSS (Swarr et al., 2016). Although powerful, the experimental methodology requires prior derivatization of the RSS before analysis and sometimes preconcentration, which may interfere with the integrity of the sample (Swarr et al., 2016).

Cathodic stripping voltammetry (CSV) at a mercury electrode is a simpler and faster technique, for detection of RSS. The method relies on the strong affinity between mercury and sulfur compounds, which causes an adsorbed complex to accumulate during the deposition step, followed by its reduction during the cathodic stripping scan. Although the reduction peak potential can be used to differentiate various sulfur compounds (Umiker et al., 2002), the peaks often coalesce when measured by CSV, resulting in a single, consolidated peak (Laglera et al., 2012). The detection of RSS has been carried out in both acidic and natural pH conditions. In acidic conditions (pH 2), two distinct peaks are attributed to RSS: one at -0.18 V and another at -0.09 V, corresponding to peak potentials for thioacetamide (TA) and glutathione (GSH), respectively (Pernet-Coudrier et al., 2013). Using this methodology in a recent study, we found that hydrothermal fluids can trigger the production of these RSS compounds by natural plankton communities (Tilliette et al., 2023). At natural pH, a single RSS peak is observed at ~ -0.52 V. Multiple RSS compounds such as glutathione, thiourea and thioacetamide produce peaks at similar potential (Whitby et al., 2018). Sulfide also produces a peak at this potential but it is unstable and tends to decrease rapidly (Al-Farawati and van den Berg, 1997). Table 1 presents a list of RSS compounds that

TABLE 1 Reduced sulfur species (RSS) detected in marine waters as well as common standards used for their quantification by voltammetry.

RSS	Location	Identification method	Approximate voltametric peak position*
Glutathione (GSH)	Subarctic Pacific Ocean	HPLC (Dupont et al., 2006) Detected to 500 m	Acidic (pH 2): -0.09 V (This study) Natural (pH 8.5): -0.51 V (This study)
	North Atlantic Ocean Sampled to 500 m	HPLC (Swarr et al., 2016) Detected to 500 m	
	Galveston Bay Surface water sampled	HPLC (Tang et al., 2000)	
Cysteine (Cys)	Subarctic Pacific Ocean	HPLC (Dupont et al., 2006) Detected to 500 m	Acidic (pH 1.95): -0.05 V (Pernet-Coudrier et al., 2013) Natural (pH 8.4): -0.40 V (Laglera et al., 2014) Natural (Cu(I)-Cys complex) (pH 8.5): -0.55 V (van den Berg et al., 1988)
	North Atlantic Ocean	HPLC (Swarr et al., 2016) Detected to 500 m	
γ-glutamyl-cysteine (γ-Glu-Cys)	Subarctic Pacific Ocean	HPLC (Dupont et al., 2006) Detected to 3000 m	Acidic: no data Natural: no data
Cysteinyl-arginine (Arg–Cys)	Subarctic Pacific Ocean	HPLC (Dupont et al., 2006) Detected to 500 m	Acidic (pH 1.95): -0.08 V (Pernet-Coudrier et al., 2013) Natural: no data
Cysteinyl-glutamine (Gln –Cys)	Subarctic Pacific Ocean	HPLC (Dupont et al., 2006) Detected to 500 m	Acidic: no data Natural: no data
Methanethiol (volatile)	Hydrothermal vent orifice	CSV (Dias et al., 2010)	Acidic (pH 2.3): -0.05 V (Dias et al., 2010) Natural (pH 8.15): -0.34 V (Whitby et al., 2018)
	Hydrothermal vent orifice	GC coupled with FID (Reeves et al., 2014)	
Sulfide	Hydrothermal system	Fluorescence (Radford-Knoery et al., 1998)	Acidic (pH 2): -0.18 V (This study) Natural (pH 8-8.1): -0.55 V (Al-Farawati and van den Berg, 1997)
Thioacetamide	Not naturally occurring in marine environments	CSV	Acidic (pH 2): -0.18 V (This study) Natural (pH 8.5): -0.54 V (This study) Acidic (Cu(I)-TA complex) (pH <1): -0.66 V (Jeng et al., 1990)
Thiourea	Not naturally occurring in marine environments	CSV	Acidic (pH 1.95): -0.23 V (Pernet-Coudrier et al., 2013) Natural (pH 8.4): -0.54 V (Laglera and Tovar-Sánchez, 2012)

*Peak positions are approximative because they are dependent on the chemical (e.g. pH, analyte concentration) and experimental (e.g. accumulation time, stripping parameters) conditions.

have been detected in marine waters along with their peak potential at the mercury electrode.

An alternative approach is cathodic pseudopolarography (CP). CP is a qualitative voltammetric technique (Laglera et al., 2014; Laglera and Tovar-Sánchez, 2012) that distinguishes between similar RSS compounds based on their potential-dependent adsorbing behaviour at the mercury surface. This technique consists of successive CSV measurements at varying deposition potentials (E_{dep}). By plotting the peak intensity vs E_{dep}, these pseudopolarograms may present waves that are characteristic of specific RSS compounds; the position and shape of these waves can be compared to those obtained from standards to help characterise the RSS present in the sample.

In this work, we use both CSV in acidic conditions and CP at natural pH to characterise the presence of RSS compounds throughout the water column and to identify their sources and sinks in the WTSP. This study was part of the French GEOTRACES TONGA project (shallow hydroThermal sOurces of trace elemeNts: potential impacts on biological productivity and the bioloGicAl carbon pump, GPpr14). We sampled from the mesotrophic Melanesian waters and North Fiji basin, through the hydrothermally active Lau Basin to the oligotrophic western south Pacific Gyre. We discuss the potential sources and sinks of RSS and we also compare pseudopolarograms of water column RSS to those of model standards (sulfide, GSH and TA) to further characterise these species.

2 Experimental

2.1 Sampling strategy

Samples were collected during the GEOTRACES TONGA (GPpr14) (Guieu and Bonnet, 2019) research cruise, which took place onboard the R/V L'Atalante from 31st October to 5th December 2019, a transect extending from New Caledonia to the western end of the South Pacific Gyre (Figure 1A).

Stations 2 and 3 were both in Melanesian waters in the western part of the transect. Station 2 was in the North Fiji Basin, north-west of the Hunter fracture zone while station 3 was situated in the South Fiji basin. Stations 4, 11 and 12 were in the Lau Basin in the central

10.3389/fmars.2024.1426906

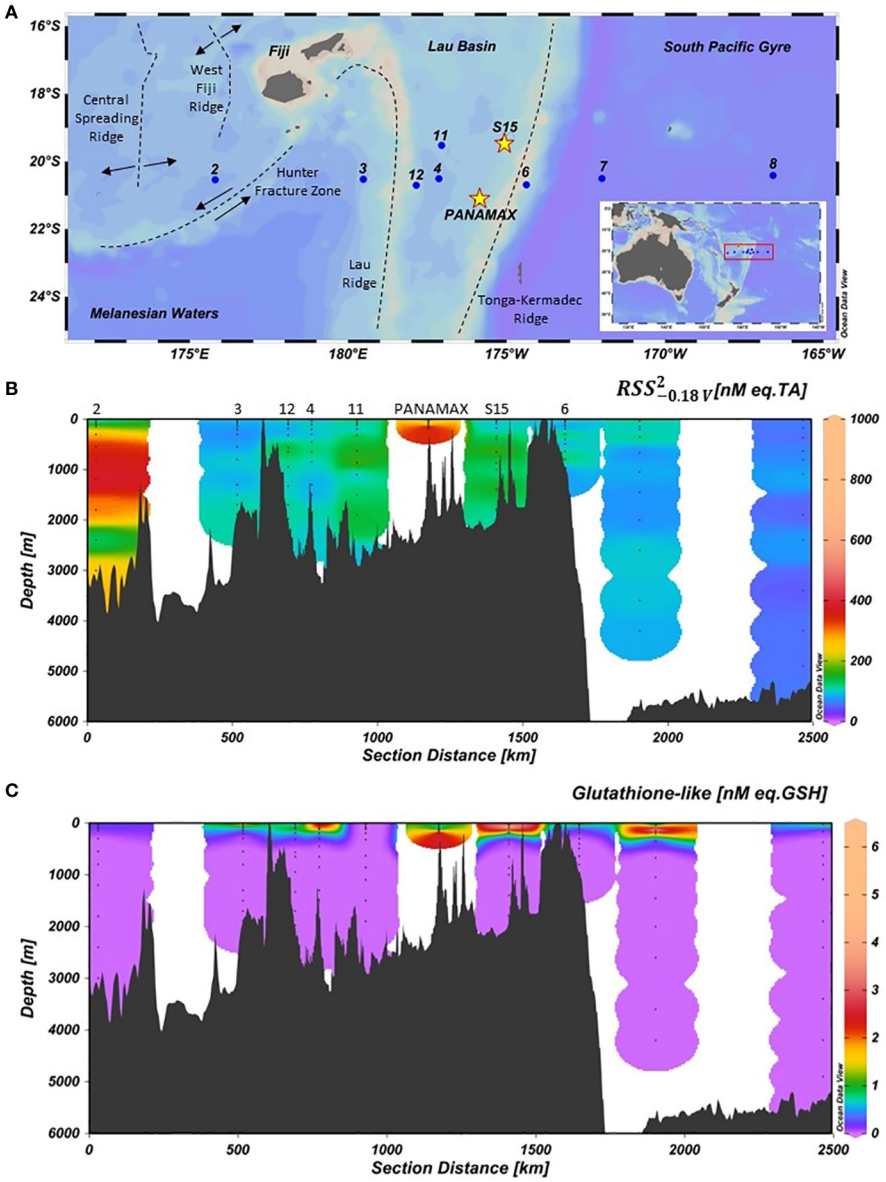

FIGURE 1
(A) Map of stations sampled during the TONGA 2019 cruise across the Western Tropical South Pacific Ocean (WTSP). In the WTSP there are three distinct regions: Melanesian waters, Lau Basin and South Pacific Gyre. The dashed lines represent plate boundaries. The numbers are the stations. The stars show the two shallow hydrothermal vents, PANAMAX and SIMONE. S15 was 15 km away from the SIMONE hydrothermal source but S15 still had high acoustic anomalies (Tilliette et al., 2022). **(B)** The distribution of $RSS^2_{-0.18\ V}$ compounds in nM eq. TA and **(C)** GSH-like compounds in nM eq. GSH. Figures were generated using ODV software (Schlitzer, 2021).

part of the transect while stations 6, 7 and 8 were in the South Pacific Gyre in the eastern part of the transect (Figure 1A). The transect also crossed two hydrothermal stations, PANAMAX and SIMONE, that were identified by acoustic anomalies (Bonnet et al., 2023a). At PANAMAX, strong and continuous anomalies of Eh, pH, redox potential and turbidity were detected, suggesting the presence of a hydrothermal plume. The sampling procedure followed at PANAMAX has been described elsewhere (Bonnet et al., 2023a). The SIMONE site also displayed multiple acoustic anomalies suggesting the presence of multiple weak hydrothermal sources (Tilliette et al., 2022). Four substations were sampled in the vicinity of SIMONE (T1, T2, T3 and T5) but only the furthest away (T1, 15 km away from hydrothermal vent) was analysed in this study. This station is referred as "S15".

2.2 Sample collection and storage

Samples were collected using a trace metal clean polyurethane powder-coated aluminium frame rosette (TMR, General Oceanics Inc. Model 1018 Intelligent Rosette), which was attached to a 6 mm diameter Kevlar line. The Go-Flo bottles were then transferred into a trace metal clean container (class 100) and pressurized with 0.2 µm-filtered nitrogen for sampling. Seawater was filtered through a

0.45 µm acid-cleaned polyethersulfone filter (Supor®) and collected in 125 mL Nalgene LDPE bottles, that had been acid-cleaned according to the GEOTRACES protocol (Cutter et al., 2017). Samples were collected after rinsing the bottle three times with around 20 mL of filtered sample, then double bagged and stored at −20°C until analysis.

2.3 Reagents

Water used for rinsing and dilution of reagents was ultrapure deionized water (>18 MΩ) from a Milli-Q (MQ) system (Millipore, UK). Thioacetamide (TA) (Fisher Scientific, UK) and glutathione (GSH) (reduced, Sigma-Aldrich, UK) were used as model RSS standards. Standards were acidified with HCl (laboratory reagent grade 32%, Fisher Scientific, UK) to pH 2. Hg plating solution was prepared from $Hg(NO_3)_2$ (Fluka, UK) in a 0.1 M sodium nitrate (Sigma-Aldrich, UK) and 10 mM HCl (Fisher, UK) solution. Stock solutions of 0.1 M sodium sulfide were prepared from hydrated $Na_2S.xH_2O$ (60-63%, Sigma-Aldrich, UK) on a daily basis. RSS standards were replaced when the concentration of the internal standard was no longer reproducible. All standards were kept in the dark to avoid photodegradation. When not in use, standards were kept in the fridge. For sulfide analysis, a borate buffer stock solution (1 M boric acid, reagent grade, Fisher Scientific, UK) was prepared in 0.35 M ammonia (trace metal grade, Fisher Scientific, UK), with the pH adjusted to 8.1. Organic contaminants were first removed from the buffer solution by UV-digestion; the solution was cleaned of trace metals by addition of 100 µM MnO_2 (van den Berg, 1982) and filtration using an acid cleaned 0.2 µm cellulose nitrate membrane (Whatman) after overnight equilibration.

2.4 Voltammetric equipment

For the quantifications of RSS and for the majority of CP, a µAutolabIII potentiostat (Ecohemie, Netherland) connected to a Metrohm 663 VA stand through the IME663 interface was used. A three-electrode cell consisted of a static mercury drop electrode (SMDE) as working electrode, a glassy carbon rod counter electrode and a Ag/AgCl//KCl (3 M) with glass salt bridge (Metrohm, filled with 3 M KCl) reference electrode. Connected to the VA stand was a V1 autosampler (https://sites.google.com/site/daromasoft/home/autosampler) allowing for the automatic loading and emptying of the voltammetric cell. Standard additions of TA and GSH standards were made automatically using Cavro syringe burettes. The voltammetric cell was rinsed twice with MQ for 30 seconds between each sample. Voltammetric analyses were controlled by NOVA software (version 2.1.4).

For CP of samples suspected to contain sulfide, a µAutolab potentiostat was connected to a Metrohm 663 VA stand through the IME663 interface and was controlled by the GPES software (Version 4.9) installed on a 32-bit laptop. A three-electrode system was also used. The working electrode was a 25 µm silver mercury amalgam microwire (silver microwire from Goodfellow, UK) fitted in a polypropylene pipette tip onto which a small vibrating rotor was fixed (1.5 V, 170 Hz) as described previously (Bi et al., 2013). Briefly, a Cu wire was inserted through a 100 µL pipette tip. The wire was connected to a 25 µm silver wire using a conductive, adhesive silver solution (Leitsilber L100, Maplin, UK). The Cu wire was pulled back leaving the silver microwire exposed out of the pipette tip. The tip was melted to secure the microwire by holding it in the mouth of a tubular oven set to 400 °C. The silver microwire was amalgamated with mercury by plating 2 mM Hg(II) (acidified at pH 2) at −0.4 V for 600 s in stagnant conditions. The amalgam electrode was then transferred to Milli-Q water and left overnight. The counter electrode was an iridium wire (approximately 2 cm in length, 150 µm diameter), and the reference electrode was an Ag/AgCl//KCl (3M) with a glass salt bridge filled with 3 M KCl.

2.5 Quantification of RSS concentrations

The voltammetric method used here was described by Pernet-Coudrier et al. (2013) to simultaneously quantify RSS and electroactive humic substances (referred to as refractory organic matter in the original paper). The concentrations and pseudopolarographic response of electroactive humic substances in these samples are reported elsewhere (Dulaquais et al., 2023; Portlock et al., in prep). Prior to analysis, 10 mL of seawater was acidified by adding 18µl of 1:1 MQ: HCL (reagent grade 32%) solution (final pH 2.04). Samples were also spiked with 100 nM molybdenum (Fisher scientific) for the determination of electroactive humic substances. Under a laminar flow hood, acidified seawater sample was automatically loaded into an acid-cleaned voltammetric quartz cell. Each new sample was purged with nitrogen (300s) before starting the analysis by CSV in differential pulse mode. The measurement consisted of a 30 s purge time, 150 s deposition at a potential (E_{dep}) of 0 V (with stirring on (setting 4 on the VA stand) followed by a 5 s rest (stirrer off) before the stripping scan (from 0 V to −0.6 V, modulation time of 60 ms, modulation amplitude of 60 mV, step potential of 2 mV and interval time of 0.1 s).

Similar to other studies (Fourrier and Dulaquais, 2024; Pernet-Coudrier et al., 2013), a well-defined peak was observed in all our acidified samples (pH 2) at a potential ~ −0.18 V, which was quantified using the standard thioacetamide (TA). Although the detected compound exhibits electrochemical characteristics similar to TA, TA is not naturally occurring in marine environments. Therefore, throughout the text, we refer to this peak in acidified conditions as a $RSS^2_{-0.18\ V}$ signal and give its concentration as TA equivalent. Similarly, in some samples, an additional broad peak was obtained at ~ −0.09 V. The $RSS^2_{-0.09\ V}$ signal exhibited a peak potential and shape similar to GSH; we refer to this peak as a GSH-like signal and we quantify its concentration in GSH equivalent. Quantification was done by standard additions (2 additions for each sample) of TA and GSH standards, added simultaneously. Typically, 4 repeat scans were performed for the analysis of the sample and after each of the 2 additions, giving a total of 12 scans for each determination and an approximate analysis time of 75 minutes per sample, including rinsing of the cell. In most cases, fixed standard additions of 80 nM TA and 1.6 nM GSH were made, unless the intensity of the initial peaks suggested a higher or lower concentration addition was required to quantify the peaks (see

Supplementary Figure S1 for example of voltammograms). For each measurement, the peak heights of $RSS^2_{-0.09\ V}$ and GSH-like signals were measured using ECDSOFT (Omanovic and Branica, 1998) after smoothing (Savitsky-Golay, smoothing factor 10).

Although TA is known to precipitate metals (Carrillo et al., 2018) and can form a Cu(I) complex in acidic conditions whose peak appear at -0.66 V (Table 1; Jeng et al., 1990) and interact with molybdenum (Farr and Laditan, 1974a and 1974b), all our standard additions were linear. This suggests that if complexation occurred, it had a negligible to impact the free TA concentration and/or the complexes are labile.

For quality control purposes, a Deep Sea Reference (DSR) seawater (Hansell lab, Batch 21 – 2021 – Lot 08-18, collected from 700m depth in the Florida Straits and acidified with HCl to pH 2) was used daily to check reproducibility. This was particularly important for TA because of instability in acidic conditions (Butler et al., 1958; Rosenthal and Taylor, 1957). The concentration of $RSS^2_{-0.18\ V}$ obtained in this reference seawater was measured at 56.1 ± 7.8 nM eq. TA (N=10, RSD =13.9%). If the daily check was not satisfactory, a new standard was made, which happened approximately on a monthly to bimonthly basis. Concentrations of GSH-like in the DSR were below the detection limits. The limit of detection was obtained by 3 times the standard deviation of 4 consecutive measurements of a seawater sample with low levels of TA (34 nM eq. TA) and GSH (2.5 nM eq. GSH). The limit of detection for TA was calculated to be 18 nM eq. TA and 0.43 nM for GSH. Error bars show the standard deviation of the intercept, determined by standard addition using Equation 1 (Harris, 2010).

$$s_x = \frac{s_y}{|\mathrm{m}|}\sqrt{\frac{1}{n}+\frac{\bar{\mathrm{y}}^2}{m^2\ \sum (x_i-\bar{\mathrm{x}})^2}} \quad (1)$$

Where s_x is the standard deviation of the compound being measured, s_y is the standard deviation in peak intensity across all data points, m is the slope of the standard addition, n is the number of data points (typically 12), $\bar{y}$ is the average peak height across all data points, x_i is the concentration of added standard for data points i, and $\bar{x}$ is the average concentration across all data points of the standard addition procedure.

2.6 Cathodic Pseudopolarography

CP was carried out on selected seawater samples, in unbuffered conditions (pH ~ 8.5), by recording the influence of the deposition potential on the intensity of the only RSS peak that we obtained at this pH (Supplementary Figure S1). This peak was located at ~ -0.52 V, similar to the peak reported in previous studies which is often attributed to the reduction of the Hg-S complex formed at the surface of the mercury during the accumulation step. In contrast to the quantification of $RSS^2_{-0.18\ V}$ and GSH-like signals, CP was achieved here only at natural pH because the peak is much more cathodic than the mercury oxidation wave (located in seawater at around -0.05 V), allowing for a wide range of deposition potentials to be tested. In acidic conditions, the $RSS^2_{-0.18\ V}$ and GSH-like peaks are present at relatively high potential thus limiting the range of deposition potential that could be tested.

For samples where the presence of sulfide was not expected, analysis was done on the SMDE in unbuffered, deoxygenated seawater samples. For comparison purposes, pseudopolarograms of TA and GSH standards (at 100 and 150 nM respectively) were obtained in UV digested seawater, also unbuffered and deoxygenated. For each pseudopolarographic experiment, 10 mL of seawater sample was loaded into an acid-cleaned voltammetric quartz cell and purged for 300 s. Pseudopolarograms started with an E_{dep} of 0 V and decreased by increments of -0.03 V until -0.72 V. The deposition time was 150 s at each E_{dep}, followed by a quiescence period of 5 s before the stripping scan (differential pulse from -0.3 V to -0.85 V, 20 ms modulation time, 60 mV modulation amplitude, 4 mV step potential 0.3 s interval time). Each pseudopolarogram took approximately 100 minutes to complete. Under these conditions of pH, only one natural RSS peak is detected at ~ -0.52 V and is referred here as $RSS^{8.5}_{-0.52\ V}$, much more cathodic than the 2 peaks obtained at pH 2 ($RSS^2_{-0.18\ V}$ and GSH-like), a change of approximately 55-63 mV/pH).

CP of samples suspected to contain sulfide were carried out using a Hg amalgam wire. Pseudopolarograms were obtained from an initial E_{dep} of -0.9 V up to 0 V, with +50 mV increment between successive measurements. The stripping parameters were as follows: differential pulse from -0.3 to -0.8 V, step of 6 mV, modulation amplitude of 50 mV, modulation time of 8 s and an interval time 0.1 s. The measurements were carried out without any purging nor stirring of the solution (instead the wire electrode was vibrated during the E_{dep}) to minimise the loss of sulfide during the experiment. A pseudopolarogram of the sulfide standard was obtained in 0.6 M NaCl (Fisher Scientific, UK) buffered at pH 9.2 with borate to minimise loss of sulfide through volatilisation (Aumond et al., 2012). The concentration of sulfide added was high (1 µM) allowing for a short deposition time (10 s). The sulfide peak potential was ~ -0.60 V, approximately 60 mV more cathodic than the TA peak (-0.54 V, Supplementary Table S1), even though these 2 peaks have been reported to have the same peak potential (e.g. Al-Farawati and van den Berg, 1997). The difference of 60 mV observed here can be attributed to differences in pH (9.2 vs 8.5, corresponding to around 40 mV cathodic shift) and differences in the working and reference electrodes. To account for these differences, the pseudopolarograms of all samples detected at the Hg amalgam wire were shifted anodically by 60 mV.

For comparison purposes, pseudpolarograms are given here as normalised to the highest intensity. Non-normalised pseudopolarograms of selected samples are given in Supplementary Figure S3.

3 Results

3.1 Hydrography and local conditions

A detailed account of the hydrography in this region has been previously described (Tilliette et al., 2022). Briefly, the Subtropical Underwater on the east and the Western South Pacific Central Water on the west dominated the main thermocline at a depth of 200 - 700 m, below the mixed layer (70 to 140 m). Immediately below were Antarctic Intermediate Waters, from 700-1300m, while the deep layer (> 1,300 m) composed two water masses: Pacific Deep Water (PDW)

and Lower Circumpolar Deep Water (LCDW). Across the cruise transect, the different water masses were distributed uniformly, except for the PDW and the LCDW. PDW was dominant in the Melanesian waters and Lau basin. In the Melanesian waters, LCDW was only present between 2,500 m and the seafloor. The Lau Basin had a low contribution of LCDW. However, in the deepest waters of the South Pacific Gyre, LCDW was the sole contributor.

Salinities ranged from 35.06 to 35.47 and temperature varied from 23.04 to 27.32 °C in the upper 100 m. The mixed layer ranged from 70-140 m deep during the cruise. The Lau basin is influenced by shallow hydrothermal activity, with at least two hydrothermal sites, PANAMAX and SIMONE (Figure 1A). Furthermore, a volcanic eruption in the region (Late'iki, previously Metis Shoal) began mid-October 2019, the month before the cruise. The main eruption continued until the 23rd October 2019 and minor eruptions continued into 2020. Satellite imagery suggested that there was a minor eruption on the 19th November (Yeo et al., 2022). S15 was the closest station in this study to Late'iki (~40 km south-west of Late'iki). S15 was sampled on the 24th November, 32 days after the main eruption ended and 5 days after the minor eruption.

3.2 Distribution of RSS in the WTSP Ocean

The distribution of $RSS^2_{-0.18\ V}$ and GSH-like compounds along the cruise transect are presented in Figures 1B, C respectively and the upper 500 m of all individual profiles are given in Figure 2. $RSS^2_{-0.18\ V}$ compounds were present throughout the whole water column at all stations, ranging from 48 to 984 nM (Figure 1B) with an average of 131 ± 16 nM across the transect (TA equivalent, N = 119). The average concentrations of $RSS^2_{-0.18\ V}$ compounds per station are given in Table 2. In the Lau Basin (stations 4, 11, 12, S15 and PANAMAX), the concentrations of $RSS^2_{-0.18\ V}$ compounds were higher than at adjacent stations (station 3 in the Melanesian waters and station 6 on the east side of the Tonga-Kermadec ridge). Moving further east to station 7 and 8 in the South Pacific Gyre, average TA concentrations decreased, with the lowest concentrations recorded at station 8. For most stations (3, 4, 6, 7, 8, 11 and 12), there were no clear trends with depth and the concentration remained quasi-uniform. The highest concentration (984 nM TA equivalent) was at PANAMAX (181 m). At the same depth, a strong decrease in Eh (Figure 2I) was observed (characteristic of reducing conditions), suggesting that the sample was collected in the hydrothermal plume. Station 2 (away from known hydrothermal activity) was characterised by high concentrations of $RSS^2_{-0.18\ V}$ compounds compared to the rest of the transect. At station 2, the average concentration of $RSS^2_{-0.18\ V}$ compounds were 242 ± 31 nM compared to the average concentration of 98 ± 12 nM across the cruise transect (excluding the PANAMAX station). $RSS^2_{-0.18\ V}$ concentrations at station 2 were similar to station 3 in the surface waters but were much higher at depth. While $RSS^2_{-0.18\ V}$ concentrations at station 3 remained between 66 and 112 nM throughout the water column, at station 2, there was a band of high $RSS^2_{-0.18\ V}$ material between 100 m and 3500 m, with a maximum concentration of 382 nM at 1200 m and high concentrations also in bottom waters, reaching 275 nM (Figure 1B). This pattern appears to be unrelated to water masses. GSH-like compounds were only detected in surface waters (upper 200 m) of most stations (Figure 1C). The concentrations ranged from 0.61 to 6.23 nM, with the maximum concentration observed at 46 m at station S15 in the Lau Basin (Figure 2D). Similar to $RSS^2_{-0.18\ V}$, GSH-like concentrations detected in the Lau Basin were slightly higher than those in adjacent waters (Table 2). At PANAMAX, concentrations of GSH-like compounds were also elevated (reaching almost 6 nM; Figure 2H) at the same depth as where the lowest Eh value was recorded suggesting that these samples were from the hydrothermal plume. In contrast to $RSS^2_{-0.18\ V}$, GSH-like concentrations detected at station 2 were relatively low, at similar levels as those encountered in the surface waters of station 7 and 8 of the oligotrophic South Pacific Gyre (Table 2). However, a high concentration (6.06 ± 0.9 nM) of GSH-like compounds was detected at 150m at station 7 (Figure 2D).

3.3 Pseudopolarography

3.3.1 Sulfide, glutathione and thioacetamide standards

Pseudopolarograms of sulfide, GSH and TA standards were recorded to be compared to those from selected samples at various stations. Although sulfide, GSH and TA all produce a peak located at a similar potential (at ~ -0.6, -0.51 and -0.50 V respectively), their pseudopolarographic response is different (Figure 3): sulfide can be detected at E_{dep} > -0.65 V (wave at around -0.63 V), GSH at E_{dep} > -0.5 V (wave around -0.45 V) while TA is only detected at E_{dep} > -0.075 V (wave around -0.04 V, Figure 3). The potential at which the pseudopolarographic waves occur is dependent on the stability of the adsorbed complex at the mercury surface. In the case of sulfide, mercury is easily oxidised due to the formation of the highly insoluble HgS complex pushing the reduction wave towards negative values. For GSH and TA, the waves are more positive and well separated. While GSH and TA are stable compounds during the experimental time (same pseudopolarograpms were obtained when repeated in the same solution), sulfide is well-known for its instability and rapid loss of signal, preventing analysis using the SMDE (Al-Farawati and van den Berg, 1997). Instead, we recorded the pseudopolarogram of sulfide under conditions that minimise its loss (see experimental section). Sulfide can be detected without any interference from GSH and TA when using a E_{dep} of -0.6 V. When E_{dep} is increased above that value, the sulfide signal intensity tends to decrease which is likely due to some loss of sulfide from solution, either through volatilisation, oxidation or complexation.

3.3.2 Marine samples

Surface, mid-water depth and bottom water samples from hydrothermal stations in the Lau Basin and from station 8 (the most representative open ocean sample), were analysed by CP to determine whether $RSS^{8.5}_{-0.52\ V}$ changed with depth and between both biogeochemical provinces. In addition, one sample from mid-depth at station 2, where high $RSS^2_{-0.18\ V}$ concentrations were detected, was chosen at random for characterisation of these RSS.

3.3.2.1 The Lau basin

Pseudopolarograms were performed on samples collected at PANAMAX (25, 110, 181 m) and at S15 (19, 399 and 1780 m

10.3389/fmars.2024.1426906

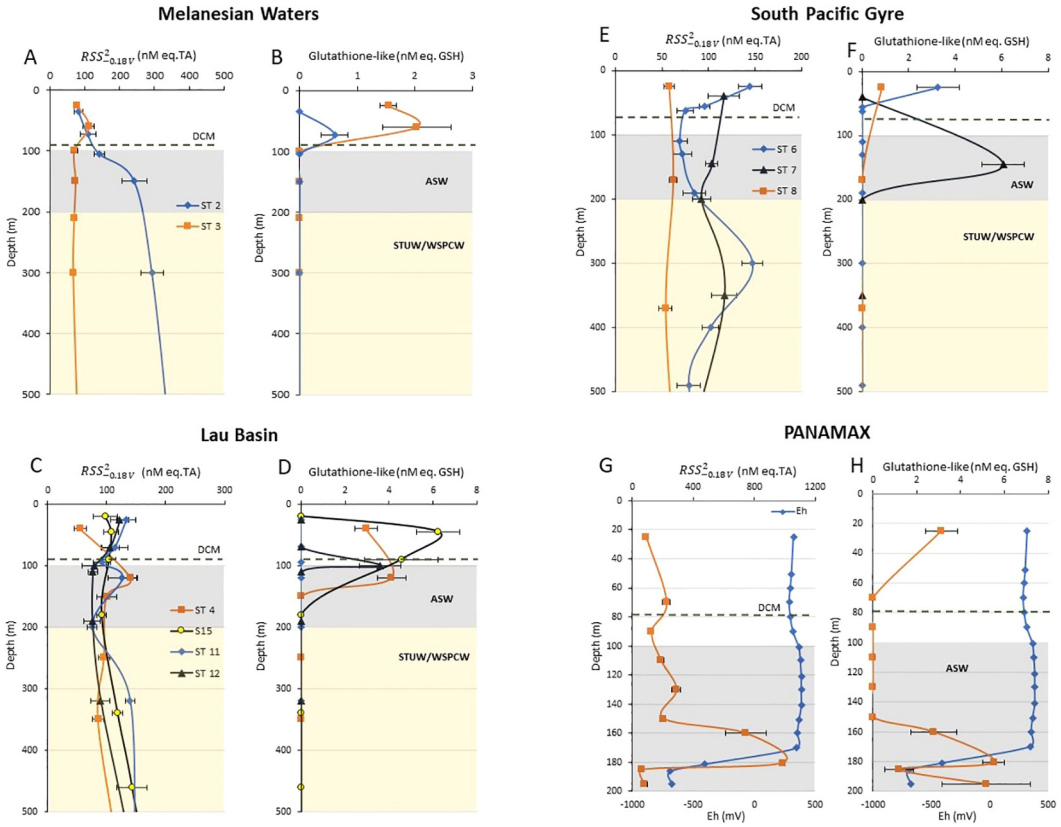

FIGURE 2
Concentrations of $RSS^2_{-0.18\ V}$ compounds in nM eq. TA and GSH-like compounds in nM eq. GSH in the upper 500 m of the Melanesian Basin **(A, B)**, Lau Basin **(C, D)** and South Pacific Gyre **(E, F)**. S15 was 15 km away from the SIMONE hydrothermal source. The shallow hydrothermal vent PANAMAX **(G, H)** was plotted separately along with Eh. Dashed line represents the average deep chlorophyll max (DCM) in each oceanographic region. There is no FluoChl data for stations 7 and 8, as the fluorimeter was unmounted at these stations. Concentrations were obtained using standard additions. Colour blocks show the different water masses. Artifactual Surface Water (ASW), Subtropical Underwater (STUW) and Western South Pacific Central Water (WSPCW) (Tilliette et al., 2022). Each of the profiles from each oceanographic region was plotted over 0–500 m **(A–F)**, except for PANAMAX which is plotted over 0–200 m **(G, H)**. Note that the scale of the x axis differs.

TABLE 2 Average concentration of $RSS^2_{-0.18\ V}$ and GSH-like compounds at each station. $RSS^2_{-0.18\ V}$ compounds were detected throughout the entire whole water column. GSH-like compounds were detected only detected in the upper 200 m.

Location	Station	Average $RSS^2_{-0.18\ V}$ compounds (nM eq.TA)	Average GSH-like concentration (nM eq.GSH)
Melanesian waters	2	242 ± 31	0.61 ± 0.23
	3	87 ± 7	1.76 ± 0.37
Lau Basin	4	99 ± 16	3.54 ± 0.57
	S15	122 ± 17	5.40 ± 1.34
	11	121 ± 18	<LOD
	12	104 ± 14	3.6 ± 0.95
	PANAMAX	285 ± 27	3.56 ± 0.99
South Pacific Gyre	6	98 ± 10	3.26 ± 0.91
	7	91 ± 10	6.06 ± 0.9
	8	61 ± 6	0.83 ± 0.13

<LOD, below detection limit.

depth). One sample of particular interest was the deep sample at PANAMAX (depth of 181 m), collected within the hydrothermal plume. As sulfide was likely present in this sample, pseudopolarograms were obtained at both the SMDE and Hg-Ag wire electrode (Figure 4). Firstly, the response of the sample at the Hg-Ag wire is very similar to that of the sulfide standard, highlighting the presence of sulfide. The concentration in the voltammetric cell was estimated to be >225 nM (estimation made from sensitivity obtained with 1 µM sulfide at E_{dep} = -0.59 V). Secondly, the response obtained at the SMDE following purging (assuming a complete loss of sulfide) with the peak height increasing with increasing E_{dep} suggests the presence of several RSS compounds: the lowest reduction wave detected at around -0.44 V was similar to GSH (reduction wave around -0.45 V). However, comparison with the pseudopolarogram of the TA standard strongly suggests that TA is not present at any significant concentration in this sample, if at all. The pseudopolarogram of the plume sample obtained at the SMDE did not experience sulfide interference as the sample was purged prior to analysis.

The other five samples tested from the Lau Basin (from 25 and 110m at PANAMAX and 19, 399 and 1780 m at S15) displayed pseudopolarograms with a very similar pattern (Figure 5), all having

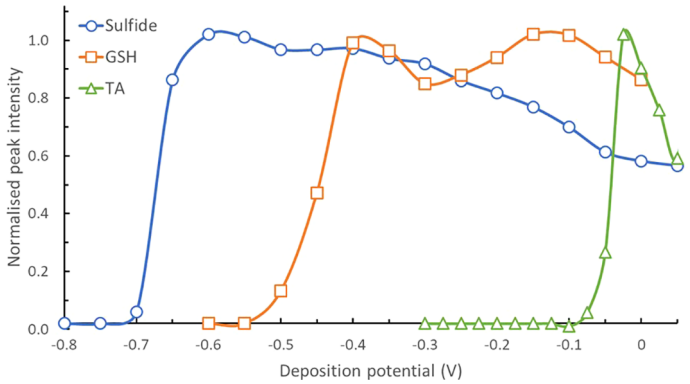

FIGURE 3
Normalised pseudopolarograms of sulfide, GSH and TA obtained (using SMDE at pH 8.5 see conditions in experimental section). For comparison purposes, pseudopolarograms are displayed as normalised to their highest peak intensity. In each case, the RSS peak being monitored is located at around -0.52 V (see Supplementary Table S1). Note that the sulfide data was obtained at a pH of 9.2 at the Hg-Ag wire and has been normalised to a pH of 8.5 at the HMDE by shifting the potential anodically by 60 mV. Peak potentials are in Supplementary Table S1.

a relatively positive reduction wave (from -0.15 to -0.05 V) irrespective of depth, indicating that GSH is not present in those samples. This is in agreement with results obtained in acidic conditions where GSH-like compounds were below detection limits for the PANAMAX 110 m sample and S15 19 m, 339 m and 1780 m samples (Figure 2). However, for the surface sample at PANAMAX (25 m), GSH-like compounds were found in acidic conditions but the pseudopolarogram did not display any reduction wave similar to that of GSH standard.

3.3.2.2 Station 8 – South Pacific Gyre

Pseudopolarograms of $RSS^{8.5}_{-0.52\ V}$ at station 8 (at depths of 25, 2400 and 5462 m) are shown in Figure 6. In contrast to other non-hydrothermal stations, the pseudopolarograms at station 8, particularly at 25m, extend much further cathodically: in the sub-surface sample, a reduction wave at around -0.47 V was observed, similar to the sample within the hydrothermal plume at PANAMAX after sulfide removal (obtained at the SMDE, Figure 4), both of which occurred at a similar potential as the reduction wave obtained for GSH. A second wave at ~ -0.15 V was also observed together with a slight increase at 0 V, similar to that of the TA. As depth increased (depth 2400 m), this most cathodic wave decreased in intensity and shifted slightly anodically (to ~ -0.44 V), still similar to GSH but no GSH-like signal was detected in acidic conditions. The signal intensity increased strongly and almost continuously at E_{dep} > -0.1 V highlighting the presence of unidentified compounds. In the deep sample (5462 m), a signal was only obtained for E_{dep} > -0.2 V with the presence of a wave at -0.15 V and -0.05 V, similar to that of TA standard.

3.3.2.3 Station 2 – North Fiji Basin

Figure 7 presents the pseudopolarogram of $RSS^{8.5}_{-0.52\ V}$ in a sample from station 2 where the TA concentration was particularly high ([TA] = 367 ± 33 nM, depth of 797 m,

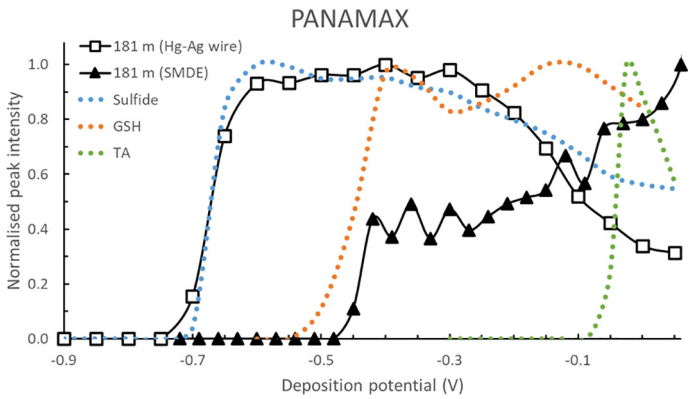

FIGURE 4
Normalised pseudopolarograms $RSS^{8.5}_{-0.52\ V}$ of the PANAMAX sample collected at 181 m (within the hydrothermal plume) using the Hg-Ag wire (15 s deposition time, for detection of sulfide) and using the SMDE (150 s deposition time for detection of other RSS). For comparison purposes, the response of the sulfide (most cathodic wave), GSH (middle wave) and TA (most anodic wave) standards are shown in dotted lines. The arrows represent the direction that the Edep was varied: anodic for the wire (sample and sulfide standard) and cathodic at the SMDE (sample, GSH and TA standards). In each case, the RSS peak being monitored is located at around -0.52 V (see Supplementary Table S1). Note that the sulfide data was obtained at a pH of 9.2 at the Hg-Ag wire and has been normalised to a pH of 8.5 at the SMDE by shifting the potential anodically by 60 mV. Peak potentials are in Supplementary Table S1.

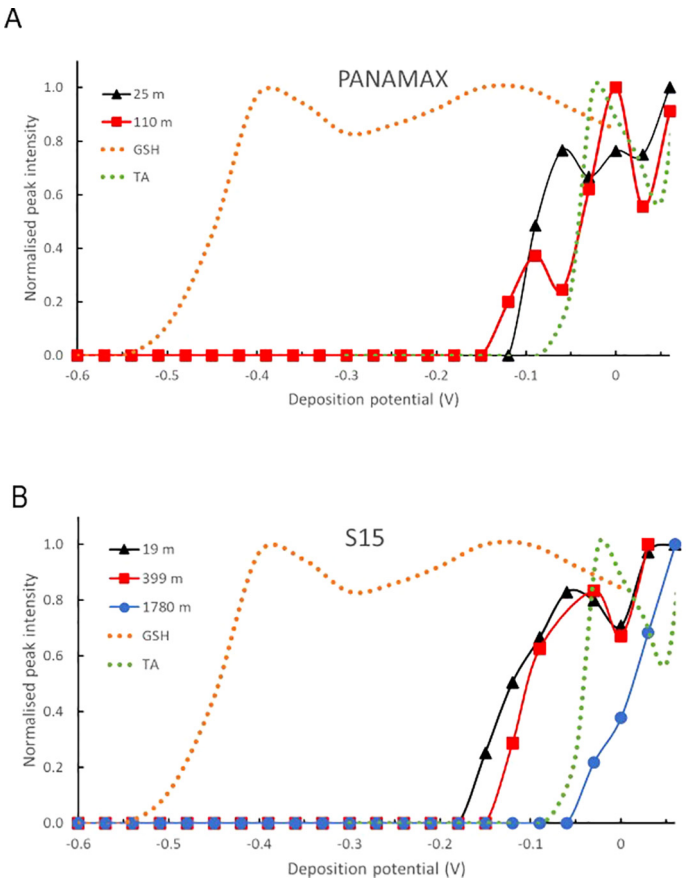

FIGURE 5
Normalised pseudopolarograms of $RSS^{8.5}_{-0.52\ V}$ in samples collected in the Lau Basin at various depths **(A)** at PANAMAX (25 and 110 m) and **(B)** at S15 (19, 399 and 1780 m). Pseudopolarograms obtained using the SMDE electrode, 150s deposition time. For comparison purposes, the response of the GSH (most cathodic wave) and TA (most anodic wave) standards are shown in dotted lines. In each case, the RSS peak being monitored is located at around -0.52 V (see Supplementary Table S1). Peak potentials are in Supplementary Table S1.

Figure 1B). A reduction wave at around -0.58 V was observed, ~ 50 mV more anodic than that of sulfide and 130 mV more cathodic than GSH. The peak intensity increased when increasing the E_{dep}, with two faint reduction waves seen at -0.32 V and -0.13 V, highlighting the presence of other unidentified RSS compounds. The expected increase at high E_{dep} observed with the TA standard was not seen in this seawater sample, showing that TA is not present in significant concentrations in this sample.

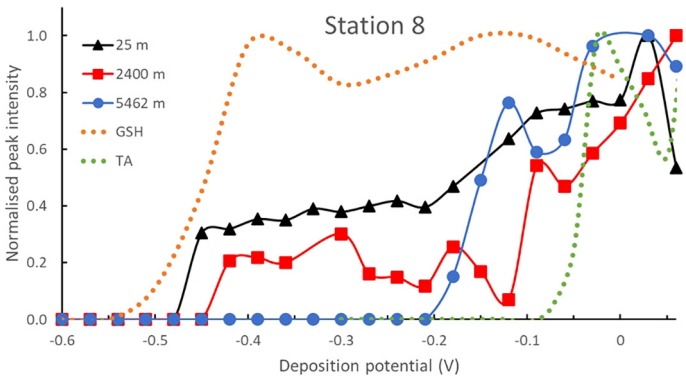

FIGURE 6
Normalised pseudopolarograms of $RSS^{8.5}_{-0.52\ V}$ in samples collected in the oligotrophic South Pacific Gyre, at Station 8 (25, 2400 and 5462 m). Pseudopolarograms obtained using the SMDE electrode, 150s deposition time. For comparison purposes, the response of the GSH (most cathodic wave) and TA standards (most anodic wave) are shown in dotted lines. In each case, the RSS peak being monitored is located at around -0.52 V (see Supplementary Table S1). Peak potentials are in Supplementary Table S1.

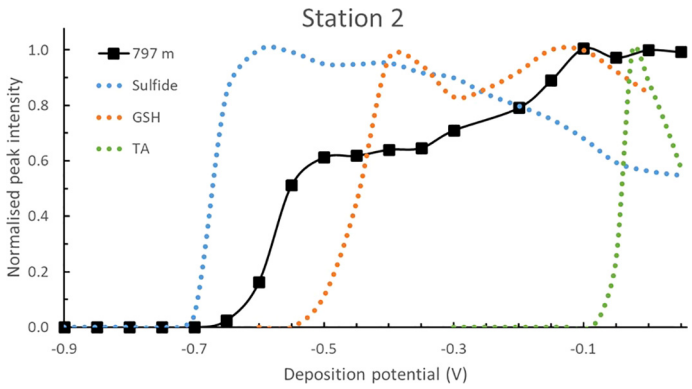

FIGURE 7
Normalised pseudopolarograms of $RSS^{8.5}_{-0.52\ V}$ in the sample collected at station 2, 797 m depth using the Hg-Ag wire (90 sec deposition time). For comparison purposes, the response of the sulfide (most cathodic wave), GSH (middle wave) and TA (most anodic wave) standards are shown in dotted lines. Peak potentials are in Supplementary Table S1. The peak potentials of the peaks being monitored in each pseudopolarograms are given in Supplementary Table S1. Note that both the sulfide and the 797 m sample data was obtained at a pH of 9.2 at the Hg-Ag wire. They have been normalised to a pH of 8.5 at the SMDE by shifting the pseudopolarogram anodically by 60 mV. Peak potentials are in Supplementary Table S1.

4 Discussion

4.1 RSS distribution in the WTSP

The vertical profiles of $RSS^2_{-0.18\ V}$ and GSH-like compounds suggest a combination of distinct and common processes drive their biogeochemical cycling. Both show some evidence of photodegradation, with near surface samples typically having a lower concentration than in underlying waters. For GSH-like compounds, this was seen at most stations, whereas for $RSS^2_{-0.18\ V}$ compounds, this was only observed at stations 2, 3 and 4. Photochemical destruction of RSS has been demonstrated to occur on the order of hours (Gomez-Saez et al., 2017; Laglera and van den Berg, 2006; Moingt et al., 2010). In the presence of UV-light, TA was reported to photodegrade at a faster rate than GSH (Laglera and van den Berg, 2006). In this study, $RSS^2_{-0.18\ V}$ compounds showed less evidence of photodegradation compared to GSH-like compounds, suggesting that active production of $RSS^2_{-0.18\ V}$ compounds is higher, or at the same rate of the photodegradation, or that the $RSS^2_{-0.18\ V}$ compounds do not behave identically to TA. Complexation with metals can affect photodegradation of RSS. Cu complexation has been shown to extend the half-life of TA, whereas it has been shown to accelerate the oxidation of GSH (Laglera and van den Berg, 2006; Moingt et al., 2010). The ratio of RSS to Cu determines how Cu complexation affects RSS photodegradation. In the surface waters (upper 200 m) of TONGA, the average concentration of total dCu was ~ 0.4 nmol kg^{-1} (Gonzalez-Santana., pers. comms. March 2024), which is relatively low compared to the RSS concentrations obtained in this study, suggesting that Cu complexation do not play a substantial role in RSS photodegradation.

Marine microbes have been shown to produce RSS both intracellularly and extracellularly when exposed to light in order to reduce stress from ROS (Mangal et al., 2020; Sunda et al., 2002). Previous studies have found a correlation between RSS, particularly GSH-like, with Chl *a* (Al-Farawati and van den Berg, 2001; Hu et al., 2006). In November 2019 in the WTSP, marine microbes were exposed to sunlight for ~ 13 h per day, which may have stimulated the production of RSS.

GSH-like compounds were only detected in the upper 200 m, suggesting biological production in surface waters, at concentrations similar to previous studies using a range of methods (Dupont et al., 2006; Kading, 2013; Le Gall and van den Berg, 1998; Swarr et al., 2016; Whitby et al., 2018). In this study, we found no correlation between the distribution of GSH-like compounds with Chl *a* (data not shown). For the majority of stations, a GSH-like maxima were observed sub-surface but above the deep chlorophyll max. Heterotrophic bacteria have also been suggested as a source of GSH-like compounds, which may explain the lack of correlation between GSH-like compounds and Chl *a* observed here, consistent with previous studies (Cameron and Pakrasi, 2011; Carfagna et al., 2016; Swarr et al., 2016). While heterotrophic bacteria are more abundant in the photic layer (0-100 m), unlike phototrophs, heterotrophic bacteria are present throughout the water column, therefore GSH-like compounds would be expected throughout the water column. However, GSH-like compounds were confined to the surface, possibly indicating low abundance and/or low metabolic activity of heterotrophs at depth. GSH-like compounds may still be produced at depth, but their turnover rate may be slower than their oxidation rate, which is only a few hours (Petzold and Sadler, 2008). The highest surface GSH concentration was detected at station S15 (6.23 nM at 46 m) in the hydrothermally active Lau Basin, possibly following the Late'iki eruption.

In comparison, $RSS^2_{-0.18\ V}$ compounds were detected at all depths across the transect (Figure 1B). $RSS^2_{-0.18\ V}$ compounds did not experience the same sub-surface maxima as GSH-like compounds, and there was no correlation between the distribution of $RSS^2_{-0.18\ V}$ compounds and Chl *a* (data not shown). However, this does not mean that $RSS^2_{-0.18\ V}$ compounds are not of biological origin. A previous study found that phytoplankton actively exude a compound electrochemically similar to TA (Leal et al., 1999). The lack of

correlation could be due to the stability of $RSS^2_{-0.18\ V}$ compounds away from direct sunlight, similar to TA which is relatively stable for long periods depending on environmental conditions (Howard et al., 2017; Mallory, 1968) allowing for its accumulation throughout the water column. TA can be a source of sulfur for marine microbes (Schmidt et al., 1982) which might also be the case for $RSS^2_{-0.18\ V}$. The persistence of $RSS^2_{-0.18\ V}$ compounds with depth could suggest that their uptake is slower than their rate of production.

We found slightly higher average concentration of GSH-like compounds than in previous studies, with a mean concentration of 3.4 ± 0.8 nM across the transect, compared to maximum concentrations of 0.8, 1.7 and 2.2 nM GSH in studies by Dupont et al. (2006); Kading (2013) and Swarr et al. (2016) respectively. The concentrations of $RSS^2_{-0.18\ V}$ compounds were lower than those detected in the North Pacific (Fourrier and Dulaquais, 2024) where they ranged from 118 ± 14 to 1140 ± 137 nM, with concentrations decreasing from surface to deep water. These nanomolar concentrations levels are much higher than those detected at natural pH in the North East Pacific where sub nM concentrations of RSS compounds were reported (Whitby et al., 2018). This large difference has to come from different experimental conditions (pH, standard, deposition potential) and different behaviour to these changes between the natural compounds and the standard. For instance, in our experiments, the intensity of the peaks at natural pH and in acidic conditions are in the same order of magnitude (nA range) while the sensitivity of the TA sharply decreases from natural pH to acidic conditions by a factor of at least 200 times. Although the reason for this loss in sensitivity is unclear (it cannot be explained by the protonation of TA in acidic conditions (pK of 1.76, (Rosenthal and Taylor, 1957)), this difference between the natural peak and the TA standard provides further evidence that the RSS peak at natural pH ($RSS^{8.5}_{-0.52\ V}$) is certainly not TA. Consequently, the concentration values reported here are conditional to the experimental parameters, are not relevant to TA and should therefore only be compared with great care to concentrations obtained by other techniques (or other pH).

Concentrations of both $RSS^2_{-0.18\ V}$ compounds and GSH-like compounds at the surface were higher in the Lau Basin than in the adjacent Melanesian Basin and South Pacific Gyre (Table 2), with concentrations decreasing with distance away from the Lau Basin. The Lau Basin experiences high primary production and high diazotrophic activity due to extensive shallow hydrothermal activity (Bonnet et al., 2023b) which might explain the higher levels of $RSS^2_{-0.18\ V}$ and GSH-like compounds. Hydrothermal vents also release trace metals such as copper, nickel, zinc and lead which can all be toxic to marine microbes, triggering biological production of RSS to reduce metal toxicity (Bjørklund et al., 2019; Courbot et al., 2004; Dupont and Ahner, 2005; Huang et al., 2018; Kumar et al., 2021; Navarrete et al., 2019; Pál et al., 2018; Steffens, 1990; Vasconcelos and Leal, 2001). In sulfidic conditions, high RSS concentrations (>500 nM) have been measured, such as in the Black Sea (Mopper and Kieber, 1991) and in sediment pore waters (Chapman et al., 2009). While such high concentrations were not observed here, the nearby volcanic and hydrothermal activity could also contribute to higher RSS concentrations.

The concentrations of $RSS^2_{-0.18\ V}$ compounds in the South Pacific Gyre decreased with distance away from the Lau Basin, suggesting an apparent dilution or weakening of the process responsible for its production in the Lau Basin, similar to what was previously observed for iron-binding ligands and DOM more broadly in this region (Mahieu et al., 2024). Station 8 displayed the lowest concentration of TA (average of 62 ± 5 nM in acidic conditions). In contrast, electroactive humic substances, which can also act as organic metal-binding ligands, were elevated at this station relative to other stations (Dulaquais et al., 2023; Portlock et al., in prep.).

4.2 Hydrothermal influence on sulfide and RSS production

In the PANAMAX plume (181 m), elevated concentrations of $RSS^2_{-0.18\ V}$ (984 ± 19 nM; Figure 2G) and GSH-like compounds (5.5 ± 0.5 nM; Figure 2H) were detected along with the presence of sulfide (>225 nM), suggesting active production of these compounds related to hydrothermal activity, either through abiotic or biotic processes. While µM levels of methanethiol have been detected in hydrothermal fluids (Dias et al., 2010; Reeves et al., 2014), no voltammetric signal was observed at its expected potential (Table 1; acidic pH -0.09 V; natural pH -0.43 V), probably because of dilution of the plume as well as a known short residence time for CH_3SH (Schäfer and Eyice, 2019).

Abiotic production of RSS in hydrothermal systems is tied to the thermodynamic and geochemical constraints of the system (temperature, pressure and chemical elements/starting materials). PANAMAX was characterised as having low O_2 concentrations (<150 µM), high CH_4 (>104 nM), high CO_2 (>645 µM), relatively high Fe (>50 nM) (Tilliette et al., 2022) and high H_2S (estimated at >225 nM, this study). The temperature and pH of the end-member fluids released from PANAMAX were not measured in this study, but the plume was recorded to be 21.2°C (mean of rest of transect (~200 m) 20.8°C) and the pH was found to be around 6.5 (Tilliette et al., 2023). The temperature of the fluids released from PANAMAX can be estimated from seawater boiling curves (Hannington et al., 2005; Stoffers et al., 2006). As PANAMAX is at a depth of around 200 m, it would imply that the temperature of end-member fluid would be no higher than 200°C. Although the pH of the end-member fluid is not known, other hydrothermal vents in the TONGA region have been reported to range from pH 1.2 to 6.1 (Hsu-Kim et al., 2008; Peters et al., 2021; Stoffers et al., 2006). The abiotic production of methanethiol can occur from the reaction of H_2S with hydrogen and CO/CO_2 (at 25°C and 1 bar) and theoretical calculations indicate that this reaction is viable in hydrothermal systems (Schulte and Rogers, 2004). CO was not measured in this study and has not been reported in hydrothermal systems, but experimental studies indicated that CO and CO_2 equilibrate at temperatures of ≥150°C (Foustoukos et al., 2001; Schulte and Rogers, 2004). Methanethiol can be a precursor for other RSS. Another chemical pathway is the reaction of H_2S, CO_2 and iron sulfide (FeS), a common component of hydrothermal systems (Findlay et al., 2019; Yücel et al., 2011), under anaerobic conditions, which yields a wide variety of organic sulfur compounds, mainly RSS, the production rate being largely influenced by the temperature (Heinen and Lauwers, 1996).

The production of RSS could also be due to biotic processes. Hydrothermal vents are able to sustain a wide variety of organisms due to the release of high concentrations of both metals and non-metals (Klinhammer et al., 1977; Resing et al., 2015), which can act as bio-essential nutrients for marine microbes (Aparicio-González et al., 2012; Lohan and Tagliabue, 2018). However, elevated concentrations of some chemicals can be harmful to marine microbes. In addition to the native biology around hydrothermal vents, buoyant hydrothermal plumes of the shallow vents (<200 m) can also reach the surface waters, affecting biological activity and RSS production. A recent study by Tilliette et al., 2023, found that when surface communities collected during the cruise in TONGA were exposed to hydrothermal fluids from PANAMAX, there was production of $RSS^{2}_{-0.18\ V}$ and GSH-like compounds (referred to as TA-like and GSH-like compounds). The addition of hydrothermal fluids led to the immediate production of $RSS^{2}_{-0.18\ V}$ compounds, thought to be produced by Synechococcus ecotypes to detoxify their environment. In contrast, GSH-like compounds were produced gradually over time, suggesting that they were not produced to detoxify the environment. Marine microbes have been found to produce GSH-like compounds to disassociate strongly bound Cu and act as a 'weak ligand shuttle', to make Cu accessible (Semeniuk et al., 2015). The use of GSH-like compounds as a 'weak ligand shuttle' may not be limited to Cu.

GSH also plays a vital role in the growth and regulation of marine microbes and therefore is abundant intracellularly (Ahner et al., 2002; Dupont et al., 2004; Giovanelli, 1987). The elevated concentrations of GSH-like compounds at PANAMAX could also be due to the breakdown of cyanobacteria. In the study by Tilliette et al., 2023, the abundance of cyanobacteria decreased after the addition of PANAMAX hydrothermal fluids, possibly due to addition of metal rich fluids. Cyanobacteria are extremely sensitive to dCu (Brand et al., 1986). Concentrations of dCu within the PANAMAX plume were similar to the rest of the transect (hydrothermal plume 0.4 nmol kg^{-1}; Gonzalez-Santana., pers. comms. March 2024), however Cu toxicity depends on its speciation. In some hydrothermal systems, dCu concentrations have been found to exceed ligand concentrations (Kleint et al., 2015), which could increase Cu toxicity and stimluate the production of GSH or the release of intracellular GSH-like compounds into the marine environment from cellular breakdown.

Hydrothermal vents are well-known to be a source of sulfides (Cotte et al., 2018; Damm et al., 1995; Dias et al., 2010), including those from the Lau Basin (Hsu-Kim et al., 2008; Yücel et al., 2011). Here, sulfide was identified only in the sample collected in the plume (Figure 4), with an estimated concentration > 225 nM. In this sample, a reduction wave at -0.44 V was apparent at the SMDE, similar to GSH-like compounds, and in agreement with the signal detected in acidic conditions (quantified as 5.5 nM). The signal increased with increasing E_{dep} highlighting the presence of other, unidentified RSS compounds in the plume. Although the PANAMAX vent is shallow at around 200 m, pseudopolarograms of $RSS^{8.5}_{-0.52\ V}$ in samples collected at the sub-surface (25 m) and below the deep chlorophyll max (110 m) did not show reduction waves characteristic of sulfide or GSH standards (Figure 5A), suggesting that RSS present in the plume at 180 m depth are not sufficiently stable to reach surface waters.

4.3 Station 2 – North Fiji Basin

$RSS^{2}_{-0.18\ V}$ concentrations were high throughout the water column at station 2 compared to the rest of the transect. Meanwhile, GSH-like were only detected in surface waters (Figure 1C). High concentrations of Fe-binding ligands were also found at depth at station 2 (max concentration at 1800 m, see Mahieu et al., 2024). The presence of high RSS and Fe-binding ligands at this station suggests either the production of these compounds within the water column or input from hydrothermal systems. Station 2 is located in the North Fiji Basin, which is a highly complex back arc-basin. To our knowledge, the North Fiji Basin has two spreading ridges (Central spreading ridge and West Fiji Ridge, Figure 1), as well as multiple fracture zones. Other oceanographic regions with multiple plate boundaries experience intense hydrothermal activity. Active venting has been confirmed in the North Fiji basin (Bendel et al., 1993), along with evidence of a 'megaplume' (Nojiri et al., 1989). Megaplumes have also been observed in the neighbouring Lau Basin (Baumberger et al., 2020). Megaplumes or event plumes are a significant, intermittent release of hydrothermal activity. These eruptions produce a buoyant plume that can be observed up to 1000 m above the sea floor. Previous megaplumes have been found to be 20 km in diameter and have a thickness of 700 m (Baker et al., 1987), which could explain why we observe high concentrations of $RSS^{2}_{-0.18\ V}$ compounds, at depth. While no active vents have yet been reported near station 2, their existence cannot be ruled out definitively. These areas are rarely investigated as most studies focus on the plate boundaries.

High metal concentrations are typically evidence for the presence of hydrothermal vents, however this is not the case at station 2. Dissolved Fe concentrations increased from 1000 m to the seafloor (above 0.5 nmol kg^{-1}) but this increase was not significant compared to the rest of the transect (Tilliette et al., 2022). Other dissolved metals such as Cu and Zn did not show an increase compared to the rest of the transect (Gonzalez-Santana, pers. comms. March 2024). Hydrothermal vent fluid chemistry is linked to the conditions which the vent is situated in and may release metal concentrations similar to seawater (Hodgkinson et al., 2015; Seyfried et al., 2015). These low metal vents have been found in ultramafic rocks, where metals in the fluids precipitate out in sub surface reactions. Dredges from the Hunter Fracture Zone have a large amount of ultramafic rock (Tararin et al., 2003). In addition, hydrothermal vents hosted in ultramafic rock are thought to produce ideal conditions for the production of organic compounds (Konn et al., 2009; Lang et al., 2010; Sander and Koschinsky, 2011).

At the time of the cruise, station 2 was on the convergence of two counter-rotating eddies, which saw high abundance of *Trichodesmium* compared to the surrounding areas (Benavides et al., 2021). Over time these communities sink. While N_2 fixation rates decrease with depth, *Trichodesmium* and other diazotrophs are still active in the mesopelagic zone (Benavides et al., 2022). For some diazotrophic bacteria there is a link between N_2-fixation and RSS biosynthesis. Diazotrophs are able to produce RSS to complex with ROS generated during N_2-fixation (Bocian-Ostrzycka et al., 2017). It is also thought that RSS play a role in N_2-fixation,

potentially as cofactors for enzymes involved in N_2-fixation or as signalling molecules that regulate the activity of genes related to N-fixation (Kalloniati et al., 2015). This link of N_2-fixation and RSS biosynthesis is primarily linked to terrestrial diazotrophs and should be investigated for marine diazotrophs. As diazotrophs sink and experience stress/death, they may release intracellular RSS, which may have contributed to the elevated concentrations of $RSS^{2}_{-0.18\ V}$ compounds at this station.

4.4 RSS diversity in the WTSP

RSS encompass a wide range of sulfur-bearing compounds and pseudopolarography is helpful to differentiate compounds (e.g. Figure 3). For instance, when comparing the pseudopolarograms of the samples collected in the plume at PANAMAX (Figure 4) or at depth at station 2 (Figure 7) with that of the TA standard, the characteristic reduction wave at -0.04 V is missing, indicating that TA is not present in significant concentrations in any of those samples. The $RSS^{2}_{-0.18\ V}$ signal detected at low pH is therefore due to other RSS compounds whose peak potential is the same as TA in acidic conditions. $RSS^{2}_{-0.18\ V}$ compounds (often referred to as TA-like compounds) have been observed in estuarine and river waters (Marie et al., 2017, 2015; Superville et al., 2013) and phytoplankton have also been shown to exude a RSS electrochemically similar to TA (Leal et al., 1999). However, TA is not known to be present in marine environments and is toxic to marine organisms with concentrations of 50 nM causing inhibition of growth in phytoplankton (Vasconcelos et al., 2002). In contrast to TA, GSH is thought to be common in marine waters (Dupont et al., 2006; Kading, 2013; Tang et al., 2000). The shape of the pseudopolarograms from PANAMAX (depth 181 m) and station 8 (surface at 25 m) were similar to that of GSH (Figures 4 and 6 respectively). While pseudopolarography cannot provide the exact identification of the RSS present, it can provide interesting details on the behaviour of various RSS that exist in the marine environment.

5 Conclusion

This study provides a quantitative and qualitative data set of species-specific RSS ($RSS^{2}_{-0.18\ V}$ and GSH-like compounds) in the WTSP Ocean. We find RSS are ubiquitous in the WTSP and concentrations are higher in the Melanesian waters and Lau basins than in the South Pacific Gyre, most likely because of sources linked to hydrothermal activity. Vertical profiles of $RSS^{2}_{-0.18\ V}$ and GSH-like compounds suggest a combination of distinct and common processes drive their biogeochemical cycling. $RSS^{2}_{-0.18\ V}$ compounds were detected in all sampled depths, while GSH-like compounds were confined to the upper 200 m, with both showing some evidence of photodegradation. Hydrothermal influence was particularly evident at the PANAMAX site, the only site where sulfide was detected (within a hydrothermal plume sample). Relatively high concentrations of $RSS^{2}_{-0.18\ V}$ and GSH-like compounds were also obtained in the hydrothermal plume, possibly due to a mixture of biotic and abiotic processes. Station 2 in the Melanesian Basin also saw elevated concentrations of $RSS^{2}_{-0.18\ V}$ compounds relative to other stations excluding the hydrothermal station, along the entire water column and at depth. The elevated concentrations suggest the production of these compounds, likely through unidentified local hydrothermal input, or possibly through *in-situ* production at this station.

Pseudopolarography of $RSS^{8.5}_{-0.52\ V}$ highlights the diversity of RSS compounds present in water. Most samples selected for pseudopolarography did not show a characteristic wave for TA suggesting that the $RSS^{2}_{-0.18\ V}$ signal detected in acidic conditions in these samples is not TA, while pseudopolarography supported the presence of GSH. Pseudopolarograms varied significantly between samples and highlighted the presence of various RSS substances, based on the variation and shape of the pseudopolarographic wave. While voltammetry is always prone to coalescence of peaks, pseudopolarography may be used as a tool to identify, and possibly quantify, some RSS species but this is a challenging task if many unknown RSS are present altogether. Studying the chemical stability of these RSS in relation to their reduction wave potential might provide further insights into their identity and biogeochemical cycling.

Data availability statement

The datasets presented in this study can be found in online repositories. The names of the repository/repositories and accession number(s) can be found below: http://www.obs-vlfr.fr/proof/php/TONGA/tonga.php#SA.

Author contributions

GP: Writing – original draft, Writing – review & editing, Investigation. HW: Supervision, Writing – review & editing. PS: Supervision, Writing – review & editing.

Funding

The author(s) declare financial support was received for the research, authorship, and/or publication of this article. The work presented in this publication was funded by the Natural Environment Research Council (NERC) EAO Doctoral Training Partnership (grant NE/L002469/1). This work contributes to the TONGA project (Shallow hydrothermal sources of trace elements: possible consequences on biological productivity and the biological carbon pump). The TONGA cruise (GEOTRACES GPpr14, November 2019, https://doi.org/10.17600/18000884) was funded by the TGIR Flotte Océanographique Française, the A-MIDeX foundation of Aix-Marseille University, the LEFE-CYBER and GMMC programs, and the ANR (grant TONGA ANR-18- CE01-0016). This work was partially supported by the "PHC Alliance" programme, funded by the UK Department for Business, Energy & Industrial Strategy (now DSIT), the French Ministry for Europe and Foreign Affairs, and the French Ministry of Higher Education, Research and Innovation. The International GEOTRACES

Programme is possible in part thanks to the support from the U.S. National Science Foundation (OCE-2140395) to the Scientific Committee on Oceanic Research (SCOR).

Acknowledgments

We warmly thank the scientific team, the captain, and the crew of the R/V L'Atalante for their cooperative efforts at sea throughout the TONGA cruise. We thank the members of the trace metal sample team, and V. Taillander for the CTD acquisition and data treatment. We also acknowledge S. Bonnet for her helpful input on the manuscript.

Conflict of interest

The authors declare that the research was conducted in the absence of any commercial or financial relationships that could be construed as a potential conflict of interest.

The reviewer RB declared a past co-authorship with the author HW to the handling editor.

Publisher's note

Supplementary material

The Supplementary Material for this article can be found online at: https://www.frontiersin.org/articles/10.3389/fmars.2024.1426906/full#supplementary-material

References

Ahner, B., Wei, L., Oleson, J., and Ogura, N. (2002). Glutathione and other low molecular weight thiols in marine phytoplankton under metal stress. *Mar. Ecol. Prog. Ser.* 232, 93–103. doi: 10.3354/meps232093

Al-Farawati, R., and van den Berg, C. M. G. (1997). The determination of sulfide in seawater by flow-analysis with voltammetric detection. *Mar. Chem.* 57, 277–286. doi: 10.1016/S0304-4203(97)00014-5

Al-Farawati, R., and van den Berg, C. M. G. (2001). Thiols in coastal waters of the western North Sea and English Channel. *Environ. Sci. Technol.* 35, 1902–1911. doi: 10.1021/es000073i

Aparicio-González, A., Duarte, C. M., and Tovar-Sánchez, A. (2012). Trace metals in deep ocean waters: A review. *J. Mar. Syst.* 100–101, 26–33. doi: 10.1016/j.jmarsys.2012.03.008

Apel, K., and Hirt, H. (2004). REACTIVE OXYGEN SPECIES: metabolism, oxidative stress, and signal transduction. *Annu. Rev. Plant Biol.* 55, 373–399. doi: 10.1146/annurev.arplant.55.031903.141701

Ardyna, M., Lacour, L., Sergi, S., d'Ovidio, F., Sallée, J.-B., Rembauville, M., et al. (2019). Hydrothermal vents trigger massive phytoplankton blooms in the Southern Ocean. *Nat. Commun.* 10, 2451. doi: 10.1038/s41467-019-09973-6

Aumond, V., Waeles, M., Salaün, P., Gibbon-Walsh, K., van den Berg, C. M. G., Sarradin, P.-M., et al. (2012). Sulfide determination in hydrothermal seawater samples using a vibrating gold micro-wire electrode in conjunction with stripping chronopotentiometry. *Anal. Chim. Acta* 753, 42–47. doi: 10.1016/j.aca.2012.09.044

Baba, S. P., and Bhatnagar, A. (2018). Role of thiols in oxidative stress. *Curr. Opin. Toxicol.* 7, 133–139. doi: 10.1016/j.cotox.2018.03.005

Baker, E. T., Massoth, G. J., and Feely, R. A. (1987). Cataclysmic hydrothermal venting on the Juan de Fuca Ridge. *Nature* 329, 149–151. doi: 10.1038/329149a0

Baker, E. T., Walker, S. L., Massoth, G. J., and Resing, J. A. (2019). The NE Lau Basin: Widespread and abundant hydrothermal venting in the back-arc region behind a superfast subduction zone. *Front. Mar. Sci.* 6. doi: 10.3389/fmars.2019.00382

Baumberger, T., Lilley, M. D., Lupton, J. E., Baker, E. T., Resing, J. A., Buck, N. J., et al. (2020). Dissolved gas and metal composition of hydrothermal plumes from a 2008 submarine eruption on the northeast lau spreading center. *Front. Mar. Sci.* 7. doi: 10.3389/fmars.2020.00171

Benavides, M., Bonnet, S., Le Moigne, F. A. C., Armin, G., Inomura, K., Hallstrøm, S., et al. (2022). Sinking Trichodesmium fixes nitrogen in the dark ocean. *ISME J.* 16, 2398–2405. doi: 10.1038/s41396-022-01289-6

Benavides, M., Conradt, L., Bonnet, S., Berman-Frank, I., Barrillon, S., Petrenko, A., et al. (2021). Fine-scale sampling unveils diazotroph patchiness in the South Pacific Ocean. *ISME Commun.* 1. doi: 10.1038/s43705-021-00006-2

Bendel, V., Fouquet, Y., Auzende, J.-M., Lagabrielle, Y., Grimaud, D., and Urabe, T. (1993). The White Lady hydrothermal field, North Fiji back-arc basin, Southwest Pacific. *Economic Geology* 88, 2237–2245. doi: 10.2113/gsecongeo.88.8.2237

Bi, Z., Salaün, P., and van den Berg, C. M. G. (2013). Determination of lead and cadmium in seawater using a vibrating silver amalgam microwire electrode. *Anal. Chim. Acta* 769, 56–64. doi: 10.1016/j.aca.2013.01.049

Bjørklund, G., Crisponi, G., Nurchi, V. M., Cappai, R., Djordjevic, A. B., and Aaseth, J. (2019). A review on coordination properties of thiol-containing chelating agents towards mercury, cadmium, and lead. *Molecules.* 24, 3247. doi: 10.3390/molecules24183247

Bluhm, K., Croot, P., Wuttig, K., and Lochte, K. (2010). Transformation of iodate to iodide in marine phytoplankton driven by cell senescence. *Aquat Biol.* 11, 1–15. doi: 10.3354/ab00284

Bocian-Ostrzycka, K. M., Grzeszczuk, M. J., Banaś, A. M., and Jagusztyn-Krynicka, E. K. (2017). Bacterial thiol oxidoreductases — from basic research to new antibacterial strategies. *Appl. Microbiol. Biotechnol.* 101, 3977–3989. doi: 10.1007/s00253-017-8291-8

Bonnet, S., Benavides, M., Le Moigne, F. A. C., Camps, M., Torremocha, A., Grosso, O., et al. (2023b). Diazotrophs are overlooked contributors to carbon and nitrogen export to the deep ocean. *ISME J.* 17, 47–58. doi: 10.1038/s41396-022-01319-3

Bonnet, S., Caffin, M., Berthelot, H., Grosso, O., Benavides, M., Helias-Nunige, S., et al. (2018). In-depth characterization of diazotroph activity across the western tropical South Pacific hotspot of N2 fixation (OUTPACE cruise). *Biogeosciences* 15, 4215–4232. doi: 10.5194/bg-15-4215-2018

Bonnet, S., Caffin, M., Berthelot, H., and Moutin, T. (2017). Hotspot of N2 fixation in the western tropical South Pacific pleads for a spatial decoupling between N2 fixation and denitrification. *PNAS* 114, E2800–E2801. doi: 10.17600/15000900

Bonnet, S., Guieu, C., Taillandier, V., Boulart, C., Bouruet-Aubertot, P., Gazeau, F., et al. (2023a). Natural iron fertilization by shallow hydrothermal sources fuels diazotroph blooms in the ocean. *Science 1979* 380, 812–817. doi: 10.1126/science.abq4654

Brand, L. E., Sunda, W. G., and Guillard, R. R. L. (1986). Reduction of marine phytoplankton reproduction rates by copper and cadmium. *J. Exp. Mar. Biol. Ecol.* 96, 225–250. doi: 10.1016/0022-0981(86)90205-4

Butler, E. A., Peters, D. G., and Swift, E. H. (1958). Hydrolysis reactions of thioacetamide in aqueous solutions. *Anal. Chem.* 30, 1379–1383. doi: 10.1021/ac60140a027

Caffin, M., Moutin, T., Ann Foster, R., Bouruet-Aubertot, P., Michelangelo Doglioli, A., Berthelot, H., et al. (2018). N2 fixation as a dominant new N source in the western tropical South Pacific Ocean (OUTPACE cruise). *Biogeosciences* 15, 2565–2585. doi: 10.5194/bg-15-2565-2018

Cameron, J. C., and Pakrasi, H. B. (2011). Glutathione facilitates antibiotic resistance and photosystem I stability during exposure to gentamicin in cyanobacteria. *Appl. Environ. Microbiol.* 77, 3547–3550. doi: 10.1128/AEM.02542-10

Carfagna, S., Bottone, C., Cataletto, P. R., Petriccione, M., Pinto, G., Salbitani, G., et al. (2016). Impact of sulfur starvation in autotrophic and heterotrophic cultures of the extremophilic microalga galdieria phlegrea (Cyanidiophyceae). *Plant Cell Physiol.* 57, 1890–1898. doi: 10.1093/pcp/pcw112

Carrillo, A., Mota, M. L., Carrasco, L. A., Cruz, E. C., Luque, P. A., Mireles, M. C., et al. (2018). Low-Temperature synthesis of CdS and ZnS nanoparticles by solution method using an anionic surfactant. *Chalcogenide Lett.* 15, 565–571.

Chapman, C. S., Capodaglio, G., Turetta, C., and van den Berg, C. M. G. (2009). Benthic fluxes of copper, complexing ligands and thiol compounds in shallow lagoon waters. *Mar. Environ. Res.* 67, 17–24. doi: 10.1016/j.marenvres.2008.07.010

Chu, C., Stamatelatos, D., and McNeill, K. (2017). Aquatic indirect photochemical transformations of natural peptidic thiols: impact of thiol properties, solution pH, solution salinity and metal ions. *Environ. Sci. Process Impacts* 19, 1518–1527. doi: 10.1039/C7EM00324B

Ciglenečki, I., and Ćosović, B. (1996). Electrochemical study of sulfur species in seawater and marine phytoplankton cultures. *Mar. Chem* 52, 87–97. doi: 10.1016/0304-4203(95)00080-1

Cotte, L., Omanović, D., Waeles, M., Laës, A., Cathalot, C., Sarradin, P. M., et al. (2018). On the nature of dissolved copper ligands in the early buoyant plume of hydrothermal vents. *Environ. Chem.* 15, 58–73. doi: 10.1071/EN17150

Courbot, M., Diez, L., Ruotolo, R., Chalot, M., and Leroy, P. (2004). Cadmium-responsive thiols in the ectomycorrhizal fungus Paxillus involutus. *Appl. Environ. Microbiol.* 70, 7413–7417. doi: 10.1128/AEM.70.12.7413-7417.2004

Cutter, G., Casciotti, K., Croot, P., Geibert, W., Geochemistry, M., Heimbürger, L.-E., et al. (2017). *Sampling and sample-handling protocols for GEOTRACES cruises.*

Damm, K. L., Oosting, S. E., Kozlowski, R., Buttermore, L. G., Colodner, D. C., Edmonds, H. N., et al. (1995). Evolution of East Pacific Rise hydrothermal vent fluids following a volcanic eruption. *Nature* 375, 47–50. doi: 10.1038/375047a0

Dias, D., do Nascimento, P. C., Jost, C. L., Bohrer, D., de Carvalho, L. M., and Koschinsky, A. (2010). Voltammetric determination of low-molecular-weight sulfur compounds in hydrothermal vent fluids – studies with hydrogen sulfide, methanethiol, ethanethiol and propanethiol. *Electroanalysis* 22, 1066–1071. doi: 10.1002/elan.200900472

Dulaquais, G., Fourrier, P., Guieu, C., Mahieu, L., Riso, R., Salaun, P., et al. (2023). The role of humic-type ligands in the bioavailability and stabilization of dissolved iron in the Western Tropical South Pacific Ocean. *Front. Mar. Sci.* 10. doi: 10.3389/fmars.2023.1219594

Dupont, C. L., and Ahner, B. A. (2005). Effects of copper, cadmium, and zinc on the production and exudation of thiols by Emiliania huxleyi. *Limnol. Oceanogr.* 50, 508–515. doi: 10.4319/lo.2005.50.2.0508

Dupont, C. L., Moffett, J. W., Bidigare, R. R., and Ahner, B. A. (2006). Distributions of dissolved and particulate biogenic thiols in the subartic Pacific Ocean. *Deep Sea Res. 1 Oceanogr. Res. Pap.* 53, 1961–1974. doi: 10.1016/j.dsr.2006.09.003

Dupont, C. L., Nelson, R. K., Bashir, S., Moffett, J. W., and Ahner, B. A. (2004). Novel copper-binding and nitrogen-rich thiols produced and exuded by Emiliania huxleyi. *Limnol. Oceanogr.* 49, 1754–1762. doi: 10.4319/lo.2004.49.5.1754

Farr, J. P. G., and Laditan, G. O. A. (1974a). The polarography of molybdate in the presence of organic sulphur and nitrogen compounds part II. The polarographic estimation of molybdenum (VI) with thioacetamide. . *J. Less Common Metals* 36, 161–168. doi: 10.1016/0022-5088(74)90095-2

Farr, J. P. G., and Laditan, G. O. A. (1974b). The polarography of molybdate in the presence of organic sulphur and nitrogen compounds part I. The electrochemical behaviour of aqueous acidified solutions of ammonium molybdate with thioacetamide. *J. Less Common Metals* 36, 151–160. doi: 10.1016/0022-5088(74)90094-0

Feely, R. A., Baker, E. T., Marumo, I. K., Urabe, T., ISHIBASHI, J., Gendron, J., et al. (1996). Hydrothermal plume particles and dissolved phosphate over the superfast-spreading southern East Pacific Rise. *Geochim. Cosmochim. Acta* 60, 2297–2323. doi: 10.1016/0016-7037(96)00099-3

Findlay, A. J., Estes, E. R., Gartman, A., Yücel, M., Kamyshny, A., and Luther, G. W. (2019). Iron and sulfide nanoparticle formation and transport in nascent hydrothermal vent plumes. *Nat. Commun.* 10, 1597. doi: 10.1038/s41467-019-09580-5

Fourrier, P., and Dulaquais, G. (2024). Low-molecular-weight reduced sulfur substances: A major component of nonvolatile dissolved organic sulfur in the Pacific Ocean. *Limnol Oceanogr Lett.* doi: 10.1002/lol2.10417

Foustoukos, D. I., Allen, D. E., Fu, Q., and Seyfried, W. E. (2001). "Experimental study of CO2(aq)/CO(aq) redox equilibria at elevated temperatures and pressures: The effect of pH on reaction relations," in *Goldschmidt Conference.*

Gao, Z., and Guéguen, C. (2018). Distribution of thiol, humic substances and colored dissolved organic matter during the 2015 Canadian Arctic GEOTRACES cruises. *Mar. Chem.* 203, 1–9. doi: 10.1016/j.marchem.2018.04.001

German, C. R., Baker, E. T., Connelly, D. P., Lupton, J. E., Resing, J., Prien, R. D., et al. (2006). Hydrothermal exploration of the fonualei rift and spreading center and the northeast lau spreading center. *Geochemistry Geophysics Geosystems* 7, 1-15. doi: 10.1029/2006GC001324

Giovanelli, J. (1987). Sulfur amino acids of plants: an overview. *Methods Enzymol.* 143, 419–426. doi: 10.1016/0076-6879(87)43073-5

Gomez-Saez, G. V., Dittmar, T., Holtappels, M., Pohlabeln, A. M., Lichtschlag, A., Schnetger, B., et al. (2021). Sulfurization of dissolved organic matter in the anoxic water column of the Black Sea. *Sci. Adv.* 7. doi: 10.1126/sciadv.abf6199

Gomez-Saez, G. V., Pohlabeln, A. M., Stubbins, A., Marsay, C. M., and Dittmar, T. (2017). Photochemical alteration of dissolved organic sulfur from sulfidic porewater. *Environ. Sci. Technol.* 51, 14144–14154. doi: 10.1021/acs.est.7b03713

Guieu, C., and Bonnet, S. (2019). *TONGA 2019 cruise, R/V L'Atalante [WWW document].* doi: 10.17600/18000884

Guieu, C., Bonnet, S., Petrenko, A., Menkes, C., Chavagnac, V., Desboeufs, K., et al. (2018). Iron from a submarine source impacts the productive layer of the Western Tropical South Pacific (WTSP). *Sci. Rep.* 8, 1-9. doi: 10.1038/s41598-018-27407-z

Hannington, M. D., De Ronde, C. E. J., and Petersen, S. (2005). "Sea-floor tectonics and submarine hydrothermal systems," in *Economic geology 100th anniversary*, 111–141. doi: 10.5382/av100.06

Harris, D. C. (2010). *Quantitative chemical analysis. 8th edition* (New York: W.H. Freeman and Company), 108.

Heinen, W., and Lauwers, A. M. (1996). Organic sulfur compounds resulting from the interaction of iron sulfide, hydrogen sulfide and carbon dioxide in an anaerobic aqueous environment. *Origins Life Evol. Biospheres* 26, 131–150. doi: 10.1007/BF01809852

Hodgkinson, M. R. S., Webber, A. P., Roberts, S., Mills, R. A., Connelly, D. P., and Murton, B. J. (2015). Talc-dominated seafloor deposits reveal a new class of hydrothermal system. *Nat. Commun.* 6, 10150. doi: 10.1038/ncomms10150

Howard, P. H., Boethling, R. S., Jarvis, W. F., Meylan, W. M., and Michalenko, E. M. (2017). *Handbook of environmental degradation rates* (CRC Press). doi: 10.1201/9780203719329

Hsu-Kim, H., Mullaugh, K. M., Tsang, J. J., Yucel, M., and Luther, G. W. (2008). Formation of Zn- and Fe-sulfides near hydrothermal vents at the Eastern Lau Spreading Center: Implications for sulfide bioavailability to chemoautotrophs. *Geochem. Trans.* 9, 1-14. doi: 10.1186/1467-4866-9-6

Hu, H., Mylon, S. E., and Benoit, G. (2006). Distribution of the thiols glutathione and 3-mercaptopropionic acid in Connecticut lakes. *Limnol. Oceanogr.* 51, 2763–2774. doi: 10.4319/lo.2006.51.6.2763

Huang, X. G., Li, S., Liu, F. J., and Lan, W. R. (2018). Regulated effects of Prorocentrum donghaiense Lu exudate on nickel bioavailability when cultured with different nitrogen sources. *Chemosphere* 197, 57–64. doi: 10.1016/j.chemosphere.2018.01.014

Jeng, H.-M., Tsai, C.-Z., and Chang, T.-Y. (1990). Voltammetric study of copper(I) thioacetamide complexes. *Fresenius J. Anal. Chem.* 338, 902–904. doi: 10.1007/BF00322029

Kading, T. (2013). Distribution of thiols in the northwest Atlantic Ocean (Thesis). Massachusetts: Massachusetts Institute of Technology and Woods Hole Oceanographic Institution. doi: 10.1575/1912/5711

Kalloniati, C., Krompas, P., Karalias, G., Udvardi, M. K., Rennenberg, H., Herschbach, C., et al. (2015). Nitrogen-fixing nodules are an important source of reduced sulfur, which triggers global changes in sulfur metabolism in lotus japonicus. *Plant Cell* 27, 2384–2400. doi: 10.1105/tpc.15.00108

Kawakami, S., Gledhill, M., and Achterberg, E. (2006). Determination of phytochelatins and glutathione in phytoplankton from natural waters using HPLC with fluorescence detection. *TrAC Trends Analytical Chem.* 25, 133–142. doi: 10.1016/j.trac.2005.06.005

Kiene, R. P. (1991). Evidence for the biological turnover of thiols in anoxic marine sediments. *Biogeochemistry* 13, 117–135. doi: 10.1007/BF00002773

Kiene, R. P., Malloy, K. D., and Taylor, B. F. (1990). Sulfur-containing amino acids as precursors of thiols in anoxic coastal sediments. *Appl. Environ. Microbiol.* 56, 156–161. doi: 10.1128/aem.56.1.156-161.1990

Kleint, C., Kuzmanovski, S., Powell, Z., Bühring, S. I., Sander, S. G., and Koschinsky, A. (2015). Organic Cu-complexation at the shallow marine hydrothermal vent fields off the coast of Milos (Greece), Dominica (Lesser Antilles) and the Bay of Plenty (New Zealand). *Mar. Chem.* 173, 244–252. doi: 10.1038/269319a0

Klinhammer, G., Bender, M., and Weiss, R. F. (1977). Hydrothermal manganese in the Galapagos Rift. *Nature* 269, 319–320. doi: 10.1038/269319a0

Klinkhammer, G., Elderfield, H., and Hudsont, A. (1983). Rare earth elements in seawater near hydrothermal vents. *Nature* 305, 185–188. doi: 10.1038/305185a0

Konn, C., Charlou, J. L., Donval, J. P., Holm, N. G., Dehairs, F., and Bouillon, S. (2009). Hydrocarbons and oxidized organic compounds in hydrothermal fluids from Rainbow and Lost City ultramafic-hosted vents. *Chem. Geol.* 258, 299–314. doi: 10.1016/j.chemgeo.2008.10.034

Kumar, V., Pandita, S., Singh Sidhu, G. P., Sharma, A., Khanna, K., Kaur, P., et al. (2021). Copper bioavailability, uptake, toxicity and tolerance in plants: A comprehensive review. *Chemosphere* 262, 127810. doi: 10.1016/j.chemosphere.2020.127810

Laglera, L. M., Downes, J., Tovar-Sánchez, A., and Monticelli, D. (2014). Cathodic pseudopolarography: A new tool for the identification and quantification of cysteine, cystine and other low molecular weight thiols in seawater. *Anal. Chim. Acta* 836, 24–33. doi: 10.1016/j.aca.2014.05.026

Laglera, L. M., and Tovar-Sánchez, A. (2012). Direct recognition and quantification by voltammetry of thiol/thioamide mixes in seawater. *Talanta* 89, 496–504. doi: 10.1016/j.talanta.2011.12.075

Laglera, L. M., and van den Berg, C. M. G. (2006). Photochemical oxidation of thiols and copper complexing ligands in estuarine waters. *Mar. Chem.* 101, 130–140. doi: 10.1016/j.marchem.2006.01.006

Lang, S. Q., Butterfield, D. A., Schulte, M., Kelley, D. S., and Lilley, M. D. (2010). Elevated concentrations of formate, acetate and dissolved organic carbon found at the Lost City hydrothermal field. *Geochim. Cosmochim. Acta* 74, 941–952. doi: 10.1016/j.gca.2009.10.045

Leal, M. F. C., and van den Berg, C. M. G. (1998). Evidence for strong copper(I) complexation by organic ligands in seawater. *Aquat. Geochemistry* 4, 49–75. doi: 10.1023/A:1009653002399

Leal, M. F. C., Vasconcelos, M. T. S. D., and van den Berg, C. M. G. (1999). Copper-induced release of complexing ligands similar to thiols by Emiliania huxleyi inseawater cultures. *Limnol. Oceanogr.* 44, 1750–1762. doi: 10.4319/lo.1999.44.7.1750

Le Gall, A. C., and van den Berg, C. M. G. (1998). Folic acid and glutathione in the water column of the North East Atlantic. *Deep Sea Res. Part I: Oceanographic Res. Papers* 45, 1903–1918. doi: 10.1016/S0967-0637(98)00042-9

Lohan, M. C., and Tagliabue, A. (2018). Oceanic micronutrients: Trace metals that are essential for marine life. *Elements* 14, 385-390. doi: 10.2138/gselements.14.6.385

Madkour, L. H. (2020a). Oxidative stress and oxidative damage-induced cell death, in: Reactive Oxygen Species (ROS), Nanoparticles, and Endoplasmic Reticulum (ER) Stress-Induced Cell Death Mechanisms. *Elsevier* pp, 175–197. doi: 10.1016/b978-0-12-822481-6.00008-6

Madkour, L. H. (2020b). "Biological mechanisms of reactive oxygen species (ROS)," in *Reactive oxygen species (ROS), nanoparticles, and endoplasmic reticulum (ER) stress-induced cell death mechanisms* (Elsevier), 19–35. doi: 10.1016/b978-0-12-822481-6.00002-5

Mahieu, L., Whitby, H., Dulaquais, G., Tilliette, C., Guigue, C., Lefevre, D., et al. (2024). Iron-binding by dissolved organic matter in the Western Tropical South Pacific Ocean (GEOTRACES TONGA cruise GPpr14). *Front. Mar. Sci.* 11. doi: 10.1021/ba-1968-0073.ch017

Mallory, E. C. (1968). A thioacetamide-precipitation procedure for determining trace elements in water, in: trace inorganics in water. *Adv. Chem.* 17, 281–295. doi: 10.1021/ba-1968-0073.ch017

Mangal, V., Phung, T., and Guéguen, C. (2020). An estimation of sulfur concentrations released by three algae (Chlorella vulgaris, Chlamydomonas reinhardtii, Scenedesmus obliquus) in response to variable growth photoperiods. *Environ. Sci. pollut. Res.* 27, 12491–12498. doi: 10.1007/s11356-020-07812-6

Marie, L., Pernet-Coudrier, B., Waeles, M., Gabon, M., and Riso, R. (2015). Dynamics and sources of reduced sulfur, humic substances and dissolved organic carbon in a temperate river system affected by agricultural practices. *Sci. Total Environ.* 537, 23–32. doi: 10.1016/j.scitotenv.2015.07.089

Marie, L., Pernet-Coudrier, B., Waeles, M., and Riso, R. (2017). Seasonal variation and mixing behaviour of glutathione, thioacetamide and fulvic acids in a temperate macrotidal estuary (Aulne, NW France). *Estuar. Coast. Shelf Sci.* 184, 177–190. doi: 10.1016/j.ecss.2016.11.018

McCollom, T. M., and Seewald, J. S. (2007). Abiotic synthesis of organic compounds in deep-sea hydrothermal environments. *Chem. Rev.* 107, 382–401. doi: 10.1021/cr0503660

McLeay, Y., Stannard, S., Houltham, S., and Starck, C. (2017). Dietary thiols in exercise: Oxidative stress defence, exercise performance, and adaptation. *J. Int. Soc Sports Nutr.* 14, 1-8. doi: 10.1186/s12970-017-0168-9

Mironov, I. V., and Tsvelodub, L. D. (1996). Complexation of copper(I) by thiourea in acidic aqueous solution. *J. Solution Chem.* 25, 315–325. doi: 10.1007/BF00972529

Moingt, M., Bressac, M., Bélanger, D., and Amyot, M. (2010). Role of ultra-violet radiation, mercury and copper on the stability of dissolved glutathione in natural and artificial freshwater and saltwater. *Chemosphere* 80, 1314–1320. doi: 10.1016/j.chemosphere.2010.06.041

Moore, J. K., Doney, S. C., Glover, D. M., and Fung, I. Y. (2001). Iron cycling and nutrient-limitation patterns in surface waters of the World Ocean. *Deep Sea Res. Part II: Topical Stud. Oceanography* 49, 463–507. doi: 10.1016/S0967-0645(01)00109-6

Moore, C. M., Mills, M. M., Arrigo, K. R., Berman-Frank, I., Bopp, L., Boyd, P. W., et al. (2013). Processes and patterns of oceanic nutrient limitation. *Nat. Geosci.* 6, 701–710. doi: 10.1038/ngeo1765

Mopper, K., and Kieber, D. J. (1991). Distribution and biological turnover of dissolved organic compounds in the water column of the Black Sea. *Deep Sea Res. Part A. Oceanographic Res. Papers* 38, S1021–S1047. doi: 10.1016/S0198-0149(10)80022-6

Moran, M. A., and Durham, B. P. (2019). Sulfur metabolites in the pelagic ocean. *Nat. Rev. Microbiol.* 17, 665–678. doi: 10.1038/s41579-019-0250-1

Morel, F. M. M., and Price, N. M. (2003). The biogeochemical cycles of trace metals in the oceans. *Science* 300, 944–947. doi: 10.1126/science.1083545

Morelli, E., and Scarano, G. (2004). Copper-induced changes of non-protein thiols and antioxidant enzymes in the marine microalga Phaeodactylum tricornutum. *Plant Sci.* 167, 289–296. doi: 10.1016/j.plantsci.2004.04.001

Morris, J. J., Rose, A. L., and Lu, Z. (2022). Reactive oxygen species in the world ocean and their impacts on 980 marine ecosystems. *Redox Biol.* 52, 102285. doi: 10.1016/j.redox.2022.102285

Navarrete, A., González, A., Gómez, M., Contreras, R. A., Díaz, P., Lobos, G., et al. (2019). Copper excess detoxification is mediated by a coordinated and complementary induction of glutathione, phytochelatins and metallothioneins in the green seaweed Ulva compressa. *Plant Physiol. Biochem.* 135, 423–431. doi: 10.1016/j.plaphy.2018.11.019

Nojiri, Y., Ishibashi, J., Kawai, T., Otsuki, A., and Sakai, H. (1989). Hydrothermal plumes along the North Fiji Basin spreading axis. *Nature* 342, 667–670. doi: 10.1038/342667a0

Omanovic, D., and Branica, M. (1998). Automation of voltammetric measurements by polarographic analyser PAR 384B*. *Croatica Chemica Acta* 71, 421–433.

Pál, M., Janda, T., and Szalai, G. (2018). Interactions between plant hormones and thiol-related heavy metal chelators. *Plant Growth. Regul.* 85, 17–185. doi: 10.1007/s10725-018-0391-7

Pernet-Coudrier, B., Waeles, M., Filella, M., Quentel, F., and Riso, R. D. (2013). Simple and simultaneous determination of glutathione, thioacetamide and refractory organic matter in natural waters by DP-CSV. *Sci. Total Environ.* 463–464, 997–1005. doi: 10.1016/j.scitotenv.2013.06.053

Peters, C., Strauss, H., Haase, K., Bach, W., de Ronde, C. E. J., Kleint, C., et al. (2021). SO2 disproportionation impacting hydrothermal sulfur cycling: Insights from multiple sulfur isotopes for hydrothermal fluids from the Tonga-Kermadec intraoceanic arc and the NE Lau Basin. *Chem. Geol* 586, 120586. doi: 10.1016/j.chemgeo.2021.120586

Petzold, H., and Sadler, P. J. (2008). Oxidation induced by the antioxidant glutathione (GSH). *Chem. Comm.* 37, 4413–4415. doi: 10.1039/b805358h

Portlock, G., Fourrier, P., Riso, R., Omanovic, D., Dulaquais, G., Whitby, H., et al. Humic substances in the oligotrophic western tropical South Pacific: an intercomparison of electrochemical techniques.

Radford-Knoery, J., Charlou, J.-L., Donval, J.-P., Aballéa, M., Fouquet, Y., and Ondréas, H. (1998). Distribution of dissolved sulfide, methane, and manganese near the seafloor at the Lucky Strike (37°17′N) and Menez Gwen (37°50′N) hydrothermal vent sites on the mid-Atlantic Ridge. *Deep Sea Res. Part I: Oceanographic Res. Papers* 45, 367–386. doi: 10.1016/S0967-0637(97)00082-4

Rea, P. A., Vatamaniuk, O. K., and Rigden, D. J. (2004). Weeds, worms, and more. Papain's long-lost cousin, phytochelatin synthase. *Plant Physiol.* 136, 2463–2474. doi: 10.1104/pp.104.048579

Reeves, E. P., McDermott, J. M., and Seewald, J. S. (2014). The origin of methanethiol in midocean ridge hydrothermal fluids. *Proc. Natl. Acad. Sci. U.S.A.* 111, 5474–5479. doi: 10.1073/pnas.1400643111

Resing, J. A., Sedwick, P. N., German, C. R., Jenkins, W. J., Moffett, J. W., Sohst, B. M., et al. (2015). Basin-scale transport of hydrothermal dissolved metals across the South Pacific Ocean. *Nature* 523, 200–203. doi: 10.1038/nature14577

Rijstenbil, J. W. (2002). Assessment of oxidative stress in the planktonic diatom Thalassiosira pseudonana in response to UVA and UVB radiation. *J. Plankton. Res.* 24, 1277–1288. doi: 10.1093/plankt/24.12.1277

Rosenthal, D., and Taylor, T. I. (1957). A study of the mechanism and kinetics of the thioacetamide hydrolysis reaction 1. *J. Am. Chem. Soc.* 79, 2684–2690. doi: 10.1021/ja01568a007

Sander, S. G., and Koschinsky, A. (2011). Metal flux from hydrothermal vents increased by organic complexation. *Nat. Geosci.* 4, 145–150. doi: 10.1038/ngeo1088

Schäfer, H., and Eyice, Ö. (2019). "Microbial cycling of methanethiol," in *Methylotrophs and methylotroph communities* (Caister Academic Press). doi: 10.21775/9781912530045.09

Schieber, M., and Chandel, N. S. (2014). ROS function in redox signaling and oxidative stress. *Curr. Biol.* 24, R453–R462. doi: 10.1016/j.cub.2014.03.034

Schine, C. M. S., Alderkamp, A.-C., van Dijken, G., Gerringa, L. J. A., Sergi, S., Laan, P., et al. (2021). Massive Southern Ocean phytoplankton bloom fed by iron of possible hydrothermal origin. *Nat. Commun.* 12, 1211. doi: 10.1038/s41467-021-21339-5

Schlitzer, R. (2021). *Ocean data view*. [Software].

Schmidt, A., Erdle, I., and Köst, H.-P. (1982). Changes of C-Phycocyanin in Synechococcus 6301 in Relation to Growth on various Sulfur Compounds Materials and Methods. *Zeitschrift für Naturforschung C* 37, 870–876. doi: 10.1515/znc-1982-1004

Schulte, M. D., and Rogers, K. L. (2004). Thiols in hydrothermal solution: Standard partial molal properties and their role in the organic geochemistry of hydrothermal environments. *Geochim. Cosmochim. Acta* 68, 1087–1097. doi: 10.1016/j.gca.2003.06.001

Semeniuk, D. M., Bundy, R. M., Payne, C. D., Barbeau, K. A., and Maldonado, M. T. (2015). Acquisition of organically complexed copper by marine phytoplankton and bacteria in the northeast subarctic Pacific Ocean. *Mar. Chem.* 173, 222–233. doi: 10.1016/j.marchem.2015.01.005

Seyfried, W. E., Pester, N. J., Tutolo, B. M., and Ding, K. (2015). The Lost City hydrothermal system: Constraints imposed by vent fluid chemistry and reaction path models on subseafloor heat and mass transfer processes. *Geochim. Cosmochim. Acta* 163, 59–79. doi: 10.1016/j.gca.2015.04.040

Shao, Z., Xu, Y., Wang, H., Luo, W., Wang, L., Huang, Y., et al. (2023). Global oceanic diazotroph database version 2 and elevated estimate of global oceanic N2 fixation. *Earth Syst. Sci. Data* 15, 3673–3709. doi: 10.5194/essd-15-3673-2023

Steffens, J. C. (1990). The heavy metal-binding peptides of plants. *Annu. Rev. Plant Physiol. Plant Mol. Biol.* 41, 553–575. doi: 10.1146/annurev.pp.41.060190.003005

Stoffers, P., Worthington, T. J., Schwarz-Schampera, U., Hannington, M. D., Massoth, G. J., Hekinian, R., et al. (2006). Submarine volcanoes and high-temperature hydrothermal venting on the Tonga arc, southwest Pacific. *Geology* 34, 453–456. doi: 10.1130/G22227.1

Sunda, W., Kieber, D. J., Kiene, R. P., and Huntsman, S. (2002). An antioxidant function for DMSP and DMS in marine algae. *Nature* 418, 317–320. doi: 10.1038/nature00851

Superville, P. J., Pižeta, I., Omanović, D., and Billon, G. (2013). Identification and on-line monitoring of reduced sulphur species (RSS) by voltammetry in oxic waters. *Talanta* 112, 55–62. doi: 10.1016/j.talanta.2013.03.045

Swarr, G. J., Kading, T., Lamborg, C. H., Hammerschmidt, C. R., and Bowman, K. L. (2016). Dissolved low-molecular weight thiol concentrations from the U.S. GEOTRACES North Atlantic Ocean zonal transect. *Deep Sea Res. Part I: Oceanographic Res. Papers* 116, 77–87. doi: 10.1016/j.dsr.2016.06.003

Tang, D., Hung, C., Warnken, K. W., and Santschi, P. H. (2000). The distribution of biogenic thiols in surface waters of Galveston Bay. *Limnol. Oceanogr.* 45, 1289–1297. doi: 10.4319/lo.2000.45.6.1289

Tararin, L. A., Chubarov, K. M., and Filosofova, T. M. (2003). *Chemical composition of rock and minerals from the ophiolite complex in the Hunter Fracture Zone [WWW Document]* (PANGAEA).

Tilliette, C., Gazeau, F., Portlock, G., Benavides, M., Bonnet, S., Guigue, C., et al. (2023). Influence of shallow hydrothermal fluid release on the functioning of phytoplankton communities. *Front. Mar. Sci.* 10. doi: 10.3389/fmars.2023.1082077

Tilliette, C., Taillandier, V., Bouruet-Aubertot, P., Grima, N., Maes, C., Montanes, M., et al. (2022). Dissolved iron patterns impacted by shallow hydrothermal sources along a transect through the Tonga-kermadec arc. *Global Biogeochem Cycles* 36, 1-27. doi: 10.1029/2022GB007363

Treude, T., Smith, C. R., Wenzhöfer, F., Carney, E., Bernardino, A. F., Hannides, A. K., et al. (2009). Biogeochemistry of a deep-sea whale fall: Sulfate reduction, sulfide efflux and methanogenesis. *Mar. Ecol. Prog. Ser.* 382, 1–21. doi: 10.3354/meps07972

Ulrich, K., and Jakob, U. (2019). The role of thiols in antioxidant systems. *Free Radic. Biol. Med.* 140, 14–27. doi: 10.1016/j.freeradbiomed.2019.05.035

Umiker, K. J., Morra, M. J., and Francis Cheng, I. (2002). Aqueous sulfur species determination using differential pulse polarography. *Microchemical J.* 73, 287–297. doi: 10.1016/S0026-265X(02)00097-8

van den Berg, C. M. G. (1982). Determination of copper complexation with natural organic ligands in seawater by equilibration with MnO2 II. Experimental Procedures and Application to Surface Seawater. *Mar. Chem.* 11, 323–342. doi: 10.1016/0304-4203(82)90029-9

van den Berg, C. M. G., Household, B. C., and Riley, J. P. (1988). Determination of cystine and cysteine in seawater using cathodic stripping voltammetry in the presence of Cu(II). *J. Electroanal. Chem. Interfacial Electrochem.* 239, 137–148. doi: 10.1016/0022-0728(88)80275-4

Vasconcelos, M. T. S. D., and Leal, M. F. C. (2001). Adsorption and uptake of Cu by Emiliania huxleyi in natural seawater. *Environ. Sci. Technol.* 35, 508–515. doi: 10.1021/es000954p

Vasconcelos, M. T. S. D., Leal, M. F. C., and van den Berg, C. M. G. (2002). Influence of the nature of the exudates released by different marine algae on the growth, trace metal uptake and exudation of Emiliania huxleyi in natural seawater. *Mar. Chem.* 77, 187–210. doi: 10.1016/S0304-4203(01)00087-1

Walsh, E. A., Smith, D. C., Sogin, M. L., and D'Hondt, S. (2015). Bacterial and archaeal biogeography of the deep chlorophyll maximum in the South Pacific Gyre. *Aquat. Microb. Ecol.* 75, 1–13. doi: 10.3354/ame01746

Wang, H., Wang, W., Liu, M., Zhou, H., Ellwood, M. J., Butterfield, D. A., et al. (2022). Iron ligands and isotopes in hydrothermal plumes over backarc volcanoes in the Northeast Lau Basin, Southwest Pacific Ocean. *Geochim. Cosmochim. Acta* 336, 341–352. doi: 10.1016/j.gca.2022.09.026

Whitby, H., Posacka, A. M., Maldonado, M. T., and van den Berg, C. M. G. (2018). Copper-binding ligands in the NE pacific. *Mar. Chem.* 204, 36–48. doi: 10.1016/j.marchem.2018.05.008

Yeo, I. A., McIntosh, I. M., Bryan, S. E., Tani, K., Dunbabin, M., Metz, D., et al. (2022). The 2019–2020 volcanic eruption of Late'iki (Metis Shoal), Tonga. *Sci. Rep.* 12, 7468. doi: 10.1038/s41598-022-11133-8

Yücel, M., Gartman, A., Chan, C. S., and Luther, G. W. (2011). Hydrothermal vents as a kinetically stable source of iron-sulphide-bearing nanoparticles to the ocean. *Nat. Geosci.* 4, 367–371. doi: 10.1038/ngeo1148

Zhang, Z., Fan, W., Bao, W., Chen, C. T. A., Liu, S., and Cai, Y. (2020). Recent developments of exploration and detection of shallow-water hydrothermal systems. *Sustainability* 12, 1–17. doi: 10.3390/su12219109

frontiers | Frontiers in Marine Science

TYPE Original Research
PUBLISHED 17 June 2025
DOI 10.3389/fmars.2025.1538835

OPEN ACCESS

EDITED BY
Jessica Nicole Fitzsimmons,
Texas A and M University, United States

REVIEWED BY
Emilie Le Roy,
Woods Hole Oceanographic Institution, United States
Wei Wei,
University of Science and Technology of China, China

*CORRESPONDENCE
Li Li
li.li@fio.org.cn
Xuefa Shi
xfshi@fio.org.cn

RECEIVED 03 December 2024
ACCEPTED 26 May 2025
PUBLISHED 17 June 2025
CORRECTED 19 June 2025

CITATION
Zhao C, Li L, Li J, Xie RC, Wang X and Shi X (2025) Impact of hydrothermal activity on marine barium isotope composition: a case study from the Southwestern Indian Ocean. *Front. Mar. Sci.* 12:1538835. doi: 10.3389/fmars.2025.1538835

Impact of hydrothermal activity on marine barium isotope composition: a case study from the Southwestern Indian Ocean

Chunxiao Zhao[1], Li Li[1,2,3]*, Jiejun Li[1], Ruifang C. Xie[4,5], Xiaojing Wang[1,2] and Xuefa Shi[1,2,3]*

[1]Key Laboratory of Marine Geology and Metallogeny, First Institute of Oceanography, Ministry of Natural Resources, Qingdao, China, [2]Laboratory for Marine Geology, Qingdao Marine Science and Technology Center, Qingdao, China, [3]Shandong Key Laboratory of Deep Sea Mineral Resources Development, Qingdao, China, [4]Key Laboratory of Polar Ecosystem and Climate Change, Ministry of Education, School of Oceanography, Shanghai Jiao Tong University, Shanghai, China, [5]Shanghai Key Laboratory of Polar Life and Environment Sciences, School of Oceanography, Shanghai Jiao Tong University, Shanghai, China

The cycling of barium (Ba) is closely linked to marine biogeochemical processes. Barium and its isotopes are commonly used as tracers for marine productivity, seawater alkalinity, and ocean circulation. Mid-ocean ridge hydrothermal systems significantly impact marine chemistry, acting as key sources of trace elements in deep seawater. However, the overall contribution of hydrothermal Ba to the global Ba cycle remains poorly quantified, and studies on hydrothermal Ba isotopes are limited, hindering a comprehensive understanding of the marine Ba cycle. This study investigated the concentration of dissolved Ba and other elements, along with Ba isotope composition (δ^{138}Ba), in the hydrothermal influenced water and sediment samples collected near the Longqi and Tiancheng vents in the southwestern Indian Ocean. This constitutes the first such investigation in this region. The vertical profiles of dissolved Ba and its isotope compositions mirrored each other in the southwestern Indian Ocean, consistent with prior observations in other ocean basins. For near-field water samples, Ba isotope compositions (-0.10‰ to 0.05‰) are significantly lower than background seawater (~0.29‰). In addition, Hydrothermal sediments exhibited Ba isotopic values (-0.16‰ to 0.01‰) markedly lower than background sediments (0.01‰ to 0.14‰). The depleted δ138Ba values of near-field water samples indicate preferential removal of lighter Ba isotopes during the mixing of hydrothermal fluids with seawater. Consequently, precipitated particles acquire lighter Ba isotope signatures, explaining the low values in hydrothermal sediments. This demonstrates that sediments effectively capture and preserve hydrothermal Ba signals. Collectively, these findings provide new insights into hydrothermal influences on the marine Ba cycle.

KEYWORDS

Barium (Ba), isotope composition, hydrothermal activity, Indian Ocean, seawater, sediment

1 Introduction

The marine barium (Ba) cycle is closely linked to marine biogeochemistry (Horner and Crockford, 2021). The primary sources of Ba in the ocean are rivers, groundwater, and hydrothermal vents (Kumagai et al., 2008; Cao et al., 2016; Carter et al., 2020; Hsieh et al., 2021). Once introduced into seawater, the dissolved Ba is removed from seawater and accumulated in marine sediments primarily in the form of the barite and in association with iron and manganese oxides (Dymond et al., 1992; Paytan and Kastner, 1996; Carter et al., 2020). The concentration of dissolved Ba in seawater is found to be associated with the concentration of the major nutrient silicon (Lea and Boyle, 1989; Jacquet et al., 2005; Roeske et al., 2012). Its sinking flux is closely linked with organic carbon flux, and it is commonly used as a tracer for marine productivity (Eagle et al., 2003; McManus et al., 1999; McCulloch et al., 2003; Paytan and Griffith, 2007). In addition, Ba displays a positive correlation with ocean alkalinity and dissolved inorganic carbon. The Ba/Ca ratio in foraminifera, for instance, can serve as a proxy for past seawater alkalinity (Lea, 1993; McManus et al., 1999).

Recently, Ba isotopes (δ^{138}Ba) have been recognized as a valuable tool for exploring the oceanic Ba cycle, providing important insights into its processes and behavior, such as, to trace the movement and mixing of deep-water masses, to serve as a proxy for marine biological productivity and to indicate riverine inputs (Horner et al., 2015; Bates et al., 2017; Hsieh and Henderson, 2017; Bridgestock et al., 2018; 2021; Crockford et al., 2019; Cao et al., 2021; Middleton et al., 2023). The Ba isotope composition in seawater ranges from 0.24‰ – 0.65‰, and the primary factor influencing the observed variations in seawater δ^{138}Ba is the formation and dissolution of barite (Horner et al., 2015; Bates et al., 2017; Hsieh and Henderson, 2017; Cao et al., 2021; Whitmore et al., 2022). Modern oceans show a significant δ^{138}Ba gradient from surface to depth, characterized by higher δ^{138}Ba values in surface water masses and lighter δ^{138} Ba values in deep water masses (Hsieh and Henderson, 2017; Bridgestock et al., 2018; Carter et al., 2020). This type of vertical distribution is a result of the precipitation process as barite from seawater, which is marked by significant isotopic fractionation, with lighter Ba isotopes preferentially incorporated into biogenic barite crystals (Horner et al., 2015; Bates et al., 2017; Hsieh and Henderson, 2017; Bridgestock et al., 2018). Similarly, adsorption onto biological particles preferentially removes lighter Ba isotopes from ambient seawater (Cao et al., 2020). Both adsorption and barite precipitation increase the δ^{138}Ba values of seawater in the upper ocean (~ 600 m), whereas the dissolution processes re-introduce lighter Ba isotopes into deeper waters.

The degree to which Ba isotopes behave conservatively in the deep ocean remains uncertain. Moreover, available published data suggest an imbalance between the sources and sinks of Ba isotopes in the modern ocean. Specifically, Ba isotope compositions from terrestrial sources range from 0.1‰ to 0.2‰, while sediment values, representing sinks, range from 0‰ to 0.1‰ (Horner and Crockford, 2021). Therefore, it is proposed that lighter Ba isotope sources or heavier isotope sinks may be missing and not fully accounted for (Horner and Crockford, 2021; Zhang et al., 2024). Bates et al. (2017) suggested that Ba isotopes exhibit conservative behavior during the mixing of North Atlantic Deep Water (NADW) and Antarctic Bottom Water (AABW) in the Atlantic. However, Hsieh and Henderson (2017) observed that in deep water between 2000 and 3000 meters, Ba isotope compositions exceeded conservative mixing predictions, reflecting additional inputs or sinks of Ba during transport, a phenomenon later explained by Hsieh et al. (2021) as resulting from hydrothermal vents imparting distinct Ba isotopic signatures to deep water masses.

Hydrothermal systems at mid-ocean ridges play a critical role in trace element recycling processes in marine system (Elderfield and Schultz, 1996; Coogan et al., 2019). Barium in source rocks is released into hydrothermal fluids through water-rock interactions under high temperatures and pressures (Von Damm, 1985), resulting in fluids highly enriched in dissolved Ba. Barium concentrations in hydrothermal fluids (1-119 μM) can be up to three orders of magnitude higher than those in seawater (30-150 nM) (Butterfield and Massoth, 1994; Kumagai et al., 2008; Seyfried et al., 2011). However, when these fluids mix with seawater, Ba precipitates as barite and is largely removed (Jamieson et al., 2016; Gartman et al., 2019). Ba also co-precipitates with metals like Fe and Cu, resulting in minimal or no net Ba flux into seawater (Carter et al., 2020). Additionally, the ultramafic lithology contrasts with the mafic-dominated settings in mid-ocean ridge vents, which may lead to unique fluid-rock interactions that modulate Ba release and isotopic fractionation (Hsieh et al., 2021; Zhang et al., 2024). To date, the research on Ba isotopes in hydrothermal systems primarily focuses on hydrothermal fluids and non-buoyant plumes, with very limited empirical data available.

To advance the understanding of the marine Ba cycle, this study investigates the geochemical characteristics and Ba isotope compositions of hydrothermal fluids, ambient seawater, and sediments from the Longqi and Tiancheng hydrothermal fields along the Southwest Indian Ridge. This research fills a gap in the study of Ba isotopes in Indian Ocean seawater and reveals the Ba isotope composition of hydrothermal end-member inputs. It is also the first investigation of Ba isotopes in hydrothermal sediments, exploring how these sediments record hydrothermal Ba inputs. The study systematically examines the mechanisms driving Ba cycling within the Southwest Indian Ridge hydrothermal system.

2 Materials and methods

2.1 Study region

The study area is located along the Southwest Indian Ridge (SWIR), an ultra-slow spreading mid-ocean ridge (Figure 1) (Demets et al., 1994; Cannat et al., 2008). The SWIR is characterized by distinctive tectonic features, including a series of large north-south trending transform faults that formed due to lateral spreading during ridge evolution. This study focuses on the Longqi and Tiancheng hydrothermal fields. The Longqi Hydrothermal Field, located at 37°47′S, 49°39′E, at a depth of

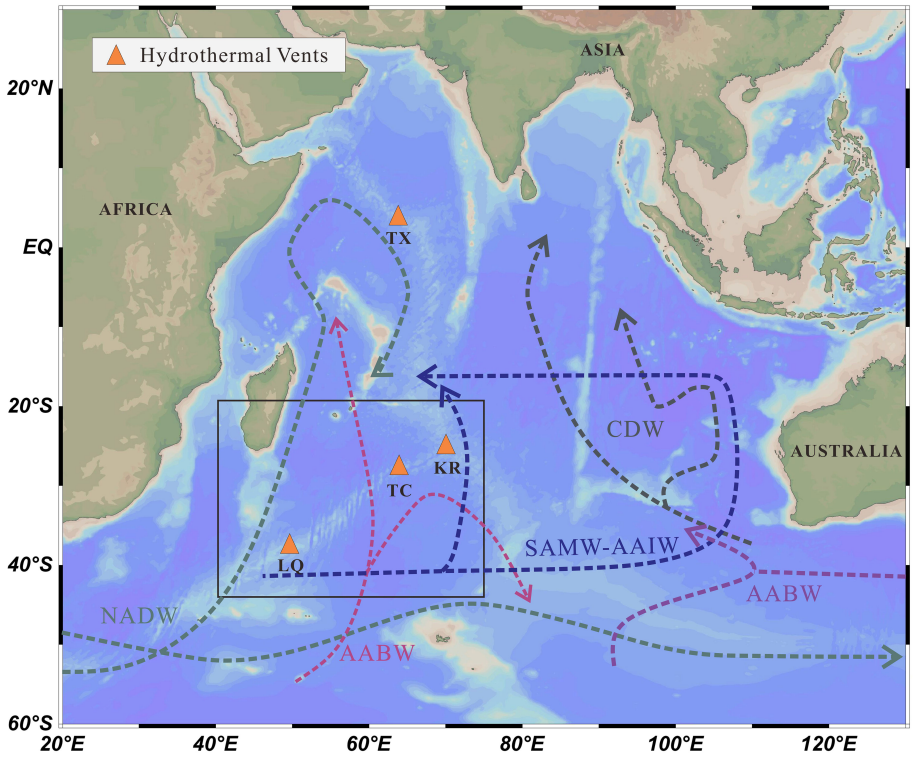

FIGURE 1
Hydrological map of india ocean the map shows the hydrothermal vent locations (orange triangles),along with the labeled main water masses SAMW (Subbantarctic Mode water) CDW (Circumpolar Deep Water AAIW) Antarctic Intermediate Water) and AABW (Antarctic Bottom Water).

2775 m, is the first active high-temperature hydrothermal field (> 300°C) discovered on the SWIR, situated on a mafic rock substrate (Tao et al., 2012). The Tiancheng Hydrothermal Field, situated at 27°51′S, 63°55′E, at a depth of 2750 meters, is the first confirmed area of low-temperature hydrothermal activity on the SWIR, with fluid temperatures around 13.2°C (Tao et al., 2014). This region experiences limited magmatic supply and intense tectonic activity, with fractured basalt as the dominant substrate (Chen et al., 2018). As shown in Figue 1, the sub-surface, intermediate, and deep layers of seawater in the study area are respectively influenced by water masses Subantarctic Mode Water (SAMW), Antarctic Intermediate Water (AAIW), Circumpolar Deep Water (CDW), and Antarctic Bottom Water (AABW) (Rippert et al., 2015; Zhang et al., 2022).

2.2 Sample collection

Water samples were collected during the DY-52 and DY-78 expeditions aboard the *R/V Da Yang 1* in April 2019 and *R/V Da Yang* in 2023, respectively. Three full-depth seawater stations (S1, S2, S3) were collected (Figure 2). Among them, S1 and S3 located directly above the Longqi and Tiancheng hydrothermal vents, respectively, and S2 represents background seawater between the two vent sites. The samples were obtained using Niskin bottles mounted on a stainless-steel rosette equipped with a CTD system (Sea-Bird® 911plus). Immediately after collection, the seawater was filtered through AcroPak capsule filters (0.2 μm, Pall Corporation®) and transferred to acid-clean low-density polyethylene (LDPE) bottles. The samples were then acidified to pH ~ 2 using high-purity nitric acid (Fisher Scientific®, Optima grade) and stored at room temperature in sealed containers. All sampling equipment, including tubes, filters, and bottles, were pre-cleaned following the protocols of Li et al. (2015).

Near-vent seawater samples (LQ-1, LQ-2, LQ-3, TC-1, TC-2, TC-3, TC-4) were collected using a custom-designed sampler mounted on the Remotely Operated Vehicle (ROV) Sea Dragon III during DY-52. The sampler was composed of a hydraulic piston, an acid-clean polycarbonate bottle, and a Teflon inlet attached to the silicone sampling tube. During DY-78, hydrothermal fluids (LQ-LT) were sampled with a titanium alloy “Pressure-Resistant Fluid Sampler” and the titanium inlet collected the fluid within the vent. Immediately after recovery of the ROV sampler, samples were filtered through polyethersulfone (PES) membranes (0.45 μm, 47 mm, Pall) and filtrate transferred to acid-cleaned LDPE bottles. They were then acidified to pH ~2 with high-purity nitric acid (Fisher Scientific®, Optima grade) and stored at room temperature. Filter membranes were preserved and stored in sealed bags for subsequent analysis.Surface sediment samples (P1–P15) were obtained from the China Ocean Sample Repository, collected during various expeditions (DY-19, 20, 21, 26, 30, 34, 35, 40, 49) using a TV grab sampler. These samples were stored in clean, sealed bags and frozen at -20°C for preservation.

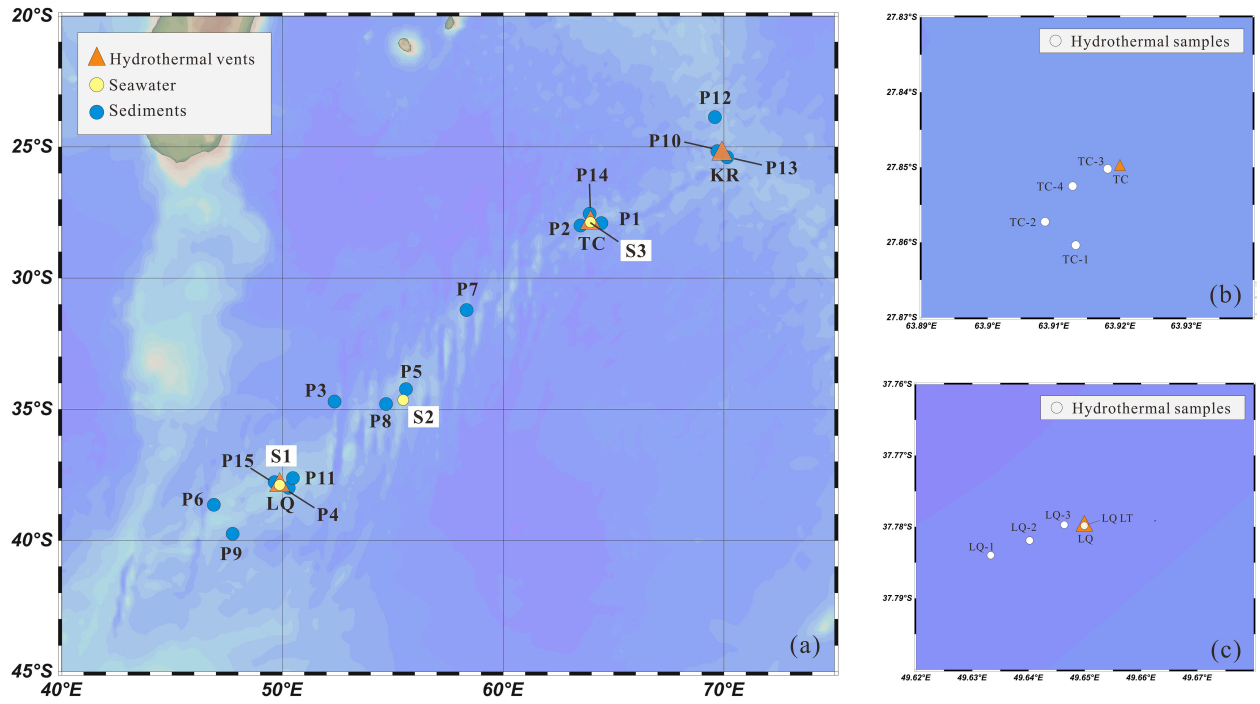

FIGURE 2
Sampling locations for seawater depth profiles hydrothermal samples and sediments Panel **(a)** presents the station locations for seawater depth profiles and sediments sampling panels **(b)** and **(c)** indicate the hydrothermal fluid and plume sampling sites at Tiancheng (TC) and longqi(LQ) .

2.3 Sample analysis

2.3.1 Analysis of seawater and hydrothermal fluid dissolved samples

Seawater and hydrothermal fluid samples were diluted 20-fold with 2% HNO_3 (Optima grade) and spiked with indium (In) as an internal standard with a final concentration of 10 ppb. Concentrations of dissolved Fe, Mnand Bawere determined using an inductively coupled plasma mass spectrometer (ICP-MS, iCAP–RQ, Thermo Fisher Scientific) in collision cell-mode at the First Institute of Oceanography of China. The precision and accuracy of Ba, Fe, Mn measurements were verified using certified reference seawater CASS-5 (National Research Council®, Canada), and the analytical results are shown in Table 1. Since no Ba data are reported in certified values of the reference seawater, the analytical results reported here are compared with data published previously by (Mori et al., 2019).

Approximately 60 ng of Ba was extracted from each stock solution and spiked with a suitable amount of the ^{130}Ba-^{135}Ba double spike. Following the methods outlined by Lin et al. (2020), the spike-sample mixtures were dried, redissolved in 2.5 mol/L HCl, and purified via column separation using AG 50 W-X8 cation-exchange resin. Procedural blanks were measured for each batch, with Ba concentrations < 0.6 ng, which was <0.1% of the total Ba in the samples. The purified samples were then dried and redissolved in 3% HNO_3 (with Ba concentrations ~ 60 ppb), and Ba isotope ratios were analyzed using a Thermo Neptune XT MC-ICP-MS at the Key Laboratory of Surficial Geochemistry, Nanjing University.

TABLE 1 Analytical results of certified reference seawater samples (CASS-5) compared to the certified values.

Parameter	Ba (nM)	Fe (ppb)	Mn (ppb)
Measured value[a]	51.84 ± 0.69(*n*=4)	1.41±0.01 (*n*=3)	2.39±0.02 (*n*=3)
Certified value	53.75[b]	1.44±0.11	0.2

[a]The data is mean ± standard deviation;
[b]Reference values are sourced from Mori et al. (2019).

Ba isotope compositions in this study are expressed as ‰ deviations (δ^{138}Ba) relative to the international Ba standard NIST SRM 3104a (Equation 1):

$$\delta^{138}\mathrm{Ba}(‰) = \left(\frac{^{138}\mathrm{Ba}/^{134}\mathrm{Ba}_{\mathrm{sample}}}{^{138}\mathrm{Ba}/^{134}\mathrm{Ba}_{\mathrm{NIST\ 3104a}}} - 1\right) \times 1000 \quad (1)$$

The standard solution NIST SRM3104a and a seawater standard IAPSO were analyzed after every five samples. The Ba isotope compositions (δ^{138}Ba) of the NIST 3104a standard and IAPSO standard seawater were 0.00 ± 0.05‰ (2SD, n=11) and -0.04 ± 0.05‰, respectively. The δ^{138}Ba value for IAPSO in this study is consistent with the 0.05 ± 0.04‰ reported in a previous study (Pretet, 2013). We determined the error of the Ba isotope compositions (δ^{138}Ba) for all samples to be 0.05‰, based on the measurements of the standard SRM3104a for δ^{138}Ba (n=11).

2.3.2 Analysis of sediments

The sediment samples were freeze-dried for 48 hours and then ground into a fine powder (200-mesh). For bulk concentration

analysis, approximately 50 mg of sediments (weighed to a precision of 0.1 mg) were digested in a concentrated acid mixture (HNO_3/HF, 1:1). The major elements were analyzed using inductively coupled plasma optical emission spectrometry (ICP-OES, iCAP 6300, Thermo Fisher Scientific®) with RSD < 5%, and trace elements and rare earth elements (REEs) were analyzed using ICP-MS. Sediment reference standards GBW07309 (China Reference Material) were analyzed to evaluate the reproducibility of this method (n=3). The measured values agreed well with certified values for all targeted elements (96 ± 0.6% – 105 ± 1%) and detailed information can be found in the supplementary material (Supplementary Table S1).

Approximately 100 ng of Ba was extracted from each stock digest solution for Ba isotope analysis, following the same procedure as for seawater and hydrothermal samples (Section 2.3.1). The standard solution NIST SRM3104a and a coral standard SH-1 were analyzed after every five samples. The Ba isotope compositions (δ^{138}Ba) of the coral standard SH-1 was 0.29 ± 0.04‰ (2SD, *n*=8), which was consistent with the published value of 0.31 ± 0.04‰ (Lin et al., 2022).

2.3.3 Analysis of filter membrane

The hydrothermal filter membrane was analyzed using scanning electron microscopy with energy-dispersive X-ray spectroscopy (SEM-EDX; FEI Quanta 200, Netherlands). A piece of the filter membrane (~ 0.5 cm × 0.5 cm) was attached to conductive adhesive using tweezers. The sample was then coated with gold for 25 seconds under vacuum conditions, after which it was placed under the scanning electron microscope for observation, with the aim of identifying as many different types of mineral particles as possible.

3 Result and discussion

3.1 Dissolved Ba concentrations and its isotope compositions of seawater

3.1.1 Characteristics of barium concentrations and isotopic distributions in this study

Vertical distribution of dissolved Ba concentrations ($[Ba]_{diss}$) at stations S1, S2 and S3 are shown in Figure 3 and Table 2. The dissolved Ba concentrations range from approximately 37 to 107 nM, with a typical increasing pattern from surface to bottom. The concentration varied slightly within the surface 1000 m (37 – 50 nM), and increased sharply to over 80 nM at 2000 m. S3, the station located above the Tiancheng hydrothermal vent, had a higher $[Ba]_{diss}$ (~ 90 nM) compared to the ones further south (S1 and S2). Barium is considered a bio-intermediate element, with its dissolved concentrations ($[Ba]_{diss}$) in the water column typically following a nutrient-like depth profile. In surface waters, $[Ba]_{diss}$ is reduced due to its removal via association with marine particles. However, $[Ba]_{diss}$ becomes enriched in deep water, primarily as a result of the decomposition and remineralization of settling particles (Lea and

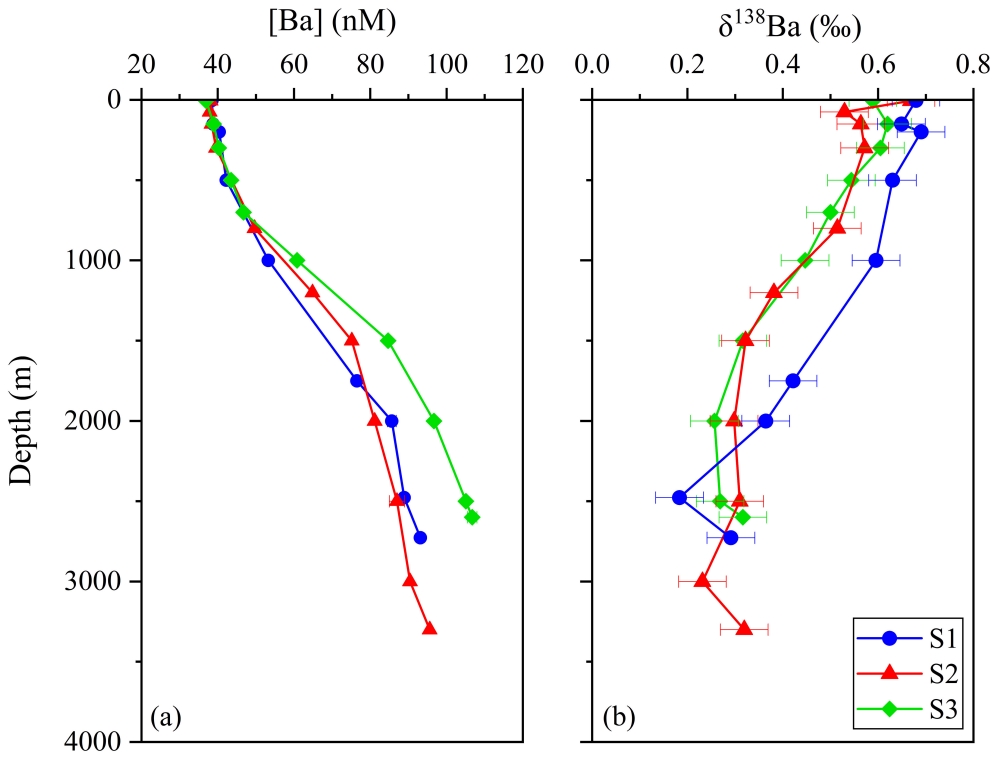

FIGURE 3
Depth profiles of seawater showings **(a)** dissolved Ba concentrations and **(b)**.

10.3389/fmars.2025.1538835

TABLE 2 The concentrations of Ba and Ba isotope compositions in seawater samples.

Station	Depth(m)	Ba(nM)	δ^{138}Ba
S1	3	38.49	0.68
	150	38.78	0.65
	200	40.37	0.69
	500	42.26	0.63
	1000	53.27	0.60
	1750	76.52	0.42
	2000	85.65	0.36
	2477	88.89	0.18
	2727	93.14	0.29
S2	5	38.13	0.67
	75	37.91	0.53
	150	38.38	0.56
	300	39.58	0.57
	800	49.68	0.51
	1200	64.87	0.38
	1500	75.17	0.32
	2000	81.18	0.30
	2500	86.98	0.31
	3000	90.42	0.23
	3300	95.60	0.32
S3	5	36.93	0.59
	50	38.30	no data
	150	38.96	0.62
	300	40.31	0.61
	500	43.52	0.54
	700	46.76	0.50
	1000	60.80	0.45
	1500	84.70	0.32
	2000	96.74	0.26
	2500	105.10	0.27
	2600	106.74	0.32

Boyle, 1991; Hsieh and Henderson, 2017; Carter et al., 2020; Yu et al., 2022).

In contrast, δ^{138}Ba values decrease from 0.65‰ near the surface to about 0.20‰ at greater depths (Figure 3). This inverse relationship between Ba concentration and isotope composition mirrors the vertical distributions that have also been observed in the Atlantic and Pacific Oceans (Figure 4) (Horner et al., 2015; Hsieh and Henderson, 2017). The observed profiles are attributed to isotopic fractionation that occurs during pelagic barite precipitation while its dissolution process shows negligible isotopic fractionation. Different from $[Ba]_{diss}$ in which all three water profiles shown similar trends and values with depth, the vertical profiles of δ^{138}Ba for stations S2 and S3 are quite similar, and δ^{138}Ba for stations S1 and S2 are also exactly similar (S1: 0.68‰;S2: 0.67‰) while the ones for S1 are heavier by ~ 0.1——0.2 ‰ within the top 2000 m. At 2500 m, the δ^{138}Ba at S1 (0.18 ± 0.05‰) is marginally lower than at S2 (0.31± 0.05‰) and S3 (0.27 ± 0.05‰), though the difference is within analytical uncertainty (Figure 3). The relationship between dissolved Ba concentrations and Ba isotope compositions (δ^{138}Ba) is displayed in Supplementary Figure S1, revealing a statistically significant negative correlation ($p < 0.01$). In addition, the temperature and salinity of the seawater samples are plotted in the T-S diagram (Figure 5). With the exception of a few surface seawater samples, all data points form distinct curves or clusters, and no extreme temperature or salinity characteristics are observed. These results indicate that the analyzed seawater samples do not exhibit significant influence from hydrothermal input.

3.1.2 Comparison with global barium cycling trends

The comparison of the vertical profile of station S2 with the ones in other ocean basins is shown in Figure 4. Except for the vertical distribution in the Southern Ocean, $[Ba]_{diss}$ in S2 in this study always lie between those from the Pacific Ocean and Atlantic Ocean, both in surface waters and deep waters. In surface waters, the $[Ba]_{diss}$ are relatively higher (~ 45 nM) in the Atlantic Ocean and lower (~ 30 nM) in the Pacific Ocean, while the opposite is true in deep waters. The $[Ba]_{diss}$ in deep waters are relatively higher (~130 nM) in the Pacific Ocean and lower in the Atlantic Ocean (~ 70 nM), with the ones found in this study similar to the deep water in the Southern Ocean (~ 90 nM).

While the study by Jacquet et al. (2005) on barium in the Crozet–Kerguelen Basin demonstrated that barite precipitation can induce surface water alterations in the Southern Ocean, recent investigations of dissolved Ba concentrations in water column profiles from the high-latitude Southern Ocean (Weddell Sea) have revealed that the Southern Ocean exhibits relatively high $[Ba]_{diss}$ in surface waters, with minimal variation between surface and deep waters (Yu et al., 2022). This limited variation is attributed, in part, to the region's classification as a high nutrient, low chlorophyll (HNLC) zone, where restricted barite formation leads to minor changes in surface water $[Ba]_{diss}$ (Fu and Wang, 2022; Yu et al., 2022). Additionally, the strong upwelling of Circumpolar Deep Water (CDW) from below further reduces the extent of $[Ba]_{diss}$ variation throughout the water column (Hsieh and Henderson, 2017; Yu et al., 2022).

Overall, deep-water $[Ba]_{diss}$ follows the sequence: North Pacific > South Pacific > Southern Ocean > Southwest Indian Ocean > South Atlantic > North Atlantic. This trend correlates positively with the age of the water masses, i.e., the older the water mass, the higher the $[Ba]_{diss}$, which again is the accumulation result of the dissolution of barite in deep water.

The comparison of the δ^{138}Ba values of the vertical profile of station S2 with the ones in other ocean basins is shown in Figure 4. Similar to the distribution of $[Ba]_{diss,}$ the δ^{138}Ba found in S2 in this study is between those in the Pacific and Atlantic Oceans in deep waters. The δ^{138}Ba values in deep waters are relatively higher (~ 0.45‰) in Atlantic Oceans and lower in Pacific Oceans (~ 0.25‰), and the ones found in this study is ~ 0.30‰. Likewise, The Southern Ocean exhibits relatively light Ba isotope compositions in deep water, with minimal variation between surface and deep waters. The δ^{138}Ba values show an inverse relationship to water mass age, indicating that lighter Ba isotopes are released into seawater during barite particle dissolution.

3.2 Geochemical processes near hydrothermal vents

3.2.1 Dissolved Mg, Fe and Mn distributions

Deep-sea hydrothermal vent fluids are in a reduced state and highly enriched in dissolved trace metals such as Fe, Mn, Cu, and Zn, with concentrations several orders of magnitude higher than those in surrounding seawater (Rouxel et al., 2008; Findlay et al., 2019; Gartman et al., 2019). When these high-temperature, reducing hydrothermal fluids mix with cooler, oxygenated seawater, most trace metals precipitate as sulfides or oxides near the vent (Rouxel et al., 2016; Yuan et al., 2018). Recently, GEOTRACES studies have shown that a portion of these metals (Fe, Zn, Cu) released from the hydrothermal vents can be stabilized as organic complexes or nanoparticles, remaining in the dissolved phase, and transported over thousands of miles (Bennett et al., 2009; Hawkes et al., 2013; Li et al., 2014; Fitzsimmons et al., 2017; Lough et al., 2019).

Dissolved Mg, Fe, Mn, Ba concentrations and Ba isotope compositions in samples collected in and near the hydrothermal vents in this study are reported in Table 3. Dissolved Mg concentrations are commonly used to indicate the extent of seawater mixing with hydrothermal fluids. During hydrothermal fluid-rock interactions, Mg is typically removed as magnesium silicates, so that Mg concentration in hydrothermal fluids that is not mixed with seawater (termed unmixed hydrothermal fluids hereafter) should approach zero theoretically (Alt, 1995; Mottl et al., 1978). This inference is supported by Ji et al. (2017) who reported that Mg concentration in unmixed hydrothermal fluids from the Longqi hydrothermal field is 1.41 mM. Conversely, the background seawater adjacent to Longqi hydrothermal vent has a concentration of Mg of 52.5 mM (Gallant and Von Damm, 2006), significantly higher than that in unmixed hydrothermal fluids.

In this study, the Mg concentrations were found to range from 40.9 to 54.2 mM. One sample, referred to as "hydrothermal fluid" (LQ-LT), collected within the vent during the DY-78 expedition, had a Mg concentration of 40.9 mM, suggesting that mixing with background seawater had already occurred within the vent. In addition, the plume samples (LQ-1, LQ-2, LQ-3, TC-1, TC-2, TC-3, TC-4), collected near hydrothermal vents, exhibited Mg concentrations between 51.8 and 54.2 mM, indicating that these samples were highly mixed with seawater.

Despite the high degrees of mixing with background seawater, dissolved Fe and Mn concentrations in these samples were significantly higher than those reported in background seawater (Fang and Wang, 2021), indicating a notable contribution from hydrothermal sources. The relationship between Fe and Mn concentrations and their distance from hydrothermal vents is shown in Figure 6. The results reveal that among the hydrothermal samples from the Longqi vent, the fluid sample LQ-LT collected from

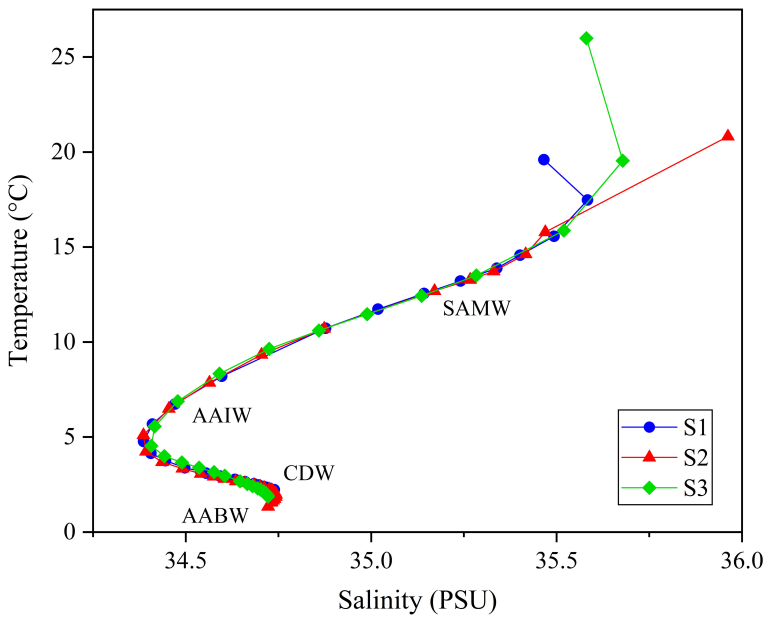

FIGURE 4
Temperature-Salinity(T-S) diagram of seawater.

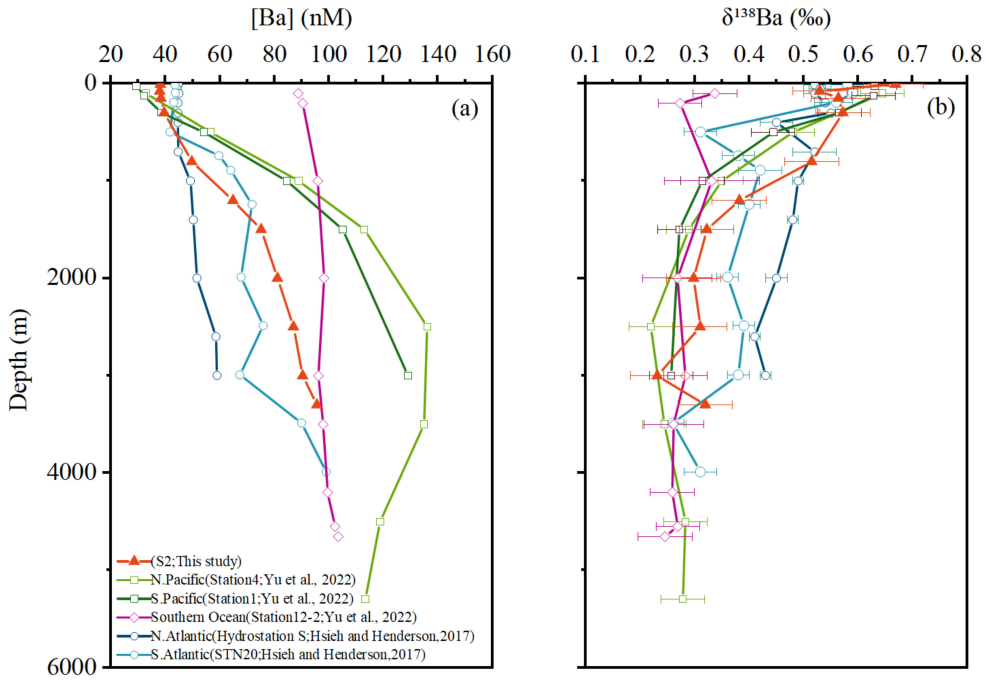

FIGURE 5
Depth profiles of **(a)** dissolved Ba concentrations and **(b)** Ba isotope compositions Data for the North pacific south Pacific and souththern Ocean are from Yu et al (2022) while data for the North atlantic and South atlantic are from Hsieh and Henderson (2017).

the vent interior exhibits the highest dissolved Fe and Mn concentrations, with concentrations rapidly declining in the remaining plume samples. All hydrothermal samples from the Tiancheng vent belong to plume samples, showing significantly lower Fe and Mn concentrations compared to the fluid sample (LQ-LT). Furthermore, Fe and Mn data from both vents indicate that only two samples (LQ-LT and TC-3) collected in close proximity to the hydrothermal vents display higher Fe concentrations than Mn concentrations. In all other plume samples, Mn concentrations decline at a slower rate relative to Fe. Previous studies have reported that during the mixing of hydrothermal fluids and seawater, dissolved Mn tends to be more stabilized in dissolved phase compared to Fe, the latter of which is removed as particles quite quickly during this process (Resing et al., 2015; Fitzsimmons et al., 2017). The distribution characteristics of these metals provide critical fluid mixing context for understanding barium isotope fractionation in hydrothermal systems.

3.2.2 The dissolved Ba distributions and Ba isotope composition

The hydrothermal samples exhibited dissolved barium concentrations ($[Ba]_{diss}$) ranging from 93 to 869 nM (Figure 6). Notably, two samples showed exceptionally high values: the hydrothermal fluid LQ-LT (869 nM) and the plume sample TC-3

TABLE 3 The concentrations of Fe, Mn, Mg, Ba, Ba isotope compositions and distance from vents in hydrothermal samples.

Sample ID	Sample type	Distance (km)	Fe (nM)	Mn (nM)	Mg (mM)	$[Ba]_{diss}$ (nM)	$\delta^{138}Ba$ (‰)
LQ-LT	fluid	0	310 μM	130 μM	40.9	869	-0.01
LQ-1	plume	1.56	8.84	107	52.5	93	0.27
LQ-2	plume	0.86	153	1.31 μM	53.4	97	0.26
LQ-3	plume	0.26	395	684	52.3	102	0.20
TC-1	plume	1.40	68.0	439	54.2	113	0.22
TC-2	plume	1.48	37.8	374	52.8	126	0.23
TC-3	plume	0.20	1.81 μM	930	51.8	738	-0.10
TC-4	plume	0.82	72.8	1.65 μM	54.0	198	0.05
Background seawater			0.54-1.07[c]	0.18-0.24[c]	52.5 [c]	89[d]	0.29 [d]

[c]The concentration values of Fe, Mn, and Mg were referenced from previous published data (Nishioka et al., 2013; Schlitzer et al., 2018; Gallant and Von Damm, 2006).
[d]The [Ba]diss and $\delta^{138}Ba$ data of background seawater were calculated as averages based on data measured in this study at station S2 from samples collected at depth of 2000 meters and below.

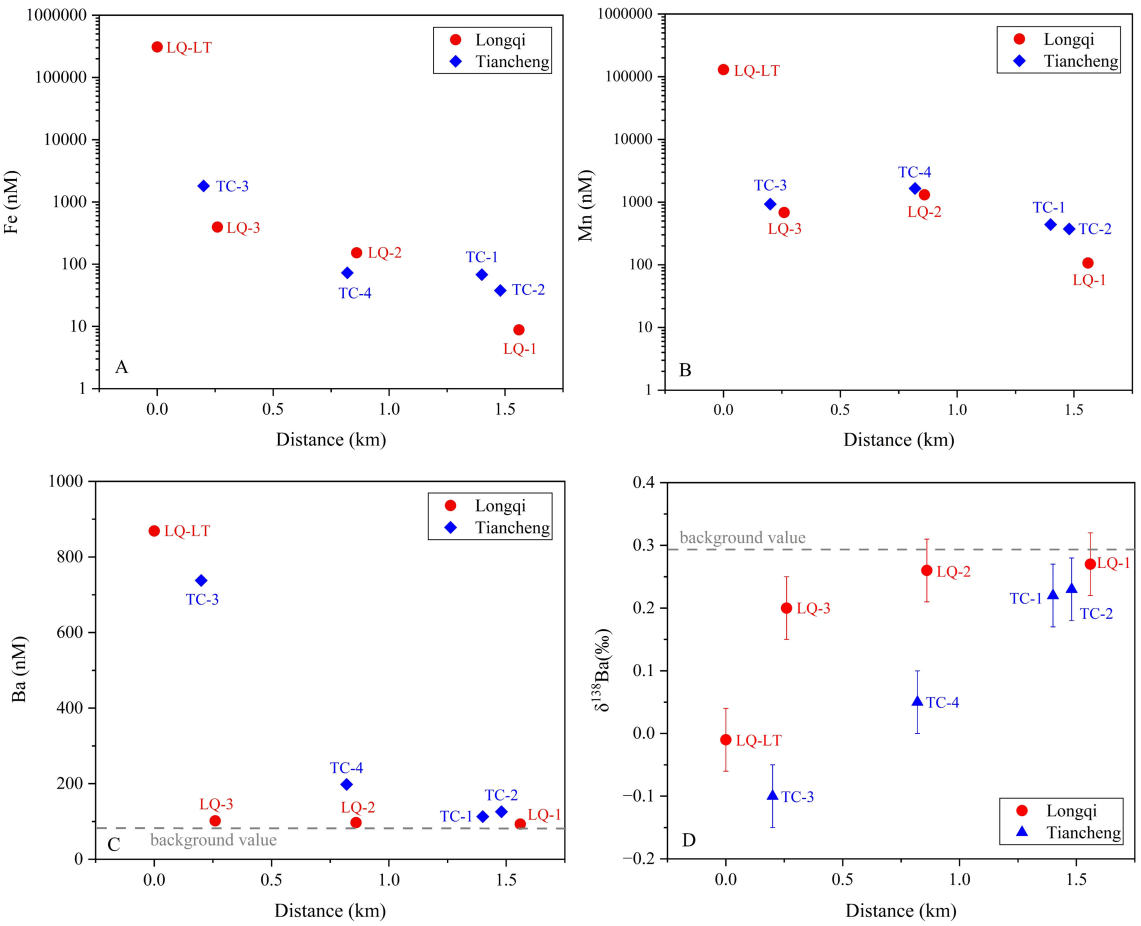

FIGURE 6
Fe, Mn, Ba concentrations and δ^{138}Ba with distance from the Tiancheng (TC) and Longqi (LQ) hydrothermal vents.

(738 nM). Excluding these, the remaining of plume samples displayed a narrower concentration range (93-198 nM). Given the limited reported [Ba]diss data for the Indian Ocean, we calculated a background seawater value (~89 nM) by averaging measurements from station S2 (located away from hydrothermal vents) at depths≥2000 m. All hydrothermal samples exceeded this background value, demonstrating a clear influence of hydrothermal input on Ba enrichment.

The δ^{138}Ba in hydrothermal samples ranged from -0.10 to 0.27‰ and it exhibits a positive correlation with the distance from the hydrothermal vent (Figure 6). The two samples with the nearest distance and highest $[Ba]_{diss}$, LQ-LT and TC-3, had lightest isotope composition -0.01‰ and -0.10‰, respectively, significantly lower than δ^{138}Ba values found in background seawater (0.29 ‰) in this study. The station with the third highest Ba concentration, TC-4, also had a light Ba isotope composition, being 0.05‰. The Ba isotopic compositions (δ^{138}Ba) of samples from the Tiancheng (TC) hydrothermal vent exhibit relatively lower values compared to those from the Longqi (LQ) vent, albeit within analytical uncertainty. Furthermore, the δ^{138}Ba values of TC samples display a slower rate of change with increasing distance from the vent, whereas LQ samples show a rapid increase in δ^{138}Ba values as distance from the vent increases. This contrast likely reflects differences in Ba isotope behavior under distinct geological settings. The Longqi Hydrothermal Field is an active high-temperature system (>300° C) hosted in mafic rocks (Tao et al., 2012). In contrast, the Tiancheng Hydrothermal Field is characterized by low-temperature hydrothermal activity (fluid temperatures ≈13.2°C; Tao et al., 2014), limited magmatic supply, and intense tectonic activity, with fractured basalt dominating the substrate (Chen et al., 2018). These geological disparities—specifically, variations in thermal regimes, host rock composition, and tectonic stress—may govern the observed differences in Ba isotope fractionation and transport dynamics between the two vent fields. Overall, the hydrothermal samples closer to the vents with high $[Ba]_{diss}$ (LQ-LT, TC-3, TC-4) have a mean δ^{138}Ba value of -0.02‰(SD=0.07‰), significantly lower than that of background seawater (0.29‰, SD=0.04‰), which suggests that the hydrothermal vent introduce lighter Ba into surrounding seawater. The Ba isotope compositions of hydrothermal fluids from the Longqi vent field (δ^{138}Ba = −0.01‰) and plume samples near the Tiancheng vent field (δ^{138}Ba = −0.10‰ to +0.05‰) on the Southwest Indian Ridge (SWIR) align closely with the range of initial endmember vent fluids (−0.17‰ to +0.09‰) reported by Hsieh et al. (2021) for mid-ocean

ridge (MOR) systems. This consistency suggests that the Ba isotopic signatures of the SWIR fluids are primarily controlled by water-rock interactions with oceanic crustal lithologies, similar to other MOR hydrothermal systems. The Longqi fluid value (−0.01‰) approaches the range of mid-ocean ridge basalts (MORBs: +0.02‰ to +0.15‰; Nielsen et al., 2018) and falls within the range of pelagic sediments (−0.21‰ to +0.11‰; Bridgestock et al., 2018), supporting Hsieh et al.'s conclusion that Ba isotopes are not significantly fractionated during high-temperature fluid-rock reactions. Notably, the SWIR data lack the extremely heavy δ^{138}Ba values (up to +0.91‰) observed in sediment-influenced systems like the Main Endeavour Field (MEF) (Hsieh et al., 2021). This absence reinforces Hsieh et al.'s finding that sediment interaction can elevate fluid Ba isotope ratios, a process unlikely in the ultramafic- or basalt-hosted SWIR vents. Instead, the SWIR results align more closely with basalt-dominated systems (e.g., East Pacific Rise), further emphasizing the role of host rock composition in shaping initial fluid signatures. These comparisons highlight the utility of Ba isotopes in tracing hydrothermal contributions to oceanic Ba cycling, while underscoring the need to account for local geological and physicochemical conditions when interpreting isotopic variability.

3.2.3 Ba isotopic fractionation during hydrothermal fluids-seawater mixing

Previous studies on Ba isotopes in hydrothermal systems remain limited (Hsieh et al., 2021; Zhang et al., 2024). Hsieh et al. (2021) examined Ba isotopes in hydrothermal fluids and particulates from multiple vents. After correcting for particulate data, they reported Ba isotope compositions in endmember hydrothermal fluids ranging from -0.17‰ to 0.09‰, which are lighter than background seawater. They calculated an isotope fractionation factor ($\Delta^{138}/^{134}Ba_{\text{Dregs-fluid}}$) of -0.35‰ during the mixing of hydrothermal fluids with seawater, suggesting preferential removal of lighter Ba isotopes. Modeling with this fractionation value, they further inferred that the Ba isotope composition would increase to +1.7 ± 0.7‰ when barite becomes undersaturated, indicating a potential contribution of heavier Ba isotopes from hydrothermal systems to the ocean. In contrast, Zhang et al. (2024) performed direct measurements on non-buoyant plume samples from the Rainbow hydrothermal field and found the δ^{138}Ba values of hydrothermally affected deep seawater exhibit a lighter isotopic signature (~ 0.3‰) compared to those found at similar depths at distant locations in the Atlantic Ocean (~ 0.45‰). Interestingly, they found that dissolved Ba undergoes conservative mixing between Rainbow hydrothermal endmember fluids and the non-buoyant plume, as evidenced by a significant linear correlation between dBa and ^{3}He. However, the Rainbow is an ultramafic system, distinct from most mafic-hosted vents. The linear regression used for Rainbow is based on a single sample and whether the conservative Ba behavior observed in the Rainbow field also occurs in other hydrothermal systems is unknown. To better constrain the global hydrothermal Ba inputs, more observations in hydrothermal plumes are required.

In this study, we also found the hydrothermal fluid and plume samples with high concentration of Ba exhibited lighter Ba isotope compositions, ranged from -0.10‰ to 0.05 ‰, which is consistent with the result reported in the previous study (Zhang et al., 2024). The relationship between dissolved Ba concentrations and Ba isotope compositions (δ^{138}Ba) is displayed in Supplementary Figure S2. One station in our samples (TC-4) exhibited a dissolved Ba concentration of 198 nM, closely matching the effective input Ba concentration of 200 nM calculated in Hsieh et al. (2021). However, the Ba isotope composition at TC-4 was 0.05‰, substantially lighter than the model-based value (+1.7 ± 0.7‰) reported by Hsieh et al. (2021). This significant discrepancy between the observed isotopic composition and the model-predicted endmember values raises a critical question: what mechanisms drive the marked deviation, particularly given the opposing trends?

It is critical to consider that Ba may be sequestered from hydrothermal fluids via coprecipitation with iron-manganese oxides and sulfide minerals, as well as adsorption onto authigenic particulates, processes that can significantly influence its isotopic fractionation (Rouxel et al., 2016; Yuan et al., 2018). Previous studies indicate that in high-temperature hydrothermal environments, anhydrite has a higher saturation index than barite, which suggests that anhydrite may precipitate firstly, thereby limiting barite precipitation (Jamieson et al., 2016). Zhang et al. (2024) also highlighted the complexity of barite precipitation and Ba removal in hydrothermal systems. Therefore, assuming the Ba removal is solely due to barite formation, as proposed by Hsieh et al. (2021), may not be correct. As reported by previous studies, trace elements are often precipitated with particles released from hydrothermal vents (Rouxel et al., 2016; Yuan et al., 2018). Analysis of filter membranes from Longqi and Tiancheng hydrothermal vents samples using Scanning Electron Microscopy and Energy-Dispersive X-ray Spectroscopy (SEM-EDX; FEI Quanta 200) revealed that, various mineral species exist in addition to barite, such as Fe oxides, FeS, FeS_2, $Fe_{(1-x)}Sx$, CeO_2, ZnS, and SiO_2, etc. (Figures 7A; 7B). Therefore, barium may co-precipitate with iron-manganese oxides and metal sulfide particles in addition to forming barite; these various processes could result in different isotopic fractionation. Further studies should be conducted to investigate the Ba isotopic fractionation associated with different removal processes.

3.3 Sediments near hydrothermal field

3.3.1 Geochemical characteristics

As discussed in the previous section, some elements (e.g. Fe, Mn, Cu, Zn) enriched in hydrothermal fluids typically precipitate with particles, and eventually settle to the seafloor near the vents (Liao et al., 2018). Even after alteration during early diagenesis processes, the hydrothermal elements that are enriched in sediments in general remain stable (Feely et al., 1987; Li et al., 2015; Agarwal et al., 2020). These sediments preserve geochemical

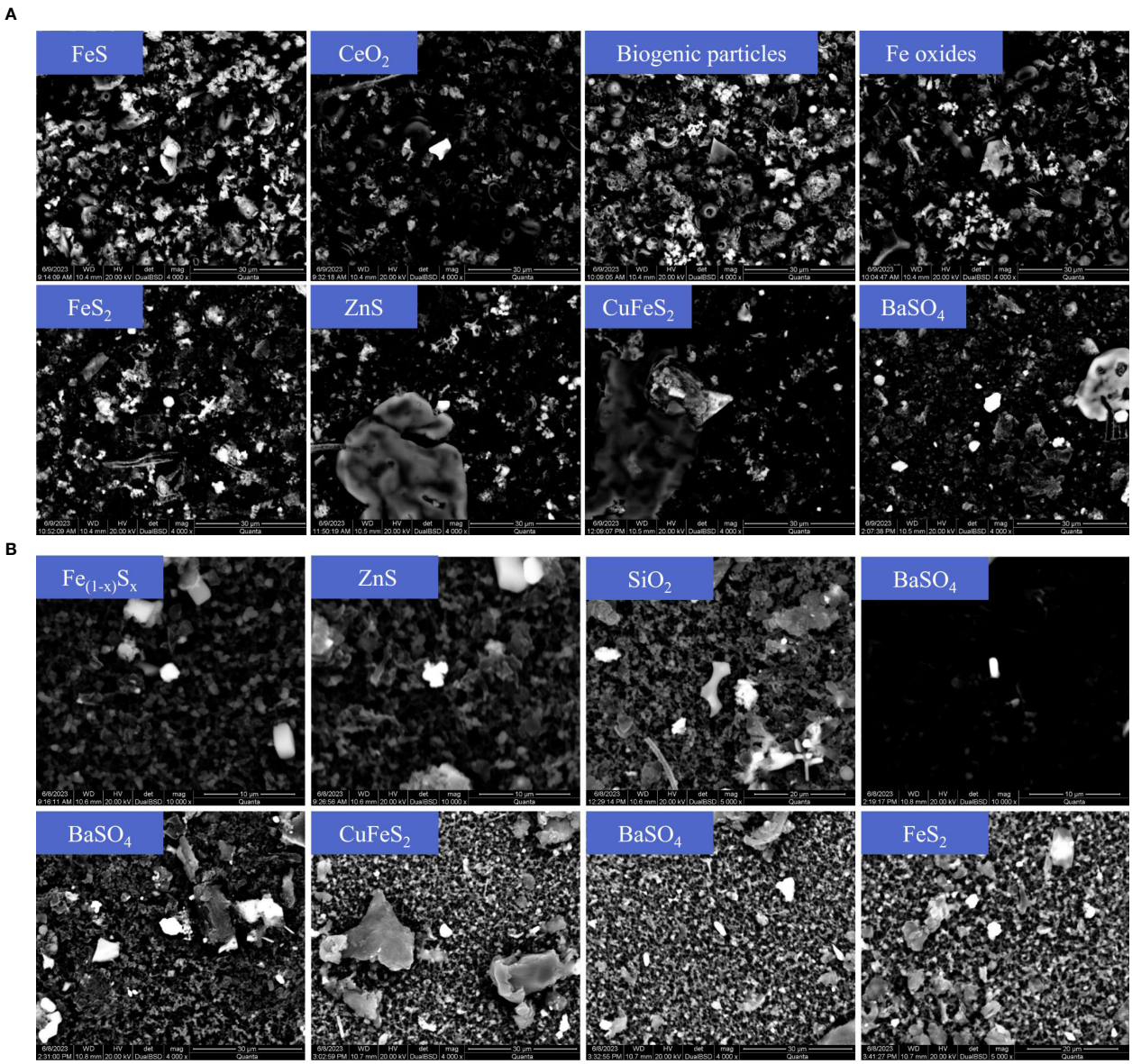

FIGURE 7
(A) SEM images of filter near the hydrothermal vent of Longqi. **(B)** SEM images of filter near the hydrothermal vent of Tiancheng.

information related to hydrothermal activities, offering valuable insights into complex hydrothermal systems (Dias and Barriga, 2006; Liao et al., 2018).

The measured major and minor element contents in selected sediment samples are reported in Table 4A. Visual observation on the selected surface sediment samples revealed that samples P1 to P9 are light gray, while P10 to P15 are reddish-brown, likely due to higher metal content from hydrothermal influence. The analytical results show that sediments P10–P15 have Fe contents ranging from 8.8% to 32.3%, with an average of 20.8%, significantly higher than those in sediments P1–P9 (0.4% – 3.2%, with an average of 1.21%). The Cu and Zn contents in sediments P10–P15 range from 182 μg/g to 130 mg/g (averaged to be 47 mg/g) and 74 μg/g to 33 mg/g (averaged to be 8.8 mg/g), respectively. These values are substantially higher than those in sediments P1–P9, where Cu and Zn contents range from 19 to 100 μg/g (averaged to be 52.8 μg/g) and 15 to 66 μg/g (averaged to be 40.6 μg/g), respectively.

The principal component analysis of the geochemistry data set was performed using IBM SPSS Statistics 25.0 software to further constrain the factors influencing the geochemistry data for the surface sediments in the study area (Supplementary Table S2). Three major factors with eigen values greater than 1 that together explain approximately 80% of the variance of the data set were extracted. And the PCA scores and loading Plot of surface sediment geochemistry is showed in Supplementary Figure S3. The dominant factor (Factor 1 (F1)) explains approximately 42% of the total

10.3389/fmars.2025.1538835

TABLE 4A Major and trace element concentrations of surface sediments.

Sample ID	Distance (km)	Fe (%)	Mn (mg/g)	Cu (μg/g)	Zn (μg/g)	Al (μg/g)	Ti (μg/g)	Ca (mg/g)	REY (μg/g)	$(Eu/Eu^*)_N$
P1	51.79	2.0	2.44	85	49	17	1073	261	156	0.72
P2	35.54	3.2	2.39	100	66	13	696	194	99	0.71
P3	418.71	1.2	0.72	69	72	9	601	320	79	0.67
P4	20.06	0.5	0.34	19	20	6	340	353	39	0.68
P5	658.94	0.7	0.56	35	25	8	515	330	66	0.70
P6	258.90	0.6	0.24	32	23	9	481	325	56	0.69
P7	655.96	1.8	1.52	64	56	20	1810	239	100	0.74
P8	558.30	0.4	0.29	25	15	4	278	347	46	0.70
P9	274.91	0.5	0.69	46	39	8	498	321	51	0.70
P10	1.03	18.5	0.80	130400	1277	2	41	6	17	1.10
P11	73.15	16.3	2.97	35260	33940	14	669	119	65	0.90
P12	166.58	32.3	0.01	58750	6878	1	5	2	7	3.39
P13	1.09	19.1	3.32	28860	4200	4	109	5	43	1.31
P14	0.08	8.8	3.21	182	74	76	4785	64	76	1.08
P15	0.37	29.8	24.8	29550	6609	2	181	4	16	2.18

TABLE 4B The Ba concentrations and Ba isotope compositions in surface sediments.

Sample ID	Type	Ba Concentrations (μg/g)	δ^{138}Ba ‰
P1	Background sediment	636	
P2	Background sediment	488	
P3	Background sediment	1109	0.14
P4	Background sediment	191	
P5	Background sediment	475	0.12
P6	Background sediment	548	
P7	Background sediment	1065	0.01
P8	Background sediment	350	
P9	Background sediment	645	
P10	Hydrothermal-impacted sediment	869	
P11	Hydrothermal-impacted sediment	413	-0.06
P12	Hydrothermal-impacted sediment	917	-0.14
P13	Hydrothermal-impacted sediment	273	0.01
P14	Hydrothermal-impacted sediment	248	-0.07
P15	Hydrothermal-impacted sediment	110	-0.16

variance and is loaded primarily with lithogenic elements, e.g., Fe, Cu, Pb, S, V, Zn, which frequently reflect the hydrothermal component. Factor 2 (F2), explaining a significant portion of the remaining variance, was predominantly associated with elevated Al and Ti concentrations, which are commonly used as lithogenic tracers. Factor 3 (F3) highlighted Ba enrichment, likely linked to marine authigenic processes, such as biogenic barite precipitation or scavenging by sinking organic matter. This tripartite structure

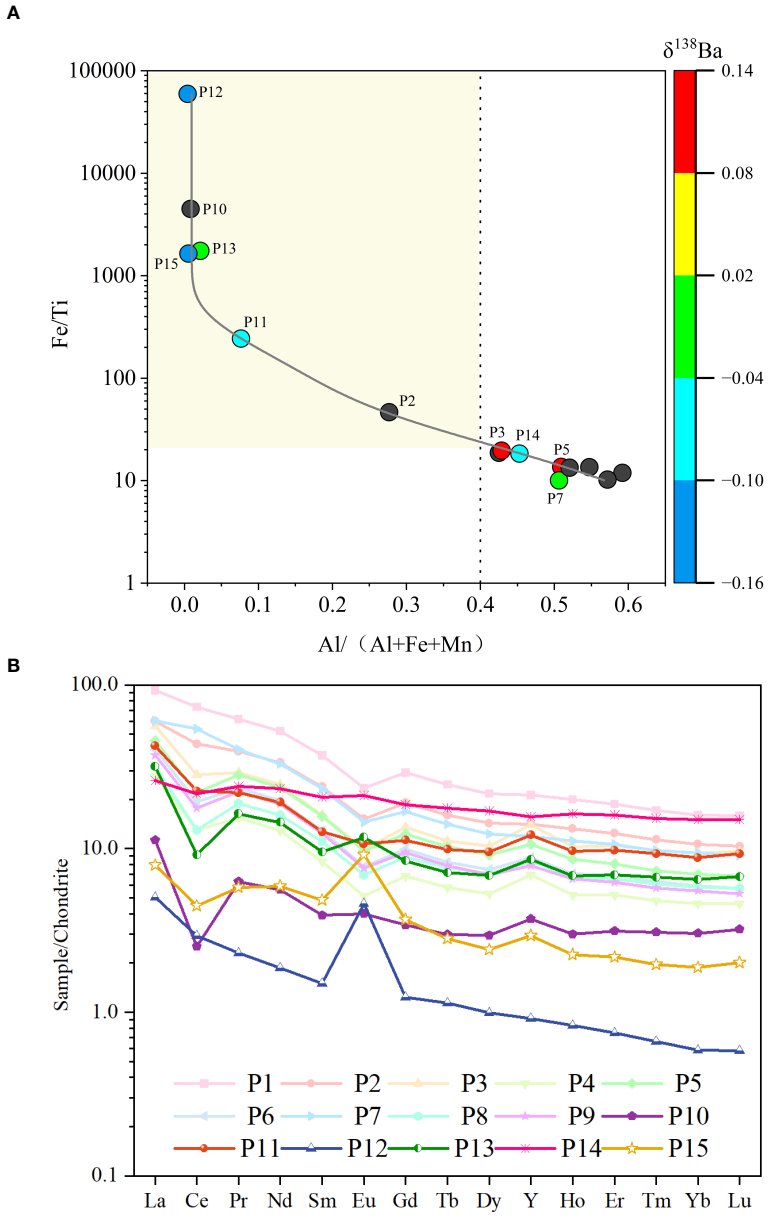

FIGURE 8
(A) Al/(Al+Fe+Mn) vs. Fe/Ti diagram (δ^{138}Ba as as X-axis color bar) of sediments. The black dots represents samples not analyzed for barium isotopes. **(B)** Chondrite-normalized REE distributions of the study area sediments. The chondrite data are from Boynton (1984).

underscores the interplay of hydrothermal activity, terrestrial sediment supply, and pelagic marine influences in shaping the geochemical signatures of the studied sediments.

The elemental ratios serve as a robust proxy for assessing hydrothermal input intensity (Qiu et al., 2023). To evaluate hydrothermal influence on sediments along the Southwest Indian Ridge, two geochemical indices were employed: (1) the metal enrichment index Al/(Al + Fe + Mn) and (2) the Fe/Ti ratio. These indices effectively differentiate hydrothermal contributions from detrital components in marine sediments.

The Al/(Al + Fe + Mn) index distinguishes metal-rich hydrothermal sediments from background sediments. Previous studies (e.g., Fisher et al., 1969; Dias and Barriga, 2006) established that background deep-sea sediments, devoid of hydrothermal input, typically exhibit values >40% due to higher detrital aluminosilicate content. In contrast, hydrothermal sediments near vent systems are characterized by lower values, reflecting Fe-Mn oxide dominance. Concurrently, the Fe/Ti ratio quantifies hydrothermal metal enrichment relative to detrital inputs, with ratios >20 indicating significant hydrothermal

influence (Zhou et al., 2020). By cross-plotting these indices (Figure 8A), hydrothermal and detrital sediment sources can be systematically discriminated (Liao et al., 2018).

Application of this dual-index approach to 15 surface sediment samples revealed distinct geochemical signatures. Six samples (P2, P10–P13, P15) exhibited Fe/Ti >20 coupled with Al/(Al + Fe + Mn) <40%, unambiguously identifying them as hydrothermal-impacted sediments (Figure 8A). These results align with established thresholds and underscore the utility of combining elemental ratios to disentangle complex sedimentary provenance.

Another way to identify the significance of hydrothermal activity on surface sediments is by looking into the rare earth element (REE) composition in sediments. The hydrothermal fluids from mid-ocean ridges are characterized by Light REE (LREE) enrichment and positive Eu anomalies (Douville et al., 1999; Allen and Seyfried, 2005; Cao et al., 2012). Consequently, sediments affected by hydrothermal activity often exhibit similar characteristics (Gillis and Thompson, 1993; Liao et al., 2018; Zhou et al., 2020). The Chondrite-normalized REE patterns of the sediment samples are shown in Figure 8B. In general, all sediment samples showed a trend of LREE enrichment. Whilst, several samples (from P10 to P15), to different extents, showed apparent positive Eu anomaly ($(Eu/Eu^{*})_N$ = 0.90–3.39) compared to the value (0.71) reported by Liao et al. (2018) for the background sediments.

It is specifically noted that although the metal ratios of P14 exceed the predicted range, they fall near the threshold boundaries. Additionally, P14 exhibits elevated Fe, Cu, and Zn concentrations compared to samples P1–P9, while its Ca content is significantly lower. Visually, the sample displays a reddish-brown coloration—a characteristic indicative of hydrothermal activity. Based on this integrated evidence, we have classified P14 as hydrothermal-impacted sediment. The sediment types are explicitly detailed in Table 4B. Overall, by taking into consideration of the results, we considered that, among the 15 surface sediment samples, P10 to P15 can be identified as hydrothermal-impacted sediments, and that P1 to P9 represent background sediments.

3.3.2 Ba contents and Ba isotope compositions

Following sediment classification, we measured the Ba contents across all samples and selected eight representative samples for Ba isotope analysis. This subset included three background sediments (P3, P5, P7) and five hydrothermal sediments (P11 to P15). The Ba contents and its isotopic compositions in sediment samples are reported in Table 4B. The Ba content ranged from 110–1109 μg/g, and there is no apparent elevation in Ba content in hydrothermal influenced samples. Paytan and Griffith (2007) reported that the content of Ba in marine sediments can be significantly affected by dilution effects due to the accumulation of other sedimentary components.

To the contrary, the δ^{138}Ba values in background samples (P3, P5,P7) ranged from 0.01‰ to 0.14‰, similar to the deep-sea sediments reported in previous study (0 – 0.10‰) (Bridgestock et al., 2018). In hydrothermal-impacted sediments (P11 to P15), δ^{138}Ba values ranged from -0.16‰ – 0.01‰. The average δ^{138}Ba of hydrothermal sediments (-0.08‰, SD=0.07‰, *n=5*) is notably lower than that of the background sediments (0.09‰, SD=0.07‰, *n=3*). The relationship of Ba contents and δ^{138}Ba is shown in Supplementary Figure S4. The results show that the data points do not follow a distinct fractionation trend (i.e., lighter Ba isotopes correlating with higher Ba concentrations). Instead, samples with lighter Ba isotopes exhibit both high and low Ba concentrations. We therefore propose that the Ba concentrations in hydrothermal-impacted sediments are influenced by dilution effects from co-occurring hydrothermal metal elements.

As we discussed in section 3.2.3, during the mixing process between hydrothermal fluid and seawater, lighter Ba isotopes are preferentially removed, resulting the settling particles compose lighter Ba isotope. This is consistent with our observation in the hydrothermally influenced sediment samples in this study. As conclusion, while the Ba content of hydrothermal sediments cannot be distinguished from the background sediments, the Ba isotope retains lighter isotopic signature, potentially can serve as an indicator of hydrothermal influence on sediment of the study region.

4 Conclusion

Although the overall Ba cycle in the ocean is relatively well understood, studies focusing on specific processes, such as hydrothermal activities, remain limited. This study presents the first Ba isotope study in hydrothermal fluid, seawater, and sediment near Southwest Indian Ocean hydrothermal vent field.

The vertical profiles of dissolved Ba and its isotope compositions is similar with previous results of other oceans. The $[Ba]_{diss}$ in several water samples collected using ROV near hydrothermal vents are significantly higher than background seawater, while the Ba isotope compositions in those samples (-0.10 – 0.05‰) are distinctly lower than those of background seawater(~ 0.29‰), suggesting that the hydrothermal fluids in the study region bearing lighter Ba isotopes.

Analysis of filter membranes from Longqi and Tiancheng hydrothermal vents samples using Scanning Electron Microscopy and Energy-Dispersive X-ray Spectroscopy revealed that, various mineral species exist, not only barite, but also Fe oxides, FeS, FeS_2, $Fe_{(1-x)}$ Sx, CeO_2, ZnS, and SiO_2, etc. Therefore, barium may co-precipitate with iron-manganese oxides and metal sulfide particles in addition to forming barite, which processes could result in different isotopic fractionation.

Analysis of hydrothermally influenced sediment showed that the Ba isotope compositions are significantly lighter (-0.16‰ – 0.01‰) compared to those in background sediments (0.01 – 0.14‰), which is consistent with lighter isotope composition found in hydrothermal fluid and also align with the calculation result of the Rayleigh fractionation model, suggesting lighter isotopes are preferable removed during the mixing process between hydrothermal fluid and seawater. Therefore, the Ba isotope may serve as a valuable indicator of hydrothermal influence in future studies on sediment.

Data availability statement

The original contributions presented in the study are included in the article/Supplementary Material. Further inquiries can be directed to the corresponding authors.

Author contributions

CZ: Formal Analysis, Investigation, Visualization, Writing – original draft. LL: Conceptualization, Data curation, Project administration, Supervision, Validation, Writing – original draft, Writing – review & editing. JL: Data curation, Investigation, Methodology, Writing – original draft. RX: Conceptualization, Data curation, Formal Analysis, Writing – review & editing. XW: Data curation, Investigation, Methodology, Writing – original draft. XS: Funding acquisition, Project administration, Resources, Writing – review & editing.

Funding

The author(s) declare that financial support was received for the research and/or publication of this article. Natural Science Foundation of China (42076046,42376035)National Key Research and Development Program of China (2022YEE0136055).

Acknowledgments

The authors would like to thank the captain and crew of the *R/V Da Yang 1* and *R/V Dayang* and the pilots of the ROV *Hailong III* for their skilled operations and technical support at sea. We want to thank all the colleagues and students who have helped at sea or in the laboratory to make this work possible. This work was supported by the Natural Science Foundation of China (42076046, 42376035), the National Key Research and Development Program of China (2022YFE0136500).

Conflict of interest

The authors declare that the research was conducted in the absence of any commercial or financial relationships that could be construed as a potential conflict of interest.

Generative AI statement

The author(s) declare that no Generative AI was used in the creation of this manuscript.

Correction note

This article has been corrected with minor changes. These changes do not impact the scientific content of the article.

Publisher's note

All claims expressed in this article are solely those of the authors and do not necessarily represent those of their affiliated organizations, or those of the publisher, the editors and the reviewers. Any product that may be evaluated in this article, or claim that may be made by its manufacturer, is not guaranteed or endorsed by the publisher.

Supplementary material

The Supplementary Material for this article can be found online at: https://www.frontiersin.org/articles/10.3389/fmars.2025.1538835/full#supplementary-material

References

Agarwal, D. K., Roy, P., Prakash, L. S., and Kurian, P. J. (2020). Hydrothermal signatures in sediments from eastern Southwest Indian Ridge 63°E to 68°E. *Mar. Chem.* 218, 103732. doi: 10.1016/j.marchem.2019.103732

Allen, D. E., and Seyfried, W. E. (2005). REE controls in ultramafic hosted MOR hydrothermal systems: An experimental study at elevated temperature and pressure. *Geochimica Cosmochimica Acta* 69, 675–683. doi: 10.1016/j.gca.2004.07.016

Alt, J. C. (1995). Subseafloor processes in mid-ocean ridge hydrothermal systems. *Seafloor Hydrothermal Systems: Physical Chemical Biological Geological Interact.* 91. doi: 10.1029/GM091p0085

Bates, S. L., Hendry, K. R., Pryer, H. V., Kinsley, C. W., Pyle, K. M., Woodward, E. M. S., et al. (2017). Barium isotopes reveal role of ocean circulation on barium cycling in the Atlantic. *Geochimica Cosmochimica Acta* 204, 286–299. doi: 10.1016/j.gca.2017.01.043

Bennett, S. A., Rouxel, O., Schmidt, K., Garbe-Schönberg, D., Statham, P. J., and German, C. R. (2009). Iron isotope fractionation in a buoyant hydrothermal plume, 5 S Mid-Atlantic Ridge. *Geochimica Cosmochimica Acta* 73, 5619–5634. doi: 10.1016/j.gca.2009.06.027

Boynton, W. V. (1984). Cosmochemistry of the rare earth elements: meteorite studies[J]. *Dev. Geochem.* 2, 63–114. doi: 10.1016/B978-0-444-42148-7.50008-3

Bridgestock, L., Hsieh, Y.-T., Porcelli, D., Homoky, W. B., Bryan, A., and Henderson, G. M. (2018). Controls on the barium isotope compositions of marine sediments. *Earth Planetary Sci. Lett.* 481, 101–110. doi: 10.1016/j.epsl.2017.10.019

Bridgestock, L., Nathan, J., Paver, R., Hsieh, Y.-T., Porcelli, D., Tanzil, J., et al. (2021). Estuarine processes modify the isotope composition of dissolved riverine barium fluxes to the ocean. *Chem. Geology* 579, 120340. doi: 10.1016/j.chemgeo.2021.120340

Butterfield, D. A., and Massoth, G. J. (1994). Geochemistry of north Cleft segment vent fluids: Temporal changes in chlorinity and their possible relation to recent volcanism. *J. Geophysical Research: Solid Earth* 99, 4951–4968. doi: 10.1029/93jb02798

Cannat, M., Sauter, D., Bezos, A., Meyzen, C., Humler, E., and Le Rigoleur, M. (2008). Spreading rate, spreading obliquity, and melt supply at the ultraslow spreading Southwest Indian Ridge. *Geochemistry Geophysics Geosystems* 9 (4). doi: 10.1029/2007gc001676

Cao, Z., Cao, H., Tao, C., Li, J., Yu, Z., and Shu, L. (2012). Rare earth element geochemistry of hydrothermal deposits from Southwest Indian Ridge. *Acta Oceanologica Sin.* 31, 62–69. doi: 10.1007/s13131-012-0192-1

Cao, Z., Li, Y., Rao, X., Yu, Y., Hathorne, E. C., Siebert, C., et al. (2020). Constraining barium isotope fractionation in the upper water column of the South China Sea. *Geochimica Cosmochimica Acta* 288, 120–137. doi: 10.1016/j.gca.2020.08.008

Cao, Z., Rao, X., Yu, Y., Siebert, C., Hathorne, E. C., Liu, B., et al. (2021). Stable barium isotope dynamics during estuarine mixing. *Geophysical Res. Lett.* 48 (19). doi: 10.1029/2021gl095680

Cao, Z., Siebert, C., Hathorne, E. C., Dai, M., and Frank, M. (2016). Constraining the oceanic barium cycle with stable barium isotopes. *Earth Planetary Sci. Lett.* 434, 1–9. doi: 10.1016/j.epsl.2015.11.017

Carter, S. C., Paytan, A., and Griffith, E. M. (2020). Toward an improved understanding of the marine barium cycle and the application of marine barite as a paleoproductivity proxy. *Minerals* 10, 421. doi: 10.3390/min10050421

Chen, J., Tao, C. H., Liang, J., Liao, S. L., Dong, C. W., Li, H. M., et al. (2018). Newly discovered hydrothermal fields along the ultraslow-spreading Southwest Indian Ridge around 63°E. *Acta Oceanologica Sin.* 37, 61–67. doi: 10.1007/s13131-018-1333-y

Coogan, L. A., Seyfried, W. E., and Pester, N. J. (2019). Environmental controls on mid-ocean ridge hydrothermal fluxes. *Chem. Geology* 528, 119285. doi: 10.1016/j.chemgeo.2019.119285

Crockford, P. W., Wing, B. A., Paytan, A., Hodgskiss, M. S. W., Mayfield, K. K., Hayles, J. A., et al. (2019). Barium-isotopic constraints on the origin of post-Marinoan barits. *Earth Planetary Sci. Lett.* 519, 234–244. doi: 10.1016/j.epsl.2019.05.018

Demets, C., Gordon, R. G., Argus, D. F., and Stein, S. (1994). Effect of recent revisions to the geomagnetic reversal time scale on estimates of current plate motions. *John Wiley Sons Ltd.* 21, 2091–2094. doi: 10.1029/94GL02118

Dias, A. S., and Barriga, F. J. (2006). Mineralogy and geochemistry of hydrothermal sediments from the serpentinite-hosted Saldanha hydrothermal field (36 34′ N; 33 26′ W) at MAR. *Mar. Geology* 225, 157–175. doi: 10.1016/j.margeo.2005.07.013

Douville, E., Bienvenu, P., Charlou, J. L., Donval, J. P., Fouquet, Y., Appriou, P., et al. (1999). Yttrium and rare earth elements in fluids from various deep-sea hydrothermal systems. *Geochimica Cosmochimica Acta* 63, 627–643. doi: 10.1016/S0016-7037(99)00024-1

Dymond, J., Suess, E., and Lyle, M. (1992). Barium in deep-sea sediment: A geochemical proxy for paleoproductivity. *PALEOCEANOGRAPHY*. 7, 163–181. doi: 10.1029/92PA00181

Eagle, M., Paytan, A., Arrigo, K. R., van Dijken, G., and Murray, R. W. (2003). A comparison between excess barium and barite as indicators of carbon export. *Paleoceanography* 18 (1). doi: 10.1029/2002pa000793

Elderfield, H., and Schultz, A. (1996). Mid-ocean ridge hydrothermal fluxes and the chemical composition of the ocean. *Annu. Rev. Earth Planetary Sci.* 24, 191–224. doi: 10.1146/annurev.earth.24.1.191

Fang, Z., and Wang, W.-X. (2021). Size speciation of dissolved trace metals in hydrothermal plumes on the Southwest Indian Ridge. *Sci. Total Environ.* 771, 145367. doi: 10.1016/j.scitotenv.2021.145367

Feely, R. A., Lewison, M., Massoth, G. J., Robert-Baldo, G., Lavelle, J. W., Byrne, R. H., et al. (1987). Composition and dissolution of black smoker particulates from active vents on the Juan de Fuca Ridge. *J. Geophysical Research: Solid Earth* 92, 11347–11363. doi: 10.1029/JB092iB11p11347

Findlay, A. J., Estes, E. R., Gartman, A., Yücel, M., Kamyshny, A. Jr., and Luther, III, G. W. (2019). Iron and sulfide nanoparticle formation and transport in nascent hydrothermal vent plumes. *Nat. Commun.* 10, 1597. doi: 10.1038/s41467-019-09580-5

Fisher, D. E., Joensuu, O., and Boström, K. (1969). Elemental abundances in ultramafic rock and their relation to the upper mantle. *J. Geophysical Res.* 74, 3865–3873. doi: 10.1029/JB074i015p03865

Fitzsimmons, J. N., John, S. G., Marsay, C. M., Hoffman, C. L., Nicholas, S. L., Toner, B. M., et al. (2017). Iron persistence in a distal hydrothermal plume supported by dissolved–particulate exchange. *Nat. Geosci.* 10, 195–201. doi: 10.1038/ngeo2900

Fu, W. W., and Wang, W. L. (2022). Biogeochemical equilibrium responses to maximal productivity in high nutrient low chlorophyll regions. *J. Geophysical Research-Biogeosciences* 127 (5). doi: 10.1029/2021jg006636

Gallant, R. M., and Von Damm, K. L. (2006). Geochemical controls on hydrothermal fluids from the Kairei and Edmond Vent Fields, 23°-25°S. *Cent. Indian Ridge Geochemistry Geophysics Geosystems* 7 (6). doi: 10.1029/2005gc001067

Gartman, A., Findlay, A. J., Hannington, M., Garbe-Schönberg, D., Jamieson, J. W., and Kwasnitschka, T. (2019). The role of nanoparticles in mediating element deposition and transport at hydrothermal vents. *Geochimica Cosmochimica Acta* 261, 113–131. doi: 10.1016/j.gca.2019.06.045

Gillis, K. M., and Thompson, G. (1993). Metabasalts from the Mid-Atlantic Ridge: new insights into hydrothermal systems in slow-spreading crust. *Contributions to Mineralogy Petrology* 113, 502–523. doi: 10.1007/BF00698319

Hawkes, J. A., Connelly, D., Gledhill, M., and Achterberg, E. P. (2013). The stabilisation and transportation of dissolved iron from high temperature hydrothermal vent systems. *Earth Planetary Sci. Lett.* 375, 280–290. doi: 10.1016/j.epsl.2013.05.047

Horner, T. J., and Crockford, P. W. (2021). Barium Isotopes, geochemical tracers in earth system science. doi: 10.1017/9781108865845

Horner, T. J., Kinsley, C. W., and Nielsen, S. G. (2015). Barium-isotopic fractionation in seawater mediated by barite cycling and oceanic circulation. *Earth Planetary Sci. Lett.* 430, 511–522. doi: 10.1016/j.epsl.2015.07.027

Hsieh, Y.-T., Bridgestock, L., Scheuermann, P. P., Seyfried, W. E., and Henderson, G. M. (2021). Barium isotopes in mid-ocean ridge hydrothermal vent fluids: A source of isotopically heavy Ba to the ocean. *Geochimica Cosmochimica Acta* 292, 348–363. doi: 10.1016/j.gca.2020.09.037

Hsieh, Y.-T., and Henderson, G. M. (2017). Barium stable isotopes in the global ocean: Tracer of Ba inputs and utilization. *Earth Planetary Sci. Lett.* 473, 269–278. doi: 10.1016/j.epsl.2017.06.024

Jacquet, S. H. M., Dehairs, F., Cardinal, D., Navez, J., and Delille, B. (2005). Barium distribution across the Southern Ocean frontal system in the Crozet–Kerguelen Basin. *Mar. Chem.* 95, 149–162. doi: 10.1016/j.marchem.2004.09.002

Jamieson, J. W., Hannington, M. D., Tivey, M. K., Hansteen, T., Williamson, N. M. B., Stewart, M., et al. (2016). Precipitation and growth of barite within hydrothermal vent deposits from the Endeavour Segment, Juan de Fuca Ridge. *Geochimica Cosmochimica Acta* 173, 64–85. doi: 10.1016/j.gca.2015.10.021

Ji, F., Zhou, H., Yang, Q., Gao, H., Wang, H., and Lilley, M. D. (2017). Geochemistry of hydrothermal vent fluids and its implications for subsurface processes at the active Longqi hydrothermal field, Southwest Indian Ridge. *Deep Sea Res. Part I: Oceanographic Res. Papers* 122, 41–47. doi: 10.1016/j.dsr.2017.02.001

Kumagai, H., Nakamura, K., Toki, T., Morishita, T., Okino, K., Ishibashi, J., et al. (2008). Geological background of the Kairei and Edmond hydrothermal fields along the Central Indian Ridge: Implications of their vent fluids' distinct chemistry. *Geofluids* 8, 239–251. doi: 10.1111/j.1468-8123.2008.00223.x

Lea, D. W. (1993). CONSTRAINTS ON THE ALKALINITY AND CIRCULATION OF GLACIAL CIRCUMPOLAR DEEP-WATER FROM BENTHIC FORAMINIFERAL BARIUM. *Global Biogeochemical Cycles* 7, 695–710. doi: 10.1029/93gb01536

Lea, D., and Boyle, E. (1989). Barium content of benthic foraminifera controlled by bottom-water composition. *Nature* 338, 751–753. doi: 10.1038/338751a0

Lea, D. W., and Boyle, E. A. (1991). BARIUM IN PLANKTONIC-FORAMINIFERA. *Geochimica Et Cosmochimica Acta* 55, 3321–3331. doi: 10.1016/0016-7037(91)90491-m

Li, L., Liu, J., Wang, X., and Shi, X. (2015). Dissolved trace metal distributions and Cu speciation in the southern Bohai Sea. *China Mar. Chem.* 172, 34–45. doi: 10.1016/j.marchem.2015.03.002

Li, M., Toner, B. M., Baker, B. J., Breier, J. A., Sheik, C. S., and Dick, G. J. (2014). Microbial iron uptake as a mechanism for dispersing iron from deep-sea hydrothermal vents. *Nat. Commun.* 5, 3792. doi: 10.1038/ncomms4192

Liao, S., Tao, C., Li, H., Zhang, G., Liang, J., Yang, W., et al. (2018). Surface sediment geochemistry and hydrothermal activity indicators in the Dragon Horn area on the Southwest Indian Ridge. *Mar. Geology* 398, 22–34. doi: 10.1016/j.margeo.2017.12.005

Lin, Y.-B., Wei, H.-Z., Jiang, S.-Y., Hohl, S., Lei, H.-L., Liu, X., et al. (2020). Accurate determination of barium isotopic compositions in sequentially leached phases from carbonates by double spike-Thermal ionization mass spectrometry (DS-TIMS). *Analytical Chem.* 92, 2417–2424. doi: 10.1021/acs.analchem.9b03137

Lin, Y.-B., Wei, H.-Z., Zhang, F., Hohl, S. V., Wei, G.-Y., Li, T., et al. (2022). Evaluation of shallow-water corals and associated carbonate sediments as seawater Ba isotope archives in the South China Sea. *Palaeogeography Palaeoclimatology Palaeoecol.* 605. doi: 10.1016/j.palaeo.2022.111196

Lough, A., Homoky, W., Connelly, D., Comer-Warner, S., Nakamura, K., Abyaneh, M., et al. (2019). Soluble iron conservation and colloidal iron dynamics in a hydrothermal plume. *Chem. Geology* 511, 225–237. doi: 10.1016/j.chemgeo.2019.01.001

McCulloch, M., Fallon, S., Wyndham, T., Hendy, E., Lough, J., and Barnes, D. (2003). Coral record of increased sediment flux to the inner Great Barrier Reef since European settlement. *Nature* 421, 727–730. doi: 10.1038/nature01361

McManus, J., Berelson, W. M., Hammond, D. E., and Klinkhammer, G. P. (1999). Barium cycling in the north pacific: implications for the utility of ba as a paleoproductivity and paleoalkalinity proxy. *Paleoceanography* 14, 53–61. doi: 10.1029/1998pa900007

Middleton, J. T., Hong, W. L., Paytan, A., Auro, M. E., Griffith, E. M., and Horner, T. J. (2023). Barium isotope fractionation in barite–fluid systems at chemical equilibrium. *Chem. Geology* 627, 121453. doi: 10.1016/j.chemgeo.2023.121453

Mori, C., Santos, I. R., Brumsack, H.-J., Schnetger, B., Dittmar, T., and Seidel, M. (2019). Non-conservative behavior of dissolved organic matter and trace metals (Mn, Fe, Ba) driven by porewater exchange in a subtropical mangrove-estuary. *Front. Mar. Sci.* 6. doi: 10.3389/fmars.2019.00481

Mottl, M. J., Holland, H. D., and Corr, R. F. (1978). Chemical exchange during hydrothermal alteration of basalt by seawater—II. Experimental results for Fe, Mn, and sulfur species. *Geochimica Et Cosmochimica Acta* 43, 869–884. doi: 10.1016/0016-7037(79)90225-4

Nielsen, S. G., Horner, T. J., Pryer, H. V., Blusztajn, J., Shu, Y., Kurz, M. D., et al. (2018). Barium isotope evidence for pervasive sediment recycling in the upper mantle. *Sci. Adv.* 4, sciadv.aas8675. doi: 10.1126/sciadv.aas8675

Nishioka, J., Obata, H., and Tsumune, D. (2013). Evidence of an extensive spread of hydrothermal dissolved iron in the Indian Ocean. *Earth Planetary Sci. Lett.* 361, 26–33. doi: 10.1016/j.epsl.2012.11.040

Paytan, A., and Griffith, E. M. (2007). : Marine barite: Recorder of variations in ocean export productivity. *Deep Sea Res. Part II: Topical Stud. Oceanography* 54, 687–705. doi: 10.1016/j.dsr2.2007.01.007

Paytan, A., and Kastner, M. (1996). Benthic Ba fluxes in the central Equatorial Pacific, implications for the oceanic Ba cycle. *Earth Planetary Sci. Lett.* 142, 439–450. doi: 10.1016/0012-821X(96)00120-3

Pretet, C. (2013). *Non-traditional isotopes (Barium and Calcium) and elemental ratios in scleractinian coral skeleton: new look into geochemical cycles, environmental proxies and bio-calcification processes* (Switzerland: Section des sciences de la Terre et de l'environnement, Université de Genève). doi: 10.13097/archive-ouverte/unige:33163

Qiu, Z., Han, X., Fan, W., Wang, Y., Li, M., and Cai, Y. (2023). Hydrothermal signatures and prospecting indicators in sediments along the Carlsberg Ridge. *Sedimentary Geology* 458, 106536. doi: 10.1016/j.sedgeo.2023.106536

Resing, J. A., Sedwick, P. N., German, C. R., Jenkins, W. J., Moffett, J. W., Sohst, B. M., et al. (2015). Basin-scale transport of hydrothermal dissolved metals across the South Pacific Ocean. *Nature* 523, 200–U140. doi: 10.1038/nature14577

Rippert, N., Baumann, K.-H., and PÄTzold, J. (2015). Thermocline fluctuations in the western tropical Indian Ocean during the past 35 ka. *J. Quaternary Sci.* 30, 201–210. doi: 10.1002/jqs.2767

Roeske, T., Rutgers vd Loeff, M., Middag, R., and Bakker, K. (2012). Deep water circula-tion and composition in the Arctic Ocean by dissolved barium, aluminium and silicate. *Mar. Chem.* 132–133, 56–67. doi: 10.1016/j.marchem.2012.02.001

Rouxel, O., Shanks, W. C. III, Bach, W., and Edwards, K. J. (2008). Integrated Fe-and S-isotope study of seafloor hydrothermal vents at East Pacific Rise 9–10 N, Chemical Geology. *Chemical Geology* 252, 214–227. doi: 10.1016/j.chemgeo.2008.03.009

Rouxel, O., Toner, B. M., Manganini, S. J., and German, C. R. (2016). Geochemistry and iron isotope systematics of hydrothermal plume fall-out at East Pacific Rise 9°50′N. *Chem. Geology* 441, 212–234. doi: 10.1016/j.chemgeo.2016.08.027

Schlitzer, R., Anderson, R. F., Dodas, E. M., Lohan, M., Geibert, W., Tagliabue, A., et al. (2018). The GEOTRACES intermediate data product 2017. *Chem. Geology* 493, 210–223. doi: 10.1016/j.chemgeo.2018.05.040

Seyfried, W. E., Pester, N. J., Ding, K., and Rough, M. (2011). Vent fluid chemistry of the Rainbow hydrothermal system (36°N, MAR): Phase equilibria and in *situ* pH controls on subseafloor alteration processes. *Geochimica Cosmochimica Acta* 75, 1574–1593. doi: 10.1016/j.gca.2011.01.001

Tao, C., Lin, J., Guo, S., Chen, Y. J., Wu, G., Han, X., et al. (2012). First active hydrothermal vents on an ultraslow-spreading center: Southwest Indian Ridge. *Geology* 40, 47–50. doi: 10.1130/g32389.1

Tao, C., Xiong, W., Xi, Z., Deng, X., and Xu, Y. (2014). TEM investigations of South Atlantic Ridge 13.2°S hydrothermal area. *Acta Oceanologica Sin.* 32, 68–74. doi: 10.1007/s13131-013-0392-3

Von Damm, ,. K. L. (1985). Chemistry of submarine hydrothermal solutions at 21°N, East Pacific Rise. *Geochimica Et Cosmochimica Acta* 49, 2197–2220. doi: 10.1016/0016-7037(85)90222-4

Whitmore, L. M., Shiller, A. M., Horner, T. J., Xiang, Y., Auro, M. E., Bauch, D., et al. (2022). Strong margin influence on the arctic ocean barium cycle revealed by pan-arctic synthesis. *J. geophysical Res. Oceans* 127, e2021JC017417. doi: 10.1029/2021JC017417

Yu, Y., Xie, R. C., Gutjahr, M., Laukert, G., Cao, Z., Hathorne, E., et al. (2022). High latitude controls on dissolved barium isotope distributions in the global ocean. *Geochemical Perspect. Lett.* 24, 22–26. doi: 10.7185/geochemlet.2242

Yuan, B., Yang, Y. M., Yu, H. J., Zhao, Y. X., Ding, Q. F., Yang, J. C., et al. (2018). Geochemistry of pyrite and chalcopyrite from an active black smoker in 49.6A°E Southwest Indian Ridge. *Mar. Geophysical Res.* 39, 441–461. doi: 10.1007/s11001-017-9324-5

Zhang, H., Luo, Y., Yu, J., Zhang, L., Xiang, R., Yu, Z., et al. (2022). Indian Ocean sedimentary calcium carbonate distribution and its implications for the glacial deep ocean circulation. *Quaternary Sci. Rev.* 284, 107490. doi: 10.1016/j.quascirev.2022.107490

Zhang, Z., Zhou, L., Chen, X.-G., Achterberg, E. P., Yu, Y., Hathorne, E., et al. (2024). Introduction of isotopically light barium from the Rainbow hydrothermal system into the deep Atlantic Ocean. *Earth Planetary Sci. Lett.* 625, 118476. doi: 10.1016/j.epsl.2023.118476

Zhou, T., Shi, X., Huang, M., Yu, M., Bi, D., Ren, X., et al. (2020). The influence of hydrothermal fluids on the REY-rich deep-sea sediments in the yupanqui basin, eastern south pacific ocean: constraints from bulk sediment geochemistry and mineralogical characteristics. *Minerals* 10, 1141. doi: 10.3390/min10121141

Frontiers in Marine Science

Explores ocean-based solutions for emerging global challenges

The third most-cited marine and freshwater biology journal, advancing our understanding of marine systems and addressing global challenges including overfishing, pollution, and climate change.

Discover the latest Research Topics

See more →

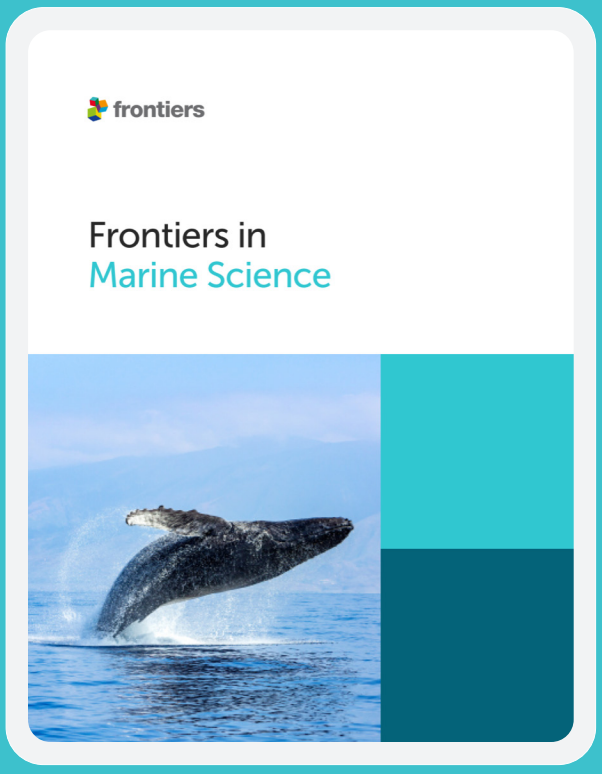

Frontiers

Avenue du Tribunal-Fédéral 34
1005 Lausanne, Switzerland
frontiersin.org

Contact us

+41 (0)21 510 17 00
frontiersin.org/about/contact